UNIVERSITY OF LONDON THESIS

Degree PhD Year 2008 Name of Author PAPAKONSTANTINOU, Ioannis

ANALYSIS DESIGN AND MEASUREMENT OF GUIDED WAVE OPTICAL BACKPLANE INTERCONNECTION

IOANNIS PAPAKONSTANTINOU

DEPARTMENT OF ELECTRONIC AND ELECTRICAL ENGINEERING

UNIVERSITY COLLEGE LONDON (UCL)

SUPERVISORS

DAVID R. SELVIAH

F. ANNIBAL FERNANDEZ

THESIS SUBMITTED FOR THE DEGREE OF DOCTOR OF PHILOSOPHY (PH.D)

AT THE UNIVERSITY COLLEGE LONDON

FEBRUARY 2008

ProQuest LLC
789 East Eisenhower Parkway
P.O. Box 1346
Ann Arbor, MI 48106-1346

To my Dad who has been
both my Dad and my Mum

ACKNOWLEDGEMENTS

I am particularly grateful to my supervisor Dr. David R. Selviah for his continuous support, guidance and enthusiasm. Most of all David has taught me an important lesson; the key to happiness is to make the right but difficult decisions your priorities. David has set the right example to me by being a pure researcher and an incredible lecturer who really cares about his students and not only about grants and promotions. I would also like to express my gratitude to my second supervisor Dr. F. Annibal Fernandez, for his help and the useful discussions we had on numerical modelling. I could not forget to express my thanks to Prof. Izzat Darwazeh. He significantly helped me and gave me his invaluable advice in very difficult times. In addition, I would like to thank my friends at UCL. Kai Wang for his help in the lab, all the fun in the office and for honouring me by making me his best man. Dr. Margret Bauer for all the discussions and the cups of coffee that we had together. Dr. Richard James, without whom I would never manage to finish the parallel computing part of my work, and also for showing me that being clever and modest is a virtue not a weakness. Finally, I acknowledge the help I received from the IT support staff, Scott Landers, Lee Heagney and Tom Crummey and the undergraduate lab technicians Andy Moss and Gerald McBrearty for repairing the boards I burnt over my time at UCL.

I am indebted to Xyratex Ltd. for funding my PhD and for introducing me to industrial culture. Specifically, I am grateful to Steve Thompson CTO, who approved the funding and who came up with the idea for this project, Dave Milward who has been supportive, and caring and who made me realise that project managers stand not only to claim the victory but can also add significant value to a project. My good friend Richard Pitwon for our excellent collaboration and Ken Hopkins for all his technical advice. Also, I would like to thank Dr. Frank Tooley for his technical advice during the initial stages of my PhD and Dr. Navin Suyal of Exxelis Ltd. for fabricating the polymer waveguides and for guidance with the optical waveguide measurements. I am grateful to Prof. Ronald Atkinson from Queen's University Belfast, for his supporting letters.

I would like to express my gratitude to the Engineering and Physical Sciences Research Council (EPSRC) for granting me a Doctoral Training Award and to the Centre for

Scientific Enterprises Limited (CSEL) for allowing me to follow the unusual route of exploring the commercial potential of my research by awarding me a PhD scholarship. I am very grateful to Dr. Steven Schooling for being an inspiring mentor in this business exercise and for his contribution to me being awarded this scholarship. I am indebted to the *IEEE-Laser Electro-Optics Society* for financially supporting my trip to Santa Fe to present my work at the 17th *IEEE-LEOS* workshop on interconnections within high-speed digital systems, and for allowing me to be a member of the program committee of the 18th and 19th workshops, and to chair the system session at the 18th workshop. I also acknowledge the Canon Foundation in Europe for granting me a 2007 Research Fellowship.

I owe a big thank you to all my Greek friends for being REAL friends. I am grateful to those living in the UK, my flatmates Dora and Marina Antonakaki for the great time I spent with them, Dora Karveli for always coming up with a good piece of advice when I needed it and Manos Mavrikos. Also to my friends who live in Greece, Kostas Oikonomopoulos, Gregoris Michailos, Pavlos Vlahos, Sozos Banavos, Nikos Mastrokostas, Panos Avramidis, Panos Xenoulis, Vassilis Leris, Manthos Stamelos, Exarhos Kalovirnas, Konstantinos Zacharopoulos, Georgia and Eirini Tsouri, Martzi Polydorou, George Gialamas, Fofi and Rania Pilidou. You have all been amazing.

As it is common in these occasions, I left the special people for the end. I am very grateful to Katie Lamb for her love, patience, and for allowing me to share my dreams with her. To Jane and Adrian Lamb for embracing me with warmth and for providing me with a family in England. Finally, to my sister and my Dad. My sister because she has been my most enthusiastic and supportive fan and has looked after me for a number of years and my Dad for bringing us up entirely on his own. I owe them everything.

ABSTRACT

Optics has been long regarded as the prominent alternative to electronics, to address the serious interconnects bottleneck in high-speed backplane printed circuit boards. In this thesis, we present our work towards the realization of a robust and cost effective 10 Gb/s optically interconnected backplane aimed at switching and storage applications. In the course of this work, we experimentally analyzed optical waveguides and advanced electromagnetic theories and algorithms to explain light propagation phenomena.

We experimentally characterized the insertion loss for dielectric waveguide bends of rectangular cross-section for a range of radii of curvature and waveguide widths and generated useful design rules. We then used the Beam Propagation Method (BPM) to separate insertion loss into its individual loss components and developed a ray-tracing model to gain further insight into propagation in waveguide bends.

We developed a novel waveguiding component called the tapered bend, which integrated a tapered waveguide with a bend. We expanded intrinsic mode theory, widely known in the acoustic wave field, to explain adiabatic propagation phenomena in tapered bends before, at and after modal cut-off. The proposed electromagnetic theory has significant implications since it can be used for tapered waveguides in general inhomogeneous media. We experimentally measured the insertion loss of the tapered bend and characterized the coupling efficiency tolerance under source misalignment for a range of radii and taper ratios.

We developed a semi-analytic algorithm to calculate the radiation modes of rectangular waveguides, based on a non-liner transformation of the wave equation and a Fourier decomposition method. The proposed method is very powerful and can be used in waveguides of arbitrary shape with some additional computational complexity. We applied the coupled mode theory to the computed radiation modes and we calculated the equilibrium distance, the steady state power distribution, and the propagation loss for multimode rectangular waveguides with sidewall roughness. These are the first reported calculations of this kind for rectangular waveguides, to the best of our knowledge.

Finally, we designed a novel optical connector based on the mechanically transferable (MT) technology for accurate passive alignment between arrays of waveguides and active

devices. In addition, we built a prototype optical backplane system to demonstrate the operation of our connector, and we monitored its performance by subjecting it to a test cycle of a number of engagements. We experimentally characterized the VCSEL sources used in the prototype and generated contour maps of coupling loss as a function of source misalignments. For the first time reported in literature, we measured cross-talk as a function of VCSEL lateral misalignment.

GLOSSARY

α	Insertion Loss
AFM	Atomic Force Microscope
AWG	Arrayed Waveguide Grating
BER	Bit Error Rate
β	Propagation Constant
BPM	Beam Propagation Method
d	Waveguide Thickness
Δn	Core-Cladding Refractive index Difference (percentage)
Ebeam	Electron Beam (mask)
FDM	Fourier Decomposition Method
FR4	Flame Resistant 4
FTDM	Finite Time Difference Method
FWHM	Full Width at Half Maximum
GaAs	Gallium-Arsenide
GRIN	Graded-Index (lens)
I_{bias}	Bias Current
I_{th}	Threshold Current
k	Free-Space Wavenumber
k_x	wavenumber in x-direction
k_y	wavenumber in y-direction
λ	Free-Space Wavelength
L_c	Autocorelation Length
LSI	Large Scale Integration
MM	Multimode
MT	Mechanically Transferable
NA	Numerical Aperture
n_{cl}	Cladding Refractive index
n_{co}	Core Refractive Index
OPCB	Optical Printed Circuit Board
PCB	Printed Circuit Board
PD	Photodiode
R	Radius of Carvature
r	Transverse Wavenumber
RMS	Random Mean Square
SCR	Signal to Cross-Talk Ratio
Si	Silicon
σ	Standard Deviation
SM	Singlemode
S_z	Poynting Vector
TR	Taper Ratio
UV	Ultra-Violet
VCSEL	Vertical Cavity Surface Emitting Laser
w	Waveguide Width
WKB	Wentzel-Krammer-Brilouin
XFP	Small Form Factor Pluggable

CHAPTER 1

INTRODUCTION

1.1. THE AIM

The aim of this thesis was to address the electronic interconnect bottleneck at high data-rates, by developing an affordable optical backplane interconnect system for board-to-board communication. In order to serve this purpose, optical links with polymer multimode buried channel waveguides were designed, modelled and tested and electromagnetic theories of light propagation within the waveguides were developed.

1.2. MOTIVATION

In the last three decades, the number of transistors per integrated circuit has been scaling up according to Moore's law, which predicts doubling every 18-24 months. Moreover, as microelectronic device integration techniques have been considerably improved to provide denser integration, the number of chips per board has been scaling up as well. In addition, the boards themselves have been shrinking in size and so, the number of boards that can be accommodated on a specific backplane or motherboard area has been also following an increasing trend. As a result, the growth on the number of devices has lead to a burst on the demand for interconnections. However, for several reasons to be explained in the following, the number of interconnections, as well as the data-rates they can deliver is both not keeping up with the pace of the device expansion, which is leading towards what has been described as the interconnection crisis. In order to resolve this bottleneck, optical interconnections, which is the subject of this thesis, have been proposed to replace the electronic ones.

In general, short-distance interconnections are divided into four categories. The on-chip interconnects whose lengths are limited to <2 cm, the chip-to-chip interconnections with lengths in the range of 1 cm – 10 cm, the board-to-board in the range of 1cm – ~1m, and the cabinet level interconnects in the range of 1 m – 10 m. The focus of this thesis resides in the board-to-board interconnects.

The main factors contributing to the previously mentioned interconnect bottleneck are:

- The skin-effect resistance, which increases according to the square root of the interconnect length [1], and limits the bandwidth of a transmission line.
- The dielectric leakage or loss, which increases linearly with the clock frequency [1]. Dielectric loss dominates over skin-effect resistance at clock rates of more than 1 GHz in FR4 laminate [2].
- The propagation delay (or latency as often met in the on-chip level terminology) which increases quadratically with propagation length [3]. Even for a certain length as frequency increases, propagation delay accounts for a larger fraction of the clock duty-cycle. Since most integrated circuit architectures to date are based on synchronous architectures, only a specific amount of delay can be tolerated before synchronization is lost.
- The intrachannel cross-talk, which increases as the density of interconnections increases resulting in intersymbol interference (ISI) and degrading the system's bit error rate (BER), [4].
- The impedance mismatches between transmission lines and electronic components, which results to reflections and signal degradation. Reflections become more severe and impedance matching becomes more difficult as the clock frequency increases [4].
- The finite inductance of the pins at the edge of the electronic connectors [5], which result in signal deterioration. Electronic connectors are also suffering from reflections and impedance mismatch.

Numerous solutions in the electronic domain have been proposed to overcome the above limitations with the most popular being: Equalization of the transmission lines so that they have a uniform response over a broad bandwidth [6]; Use of low-k dielectric materials such as Rogers 4000 and GETEK to reduce dielectric loss [1], [7]; Repartition of the lines and use of repeaters [5]; Increase of the number of layers to widen the spacing between wires; Use of differential signals to reduce noise levels; Use of more efficient coding schemes such as the Manchester coding or use of multilevel signaling; Use of asynchronous circuit design architectures which eliminate the need of low skew clock. All of these complicated techniques might provide a temporary relief to the interconnect bottleneck but their ability to give a permanent solution, which also has to be scalable for future applications, is questionable. Most important, they all involve increased circuit

complexity, which results in higher development costs and increased power consumption. For example, backplanes with Rogers materials are in general 5 times more costly [7], than conventional FR4 backplanes, although they manage to increase the bandwidth density from 400 Mb/s/mm in FR4 to 1 Gb/s/mm in Rogers.

Even further, the data rates delivered by electrical wires cannot indefinitely increase for an even more fundamental reason. The study in [10], showed that there is an absolute physical limit in electronic data transmission, which for Non-Return to Zero (NRZ) coding, is proportional to the length of the line and inversely proportional to the square root of the line cross-section [10]. This limit is related to the *RC* nature of the transmission lines and sets an upper boundary on the data rates that can be delivered by electrical wires in the range of Tb/s for a few cm of propagation.

As electronic interconnects approach their limits, optical technology emerges as a very promising substitute. However, before optical technology can be used, it has to outperform the electronic solution in the following five areas; Signal delay, bandwidth of the link, cross-talk, power consumption and interconnect density. A number of papers have been recently published comparing the electrical to the optical interconnects [1]-[3], [11]-[18]. According to these publications the most significant benefits that optics can bring are:

- The bandwidth of optical waveguides is several orders of magnitude larger than the bandwidth of electrical transmission lines. In addition, optical waveguides need not to be redesigned according to the clock frequency.
- Optical connectors can be denser. Fiber ribbon connectors with 250 μm spacing give 36 times higher signal density compared to current electrical connectors [2].
- Optical waveguides exhibit less propagation delay. In the specific case of the on-chip communications optical interconnects can deliver a clock with less skew and jitter helping, therefore, at the synchronization of the chips.
- Optics has the potential to reduce power consumption.
- Optics does not have the same physical bandwidth limitations as electronics, [10]. The physical limits of optic communications are orders of magnitude larger than the electronics ones.
- A new dimension of interconnection architectures can be opened up by utilizing

techniques in the optical domain such as the wavelength division multiplexing (WDM).

1.3. KEY CONTRIBUTIONS

The main contributions derived from the work reported in this thesis are:

- Waveguide bends have been investigated theoretically and experimentally that resulted in separating out the various loss components involved and thus in identifying the most severe ones.
- Tapered waveguide bends have been investigated experimentally and theoretically. The resulted theory can be used to analyze adiabatic mode propagation in any waveguide with inhomogeneous refractive index.
- The radiation modes and the coupling coefficients between bound and radiation modes have been derived for the first time in multimode buried channel waveguides, and modal propagation in waveguides with sidewall roughness has been described.
- A novel connector design for butt-coupling of arrays of active components into the backplane waveguides passively, accurately and repeatedly has been designed fabricated and tested.

1.4. STRUCTURE OF THESIS

Chapter 2 reviews the optical backplane interconnect systems reported in the literature. Emphasis has been given to optical backplanes systems consisting of VCSELs and multimode buried channel polymer waveguides.

Chapter 3, reviews two electromagnetic theories that have been utilized in this thesis, the intrinsic mode theory, and the coupled mode and coupled power theories. The intrinsic mode theory, which is mainly known in the acoustic field, is extended to analyze the tapered bends in Chapter 5, and Marcuse's coupled mode and coupled power theories are used to describe propagation in multimode buried channel waveguides with randomly deformed sidewalls in Chapter 6.

Chapter 4 investigates one of the most important components in optical backplanes, the waveguide bend. Waveguide bends of a range of radii of curvature and width have been experimentally measured and theoretically investigated with the Beam Propagation Method (BPM). Design rules for curved multimode waveguides are extracted and

reported.

Chapter 5 introduces a novel waveguiding component, which we called the tapered bend. This component integrates a waveguide bend and a tapered waveguide. Compared to a straight waveguide taper, the tapered bend is more compact managing to conserve board space. In order to analyze adiabatic mode propagation in a tapered bend, we extended the intrinsic mode theory. The proposed electromagnetic theory has important value, since with some modifications it can be used to analyze tapered dielectric waveguides of inhomogeneous refractive index. The second part of Chapter 5 focuses on the experimental investigation of tapered bends. In particular, the component tolerance under source misalignment and the insertion loss for a number of taper ratios and range of radii of curvature has been investigated.

Chapter 6 investigates modal propagation in waveguides whose sidewalls have been randomly perturbed, as often happens in photolithographically fabricated waveguides. For the first time in buried channel waveguides the equilibrium power distribution, the distance needed for equilibrium to be reached and the steady-state propagation loss have been calculated. The proposed method is applicable not only to rectangular but also to arbitrarily shaped waveguides, operating in the weakly guiding regime.

Chapter 7 describes a novel optical backplane connector. The connector carries an array of four 10 Gb/s VCSELs and an array of four photodetectors giving an aggregated bandwidth of 80 Gb/s. The fully passive alignment method between the connector active devices and the backplane waveguides is presented. A rigorous experimental investigation of the insertion loss as a function of the connector misalignment is given. The first reported experiments on optical cross-talk under connector misalignment are presented. Finally, the repeatability performance of the connector has been explored by exposing the connector to a test cycle of a number of engagements.

Chapter 8 concludes and gives directions for future work.

Finally, Appendix A is assessing the commercial opportunity for the optical backplane connector presented in Chapter 7. The work in Appendix A was carried out under the sponsorship of the Center of Scientific Enterprises Limited (CSEL), a joint venture between UCL and London Business School, and aims at a business audience with interest in the optoelectronics industry. The electronic backplane connector market and industry

are analyzed in Appendix A and possible routes to the market for an optical product are identified.

REFERENCES

[1]. H. Cho, P. Kapur, and K. C. Saraswat, "Power Comparison Between High-Speed Electrical and Optical Interconnects for Interchip Communication", *J. Lightw. Technol.*. vol.22, pp.2021-2033, 2004.

[2]. D. Huang, T. Sze, A. Landin, R. Lytel, and H. L. Davidson,, "Optical Interconnects: Out of the Box Forever?," *IEEE J. Sel. Top. Quantum. Electron*, vol. 9, pp. 614-623, Mar/Apr 2003.

[3]. E. Cassan, D. Marris, M. Rouvière, L. Vivien, and, S. Laval, "Comparison between electrical and optical global clock distributions for CMOS integrated circuits," *Opt. Eng.*, vol.44, pp. 15402-1 – 15402-10, Oct. 2005.

[4]. A. Deutsch, "Electrical characteristics of interconnections for high performance systems," *Proc. IEEE*, vol. 86, pp. 315–357, 1998.

[5]. D. A. B. Miller, "Rationale and Challenges for Optical Interconnects to Electronic Chips", *Proc. IEEE*, vol. 88, pp. 728 – 749, Jun. 2000.

[6]. W. J. Dally and J. Poulton, "Transmitter equalization for 4-Gbps signaling," *IEEE Micro*, pp. 48–56, Jan./Feb. 1997.

[7]. D. Huang, T. Sze, A. Landin, R. Lytel, and Howard L. Davidson,, "Optical Interconnects: Out of the Box Forever?," *IEEE J. Sel. Top. Quantum. Electron*, vol.12, pp. 614-623, Mar/Apr 2003.

[8]. J. A. Davis and J. D. Meindl, "Is interconnect the weak link?," *IEEE Circuits Devices Mag.*, vol. 14, no. 2, pp. 30–36, Mar. 1998.

[9]. A. Deutsch, G. V. Kopcsay, P. J. Restle, H. H. Smith, G. Katopis,W. D. Becker, P.W. Coteus, C.W. Surovic, B. J. Rubin, R. P. Dunne Jr., T. Gallo, K. A. Jenkins, L. M. Terman, R. H. Dennard, G. A. Sai-Halasz, B. L. Krauter, and D. R. Knebel, "When are ransmission-line effects important for on-chip interconnections?," *IEEE Trans. Microwave Theory Tech.*, vol. 45, pp. 1836–1846, 1997.

[10]. D. A. B. Miller, and H. M. Ozaktas, "Limit to the bit-rate capacity of electrical interconnects from the aspect ratio of the system architecture," *J. Paral. Distr. Comp.*, vol. 41, pp. 42-52, 1997.

[11]. M. Haurylau, G. Chen, H. Chen, J. Zhang, N. A. Nelson, D. H. Albonesi, E. G. Friedman, and P. M. Fauchet, "On-Chip Optical Interconnect Roadmap: Challenges and Critical Directions", *IEEE J. Sel. Top. Quantum. Electron*, vol.12, pp. 1699-1705, Nov/Dec 2006.

[12]. G. I. Yayla, P. J. Marchand, and S. C. Esener, "Speed and energy analysis of digital interconnections: comparison of on-chip, off-chip, and free-space technologies," *Appl. Opt.*, vol. 37, pp. 205-227, Jan. 1998.

[13]. E. Berglind, L. Thylen, B. Jaskorzynska, and C. Svensson, "A Comparison of Dissipated Power and Signal-to-Noise Ratios in Electrical and Optical Interconnects", *J. Lightw. Technol.*, vol. 17, pp. 68-73, Jan. 1999.

[14]. E. Griese, "Reducing EMC Problems Through an Electrical/Optical Interconnection Technology," *IEEE Trans. Electr. Compat.*, vol. 41, pp. 502-509, Nov. 1999.

[15]. F. E. Kiamilev, P. Marchand, A. V. Krishnamoorthy, S. C. Esener, and S. H. Lee, "Performance Comparison Between Optoelectronic and VLSI Multistage Interconnection Networks," *J. Lightw. Technol.*, vol.9, pp. 1674-1692, Dec. 1991.

[16]. R. Lytel, H. L. Davidson, N. Nettleton, and T. Sze, "Optical Interconnections Within Modern High-Performance Computing Systems," *Proc. IEEE*,

[17]. J. Tanida, K. Nitta, T. Inoue and Y. Ichioka, "Comparison of electrical and optical interconnection for large fan-out communication," *J. Opt. A: Pure Appl. Opt.*, vol. 88, pp. 758-763, Jun. 2000

[18]. A. Naeemi, A. V. Mule, J. D. Meindl, " Partition length between board-level electrical and optical interconnects," *In Proc. Interconnect Technology Conf.*, 2-4 June 2003, pp. 230-232.

CHAPTER 2

REVIEW OF OPTICAL BACKPLANE SYSTEMS WITH INTEGRATED POLYMER WAVEGUIDES

2.1. INTRODUCTION

In this chapter, the research prior to this thesis, on optical printed circuit board (OPCB) systems with embedded polymer buried channel waveguides is reviewed. Research on optical backplanes has attracted the attention of a large number of groups in both academia and industry worldwide in the last 15 years. In Germany, groups involved in OPCB research include (or included in the past) DaimlerChrysler [2.2.1]-[2.2.5], ULM University [2.2.3], Siemens in collaboration with the University of Paderborn [2.2.6]-[2.2.10], Infineon [2.2.7], Dortmund University [2.2.12]-[2.2.13], the University of Hagen [2.2.8] and the Fraunhofer Institute for Reliability and Microintegration [2.2.14]-[2.2.15]. In Switzerland, similar work has been carried out by IBM Zurich [2.2.16]–[2.2.20], the Swiss Federal Institute of Technology (ETH) Zurich [2.16]-[2.19] and by Varioprint [2.20]. In Sweden, Linköping University has produced a number of papers on the subject in recent years [2.13], [2.22]-[2.23]. In Finland, a joint academic and industrial collaboration between the University of Helsinki, VTT Electronics and Aspocomp Perlos Company, [2.24]-[2.29] is active in the area. In France, we find some industrial involvement in OPCB design from, Supelec, Service de Mesures [2.8] and from INTEXYS Photonics [2.20]-[2.21] mainly through pan-European projects. In Belgium, Ghent University [2.30]-[2.34] has been active in the area for a number of years. Finally, in the UK, we find Herriot-Watt University [2.35]-[2.36], Exxelis Ltd. (former Terahertz photonics) [2.37], Cambridge University [2.38]-[2.39] and in the early 1990s Marconi [2.33]-[2.34]. In the US, groups which have been involved in the past or are still actively researching the area include Fujitsu Laboratories of America [2.40]-[2.42], Texas University in Austin [2.43]-[2.46], Georgia Institute of Technology [2.47]-[2.51], Duke University [2.48], [2.50]-[2.51], Honeywell [2.45], [2.52]-[2.54], General Electric [2.45], [2.52]-[2.53], AMP Global Optoelectronic Technology [2.52]-[2.53], Cray Research [2.45] and DuPont Photonics [2.55]. In Japan, Nippon Telegraph and Telephone (NTT) is

the main player in the area [2.56]-[2.61], but Matsushita Electrical Industrial, Toray Industries and Hitachi Chemical [2.48] have also shown interest in OPCB products. In Korea, significant work has been carried out by the Electronics and Telecommunications Research Institute (ETRI) [2.62]-[2.66], iTEC Technology, Information and Communication University Daejeon [2.62]-[2.66], Samsung [2.61], [2.64]-[2.66] and Kyungpook National University [2.65]. Finally, in Taiwan, the Advanced Packaging Technology Center, Electronics and Service Organization and the Industrial Technology Research Institute [2.67] have demonstrated some research activity in the OPCB area.

In reviewing the various backplane systems, we will specifically focus on the research results and system properties most relevant to this thesis, namely:

- The waveguide fabrication method and materials used
- The waveguide physical parameters such as cross-section dimension and numerical aperture (NA)
- The alignment method between active devices (laser sources, photodetectors) and waveguides, the optical connector design, and the alignment tolerances
- The implementation of optical vias
- The use of microlens arrangements for facilitating coupling between active devices and OPCB waveguides
- The coupling efficiency
- The propagation and total insertion loss
- The transmission length
- The bit-rate that the systems can support.

2.2. OPTICAL BACKPLANE SYSTEM REVIEW

2.2.1. DaimlerChrysler optical backplane

DaimlerChrysler work [2.1]-[2.5], mainly aimed at relatively low data-rate, 1 Gb/s, avionic applications. The prototype they made [2.2], Fig. 2-1, supported two processor cards, which were interconnected to each other via a 55 cm long optical backplane. Light from an edge emitting laser diode at 780 nm was coupled into the backplane waveguides with the aid of two half-ball lenses and a 45° degree mirror. The first of the two half-ball lenses, mounted in the processor card, collimated the light emitted by the laser while the

second half-ball lens, mounted on the backplane, imaged the laser output onto the 45° mirror surface, which deflected light perpendicularly to its plane into the waveguides. The dimension of the waveguide cross-section was 200 μm × 200 μm. At the receiver, a similar lens focused light from the waveguide output onto a 400 μm active area photodetector. The combination of the ball lens system with the large waveguide apertures provided large alignment tolerances, with required lateral misalignment between the two lenses in the system of more than 0.5 mm before excess loss reached 1 dB. The waveguide propagation loss was measured 0.03 dB/cm with the cutback method, while the total insertion loss for the system was 2.5 dB for the demonstrator with the ball lenses, and 4 dB for a second demonstrator where ball lenses were replaced by double convex plastic lenses for better imaging. The system operated at 1 Gb/s and successfully passed environmental tests.

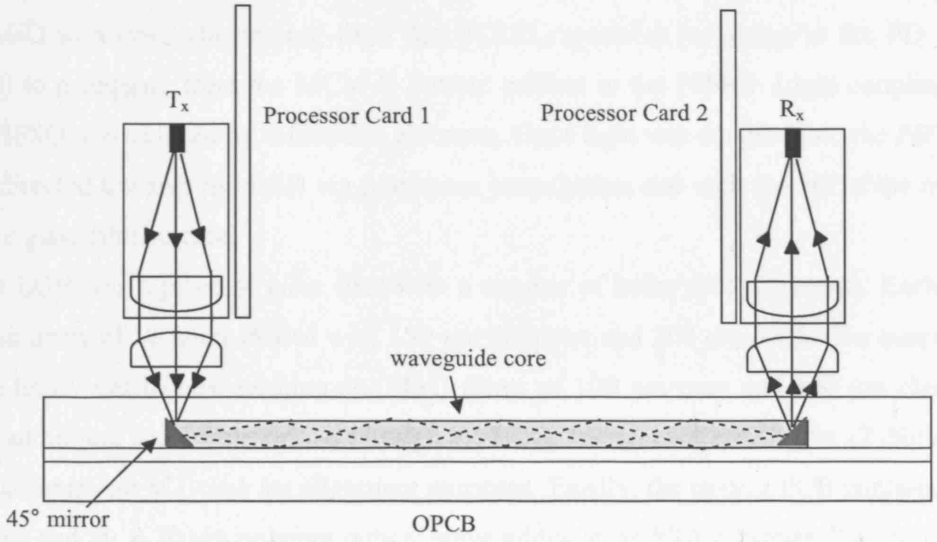

Fig. 2-1. DaimlerChrysler optical backplane prototype.

2.2.2. The High-Speed Optoelectronic Memory Systems (HOLMS) Project

HOLMS [2.8] was a European Union funded project in the early 2000s, with the contribution of Herriot-Watt University Scotland, ETH Zurich Switzerland, THALES Communications France, Siemens/C-Lab Germany, the University of Hagen Germany, SUPELEC France, the University of Paderborn Germany, and ILFA AG Germany. The objective of the project was to overcome the bottleneck of the high latency experienced in

multistage interconnect architectures such as in shared memory multiprocessors (SMPs). For this purpose, they developed a hybrid 1 Gb/s free-space / buried channel waveguide interconnection scheme, Fig. 2-2, made of an optoelectronic multi-chip-module (OE-MCM), a light guiding beak (LGB) and an optical PCB.

The OE-MCM module, Fig. 2-2 (b), comprised of two main elements: The first one was a thin glass film (called the planar integrated free-space system, PIFSO) with monolithically integrated optical components such as mirrors, diffractive elements, lenses and beam splitters, to assist light coupling into and out from the PIFSO and light propagation inside the PIFSO. The second part of the OE-MCM was a thin-film module technology (MCM-D), made of a few thin copper and dielectric layers deposited on a thicker transparent substrate. VCSELs and photodiodes (PDs) were flip-chip bonded on the bottom surface of the MCM-D module, while its transparent substrate on the opposite side was glued onto the PIFSO surface, Fig. 2-2 (b). Via holes were drilled through the MCM-D to allow light coming from the VCSEL apertures (or going to the PD active areas) to propagate from the MCM-D bottom surface to the PIFSO. Light coupling into the PIFSO was assisted by diffractive elements. Once light was coupled into the PIFSO, it was directed towards the LGB via free-space propagation and with the aid of the mirrors on the glass film surface.

The LGB was a piece of plain FR4 with a number of holes drilled through. Each LGB had an array of 12 holes drilled with 150 μm diameter and 250 μm pitch. The purpose of these holes was to host multimode (MM) fibres of 100 μm core and 140 μm cladding. Two additional holes were drilled through the LGB, one on each side of the 12-fibre array to accommodate MT-pins for alignment purposes. Finally, the optical PCB contained 45° mirrors and 70 × 70 μm polymer optical waveguides on an FR4 substrate. Two MT-holes were drilled through the optical and FR4 layers on the PCB for aligning the waveguides with the LGB fibres.

Light in the PIFSO reaching the LGB was coupled into the MM fibres of the LGB with the aid of the PIFSO diffracting elements, and propagated inside the fibres until it reached the 45° mirrors. Upon reflection on the 45° mirrors, light was reflected into the PCB waveguides. Fibre holes in the LGB were drilled with a pitch of 250 ± 10 μm, while the diameter of the fibre cladding was 10 μm less than that of the holes. Therefore, a lateral

misalignment of ±15 µm should be expected between LGB fibres and PCB waveguides. Unfortunately, the alignment tolerance between the MT-holes on the PCB and the waveguides was not quoted to allow an estimate of the total potential misalignment of their system. No characterisation or bit-rate experiments were reported for this system.

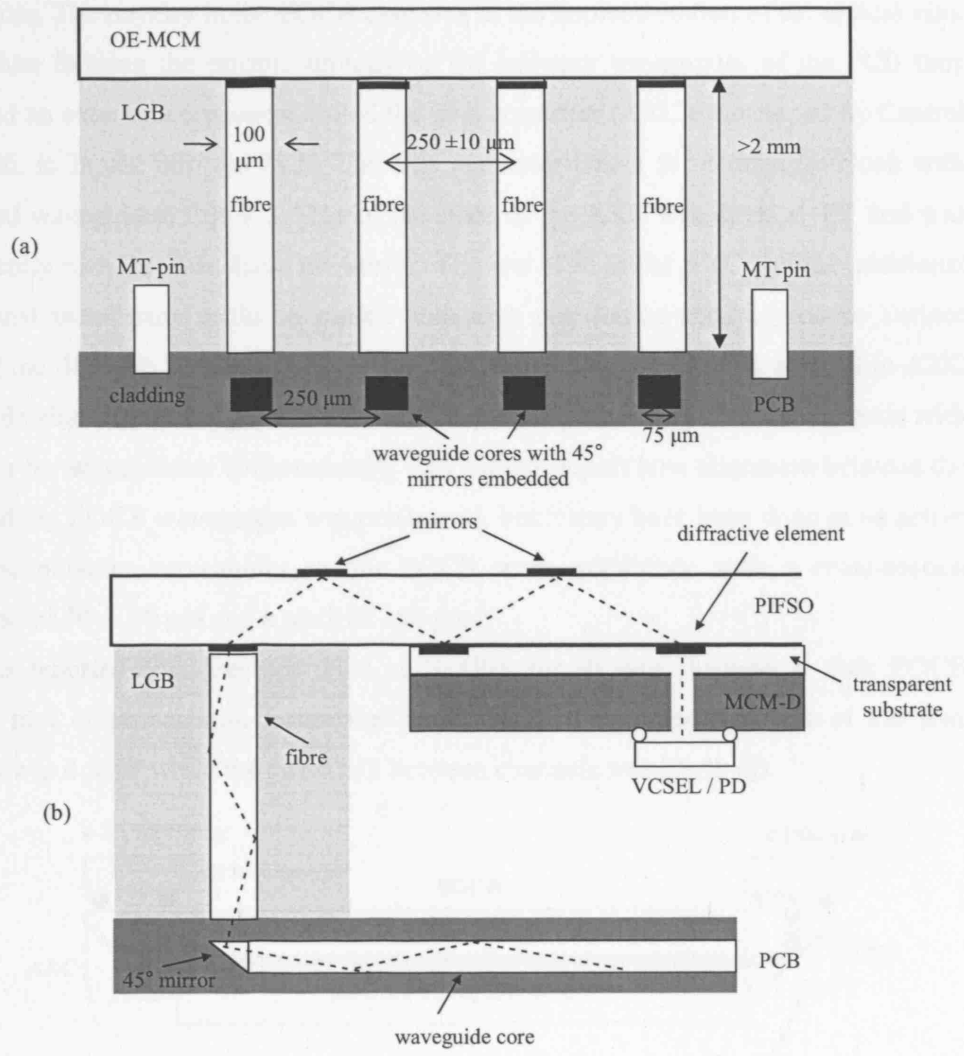

Fig. 2-2. (a) Front-view of HOLMS project OE-MCM - optical PCB interconnection scheme. (b) Side view of it.

2.2.3. Siemens / C-Lab Electrical-Optical Circuit Board (EOCB)

In 2006, Siemens announced a 4-channel, single way, 10 Gb/s/channel optical backplane system [2.9] with the acronym EOCB (Electrical-Optical Circuit Board), Fig 2-3. Their demonstrator followed the usual principle of mounting the VCSELs and PDs on the surface of the PCB and using optical vias with 45° mirrors to route light into the board waveguides. The novelty in the EOCB case was in the implementation of the optical vias. Rather than forming the mirrors directly on the polymer waveguides of the PCB they integrated an external component called the axis converter (AXC), developed by Central Glass Ltd. in Japan, into the PCB. The axis converter was a Si rectangular block with embedded waveguides, Fig. 2-3. One of the sides of the AXC was diced at 45° and was subsequently metallised to shape the mirror. The use of Si in the AXC had the additional benefit that metal pads could be placed with high positioning accuracy on its surface enabling the flip-chip bonding of the active devices. As a result, VCSEL and PD to AXC waveguide alignment were passive due to the accurate positioning of the metal pads with respect to the waveguides. Unfortunately, they did not report how alignment between the AXC and the EOCB waveguides was performed, but it may have been done in an active way. The polymer waveguides in the EOCB were multimode with a cross-section dimension of 70 × 70 μm and a pitch of 250 μm.

Siemens reported error-free operation at 10 Gb/s for all four channels in their EOCB over 60 mm of propagation inside the board. The average insertion loss of the four channels was 4.5 dB while the cross-talk between channels was 25-30 dB.

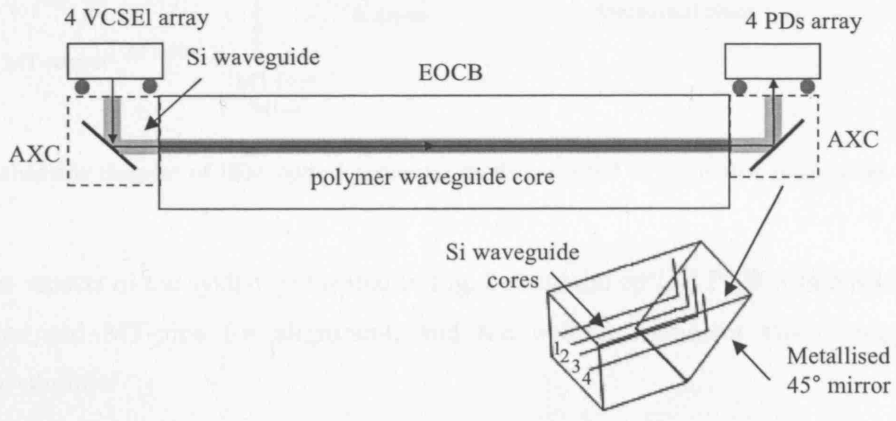

Fig. 2-3. Siemens C-Lab Electrical-Optical Circuit Board schematic diagram.

2.2.4. IBM 120 Gb/s Optical Card-to-Card Link Demonstrator

IBM reported in 2007 [2.20], an optical backplane demonstrator, which they developed jointly with the French company INTEXYS Photonics and the Swiss PCB vendor Varioprint. The objective of this work was to interconnect two electronic cards over an optical backplane with 12 parallel, 10 Gb/s channels. Their choice of delivering the optical signals to the board was by butt coupling the active devices to the PCB waveguides, without routing their signals through optical vias. In addition, they built their connector based on the Mechanically-Transferable (MT) technology. A schematic of the IBM demonstrator showing the active devices being butt-coupled onto the PCB waveguides is shown in Fig. 2-4.

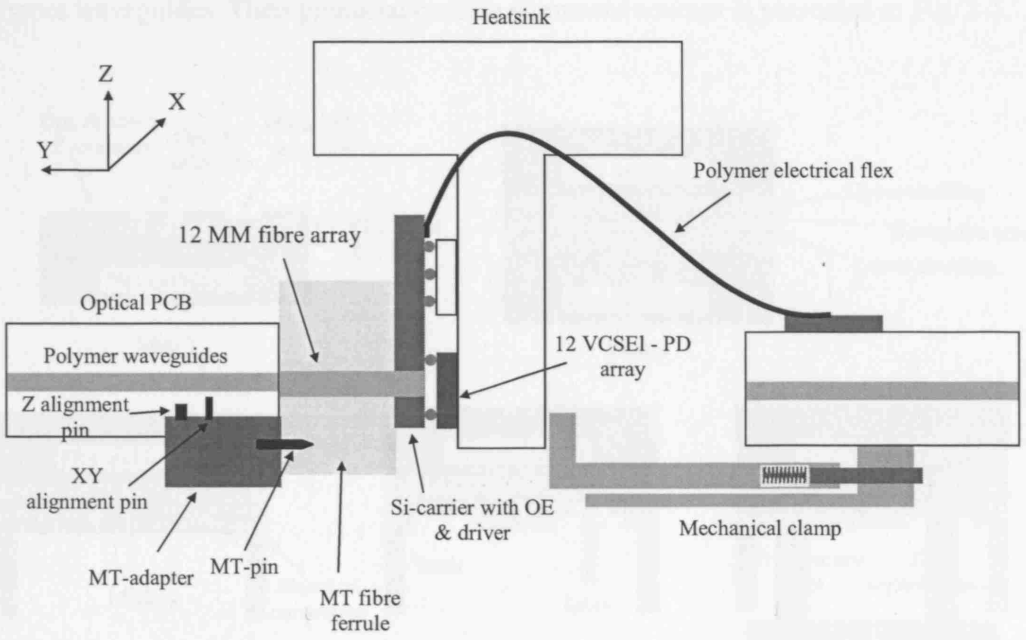

Fig. 2-4. Schematic diagram of IBM optical connector module aligned to the buried waveguides of an OPCB.

The main aspects of the system presented in Fig. 2-4 are the optical PCB with embedded MT-adapter and MT-pins for alignment, and the optical connector with integrated transceiver module.

IBM optical PCB and MT-adapter

Waveguides were patterned photolithographically on the top of a multilayer FR4 substrate. The lower- and upper-claddings were both deposited by doctor-blading and polymerized by UV flood exposure. The core layer was also deposited by doctor-blading and polymerized by UV-laser direct writing using a high precision *xyz* table. Truemode^{TM}, an acrylate polymer was used for the optical layers. The waveguides formed, had cross-section dimensions varying from 35 × 35 μm to 50 × 50 μm, while propagation loss measured was in the region of 0.03 – 0.05 dB/cm at 850 nm. Once optical layers were formed, another FR4 multilayer board was laminated on the top of the upper-cladding layer. Alignment marks and trenches were formed on the PCB to allow for passive physical alignment between the transceiver components and the embedded polymer waveguides. Their proposed passive alignment concept is presented in Fig. 2-5.

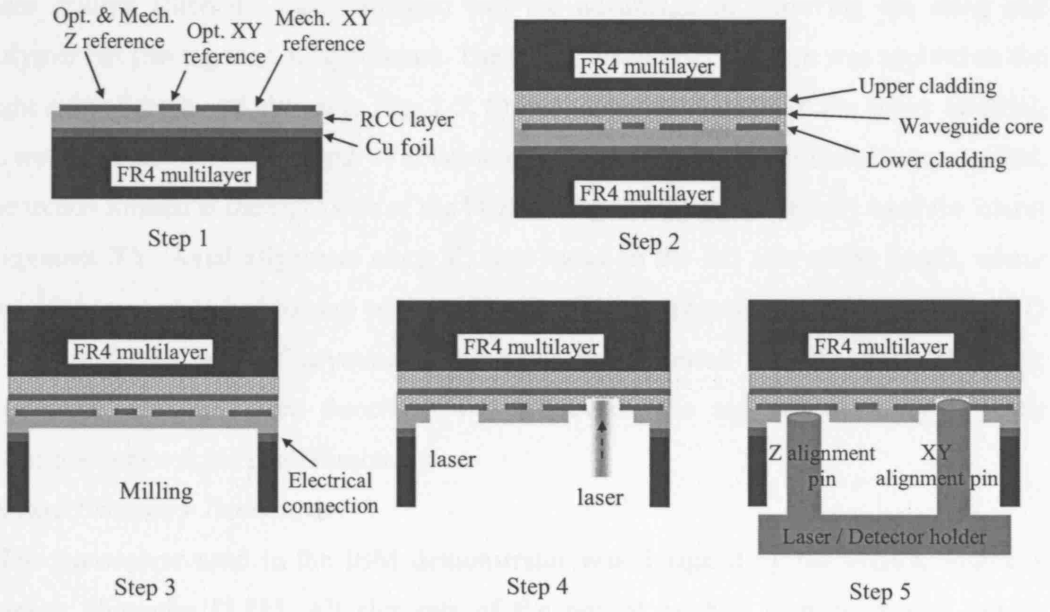

Fig. 2-5. Fabrication steps of IBM optical PCB and alignment markers.

Their alignment method relied on trenches and visual marks being placed on a copper layer in the PCB. The fabrication of their PCB started with a multilayer FR4 with a copper layer on the top of it. Then on the top of this Cu layer, they laminated a thin RCC

(resin-coated copper) foil. Finally, on the top of the RCC layer, another copper layer was deposited and alignment marks were defined (Step 1, in Fig. 2-5). These four layers (FR4 - Cu – RCC - Cu) formed the substrate for the optical layers. It is worth mentioning that the position of the waveguide cores was defined with reference to the copper alignment marks, which were visible through the transparent polymer material used. Upon formation of the optical layers, the top FR4 layer was laminated, completely burying the alignment trenches and marks (Step 2, in Fig. 2-5).

To recover the alignment features, milling was firstly used to remove the bottom FR4 layer (Step 3). The milling depth was controlled by the continuous Cu layer below the RCC layer. Once the milling tool reached the Cu layer, electrical contact was made signalling the end of the milling process. In reality, the milling process continued for a few further micrometres until the entire Cu layer had been removed and stopped only when the resin of the RCC foil had been exposed. The remaining resin was ablated by laser drilling (Step 4). Laser ablation had the advantage of removing the resin and polymer but leaving the Cu layer intact. Therefore, when laser ablation was applied on the right side of the board shown in Fig. 2-5, Step 4, it removed some of the lower cladding as well. Because the exact depth of ablation of the lower cladding could not be controlled, the trench formed at the right side of the PCB, in Fig. 2-5 Step 5, was only used for lateral alignment XY. Axial alignment along Z, was based on the left side of the board, where the ablation process had to stop on the copper back-stop. Therefore, when a VCSEL / PD holder with two pins of asymmetrical lengths was inserted into the holes (Step 5), alignment along all three directions was achieved. The reported accuracy of their technique was ± 5 μm in all directions.

Intexys Photonics Transceiver

The transceiver used in the IBM demonstrator was designed by the French company Intexys Photonics [2.21]. All elements of the optical module were integrated onto a highly resistive Si motherboard. These elements were an array of 12 VCSELs (or PDs) operating at 850 nm, a laser (receiver) driver, a multimode fibre MT-ferrule with protruding fibres and an LCP polymer flexible circuit, Fig. 2-4. The VCSELs (PDs) were at first flip-chip bonded on the Si motherboard. Then 12 holes were accurately drilled through the Si motherboard against the VCSEL and PD active apertures, by using the

DRIE etching method, with ~125 μm diameters. Once the holes on the motherboard were drilled, the fibres of an MT-ferrule with an array of 12 protruded, 50/125 multimode fibres were inserted. Since the length of the protruding fibres was designed to match the thickness of the motherboard, butt coupling of the fibre to the VCSEL (PD) array was achieved. Therefore, when the MT-pins of the MT-adaptor on the optical PCB registered into the MT-holes of the fibre ferrule, Fig. 2-4, the coupling between the VCSELs (PDs) and the OPCB polymer waveguides was accomplished. The insertion loss of their system was 2 dB at the VCSEL – waveguide end and 3 dB at the waveguide – PD end. Finally, they reported error-free operation at 10 Gb/s over 30 cm of propagation in the optical PCB for all 12 channels, giving an aggregated OPCB bandwidth of 120 Gb/s.

2.2.5. Parallel Optical Interconnect between Ceramic Ball Grid Array Packages on FR4 Board (Finland)

In 2006 a consortium of two Finnish companies (VTT Technical Research Centre, Aspocomp Oy) and one university (University of Helsinki) presented their work on a 4 × 10 Gb/s optically interconnected printed circuit board [2.28]. Their design consisted of four VCSELs at 850 nm and four PDs, wire bonded on the top of low-temperature co-fires ceramic (LTCC) substrates. Ball grid arrays (BGAs) were utilised to mount the LTCC with the transceivers on the PCB and for alignment. Two microlens arrays, one mounted in a cavity opened in the LTCC and the other mounted on the PCB, assisted light coupling into the waveguides. An individual 45° mirror component, reflected light perpendicularly from its initial propagation axis into the waveguides, Fig. 2-6 (a). An array of four parallel polymer waveguides was patterned on the top of the PCB, Fig. 2-6. The material used for the cladding and core waveguide layers was the epoxy based Nano SU-8-25 by Micro Chem Corp and waveguides were formed by UV mask photolithography. The thickness of the waveguides was 40 μm, while two of the waveguides were 50 μm wide and the other two were 75 μm wide, with waveguides being arranged in a 250 μm pitch. The transmitter and receiver modules were integrated onto the LTCC, which was the new concept they introduced. Through holes (optical vias) were cut in the LTCC and VCSELs (and PDs) were flip-chipped on the top of the LTCC, with their emitting aperture pointing toward the vias. VCSELs (PDs) were wire bonded to the drivers / receiver ICs also integrated in the LTCC. Another set of four holes was cut

through the LTCC at the same step as the optical vias to assist alignment with the microlens array underneath. Once the microlens array was aligned to the VCSEL/PD array, it was permanently attached to a specially formed cavity in the bottom of the LTTC with UV glue.

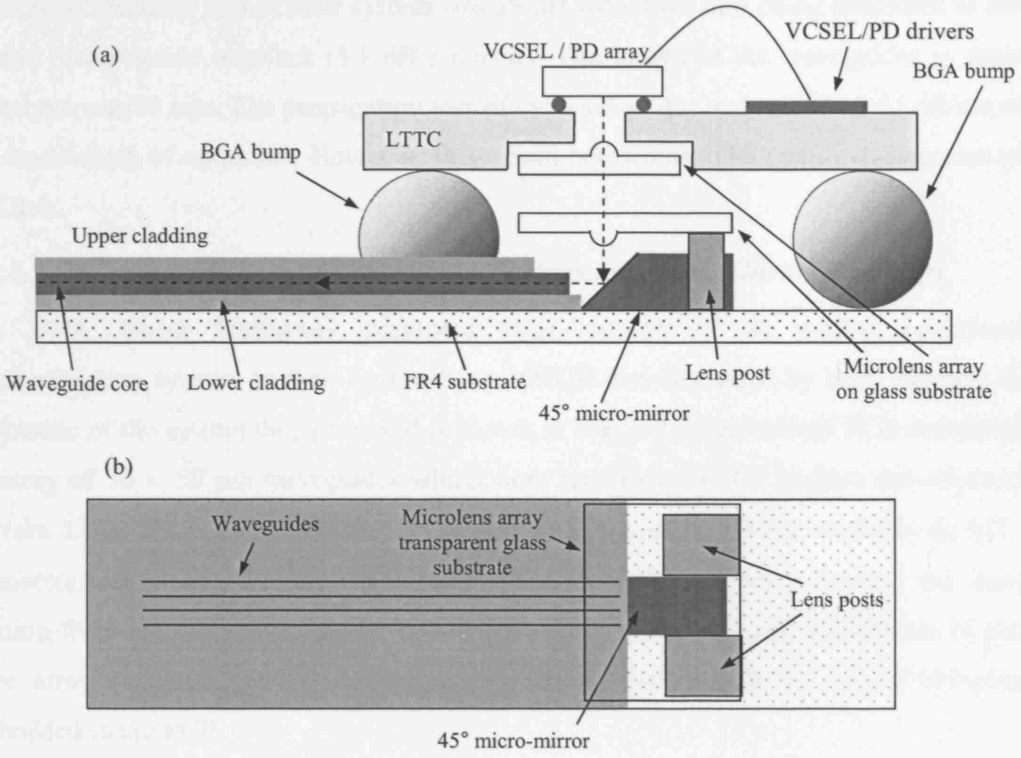

Fig. 2-6. (a) Side-view of the optical backplane interconnection system proposed by the Finnish consortium. (b) Top-view of the optical backplane system.

The 45° mirror was made by grinding and polishing one side of a 100 μm thick glass block. After polishing, a layer of aluminium was coated to enhance mirror reflectivity. The width of the glass was arranged to coincide with the gap between two lens posts standing out from the PCB, which served for both holding the second microlens array and for aligning the micro-mirror to the PCB waveguides, Fig. 2-6 (b). The lens posts were made photolithographically by core material at the same step as the waveguides and so, when the mirror module was slid through the two posts, lateral alignment with the waveguide cores was achieved. Axial alignment was achieved with the aid of the lower cladding, which served as a stop for the mirror module. Once the mirror was in place, the

second microlens array was mounted on the PCB. Alignment between the lens array and the micro-mirror was achieved by fiducial marks left on the PCB during the waveguide core fabrication step. Once the transceiver module and the micro-optics were assembled, the LTCC was mounted on the PCB with the aid of the BGA bumps, Fig 2-6 (a).

The total insertion loss of their system was 19 dB with most of it being attributed to the mirror – waveguide interface (5.1 dB / mirror). The length of the waveguides in their prototype was 83 mm. The propagation loss of the waveguides measured to 0.55 dB/cm at the wavelength of operation. However, they could not demonstrate open eye diagrams at 10 Gb/s.

2.2.6. MT-Compatible Laser Ablated Optical Interconnections (Ghent University)

In 2004, Ghent University presented their version of an optical backplane interconnection system. In their approach, the OPCB was fabricated by laser ablation. A schematic of the system they proposed is shown in Fig. 2-7. Their optical PCB contained an array of 50 × 50 μm waveguides which were terminated at 45° to form out-of-plane mirrors. Light was coupled into the OPCB from an array of MM fibres carried by an MT-connector. An array of microlenses made on a glass plate slightly focused the light coming from the fibre array before reaching the mirror surface. The MT-ferrule of the fibre array was mounted on the top surface of the board with the aid of MT-pins embedded in the PCB.

The fabrication of the optical backplane took place as following: A layer of lower cladding material (ORMOCER - Organic Modified Ceramic) was spun on top of the FR4 and was polymerized with UV radiation. Then a second layer of core material was deposited in exactly the same way. Waveguides were formed with laser ablation by a KrF excimer laser. After each waveguide was written, the laser was tilted by 45° and mirrors were formed. When all of the waveguides were made, the laser was used to shape alignment marks on the core layer that determined the position for MT-holes to be placed. Once waveguide core and alignment mark fabrication was finished, an upper-cladding layer was deposited, again with spin coating and UV lithography. Finally, when all optical layers were made, MT-holes were cut with the KrF laser at the position of the alignment marks and MT-pins were inserted and permanently glued.

The fabrication of the microlenses was also accomplished by laser ablation. In this case,

two MT-holes were cut on a 250 μm thick glass plate and the pins of an MT-ferrule, similar to the one used in the PCB, were registered to the holes of the plate. The fibre ribbon carried by the MT-ferrule was then illuminated from the opposite side and the mirrors were written actively on the glass plate with laser ablation, at the positions defined by the spots projected from the fibres onto the glass surface. The final steps of the assembly were to insert the lens plate into the MT-pins of the board, align it visually with respect to the mirrors with the aid of the alignment marks in the core and mount an MPO (multi-fibre push on) plug adaptor. No characterisation was performed on the board and so we have no information about the insertion loss in their system.

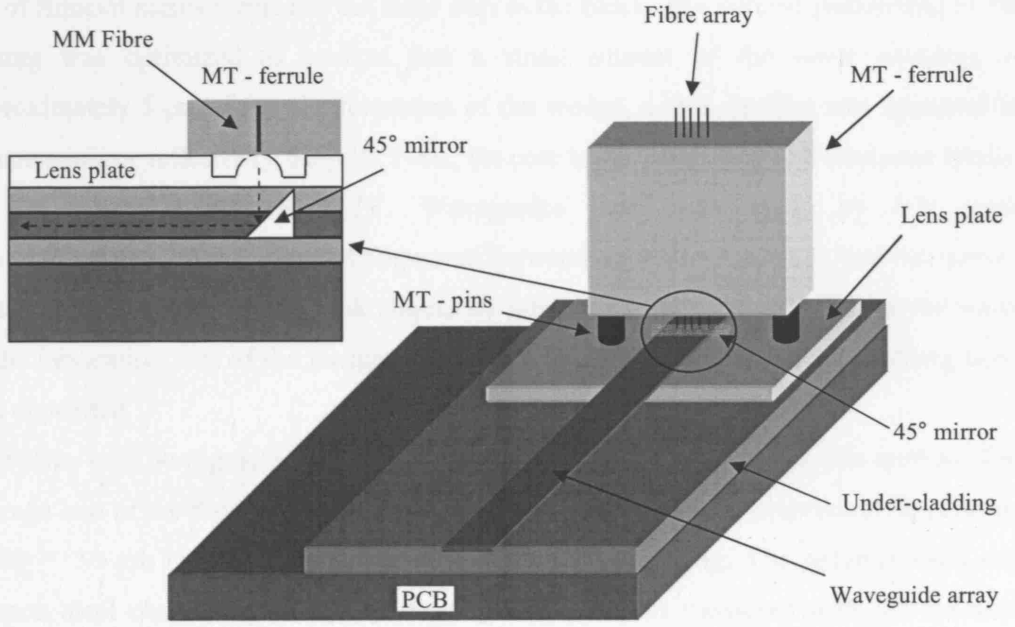

Fig. 2-7. Ghent university interconnection concept based on laser ablation and MT alignment.

2.2.7. Fujitsu Laboratories of America, Board-to-Board Optical Interconnect (B^2OI) Demonstrator

Fujitsu Laboratories introduced their own board-to-board optical interconnect (B^2OI) demonstrator in 2005 [2.40]-[2.42]. In their approach, an adaptor compatible to an MT-connector (mechanical transfer-connector) was mounted on the surface of the optical PCB and was passively aligned to the 45° mirrors formed at the edge of the waveguides in the

board, Fig. 2-8 (a). An array of microlences was integrated into the adaptor to facilitate coupling between fibres and board waveguides and to relax alignment tolerances. 45° mirrors were made by a fabrication method, which they named wedge reflector mirror technology.

The fabrication steps of the optical PCB and wedge reflection mirror technology are shown in Fig. 2-8 (b). During Step I, they deposited a layer of ~15 μm lower cladding polymer on the FR4 substrate and polymerized it with UV photolithography. Then they spin coated a layer of core material from which they only polymerized a part of it to form a wedge block. In Step II, they micromachined the wedge block with a 45° dicing saw to form the mirror surface. The dicing saw was aligned laterally to the wedge block with the aid of fiducial marks formed in the same step as the block. The vertical positioning of the cutting was optimized to overcut just a small amount of the lower cladding of approximately 5 μm. After the formation of the wedge, a thin Au film was sputtered to enhance mirror reflectivity, Step III. Next, the core layer was coated in a thickness similar to the wedge height, Step IV. Waveguides were then made by UV mask photolithography, Step V. Lateral alignment between the waveguide mask and the mirrors was achieved visually in the mask aligner by reference marks that were left on the wafer at the fabrication step of the wedge. In the final step (Step VI), the upper cladding layer was deposited.

An array of 8 waveguides with embedded mirrors was fabricated with this method. The average loss of the 8 mirrors was 0.8 dB. The waveguides had cross-sectional dimensions of 30 × 30 μm in a pitch of 250 μm, and were 80 mm long. The polymer used was Nippon steel chemical photoepoxy. Propagation loss was measured with the cut-back method and it was 0.2 dB/cm at 850 nm.

Microlenses were integrated into the PCB adaptor to relax the alignment tolerances between the fibre array and the mirrors on the board. Biconvex silica microlenses with 230 μm and 120 μm radii of curvature were formed on a 950 μm silica plate. The lateral dimension of the lenses was slightly less than 250 μm to accommodate the 250 μm waveguide pitch. The height of the microlenses in the adaptor was optimized so that light coming from the fibre array was focused on the mirrors. The adaptor consisted of two parts, the lower subassembly and the top part with the latch mechanism for the MTP

connector. The lower subassembly was mounted on the PCB and aligned passively to reference marks formed in the core layer. The upper part was then attached to the lower part with the aid of precision alignment pins. Within the adaptor, microlenses were aligned to ± 5 μm with respect to the connector.

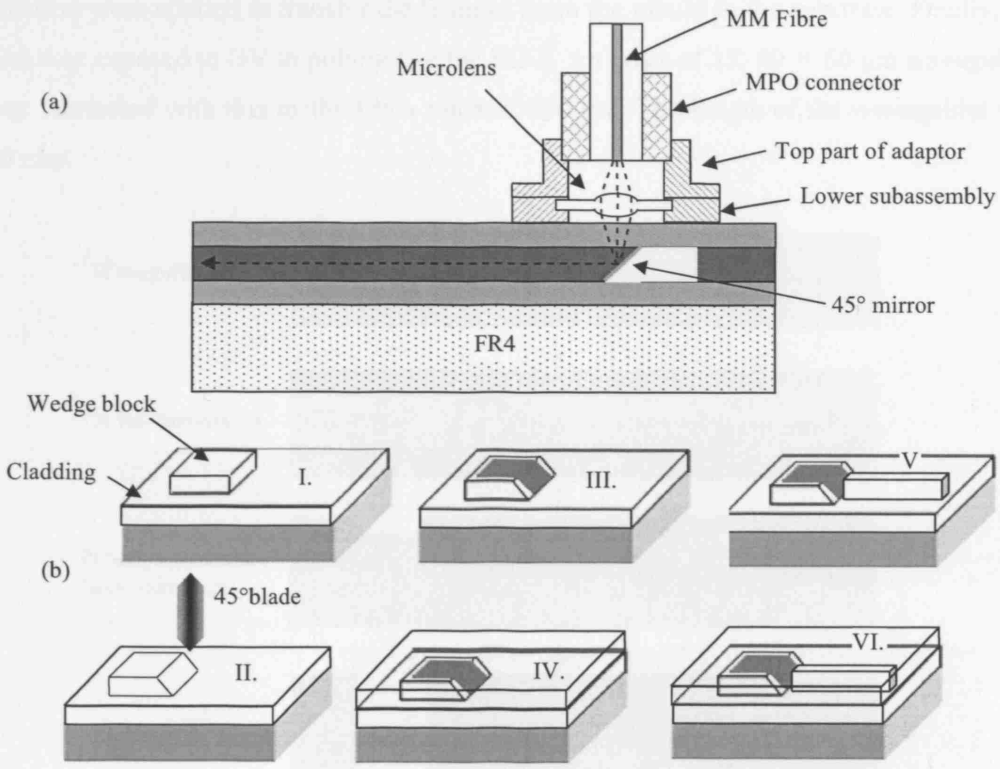

Fig. 2-8. (a) Fujitsu B^2OI optical backplane. (b) wedge reflection mirror technology fabrication steps.

The insertion loss was measured in the range of 5 – 6 dB for all 8 channels. Open and symmetric eye-diagrams with 25 ps jitter were measured for 10 Gb/s operation.

2.2.8. Flexible Optical Waveguide Film Interconnects (University of Texas)

In 2004 the University of Texas presented an interconnection scheme where they integrated optoelectronic devices onto a flexible optical substrate, [2.45]. Waveguides were fabricated by soft moulding and mirrors by cutting the core layer at 45° with a microtome blade. A novel heat management system was proposed to enhance VCSEL source reliability.

Hot embossing and moulding was used to fabricate the waveguides. SU-8 was used for the core and an optically transparent film called Topas 5013 was used for the cladding layers. The master of the mould was made of Si and the mould of poly-dimethylsiloxane (PDMS). To make the waveguides, the mould was heated up and was filled with SU-8. Then the 127 μm thick Topas cladding was placed on the top of the mould and heat and pressure were applied to transfer the features from the mould to the substrate. Finally, the film was exposed to UV to polymerize the SU-8. An array of 12, 50 × 50 μm waveguides was fabricated with this method in a pitch of 250 μm. The length of the waveguides was 50 mm.

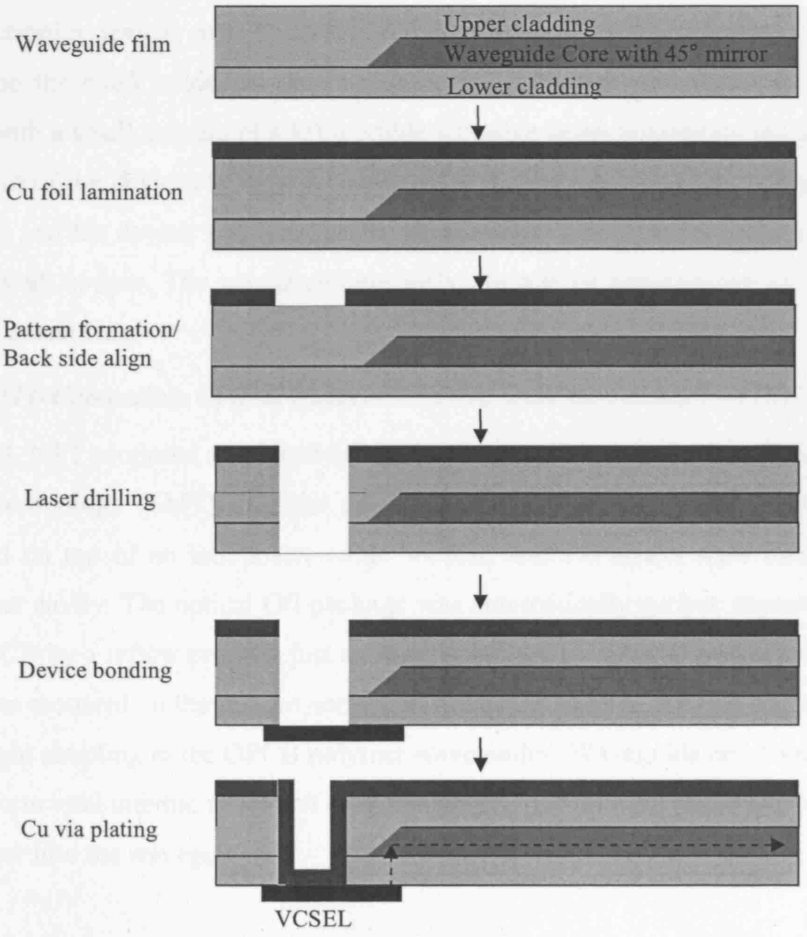

Fig. 2-9. Integration of devices and heat-sink management processing flowchart.

To shape the mirrors a tilted microtome blade was used. The film was heated to soften and the blade was slid down to the waveguide layer at a 45° slope. In this way, the optical film was cut at a 45° angle. After cutting the film, the mirrors were coated with aluminium. Once mirrors were made, another layer of Topas was coated to form the upper cladding layer. The waveguide propagation loss measured was 0.6 dB/cm, while mirror coupling efficiency was 92%.

The optoelectronic devices were integrated, in the way shown in Fig. 2-9. At the beginning, a thin Cu film of ~25 μm was laminated on the top of the upper cladding. This copper layer was then appropriately patterned to form the top pads for the VCSELs and PDs to be bonded. Next, vias were drilled through the film with laser ablation and the optoelectronics devices were bonded in a mask aligner. The flexible waveguide film was placed on the mask holder and the device to be integrated was placed on the substrate holder with a small amount of a UV curable adhesive being applied on the devices. Upon alignment of the devices to the micromirrors of the flexible film, UV radiation cured the adhesive and the device was glued onto the substrate. The final step was to electroplate the via with copper. The via played not only the role of bonding the VCSEL but also acted as a heat sink.

2.2.9. SMT-Compatible Optical Interconnections with Microlenses (NTT)

In 2003, NTT proposed an optical-I/O packaging concept, Fig. 2-10, utilising the surface mount technology (SMT). In their approach, a LSI (large scale integration) chip was mounted on top of an interposer, while VCSEL and PD arrays were integrated in the interposer cavity. The optical O/I package was automatically surface mounted on the top of the PCB by a reflow process, just as for ordinary electronics IC-packages. A microlens array was mounted on the bottom surface of the interposer and another one on the PCB to assist light coupling to the OPCB polymer waveguides. Waveguide end facets were cut at 45° to form total internal reflection (TIR) mirrors to deflect light perpendicularly from the interposer into the waveguides.

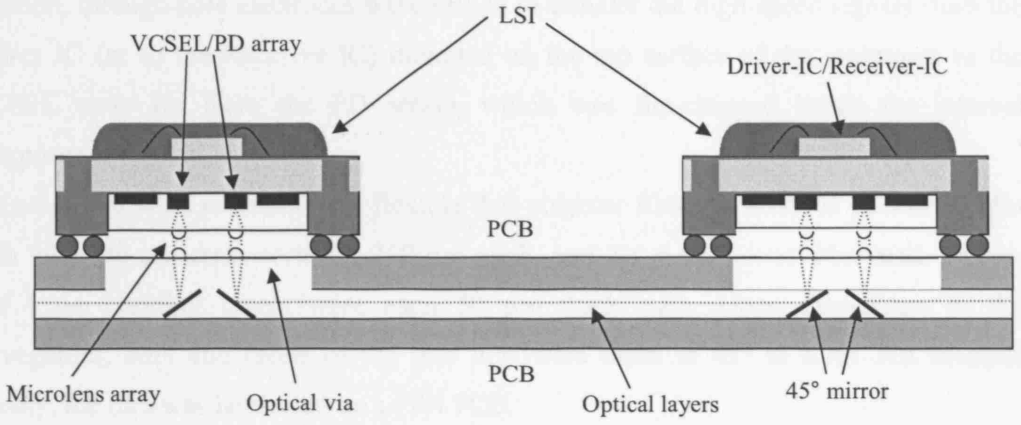

Fig. 2-10. NTT, optical SMT compatible board with microlense array interface.

NTT developed two prototype packages, a transmitter (Tx) and a receiver (Rx). The Tx-package consisted of a 1×3 array of 850 nm VCSELs. A thin transparent polymer film encapsulation was used to protect the VCSEL emitting apertures. Driver-ICs were mounted on top of the interposer. The R_x package contained an 1×3 array of pin-photodiodes and receiver ICs on the top of the interposer. Microlenses were formed on the surface of the polymer encapsulation by the polymer-dispensing method. According to this method, small droplets of liquid resin were dispensed one by one and UV radiation solidified each droplet to form the lenses. The lens diameter of curvature was 480 μm, and the centre-to-centre spacing between the lenses was 500 μm. The waveguides had a cross-sectional dimension of 50 × 50 μm arranged in a pitch of 500 μm, and were 30 mm long. Passive alignment between the interposer and the PCB was performed by utilising the self-alignment effect of the solder balls. The lateral misalignment occurring between interposer and PCB was 11 μm while the total insertion loss for the link measured was 5.4 dB. With this system, NTT demonstrated error-free operation at 1.25 Gb/s.

2.2.10. Active Interposers for High-Speed Chip Level Interconnects (NTT)

NTT developed a second prototype based on the idea of the active interposers, [2.61]. The design, which was made public in 2006, is shown in Fig. 2.11. The main differences from the previous demonstrator were that the active interposers were mounted on the top of accurately defined metal posts rather than on BGA bumps and the coupling between VCSELs and PCB waveguides was direct without the assistance of microlenses. In

addition, through-hole electrodes were drilled to transfer the high-speed signals from the Driver IC (or to the Receiver IC) mounted on the top surface of the interposer to the VCSEL array (or from the PD array), which was flip-chipped inside the internal interposer cavity.

Waveguides were patterned in a flexible thin polymer film. An array of 10 waveguides with 40 × 40 μm cross-sections, 250 μm pitch, and NA = 0.24, was fabricated. Upper- and lower-cladding layers were each 50 μm thick each. Upon fabrication of the waveguides, both end facets of the thin film were diced at 45° to form TIR mirrors. Finally, the film was laminated on a FR4 PCB.

A 1 × 10 array of VCSELs was used in the T_x interposer. The Driver-IC was wire-bonded to surface pads made on the top surface of the interposer. The VCSEL array was flip-chipped on the bottom surface of the interposer. The bottom and top surface pads were interconnected via through-hole electrodes for high-speed signal integrity. Fan-shape electrodes printed on polyimide brought high-speed signals into the interposer. The R_x interposer was constructed in a similar way. An array of 10 metal-semiconductor-metal (MSM) photodiodes with 100 × 100 μm active areas, were used in the R_x assembly. Interposers were made of ceramic for better thermal management.

Metal posts were attached to the transmitter and receiver interposers to hold them on the top of the optical PCB. Alignment was achieved passively with the aid of alignment marks on the active devices (VCSELs and PDs) and on the waveguide film. Once the interposer was aligned, it was glued to the PCB with polymer adhesive. The clearance between the VCSELs / PDs and the top surface of the OPCB upper cladding was 60 ± 14 μm. The lateral alignment tolerance was ± 7 μm. The average total insertion loss for the 10 channels of the active interposer interconnection system was 4 dB. Clear eye-diagrams were demonstrated at 2 Gb/s.

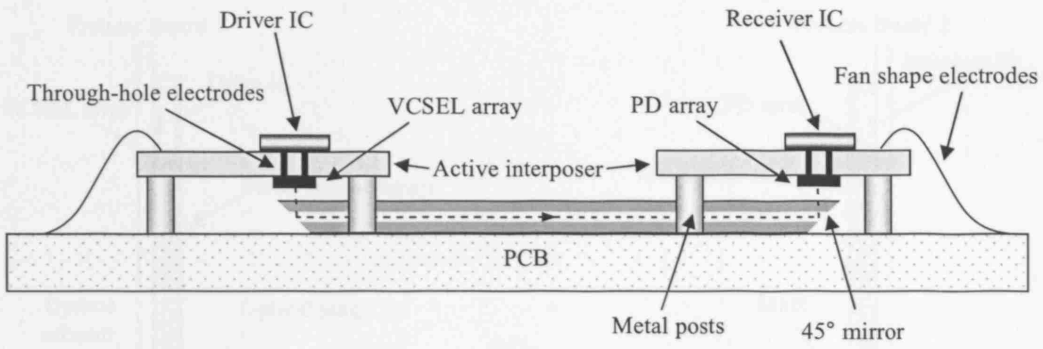

Fig. 2-11. NTT, Optical interconnect utilising active interposers.

2.2.11. Electronics and Telecommunications Research Institute (ETRI) Optical Backplane System.

ETRI presented their own version of a board-to-board optically interconnected backplane system in 2004 [2.63]-[2.66], incorporating a pluggable connector. In their approach, coupling between laser sources and backplane waveguides was achieved by registering an optical plug located at the edge of the processor cards into the permanently attached backplane optical adaptor, Fig. 2-11. VCSEL and PD arrays, as well as their drive and receiver circuits, were integrated onto a metal optical bench (MOB) in the processor cards. Optical waveguiding components were placed in both processor cards and optical backplane. Light from a VCSEL was first coupled into a thin polymer film, also mounted in the MOB (Fig. 2-13 (a)), and then was subsequently coupled to a multimode fibre array mounted in the optical plug module. A 45° mirror component placed at the end of the fibre reflected light, which was focused by microlenses before collected by the PCB waveguides, Fig. 2-13 (b).

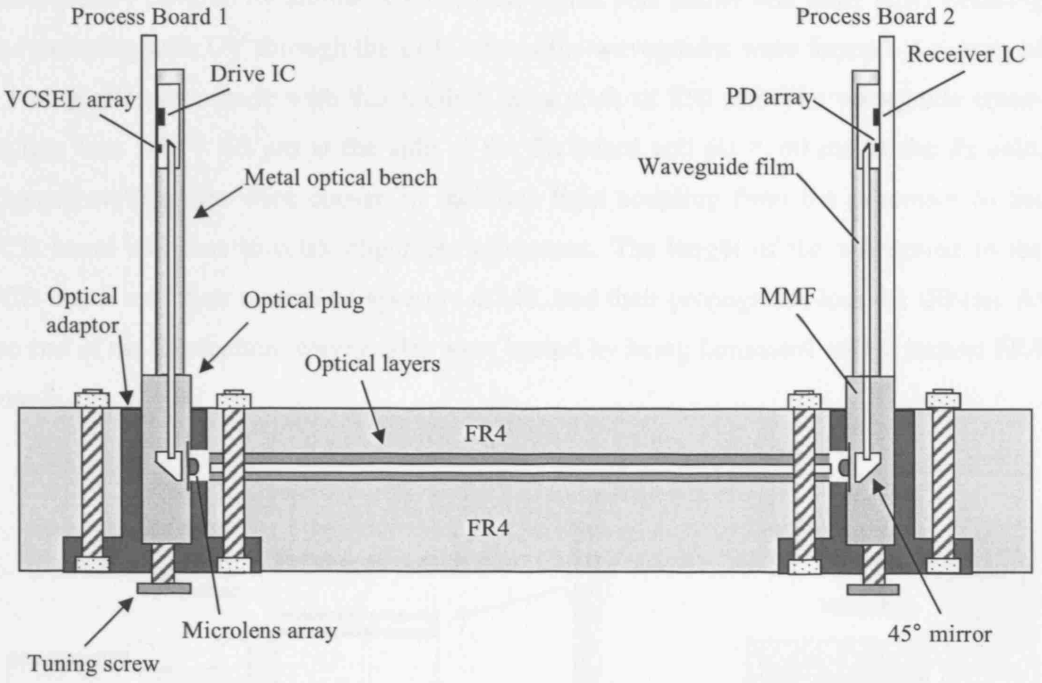

Fig. 2-12. ETRI board-to-board interconnection through optical backlpane.

An array of 4 VCSELs, 850 nm, were mounted on the Tx processor board and an array of 4 PDs on the Rx board together with their drive and receiver circuits. A novel wire bonding technique was introduced in the MOB to reduce the size of the bond-wires and, thus, to minimise parasitic capacitance and optimise channel bandwidth, Fig. 2-13 (a). According to their method, a three-stepped trenched structure was included in the MOB. Access lines were mounted on the bottom step, driver and receiver ICs were die-bonded on the middle step and VCSEL and PD arrays wire-bonded on the top step. All wire bond lengths made in this way were less then 600 μm resulting in high-bandwidth channels. Light generated from the VCSELs was coupled into a thin waveguide film mounted in the MOB. The waveguide film had one of its facets cut at 45° and was aligned against the VCSEL active apertures.

Optical waveguides for the processor and PCB boards were made by the hot-embossing process. A cycloolefin copolymer (COC) was used for the cladding and a UV curable resin for the core. At the beginning, waveguide patterns were transferred from a Si master to a COC sheet by means of heating and pressing. After the waveguide patterns were transferred to the COC sheet, they were filled with the core UV resin and were

subsequently covered by another COC sheet, which was planar this time. After pressing and radiating with UV through the COC sheets the waveguides were formed. An array of 4 waveguides was made with this method on a pitch of 250 μm. The waveguide cross-section was 100 × 60 μm at the side of the Tx board and 60 × 60 μm at the *Rx* side. Tapered waveguides were chosen to facilitate light coupling from the processor to the PCB board and thus to relax alignment tolerances. The length of the waveguide in the PCB was 8 cm, their numerical aperture 0.248, and their propagation loss 0.1 dB/cm. At the end of the fabrication, waveguides were buried by being laminated with a second FR4 board.

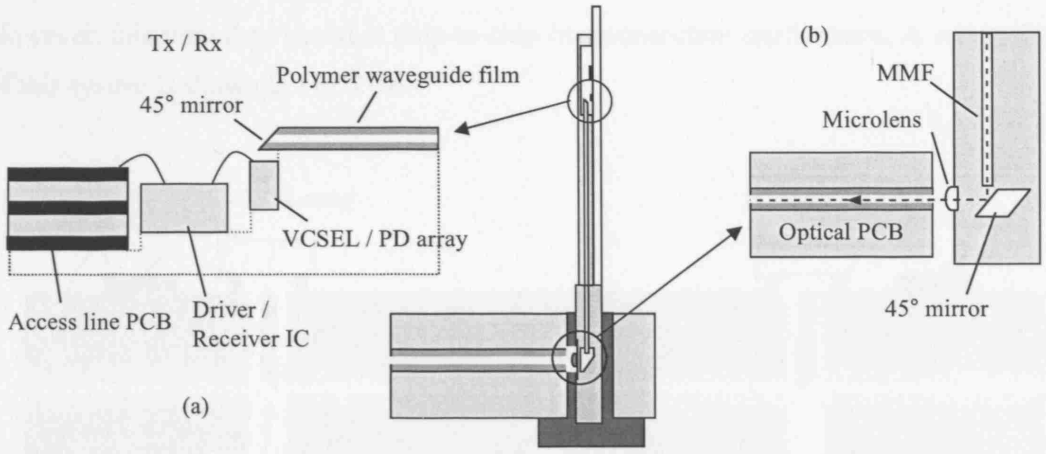

Fig. 2-13. (a) Close up view of the VCSEL / PD - MOB waveguide interface, (b) Close up view of the optical plug – PCB interface.

Coupling from the processor board to the optical backplane was achieved through an optical adaptor – plug strategy, Fig. 2-12. The optical adaptor with the plug registered was first placed into the backplane hole and aligned actively to the backplane waveguides. Then the adaptor was fixed in the board with the aid of bolts and nuts. Once the optical adaptor was installed, the optical plug was free to be removed and reinserted. Although no lateral adjustment was required when the plug was inserted for a second time, an axial correction was necessary, which was achieved with the aid of a fine tune screw installed at the bottom of the adaptor.

The polymer waveguide array on the MOB was butt-coupled to a 62.5 μm multimode

fibre array at the MBO – optical plug interface. This ensured reliability of the optical coupling against potential vibrations, which would be absorbed by the fibre array. An optical deflecting mirror was attached to the end of the fibres to redirect light towards the backplane waveguides, Fig. 2-13 (b). An array of microlenses coupled the adaptor-to-backplane.

In terms of performance, the ETRI backplane exhibit clean eye-diagrams up to 8 Gb/s. However, it suffered from rather high insertion loss of 14 dB.

2.2.12. PCB Compatible Optical Interconnections using 45°-Ended Connection Rods and Via-Holes (ETRI).

In 2004, ETRI presented a second PCB optical interconnection scheme, [2.62]. However, this time they aimed at chip-to-chip interconnection applications. A schematic of this system is shown in Fig. 2-14.

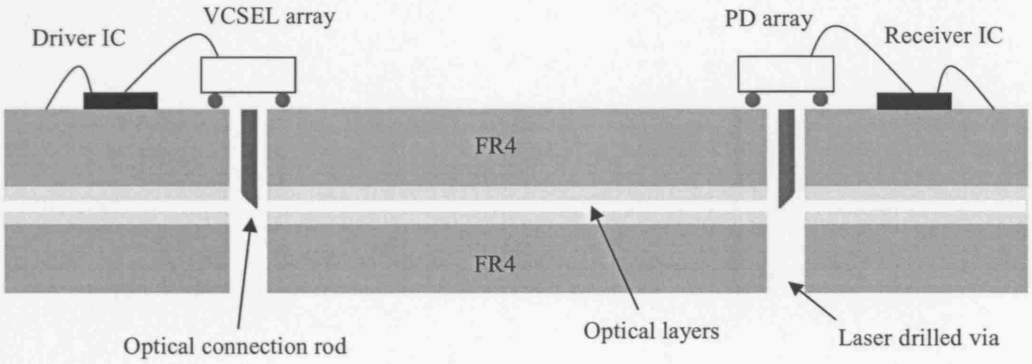

Fig. 2-14. ETRI optical interconnection scheme utilising 45° connection rods and laser drilled optical vias.

Coupling between the VCSEL / PD arrays and the waveguides, was achieved through an array of fibres mounted in an MT-ferrule. The waveguides were made by use of UV photolithography on an FR4 substrate. SU-8 was used for the core while a polymer material called ZP2145M from ZenPhotonics, Deajeon, Korea was used for the cladding layers. An array of 1 × 12 waveguides, 50 mm long, was fabricated in 250 μm pitch. The dimensions of the waveguides were 100 μm width × 65 μm thickness. Upon fabrication, the waveguides were laminated between two FR4 boards. Propagation loss was measured 0.6 dB/cm and was not affected by the lamination process.

After the lamination process, optical vias were drilled through the FR4 and polymer layers with a CO_2 laser. Twelve such vias were drilled with 140 μm diameter and 250 μm centre-to-centre spacing. Unfortunately, it was not reported how the CO_2 laser was aligned to drill at the exact position corresponding to the waveguide cores.

Once the vias were formed, the optical connection rod was inserted. The optical connection rod consisted of an MT-ferrule with an array of 12 protruding fibre. The fibre end facets were mechanically polished to 45° to shape TIR mirrors. The accuracy of the mirror angle was ±1°. 62.5 μm core fibres were used at the transmitter side and 100 μm core fibres at the receiver side. Active alignment between the fibre and waveguides arrays was performed by mounting the MT-ferrule on a *xyz*-motorized stage. The total insertion loss of the system was 8 dB while error-free operation was demonstrated at 1.25 Gb/s.

The following table summarizes the main technical aspects of the 12 above optical backplane systems:

	DaimlerChrysler	HOLMS	EOCB	IBM
Polymer material	—	—	—	Truemode™
Fabrication method	—	—	UV photolithography	UV photolithography
Propagation loss at 850 nm (dB/cm)	0.03	—	—	0.03 – 0.05
45° mirror	Yes	Yes	Yes	No
Mirror loss (dB/mirror)	—	—	—	—
Microlens assisted coupling	Yes	No	No	No
Waveguide size (μm × μm)	200 × 200	70 × 70	70 × 70	35 × 35, 50 × 35
Total insertion loss (dB)	2.5 / 4	—	4.5	6.5
Transmission length (cm)	55	—	6	30
BER (Gb/s)	1	1	10	10

	Finnish consortium	University of Ghent	Fujitsu	University of Texas
Polymer material	SU-8	—	Nippon steel chemical photoepoxy	SU-8
Fabrication method	UV photolithography	Laser ablation	UV photolithography	Soft moulding
Propagation loss at 850 nm (dB/cm)	0.55	—	0.2	0.6
45° mirror	Yes	Yes	Yes	Yes
Mirror loss (dB/mirror)	5.1	—	—	0.36
Microlens assisted coupling	No	Yes	Yes	No

Waveguide size (μm × μm)	50 × 40, 75 × 40	50 × 50	30 × 30	50 × 50
Total insertion loss (dB)	19	—	5 - 6	3.72
Transmission length (cm)	8.3	—	8	5
BER (Gb/s)	10 (not demonstrated)	—	10	—

	NTT 1	NTT 2	ETRI 1	ETR 2
Polymer material	—	—	Cycloolefin Copolymer (COC_ / UV curable resin	ZP2145M, Zenophotonics
Fabrication method	—	—	Hot embossing	UV photolithography
Propagation loss at 850 nm (dB/cm)	—	—	0.1	0.6
45° mirror	Yes	Yes	Yes	Yes
Mirror loss (dB/mirror)	—	—	—	—
Microlens assisted coupling	Yes	No	No	No
Waveguide size (μm × μm)	50 × 50	40 × 40	100 × 60 tapered to 60 × 60	100 × 65
Total insertion loss (dB)	5.4	4	14	8
Transmission length (cm)	3	3	8	5
BER (Gb/s)	1.25	2	8	1.25

2.3. CONCLUSIONS

This chapter reviewed the most important optical backplane systems reported up to date. We have found a large diversity in the polymer materials and the fabrication methods used to make the waveguides and it is not obvious which ones will dominate in the end.

All systems reported suffer from relatively high insertion loss, compared to single mode fibre systems, which is an aspect in the system design that all groups are working to improve. In addition, most optical backplanes employ the surface mounting approach for the VCSELs / PDs with via holes and 45° mirrors responsible to deliver the light into and out of the waveguides. Since there are still many imperfections at fabricating mirrors and as the use of mirrors introduces an additional alignment step compared to the butt coupling approach, mirrors contribute to even higher insertion loss. The transmission length varied in the reported systems from 1cm – 10cm depending on the application (chip-to-chip or board-to-board interconnects) but the maximum length was mainly limited from the size of the available mask aligners in the photolithographic case or the maximum path length of the translational stages in the case of laser writing or ablation. The size of the waveguides varied from 30 × 30 μm to 200 × 200 μm depending on the accuracy of the alignment method used. Connector mechanisms that can ensure reliable, robust and accurate alignment between the VCSELs / PDs and the waveguides are very important elements in optical backplane systems. However, a detachable connector carrying active components was reported only in [2.20]. The alignment methods for the rest of the systems were either fibre based or VCSEL / PD arrays were permanently flip-chipped on the surface of the backplanes. Therefore, there is still lots of room for innovation in this area.

REFERENCES

[2.1]. B. Lunitz, J. Guttmann, H.-P. Huber, J. Moisel, and M. Rods, "Experimental demonstration of 2.5 Gbit/s transmission with 1 m polymer optical backplane," *Electron. Lett.* Vol. 37, pp. 1079, 2001.

[2.2]. J. Moisel, J. Guttmann, H-P Huber, O. Krumpholz, M. Rode, R. Bogenberger and K.-P. Kuhn, "Optical backplanes with integrated polymer waveguides," *Opt. Eng.*, vol. 39, pp. 673-679, 2000.

[2.3]. F. Mederer, R. Michalzik, J. Guttman, H.-P. Huber, B. Lunitz, J. Moisel, and D. Wiedenmann, "10 Gb/s data transmission with TO-packaged multimode GaAs VCSELs pver 1m long polymer waveguides for optical backplane applications," *Opt. Commun.*, vol. 206, pp. 309-312, 2002.

[2.4]. M. Rode, J. Moisel, O. Krumpholz, O. Schickl, "Novel optical backplane board-to-board interconnection," *Proc. ECOC '97*, paper no. 448, 1997.

[2.5]. J. Moisel, "Optical backplane for avionic applications using polymer multimode waveguides," *Proc. 13th LEOS annual meeting*, pp. 567-568, 2000.

[2.6]. T. Bierhoff and J. Schrage, "Design and simulation of board-integrated optical interconnects," *Proc. IEEE 18th Annual Workshop on Interconnections within High Speed Digital Systems*, 2007.

[2.7]. P. Demmer, R. Modinger, J. Bauer, F. Eblin, H. Schroder, P. Beill, H. Albrecht, A. Beier, K. Pfeifferd, M. Franke, E. Griese, M. Reubere, and J. Kostelnikg, "New generation interconnection technology: printed circuit boards with integrated optical layers," *Proc. 9th IEEE Workshop on Signal Propagation on Interconnects*, 2005.

[2.8]. P. Lukowicz, J. Jahns, R. Barbieri, P. Benabes, T. Bierhoff, A. Gauthier, M. Jarczynski, G. A. Russell, J. Schrage, W. Süllau, J. F. Snowdon, M. Wirz, and G. Tröster, "Optoelectronic interconnection technology in the HOLMS system," *IEEE J. Sel. Top. Quantum. Electron*, vol. 9, pp. 624-635, Mar/Apr 2003.

[2.9]. E. Griese, "Reducing EMC problems through an electrical/optical interconnection technology," *IEEE Trans. Electromagnetic Compatibility*, vol. 41, pp. 502-509, Nov. 1999.

[2.10]. E. Griese, "A high-performance hybrid electrical-optical interconnection technology for high-speed electronic systems," *IEEE Trans. Adv. Packag.*, vol. 24, pp. 375-383,Aug. 2001.

[2.11]. T. Happel, M. Franke, H. Nanai, J. Schrage, "Demonstration of Optical Interconnection and Assembly Technique for Fully-Embedded Optical PCB at Data Rates of 10 Gbps/ch, " *Proc. 1st Electronics System Integration Technology Conference*, 2006.

[2.12]. A. Neyer, S. Kopetz, E. Rabe, W. J. Kang, S. Tombrink, "Electrical-optical circuit board using polysiloxane optical waveguide layer," *Proc. Electronic components and technology conference*, 2005.

[2.13]. S. Kopetz, E. Rabe, W. J. Kang, and A. Neyer, "Polysiloxane optical waveguide layer integrated in printed circuit board," *Electron. Let.* Vol. 40, pp. 668-669.

[2.14]. H. Scrhoder, J. Bauer, F. Ebling, and W. Scheel, "Polymer optical interconnects for PCBs," *Proc. 1st IEEE conf. on Polymers and Adhesives in Microelectronics and Photonics*, 2001.

[2.15]. S. Uhlig, L. Fröhlich, M. Chen, N. A.-Staufenbiel, G. Lang, H. Schröder, R. Houbertz, M. Popall, and M. Robertsson, "Polymer Optical Interconnects-A Scalable Large-Area Panel Processing Approach," *IEEE Trans. Adv. Packag.*, vol. 29, pp. 158-170, Nov. 2006.

[2.16]. G.L. Bona, B.J. Offrein, U. Bapst, C. Berger, R. Beyeler, R. Budd, R. Dangel, L. Dellmann, and F. Horst, "Characterization of parallel optical-interconnect waveguides integrated on a printed circuit," *Proc. SPIE*, vol. 5453, pp. 134-141, 2004.

[2.17]. R. Dangel, U. Bapst, C. Berger, R. Beyeler, L. Dellmann, F. Horst, B. Offrein, and G.-L. Bona, "Development of a low-cost low-loss polymer waveguide technology for parallel optical interconnect applications," *Digest of LEOS Summer Topical Meetings*, pp. 337-343, 2004.

[2.18]. L Dellmann, T. Lamprecht, S. Oggioni, M. Witzig, R. Dangel, R. Beyeler, C. Berger, F. Horst, and B.J. Oifrein, " Butt-coupled optoelectronic modules for high-speed optical interconnects," *Proc. CLEO*, 2005.

[2.19]. C. Berger, U. Bapst, G.-L. Bona, R. Dangel, L. Dellmann, P. Dill, M. A. Kossel, T. Morf, B. Offrein, M. L. Schmatz, "Design and implementation of an optical

interconnect demonstrator with board-integrated waveguides and microlens coupling," *Digest of LEOS Summer Topical Meetings*, pp. 19-20, 2005.

[2.20]. L. Dellmann, C. Berger, R. Beyeler, R. Dangel, M. Gmur, R. Hamelin, F. Horst, T. Lamprecht, N. Meier, T. Morf, S. Oggioni, Mauro Spreafico, R. Stevens, B. J. Offrein, "120 Gb/s Optical Card-to-Card Interconnect Link Demonstrator with Embedded Waveguides," *Proc. Electronic Components and Technology Conference*, 2007.

[2.21]. S. Bernabe, R. Stevens, M. Volpert, R. Hamelin, C. Rossat, F. Berger, L. Lombard, C. Kopp, J. Berggren, P. Sundgren, and M. Hammar," Highly integrated VCSEL-based 10Gb/s miniature optical sub-assembly," *Proc. Electronic Components and Technology Conference*, 2005.

[2.22]. S. Uhlig, and M. Robertsson, "Flip chip mountable optical waveguide amplifier for optical backplane systems," *Proc. Electronic Components and Technology Conference*, 2005.

[2.23]. S. Uhlig, and M. Robertsson, "Limitations to and solutions for optical loss in optical backplanes," *J. Lightw. Technol.*, vol. 24, pp. 1710-1724, Apr. 2006.

[2.24]. M. Immonen, M. Karppinen, and J. Kivilahti, "Fabrication and characterization of polymer optical waveguides with integrated micromirrors for three-dimensional board-level optical interconnects," *IEEE Trans. on Electron. Packag. Manuf.*, vol. 28, pp. 304-311, Oct. 2005.

[2.25]. M. Immonen, J. Wu, and J. Kivilahti, "Influence on environmental stresses on board-level integrated optics," *Proc. Electronic Components and Technology Conference*, 2005.

[2.26]. M. Immonen, and T. R.-Virtanen, "Fabrication of low-cost panel sized optical-printed circuit boards," *Proc. Electronics Packaging Technology Conference*, 2005.

[2.27]. M. Immonen, J. Wu, and J. Kivilahti, "Fabrication of polymer optical waveguides with integrated micromirros for out-of-plane surface normal optical interconnects," *Proc. of 4th International Conference on Polymers and Adhesives in Microelectronics and Photonics*, 2004.

[2.28]. M. Karppinen, T. Alajoki, A. Tanskanen, K. Kataja, J.-T. Mäkinen, K. Kautio, P. Karioja, M. Immonen, and J. Kivilahti, "Parallel Optical Interconnect between Ceramic

BGA Packages on FR4 Board using Embedded Waveguides and Passive Optical Alignments," *Proc. Electronic Components and Technology Conference*, 2006.

[2.29]. J. Hietala, E. Muukkonen, T. V.-Lerber, M. Immonen and A. Oy, "Volume production of on-board optical waveguides," *Proc. Electronic Components and Technology Conference*, 2005.

[2.30]. E. Bosman, G. Van Steenberge, P. Geerinck, W. Christiaens, J. Vanfleteren, and P. Van Daele, "Embedding of Optical Interconnections in Flexible Electronics," *Proc. Electronic Components and Technology Conference*, 2007.

[2.31]. G. V. Steenberge, P. Geerinck, S. V. Put, J. V. Koetsem, D. Morlion, P. V. Daele, "Demonstration of an MT-compatible connectorisation of a laser-ablated optical interconnection on a printed circuit board," *Proc. Electronic Components and Technology Conference*, 2004.

[2.32]. Geert Van Steenberge, Peter Geerinck, Steven Van Put, Jan Van Koetsem, Heidi Ottevaere, Danny Morlion, Hugo Thienpont, and Peter Van Daele, "MT-compatible laser-ablated interconnections for optical printed circuit boards," *J. Lightw. Technol.*, vol. 22, pp. 2083-2090, Sep. 2004.

[2.33]. D. Israel, R. Baets, M. J. Goodwin, N. Shaw, M. D. Salik, and C. J. Groves-Kirkby, " Multimode polymeric Y junctions for star couplers in backplane optical interconnect," *Appl. Opt.*, vol 36, pp. 5091-5096, Jul. 1996.

[2.34]. D. Israel, R. Baets, M. J. Goodwin, N. Shaw, M. D. Salik, and C. J. Groves-Kirkby, "Comparison of different polymeric multimode star couplers for backplane optical interconnect," *J. Lightw. Technol.*, vol. 13, pp. 1057-1064, Sep. 1995.

[2.35]. A. McCarthy, H. Suyal, and A. C. Walker. "45° Out-of-plane Turning Mirrors for Optoelectronic Chip Carriers based on Multimode Polymer Waveguides." *Proc. ECOC 2004*, 2004.

[2.36]. A. C. Walker, "Polymer optical interconnects – from optoelectronic chip integration to optical backplanes," invited talk, *18th Annual Workshop on Interconnections within High Speed Digital Systems*, 2007.

[2.37]. Exxelis Ltd., http://www. exxelis.com. Last time accessed 10/08/07.

[2.38]. J. D. Ingham, N. Bamiedakis, R. V. Penty, I. H. White, J. V. DeGroot, Jr., T. V.

Clapp, "Multimode siloxane polymer waveguides for robust high-speed interconnects", *Proc. Conference on Lasers and Electro-Optics (CLEO)*, 2006.

[2.39]. N. Bamiedakis, J. Beals, R. V. Penty, I. H. White, J. V. DeGroot Jr., T. V. Clapp, "Low Loss and Low Crosstalk Multimode Polymer Waveguide Crossings for High-Speed Optical Interconnects", *Proc. Conference on Lasers and Electro-Optics (CLEO)*, 2007.

[2.40]. D. Gwyer, P. Misselbrook, C. Bailey, P. Conway, and K. Williams, "Polymer waveguide and VCSEL array multi-physics modeling for OECB based optical backplanes," *Proc. 5th Intern. Conference on Thermal and Mechanical Simulation and Experiments in Micro-electronics and Micro-Systems,* 2004.

[2.41]. A. L. Glebov, J. Roman, M. G. Lee, and K. Yokouchi, "Optical interconnect modules with fully integrated reflector mirrors," *IEEE Photon. Technol. Lett.*, vol. 17, pp. 1540-1542, Jul. 2005.

[2.42]. A. L. Glebov, M. G. Lee, and K. Yokouchi, "Integration technologies for pluggable backplane optical interconnect systems," *Opt. Eng.*, vol. 46, pp. 015403 1-10, Jan. 2007.

[2.43]. A. L. Glebov, M. G. Lee, and K. Yokouchi, "10+ Gb/s board-level optical interconnects: fabrication, assembly, and testing," *Proc. SPIE Micro-Optics, VCSELs, and Photonic Interconnects II: Fabrication, Packaging, and Integration,* 2006.

[2.44]. R. T. Chen, S. Tang, T. Jannson, and J. Jannson, "45-cm long compression-molded polymer-based optical bus," *Appl. Phys. Lett.*, vol. 63, pp. 1032-1034, Aug. 1993.

[2.45]. R. T. Chen, H. Lu, D. Robinson, Z. Sun, T. Jannson, D. V. Plant and H. R. Fetterman, "60 GHz board-to-board optical interconnection using polymer optical buses in conjuction with microprism couplers," *Appl. Phys. Lett.*, vol. 60, pp. 536-538, Feb. 1992.

[2.46]. R. T. Chen, L. Lin, C. Choi, Y. J. Liu, B. Bihari, L. Wu, S. Tang, R. Wickman, B. Picor, M. K. Hibbs-Brenner, J. Bristow, and Y. S. Liu, "Fully embedded board-level guided-wave optoelectronic interconnects," *Proc. of the IEEE,* pp. 780-793, Jun 2000.

[2.47]. Chulchae Choi, Lei Lin, Yujie Liu, Jinho Choi, Li Wang, David Haas, Jerry Magera, and Ray T. Chen, "Flexible optical waveguide film fabrications and optoelectronic devices integration for fully embedded board-level optical interconnects,"

J. Lightw. Technol., vol. 22, pp. 2168-2176, Sep. 2004.

[2.48]. G.-K. Chang, D. Guidotti, F. Liu, Y.-J. Chang, Z. Huang, V. Sundaram, D. Balaraman, S. Hegde, and R. R. Tummala, "Chip-to-Chip Optoelectronics SOP on Organic Boards or Packages," *IEEE Trans. Adv. Packag.*, vol. 27, pp. 386-397, May 2004.

[2.49]. T. Suzuki, T. Nonaka, N. Ogawa, S.-Y. Cho, S.-W. Seo, and N. M. Jokerst, "Embedded Optical Interconnections on Printed Wiring Boards," *Proc. Electronic Components and Technology Conference*, 2004.

[2.50]. S. Hedge, and S. K. Sitaraman, "Thermo-mechanical evaluation of embedded optical interconnects on board," *Proc. 9th Intersociety Conference in Thermal and Thermomechanical Phenomena in Electronic Systems*, 2004.

[2.51]. S.-Y. Cho, S.-W. Seo, N. M. Jokerst, M. A. Brooke, ""Board-Level Optical Interconnection and Signal Distribution Using Embedded Thin-Film Optoelectronic Devices," *J. Lightw. Technol.*, vol. 22, pp. 2111-2118, Sep. 2004.

[2.52]. N. M. Jokerst, T. K. Gaylord, E. Glytsis, M. A. Brooke, S. Cho, T. Nonaka, T. Suzuki, D. L. Geddis, J. Shin, R. Villalaz, J. Hall, A. Chellapa, and M. Vrazel, "Planar lightwave integrated circuits with embedded actives for board and substrate level optical signal distribution," *IEEE Trans. Adv. Packag.*, vol. 27, pp. 376-385, May 2004.

[2.53]. Y. S. Liu, R. J. Wojnarowski, W.A. Hennessy, P.A. Piacente, J. Rowlette, Jr, M. Kadar-Kallen, J. Stack, Y. Liu, A. Peczalski, A. Nahata and J. Yardley, "Plastic VCSEL array packaging and high density polymer waveguides for board and backplane optical interconnect," *Proc. 48th Electronic Components and Technology Conference*, 1998.

[2.54]. Y. S. Liu, R. J. Wojnarowski, W. A. Hennessy, J. Rowlette. J. Stack, M. K.-Kallen, Y. Liu, J. P. Bristow, A. Peczalski, L. Eldada, J. Yardley, R.M. Osgood, R Scarmozzino, S. H. Lee, S. Patra, "High density optical interconnects using VCSEL and polymer Waveguides for board and backplane applications," *Proc. 47th Electronic Components and Technology Conference*, 1997.

[2.55]. L. Eldada, and L. W. Shacklette, "Advances in Polymer Integrated Optics," *IEEE J. Sel. Top. Quantum. Electron*, vol. 6, pp. 54-68, Jan/Feb 2000.

[2.56]. L. Eldada, "Advances in polymer optical interconnects," *Proc. 18th Annual LEOS*

Meeting, 2005.

[2.57]. Makoto Hikita, Ryoko Yoshimura, Mitsuo Usui, Satoru Tomaru, and Saburo Imamura, "Polymeric optical waveguides for optical interconnection," *Thin Solid Films*, vol. 331, pp. 303-308, 1998.

[2.58]. Makoto Hikita, Satoru Tomarum Koji Enbutsu, Naoki Ooba, Ryoko Yoshimura, Mitsuo Usui, Takashi Yoshida, and Saburo Imamura, , "Polymeric optical waveguide films for short-distance optical interconnects," *IEEE J. Sel. Top. Quantum. Electron*, vol. 5, pp. 1237-1242, Sep/Oct 1999.

[2.59]. T. Sakamoto, H. Tsuda,M. Hikita T. Kagawa K. Tateno, and C. Amano," Optical interconnection using VCSELs and polymeric waveguide circuits," *J. Lightw. Technol.*, vol. 18, pp. 1487-1492, Nov. 2000.

[2.60]. Y. Ishii, N. Tanaka, T. Sakamoto, H. Takahara, "Fully SMT-compatible optical-I/O package with microlens array interface," *J. Lightw. Technol.*, vol. 21, pp. 275-280, Jan. 2003.

[2.61]. Seiki Hiramatsu, and Masao Kinoshita, "Three dimensional waveguide arrays for coupling between fibre-optic connectors and surface-mounted optoelectronic devices," *J. Lightw. Technol.*, vol. 23, pp. 2733-2739, Sep. 2005.

[2.62]. Seiki Hiramatsu, and Takashi Mikawa, "Optical design of active interposer for high-speed chip level optical interconnects," *J. Lightw. Technol.*, vol. 24, pp. 927-934, Sep. 2006.

[2.63]. Byung Sup Rho, Han Seo Cho, Hyo-Hoon Park, Sang-Won Ha, and Byoung-Ho (Tiger) Rhee, "PCB-compatible optical interconnection using 45°-ended connection rods and via-holed waveguides," *J. Lightw. Technol.*, vol. 22, pp. 2128-2134, Sep. 2004.

[2.64]. Keun Byoung, In-Kui Cho, Seung Ho Ahn, Myung Yong Jeong, Deug Ju Lee, Young Un Heo, Byung Sup Rho, Hyo-Hoon Park, and Byoung-Ho Rhee, "Optical backplane system using waveguide-embedded PCBs and optical slots," *J. Lightw. Technol.*, vol. 22, pp. 2119-2127, Sep. 2004.

[2.65]. In-Kui Cho, Keun Byoung Yoon, Seung Ho Ahn, Myung Yong Jeong, Hee-Kyung Sung, Byung Ho Lee, Young Un Heo, and Hyo-Hoon Park, "Board-to-board optical interconnection system using optical slots," *IEEE Photon. Technol. Lett.*, vol. 7,

pp. 1754-1756, Jul. 2004.

[2.66]. Seung-Ho Ahn, In-Kui Cho, Sang-Pil Han, Keun Byoung Yoon, Man-Seop Lee, "Demonstration of high-speed transmission through waveguide-embedded optical backplane," *Opt. Eng.*, vol. 45, pp. 085401 1-6, Aug. 2006.

[2.67]. In-Kui Cho, Keun Byoung Yoon, Seung Ho Ahn, Hee-Kyung Sung, Sang won Ha, Young Un Heo, "Experimental demonstration of 10 Gbit/s transmission with an optical backplane system using optical slots," *Opt. Lett.*, vol. 30, pp. 1635-1637, Jul. 2005.

[2.68]. Li-Cheng Shen, Wei-Chung Lo, Hsiang-Hung Chang, Huan-Chun Fu, Yuan-Chang Lee, Shu-Ming Chang, Yu-Chih Chen, and Wun-Yan Chen, "Flexible Electronic-Optical Local Bus Modules to the Board-to-Board, Board-to-Chip, and Chip-to-Chip Optical Interconnection," *Proc. Electronic Components and Technology Conference*, 2005.

CHAPTER 3

REVIEW OF THE INTRINSIC MODE THEORY AND THE COUPLED MODE THEORY

3.1. INTRODUCTION

This chapter provides the background theory for the work that will follow in Chapter 5, "Theoretical and experimental investigation of tapered waveguide bends", and in Chapter 6, "Radiation modes, coupled power theory and modal power distribution for weakly guiding dielectric waveguides". Here we review the intrinsic mode theory [3.1]–[3.8] developed by Arnold and Felsen and the coupled mode and power theories [3.13]–[3.20] developed by Marcuse. The intrinsic mode theory describes wave propagation in slab tapered waveguides and was initially developed for sound propagation in wedge shaped oceans, [3.1]-[3.5], although it was later extended to optical dielectric waveguides [3.6]-[3.8]. The most powerful feature of the intrinsic mode theory is that it can describe modal propagation in all, before, during, and beyond cut-off waveguide regions. Intrinsic mode theory is in this sense superior to other methods, such as the coupled mode theory [3.9], which usually fail at the transition region where a mode changes from being bound to radiating into the cladding. Our aim at using the intrinsic mode theory is to describe adiabatic mode propagation in tapered waveguide bends. This extension to the intrinsic mode theory is presented in Chapter 5.

Marcuse's coupled mode and power theories [3.13]-[3.20], are reviewed in relation to a waveguide with randomly deformed sidewalls. The significance of these methods is that they predict how energy is exchanged between bound and radiation modes, which are coupled due to the sidewall roughness, and in this way, important parameters such as the waveguide propagation loss and the distribution of the modes can be calculated. The first application of the couple mode and power theories to multimode buried channel waveguides is presented in Chapter 6.

3.2. INTRINSIC MODE THEORY FOR TAPERED SLAB WAVEGUIDES

3.2.1 Plane Wave Propagation in Tapered Slab Waveguide

The slab waveguide geometry that Arnold and Felsen analyzed in their intrinsic mode theory [3.1]-[3.8] is shown in Fig. 3-1 (b). It consists of two plane boundaries S_1 and S_2, which form an angle ω with respect to each other. The bottom boundary, S_1, represents the dielectric interface between two media filled with homogenous refractive index n_{co} (core) and n_{cl} (cladding). The top boundary, S_2, is assumed metallic and so all tangent electric components are zero there. Due to the difference of the boundary conditions imposed on S_1 and on S_2 the modes that are supported by this waveguide are asymmetric. The propagation axis (z-axis) of our coordinate system runs parallel to the bottom surface S_1. As we see in Fig. 3-1 (b), the width of the waveguide w reduces as we move towards positive z, and a taper is shaped in the xz-plane. The centre of the coordinate system O, is placed at the apex of the taper.

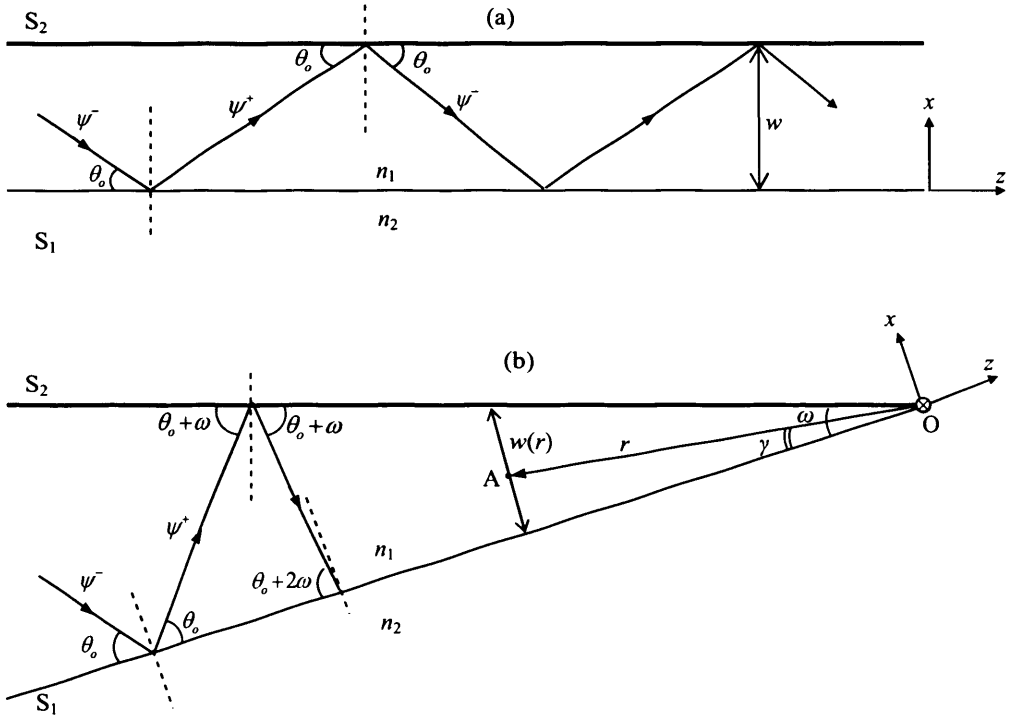

Fig. 3-1. (a) Ordinary slab waveguide geometry and (b) Tapered slab waveguide geometry under consideration consisted of two semi-infinite dielectric planes, which are tilted with respect to each other with a very small angle $\omega \sim 0$. The bottom surface S_2 separates the core, with refractive index n_{co}, from the cladding with refractive index n_{cl}. The upper surface S_2 is assumed to be perfectly reflecting (metallic).

The fields $\psi(x,z)$, that propagate in the slab waveguide, Fig. 3-1 (b), must satisfy the 2D Cartesian wave-equation

$$\left[\frac{\partial^2}{\partial x^2}+\frac{\partial^2}{\partial z^2}-k^2n^2(x,z)\right]\psi=0 \tag{3.1}$$

where $k = 2\pi/\lambda$ stands for the free-space wavenumber, λ the free-space wavelength of light, and $n(x,z)$ is the waveguide refractive index distribution ($n(x,z) = n_{co}$ in the core area and $n(x,z) = n_{cl}$ in the cladding area). Since the waveguide geometry is infinite in the y direction, we assume that $\partial\psi/\partial y = 0$ in (3.1). The elementary solutions of the wave-equation (3.1), inside the core of the waveguide, are upward propagating (towards positive x), ψ^+, and downward propagating (towards negative x), ψ^-, plane waves

$$\psi^{\pm}(x,z;\theta) = u^{\pm}(\theta)e^{\mp ikx\sin\theta}e^{-ikz\cos\theta} \tag{3.2}$$

where, θ is the angle that a plane wave forms with respect to the z-axis, and $u^{\pm}(\theta)$ the amplitude of the upward (+) and downward (-) propagating wave of angle θ correspondingly. Note that we only consider waves propagating towards increasing z (towards the apex of the taper) in (3.2). If the boundaries S_1 and S_2 were running parallel to each other, Fig. 3-1 (a), then a downward propagating plane wave $\psi^-(x,z;\theta)$ would translate to an upward propagating wave $\psi^+(x,z;\theta)$, upon reflection on the bottom boundary S_1, with the addition of a Goos-Hänchen phase shift due to the reflection on the dielectric interface. Proportionally, a reflection on the top boundary S_2 would translate the upward propagating plane wave $\psi^+(x,z;\theta)$ back to the original downward propagating wave $\psi^-(x,z;\theta)$ with the addition of a π phase shift, due to the reflection on the metallic surface. The demand for single valued fields between upward propagating (or downward propagating) waves after this double reflection process would result in an eigenvalue problem, the solutions of which would correspond to the discrete set of angles θ, that the plane waves are allowed to take in the slab (slab waveguide modes). The previously described situation, changes quite significantly in the case of the tapered slab waveguide, Fig. 3-1 (b). In this case, a downward propagating plane wave $\psi^-(x,z;\theta)$, which forms an angle θ with the z-axis (note that z-axis in Fig. 3-1 (b) has been tilted compared to Fig. 3-1 (a)), still translates to an upward wave $\psi^+(x,z;\theta)$, upon reflection on the bottom surface S_1, as also happened in the slab waveguide. However, reflection on

the top surface S_2, results in a downward propagating plane wave $\psi^-(x,z;\theta+2\omega)$, with a propagation angle tilted by 2ω (ω the angle of the taper), compared to $\psi^-(x,z;\theta)$. This new wave $\psi^-(x,z;\theta+2\omega)$ would then translate to the upward plane wave $\psi^+(x,z;\theta+2\omega)$ upon reflection on the bottom surface S_1, but its propagation angle would be tilted by a further 2ω upon reflection on S_2, to form the downward propagating wave $\psi^-(x,z;\theta+4\omega)$ and so on. Therefore, due to the presence of the slope, the propagation angle of a plane wave changes by 2ω every time the wave reflects on the top surface S_2. The intrinsic mode theory relies on tracing successive reflections of elementary upward and downward propagating waves $\psi^\pm$ on the top and bottom boundaries, and demanding single valued fields to exist inside the taper.

Since the elementary solutions of the wave equation in the waveguide core are the plane waves $\psi^\pm$, which form a complete set of solutions, we can express the total field $V^\pm$ at any waveguide cross-section, as a linear combination of all possible upward and downward propagating plane waves as

$$V^\pm(r,\gamma) = \int_c u^\pm(\theta)\cdot\psi^\pm(r,\gamma;\theta)d\theta$$

$$V^\pm(r,\gamma) = \int_c u^\pm(\theta)\cdot\exp[\,ikr\cos(\theta\pm\gamma)]d\theta \qquad (3.3)$$

where in (3.3) V^+ corresponds to the contribution from all upward propagating waves and V^- corresponds to the contribution from all downward propagating plane waves. The parameters $u^\pm(\theta)$ are the (yet undetermined) amplitude coefficients of the plane waves with propagation angle θ. Note that rather than using the Cartesian expressions for the plane waves (3.2), we switched to a convenient cylindrical coordinate system $(x,z) = (r\sin\gamma, -r\cos\gamma)$ in (3.3), where the radius r is measured from the apex of the taper and the polar angle γ measured from the z-axis, as shown in Fig. 3-2. The reasons for this switch will become more apparent in the following. The total field V, at any point (r,γ) in the taper is the sum of all upward and downward waves:

$$V(r,\gamma) = V^+(r,\gamma) + V^-(r,\gamma) \qquad (3.4)$$

The integration contour c in (3.3) is an appropriate Sommerfeld contour c, Fig. 3-2, which guarantees that the set of plane waves in the spectral representation (3.3) is complete. Our contour c, covers the real angles in the range $0 \le \theta \le \pi$, and the imaginary

angles in the range , $-\infty \leq \mathrm{Im}\theta \leq 0$, and $0 \leq \mathrm{Im}\theta \leq +\infty$, Fig. 3-2. The selected angular range implies that we consider both oscillating (real angles) and evanescent waves (imaginary angles) in our spectral representation (3.3). Our objective in the following is to calculate the integral in (3.3) which gives the propagating field in the taper. We note that the integral implied in (3.4) is valid everywhere except exactly at the apex of the waveguide. The theory that will be presented here collapses when the width of the waveguide becomes comparable to the wavelength of the light but is valid everywhere else, which covers the majority of the tapers of interest.

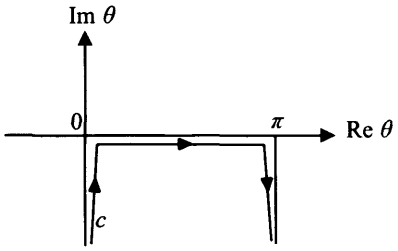

Fig. 3-2. Sommerfeld integration contour c, in the complex θ domain. Contour extends over all real angles $0 < \theta < \pi$ and is complemented by the imaginary angles $-\infty \leq \mathrm{Im}\theta \leq 0$, and $0 \leq \mathrm{Im}\theta \leq +\infty$ to consider evanescent wave contributions.

As we mentioned before, the elementary downward propagating plane wave $\psi^{-}(r,\gamma;\theta)$ translates to the upward propagating wave $\psi^{+}(r,\gamma;\theta)$ after being reflected by the bottom surface S_1, expressed as $\gamma = 0$ in the polar system, with the addition of a phase shift. Therefore, for the boundary conditions to be satisfied at $\gamma = 0$, we must require

$$u^{+}(\theta) = u^{-}(\theta)e^{i\Phi(\theta)} \tag{3.5}$$

where the Rayleigh coefficient $e^{i\Phi(\theta)}$ for reflection between two dielectric surfaces is given by

$$\Phi(\theta) = 2\arctan\left[i\frac{n_{cl}\sin\dot{\theta}}{n_{co}\sin\theta}\right] \tag{3.6}$$

In (3.6), the parameter $\dot{\theta}$, corresponds to the angle of refraction, which is calculated by Snell's law

$$n_1\cos\theta = n_2\cos\dot{\theta} \tag{3.7}$$

If $\theta < \theta_c$, with $\cos\theta_c = n_2/n_1$ the critical angle for total internal reflection (TIR), then from (3.7) $\dot{\theta}$ becomes imaginary, resulting to a real and negative $\Phi(\theta)$ in (3.6) in agreement with the Goos-Hänchen shift. In this case, all waves are reflected back to the core without any attenuation. In contrast if $\theta > \theta_c$, then $\Phi(\theta)$ becomes positive imaginary corresponding to the Fresnel loss. Every time a plane wave is reflected by the bottom boundary S_1 loses energy, which radiates into the cladding due to refraction, in this case. It is very important to note that θ_c, is a branch-point of the *arctan* function in (3.6), which generates branch-cuts in the complex angular domain that might interfere with the integration contour c, in (3.3). The interaction between branch-points and spectral integral (3.3) is very important and will be further investigated in the following.

Reflection of $\psi^+(r,\gamma;\theta)$ on the metallic boundary S_2, on the other hand, translates the plane wave $\psi^+(r,\gamma;\theta)$ into the downward propagating plane wave $\psi^-(r,\gamma;\theta+2\omega)$, angularly tilted by 2ω with respect to the z-axis, Fig. 3-1 (b). A π phase shift is involved due to the boundary conditions on the metallic surface S_2 and so the relationship between the amplitudes of the upward and downward propagating plane waves is altered in this case as

$$u^-(\theta + 2\omega) = u^+(\theta)e^{i\pi} \tag{3.8}$$

By combining (3.5) and (3.8) we obtain

$$u^-(\theta + 2\omega) = u^-(\theta)e^{i(\Phi(\theta)+\pi)} \tag{3.9}$$

If $u^-(\theta)$ is represented (all complex functions can be written in this way) by

$$u^-(\theta) = e^{iS(\theta)} \tag{3.10}$$

with $S(\theta)$ some complex function to be later defined, then by combining (3.10) with (3.9) we get

$$S(\theta + 2\omega) - S(\theta) = \Phi(\theta) + \pi - 2q\pi \tag{3.11}$$

where q can be any integer value in (3.11). By tracing the plane wave $\psi^-(r,\gamma;\theta+2\omega)$ through its further two reflections, firstly on S_1 and then on S_2, we can extract a similar to (3.9) relationship between $u^-(\theta+2\omega)$ and $u^-(\theta+4\omega)$ as

$$u^-(\theta + 4\omega) = u^-(\theta + 2\omega)e^{i(\Phi(\theta+2\omega)+\pi)} \tag{3.12}$$

which with the aid of the definition (3.10) can be written as

$$S(\theta + 4\omega) - S(\theta + 2\omega) = \Phi(\theta + 2\omega) + \pi - 2q\pi \tag{3.13}$$

Similarly, by tracing $\psi^{+}(r,\gamma;\theta)$ through m successive reflections on the bottom and top surfaces we obtain

$$S(\theta^{(m)}) - S(\theta^{(m-1)}) = \Phi(\theta^{(m-1)}) + \pi - 2q\pi \tag{3.14}$$

with the abbreviation

$$\theta^{(m)} = \theta + 2m\omega \tag{3.15}$$

Equation (3.14) can be solved with the Euler-Maclaurin formula, Appendix B. We first sum (3.14) m-times for $m = 1,2 \ldots m$

$$\begin{array}{l} S(\theta^{(1)}) - S(\theta) = \Phi(\theta) + \pi - 2q\pi \\ S(\theta^{(2)}) - S(\theta^{(1)}) = \Phi(\theta^{(1)}) + \pi - 2q\pi \\ \vdots \\ S(\theta_o^{(m)}) - S(\theta_o^{(m-1)}) = \Phi(\theta^{(m-1)}) + \pi - 2q\pi \end{array} \quad (+)$$

$$S(\theta^{(m)}) - S(\theta) = -\Phi(\theta^{(m)}) + \sum_{l=0}^{m} \Phi(\theta^{(l)}) + m\pi - 2qm\pi \tag{3.16}$$

Equation (3.16) contains a series, which is cumbersome to calculate. However, with the aid of the Euler-Maclaurin formula (see (B5)-(B6) in appendix B), (3.16) is spanned to continuous angles $\theta^{(l)}$, and the series is transformed to an integral as

$$\sum_{l=0}^{m} \Phi(\theta^{(l)}) = \frac{1}{2}\left[\Phi(\theta^{(m)}) + \Phi(\theta)\right] + \int_{0}^{m} \Phi(\theta^{(l)})\,dl + \hat{E}(\theta^{(m)},\theta) \tag{3.17}$$

$$\hat{E}(\theta^{(m)},\theta) = 2\sum_{q=1}^{\infty} \int_{0}^{m} \Phi(\theta^{(l)}) \cdot \cos(2q\pi l)\,dl \tag{3.18}$$

Furthermore, with the aid of the variable change

$$\hat{\theta} = \theta + 2l\omega = \theta^{(l)} \tag{3.19}$$

from, which we get

$$dl = \frac{d\hat{\theta}}{2\omega} \tag{3.20}$$

we can write (3.17) and (3.18) as

$$\sum_{l=0}^{m} \Phi(\theta^{(l)}) = \frac{1}{2}\left[\Phi(\theta^{(m)}) + \Phi(\theta)\right] + \frac{1}{2\omega} \int_{\theta}^{\theta^{(m)}} \Phi(\hat{\theta})\,d\hat{\theta} + \hat{E}(\theta^{(m)},\theta) \tag{3.21}$$

$$\hat{E}(\theta^{(m)},\theta)=\frac{1}{\omega}\sum_{q=1}^{\infty}\int_{\theta}^{\theta^{(m)}}\Phi(\hat{\theta})\cdot\cos\left(\frac{q\pi}{\omega}(\hat{\theta}-\theta)\right)d\hat{\theta} \tag{3.22}$$

In (3.21) - (3.22) the angle $\theta^{(l)}$ takes only discrete values that differ by 2ω, (3.15). However, equations (3.21) and (3.22), can be extended to arbitrary angular values $\theta^{(l)}$ and θ. Firstly, we express (3.22) in its alternative form [3.2]:

$\hat{E}(\theta^{(m)},\theta)=E(\theta^{(m)})-E(\theta)$,

$$E(\theta)=\omega^{-1}\sum_{q=1}^{+\infty}\int_{+i\infty}^{0}\Phi(\theta+\psi)\cdot\exp(iq\pi\psi/\omega)d\psi+\omega^{-1}\sum_{q=1}^{+\infty}\int_{-i\infty}^{0}\Phi(\theta+\psi)\cdot\exp(-iq\pi\psi/\omega)d\psi \tag{3.23}$$

The $E(\theta)$ term is now a function of the angular variable θ, which can be treated as being continuous. Similarly, $E(\theta^{(m)})$ term is now a function of the angular variable $\theta^{(m)}$ only. Parameter l, can also be extended to continuous values if it is written with the aid of (3.19) as

$$l=\frac{\theta^{(l)}-\theta}{2\omega} \tag{3.24}$$

Now, by using (3.23)-(3.24), equation (3.16) takes the form

$S(\theta^{(m)})-S(\theta)=$

$$-\frac{1}{2}\Phi(\theta^{(m)})+\frac{1}{2\omega}\int_{\theta_c}^{\theta^{(m)}}\Phi(\hat{\theta}^{(m)})d\hat{\theta}^{(m)}-\frac{q\pi\theta^{(m)}}{\omega}+\frac{\pi\theta^{(m)}}{2\omega}+E(\theta^{(m)})+\frac{1}{2}\Phi(\theta)-\frac{1}{2\omega}\int_{\theta_c}^{\theta}\Phi(\hat{\theta})d\hat{\theta}+\frac{q\pi\theta}{\omega}-\frac{\pi\theta}{2\omega}-E(\theta) \tag{3.25}$$

and finally, by separating terms depending on $\theta^{(m)}$ only, from terms depending on θ only we get the formal solution for $S(\theta)$ as:

$$S(\theta)=-\frac{1}{2}\Phi(\theta)+\frac{1}{2\omega}\int_{\theta_c}^{\theta}\Phi(\hat{\theta})d\hat{\theta}-\frac{q\pi\theta}{\omega}+\frac{\pi\theta}{2\omega}+E(\theta) \tag{3.26}$$

In (3.26), θ_c can be any arbitrary angle but when calculating the integral (3.3), it is convenient to use the critical angle θ_c, for total internal reflection on the bottom surface

$$\cos\theta_c=n_{cl}/n_{co} \tag{3.27}$$

The $E(\theta)$ term in (3.26) is, as we will prove in 3.2.3, very small compared to the rest of the terms and as a first order approximation, it can be ignored. We refer to $E(\theta)$ as the error term in the following.

3.2.2 Analytical continuation of phase function

The spectral integral (3.3) involves the phase function $\Phi(\theta)$, through (3.10) and (3.26). However, $\Phi(\theta)$ contains branch-points, which do not permit direct integration over the entire contour c. This problem can be overcome by analytically continuing the phase function $\Phi(\theta)$ so that the integral in (3.3) is defined everywhere on c. We proceed by explaining how to achieve this analytical continuation.

The phase function $\Phi(\theta)$ is given from (3.6) and (3.7) and has a branch-point due to the numerator, when its argument equals to the critical angle for reflection on the upper surface θ_c. Note that due to the symmetry of the sin functions in (3.6) around π, the point π-θ_c is also a branch point of $\Phi(\theta)$. Around $\theta \rightarrow \theta_c$, $\Phi(\theta)$ has a first order Taylor expansion, which is written by using (3.27) in the form:

$$\begin{aligned}\Phi(\theta)\big|_{\theta\to\theta_c} &= 2\arctan\left[i\frac{n_2\sin\dot{\theta}}{n_1\sin\theta}\right]\Bigg|_{\theta\to\theta_c} = 2\arctan\left[-\frac{\sqrt{\cos^2\theta-\cos^2\theta_c}}{\sin\theta}\right]\Bigg|_{\theta\to\theta_c} \\ &\cong -2\frac{\sqrt{\cos^2\theta-\cos^2\theta_c}}{\sin\theta} \cong -2\sqrt{2\cot\theta_c}\cdot\sqrt{\sin\frac{1}{2}(\theta_c-\theta)} \\ &\cong -2\sqrt{2\cot\theta_c}(\theta_c-\theta)^{1/2} \quad a_o>0,\ \theta\to\theta_c\end{aligned} \tag{3.28}$$

It is the square root function $(\theta_c - \theta)^{1/2}$ in (3.28), which is responsible for the discussed branch-point as $\theta \rightarrow \theta_c$. Analytical continuation of $\Phi(\theta)$ close to $\theta = \theta_c$ is achieved by considering instead, the function $\Phi(\theta)$ on a hemi-circle with infinitely small radius which passes from $\mathrm{Re}(\theta) < \theta_c$ to $\mathrm{Re}(\theta) > \theta_c$ in a clockwise manner as shown in Fig. 3-3. The right branch over which $\Phi(\theta)$ should be defined is the one that forces it to be real and negative for $\theta < \theta_c$, and positive imaginary for $\theta > \theta_c$. This establishes the correct physical behaviour of the reflection coefficient which should connect incident and reflected waves with a negative phase shift for $\theta < \theta_c$ (Goos-Hänchen shift) and with an attenuation coefficient for $\theta > \theta_c$ (Fresnel loss).

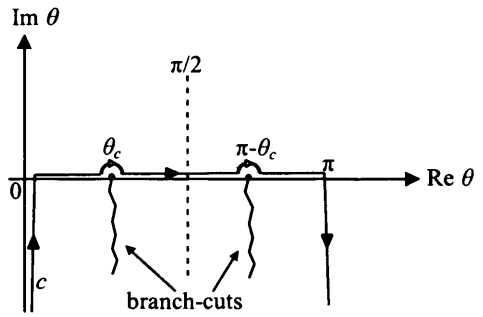

Fig. 3-3. Integration contour c, and analytical continuation of the phase function $\Phi(\theta)$, in the complex θ, domain.

3.2.3 Evaluation of Error Terms

This section provides an approximation of the error term $E(\theta)$ involved in (3.26). Two cases need to be distinguished:

I) Critical angle is larger than θ, ($\theta<\theta_c$):

In this region $E(\theta)$ is analytic and since it does not involve any singularities or branch-points, the error is according to appendix B

$$E(\theta) \approx \mathrm{O}(\omega) \tag{3.29}$$

where the symbol O(ω) means that the error is of order ω

II) Critical angle is smaller than θ, ($\theta>\theta_c$) :

In the view of the analytical continuation of $\Phi(\theta)$ (Fig. 3-3), the second integral in (3.23) might traverse the branch-point in which case we need the inclusion of a branch-cut integral. The result of the integral in (3.23) by the steepest descent method [3.10] is

$$E(\theta) \cong -a_o \omega^{1/2} \sum_{q=1}^{\infty} e^{iq\pi/4} \frac{2\sqrt{\pi}}{(q\pi)^{3/2}} + \mathrm{O}(\omega) \tag{3.30}$$

since the geometric series in (3.30) is definitely convergent (the power of q in the denominator is larger than 1) we can write as a total estimate for the error

$$E(\theta) \approx \mathrm{O}(\omega^{1/2}) \tag{3.31}$$

As a consequence of (3.29) and (3.31), we see that the error $E(\theta)$, is O(ω) if the critical angle is smaller than the angle of incidence while it is O($\omega^{1/2}$) if the critical angle is larger. However, we emphasize that in both cases the error goes ***uniformly*** to zero as

$\omega \rightarrow 0$, and so for shallow tapers as the ones we are considering here, the error is negligible compared to the rest of the terms in (3.36).

3.2.4 Saddle point approximation and adiabatic modes

In this section, we asymptotically calculate the spectral integral (3.3) with the saddle-point method [3.10]-[3.11]. The calculation of the spectral integral (3.3) furnish the adiabatic modes that propagate in the taper, as we will see.

Combining (3.5), (3.10), and (3.26) we for get the amplitudes of the upward and downward propagating plane waves

$$u^{\pm}(x,\theta_o) = \exp\left[iR(\theta_o) \mp \frac{1}{2}\Phi(\theta_o) \right] \cdot \exp\left[-iq\pi\theta_o / \omega \right] \tag{3.32}$$

$$R(\theta_o) = \frac{1}{2\omega}\int_{\theta_c}^{\theta} \Phi(\hat{\theta}) d\hat{\theta} + \frac{\pi\theta}{2\omega} \tag{3.33}$$

Note that in (3.32) and (3.33) we ignored the error term $E(\theta)$, included in (3.26), as a first order approximation for the amplitudes $u^{\pm}$, since we are only considering very swallow angles $\omega \sim 0$ for which $E(\theta) \rightarrow 0$ as we showed in the previous section. Now, by combining (3.3) with (3.32) - (3.33) we get for the upward and downward propagating fields inside the taper

$$V^{\pm}(r,\gamma) = \int_c \exp[\, iQ^{\pm}(r,\gamma;\theta)] \cdot \exp\left[-iq\pi\theta / \omega \right] d\theta \tag{3.34}$$

with

$$Q^{\pm}(r,\gamma;\theta) = R(\theta) \mp \frac{1}{2}\Phi(\theta) + kr\cos(\theta \pm \gamma) \tag{3.35}$$

The integral in (3.34) can be asymptotically evaluated by the steepest descent method, (see Appendix C for a brief review of the method) as $\omega \rightarrow 0$. This is because, both exponents in (3.34) express high frequency oscillating terms as $\omega \rightarrow 0$, since they both contain terms depending on $1/\omega$, and therefore, are amended to asymptotic analysis. According to the steepest descent method, we only need to consider the leading order Taylor expansion (with respect to the asymptotic parameter $1/\omega$) of the terms in the exponents, for a first order approximation of the integral (3.34). Thus, if

$$Q_o^{\pm}(r,\gamma;\theta) = \lim_{\omega \rightarrow 0}\left[\omega Q^{\pm}(r,\gamma;\theta) \right] \tag{3.36}$$

so that for $\omega \rightarrow 0$

$$Q^{\pm}(r,\gamma;\theta) = \omega^{-1}Q_o^{\pm}(r,\gamma;\theta) + \mathrm{O}(1) \tag{3.37}$$

then the leading order Taylor approximation of $Q^{\pm}(r,\gamma;\theta)$ is the $Q_o^{\pm}(r,\gamma;\theta)$ term and the saddle-points of the integral in (3.34) are calculated as solutions of

$$\frac{\partial Q_o^{\pm}(r,\gamma;\theta)}{\partial\theta} = q\pi \tag{3.38}$$

The asymptotic behaviour of the waveguide geometry for $\omega\rightarrow 0$, necessary for the asymptotic calculation of the spectral integral, is explained with the aid of Fig. 3-4. For a given observation point A, inside the taper, the upper boundary S_2 rotates about A, until for $\omega = 0$ the two boundaries S_1 and S_2 become parallel. As the two boundaries S_1 and S_2 become parallel to each other, the local width of the waveguide w, at the point of observation A remains constant.

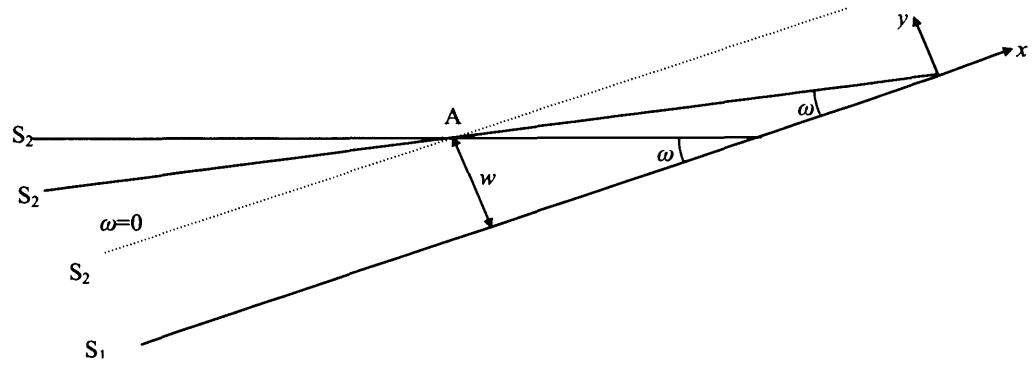

Fig. 3-4. Asymptotic behaviour of the taper as $\omega\rightarrow 0$. For a given point A inside the taper, boundaries of the waveguide tend to become parallel as $\omega\rightarrow 0$, while their separation is kept constant and equals to the ***local*** width of the cross-section w.

Under these assumptions, we get for $Q_o^{\pm}$ by combining (3.32), (3.33) and (3.35)

$$Q_o^{\pm}(x,y;\theta) = -kn_{co}h\cos(\theta) + \frac{1}{2}\int_{\theta_c}^{\theta_o}\Phi(\hat{\theta})d\hat{\theta} + \frac{\pi\theta}{2} = Q_o(x,y;\theta) \tag{3.39}$$

In (3.39) we omitted the ± subscript for Q_o since it takes the same form for both upward and downward waves and we need not distinguish between them any more. The saddle points θ_q are then determined from (3.38) and (3.39) as solutions of the transcendental equation

$$-kn_{co}h\sin(\theta_q) + \frac{1}{2}\Phi(\theta_q) + \frac{\pi}{2} = q\pi \tag{3.40}$$

Equation (3.40) coincides precisely with the eigenvalue equation of a normal (non-tapered) slab waveguide, whose width equals to the local width w, of the tapered waveguide at the point of observation A. Therefore, the saddle-points θ_q correspond to the angles that the modes of an ordinary slab waveguide with width w, would have. This is an important observation, since it connects the field in the tapered waveguide to the modes of a local non-tapered waveguide, (local modes). Similar associations between tapered and local waveguides have been made in other theories as well, such as the coupled mode theory for example, [3.9]. Also note that due to the symmetry of the functions in (3.40) about π, if θ_q is a saddle-point, then $\pi-\theta_q$ is a saddle-point as well.

The function $V(r,\gamma)$, (3.4) defined through (3.34), (3.35), (3.33) and (3.6), has been termed as the tapered waveguide intrinsic mode by Arnold and Felsen, [3.1]-[3.8]. It consists of a combination of two wavefunctions (3.34), one upward propagating wavefunction $V^+(r,\gamma)$ and one downward propagating $V^-(r,\gamma)$. Each wavefunction $V^+(r,\gamma)$ and $V^-(r,\gamma)$, has been constructed as a linear combination of elementary solutions of the wave equation (plane waves) in the core region, (3.3), all of which satisfy the waveguide boundary conditions on the bottom (3.5) and top boundaries (3.8). Because each elementary wave of the intrinsic mode satisfies the boundary conditions in the waveguide, the entire intrinsic mode $V(r,\gamma)$ satisfies the boundary conditions on the bottom and top boundaries as well. Field propagation inside the tapered waveguide is therefore properly described by the intrinsic mode, which in its (3.3) form is valid for both slow (ω~0) and fast tapers (ω>>0). However, it is only when we consider slow tapers (ω~0) that the relationship between the intrinsic modes and the local waveguide modes, starts being revealed, (3.40), as both share the same eigenvalue problem. This relationship between the intrinsic mode and the local waveguide modes is further explored in the next when we proceed to the asymptotic calculation of the intrinsic mode integral (3.34).

The saddle-point method for asymptotically calculating the intrinsic mode integral (3.34), depends on the deformation of the integration contour c, along the steepest descent path c', of $Q(r,\gamma;\theta)$, Appendix C. The deformed contour is shown in Fig. 3-5. The method of saddle points for approximating oscillating integrals is thoroughly

described in [3.10]-[3.11].

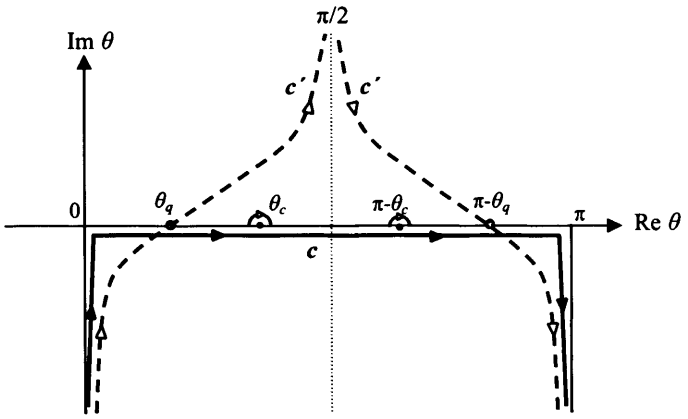

Fig. 3-5. Original contour c (solid line), and deformed contour along the steepest descent c' (dashed line), for a specific saddle point θ_q and its reciprocal $\pi-\theta_q$, in the angular θ domain. As can be seen contour c' traverses the two saddle points and asymptotically approaches the line $\mathrm{Re}\,\theta=\pi/2$.

In order to proceed to the integral approximation we need to differentiate the following three cases, according to the position of the saddle-point θ_q, in Fig. 3-5.

A) $0<\theta_q<\theta_c$. This case describes the intrinsic mode propagation in the waveguide region where it is well guided.

This case can be treated by the steepest descent method with one first-order saddle point, (Appendix C, equation C8). The result of the steepest descent integration of (3.34) is in this case

$$V^{\pm}(r,\gamma)\cong\sqrt{\pi\omega}e^{-i\pi/4}\cdot\exp[\pm i(q-1/2)\pi]\cdot\exp[\mp ikn_{co}(h-r\sin\gamma)\sin\theta_q]A_q(r,\omega)e^{-iS_q(r,\omega)} \tag{3.41}$$

The amplitude term of the intrinsic mode $A_q(r,\omega)$ is given by

$$A_q(r,\omega)=\left[\frac{1}{2}\left(kn_{co}h\cos\theta_q+\frac{1}{2}\frac{d\Phi(\theta)}{d\theta}\bigg|_{\theta=\theta_q}\right)\right]^{-1/2} \tag{3.42}$$

and the phase factor of the intrinsic mode $S_q(r,\omega)$ is given by

$$S_q(r,\omega)=\frac{1}{\omega}\left[Q_o(r,\gamma;\theta_q)-q\pi\theta_q\right] \tag{3.43}$$

The total field in the tapered waveguide is finally found by combining (3.41) and (3.4) as

$$V(r,\gamma) \cong -2\sqrt{\pi\omega}e^{-i\pi/4}\cdot e^{iq\pi}\sin[kn_{co}(h-r\sin\gamma)\sin\theta_q]A_q(r,\omega)e^{-iS_q(r,\omega)} \quad (3.44)$$

which, can be converted back to the original (x,z) coordinate system with the aid of the connection relationship $(x,z) = (r\sin\gamma, -r\cos\gamma)$, as

$$V(x,z) \cong -2\sqrt{\pi\omega}e^{-i\pi/4}\cdot e^{iq\pi}\sin[k_{xq}(h-x)]A_q(x,z)e^{-iS_q(x,z)} \quad (3.45)$$

In (3.45), we used the definition for the transverse wavenumber k_{xq} in x

$$k_{xq} = kn_{co}\sin\theta_q \quad (3.46)$$

The amplitude of the intrinsic mode $A_q(x,z)$, (3.42) can be expressed in the Cartesian system with the aid of (3.6)-(3.7) as

$$A_q(x,z) = \left[\frac{\beta_q h}{2}\left(1-\frac{1}{h\eta_q^2}\right)\right]^{-1/2} \quad (3.47)$$

In (3.46), we made use of the propagation constant β_q in the z-direction, and the wavenumber η_q, in the cladding in the x-direction defined as

$$\beta_q = kn_{co}\cos\theta_q,\ \eta_q^2 = k^2n_{cl}^2 - \beta_q^2 \quad (3.48)$$

The phase of the intrinsic mode $S_q(x,z)$, (3.43) in the Cartesian coordinates can be written with the aid of (3.39) as

$$S_q(x,z) = \frac{1}{\omega}\left[Q_o(x,z;\theta_q) - q\pi\theta_q\right] = \frac{1}{\omega}\left[-kn_{co}h\cos\theta_q + \frac{1}{2}\int_{\theta_c}^{\theta_q}\Phi(\theta')d\theta' + \frac{\pi\theta_q}{2} - q\pi\theta_q\right]$$
$$\cong kz\cos\theta_q + \frac{1}{2\omega}\int_{\theta_c}^{\theta_q}\Phi(\theta')d\theta' + \frac{\pi\theta_q}{2\omega} - \frac{q\pi\theta_q}{\omega} \quad (3.49)$$

Note that in (3.48) we used the approximation for small angles ω, $\tan\omega \cong \omega \rightarrow \frac{h}{\omega} \cong z$.

Differentiating (3.48) with respect to z (θ_q is also a function of z) gives

$$\frac{\partial S_q(x,zy)}{\partial z} \cong kn_{co}\cos\theta_q + \left(kn_{co}z\sin\theta_q + \frac{\Phi(\theta_q)}{2\omega} + \frac{\pi}{2\omega} - \frac{q\pi}{\omega}\right)\frac{\partial\theta_q}{\partial z} = kn_{co}\cos\theta_q = \beta_q \quad (3.50)$$

Due to the saddle-point condition (3.40), the argument in the parenthesis in (3.49) is 0, and so the phase $S_q(x,z)$ of the intrinsic mode becomes

$$S_q(x,z) = \int^{z} \beta_q(z')dz' \tag{3.51}$$

The final form of the first order asymptotic approximation of the intrinsic mode (3.45) therefore is by combining (3.45), with (3.46) and (3.50)

$$V(x,z) \cong -2\sqrt{\pi\omega}e^{-i\pi/4} \cdot e^{iq\pi}\left[\frac{\beta_q h}{2}\left(1-\frac{1}{h\eta_q^2}\right)\right]^{-1/2} \sin[k_{xq}(h-x)]e^{-i\int^{z}\beta_q(z')dz'} \tag{3.52}$$

Equation (3.51) is a very important relationship. It has been proved in [3.4], that (3.51), which is the first order approximation of the intrinsic mode (3.34), (3.4), ***agrees precisely*** with the adiabatic mode calculated by the coupled mode theory [3.9]. The physical interpretation of the adiabatic mode (3.51) is the following: At a given point of observation, the sin term in (3.51) corresponds to the q-th modal profile of a normal (non-tapered) slab waveguide with width w. As the mode propagates towards the apex of the taper its phase (3.50), changes according to the local mode propagation constant to reflect the change to the local width w, of the waveguide. Therefore, in contrast to the non-tapered slab modes, whose profile and propagation constant remain unchanged throughout the entire waveguide, the adiabatic mode profile and propagation constant evolve as the mode propagates inside the waveguide to adapt to the local waveguide environment. The amplitude of the adiabatic mode is not constant as well but instead it also depends on the local waveguide parameters, as seen in (3.46), in order to keep the power flow through a waveguide cross-section as the adiabatic mode propagates towards the apex constant and so for the conservation of energy requirement to be satisfied.

B) $\theta_q \cong \theta_c$. This case describes the adiabatic mode propagation as it approaches its cut-off. In other words, this region corresponds to the transition of a bound mode to a radiating mode.

The saddle-points θ_q calculated in (3.40) could approach arbitrarily close the critical angle θ_c as the waveguide width decreases. The critical angle θ_c, however, is a branch-

point of the phase function $\Phi(\theta)$, (3.6), and the asymptotic approximation of the intrinsic mode described in the previous section fails in this region. However, the intrinsic mode in (3.34) is still valid due to the analytical continuation (3.28), of the phase function described in section 3.2.2. In order to calculate the intrinsic mode behaviour as we approach cut-off more refined asymptotic approximations, than the ones described in the previous section, are required.

We first perform the variable change

$$t = (\theta_c - \theta)^{1/2} \tag{3.53}$$

with the branch of the square root function selected in accordance with our discussion in section 3.2.2. The transformation (3.53) has the effect of eliminating the branch-point and replacing it with a second saddle-point. This is easily confirmed by writing

$$\frac{\partial[Q_o(x,z;\theta(t)) - q\pi\theta(t)]}{\partial t} = \frac{\partial[Q_o(x,z;\theta) - q\pi\theta]}{\partial\theta}\cdot\frac{\partial\theta}{\partial t} = -2t\frac{\partial[Q_o(x,z;\theta) - q\pi\theta]}{\partial\theta} \tag{3.54}$$

and since the saddle-points in the new t-domain are determined by the relationship

$$\frac{\partial[Q_o(x,z;\theta(t)) - q\pi\theta(t)]}{\partial t} = 0 \tag{3.55}$$

we see that apart from the original saddle-point θ_q we have the addition of a new one at $\theta=\theta_c$ or equivalently at $t = 0$. In this way, the phase function $\Phi(\theta)$, given by (3.28) for $\theta\cong\theta_c$ is transformed to an analytic function and the asymptotic integration in (3.34) can now be carried out by considering the influence of two confluent saddle-points, in contrast to the single saddle-point in (3.45)-(3.48). A uniform asymptotic evaluation of the integral (3.34) is in this case obtained by using the Chester-Friedman-Ursell method, [3.10]-[3.11]. According to this method, we associate Q_o with a third order polynomial as

$$\omega^{-1}[Q_o(x,z;\theta(t)) - q\pi\theta(t)] = f_o - f_1\frac{s^2}{2} + i\frac{s^3}{3} = \tau(s) \tag{3.56}$$

in the new s-domain the two saddle-points s_1 and s_2 are given by

$$\frac{\partial\tau(s)}{\partial s} = s(-f_1 + is) = 0 \Rightarrow \begin{cases} s_1 = 0 \\ s_2 = -if_1 \end{cases} \tag{3.57}$$

now without loss of generality, we assume that s_1 corresponds to the saddle-point with $t = 0$ ($\theta=\theta_q$) and s_2 corresponds to the saddle point with $\theta=\theta_q$ and so, with the help of (3.56)

and (3.57) we can write

$$\omega^{-1}\left[Q_o(x,y;\theta(t=0))-q\pi\theta(t=0)\right]=\tau(s_1)=f_o \tag{3.58}$$

$$\omega^{-1}\left[Q_o(x,y;\theta(t)=\theta_q)-q\pi(\theta(t)=\theta_q)\right]=\tau(s_2)=f_o+\frac{1}{6}f_1^3 \tag{3.59}$$

The coefficient f_o is given directly by (3.58), while f_1 can be calculated from (3.58) and (3.59) as

$$f_1^3=6\omega^{-1}\left[Q_o(x,z;\theta(t=0))-Q_o(x,z;\theta_q)-(q\pi\theta_c-q\pi\theta_q)\right] \tag{3.60}$$

Calculation of the intrinsic mode $V^{\pm}$ in (3.34) with the steepest descent method involves the Airy functions this time, which are understood as transition functions. The result of the steepest descent integration for $\theta_q\cong\theta_c$ is [3.1]-[3.2]

$$V^{\pm}(x,z)\cong C_q(x,z)\exp[2i\zeta^3/3]\exp[-iq\pi\theta_c/\omega]\cdot\exp(2i\zeta^3/3)\left(Ai'\left(\zeta^2e^{i\pi/3}\right)+\zeta e^{i\pi/6}Ai\left(\zeta^2e^{i\pi/3}\right)\right) \tag{3.61}$$

with

$$C_q(x,z)=-8\pi e^{-i5\pi/12}\zeta\omega\left(\frac{d^2}{dt^2}(Q_o(x,z)-q\pi\theta)\right)^{-1}\Bigg|_{t=0} \tag{3.62}$$

and

$$\zeta=\omega^{-1/3}\left\{\frac{3}{4}\left[Q_o(x,z;\theta(t=0))-Q_o(x,z;\theta_q)-(q\pi\theta_c-q\pi\theta_q)\right]\right\}^{1/3} \tag{3.63}$$

Equation (3.63) can be significantly simplified. Firstly, for $\theta_{oq}\cong\theta_c$ the eigenvalue equation (3.40) takes the form

$$-kn_{co}h\sin(\theta_q)-\sqrt{2\cot\theta_c}(\theta_c-\theta_q)^{1/2}+\frac{\pi}{2}=q\pi \tag{3.64}$$

where in (3.64) we replaced $\Phi(\theta)$ with its value close to θ_c (3.28). On the other hand, when the saddle-point θ_q coincides exactly with the critical angle θ_c, ($\theta_q=\theta_c$), then (3.64) becomes

$$-kn_{co}h_c\sin(\theta_c)+\frac{\pi}{2}=q\pi \tag{3.65}$$

with h_c the local critical height of the waveguide where the condition $\theta_q=\theta_c$ is met. By combining (3.64) with (3.65) we get

$$(\theta_c - \theta_q)^{1/2} \cong \frac{1}{\sqrt{2\cot\theta_c}} kn_{co}(h-h_c)\sin\theta_c \tag{3.66}$$

where we used the fact that $\sin\theta_q \cong \sin\theta_c$ for $\theta_q = \theta_c$ in (3.66). Finally, by combining (3.63) with (3.66) we derive the simple expression

$$\zeta = XY^{-2/3} \tag{3.67}$$

$$X = kn_{co}(h-h_c)\sin\theta_c, \quad Y = 2\omega^{-1}\sqrt{2\cot\theta_c} \tag{3.68}$$

In deriving (3-61), we used the term "transition functions" for the Airy functions. This is because in the waveguide region just before cut-off, ($\theta_q \cong \theta_c$ with $\theta_q < \theta_c$), the argument of the Airy functions ζ^2 (defined in (3.63)), is negative. However, Airy functions with negative arguments correspond to oscillating fields [3.12]. On the other hand, in the region just after cut-off ($\theta_q \cong \theta_c$ with $\theta_q > \theta_c$) the argument of the Airy functions ζ^2, becomes complex with a positive real part. Airy functions with positive real part represents fields, whose amplitudes are diminishing as they propagate [3.12], as should happen for modes beyond cut-off, which radiate into the cladding. Equation (3.61) therefore, expresses the transition of the adiabatic mode from the region $\theta_q < \theta_c$, where it was well-guided, (3.44), to the region where it becomes cut-off (3.61). This is an important achievement of the intrinsic mode theory as most coupled mode theories fail in this region.

C) $\theta_q > \theta_c$. This case describes the intrinsic mode propagation beyond cut-off, where the mode radiates into the cladding.

The phase-function $\Phi(\theta)$ given by (3.6), becomes imaginary in this case in order to express the Fresnel loss of the plane-wave reflection on the bottom boundary. As a result, the saddle-points θ_{oq} calculated by the eigenvalue equation (3.40), cease to be real and move to the complex angular domain. The integration contour for the approximate calculation of the spectral integral (3.34) is shown in Fig. 3-6. The steepest descent path traverses the branch-cut of the phase function $\Phi(\theta)$ in this case and, therefore, we need to take into account the influence of an additional branch-cut integral around the branch-point θ_c, (Appendix C, equations C28 - C36). Therefore, apart from the main integral

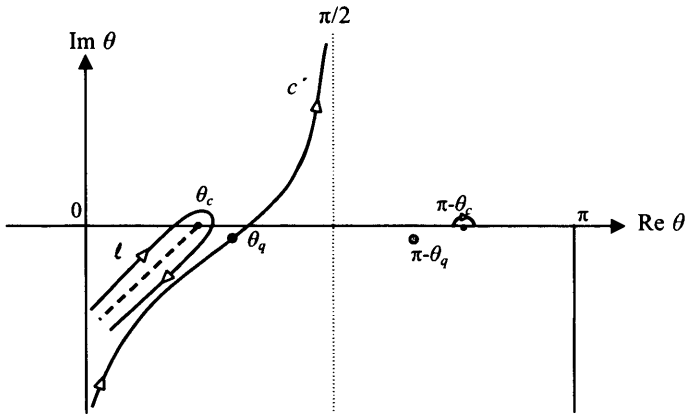

Fig. 3-6. Integration contour along the steepest descent path c' when the saddle-point θ_q is larger than the critical angle θ_c. Contour is seem to interfere with the branch point θ_c, in which case a branch-cut integral ℓ is required.

along the steepest descent contour c, we need to calculate another integral over the contour ℓ, which embraces the branch-point θ_c. These integrals can be treated with the aid of the same transformation (3.53), as in the case where modes were approaching cut-off. However, the main difference in the present case where $\theta_q > \theta_c$ from the $\theta_q \cong \theta_c$ case, is that the two resulting saddle-points (at θ_q and θ_c), generated after the transformation (3.53) can be considered to be well separated from each other and so each one of them makes a distinct contribution (as opposed to one joint contribution from the two confluent saddle-points in the $\theta_q \cong \theta_c$ case). The asymptotic solution for the intrinsic mode field $V(r,y)$ in (3.34) can be written in the $\theta_q > \theta_c$ case as [3.1]-[3.2]

$$V(x,z) \cong -2\sqrt{\pi\omega}e^{-i\pi/4} \cdot e^{iq\pi} A_q(x,z)\sin[k_{xq}(h-x)]e^{-iS_q(x,z)} + v_1(x,z) \qquad (3.69)$$

with

$$v_1(x,z) \approx \sqrt{2\pi\cot\theta_c}\,\omega^{3/2}e^{-i\pi/4}\exp\left(i\omega^{-1}[Q_o(x,z;\theta_c) - q\pi\theta_c]\right)\cdot(kn_{co}\sin\theta_c)^{-5/2} \qquad (3.70)$$

The intrinsic mode, (3.69) consists of two parts in this case. The first part is almost identical to the case were the intrinsic mode was bound (3.45). In reality the amplitude $A_q(x,z)$ and phase functions $S_q(x,z)$ are still given by the same equations ((3.46) and (3.49) respectively), as for the bound mode. However, there is a significant difference between the bound mode case $\theta_q < \theta_c$, and the $\theta_q > \theta_c$ case that we are examining now.

As we already mentioned the saddle-points move to the angular complex domain. In this case the phase function $S_q(x,z)$, which is defined in (3.49)-(3.50), becomes complex as well. Without giving the details of the calculations, it has been proved, [3.1]-[3.2], that the phase function can be written as $\partial S_q(x,z)/\partial z = \beta_{qr} - i\alpha_{qr}$, $\beta_{qr} > 0$, $\alpha_{qr} > 0$. The real part, β_{qr}, is related to the phase of the mode as it propagates. However, the imaginary part α_{qr} corresponds to the rate of power radiating from the core into the cladding, since our mode is beyond its cut-off. The second term $v_1(x,z)$, in (3.69), corresponds to the contribution from the branch-point and describes the phenomenon of "lateral waves" [3.1]-[3.2], which represents energy that radiates almost parallel to the waveguide bottom boundary.

3.3. COUPLED MODE THEORY FOR RECTANGULAR WAVEGUIDES

3.3.1 Coupled Mode Equations

In this section, we briefly review Marcuse's coupled mode theory, which describes the interaction between bound and radiation modes, and the coupled power theory, which yields the propagation loss, the equilibrium distance and the modal distribution for multimode waveguides under the influence of sidewall roughness. We refer the reader who wants a more detailed description of these theories to [3.13]-[3.20]. Coupled mode and coupled power theories are suitable for analyzing continuous wave (cw) light propagation in waveguides with randomly deformed core boundaries, such as the one in Fig. 3-7.

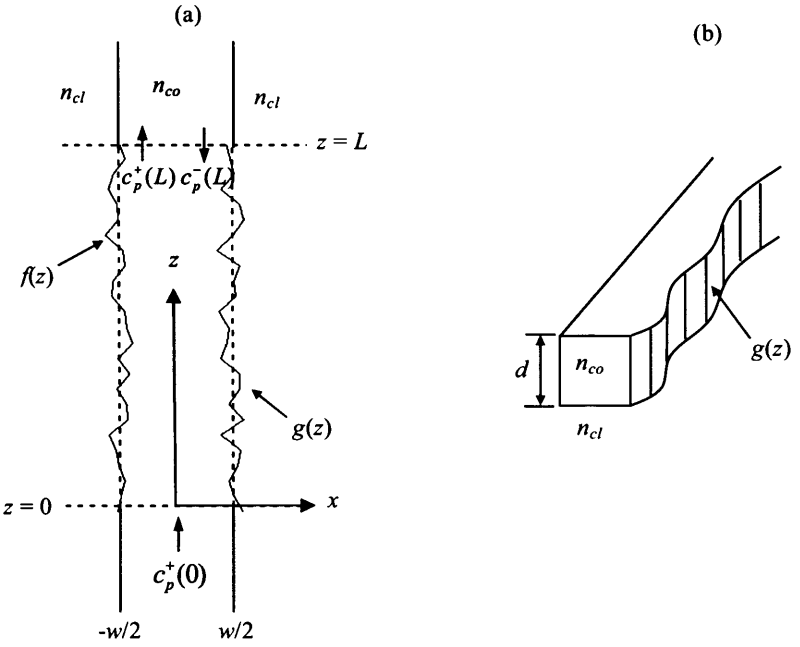

Fig. 3-7. (a) Top-view of a rectangular waveguide with randomly perturbed core boundaries. Dashed-line corresponds to the boundaries of the ideal waveguide. The structure we are investigating is a rectangular waveguide a part of which has been randomly deformed. The distorted piece extends over a length L. The distortion function of its left sidewall is a random distribution $f(z)$ while this of its right wall is the random distribution $g(z)$. Both distributions are statistically independent. (b) Angled-view of the randomly deformed waveguide. The 1D deformation, $g(z)$, affects the width of the waveguide width, while its thickness d remains unchanged.

While the coupled mode theory provides full information about how both the amplitude and the phase of the guided modes evolve as they propagate in the waveguide, the

coupled power theory deals only with their power. In highly multimode waveguides though, it is quite rare that the information about the phase of the large number of modes is of any use, and therefore the coupled power method is preferable for analyzing them. The major outcome of the coupled power method is that the distribution of (average) power between the various bound modes gradually converges to a steady state. This steady state distribution (also called equilibrium distribution) is *independent* from the excitation field at the input of the waveguide and it depends only on the statistical properties of the sidewall perturbation. It is important to note that power is still exchanged between the modes at equilibrium and the equilibrium distribution refers to the average power (averaged over the propagation length) in the modes only. The distance that modes need to travel before reaching the steady state is called the equilibrium length. Once equilibrium is reached, a unique propagation loss can be assigned to the waveguide, due to coupling of bound to radiation modes.

The theory starts by writing the Maxwell equations for the electric $\boldsymbol{E}$ and magnetic $\boldsymbol{H}$ field for a waveguide with an imperfect refractive index distribution $n = n(x,y,z)$ that expresses the sidewall roughness

$$\nabla \times \boldsymbol{H} = i\omega\varepsilon_o n^2 \boldsymbol{E} \tag{3.71}$$

$$\nabla \times \boldsymbol{E} = -i\omega\mu_o \boldsymbol{H} \tag{3.72}$$

where the bold in (3.71)-(3.72) denotes that we are dealing with vectors.

The longitudinal components E_z and H_z can be expressed as a function of the transverse components $\boldsymbol{E}_t$ and $\boldsymbol{H}_t$ as

$$\boldsymbol{E}_z = (1/i\omega\varepsilon_o n^2)\nabla_t \times \boldsymbol{H}_t \tag{3.73}$$

$$\boldsymbol{H}_z = -(1/i\omega\mu_o)\nabla_t \times \boldsymbol{E}_t \tag{3.74}$$

with the transverse curl operator defined as $\nabla_t = \hat{x}\partial/\partial x + \hat{y}\partial/\partial y$, $\hat{x}$ the unity vector in x and $\hat{y}$ the unity vector in y. If we expand (3.71)-(3.72) into transverse and longitudinal field components and replace the longitudinal components with the transverse components from (3.73)-(3.74) we obtain

$$-(1/i\omega\mu_o)\nabla_t \times (\nabla_t \times \boldsymbol{E}_t) + \hat{z} \times \partial \boldsymbol{H}_t / \partial z = i\omega\varepsilon_o n^2 \boldsymbol{E}_t \tag{3.75}$$

$$(1/i\omega\varepsilon_o n^2)\nabla_t \times ((1/n^2)\nabla_t \times \boldsymbol{H}_t) + \hat{z} \times \partial \boldsymbol{E}_t / \partial z = -i\omega\mu_o \boldsymbol{H}_t \tag{3.76}$$

Since (3.75)-(3.76) hold for any general refractive index distribution, $n = n(x,y,z)$, they also hold for an ideal waveguide with refractive index distribution, $n_o = n_o(x,y)$, (note that a perfect waveguide's index is independent of z). However, the field inside an ideal waveguide is expressed by its modes, which have a z dependence of the form $e^{-i\beta z}$ (for forward propagating modes). If the transverse electric and magnetic fields for a mode are $\mathbf{E_{qt}}$ and $\mathbf{H_{qt}}$ respectively (where the index q refers to the q–th mode) then (3.75)-(3.76) are rearranged as

$$-(1/i\omega\mu_o)\nabla_t \times \left(\nabla_t \times \mathbf{E}_{qt}\right) - i\beta_q \left(\hat{z} \times \partial \mathbf{H}_{qt} / \partial z\right) = i\omega\varepsilon_o n_o^2 \mathbf{E}_{qt} \tag{3.77}$$

$$(1/i\omega\varepsilon_o n^2)\nabla_t \times \left((1/n_o^2)\nabla_t \times \mathbf{H}_t\right) - i\beta_q \left(\hat{z} \times \partial \mathbf{E}_{qt} / \partial z\right) = -i\omega\mu_o \mathbf{H}_{qt} \tag{3.78}$$

Equations (3.75)-(3.76) and (3.77)-(3.78) contain almost all of the information required for the coupled mode theory. The first two, (3.75)-(3.76), describe the transverse fields (and through (3.73)-(3.74) the longitudinal as well) for the perturbed waveguide while (3.77)-(3.78) describe the ideal modes of an unperturbed waveguide with exactly the same physical properties (but without the distortion) with the first. The coupled mode theory relies on connecting the perturbed to the unperturbed fields and by doing so, it evaluates how the modes of the ideal waveguide, which are completely independent from each other on the perfect waveguide, are coupled to each other as they propagate inside the imperfect waveguide. In order to connect perturbed and unperturbed fields we need two more sets of equations. In the first set of equations, the electric and magnetic transverse field components $\boldsymbol{E_t}$ and $\boldsymbol{H_t}$ in the perturbed waveguide are expressed as an expansion of the bound and the radiation modes of the ideal waveguide as

$$\mathrm{E}_t = \sum_{q=1}^{N_1} A_q \mathbf{E}_{qt}^{TE} + \int_0^{\infty} A_r \mathbf{E}_{rt}^{TE} + \sum_{q=1}^{N_1} A_q \mathbf{E}_{rt}^{TM} + \int_0^{\infty} A_r \mathbf{E}_{rt}^{TM} = \sum_q A_q \mathbf{E}_{qt} \tag{3.79}$$

$$\mathrm{H}_t = \sum_{q=1}^{N_2} B_q^{TE} \mathbf{H}_{qt}^{TE} + \sum \int_0^{\infty} B_r^{TE} \mathbf{H}_{rt}^{TE} + \sum_{q=1}^{N_2} B_q^{TM} \mathbf{H}_{qt}^{TM} + \sum \int_0^{\infty} B_r^{TM} \mathbf{H}_{rt}^{TM} = \sum_q B_q \mathbf{H}_{qt} \tag{3.80}$$

where in (3.79) $\boldsymbol{E_t}$ was expressed as a sum over the N_1 propagating TE-like ($\mathbf{E}_{qt}^{TE}$) and the N_2 propagating TM-like ($\mathbf{E}_{qt}^{TM}$) bound modes of the ideal waveguides plus an integral over the continuous spectrum of the TE-like ($\mathbf{E}_{rt}^{TE}$) and TM-like ($\mathbf{E}_{rt}^{TE}$) radiation modes. This expansion is possible since the set of bound and radiation modes of the ideal

waveguide is complete, and, therefore, any field (including the field in the perturbed waveguide) can be described by this set. The magnetic field $\boldsymbol{H}_t$ is expressed in a similar way in (3.80). Note that in order to simplify notation, we used a single sum symbolism in the third leg of (3.79)-(3.80). However, it is understood that the summation symbol this time refers to both, summation over propagation and integration over radiation modes, as well as summation over both types of polarization. In the same way, the single index q has now been expanded to include both propagation and radiation modes.

The second set of equations that we need to apply the coupled mode is the orthogonality condition of the ideal modes

$$\frac{1}{2}\int_{-\infty-\infty}^{+\infty+\infty}\left(\mathbf{E}_{pt}\times\mathbf{H}_{qt}^{*}\right)_z dxdy = s_q P\delta_{pq} \tag{3.81}$$

where in (3.81) $s_q = +1$ for forward and $s_q = -1$ for backward propagating modes, P is the normalized power flow (usually fields are normalized to $P = 1$), and δ stands for the delta Kronecker function in the case where we deal with bound modes and stands for the Dirac delta function when we deal with radiation modes. Upon substitution of the field modal expansions (3.79)-(3.80) into the imperfect waveguide wave equations (3.77)-(3.88), we obtain

$$\sum_q \left\{\left[\partial B_q/\partial z + i\beta_q A_q\right](\hat{z}\times\mathbf{H}_{qt}) - i\omega\varepsilon_o(n^2-n_o^2)A_q\mathbf{E}_{qt}\right\} = 0 \tag{3.82}$$

$$\sum_q \left\{\left[\partial A_q/\partial z + i\beta_q B_q\right](\hat{z}\times\mathbf{E}_{qt}) + (1/i\omega\varepsilon_o)B_q\nabla_t\times(n^{-2}-n_o^{-2})(\nabla_t\times\mathbf{H}_{qt})\right\} = 0 \tag{3.83}$$

We now take advantage of the orthonormality relation (3.81) by multiplying (3.82) with $\mathbf{E}_{pt}^{*}$ and (3.83) with $\mathbf{H}_{pt}^{*}$ and integrating over an infinite waveguide cross-section to obtain the coupled mode differential equations

$$\partial B_p/\partial z + i\beta_p A_p = 2\sum_q Z_{pq}A_q \tag{3.84}$$

$$\partial A_p/\partial z + i\beta_p B_p = 2\sum_q \zeta_{pq}B_q \tag{3.85}$$

The two coupling coefficients Z_{pq} and ζ_{pq} appearing in (3.84) and (3.85) take the following form

$$Z_{pq} = \frac{\omega\varepsilon_o}{4s_q P}\int_{-\infty-\infty}^{+\infty+\infty}(n^2-n_o^2)\mathbf{E}_{pt}^{*}\cdot\mathbf{E}_{qt}dxdy \tag{3.86}$$

$$\zeta_{pq} = \frac{\omega\varepsilon_o}{4s_q P}\int_{-\infty-\infty}^{+\infty+\infty}\int (n_o^2/n^2)(n^2 - n_o^2)\mathbf{E}_{pz}^* \cdot \mathbf{E}_{qz}\, dxdy \tag{3.87}$$

Although Z_{pq} and ζ_{pq} appear in a rather awkward form in (3.86) and (3.87), they can be considerably simplified for weekly guiding dielectric waveguides, as we will see in the following.

We now proceed to solve the system of differential equations (3.84)-(3.85) by applying a perturbation method. In the absence of coupling we have $Z_{pq} = \zeta_{pq} = 0$ and the solutions of (3.84) and (3.85) are simply

$$A_p^+ = c_p^+ \exp(-i\beta_p z), \quad A_p^- = c_p^- \exp(+i\beta_p z) \tag{3.88}$$

$$B_p^+ = A_p^+, \quad B_p^- = -A_p^- \tag{3.89}$$

where the subscript (+) corresponds to forward and the (–) to backward propagating modes and c_p are some constants corresponding to the amplitudes of the modes. Equations (3.88)-(3.89) have the plausible physical interpretation that, in the absence of coupling, each mode has a non-changing amplitude c_p, and phase that depends on its propagation constant β_p. An observation that helps with our perturbation method, is that in (3.88) and (3.89) the terms $A_p^{+,-}$ and $B_p^{+,-}$ are rapidly varying functions of z due to the presence of the exponent. However, the amplitude coefficients c_p are constants and this will serve as the basis of the perturbation method that will be used to solve (3.86)-(3.87). The form of the solutions in the uncoupled case (3.88)-(3.89), suggests that the variables A_p and B_p in (3.84) and (3.85) can be separated out to forward and backward propagating fields as

$$A_p = A_p^+ + A_p^-, \quad B_p = B_p^+ - B_p^- \tag{3.90}$$

We are now ready to apply our perturbation method to find the solutions of the couple mode equations (3.84)-(3.85), in the presence of weak coupling between the modes. We first consider the solutions of the coupled equations (3.84)-(3.85) as a perturbation of the uncoupled solutions (3.88)-(3.89) and we let the amplitude coefficients c_p to vary slowly (compared to the phase of the modes) with z as

$$A_p^+ = c_p^+(z)\exp(-i\beta_p z), \quad A_p^- = c_p^-(z)\exp(+i\beta_p z) \tag{3.91}$$

Then we substitute (3.90) and (3.91) into (3.84)-(3.85) and after some calculations [3.1]-

[3.8] we reach to the final form of the coupled mode equations

$$\partial c_p^+ / \partial z = \sum_q \left\{ Z_{pq}^{+,+} c_q^+ \exp\left[-i(\beta_q - \beta_p)z\right] + Z_{pq}^{+,-} c_q^- \exp\left[i(\beta_q + \beta_p)z\right] \right\} = 0 \tag{3.92}$$

$$\partial c_p^- / \partial z = \sum_q \left\{ Z_{pq}^{-,+} c_q^+ \exp\left[-i(\beta_q - \beta_p)z\right] + Z_{pq}^{-,-} c_q^- \exp\left[-i(\beta_q + \beta_p)z\right] \right\} = 0 \tag{3.93}$$

with $Z_{pq}^{(s_p,s_q)}$ (s_p, s_q = ±1) being the coupling coefficient between the p-th mode with propagation direction defined by s_p (s_p = + or s_p = -) and the q-th mode with direction defined by s_q, given by

$$Z_{pq}^{(s_p,s_q)} = s_p Z_{pq} + s_q \zeta_{pq} \tag{3.94}$$

3.3.2 Coupling Coefficients for Rectangular Waveguides

In this section we calculate the coupling coefficients $Z_{pq}^{(s_p,s_q)}$ of the coupled mode differential equations (3.92) and (3.93) for the specific case of the randomly deformed rectangular waveguide shown in Fig. 3-7. The deformation of the sidewalls of the waveguides is assumed to be of one dimension, which affects its width w, but not its thickness. In other words, we assume that $\partial n(x,y,z)/\partial y = 0$. The left waveguide wall is defined by the function $x(z) = -w/2 + f(z)$, while the right wall by the function $x(z) = -w/2 + g(z)$. Both $f(z)$ and $g(z)$ are assumed to be statistically independent random distributions. The coupling coefficients $Z_{pq}^{(s_p,s_q)}$ are defined in (3.86), (3.87) and (3.94), and they depend on the difference between the square of the ideal waveguide refractive index $n_o(x,y)$ and the square of the perturbed waveguide refractive index $n(x,y,z)$. Since ideal and perturbed waveguide coincide anywhere except in the vicinity of the boundaries of the waveguide, $Z_{pq}^{(s_p,s_q)}$ will be zero everywhere except very close to the waveguide sidewalls. In regions where the core boundary moves outward from the ideal core we have

$$n^2 - n_o^2 = n_{co}^2 - n_{cl}^2 \tag{3.95}$$

while in the regions where the core moves inward

$$n^2 - n_o^2 = -(n_{co}^2 - n_{cl}^2) \tag{3.96}$$

In the rest of the area ideal and perturbed waveguides coincide and $n^2 - n_o^2 = 0$.

Now, if we consider waveguides with very slight deviations only, then we can expect the field components of the perturbed waveguide not to differ very much from the field

components of the ideal waveguide, in the area very close to the waveguide boundaries (in the area between the solid and dashed lines in Fig. 3-7 (a)). Since the tangential components are continuous at both sides of the core boundary we can take them out of the integral in (3.86), (3.87) and replace them with their values on the ideal core boundary. However, the transverse electrical component along x is discontinuous and following the dielectric boundary conditions, we have to replace it with $\mathbf{E}_x$ when the core boundary moves outward and with $n_{co}^2 / n_{cl}^2 \mathbf{E}_x$ when it moves inward.

By combining the above with (3.86)-(3.87) and (3.95)-(3.97) we obtain the coupling coefficients of lightly deformed rectangular waveguides

$$Z_{pq}^{(s_p,s_q)} = \frac{s_q \omega \varepsilon_o}{4iP} \left\{ \int_{-d/2}^{d/2} (n_{cl}^2 - n_{co}^2) g(z) \left[(n_{cl}^2 / n_{co}^2) \eta_g \mathbf{E}_{px}^* \cdot \mathbf{E}_{qx} + \mathbf{E}_{py}^* \cdot \mathbf{E}_{qy} + 1/\eta_g \mathbf{E}_{pz}^* \cdot \mathbf{E}_{qz} \right]_{x=w/2} dy \right.$$
$$\left. - \int_{-d/2}^{d/2} (n_{cl}^2 - n_{co}^2) f(z) \left[(n_{cl}^2 / n_{co}^2) \eta_f \mathbf{E}_{px}^* \cdot \mathbf{E}_{qx} + \mathbf{E}_{py}^* \cdot \mathbf{E}_{qy} + 1/\eta_f \mathbf{E}_{pz}^* \cdot \mathbf{E}_{qz} \right]_{x=-w/2} dy \right\} \tag{3.97}$$

where

$$\eta_{g,f} = \begin{cases} (n_{cl}^2 / n_{co}^2), & g(z) > 0 \text{ or } f(z) < 0 \\ (n_{co}^2 / n_{cl}^2), & g(z) < 0 \text{ or } f(z) > 0 \end{cases} \tag{3.98}$$

For weakly guided waveguides we can simplify (3.97), (3.98) even further if we replace $\eta_{g,f}$ with their geometric mean $\eta_{g,f} = \left[(n_{co}^2 / n_{cl}^2)(n_{cl}^2 / n_{co}^2) \right]^{1/2} = 1$. Therefore, the final expression for the coupling coefficients valid for weakly guiding waveguides with slightly perturbed sidewalls is given by

$$Z_{pq}^{(s_p,s_q)} = \frac{s_q \omega \varepsilon_o}{4iP} \left\{ \int_{-d/2}^{d/2} (n_{cl}^2 - n_{co}^2) g(z) \left[(n_{cl}^2 / n_{co}^2) \mathbf{E}_{px}^* \cdot \mathbf{E}_{qx} + \mathbf{E}_{py}^* \cdot \mathbf{E}_{qy} + \mathbf{E}_{pz}^* \cdot \mathbf{E}_{qz} \right]_{x=w/2} dy \right.$$
$$\left. - \int_{-d/2}^{d/2} (n_{cl}^2 - n_{co}^2) f(z) \left[(n_{cl}^2 / n_{co}^2) \mathbf{E}_{px}^* \cdot \mathbf{E}_{qx} + \mathbf{E}_{py}^* \cdot \mathbf{E}_{qy} + \mathbf{E}_{pz}^* \cdot \mathbf{E}_{qz} \right]_{x=-w/2} dy \right\} \tag{3.99}$$

or equivalently by

$$Z_{pq}^{(s_p,s_q)} = G_{pq} g(z) - T_{pq} f(z) \tag{3.100}$$

with F_{pq} and G_{pq} being just constants defined as

$$G_{pq} = \frac{s_q \omega \varepsilon_o}{4iP} (n_{cl}^2 - n_{co}^2) \left\{ \int_{-d/2}^{d/2} \left[(n_{cl}^2 / n_{co}^2) \mathbf{E}_{px}^* \cdot \mathbf{E}_{qx} + \mathbf{E}_{py}^* \cdot \mathbf{E}_{qy} + \mathbf{E}_{pz}^* \cdot \mathbf{E}_{qz} \right]_{x=w/2} dy \right.$$

$$T_{pq} = \frac{s_q \omega \varepsilon_o}{4iP}(n_{cl}^2 - n_{co}^2)\left\{\int_{-d/2}^{d/2}(n_{cl}^2/n_{co}^2)\mathbf{E}_{px}^* \cdot \mathbf{E}_{qx} + \mathbf{E}_{py}^* \cdot \mathbf{E}_{qy} + \mathbf{E}_{pz}^* \cdot \mathbf{E}_{qz}\right]_{x=-w/2} dy \tag{3.101}$$

We therefore see that the coupling coefficients take a very simple form.

3.3.3 Perturbation Solution for the Coupled Mode Theory Equation

Now that we have identified the coupling coefficients, we are ready to proceed to solve the coupled mode equations (3.92) - (3.93). In order to simplify analysis we will consider that only one of the side-walls is deformed, say the left one with deformation function $f(z)$. In addition, we assume that modes are only mildly coupled to each other and that the amplitude coefficient c_p^+ of a specific mode (the p-th mode in this case) incident to the perturbed waveguide is always much larger than the amplitude coefficients of the rest of the modes

$$|c_p^+| >> |c_q^+| \tag{3.102}$$

Since the amplitude, c_p^+ of the p-th mode does not vary too much we can treat it as approximately constant. In this case, (3.92) and (3.93) become upon integrating along z

$$c_q^+(z) = c_p^+(0)\int_0^z Z_{pq}^{+,+}(u)\exp\left[-i(\beta_q - \beta_p)u\right]du \tag{3.103}$$

$$c_q^-(z) = c_p^+(L)\int_L^z Z_{pq}^{-,+}(u)\exp\left[-i(\beta_q + \beta_p)u\right]du \tag{3.104}$$

with the following boundary conditions being imposed to obtain the solutions (3.103) - (3.104)

$$c_q^+(0) = 0,\ q \neq p \tag{3.105}$$

$$c_q^-(L) = 0 \tag{3.106}$$

If the amplitude c_p^+ does not change appreciably then we can claim that

$$c_p^+(0) \approx c_p^+(L) \tag{3.107}$$

and so after substituting (3.107) and (3.101) into (3.103)-(3.104) we get

$$c_q^+(L) = \sqrt{L}c_p^+(0)F(\beta_q - \beta_p)G_1 \tag{3.108}$$

$$c_q^-(0) = -c_q^+(0)F(\beta_p + \beta_q)G_1 \tag{3.109}$$

Equations (3.108) and (3.109) are the formal solutions of the coupled mode equations

(3.92)-(3.93). The important point in (3.108)-(3.109) is that the amplitudes of the various modes are proportional to the Fourier transform of the side wall deformation function f(z)

$$F(\beta_q - \beta_p) = 1/\sqrt{L}\int_0^L f(z)\exp\left[-i(\beta_q - \beta_p)z\right]dz \tag{3.110}$$

We also remind that when both p and q subscripts refer to bound modes then (3.108) and (3.109) can be associated with power being exchanged between the p-th and the q-th guided modes. However, if one of the modes is of the radiation type then (3.108) and (3.109) can be associated with energy being lost.

3.3.4 Coupled Power Theory

Up to now, we have dealt with the full solutions of the coupled mode equations (3.92) and (3.93) which calculate how both the amplitude and the phase of a mode changes as this mode propagates inside an imperfect multimode waveguide. However, for many applications, as for example for the evaluation of the propagation loss, the phase information is redundant and significantly complicates calculations. In this case, the important property is the power that the modes carry, and how this is exchanged between the modes as they propagate in the perturbed waveguide. The theory, which deals with the way that the power of the modes are coupled in a perturbed waveguide, and, which is directly related to the previously presented coupled mode theory, is called the coupled power theory and has also been developed by Marcuse [3.2 pp. 177-197].

The theory starts with the definition of the average power (with respect to the propagation length) carried by a mode

$$P_p = \left\langle \left|A_p\right|^2 \right\rangle = \left\langle \left|c_p\right|^2 \right\rangle \tag{3.111}$$

where the brackets <> in (3.111) represent averaging over z. The z derivative of the average power can be easily calculated to be

$$\frac{dP_p}{dz} = \left\langle \frac{dc_p}{dz} c_q^* \right\rangle + c.c \tag{3.112}$$

with $c.c$ denoting the complex conjugate in (3.112). If we consider that the statistical properties of the waveguide deformation are such that coupling from forward to backward propagating modes is neglected (which is true in most of the cases of interest) then by substituting (3.92) and (3.103) into (3.112) we obtain

$$\frac{dP_p}{dz} = \sum_{q=1}^{M} T_{pq} \left\langle c_p c_q^* f(z) \right\rangle \exp\left[-i(\beta_q - \beta_p)z\right] + c.c \tag{3.113}$$

Note that in (3.113) we focused on the power of the M ($M = N_1 + N_2$), bound modes of the waveguide.

Through a process that considers $f(z)$ as a stationary random process with a finite autocorrelation length, D the coupled power equations (3.113) takes the form [3.2, pp. 183]

$$\frac{dP_p}{dz} = \sum_{q=1}^{M} T_{pq}^2 \int_{-\infty}^{+\infty} \left\langle f(z) f(z-u) \right\rangle \exp\left[-i(\beta_q - \beta_p)u\right] du \tag{3.114}$$

Equation (3.114) is presented in a form which makes obvious that the coupled power equations are related to the Fourier transformation of the autocorrelation function $R(u) = \left\langle f(z) f(z-u) \right\rangle$, of the waveguide random distortion $f(z)$. With this comment in mind, the final form of the coupled power equations is [3.2, pp. 183]

$$\frac{dP_p}{dz} = -2a_p P_p + \sum_{q=1}^{Q} h_{pq} (P_q - P_p) \tag{3.115}$$

with the following definition

$$h_{pq} = T_{pq}^2 \int_{-\infty}^{+\infty} \left\langle f(z) f(z-u) \right\rangle \exp\left[-i(\beta_q - \beta_p)u\right] du = T_{pq}^2 \left\langle \left| F(\beta_q - \beta_p) \right|^2 \right\rangle \tag{3.116}$$

the additional term appearing in (3.115), is the loss coefficients $-2a_p$, and has been added to take into account losses in our system from coupling of the p-th bound mode to the radiation modes. These loss coefficients can be calculated as following. The Poynting vector of the field in the waveguide is given by

$$P_c = \frac{1}{2} \mathrm{Re} \int_{-\infty-\infty}^{+\infty+\infty} S_z \, dxdy = \frac{1}{2} \mathrm{Re} \int_{-\infty-\infty}^{+\infty+\infty} (E_t \times H_t^*)_z \, dxdy \tag{3.117}$$

We now substitute the series expansions (3.79) and (3.80) into (3.117) and then express the mode amplitudes in terms of forward and backward propagating waves, (3.90). Then, by using the expressions for the slowly varying field amplitudes (3.91), we obtain the power flow through a plane perpendicular to the waveguide as

$$P_c = \left[\sum_q \left|A_q^+\right|^2 - \left|A_q^-\right|^2 + \sum \int_0^{kn_{cl}} \left|A_r^+\right|^2 - \left|A_r^-\right|^2 dr \right] \tag{3.118}$$

with r, the transverse wave-vector in the cladding defined as

$$r^2 = kn_{cl}^2 - \beta_r^2 \tag{3.119}$$

and β_r, the propagation constant of the r-th radiation mode. Note that the power flowing towards positive z has been counted as positive, in (3.118), while the power flowing towards negative z has been counted as negative. If we consider that, the power coupled to both forward and backward radiation modes as being lost, then in order to calculate the attenuation that a guided mode experiences, we should count all power as positive. Therefore, the power lost in the deformed waveguide of Fig. 3-7 becomes

$$P_a = \left[\sum \int_0^{kn_{cl}} \left|A_r^+(L)\right|^2 + \left|A_r^-(0)\right|^2 dr \right] \tag{3.120}$$

By noting from (3.91) that the only difference between the amplitude coefficients A_r^+ and A_r^- is in the sign of β_r and by using (3.119) to switch the integration variable in (3.120) from the transverse wave-vector r, to the propagation constant β_r we get the formula for the power loss in the convenient form

$$P_a = \left[\sum \int_{-kn_{cl}}^{kn_{cl}} \left|A_r^+(L)\right|^2 \left(|\beta_r|/r\right) d\beta_r \right] \tag{3.121}$$

The power carried by the p-th incident mode at the beginning of the waveguide is given by $\left|c_p^+(0)\right|^2$. Therefore, by using (3.108) the attenuation coefficient $2a_p$ is given by

$$2a_p = \frac{P_a}{\left|c_p^+(0)\right|^2} L = \sum \int_{-kn_{cl}}^{kn_{cl}} \left|G_{pr}\right|^2 \left|F(\beta_r - \beta_q)\right|^2 \left(|\beta_r|/r\right) d\beta_r \tag{3.122}$$

3.3.5 Solutions of the Coupled Power Theory

In order to solve the first order differential equations system in (3.115) we try the test solutions

$$P_q = C_q e^{-\sigma z} \tag{3.123}$$

with σ corresponding to the (M) eigenvalues of the system. By replacing (3.123) into (3.115) we convert the system of differential equations to a linear system of M equations

and M unknowns C_q as

$$\sum_{q=1}^{M}\left[h_{pq}+\left(\sigma-2a_q-\tau_q\right)\delta_{pq}\right]C_q=0 \tag{3.124}$$

with the abbreviation $\tau_q=\sum_{p=1}^{M}h_{pq}$ in (3.124). The determinant of the homogenous system (3.124) must vanish in order for the system to have solutions and thus we demand

$$\det\left[h_{pq}+\left(\sigma-2a_q-\tau_q\right)\delta_{pq}\right]=0 \tag{3.125}$$

The solutions of equation (3.125) give the M independent eigenvalues $\sigma^{(i)}$, $i=1...M$, while the solutions of the system (3.124) give the M independent and orthogonal eigenvectors $C_q^{(i)}$, $i=1,...M$ of the coupled power equation system. Therefore, by combining the above with (3.123) we obtain the M, solutions of the coupled power equations as

$$P_q^i(z)=C_q^{(i)}\exp(-\sigma^{(i)}z),\quad i=1,...M \tag{3.126}$$

Since we have identified all eigenvectors $C_q^{(i)}$, the general solutions of (3.115) can be written as a linear combination of them as

$$P_q(z)=\sum_{i=1}^{M}A_iC_q^{(i)}\exp(-\sigma^{(i)}z),\quad i=1,...M \tag{3.127}$$

with A_i arbitrary coefficients. These coefficients could be defined, if we knew the power distribution at any cross-section of the waveguide, say, at the beginning of the waveguide $z = 0$ for example. Then, by taking into account the orthogonality of the eigenvectors we could calculate the expansion coefficients A_i as

$$A_i=\sum_{i=1}^{M}C_q^{(i)}P_q(0) \tag{3.128}$$

It is important to make clear the physical interpretation of the coupled power solutions (3.127). To make it more apparent we assume that all eigenvectors have been arranged in a descending order as

$$\sigma^{(1)}<\sigma^{(2)}\le...\le\sigma^{(M)} \tag{3.129}$$

Since eigenvalues are connected to the power carried by modes, they all have to be positive. In this case, all solutions (3.126) are decreasing as z increases. The ratio between

the first term and any other term in (3.127) is

$$\left(A_1 C_q^{(1)} / A_i C_q^{(i)}\right)\exp(\sigma^{(i)} - \sigma^{(1)})z \tag{3.130}$$

This ratio constantly increases as z increases and, therefore, for large z only the first term in (3.127) is important and dominates over the rest of the eigenvectors. The implication of this property is that the distribution of power between the modes after some distance of propagation becomes independent of the initial power distribution and gradually converges to a final distribution depending on the terms of A_q. The power distribution reaches an equilibrium after some distance L, given by

$$L = (\ln R)/(\sigma^{(2)} - \sigma^{(1)}) \tag{3.131}$$

Equation (3.131) implies that the equilibrium is reached when the first term (which is also the largest term) of the general solution (3.127) is R times larger than the second largest term. For most applications $R = 100$ is good enough to characterize equilibrium.

The final remark is about the evolution of the modal power distribution after equilibrium has been reached. Since the first eigenvector is the dominant one, the power distribution propagates as

$$P_{eq}(z) = \left[\sum_{q=1}^{M} C_q^{(1)} P_{eq}(0)\right] C_q^{(1)} \exp(-\sigma^{(1)} z) \tag{3.132}$$

3.3.6 Conclusions

In this chapter, we reviewed the intrinsic mode theory that is used to solve the problem of adiabatic mode theory in tapered waveguide bends in Chapter 5, and Marcuse's coupled mode and power theories that is used in Chapter 6 to investigate modal propagation in multimode buried channel waveguides with sidewall roughness. The intrinsic mode theory predicts how an adiabatic mode propagates down the apex of a tapered waveguide. In the region where the mode is well guided the adiabatic mode profile coincides to the waveguide local mode (3.50)-(3.51). The propagation constant of the adiabatic mode changes to adjust to the local waveguiding environment (3.50) while its amplitude changes to reassure conservation of energy (3.51). As the width of the waveguide reduces, the mode approaches its cut-off, in which case the adiabatic mode takes the form described in (3.61)-(3.63). In this region the modes passes from being well guided to being radiating and lateral waves are excited at the vicinity of the cut-off width.

Finally, at the region beyond cut-off, (3.69)-(3.70), the adiabatic mode has an imaginary propagation coefficient, which expresses attenuation due to leakage into the cladding.

The coupled mode theory serves as the basis for the coupled power theory, which actually is the theory of interest in multimode waveguides. The main outcome of the coupled mode theory is that in waveguides with mild side-wall roughness, like the ones fabricated by photolithography for example, the waveguide bound modes are coupled to each other and to the radiation modes with coupling coefficients that take a simple form directly depending on the values of the electric field components at the distorted waveguide boundaries (3.99)-(3.101). At the weakly guiding limit, a perturbation approach can be adopted to solve for the solutions of the coupled mode theory equations (3.108)-(3.110), in which case as it is proved the strength of the coupling between any two modes is proportional to the Fourier transform of the waveguide deformation function taken at the difference between the propagation constants of the two modes under consideration (3.110). The coupled power theory on the other hand deals directly with the power in each mode and completely ignores their relative phases. This in general is not restrictive as in multimode waveguiding systems the phase of each individual mode is a quantity, which is not only almost impossible to be measured with the means of any experiment, but also in most of the times it does not find any practical usage. The main outcome of the coupled power theory is that as modes propagate in a waveguide with randomly deformed sidewall they gradually converge after some length L, (3.131), to an equilibrium power distribution, which remains (in average) steady (3.132). This is a very important observation as the propagation loss, (3.132), in the equilibrium state also converges to a steady value, which is independent of the initial field that was used to excite the waveguide.

REFERENCES

[3.1] J. M. Arnold and L. B. Felsen, "Rays and local modes in a wedge-shaped ocean, "*J. Acoust. Soc. Am*, vol. 73, pp. 1105-1119, 1983.

[3.2] J. M. Arnold and L. B. Felsen, "Intrinsic modes in a nonseparable ocean waveguide, "*J. Acoust. Soc. Am*, vol. 76, pp. 850-860, 1984.

[3.3] J. M. Arnold and L. B. Felsen, "Spectral reconstruction of uniformized wave fields from non uniform ray or adiabatic mode forms for acoustic propagation and diffraction," *J. Acoust. Soc. Am*, vol. 87, pp. 587-600, 1990.

[3.4] J. M. Arnold and L. B. Felsen, "Coupled mode theory of intrinsic modes in a wedge," *J. Acoust. Soc. Am*, vol. 79, pp. 31-40, 1986.

[3.5] J. M. Arnold and L. B. Felsen, "Local intrinsic modes: layer with nonplanar interface," *Wave Motion*, vol. 8, pp. 1-14, 1986.

[3.6] J. M. Arnold and L. B. Felsen, "Ray invariants, plane wave spectra and adiabatic modes for tapered dielectric waveguides," *Radio Sci.*, vol. 19, pp. 1256-1264, 1984.

[3.7] I-Tai Lu, "Intrinsic modes in a wedge-shaped taper above an anisotropic substrate," *IEEE J. Quantum Electron.*, vol. 27, pp. 2373-2377, Nov. 1991.

[3.8] A. Dendane and J. M. Arnold, "Beam radiation from tapered waveguides," *IEEE J. Quantum Electron.*, vol. QE-22, pp. 1551-1556, Sep. 1986.

[3.9] A. D. Pierce, "Extension of the method of normal modes to sound propagation in an almost stratified medium," *J. Acoust. Soc. Am*, vol. 37, pp. 19-27, 1965.

[3.10] L. B. Felsen and N. Marcuvitz, *Radiation and Scattering of Waves*, ser. Microwaves and Fields Series, Prentice-Hall, Inc., New Jersey, 1973, pp. 370-441.

[3.11] R. Wong, *Asymptotic Approximations of Integrals*, ser. Computer Science and Scientific Computing, Academic Press, Inc, 1989, pp. 55-60.

[3.12] M. Abramozitz and I. Stegun, "Handbook of mathematical functions and tables," Dover, New York, 1964.

[3.13] D. Marcuse, *Light Transmission Optics*. London, U.K.: Van Nostrand Reinhold, 1972.

[3.14] D. Marcuse, *Theory of Dielectric Waveguides*, London, U.K: Academic, 1991.

[3.15] D. Marcuse, "Radiation losses of dielectric waveguides in terms of the power spectrum of the wall distortion function," *Bell Syst. Tech. J.,* vol. 48, pp. 3233-3243, Dec. 1969.

[3.16] D. Marcuse, "Mode conversion caused by surface imperfections of a dielectric slab waveguide," *Bell Syst. Tech. J.,* vol. 48, pp. 3186-3214, Dec. 1969.

[3.17] D. Marcuse, "Derivation of coupled power equations," *Bell Syst. Tech. J.,* vol. 51, pp. 229-237, Jan. 1972.

[3.18] D. Marcuse, "Power distribution and radiation losses in multimode dielectric slab waveguides," *Bell Syst. Tech. J.,* vol. 51, pp. 429-454, Feb. 1972.

[3.19] D. Marcuse, "Higher-order scattering losses in dielectric waveguides," *Bell Syst. Tech. J.,* vol. 51, pp. 1801-1817, Oct. 1972.

[3.20] D. Marcuse, "Higher-order loss processes and the loss penalty of multimode operation," *Bell Syst. Tech. J.,* vol. 51, pp. 1819-1836, Oct. 1972.

CHAPTER 4

ANALYSIS OF LOSS MECHANISMS IN CURVED MULTIMODE POLYMER WAVEGUIDES

4.1. INTRODUCTION

Current state of the art storage systems contain up to 48 pluggable sets of disk drives in a 19" rack, [4.1]. This in effect means that there are 48 connectors dispersed over the backplane area, with connector-to-connector spacing being as close as less than 2", [4.1]. Such ultra dense architectures require from the copper track layout to incorporate a large number of tight bends in order to allow to all daughtercards to be interconnected to each other, in a point-to-point interconnection scheme for example. A similar optical backplane system extending over the same backplane area, and having the same number of point-to-point links, would require very tightly bended optical waveguides to achieve full interconnectivity. Implementation of tight optical waveguide bends might prove to be challenging however, as these components introduce excessive insertion loss, crosstalk through radiated waves and reflections [4.5]-[4.16].

Multimode polymer waveguide bends, like the ones used in optical backplanes, are used not only for routing signals, but, also, in several other optical components such as in Arrayed Waveguide Gratings (AWGs) [4.2], Y-branch splitters/couplers [4.3] and port by-pass switches [4.4]. The loss as a function of bend radius has been repeatedly studied in single mode waveguides [4.5]-[4.6], in single mode fibres [4.7]-[4.8] and in multimode silica and plastic fibres [4.9]-[4.12]. However, limited research has been reported on the subject in the case of multimode polymer waveguides for optical backplane applications [4.13]-[4.16]. In addition, the work in [4.13]-[4.16] has mainly been experimental and restricted to reporting the total insertion loss in the waveguide bends as a function of the radius of curvature only.

The work presented here extends the earlier research, since not only did we experimentally measured the total insertion loss in multimode waveguide bends but we also separated out the various loss mechanisms involved, with the aid of a hybrid experimental / modelling approach. Our analysis revealed that not all loss components

are of equal magnitude but instead, there are some, which dominate over the others and future efforts should focus on minimizing their effect.

Regarding the modelling part of our work, we chose the Beam Propagation Method (BPM) to analyze our waveguide bends, among a number of available modelling techniques that have been used in the past. These modelling techniques include the ray-tracing method [4.17], the WKB approximation [4.18]-[4.19], the finite element method [4.20], the method of lines [4.21], the eigenmode expansion [4.24] and the 2 × 2 matrix numerical method reported in [4.25]. We chose BPM because it has already been successfully used to model multimode and single mode bends [4.16], [4.22]-[4.23], but also because it gives better insight into the behaviour of light compared to most of the other methods, since waveguide modes are included in the analysis. In addition, simulations are completed in reasonable time. The main drawbacks of BPM are that it cannot trace reflected light and it is governed by the paraxial limitation, which requires an indirect approach to model a full 90° bend, as we will see in the next.

This chapter is constructed as following. Section 4.2 discusses the various loss mechanisms in a straight waveguide – 90° bend – straight waveguide combination. Section 4.3 describes our experimental measurements on the insertion loss of multimode waveguide bends as a function of the radius of curvature and the waveguide width. Section 4.4 introduces the geometrical ray optics derivation of numerical aperture and transition loss. Section 4.5 describes the BPM modelling of field propagation in multimode waveguide bends. Section 4.6 compares the BPM results with the experimentally obtained results for the insertion loss. Section 4.7 presents our approach of separating the various loss components involved in waveguide bends from each other. Section 4.8 compares the experimental results, geometrical ray optic results and those from BPM modelling. Finally section 4.9 concludes.

4.2. TYPES OF WAVEGUIDE LOSS

Fig. 4-1 (a) is a schematic diagram of the waveguide structure used in our experiments to measure insertion loss in waveguide bends. The waveguide system under investigation consisted of a typical straight – 90° bend – straight waveguide cascade. Four types of loss are identified in this case

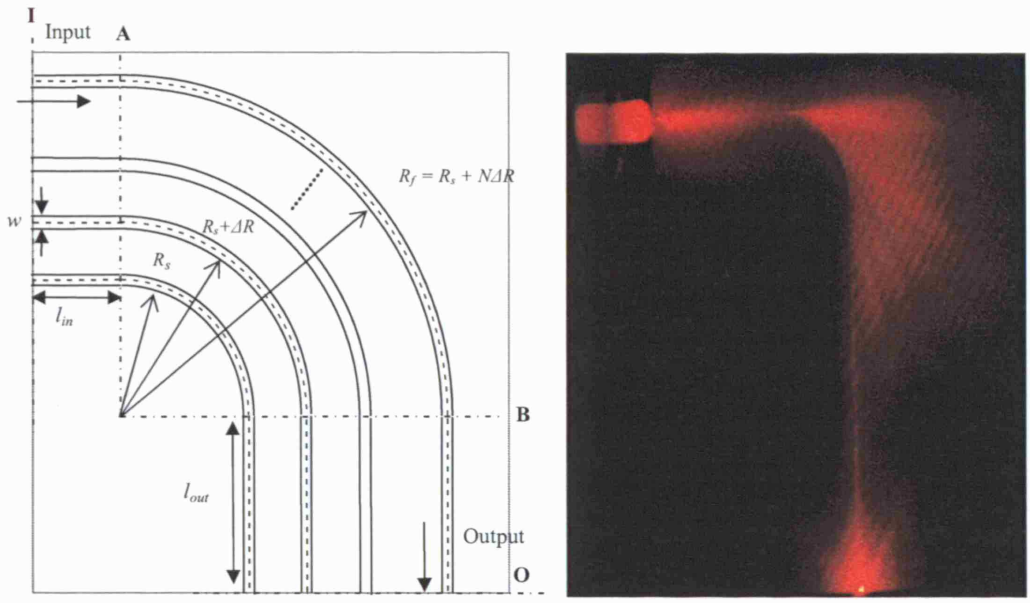

Fig. 4-1. (a) Schematic diagram of one set of waveguide bends. Three sets of waveguides with widths w = 50 μm, 75 μm, and 100 μm respectively were fabricated. Radius R, varied between 5.5 mm < R < 34.5 mm while the separation of adjacent waveguides was ΔR = 1 mm. Straight sections l_{in} = 11.5 mm and l_{out} = 24.5 mm. (b) Light through a 50 μm × 50 μm waveguide bend of R = 5.5 mm. Light lost due to scattering, transition loss, radiation loss, reflection and back-scattering at the end of the waveguide can be clearly seen. Waveguide was butt-coupled to a 50/125 μm step-index MM fibre illuminated with a 650 nm red-laser.

4.2.1 Coupling Loss

Coupling loss occurs between an incoming multimode (MM) fibre and the waveguide bend and also between the waveguide exit and a photodetector in our experiments and consists of

I. *Fresnel reflection loss* due to reflection at the interface between different refractive index media with a magnitude that strongly depends on whether an air gap exists between the waveguide and the MM fibre or the photodetector.

II. *Scattering loss* caused by the relatively rough waveguide end face, which scatters light forwards and backwards into a wide range of angles. The scattered light couples to forward and backward bound and radiation modes. We note that our waveguides have been dices but NOT polished in a low cost approach.

In Fig. 4-1 (a) coupling loss occurs along plane **I**, at the input to the waveguides and along plane **O**, at the output. Coupling loss is given by the variables, *CouplI* and *CouplO*. We note that in contrast to the rest of the loss components, which are specifically associated with waveguide bends, coupling loss is present in any waveguiding system.

Therefore for the purpose of studying the additional effects that waveguide bends contribute in a system we need to calibrate its effect out.

4.2.2 Transition Loss

Transition loss occurs at the junction between waveguides supporting dissimilar sets of modes [4.17], like for example the MM fibre and the input straight waveguide or the straight waveguide and the 90° bend in our case. The field across the waveguide cross section emerging from the input waveguide or incident externally from the fibre cannot be expanded and fully represented as a weighted combination of only the propagating modes of the waveguide into which the light travels. The modal field expansion must also include radiation modes to match the field distribution fully. Radiation modes radiate energy from the waveguide and most energy is removed along the waveguide in a short distance after the coupling plane. In Fig. 4-1 (a) transition loss occurs along plane **I,** since the fibre modes do not match those of the waveguide, and this loss is assumed to be included within the coupling loss term, *CouplI.* Transition loss also occurs along plane **A,** at the interface between the straight and the curved waveguides, *TransA* and along plane **B**, at the interface between the curved waveguide and the straight waveguide, *TransB.*

4.2.3 Propagation Loss

Propagation loss, *PL*, is caused by the scattering of energy from propagating to radiation modes due to waveguide sidewall roughness, and also direct loss due to material absorption. The core layer is spun as a liquid onto the wafer so the upper and lower surfaces of the waveguide are flat to within a few nm [4.34]. However, the vertical side walls are formed by photolithographic UV exposure and so, any sidewall roughness formed on the mask at the etching step is transferred from the mask onto the waveguides [4.26]. The scattering of guided modes at the rough sidewalls redistributes and couples energy between modes and causes loss by radiation [4.27] - [4.28].

4.2.4 Radiation Loss

Curved waveguides cannot support perfectly bound modes but instead they host leaky modes similar to those of a hollow waveguide [4.30], which radiate energy continuously around a bend causing radiation loss, *RL*. Each propagating mode loses power at a unique rate determined by its mode number and waveguide parameters such as numerical

aperture, physical dimensions and radius of curvature [4.7] - [4.25].

The total loss, *TL*, in our device can, therefore, be resolved into the following components

$$TL = CouplI + TransA + TransB + CouplO + PL + RL \quad (4.1)$$

The aim of this study is to investigate the loss components other than the input and output coupling loss *CouplI* and *CouplO*, as mentioned in section 4.2.1, so these are reduced and calibrated out by appropriately designed experiments in section 4.3.

4.3. EXPERIMENTAL MEASUREMENTS OF WAVEGUIDE BEND INSERTION LOSS

4.3.1 Waveguide Fabrication and Structure

The waveguides were formed photolithographically on the surface of a 7" diameter woven glass FR4 wafer. The fabrication of the waveguides was outsourced to the commercial company Exxelis Ltd, [4.34]. A photosensitive acrylate polymer, Truemode^{TM}, [4.34], was used for the core and the cladding. Truemode^{TM} has low absorption loss at ~ 850 nm which is compatible with readily available 10 Gb/s VCSELs. The circular wafer substrates made from a woven FR4 layer of 800 μm thickness coated in a copper layer of 17 μm were initially planarized by spinning a 50 μm layer of cladding polymer. The core polymer precursor was then spun on to a thickness of 50 μm and exposed to UV light through a dark field photomask (~ 450£) which is somewhat lower cost than an e-beam mask (~ 1000£). The polymer precursor layers were spun on wet, the mask was placed ~ 100 μm above to avoid touching the wet polymer layer, and the gap flushed with dry nitrogen at atmospheric pressure to prevent oxygen inhibition. Once the unexposed core material was washed off with an acetone solution, a second layer of cladding was spun over the core and lower cladding to a depth of 50 μm above the top of the core layer. The refractive index of the core after UV exposure was n_{co} = 1.556 and that of the cladding was n_{cl} = 1.5264, measured by the prism coupler method, giving a numerical aperture of NA_{wg} = 0.302. A large Δn was chosen to give a large enough *NA* to ensure low coupling loss to similar *NA* multimode and single mode fibres.

The mask pattern was designed Fig. 4-1 (a), to have three sets of 90° circular arc waveguides with straight waveguides at their input and output. The radius of the

waveguides in each set varied in the range 5.5 mm < R < 34.5 mm. The difference between the radius of any two adjacent arcs was ΔR = 1 mm, giving N = 30 curved waveguides. The input straight section of length, l_{in} = 11.5 mm and the output section of length, l_{out} = 24.5 mm were introduced to investigate transition loss between straight and curved waveguides (line **A**) and between curved and straight waveguides (line **B**) and to allow for tolerance of positioning a dicing saw to cut through the polymer, copper and FR4 layers in a low cost approach without polishing the waveguide end face. All three sets of waveguides had the same thickness, d = 50 μm being made on the same wafer, but they had different widths, w = 50 μm, 75 μm, and 100 μm correspondingly.

4.3.2 Experimental Measurement Technique

Light from an 850 nm VCSEL operated at 0 dBm, Fig. 4-2, was launched into a standard 50/125 μm step-index MM fibre with NA_{fibre} = 0.2 < NA_{wg} = 0.302. After mode scrambling, fibre was aligned and butt-coupled to one of the waveguides on the wafer. Mode scrambling had the effect of exciting a large number of transverse modes that filled most of the fibre's numerical aperture, as seen in Fig. 4-3, from far field angular divergence measurements.

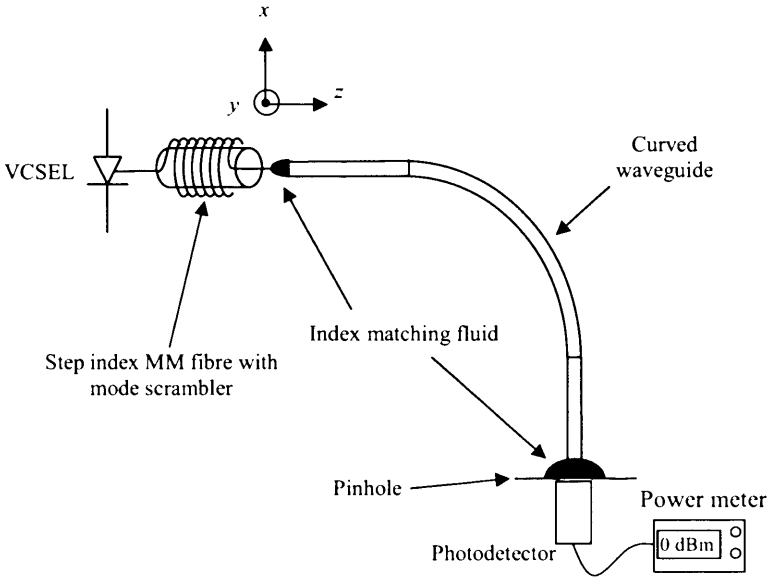

Fig. 4-2. Experimental set-up for measuring the insertion loss of the waveguide bends in Fig. 4.1.

Fibre to waveguide alignment was achieved by mounting the fibre end ferrule on a

system of one manual rotation stage and three motorized translation stages with sub-micrometer precision in x, y, and z directions, Fig. 4-2. The fibre was then butt-coupled to the waveguides of the wafer and its position was adjusted with the aid of the rotation and translational stages until the power at the output of the waveguide was maximized. The use of a mode scrambled MM fibre as the input field is a widely accepted method for measuring the insertion loss of other multimode waveguides and components [4.9]-[4.16]. Alternatively an 850nm LED could have been used to excite the waveguide high-order modes. Light at the output of the waveguides was spatially filtered by a 150 μm diameter circular pinhole to exclude much of the light travelling through the cladding, before being collected by a large area integrating sphere photodetector (PD) connected to a power meter. Index matching fluid (n = 1.4911 at 850 nm) was applied to both MM fibre - waveguide and waveguide - pinhole interfaces to reduce Fresnel reflection loss due to the refractive index mismatch at the interface and scattering loss due to the surface roughness across the waveguide face. The index matching fluid refractive index was close but did not exactly match the refractive index of the waveguide and so, some degree of scattering and reflections should still be expected.

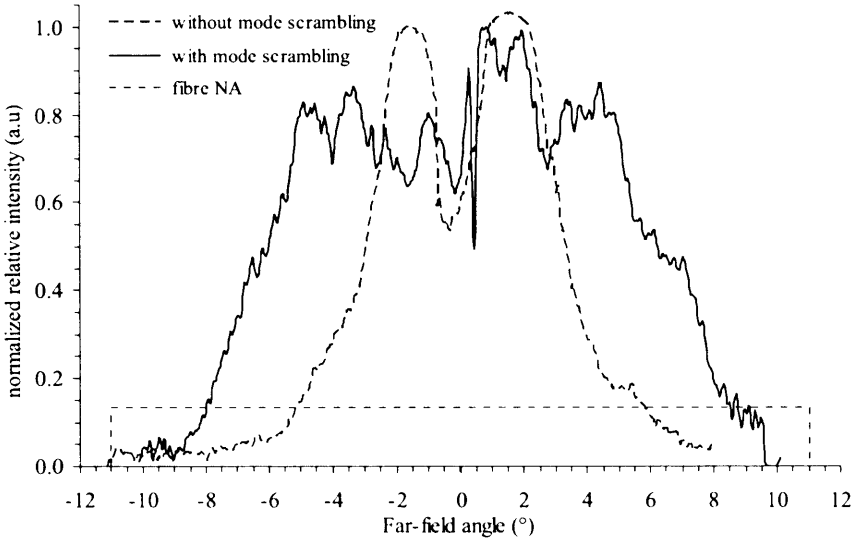

Fig. 4-3. Far-field of the 50/125 μm fibre used in the experiment with and without mode scrambling effect. In the latter case, the broadening of the angular divergence is evident, almost filling the fibre numerical aperture. The far-field intensity was normalized to unity maximum value.

4.3.3 Coupling Loss Calibration

Experimental measurements obtained with the set-up of Fig. 4-2 included the two coupling loss components *CouplI* and *CouplO*. However, as explained in section 4.2.1 coupling loss is independent from the rest of the loss components involved in the waveguide bends and its effect should be calibrated out. The calibration of the coupling loss was achieved with the following aid experiment. The real power $P_{bend}(w,R)$, measured at the output of each bend was subtracted from the power P_{str}, measured at the output of a set of straight waveguides fabricated on the same wafer. Three such straight waveguides were actually fabricated with dimensions 50 μm × 50 μm, 75 μm × 50 μm and 100 μm × 50 μm respectively and so, each one of the three sets of waveguide bends was calibrated by using the straight waveguide, which matched its cross-sectional dimension.

The power at the output of each bend P_{bend}, can be expressed with the aid of (4.1) as

$$P_{bend} = P_{in} - TL = P_{in} - (CouplI + TransA + TransB + CouplO + PL + BL) \tag{4.2}$$

where P_{in}, is the input power from the MM fibre. Similarly, the power at the output of each straight waveguide P_{str}, can be expressed as

$$P_{str} = P_{in} - (CouplI + CouplO + \alpha(w) l_{str}) \tag{4.3}$$

where $\alpha(w)$, is the propagation loss (in dB/mm) in the straight waveguide of length l_{str} = 65.5 mm, which was the longest straight waveguide we could fit on the mask. Therefore upon subtraction of (4.3) from (4.2), the normalized loss P_{norm1}, is given by

$$\begin{aligned} P_{norm1} &= P_{bend}(w,R) - P_{str} \\ &= -(TransA + TransB + PL + BL) + \alpha(w) l_{str} \end{aligned} \tag{4.4}$$

where we assumed that since straight and curved waveguides were made on the same wafer they had the same coupling loss. Equation (4.4) is the desired result since it contains the insertion loss of the waveguide bend with the coupling loss being removed. However, it also contains the additional $\alpha(w) l_{str}$, loss factor remaining due to the propagation loss in the straight calibration waveguide. This residual loss is of minor importance since its value is small compared to the rest of the components. In addition, as it is a parameter of the straight waveguides only, it does not affect the measurements for the bends of various radii in any other way other than just adding a constant value to the final results. However, for the sake of completeness even this small residual parameter

will be calibrated out in the following.

4.3.4 Experimental Results for Waveguide Bend Insertion Loss

The experimental results of the waveguide bend insertion loss P_{norml}, as a function of the radius of curvature R are shown in Fig. 4-4, for the three sets of waveguide bends with different waveguide widths. As seen in Fig. 4-4, for R < 20 mm in all three cases insertion loss increases as the radius of curvature decreases and also wider waveguides appear to have higher insertion loss compared to the narrower ones. These two trends, which have been repeatedly observed in other studies as well [4.17] - [4.22], are attributed to the increasing magnitude of the transition and radiation loss components as the radius of curvature reduces. Insertion loss, reaches its minimum value P_{min} = 0.73 dB at R_{min} = 13.5 mm for the 50 μm wide waveguide. The same values for the rest of the waveguide sets are, P_{min} = 0.84 dB at R_{min} = 15.3 mm for the 75 μm wide waveguide bends and P_{min} = 1.16 dB at R_{min} = 17.7 mm for the 100 μm wide waveguide bends, Table 4.1. As the radius increases beyond the minimum insertion loss value R_{min} loss starts increasing again, due to the enhanced contribution from the propagation loss component this time.

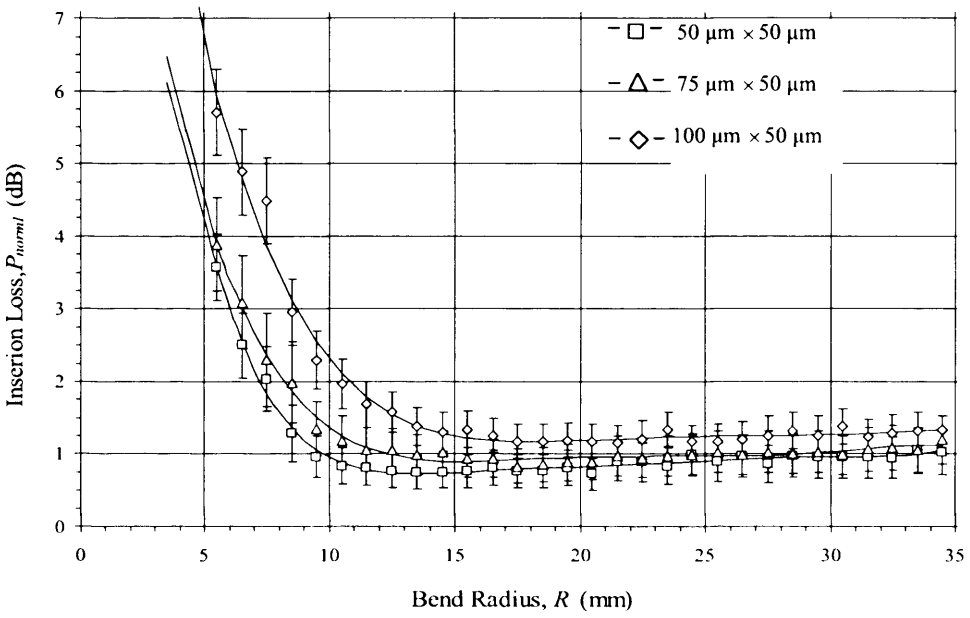

Fig. 4-4. Loss of curved waveguides for three widths w = 50 μm , 75 μm and 100 μm as a function of bend radius after normalization by subtracting the loss of similar straight waveguides to remove coupling loss.

TABLE 4.1

MINIMUM LOSS FOR SEVERAL WAVEGUIDE WIDTHS

Width (μm)	Radius of minimum loss (mm)	Minimum Loss (dB)
50	13.5	0.73
75	15.3	0.84
100	17.7	1.16

4.4. GEOMETRICAL RAY OPTIC CALCULATION OF NUMERICAL APERTURE AND TRANSITION LOSS BETWEEN STRAIGHT AND CURVED WAVEGUIDES

4.4.1 Introduction

In order to analyze the results for the waveguide bend insertion loss in Fig. 4-4, and to understand the various contributing loss mechanisms, we developed a simple geometrical ray optic model of propagation inside our multimode buried channel waveguides. It is well known that the numerical aperture of a fibre, which is related to its acceptance angle θ_a by $NA=\sin\theta_a$, is a helpful quantity as the transition loss is found from $(NA_2/NA_1)^2$, [4.35], for travel from a wider to a narrower NA fibre. We extend the concept of NA to the waveguide bend, to assess its dependence on the bend radius (R) and the width of the waveguides (w) and, hence, to calculate the transition loss between straight and curved waveguides as a function of R and w.

The following NA calculations are based on the ray model of modes in a rectangular waveguide. The use of a ray model to represent wave propagation is justified for two reasons. Firstly, the waveguides under investigation have large cross-sections compared to the wavelength of light supporting a large number of modes (1032 modes in the 50 μm × 50 μm waveguide). Ray trace simulations of wave propagation in multimode waveguides and fibres with similar cross-sectional dimensions to our waveguides have shown good agreement with experiments [4.32]-[4.33]. Secondly, the radius of curvature of the waveguides under investigation (R > 5 mm) is many times larger than the wavelength of operation (λ = 850 nm). For these macro-bends reflections can be assumed to occur on planar surfaces tangential to the waveguide core boundaries at the points of

contact between the rays and waveguide boundaries (Fig. 4-5), as has been confirmed in [4.17] and [4.31]. Therefore, we can assume at least to a first order approximation, light propagation by means of rays to be valid within both straight and curved waveguides for $R > 5$ mm.

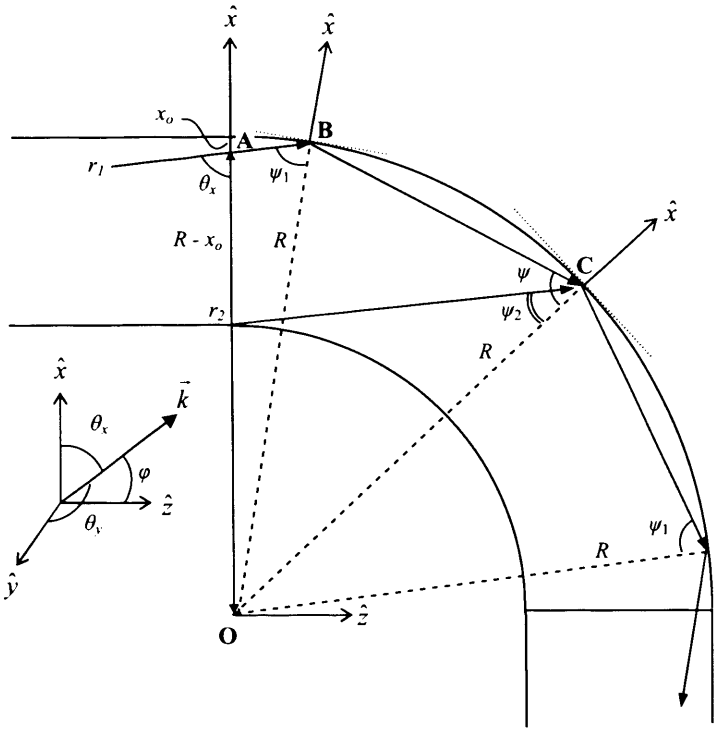

Fig. 4-5. Schematic diagram of rays entering the waveguide bend from the input straight waveguide for the geometrical ray optical calculation of acceptance angle and numerical aperture. In the diagram we observe two parallel rays r_1 and r_2, which both subtend angle θ_x with the x-axis, to enter the waveguide bend from two different points on the straight waveguide – waveguide bend interface. Due to the waveguide curvature, r_1 is reflected from the upper boundary of the bend with angle $\psi_1 < \theta_x$. If ψ_1 is smaller than the critical angle $\psi_1 < \theta_c$ then r_1 will find itself beyond cut-off inside the bend and will be lost. The second ray r_2, is reflected with angle $\psi_2 < \psi_1 < \theta_x$ inside the bend. Therefore, r_2 is more likely to be lost than r_1.

4.4.2 Calculation of Transition Loss Component between Straight Waveguides and Waveguides Bends, TransA.

According to the ray model, modes are represented by plane waves reflecting from the four waveguide walls, [4.34]. Plane waves propagate inside the input straight waveguide without attenuation if and only if they reflect at the boundaries with angles larger than the critical one, θ_c measured from the normal to the surface. The critical angle for reflection on a planar surface between two dielectrics with refractive indices n_{co} (core) and n_{cl} (cladding) is given by the relationship $\theta_c = \arcsin(n_{cl} / n_{co})$. The parameter $NA = \sin(\theta_c)$ is

termed the numerical aperture and is a useful quantity in waveguiding theory, which determines the range of angles that a waveguide can accept (angles of acceptance) for propagation.

The k-vector of such a plane wave subtends angles θ_x, θ_y, φ with the x, y, z axes as shown in Fig. 4-5. The amplitude of the k-vector is connected to the propagation constant β of the plane wave, its wavenumber k_x in x, and its wavenumber k_y in y via

$$k^2 = k_x^2 + k_y^2 + \beta^2,$$

$$k_x = k\cos\theta_x, k_y = k\cos\theta_y, \beta = k\cos\varphi \tag{4.5}$$

The intensity of such a plane wave is given by (see Appendix D, (D1-D7) for the derivation of (4.6))

$$I(\theta_x, \theta_y) = whC^2\cos\varphi = whC^2\sqrt{1-\cos^2\theta_x - \cos^2\theta_y} \tag{4.6}$$

where C is the amplitude of the plane wave (or more accurately the amplitude density per elementary θ_x and θ_y angles) at a range of angles within the acceptance angle, w the width and h the thickness of the waveguide. Equation (4.6) assumes that all the energy of the waves is confined inside the core of the waveguide, which is true for at least the strongly guided modes. In contrast to the modal theory where only a discrete set of k_x, k_y, and β is allowed, ray models assume a continuous distribution of wave vectors and propagation constants. As a result, the total power flow I_o across a straight waveguide cross-section can be expressed by integrating along the incremental power flow contributions from each plane wave guided in the waveguide, which with the aid of (4.6) becomes

$$I_o = 4\int_{\theta_x=\theta_{x,r}}^{\pi/2}\int_{\theta_y=\theta_{y,r}}^{\pi/2} I(\theta_x, \theta_y)\,d\theta_x\,d\theta_y \tag{4.7}$$

Inside the curved section, angles θ_y are preserved since reflections still occur on the planar surfaces $y = 0$ and $y = d$, (curvature is only in the xz plane). However, θ_x and so φ change to account for reflections along the curved surfaces. On the upper curved boundary rays are reflected with angles ψ_1, measured on a local polar coordinate system moving with the radius of curvature of the upper boundary R, Fig. 4-5, which is given by applying the law of sines to the **AOB** triangle as

$$\sin\psi_1 = [(R - x_o)/R]\sin\theta_x, \quad 0 < x_o < w \tag{4.8}$$

where x_o, is the distance in the x-axis between the upper curved boundary and the position where the ray enters the curved section and w the width of the waveguide. Equation (4.8) shows that $\sin\psi_1 < \sin\theta_x$ and so, $\psi_1 < \theta_x$ and therefore some rays, which previously belonged to propagating waves in the straight waveguide section might reflect at angles less than the critical angle inside the bend resulting in radiation loss. In addition, for rays entering from the same position x_o, decreasing θ_x leads to decreasing ψ_1 and so it is easier for the high order modes ($\theta_x \sim \theta_c$) of the straight waveguide to go beyond cut-off in the bend, rather than the low order modes ($\theta_x \sim \pi/2$). This implies that curved waveguides behave like mode filters, filtering out the higher order modes. The worst case is for rays passing through $x_o = w$, as these rays travel furthest into the waveguide before reflecting from its walls, as happens with ray r_1 compared to r_2 shown in Fig. 4-5. Therefore, the first ray to be lost passes from $x_o = w$, and it is reflected by the upper bent boundary with the critical angle ($\psi_1 = \theta_c$). By replacing $\sin\psi \rightarrow \sin\theta_{cr} = n_{cl}/n_{co}$ and $x_o = w$ in (4.8), we find that all plane waves with angles θ_x satisfying the condition

$$\theta_x < \theta_o = \arcsin\left[\frac{n_{cl}}{n_{co}}\frac{(R-w)}{R}\right] \tag{4.9}$$

contain rays which are reflected with angles beyond the critical angle inside the bend and thus, are rapidly lost. Each plane wave with $\theta_x < \theta_o$, has a window on its wavefront, which radiates away from the waveguide. This is the part in the range $x_o'(\theta_x) < x_o < w$ where $x_o'(\theta_x)$ is found from (4.8) as ψ_1 approaches the critical angle

$$x_o'(\theta_x) = R\left(1 - \frac{n_{cl}}{n_{co}}\frac{1}{\sin\theta_x}\right) \tag{4.10}$$

If (4.8) was solved for θ_x, as $\sin\psi \rightarrow \sin\theta_{cr}$ instead, then we could interpret in an alternative way

$$\theta_x = \theta_o(x) = \arcsin\left[\frac{n_{cl}}{n_{co}}\frac{R}{R-x_o}\right] \tag{4.11}$$

Equation (4.11) implies that rays entering the curved section from a given x_o survive as they propagate inside the bend if they belong in the range $\theta_o < \theta_x < \pi/2$ while they go beyond cut-off inside the bend if they belong in the range $\theta_c < \theta_x < \theta_o$. Therefore, the angle θ_o is in some ways, the equivalent to the acceptance angle which determines the *NA*

in straight waveguides.

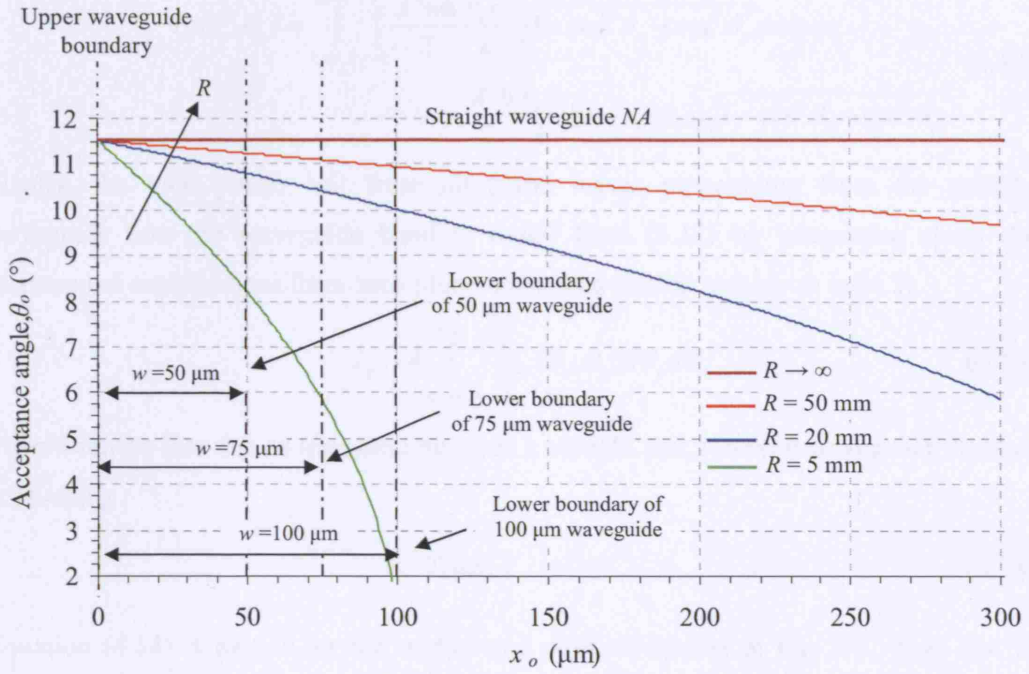

Fig. 4-6. Acceptance angle θ_o at a straight-curved waveguide join as a function of distance across the waveguide from the outside of the bend, x_o for several bend radii.

The difference is that in curved waveguides θ_o, and thus, the *NA* varies along the waveguide aperture with x. Fig. 4-6 plots the acceptance angle, $\theta_o(x)$ of rays as a function of the distance from the waveguide bend upper boundary x_o for three different radii of curvature R = 5 mm, R = 20 mm and R = 50 mm. The acceptance angle for curved waveguides of any radius of curvature R, starts off by being equal to the straight waveguide *NA* for rays entering from $x_o = 0$, but it drops monotonically with x_o, as rays enter from $0 < x \leq w$. Waveguides with small radius of curvature R, have an acceptance angle which drops rapidly across their aperture. As the radius of curvature increases, the acceptance angle asymptotically approaches the *NA* of the straight waveguide. Finally, the acceptance angle varies more for wider waveguides than for narrower ones implying that wide waveguides exhibit higher transition loss.

Each plane wave with $\theta_x < \theta_o$ experiences some degree of attenuation while those with $\theta_x > \theta_o$ do not notice any transition loss. For a certain plane wave, the power I_α which is

radiated is given by (see D12 for derivation)

$$I_\alpha(\theta_x,\theta_y)=\int_{x_o(\theta_x)}^{x_o=w}\int_{y=0}^{h}\frac{A^2wh}{2}\frac{\varepsilon_o\omega}{k}\sqrt{1-\cos^2\theta_x-\cos^2\theta_y}\,dxdy= \\ \frac{A^2h}{2}\frac{\varepsilon_o\omega}{k}(w-x_o(\theta_x))\sqrt{1-\cos^2\theta_x-\cos^2\theta_y} \tag{4.12}$$

Finally, the total power lost from all plane waves propagating from the straight waveguide into the waveguide bend is found from (4.12) by integrating along the incremental contributions from each plane wave, in a similar manner as in (4.7)

$$I_\alpha=4\int_{\theta_x=\theta_0}^{\pi/2}\int_{\theta_y=\theta_{cr}}^{\pi/2}I_\alpha(\theta_x,\theta_y)d\theta_x d\theta_y \tag{4.13}$$

Therefore, the loss due to transition between a straight and a curved waveguide *TransA*, is given by

$$TransA=\frac{I_\alpha}{I_o} \tag{4.14}$$

Equation (4.14) is plotted for the widths and radii of interest in Fig. 4-7. Note that in order to obtain these results we assumed that the whole *NA* of the input straight waveguide was filled with rays, which were assigned with a uniform angular (θ_x, θ_y) power distribution. There are two main conclusions arising from Fig. 4-7. Firstly, transition loss *TransA*, increases as the waveguide width w, increases for the same radius of curvature. This can be readily explained with the aid of Fig. 4-6, where we see that the acceptance angle of the waveguide bend reduces more for wider waveguides than it reduces for narrower waveguides. In other words, for a given plane wave there are more rays that will find themselves beyond cut-off after entering the waveguide bend for a wider waveguide than for a narrower one. The second observation is that as expected, transition loss asymptotically approaches zero when the radius of curvature increases for any waveguide width. This is easily understood if we consider that for $R \rightarrow +\infty$ the curved waveguide turns to a straight one.

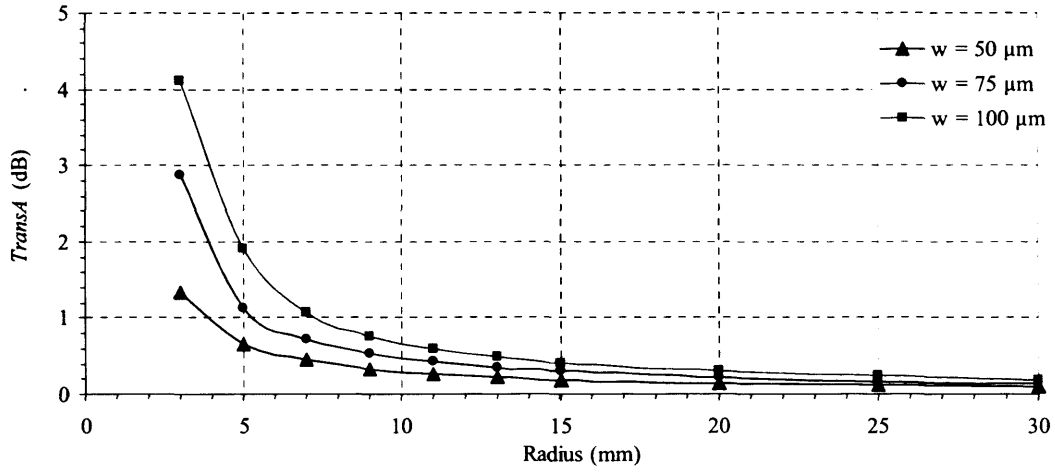

Fig. 4-7. Transition loss component between a straight waveguide and a waveguide bend loss, *TransA*, as a function of the bend radius calculated by the geometric ray optic approach.

4.4.3 Transition Loss Component between Waveguide Bends and Straight Waveguides, TransB

Rays not lost at the first transition, propagate in the waveguide bend by reflecting back and forth according to the generalized Fresnel reflection coefficients [4.31], until they reach the output straight waveguide. These rays suffer loss as a result of their leaky nature, but this is not adequately modelled by our geometric ray optics approach. The new transition between the curved and the second straight waveguide can be analyzed by considering it to be the reverse of Fig. 4-5. Equation (4.8) still applies and rays enter the output straight waveguide at exactly the same angles as they exited the input straight waveguide. The difference is that in this case the higher order modes have already died away due to the mode filtering effect of *TransA*, and the remaining low order modes are the only ones to be coupled. The angular range of rays emerging from the curved waveguide is well within the *NA* of the output straight waveguide and no loss occurs in the geometrical ray optic model. So, *TransA* (straight waveguide - bend) is much larger than *TransB* (bend - straight waveguide), which may be considered to be negligible for highly multimode waveguides. In waveguides with only one or a few modes though, overlap integrals rather than the ray-model give the transition loss. In this case situation is completely different. The energy in the modes in the single mode waveguide bend is offset towards the outside of the bend and does not match the modes in the straight

waveguide in which the energy is more centralized. Reciprocity shows that at both ends the loss should be the same [4.18] since overlap integrals of the modes at both ends are the same, apart from an interchange of the terms in the integrands which does not affect the results. However, single mode waveguides are not the topic of this chapter.

4.5. BPM MODELLING OF MULTIMODE WAVEGUIDE BENDS

4.5.1 Introduction

Although our the ray model is adequate for qualitative analysis of wave propagation, we need a more advanced method to investigate the loss components involved in curved waveguides. A very popular simulation tool which provides accurate results in a reasonable simulation time is the Beam Propagation Method (BPM). In this section we present our work on modelling the waveguides in our experiments by using BPM in three dimensions. In order to conduct our simulations we used the commercial program BeamPROP by RSOFT, [4.36].

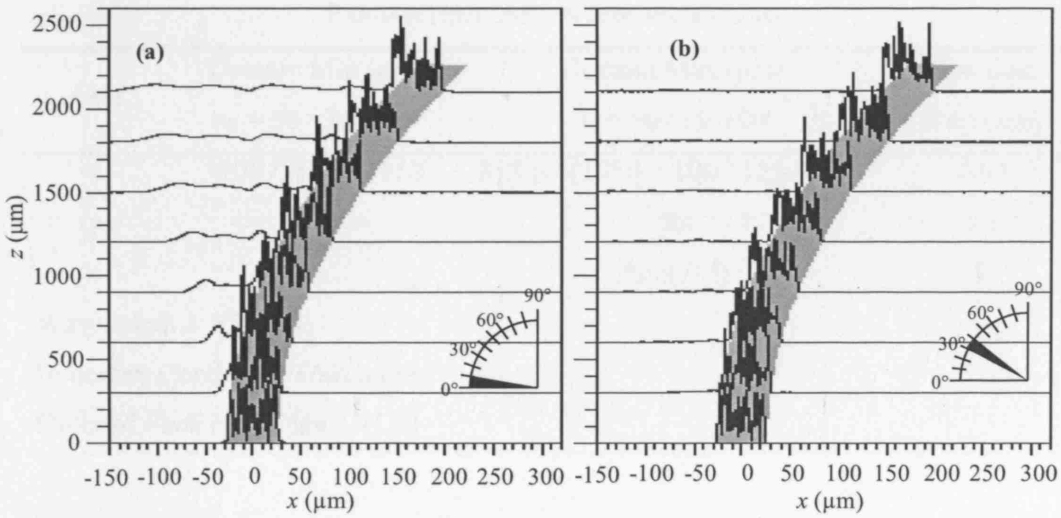

Fig. 4-8. Propagation of the optical field around two waveguide segments of a bend for a launch field consisting of fully filled straight waveguide modes for w = 50 μm, R = 13 mm (a) in the first segment (first 10°). (b) in the 30° to 40° degree segment.

Standard BPM modelling assumes a paraxial approximation in which rays travel within a small angle of the original launch direction along the initial waveguide axis. This means that direct simulation of a 90° bend could not be performed as the final rays would be at

angles of about 90° to the original rays. So, we divided our 90° bent waveguide into a number of smaller radial sectors, Fig. 4-8, within which the paraxial approximation was valid. The initial field profile was propagated through one segment and the amplitude and phase of the field profile at the end was stored and used as the initial field for the next segment, Fig. 4-8. After a set of trial simulations of insertion loss in 50 μm × 50 μm waveguide bends we concluded that we could accurately analyze waveguide segments turning through an angle of up to 10° before the algorithm gave diverging results. This approach avoided the need to use a wide angle version of BPM using higher order Padé coefficients in three dimensions which is difficult to implement in 3D. The scalar version of BPM was used as it was faster although it did not account for polarizations. This choice was confirmed by carrying out another set of test simulations using fully-vectorial BPM which showed indistinguishable results for the loss of *TE* and *TM* waveguide modes through a 10° segment. Table 4.2 lists the parameters used in the simulations.

TABLE 4.2

PARAMETERS USED IN BPM MODELLING

Axis	Domain Min (μm) $w = 50 / 75 / 100$	Domain Max (μm) $w = 50 / 75 / 100$	Compute Step (μm)
x	-100 / -125 / - 150	R[3-cos($10°$)] + 100 / 125 /150	0.05
y	- 30	30	0.1
z	0	Rsin($10°$)	1

Wavelength λ: 850 nm

Boundary Condition: Transparent

Order of *Padé* coefficients: (1,0)

4.5.2 Waveguide Sidewall Roughness Implementation

In a real system, waveguides have some sidewall roughness. Therefore, an accurate simulation should include the effect of the roughness in a direct or, at least, in an indirect way. Direct implementation of waveguide wall roughness is very challenging in BPM since it requires a very fine grid to capture the highest spatial frequency components leading to impractically long simulation times. In reality not all Fourier components of

the roughness are required in order to perform these simulations. The spectrum of the roughness in our waveguides follows a Gaussian distribution and measurements with an AFM (further details are given in Chapter 6) showed that the autocorrelation length varies in the region 2 μm < L_c < 8 μm, and the standard deviation within the range 9 nm < σ < 74 nm. As the coupling between a radiation mode and a bound mode depends at the amplitude of the roughness spectrum taken at the difference between the propagation constants of the two modes, in reality we only need to confine our simulations within the band of the roughness spectrum with significant amplitudes. However, even if we used these limited Fourier components only the simulations would still need to be too long for a practical analysis.

If we assume that roughness causes a strong coupling and mixing between modes, we can overcome this limitation by artificially exciting a large number of waveguide modes in the launched field. We investigated two different input fields in our simulations. In the first case, waveguide modes were excited by the modes of a multimode fibre with a fully filled *NA* and with parameters matching those of our experiment. In the latter case, we used a three dimensional field consisting of many straight waveguide modes filling the waveguide *NA* this time, all with equal amplitudes. The waveguides modelled had the same width, thickness and Δn as in our experiments. In each case, each mode was given a random phase to model the effect of the mode scrambler in our experiment for fibre modes or the effect of the wall roughness for the waveguide modes. To avoid inadvertently chosen special cases, three different phase profiles were created for the two cases (MM fibre, waveguide modes) by a Monte-Carlo random number generator. After generation, all three fields were summed and launched into the first rectangular straight waveguide segment. The total number of modes generated was in excess of 300.

4.5.3 BPM Simulation of Propagating Field in Waveguide Bends

After propagating 1 mm inside the straight waveguide, to ensure that almost all of the radiating components due to mode mismatch had been removed from the waveguide the amplitude and the phase of the field was stored. The input straight waveguide was 11.5 mm in length but it was sufficient to only model 1 mm of length as we found it gave the same results to a longer waveguide. This was mainly because wall roughness and the resultant intermodal coupling were not directly included in the model and so, the modal

distribution was not affected by the waveguide length as it happens in the presence of the sidewall roughness. This saved field was then launched into the first 10° bent waveguide segment. The same range of radii of curvature and waveguide widths as the waveguide bends in the experiments was modelled. Typical radial field profiles are shown in Fig. 4-8 for the first and a later segment. The modal energy within the waveguide is towards the outer side of the bend as expected [4.32]. Figure 4-8 (a), shows the light which radiates to the left of the waveguide due to mode mismatch. After the initial radiation causing transition loss, only the radiation loss eventually remains which is weaker than the transition loss and can only just be seen in Fig. 4-8 (b), on the outside of the bend. This is seen more clearly in Fig. 4-9 where the power has been integrated along the radius across the waveguide and all 9 segments have been plotted continuously as a function of angle traversed together with this power's derivative (per degree of curvature) for an example case, w = 75 μm, R = 5 mm.

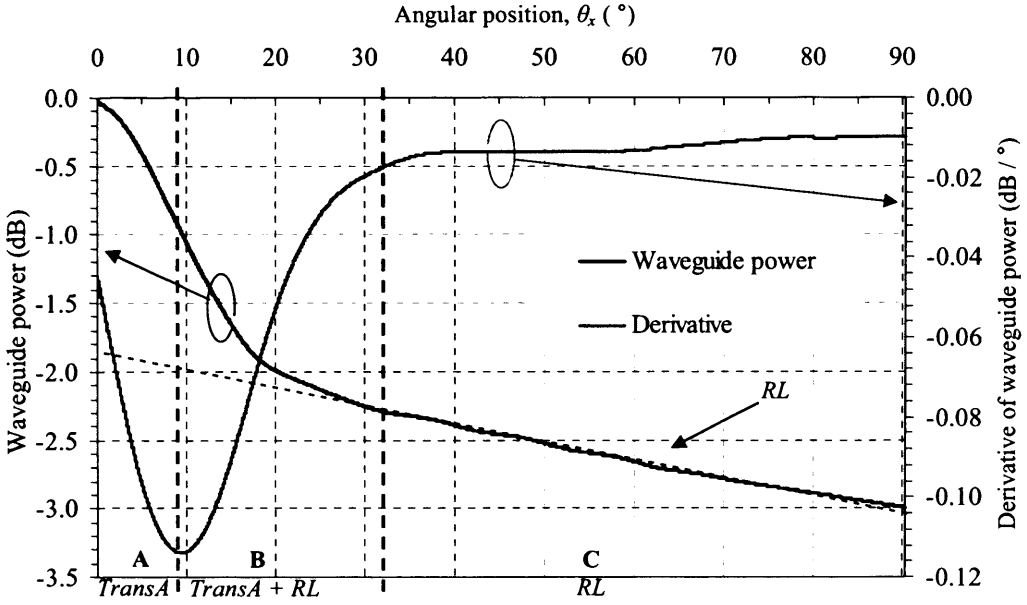

Fig. 4-9. Power as a function of angular propagation position θ_x, calculated by cascading the results from nine 10° segments and its derivative for w = 75 μm, R = 5 mm. For $0 < \theta_x < 8°$ transition loss (*TransA*) dominates and the derivative of the power is decreasing. For $8° < \theta_x < 33°$ derivate changes to becoming ascending, implying that the effect of transition loss has been mitigated. In this region, both transition and radiation loss (*RL*) components are important. Finally for $\theta x > 33°$ bend loss takes over and derivative is almost constant. By fitting a least-squares line to the results in region C we calculated the *BL* loss component.

The power at the input of the waveguide bend, $\theta_x = 0°$, has been set to 0 dBm. From

the power derivative plot we can easily identify three regions namely region A, B and C where the contribution of transition and bend loss varies. The high rate of increasing loss within a short distance or angle ~ 8°, of the waveguide entrance (region A) of between – 0.11 dB/° and 0.014 dB/° is due to a combination of transition loss, *TransA* which dominates and radiation loss, *RL*. As we progress from region A to region B energy is lost but at a decreasing rate due to the weakened contribution of *TransA*, and both types of loss are important. Finally, at larger angles >33° (region C) the much slower rate of increase of loss of 0.016 dB/° is the radiation, *RL*. In other waveguides region A was seen to extend over a much larger angular region. The radiation loss was calculated by fitting a line to the curve in section C. Then, by subtracting the radiation loss from the combined loss in section A we found and separated out the transition loss, *TransA*. Finally, we launched the field at the end of the bend into a straight waveguide, and similarly, calculated the *TransB* loss component.

4.6. COMPARISON BETWEEN BPM MODELLED RESULTS AND EXPERIMENTAL RESULTS

Fig. 4-10 (a) – (c) show the simulation results for the two input fields (MM fibre, waveguide modes) compared to the experimental results in Fig. 4-4, for the 50 μm, 75 μm and 100 μm width of waveguides correspondingly. For all three waveguide cases the modelled loss when a fibre is butt-coupled to the straight waveguide as in the experiments, is significantly lower than that when the input is considered to come from a waveguide with a fully filled *NA*. This can be explained if we consider that when a fibre with NA_{fibre} = 0.2, is aligned to a square waveguide with NA_{wg} = 0.302 it only excites a fraction of the waveguide modes. These modes maintain their relative powers throughout the straight waveguide section until they reach the start of the bend, since there is no mixing mechanism such as wall roughness to couple them in the model. On the other hand, an input from a fully filled straight waveguide excites all of the straight waveguide modes without loss which continue to the start of the bend. So, since in the second case the input field contains more high order modes and high order modes exhibit more attenuation (mainly transition) in a bend, as we saw in section 4.4, the modelled insertion loss for the waveguide mode case is higher than the modelled loss for the MM fibre case as shown, in Fig. 4-10.

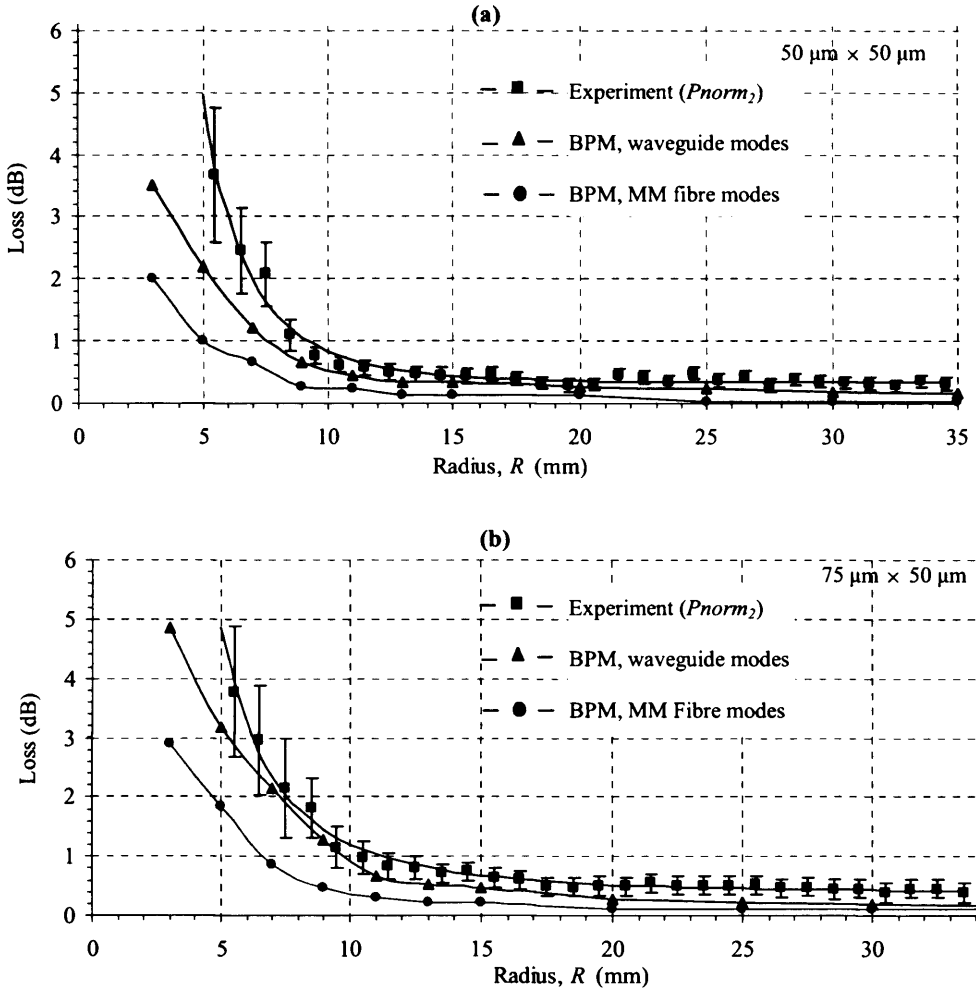
(a)
50 µm × 50 µm
Experiment (Pnorm2)
BPM, waveguide modes
BPM, MM fibre modes
Loss (dB)
Radius, R (mm)
(b)
75 µm × 50 µm
Experiment (Pnorm2)
BPM, waveguide modes
BPM, MM Fibre modes
Loss (dB)
Radius, R (mm)

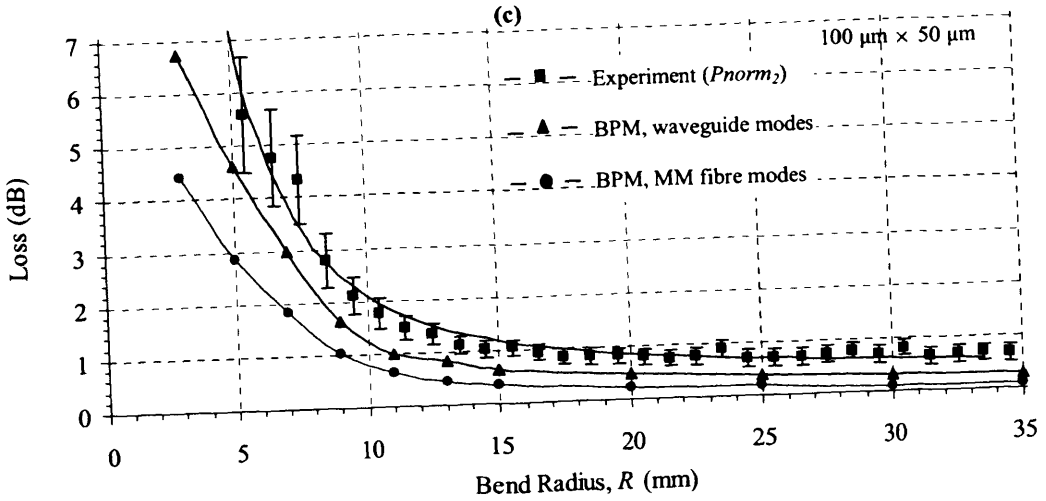

Fig. 4-10. BPM modeled loss (*TransA* + *RL*) for launched fully filled 50/125 µm MM fibre modes and for fully filled waveguide modes compared to experimental loss as a function of bend radius for 50 µm × 50 µm waveguides. A second experimental normalization removed the propagation loss to match the slope of the modelled waveguide mode curve for $R > 20$ mm, where loss was linear.

A second normalization step, (after the one in section 4.3.3 which removed the coupling loss) calibrated out the propagation loss from the experimental data plotted in Fig. 4-10. The normalized experimental results P_{norm2}, in Fig. 4-10 were obtained from those in Fig. 4-4 by subtracting the propagation loss, $\alpha(w)$. This was found by fitting a least-square line to the curves in Fig. 4-4 for radii of curvature R, beyond the minimum loss point, Table 4.1, and finding the slope, $\alpha_{expt}(w)$. Note that experimental results contain both propagation and bend loss. In order to separate them we fitted a line to the fully filled waveguide launch modeled curves in Fig. 4-10, beyond a 20 mm radius where results are linear, to find the slope $\alpha_{BPM}(w)$. Both $\alpha_{expt}(w)$ and $\alpha_{BPM}(w)$ are given in Table 4.3. The units of these slopes are in dB/ΔR mm which means per mm change in the radius of curvature. Note that since the graphs are plotted as a function of the radius the actual waveguide length is changed by δl (mm) equal to $\delta l = (\pi/2) / \Delta R$. In order to convert this to propagation loss in dB/cm along the waveguide axis the total slope figure was multiplied by $10\times2/\pi$. If we assume that the slope of the BPM modeled curves is accurate then we can subtract the two slopes to find the propagation loss.

$$PL = (l_{in} + l_{out} + l_{bend})\alpha(w) \tag{4.15}$$

$$\alpha(w) = \alpha_{BPM}(w) - \alpha_{expt}(w) \tag{4.16}$$

which, can then be used to normalize the experimental results using (4.4), assuming that the propagation loss in the straight waveguide sections is the same as that in the bend, $\alpha(w)$.

$$P_{norm2} = P_{norm1} + (l_{in} + l_{out} + l_{bend} - l_{str})\alpha(w) \tag{4.17}$$

where l_{bend} is the length of each curved section. Substituting the definition of P_{norm1} (4.4), into (4.17) we finally find

$$P_{norm2} = -BL - TransA - TransB \tag{4.18}$$

So, the normalized experimental curve in Fig. 4-10 consists only of combined bend and transition losses. All the rest of the loss components including the propagation loss remaining from the first calibration step have been removed.

4.7. WAVEGUIDE BEND LOSS COMPONENT SEPARATION

Fig. 4-11 (a)-(c) show all of the loss components after being separated. The propagation loss was found from (4.10) by comparing the experimental results and the BPM modelling for each waveguide width. Radiation loss was found by repeating the process described in Fig. 4-9 for each waveguide, and transition loss was found by subtracting the radiation loss from total loss calculated by BPM (Fig. 4.10). Fig. 4-11 shows that wider waveguides have higher transition and radiation loss but less propagation loss. The higher transition loss and higher radiation loss of the wider waveguides agrees with similar observations experimentally in [4.10], [4.16] and theoretically for slab waveguides and optical fibres in [4.18], [4.32]. Table 4.3 shows that wider waveguides have slightly less propagation loss which agrees with the theoretical predictions in [4.27]-[4.28] but the large experimental error in Table 4.3 means this cannot be asserted with confidence.

Below about 5 mm bend radius, the transition loss is large and dominates over the radiation loss. Below 10 mm bend radius, the transition loss and the radiation loss cause seriously increased total loss. At a bend radius of about 15 mm, radiation, transition and propagation losses have about the same magnitude of 0.3 dB for the 50 μm × 50 μm waveguide. The effects of transition loss and bend loss are reduced to about 0.2 dB at a bend radius of 30 mm but the propagation loss has now been increased to 0.6 dB.

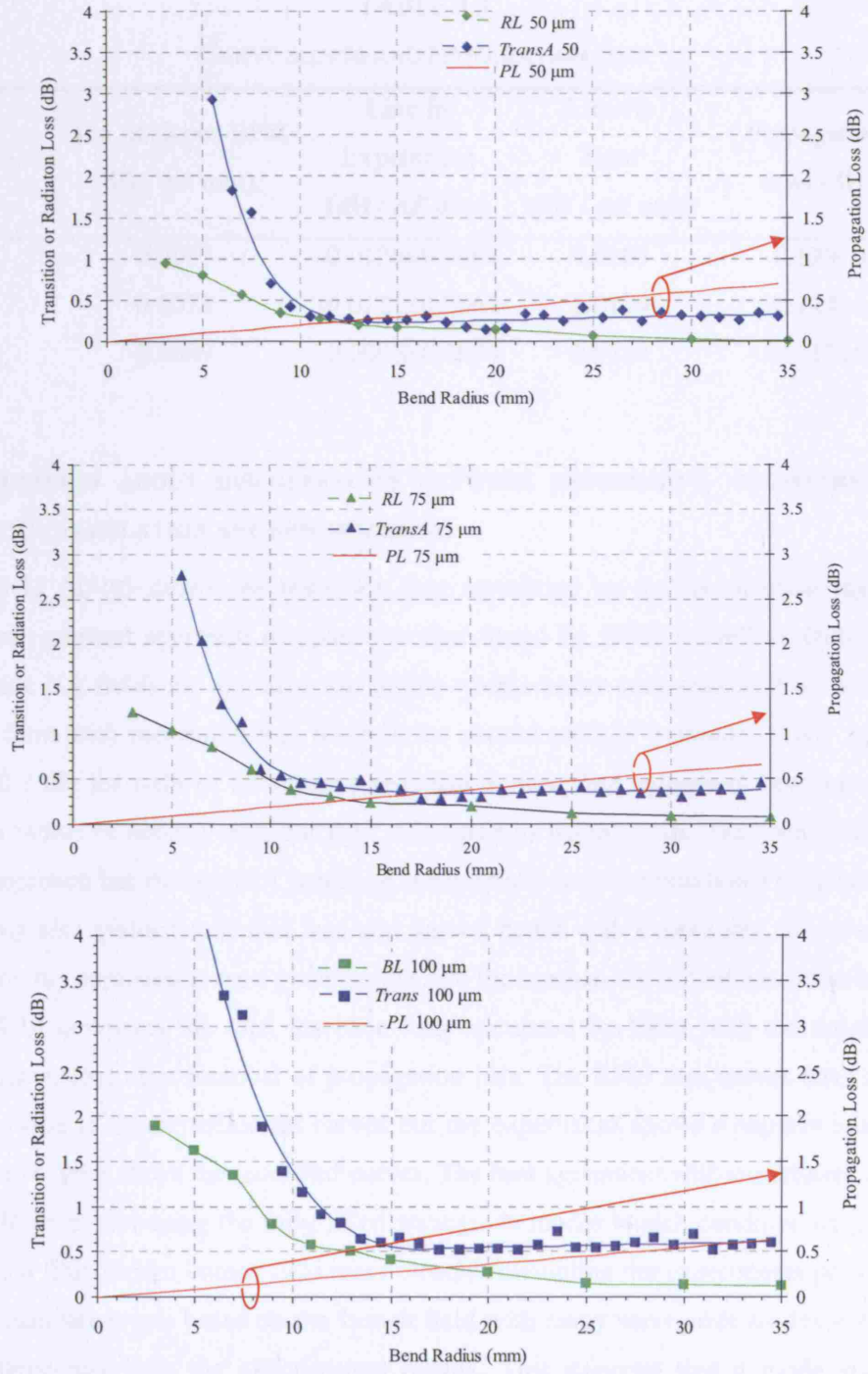

Fig. 3-11. Transition, radiation loss from the BPM modelling and propagation loss from both the experiment and BPM modeling for 50 μm × 50 μm, 75 μm × 50 μm and 100 μm × 50 μm waveguides.

TABLE 4.3

CURVE SLOPES AND PROPAGATION LOSS

Width (μm)	Line fit slopes BPM (dB / ΔR mm)	Line fit Experiment (dB / ΔR mm)	Line fit Total (dB / ΔR mm)	Propagation Loss $\alpha(w)$ (dB / cm)
50	0.0067	-0.0136±0.0064	0.0203	0.129±0.041
75	0.0073	-0.0121±0.0063	0.0194	0.124±0.040
100	0.0089	-0.0095±0.0094	0.0184	0.117±0.060

4.8. DISCUSSION ABOUT DISCREPANCIES BETWEEN EXPERIMENT, GEOMETRIC RAY OPTIC CALCULATION AND BPM MODELING

Fig. 4-12 (a)-(c) shows the transition loss calculated by the geometrical ray optic numerical aperture approach compared to that found by BPM modelling (fully filled waveguide NA field) for the three waveguide widths under examination. Curves have a similar form with increasing loss towards the shorter radii of curvature. They agree to within 0.2 dB for radii of curvature more than 9 mm. The agreement becomes worse below a radius of about 9 mm but they still agree to within 1 dB. The geometrical ray optics approach has the merit of requiring substantially less computational time but BPM modelling also yielded radiation loss and agreed better with experiment. However, the geometric ray approach gives a good insight into the mechanism behind transition loss.

Fig. 4-10 compares the total insertion loss calculated by BPM with the normalized experimental loss after removal of propagation loss. The BPM loss curves have a very similar shape to the experimental curves but the experiment shows a slightly increased loss always lying above the modelled curves. The best agreement with experiment occurs for the BPM model using the fully filled waveguide modes launch condition despite the fully filled fibre modes launch field more closely resembling the experiments performed. The normalization was based on the launch field with many waveguide modes due to its better agreement with the experimental results. This suggests that a mode coupling process is occurring and there are two possible processes. Although the matching fluid refractive index is close to the core index there is still some mismatch.

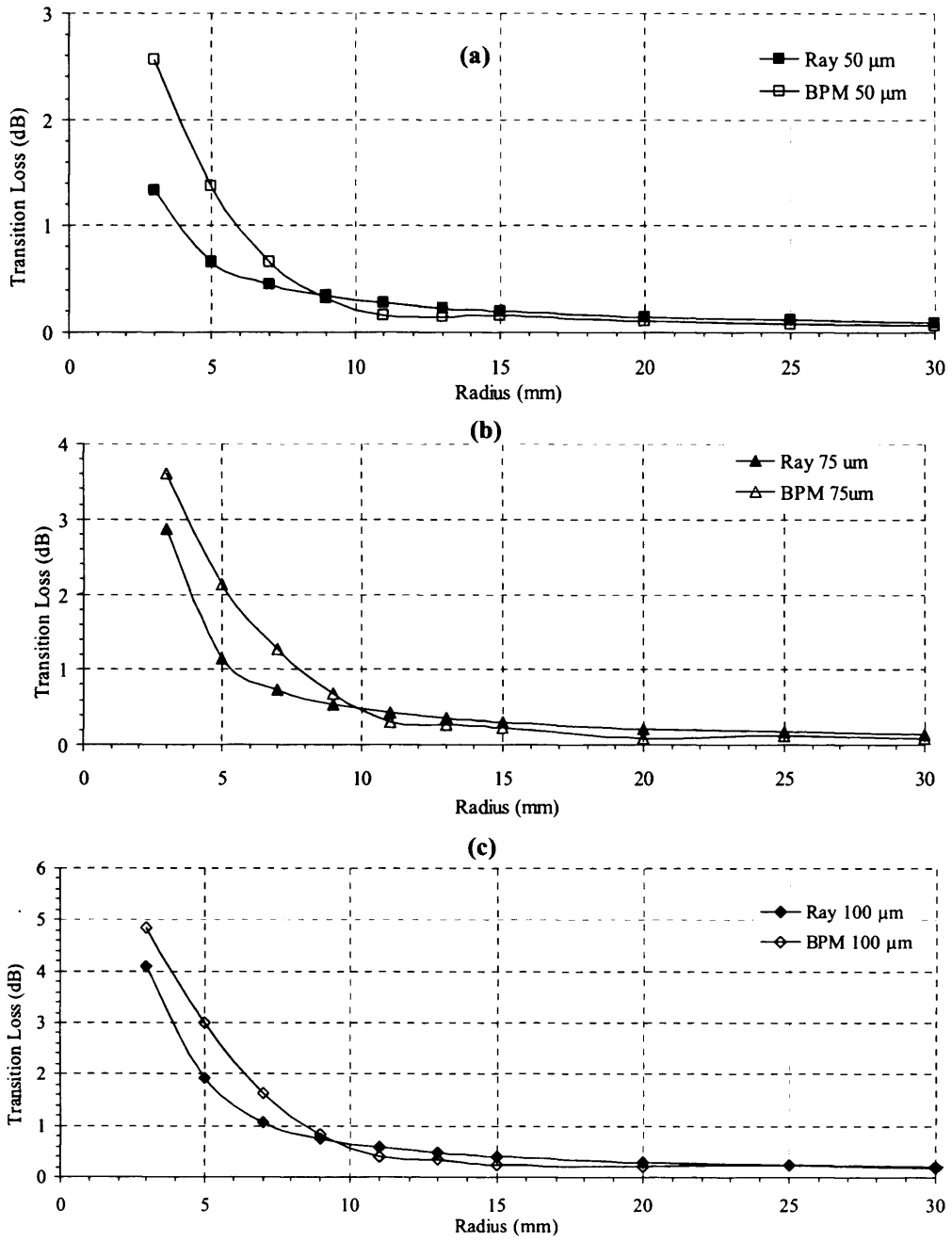

Fig. 4-12. Transition loss as a function of bend radius calculated by geometric ray optic approach compared to that by BPM modeling.

Therefore, the relatively rough front waveguide surface couples light into more waveguide modes than for a polished entry surface due to scattering and causes

additional scattering loss. In addition, the side-wall roughness not only transfers power from guided to radiation modes but also redistributes energy between them. These two mechanisms may also explain the higher loss we observed in our experiment compared to either of the modelled results.

Fig. 4-10 shows the experimental results to agree with the BPM fully filled waveguide modes launch simulation to within experimental error for radii above about 10 mm but to increasing deviate for radii below this to give a 1 dB difference at a radius of 5 mm with an increased experimental loss more than the simulation. The main differences between simulations and experiments which may account for the slight differences are

a) The facet and side-wall waveguide roughness was not included directly in the theoretical model although the choice of fully filled modal launch conditions partially accounted for it.
b) Alignment in experiments was not perfect as in the theory and was estimated to be for angular misalignment $<1°$ and lateral and axial misalignment <5 μm.
c) The dicing cut at the entrance and exit of the straight waveguides was not always at exactly 90° to the waveguide which would affect the symmetry of mode coupling and predominant propagation direction.
d) Photographs of the end face of the waveguide show that the side walls of the waveguide were slightly tilted with the waveguide being narrower at the top and having rounded convex corners at the top and concave corners at the bottom.
e) The waveguide layout was digitized onto a grid and formed from polygons in order to form the photomask. This quantization error would result in a rough wall to the curved waveguide which might be worse than for an e-beam mask made using a finer mesh.

4.9. SUMMARY – CONCLUSIONS

The loss of curved multimode polymer waveguides was measured and calculated by geometrical optics approach and by BPM modelling for a range of radii of curvature and for several waveguide widths to establish design curves to aid optical waveguide interconnect backplane designers. The best agreement was for radii of curvature larger than 10 mm. The design curves of loss as a function of bend radius were plotted after

separating out the propagation loss so that they can be used by designers using other polymers or other fabrication techniques which may alter the wall roughness and so the propagation loss. The various components making up the total loss were separated with the help of BPM modelling to separate the pure bend loss from the transition loss. For the smallest radii transition loss from the first straight waveguide to the curved waveguide was the most important. As the radius increased transition and bend loss decreased, while propagation loss increased so that at a radius of ~15 mm they were all of equal importance. Finally, at radii larger than 20 mm propagation loss was the most important.

We introduced a novel technique for measuring propagation loss as a series of nested bent waveguides have a range of lengths, so by plotting the loss as a function of radius and fitting a linear curve, propagation loss can be extracted. This is more convenient than using the conventional cut-back method since the uncertainties involved in the successive dicing of a waveguide wafer are eliminated and experiments take less time and also experiments can be reproduced as many times as desired.

We applied the geometrical ray optic calculation to find the numerical aperture and transition loss between straight and curved waveguides. This required the concept of numerical aperture being extended so that the *NA* varied across the waveguide being largest at the outside of the bend at the junction with a straight waveguide. The geometric ray optic calculation is quickly performed and can be readily programmed from the derived equations provided if BPM or other modelling software is not available and yields reasonably accurate results. BPM modelling agreed better with experiment than the geometrical ray optics approach and also gave radiation loss although at the expense of increased computational time. The geometrical optics calculation showed that the curved waveguide behaves as a mode filter which filters out higher order modes leaving only low-order modes.

The optimum bend radius for polymer waveguide backplanes, Fig. 4-3, Table 4.1, is 13.5 mm for 50 μm × 50 μm waveguide cross-sections giving 0.73 dB loss, 15.3 mm for 75 μm × 50 giving 0.84 dB loss and 17.7 mm for 100 μm × 50 giving 1.16 dB loss, as these provide a balance of pure bend and transition loss versus propagation loss. It is inadvisable to have much smaller radii of curvature than ~10 mm since loss increases quickly as the radius is reduced, although if very tight bends are required to meet layout

constraints then Fig. 4-4 can be used as a design curve to establish the loss for the link power budget calculation. Measurements of waveguide bend insertion loss in [4.13]-[4.14], agree reasonably well with the results in Fig. 4-4, for the insertion loss of our 50 μm × 50 μm waveguide, which is the most commonly used cross-section dimension in backplanes. However, in both [4.13]-[4.14], they did not report the increase of loss in the long radii regime due to propagation loss domination, nor did they separate the various loss components from each other. Insertion loss in [4.15] is significantly lower compared to this study or to [4.13]-[4.14], but in that case out-of-plane 180° bends were investigated on flexible polymer circuits which makes any direct comparison difficult.

REFERENCES

[4.1] Xyratex RS-4835-E3-EBD network storage system datasheet, available at www. xyratex.com/pdfs/products/storage-systems/ds/RS-4835-E3-EBD_1-.pdfKeun, accessed 13/06/07.

[4.2] A. M. Kok, S. Musa, A. Borreman, M. B. J. Diemeer, and A. Driessen, "Completely multimode arrayed waveguide grating-based wavelength demultiplexer," *in Proc. of IEEE International Conference on Computer as a Tool*, pp. 422-426, Sep. 2003.

[4.3] D. Israel, R. Baets, M. J. Goodwin, N. Shaw, M. D. Salik and C. J. G.-Kirkby, "Comparison of different polymeric multimode star couplers for backplane optical Interconnect," *J. Lightw. Technol.*, vol. LT-13, pp. 1057-1064, Jun. 1995.

[4.4] Y. Hida, H. Onose, and S. Imamura, "Polymer waveguide thermooptic switch with low electric power consumption at 1.3 μm," *IEEE Photon. Technol. Lett.*, vol. 5, pp. 782-784, July 1993.

[4.5] A. Kumar, and S. Aditya, "Performance of S-bends for integrated-optic waveguides," *Microwave Opt. Technol. Lett.*, vol. 19, pp. 289-292, Nov. 1998.

[4.6] S. Akiyama, M. A. Popović, P. T. Rakich, K. Wada, J. Michel, H. A. Haus, E. P. Ippen and L. C. Kimerling, "Air trench bends and splitters for dense optical integration in low index contrast," *J. Lightw. Technol.*, vol. LT-23, pp. 2271-2277, July 2005.

[4.7] A. J. Harris and P. F. Castle, "Bend loss measurements on high numerical aperture single-mode fibres as a function of wavelength and bend radius," *J. Lightw. Technol.*, vol. LT-4, pp. 34-40, Jan. 1986.

[4.8] L. Faustini and G. Martini, "Bend loss in single-mode fibres," *J. Lightw. Technol.*, vol. LT-15, pp. 671-679, Apr. 1997.

[4.9] A. P. Boechat, D. Su, D. R. Hall, and J. D. C. Jones, "Bend loss in large core multimode optical fibre beam delivery systems," *Appl. Opt.*, vol. 30, no. 3, pp. 321-327, 1991.

[4.10] M. A. Losada, I. Garcés, J. Mateo, I. Salinas, J. Lou, and J. Zubía, "Mode

coupling contribution to radiation loss in curvatures for high and low numerical aperture plastic optical fibres," *J. Lightw. Technol.*, vol. LT-20, pp. 1160-1164, July 2002.

[4.11] M. –Y. Loke, and James N. McMullin, "Simulation and measurement of radiation loss at multimode fibre macrobends," *J. Lightw. Technol.*, vol. LT-8, pp. 1250-1256, Aug. 1990.

[4.12] J. Arrue, J. Zubia, G. Fuster, and D. Kalymnios, "Light behavior when bending plastic optical fibres," *IEE Proc-Optoelectron*, vol. 145, pp. 313-318, Dec. 1998.

[4.13] S. Musa, A. Borreman, A. A. M. Kok, M. B. J. Diemeer, and A. Driessen, "Experimental study of bent multimode optical waveguides," *Appl. Opt.*, vol. 43, no. 30, pp. 5705-5707, Oct. 2004.

[4.14] L. Dellmann, R. Dangel, R. Beyeler, Ch. Berger, F. Horst, B.J. Offrein, and G.L. Bona, "Polymer waveguides for high-speed optical interconnects," *in Proceedings of EOS Topical Meeting on Optics in Computing, Engelberg, Switzerland*, pp. 131-132, 2004.

[4.15] M. Hikita, S. Tomarum K. Enbutsu, N. Ooba, R. Yoshimura, M. Usui, T. Yoshida, and S. Imamura, "Polymeric optical waveguide films for short-distance optical interconnects," *IEEE J. Sel. Top. Quantum. Electron.*, Vol. 5, pp. 1237-1242, 1999.

[4.16] J. Cardenas, L. Li, S. Kim, and G. P. Nordin, "Compact low loss single air interface bends in polymer waveguides," *Opt. Express*, vol. 12, pp. 5314-5324, Nov. 2004.

[4.17] C. Winkler, J. D. Love, and A. K. Ghatak, "Loss calculations in bent multimode optical waveguides," *Opt. Quant. Elect.*, vol. 11, pp. 173-183, 1979.

[4.18] M. Heiblum and J. H. Harris, "Analysis of curved waveguides by conformal transformation," *IEEE J. Quantum Electron.*, vol. QE-11, pp. 75-83, 1975.

[4.19] W. Berglund and A. Gopinath, "WKB analysis of bend loss in optical waveguides," *J. Lightw. Technol.*, vol. LT-18, pp. 1161-1166, Aug. 2000.

[4.20] S. S. A. Obayya, B. M. Rahman, and K. T. V. Grattan, "Fully vectorial finite element modal solution of curved optical waveguides," *Laser Phys. Lett.*, vol. 2,

pp. 131-136, Mar. 2005.

[4.21] J.-S. Gu, P.-A. Besse, and H. Melchior, "Method of lines for the analysis of the propagation characteristics of curved optical rib waveguides," *IEEE J. Quantum Electron.*, vol. QE-27, pp. 531-537, Mar. 1991.

[4.22] J. Yamauchi, M. Ikegaya and H. Nakano, "Analysis of bent step-inex optical fibres by the beam propagation method," *Proc. Inst. Elect. Eng.*, vol. 139, no. 3, pp. 201-207, 1992.

[4.23] S. Tomljenovic-Hanic, J.D. Love and A. Ankiewicz, "Effect of additional layers on bend loss in buried channel waveguides," *Proc. Inst. Elect. Eng.* Optoelectron., vol. 150, no. 3, pp. 259-265, 2003.

[4.24] P. Bienstman, E. Six, M. Roelens, M. Vanwolleghem, and R. Baets, "Calculation of bending loss in dielectric waveguides using eigenmode expansion and perfectly matched layers," *IEEE Photon. Technol. Lett.*, vol. PTL-14, pp. 164-166, Feb. 2002.

[4.25] K. Thyagarajan, M. R. Shenoy, and A. K. Ghatak, "Accurate numerical method for the calculation of bending loss in optical waveguides using a matrix approach," *Opt. Lett.*, vol. 12, pp. 296-298, Apr. 1987.

[4.26] F. Ladoucer, J. D. Love, and T. J. Senden, "Effect of side wall roughness in buried channel waveguides," *IEE Proc. Optoelectron.*, vol. 141, Aug. 1994.

[4.27] D. Marcuse, "Power distribution and radiation loss in multimode dielectric slab waveguides," *Bell Syst. Tech. J.*, vol. 51, pp. 429-454, Feb. 1972.

[4.28] D. Marcuse, "Mode conversion caused by surface imperfections of a dielectric slab waveguide," *Bell Syst. Tech. J.*, vol. 51, pp. 3186-3215, Feb. 1972.

N. Suyal, Exxelis Ltd., private communication, Feb. 2006.

[4.29] A. K. Ghatak, "Leaky modes in optical waveguides," *Opt. Quant. Elect.*, vol. 17, pp. 311-321, 1985.

[4.30] A. W. Snyder and J. D. Love, "Reflection at a curved dielectric interface - electromagnetic tunneling," *IEEE Trans. Microw. Theory Tech.*, vol. MTT-23, pp. 134-141, Jan. 1975.

[4.31] C. Goyal, R. L. Gallawa and A. K. Ghatak, "Bent planar waveguides and

whispering gallery modes: A New Method of Analysis," *J. Lightw. Technol.*, vol. LT-8, pp. 768-774, May 1990.

[4.32] L. Jacomme, "Model for ray-propagation in a multimode graded-index fibre," *Opt. Commun.*, vol. 14, pp. 134-138, 1975.

[4.33] A. Himmler, E. Griese, J. Schrage, T. Bierhoff, A. Wallrabenstein, "Modeling of highly multimodal optical interconnects for time domain analysis", *in Digest of the Leos Summer Topical Meetings*, pp. I43 – I44, Jul. 2000.

[4.34] Exxelis Ltd., "TruemodeTM wet film datasheet". Available at http://www.exxelis.com/products/truemode.php. Last time accessed 16/06/07.

[4.35] A. W. Snyder and J. D. Love, "Optical Waveguide Theory", London: Chapman and Hall (1983).

[4.36] www.rsoftdesign.com/products/component_design/BeamPROP

CHAPTER 5

THEORETICAL AND EXPERIMENTAL INVESTIGATION OF TAPERED WAVEGUIDE BENDS

5.1. INTRODUCTION

Tapered waveguides have been used extensively in the past to facilitate light coupling from a laser source into a waveguide or fibre especially in single mode systems [5.1]-[5.3]. In some cases, laterally tapered polymer waveguides have also been used in multimode systems for optical interconnections [5.4]-[5.5] but, so far, they have not found wide acceptance, although coupling in these systems is particularly challenging. Cost requirements in optical interconnection systems demand laser-to-waveguide and waveguide-to-photodetector coupling to be passive and, therefore, a potential large degree of misalignment between components should be expected and tolerated. Introducing waveguides with large physical apertures is not seen as a solution to the coupling problem in all cases, since waveguides have to be wide at their entrance to optimize laser-to-waveguide coupling but sufficiently narrow at their output to fit within the active area of the photodetectors, which has to be kept small in order to minimize their bandwidth limiting parasitic capacitance. In current electronic backplane designs, adjacent connectors are placed as close as to within 1″ from each other and, therefore, in similar optical backplanes waveguides coming from one connector would have to bend in order to bypass an adjacent connector. However, our analysis in Chapter 4 showed that the optimum radius of curvature for the multimode waveguides usually employed in optical backplanes is ~ 15 mm and therefore, almost all of the area between two connectors is taken over by the bend. The lack of space is a serious problem for the straight tapers since in order for them to be loss efficient, they have to operate in the adiabatic regime, where their width changes at a very slow rate [5.6], to minimize coupling between propagating and radiating modes. As a result, tapers usually need to be long and a compromise between the space occupied by the bend, and the space occupied by the taper has to be made, leading to higher than could have been achieved loss. A solution, which results in a

more compact device than the straight taper plus bend combination, is to merge the taper with the bend into a single component. Actually the idea of tapered bends is not new and to some extend it has been explored in the past [5.7]-[5.8]. However, the field is still lacking an "adiabatic mode" type technique, already present in the straight taper case [5.9], which can provide with insight into how modes transform as they propagate inside the tapered bend. In addition, the field is also lacking an experimental investigation of tapered bends under real system conditions, which would equip the backplane designer with design rules that determine the optimum backplane architecture.

This chapter is divided into two parts. The first part presents the fundamentals of a new propagation theory for tapered bends, in which we propose an adiabatic mode theory equivalent to that for the straight taper, where modal amplitude and phase adjusts to the local waveguide environment. In order to construct the adiabatic modes in the tapered bend we combined the Wentzel-Kramers-Brillouin (WKB) theory [5.10]-[5.11], which describes wave propagation in waveguide bends with the powerful intrinsic mode theory [5.12]-[5.17] which has successfully described propagation phenomena in straight tapered waveguides.

The second part of this chapter is dedicated to the experimental analysis of a range of tapered bends. The aim of these experiments is to investigate the effect of the taper ratio (defined as the ratio of the input to the output width) and the radius of curvature, on the loss performance of the tapers. In particular, we are investigating the effect of the taper ratio and radius of curvature on the insertion loss and the tolerance to source misalignment of the device aiming at defining regions of optimum operation.

This chapter is arranged as following. In section 5.2.1 we provide the fundamentals of the WKB theory for propagation in waveguide bends, in section 5.2.2 - 5.2.6 we present the extension of the intrinsic mode theory to the tapered bend case and in 5.2.7 – 5.2.8 we present the analytical expression for the adiabatic modes before, close to and beyond cut-off. In section 5.3.1 – 5.3.2 we introduce the layout of the tapered waveguide bends used in our experiments, in section 5.3.3 we present the experimental results for the tapered bend insertion loss and we compare them to similar results for straight tapers, and in 5.3.4 we present the experimental results of the tapered bend tolerance to source misalignment. Finally, in section 5.4 we conclude.

5.2. ADIABATIC MODE THEORY OF TAPERED BENDS

5.2.1 Slab Bend Waveguide and Conformal Transformation

The aim of this section is to provide the fundamental theory of simple step-index slab waveguide bends and their analysis after applying the conformal transformation described in [5.10]. This transformation has the effect of translating curved boundaries to straight ones and the effect of altering the refractive index profile from a step-indexed type to an inhomogeneous distribution. Solutions of the wave equation in the transformed domain are approximated by the Wentzel-Krammer-Brilouin (WKB) method. Therefore, the results of this work are valid within the limitations of the WKB approximation.

The waveguide we wish to analyze is shown in Fig. 5-1 (a). In the region $R_1 < R < R_2$, where the core lies, the refractive index equals n_{co}. In the cladding, the refractive index is $n_{cl} < n_{co}$.

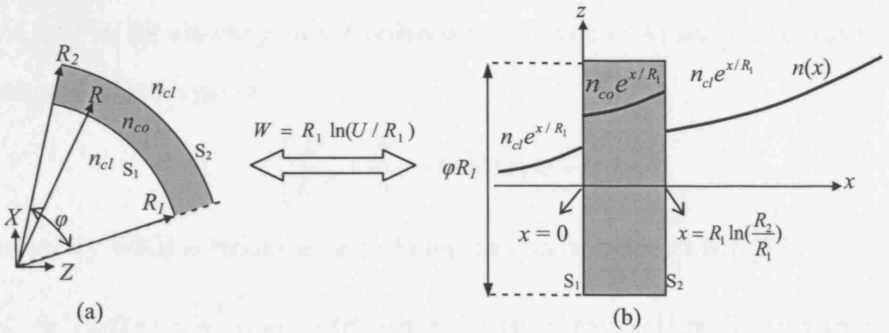

Fig. 5-1. (a) A curved slab waveguide with a step-index distribution and (b) its transformation to a linear waveguide with an exponentially perturbed index profile.

Waves ψ, propagating in the waveguide bend of Fig. 5-1 (a) must satisfy the 2D scalar wave equation which in a Cartesian X,Z coordinate system takes the usual form

$$\left[\frac{\partial^2}{\partial X^2}+\frac{\partial^2}{\partial Z^2}+k^2 n(X,Z)\right]\psi=0 \tag{5.1}$$

In the previous equation, k is the free space wavenumber, $n(X,Z)$ the refractive index distribution of the waveguide, and ψ, the solutions (wave functions) of the wave equation corresponding to the propagating fields. As mentioned before, our objective is to apply a conformal transformation, which converts the curved boundaries in Fig. 5-1 (a) to straight ones in an alternative coordinate system. If $W=x+iz=f(Z)=f(X+iZ)$, corresponds to this transformation, with f some analytic function, then the wave equation (5.1) is transformed

in the new (x, z) coordinate system to

$$\left[\frac{\partial^2}{\partial x^2}+\frac{\partial^2}{\partial z^2}+\left|\frac{dU}{dW}\right|^2 k^2 n^2\left(X(x,z),Z(x,z)\right)\right]\psi=0 \tag{5.2}$$

with $(dW/dU)^2=(\partial x/\partial X)^2+(\partial z/\partial X)^2=(\partial x/\partial Z)^2+(\partial z/\partial Z)^2$, the Jacobian of the transformation written in this form with the aid of the Cauchy-Riemann relations. The transformation [5.10],

$$W = R_1 \ln(U/R_1) \tag{5.3}$$

with

$$\left|\frac{dU}{dW}\right| = \exp(x/R_1) \tag{5.4}$$

transforms the waveguide of Fig. 5-1 (a) to the one in Fig. 5-1 (b), which has straight boundaries but a perturbed refractive index given by $n(x) = n_{co}e^{x/R_1}$, in the core area and $n(x) = n_{cl}e^{x/R_1}$ in the cladding area. Combining (5.2) with (5.4) we get the wave equation in the new coordinate system

$$\left[\frac{\partial^2}{\partial x^2}+\frac{\partial^2}{\partial z^2}+k^2 n^2(x)\right]\psi=0 \tag{5.5}$$

The elementary WKB solutions ψ, in (5.5) for the core area are [5.10]-[5.11]

$$\psi^{\pm}(x,z)=\frac{C^{\pm}}{\sqrt{kn(x)\sin\theta(x)}}\exp\left(-ikn_{co}e^{h/R_1}\cos\theta_o z\right)\cdot\exp\left(\mp i\int_s^x k_o n(x')\sin\theta(x')dx'\right) \tag{5.6}$$

with $C^{\pm}$ being the amplitude of the WKB solutions, w the width of the waveguide and the parameter s to be later defined. In order for the WKB analysis to be valid the requirement $\left|\frac{\pi}{kn^2(x)}\frac{dn(x)}{dx}\right| << 1$, [5.11], must be valid.

Equation (5.6) represents upward propagating (ψ^+) and downward propagating (ψ^-) ***local*** plane waves with wavefronts whose angle θ with respect to the propagation axis is a function of x as

$$n_1 e^{w/R_1}\cos\theta_o = n_1(x)\cos\theta(x) = e^{x/R}\cos\theta(x),\quad \cos\theta(w)=\cos\theta_o \tag{5.7}$$

Note that in (5.7), the angle that the local plane waves form with the propagation axis at the top boundary θ_o has been chosen as the reference, and the angle θ at any other point

in the waveguide is expressed relatively to θ_o.

As shown in Fig. 5-2, an equivalent ray representation of the WKB solutions (5.6)-(5.7) is the following. As rays propagate from the top waveguide boundary to the bottom boundary, they bend to take into account the change on the waveguide refractive index, which reduces, as we are moving towards negative x. Therefore, rays form steeper angles with respect to the propagation z-axis at the top of the waveguide than at the bottom. If a ray happens to change direction, from downward propagating to upward propagating, before being reflected by the bottom boundary then a whispering gallery mode is formed. The point where the whispering gallery ray becomes parallel to the waveguide boundaries is called the caustic or turning point, and in Fig. 5-2 it occurs at $x = w'$ above the bottom boundary. The parameter s in (5.6) is $s = 0$ in the non-whispering gallery case and $s = w'$ in the whispering gallery case.

In reality, WKB solutions (5.6) are not valid at the caustic of the fields. This is because $\theta(h') = 0$ and the WKB fields are singular due to the sin term in the denominator of (5.6). A more refined set of solutions based on the Airy functions, which is valid even at the caustics, will be presented in section 5.2.4.

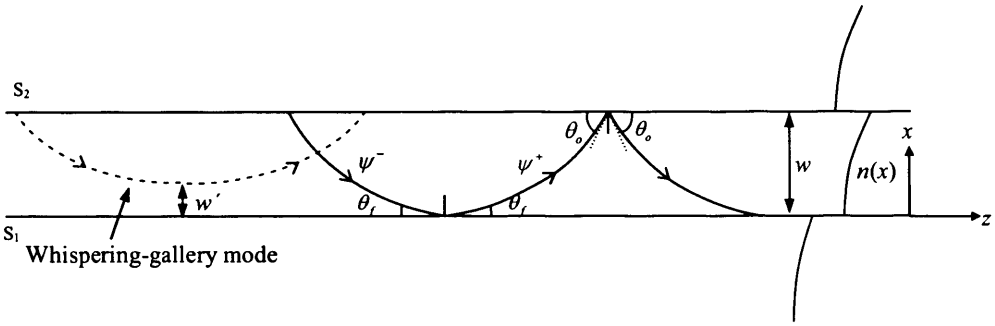

Fig. 5-2. Ray propagation in a transformed waveguide bend. Since $n(0) = n_{co} < n(w) = n_{co}\exp(R_1 / R_2)$ then $\theta_o > \theta_f$ and rays propagate at shallower angles as they move towards the bottom surface. If $\cos\theta(w') = 0$, for some depth $x = w'$ in the core, whispering gallery modes (dashed line) are formed and rays never meet the bottom surface.

Upon application of the appropriate dielectric boundary conditions at the top and bottom boundaries in (5.5), an eigenvalue problem is formed which discretises the angular spectrum in (5.6) and determines the propagation constants of the modes in the waveguide bend. Unlike straight waveguides with purely real propagation constants, bend modes have both a real and an imaginary part to include both propagation and radiation

effects [5.10].

5.2.2 Tapered Bend Analysis

In this chapter, we analyze wave propagation in a tapered bend, the geometry of which is shown in Fig. 5-3. The tapered bend under consideration, Fig. 5-3, is different from the waveguide bend in Fig. 5-1 in that the radius of curvature of its upper boundary S_2 is a function of the polar angle φ. The bottom boundary S_1 though, is still assumed a circular arc, for simplicity. The radius of curvature R_2, varies linearly with respect to the polar angle as, $R_2(\varphi) = R_2(0°) - \omega \cdot \varphi$. Therefore, as we move clockwise from $\varphi = 0$ to $\varphi = \pi/2$, the width of the waveguide decreases at a linear rate with φ, which depends on ω, and a tapered bend is formed. Applying the transformation (5.3) to the waveguide bend has the effect of tilting the top surface S_2, so that a linear straight tapered waveguide is formed in the transformed domain, Fig. 5-3. The bottom surface S_1 still appears to be parallel to the propagation axis z, as in the waveguide bend case in Fig. 5-2, but the top surface S_2 forms an angle ω with it. This problem does not have an exact solution in terms of conventional modal analysis and therefore we are seeking for approximate solutions. In the case where we are dealing with slow tapers, for which $\omega \sim 0$, the intrinsic mode theory, [5.12]-[5.17], presented in Chapter 3 can be used to analyse the tapered bend of Fig. 5-3.

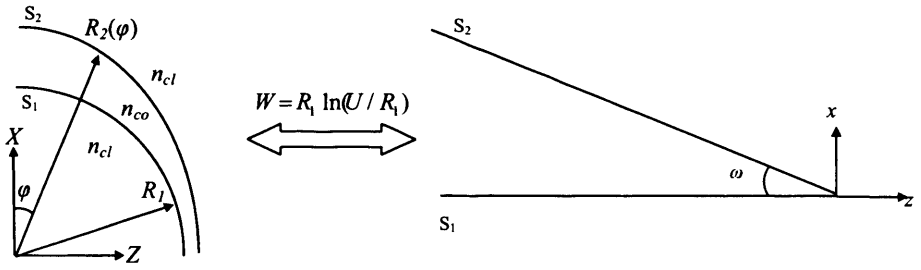

Fig. 5-3. A tapered bend in the original Cartesian coordinate system and in the transformed domain. The radius of curvature of the top boundary S_2 tapers linearly with respect to the polar angle φ while the bottom boundary S_1 remains a circular arc. In the new domain, the tapered bend is transformed to a straight taper with its top boundary S_2 being angled with respect to the propagation axis z.

The main difference between the straight tapered waveguide presented in Chapter 3 and the straight tapered waveguide in Fig. 5-3 is that the latter has an inhomogeneous refractive index profile compared to the homogenous refractive index of the former. The refractive index of the tapered bend in the transformed domain has an exponentially

perturbed refractive index in the core and cladding areas, Fig. 5-4, given as in the case of the waveguide bend by $n(x) = n_{co}e^{x/R_1}$ in the core, and $n(x) = n_{cl}e^{x/R_1}$ in the cladding.

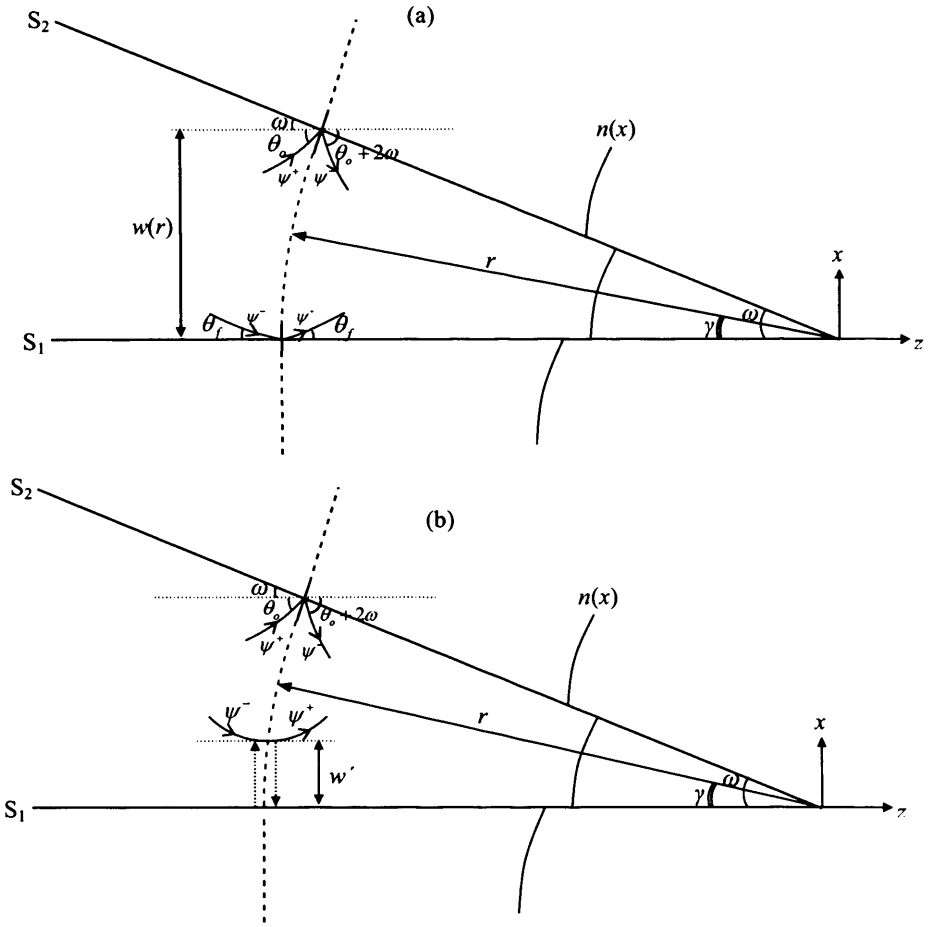

Fig. 5-4. A tapered waveguide bend with a linearly sloped upper surface (ω~0). Bottom surface remains parallel to the propagation axis implying that S_1 is still a circular arc in the original (X,Z) coordinate system. Waveguide cross-sections are defined along circular arcs the centre of which coincides with the origin of the (x,z) coordinate radius. a) Non-whispering gallery wave propagation in the taper. b) Whispering gallery waves in the taper. In this case downward propagating waves never reach the bottom surface but instead change direction at the turning point (or caustic) $y = w'$. Although not evident, there is still a phase shift involved into this direction change due to evanescent wave reflection on the bottom surface, represented by the dashed arrows, Appendix F.

Although, we will follow Arnold and Felsen [5.12]-[5.17] to describe wave propagation in the tapered bend of Fig. 5-4, their method has to be extended to include the complications arising from the inhomogeneous refractive index core and cladding. The most important differences between the waves propagating in the tapered bend of Fig. 5-4 and the straight taper of Fig. 3-1, in Chapter 3, are:

- In inhomogeneous media, rays do not propagate along straight paths but along curved ones.
- In inhomogeneous media rays belonging to the upward propagating elementary waves ψ^+ reach (and are reflected by) different points at the top boundary S_2 with different angles. This is because as can be seen from (5.6)-(5.7) the angle θ that the WKB solutions form with the propagation axis z, is not constant in the waveguide but it depends on x ($\theta = \theta(x)$). On the other hand, in the homogenous waveguide case, all rays belonging to the same plane wave, form the same angle θ with the propagation axis z, when they reach the top boundary S_2. The implication of the x-dependence of the angle θ is that, as we will see, we need to apply ***local*** boundary conditions at each point of the surface S_2 in the tapered bend case, in contrast to the ***global*** boundary conditions valid across the entire surface S_2 in the homogenous straight taper case.
- Finally, in inhomogeneous media whispering gallery modes as those in Fig. 5-2 are formed. The existence of both whispering gallery modes and non-whispering gallery modes in the tapered bend adds to the complexity of the problem, since these two cases need to be considered independently from each other.

5.2.3 WKB Spectral Element Analysis

We start our analysis by writing the field in the core along a waveguide cross-section as a linear combination of the elementary WKB solutions (5.6) in a similar manner to (3.3). We consider waveguide cross-sections to express our fields, which are circular arcs with their centre located at the apex of the taper, traversing the boundaries S_1 and S_2 perpendicularly. This selection on the waveguide cross-section optimizes the adiabatic modes in the sense of minimizing the error terms (3.22)-(3.23) as has been stated in [5.9]-[5.14]. The total upward propagating field V^+ and downward propagating field V^-, along a specific waveguide cross-section is expressed as

$$V^{\pm}(r,\gamma) = \int_c \tilde{u}^{\pm}(r,\theta_o)\cdot\psi^{\pm}(r,\gamma;\theta_o)\,d\theta_o, \tag{5.8}$$

$$\psi^{\pm}(r,\gamma;\theta_o) = \frac{1}{\sqrt{kn(r,\gamma)\sin\theta(r,\gamma)}}\exp\left(ikn_{co}e^{h/R_1}\cos\theta_o r\cos\gamma\right)\cdot\exp\left(\mp i\int_w^{r\sin\gamma} k_o n(x')\sin\theta(x')dx'\right)$$

Equation (5.8) expresses the upward and downward propagating fields $V^{\pm}$ at each cross-section, as a linear combination of upward (ψ^+) and downward (ψ^-) propagating

elementary WKB solutions (5.6), of the wave equation, (5.5), with amplitudes $\tilde{u}^{\pm}$ respectively. Note that in (5.8), we switched to a convenient cylindrical coordinate system (r,γ), Fig. 5-4, the radius r of which is measured from the taper apex and the polar angle γ with respect to the propagation axis z, to describe the field on the curved cross-sections. Cross-sections are circular arcs defined as r = constant in this system. The x and z coordinate variables in the $\psi^{\pm}$ definition (5.6), need to be taken on the cross-section under consideration and they are related to r and γ via the relationships $x = r \sin \gamma$, and $z = -r \cos \gamma$. Two points regarding (5.8) need special attention. At first, we chose to parametrize the integral (5.8) and the elementary WKB solutions $\psi^{\pm}$ (5.6), by the angle θ_o that the local plane waves form with the z-axis at the top boundary, as we did with the waveguide bend. Secondly, amplitudes $\tilde{u}^{\pm}$ are functions of r and θ_o but **NOT** of γ. This is because $\psi^{\pm}$ form a complete set of solutions and a proper linear combination of them is able to describe the total field on any arbitrary cross-section. The integration contour c is the Sommerfeld contour, in Fig. 5-5, which is similar to the contour in Fig. 3-2 and extends over both propagating and evanescent angles. The contour c, is chosen so that the set of solutions $\psi^{\pm}$, which results is complete, [5.15].

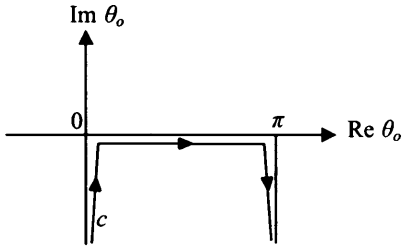

Fig. 5-5. Integration contour c, in the complex θ_o domain. Contour extends over all real angles $0 < \theta_o < \pi$ and is complemented by imaginary angles to take into account evanescent wave contributions.

The total field at any point $(r\ ,\ \gamma)$ along the waveguide cross-section under examination is:

$$V(r,\gamma) = V^{+}(r,\gamma) + V^{-}(r,\gamma) \tag{5.9}$$

We proceed in our analysis by applying boundary (local) conditions. The non-whispering gallery waves $\psi^{\pm}$, Fig. 5-4 (a), reach and are reflected by both surfaces S_1 and S_2. Each reflection is associated with a Goos-Hänchen shift, which as in the case of the homogenous waveguides, depends on the angle of reflection and the refractive index of the core and the cladding. As seen in Fig. 5-4 (a), a downward WKB wave ψ^{-}, with

reference angle θ_o, reaches the bottom boundary with an angle θ_f, which is related to θ_o according to (5.7) as

$$\cos(\theta_f) = \exp(-w(r)/R_1)\cdot\cos(\theta_o) \tag{5.10}$$

upon reflection on the bottom boundary, ψ^- will be translated to an upward propagating wave ψ^+ with the addition of a phase shift, Fig. 5-4 (a). The value of ψ^+ at the bottom boundary S_1 (r, $\gamma = 0$) is from (5.8)

$$\psi^+(r,0;\theta_o) = \frac{1}{\sqrt{kn_{co}\sin\theta_f}}\exp\left(ikn_{co}\cos\theta_f r\right)$$

while the value of ψ^- on the bottom boundary is given again by (5.8)

$$\psi^-(r,0;\theta_o) = \frac{1}{\sqrt{kn_{co}\sin\theta_f}}\exp\left(ikn_{co}\cos\theta_f r\right) = \psi^+(r,0;\theta_o)$$

According to (5.8) the amplitude of the downward propagating wave with angle θ_o on a waveguide cross-section is $\tilde{u}^-(r,\theta_o)$, while the amplitude of the upward propagating wave also with angle θ_o taken at the same cross-section is $\tilde{u}^+(r,\theta_o)$. In order for the dielectric boundary conditions to be satisfied on S_1, the value and the amplitude of the downward propagating wave should be connected with the value and the amplitude of the upward propagating wave as

$$\begin{aligned}\tilde{u}^+(r,\theta_o)\psi^+(r,0;\theta_o) &= e^{i\Phi(\theta_f)}\cdot\tilde{u}^-(r,\theta_o)\psi^-(r,0;\theta_o) \Rightarrow \\ \tilde{u}^+(r,\theta_o) &= e^{i\Phi(\theta_f)}\cdot\tilde{u}^-(r,\theta_o)\end{aligned} \tag{5.11}$$

with $\Phi(\theta_f)$ the Rayleigh coefficient associated to the phase shift due to the reflection, given by (5.13).

Similarly, a reflection of an upward propagating wave $\psi^+(r,\gamma;\theta_o)$ on the top boundary S_2 translates it to a downward propagating wave $\psi^-(r,\gamma;\theta_o + 2\omega)$ due to the slope ω, as seen in Fig. 5-4 (a). The value of $\psi^+(r,\gamma;\theta_o)$ on the top boundary S_1, (r, $\gamma = \omega$) is from (5.8)

$$\psi^+(r,\omega;\theta_o) = \frac{1}{\sqrt{kn(r,\omega)\sin\theta_o}}\exp\left(ik_o n_{co} r\cos\omega\cos(\theta_o)\right)\exp\left(-i\int_0^{w=r\sin\omega} k_o n_{co}(x')\sin\theta(x')dx'\right)$$

while the value of $\psi^-(r,\gamma;\theta_o + 2\omega)$ on the top boundary S_1, is again from (5.8)

$$\psi^{-}(r,\omega;\theta_o+2\omega)=$$

$$=\frac{1}{\sqrt{kn(r,\omega)\sin(\theta_o+2\omega)}}\exp\left(ikn_{co}r\cos\omega\cos(\theta_o+2\omega)\right)\exp\left(+i\int_0^w kn_{co}(x')\sin\theta(x')dx'\right)$$

The boundary condition on S_2, which connects the amplitudes and the values of the upward and downward propagating waves, consequently is

$$\tilde{u}^{-}(r,\theta_o+2\omega)\psi^{-}(r,0;\theta_o+2\omega)=e^{i\Phi(\theta_o+\omega)}\cdot\tilde{u}^{+}(r,\theta_o)\psi^{+}(r,0;\theta_o)\Rightarrow$$

$$\begin{aligned}&\frac{\tilde{u}^{-}(r,\theta_o+2\omega)}{\sqrt{kn(r,\omega)\sin(\theta_o+2\omega)}}\exp\left(ikn_{co}r\cos\omega\cos(\theta_o+2\omega)\right)\exp\left(+i\int_0^w kn_{co}(x')\sin\theta(x')dx'\right)\\&=e^{i\Phi(\theta_o+\omega)}\cdot\frac{\tilde{u}^{+}(r,\theta_o)}{\sqrt{kn(r,\omega)\sin\theta_o}}\exp\left(ikn_{co}r\cos\omega\cos(\theta_o)\right)\exp\left(-i\int_0^w kn_{co}(x')\sin\theta(x')dx'\right)\end{aligned}\qquad(5.12)$$

with $\Phi(\theta_o+\omega)$ the Rayleigh coefficient associated to the phase shift due to reflection of the $\psi^{+}(r,\gamma;\theta_o)$ wave on the surface S_1. Note from Fig. 5-4, that the angle of incidence of the local plane wave $\psi^{+}(r,\gamma;\theta_o)$ on S_1 is $\theta_o+\omega$.

The phase shift $\Phi(\theta)$, ($\theta=\theta_o+\omega$ or θ_f) of the local plane waves upon reflection on the top or the bottom boundaries in (5.11) and (5.12) is given as in (3.6) by the usual relationship,

$$\Phi(\theta)=2\arctan\left[i\frac{n_{cl}\sin\dot{\theta}}{n_{co}\sin\theta}\right]\qquad(5.13)$$

with the angle of refraction $\dot{\theta}$, calculated by the Snell's law as

$$n_{co}\cos\theta=n_{cl}\cos\dot{\theta}\qquad(5.14)$$

We remind that $\theta<\theta_c$, with $\cos\theta_c=n_{cl}/n_{co}$ the critical angle for total internal reflection (TIR) (which is the same for reflection on both interfaces S_1 and S_2), then $\Phi(\theta)$ is real and negative in (5.13) in agreement with the Goos-Hänchen shift. In contrast if $\theta>\theta_c$, then $\Phi(\theta)$ becomes positive imaginary corresponding to Fresnel loss.

In the whispering gallery case, equations (5.10) – (5.12) need to be modified. In this case, waves do not reach and so reflect from the bottom surface but instead change direction at the caustic point $y=h'$ as seen in Fig. 5-4 (b). However, there is still a phase shift $\Phi(\theta_f)$ between the amplitudes $\tilde{u}^{-}$ and $\tilde{u}^{+}$ involved in this process due to evanescent wave

reflection, Appendix F, and boundary conditions (5.10), (5.12) should be modified as

On $x = h'$

$$\tilde{u}^{+}(r,\theta_o) = e^{i\Phi(\theta_f)} \cdot \tilde{u}^{-}(r,\theta_o) \tag{5.15}$$

On S_2 ($x = w(r) = r\sin\omega$)

$$\begin{aligned} &\frac{\tilde{u}^{-}(r,\theta_o+2\omega)}{\sqrt{kn(r,\omega)\sin(\theta_o+2\omega)}}\exp\left(ikn_{co}r\cos\omega\cos(\theta_o+2\omega)\right)\exp\left(+i\int_{w'}^{w}kn_{co}(x')\sin\theta(x')dx'\right) \\ &= e^{i\Phi(\theta_o+\omega)}\frac{\tilde{u}^{+}(r,\theta_o)}{\sqrt{kn(r,\omega)\sin(\theta_o)}}\exp\left(ik_o n_{co}r\cos\omega\cos(\theta_o)\right)\exp\left(-i\int_{w'}^{w}k_o n_{co}(x')\sin\theta(x')dx'\right) \end{aligned} \tag{5.16}$$

As shown in Appendix F the phase coefficient $\Phi(\theta_f)$ in (5.15) is related to reflection of waves with imaginary (evanescent) angles. In (5.16) $\Phi(\theta_o)$ is again given by (5.13)-(5.14) since a reflection on S_1 still occurs but the lower limit of integration has now been changed to the turning point w'.

Now if we write

$$\frac{\tilde{u}^{+}(r,\theta_o)}{\sqrt{kn(r,\omega)\sin(\theta_o)}} = e^{iS(r,\theta_o)} \tag{5.17}$$

with $S(x,\theta_o)$ some trial function to be later defined, then by combining (5.10), (5.12) and (5.17) for the non-whispering case or (5.15), (5.16) and (5.17) for the whispering gallery wave case we derive

$$S(x,\theta_o) - S(x,\theta_o^{(1)}) = \Phi(\theta_f) + \Phi(\theta_o+\omega) - \varphi_x(\theta_o) + \varphi_x(\theta_o+2\omega) + \varphi_y(\theta_o) + \varphi_y(\theta_o+2\omega) - 2q\pi \tag{5.18}$$

in (5.18) q can be any integer and $S(x,\theta_o^{(1)}) = S(x,\theta_o+2\omega)$. By summing (5.18) m times in a process similar to (3.16), which traces successive wave reflections we get

$$\begin{aligned} S(x,\theta_o) - S(x,\theta_o^{(m)}) = &-\Phi(\theta_f^{(m)}) - \Phi(\theta_o^{(m)}+\omega) + \sum_{l=0}^{m}\Phi(\theta_f^{(l)}) + \sum_{l=0}^{m}\Phi(\theta_o^{(l)}+\omega) \\ &-\varphi_x(\theta_o) + \varphi_x(\theta_o^{(m)}) - \varphi_x(\theta_o) - \varphi_x(\theta_o^{(m)}) + 2\sum_{l=0}^{m}\varphi_x(\theta_o^{(l)}) - 2qm\pi \end{aligned} \tag{5.19}$$

with the following definitions

$$\varphi_x(\theta_o^{(l)}) = k_o n_1 r\cos\omega\cos(\theta_o^{(l)}) \tag{5.20}$$

$$\varphi_x(\theta_o^{(l)}) = \int_0^w k_o n_1(x)\sin\theta^{(l)}(x)dx = -k_o n_1\int_0^w\sqrt{e^{2x/R_1} - e^{2w/R_1}\cos^2\theta_o^{(l)}}\,dx \tag{5.21}$$

for the non-whispering case and

$$\varphi_x(\theta_o^{(l)}) = \int_{w'}^{w} k_o n_1(x)\sin\theta^{(l)}(x)dx = -k_o n_1 \int_{w'}^{w} \sqrt{e^{2x/R_1} - e^{2w/R_1}\cos^2\theta_o^{(l)}}\,dx \tag{5.22}$$

for the whispering gallery wave case. The parameters $\theta_f^{(l)}$ and $\theta_o^{(l)}$ are defined via the recurrence relationships

$$\cos\theta_f^{(l)} = \exp(-w/R_1)\cdot\cos(\theta_o + 2l\omega) \tag{5.23}$$

$$\theta_o^{(l)} = \theta_o + 2l\omega, \tag{5.24}$$

Equation (5.19) contains three series, which are cumbersome to calculate. However, these series are transformed with the aid of the Euler-Maclaurin formula, as in (3.17) - (3.18) (see also (B7) in appendix B), to integrals as

$$\sum_{l=0}^{m}\Phi(\theta_o^{(l)} + \omega) = \frac{1}{2}\left[\Phi(\theta_o^{(m)} + \omega) + \Phi(\theta_o + \omega)\right] + \int_0^m \Phi(\theta_o^{(l)} + \omega)dl + \hat{E}(\theta_o^{(m)}, \theta_o), \tag{5.25}$$

$$\hat{E}(\theta_o^{(m)}, \theta_o) = 2\sum_{q=1}^{\infty}\int_0^m \Phi(\theta_o^{(l)} + \omega)\cdot\cos(2q\pi l)dl \tag{5.26}$$

$$\sum_{l=0}^{m}\Phi(\theta_f^{(l)}) = \frac{1}{2}\left[\Phi(\theta_f^{(m)}) + \Phi(\theta_f)\right] + \int_0^m \Phi(\theta_f^{(l)})dl + \hat{E}(\theta_f^{(m)}, \theta_f), \tag{5.27}$$

$$\hat{E}(\theta_f^{(m)}, \theta_f) = 2\sum_{q=1}^{\infty}\int_0^m \Phi(\theta_f^{(l)})\cdot\cos(2q\pi l)dl \tag{5.28}$$

$$\sum_{l=0}^{m}\varphi_x(\theta_o^{(l)}) = \frac{1}{2}\left[\varphi_x(\theta_o^{(m)}) + \varphi_x(\theta_o)\right] + \int_0^m \varphi_x(\theta_o^{(l)})dl + \hat{E}_{\varphi_x}(\theta_o^{(m)}, \theta_o), \tag{5.29}$$

$$\hat{E}_{\varphi_y}(\theta_o^{(m)}, \theta_o) = 2\sum_{q=1}^{\infty}\int_0^m \varphi_y(\theta_f^{(l)})\cdot\cos(2q\pi l)dl \tag{5.30}$$

Evaluation of $\hat{E}(\theta_f^{(m)}, \theta_f)$ in (5.28) involves the phase function $\Phi(\theta_f^{(l)})$ due to reflection at the bottom surface, which can be written according to (5.13) and (5.14) as

$$\Phi(\theta_f^{(l)}) = 2\arctan\left[i\frac{n_2\sin\dot{\theta}_f^{(l)}}{n_1\sin\theta_f^{(l)}}\right],\ n_1\cos\theta_f^{(l)} = n_2\cos\dot{\theta}_f^{(l)} \tag{5.31}$$

Since our reference angle so far, has been the angle that WKB solutions form at the top surface we can write $\Phi(\theta_f^{(l)})$ as

$$\Phi(\theta_f^{(l)}) = 2\arctan\left[i\frac{\sqrt{\cos^2\theta_c - \cos^2\theta_f^{(l)}}}{\sqrt{1-\cos^2\theta_f^{(l)}}}\right] = 2\arctan\left[i\frac{\sqrt{\cos^2\theta_c - e^{2w/R}\cos^2\theta_o^{(l)}}}{\sqrt{1-e^{2w/R}\cos^2\theta_o^{(l)}}}\right] = \Phi_{\theta_f}(\theta_o^{(l)}) \tag{5.32}$$

In the case of the whispering gallery waves, $\Phi(\theta_f^{(l)})$ takes the form

$$\Phi(\theta_f^{(l)}) = \Phi_{\theta_f}(\theta_o^{(l)}) = 2\arctan\left[i\frac{\sqrt{\cos^2\theta_c e^{2w/R_1} - \cos^2\theta_o^{(l)}}}{\sqrt{e^{2w/R_1}\cos^2\theta_o^{(l)} - 1}}\right] \tag{5.33}$$

A full proof of (5.33) is given in appendix G. In (5.32)-(5.33) we used the symbolism $\Phi_{\theta_f}(\theta_o^{(l)})$ to emphasize that it refers to the phase function related to reflections on the bottom-surface but expressed as a function of the angle on the top-surface $\theta_o^{(l)}$. With the aid of (5.32) and (5.33), equations (5.27) and (5.28) can be written as

$$\sum_{l=0}^{m}\Phi(\theta_f^{(l)}) = \frac{1}{2}\left[\Phi(\theta_f^{(m)}) + \Phi(\theta_f)\right] + \int_0^m \Phi_{\theta_f}(\theta_o^{(l)})dl + \hat{E}(\theta_f^{(m)},\theta_f), \tag{5.34}$$

$$\hat{E}(\theta_f^{(m)},\theta_f) = 2\sum_{q=1}^{\infty}\int_0^m \Phi_{\theta_f}(\theta_o^{(l)})\cdot\cos(2q\pi l)dl \tag{5.35}$$

With the aid of the variable change

$$\hat{\theta}_o = \theta_o + 2l\omega \tag{5.36}$$

from which we get

$$dl = \frac{d\hat{\theta}_o}{2\omega} \tag{5.37}$$

we can write (5.25) and (5.26) as

$$\sum_{l=0}^{m}\Phi(\theta_o^{(l)} + \omega) = \frac{1}{2}\left[\Phi(\theta_o^{(m)} + \omega) + \Phi(\theta_o + \omega)\right] + \frac{1}{2\omega}\int_{\theta_o}^{\theta_o^{(m)}}\Phi(\hat{\theta}_o + \omega)d\hat{\theta}_o + \hat{E}(\theta_o^{(m)},\theta_o), \tag{5.38}$$

$$\hat{E}(\theta_o^{(m)},\theta_o) = \frac{1}{\omega}\sum_{q=1}^{\infty}\int_{\theta_o}^{\theta_o^{(m)}}\Phi(\hat{\theta}_o + \omega)\cdot\cos\left(\frac{q\pi}{\omega}(\hat{\theta}_o - \theta_o)\right)d\hat{\theta}_o \tag{5.39}$$

Similarly we can write (5.34), (5.35) as

$$\sum_{l=0}^{m}\Phi(\theta_f^{(l)}) = \frac{1}{2}\left[\Phi(\theta_f^{(m)}) + \Phi(\theta_f)\right] + \frac{1}{2\omega}\int_{\theta_o}^{\theta_o^{(m)}}\Phi_{\theta_f}(\hat{\theta}_o)d\hat{\theta}_o + \hat{E}(\theta_f^{(m)},\theta_f), \tag{5.40}$$

$$\hat{E}(\theta_f^{(m)},\theta_f)=\frac{1}{\omega}\sum_{q=1}^{\infty}\int_{\theta_o}^{\theta_o^{(m)}}\Phi_{\theta_f}(\hat{\theta}_o)\cdot\cos\left(\frac{q\pi}{\omega}(\hat{\theta}_o-\theta_o)\right)d\hat{\theta}_o \tag{5.41}$$

and finally we can write (5.29) and (5.30) as

$$\sum_{l=0}^{m}\varphi_x(\theta_o^{(l)})=\frac{1}{2}\left[\varphi_x(\theta_o^{(m)})+\varphi_x(\theta_o)\right]+\frac{1}{2\omega}\int_{\theta_o}^{\theta_o^{(m)}}\varphi_x(\hat{\theta}_o)d\hat{\theta}_o+\hat{E}_{\varphi_x}(\theta_o^{(m)},\theta_o), \tag{5.42}$$

$$\hat{E}_{\varphi_x}(\theta_o^{(m)},\theta_o)=2\frac{1}{\omega}\sum_{q=1}^{\infty}\int_{\theta_o}^{\theta_o^{(m)}}\varphi_x(\hat{\theta}_o)\cdot\cos\left(\frac{q\pi}{\omega}(\hat{\theta}_o-\theta_o)\right)d\hat{\theta}_o \tag{5.43}$$

In (5.38)-(5.43), the angle $\theta_o^{(l)}$ is discrete with values, which differ by 2ω. However (5.39), (5.41), (5.43) can be extended to arbitrary values $\theta_o^{(m)}$ and θ_o if we express the error terms with their alternative form [5.13]

$$\hat{E}(\theta_o^{(m)},\theta_o)=E(\theta_o^{(m)})-E(\theta_o),$$

$$E(\theta_o)=\omega^{-1}\sum_{q=1}^{+\infty}\int_{+i\infty}^{0}\Phi(\theta_o+\omega+\psi)\cdot\exp(iq\pi\psi/\omega)d\psi+\omega^{-1}\sum_{q=1}^{+\infty}\int_{-i\infty}^{0}\Phi(\theta_o+\omega+\psi)\cdot\exp(-iq\pi\psi/\omega)d\psi \tag{5.44}$$

$$\hat{E}(\theta_f^{(m)},\theta_f)=E_{\theta_f}(\theta_o^{(m)})-E_{\theta_f}(\theta_o),$$

$$E_{\theta_f}(\theta_o)=\omega^{-1}\sum_{q=1}^{+\infty}\int_{+i\infty}^{0}\Phi_{\theta_f}(\theta_o+\psi)\cdot\exp(iq\pi\psi/\omega)d\psi+\omega^{-1}\sum_{q=1}^{+\infty}\int_{-i\infty}^{0}\Phi_{\theta_f}(\theta_o+\psi)\cdot\exp(-iq\pi\psi/\omega)d\psi \tag{5.45}$$

$$\hat{E}_{\varphi_x}(\theta_o^{(m)},\theta_o)=E_{\varphi_x}(\theta_o^{(m)})-E_{\varphi_x}(\theta_o),$$

$$E_{\varphi_x}(\theta_o)=\omega^{-1}\sum_{q=1}^{+\infty}\int_{+i\infty}^{0}\varphi_x(\theta_o+\psi)\cdot\exp(iq\pi\psi/\omega)d\psi+\omega^{-1}\sum_{q=1}^{+\infty}\int_{-i\infty}^{0}\varphi_x(\theta_o+\psi)\cdot\exp(-iq\pi\psi/\omega)d\psi \tag{5.46}$$

Therefore, $E(\theta_o)$, $E_{\theta_f}(\theta_o)$ and $E_{\varphi_x}(\theta_o)$ are now functions of the continuous variable θ_o. The parameter l, can also be extended to continuous values with the aid of (5.24)

$$l=\frac{\theta_o^{(l)}-\theta_o}{2\omega} \tag{5.47}$$

Next, by combining (5.38), (5.40), (5.42) with (5.44)-(5.46) equation (5.19) takes the form

$$
\begin{aligned}
S(r,\theta_o)-S(r,\theta_o^{(m)})= & \\
& -\frac{1}{2}\Phi(\theta_o+\omega)-\frac{1}{2}\Phi(\theta_f)-\varphi_x(\theta_o)+\frac{1}{2\omega}\int_{\theta_c}^{\theta_o}\Phi(\hat{\theta}_o+\omega)d\hat{\theta}_o+\frac{1}{2\omega}\int_{\theta_c}^{\theta_o}\Phi_{\theta_f}(\hat{\theta}_o)d\hat{\theta}_o+\frac{1}{\omega}\int_{\theta_c}^{\theta_o}\varphi_x(\hat{\theta}_o)d\hat{\theta}_o \\
& -\frac{q\pi\theta_o}{\omega}+E(\theta_o)+E(\theta_f)+E_{\varphi_x}(\theta_o) \\
& +\frac{1}{2}\Phi(\theta_o^{(m)}+\omega)+\frac{1}{2}\Phi(\theta_f^{(m)})+\varphi_x(\theta_o^{(m)})-\frac{1}{2\omega}\int_{\theta_c}^{\theta_o^{(m)}}\Phi(\hat{\theta}_o+\omega)d\hat{\theta}_o-\frac{1}{2\omega}\int_{\theta_c}^{\theta_o^{(m)}}\Phi_{\theta_f}(\hat{\theta}_o)d\hat{\theta}_o-\frac{1}{\omega}\int_{\theta_c}^{\theta_o^{(m)}}\varphi_x(\hat{\theta}_o)d\hat{\theta}_o \\
& +\frac{q\pi\theta_o^{(m)}}{\omega}+E(\theta_o^{(m)})+E(\theta_f^{(m)})+E_{\varphi_x}(\theta_o^{(m)})
\end{aligned}
\tag{5.48}
$$

and finally by separating terms depending on $\theta_o^{(m)}$ only from terms depending on θ_o only we get the formal solution for $S(r,\theta_o)$:

$$
\begin{aligned}
S(r,\theta_o)= & -\frac{1}{2}\Phi(\theta_o+\omega)-\frac{1}{2}\Phi_{\theta_f}(\theta_o)-\varphi_x(\theta_o)+\frac{1}{2\omega}\int_{\theta_c-\omega}^{\theta_o}\Phi(\hat{\theta}_o+\omega)d\hat{\theta}_o+\frac{1}{2\omega}\int_{\theta_{wf}}^{\theta_o}\Phi_{\theta_f}(\hat{\theta}_o)d\hat{\theta}_o+\frac{1}{\omega}\int_{\theta_c}^{\theta_o}\varphi_x(\hat{\theta}_o)d\hat{\theta}_o \\
& -\frac{q\pi\theta_o}{\omega}+E(\theta_o)+E_{\theta_f}(\theta_o)+E_{\varphi_x}(\theta_o)
\end{aligned}
\tag{5.49}
$$

In (5.49) θ_c and θ_{wf} are arbitrary angles but for reasons that will become evident later, it is convenient to use the critical angle for total internal reflection on the top surface for the former and the angle which eliminates the denominator of $\Phi_{\theta_f}(\theta_o)$ in (5.32) and satisfies the condition

$$e^{w/R}\cos\theta_{wf}=1 \tag{5.50}$$

The above condition corresponds physically to rays that as they propagate downward from the top to the bottom surface they become parallel to the propagation axis exactly at the bottom boundary. Rays with angles $\theta_o < \theta_{wf}$ do not even reach the bottom boundary and change direction within the core of the waveguide forming whispering gallery waves. Although the denominator of the phase coefficient $\Phi_{\theta_f}(\theta_o)$ in (5.30), appears to be singular at $\theta_o = \theta_{wf}$, in reality this is not the case as it will be explained in the following section and, therefore, all integrals in (5.49) can be calculated.

5.2.4 Fields near and at a caustic

As already mentioned the WKB approximation is not adequate to describe fields near and at a caustic. Fields placed at a caustic correspond to singularities of the WKB

solutions and our field expressions in (5.6) need to be modified so that fields are described by analytic functions in the entire waveguide region. This can be achieved by using the solutions proposed for optical problems within media of inhomogeneous refractive index by Goyal, Gallawa and Ghatak [5.20]. According to [5.20] we can express the field in the core of the waveguide bend near the caustic (or turning point) $x = w'$ as a linear combination of Airy functions of the first kind A_i and second kind B_i as

$$\psi(x,z) = \left\{C_1[\xi'(x)]^{-1/2} A_i[\xi(x)] + C_2[\xi'(x)]^{-1/2} B_i[\xi(x)]\right\}\exp(-i\beta z) \quad 0 < x < w \tag{5.51}$$

$$\xi(x;\vartheta_o) = \left[\int_{w'}^{x}\sqrt{-\frac{3}{2}k_x^2(u)}\,du\right]^{2/3} \tag{5.52}$$

$$\beta = k_o n_1 e^{w/R_1}\cos\theta_o \tag{5.53}$$

$$k_x^2(x) = k^2 n^2(x) - \beta^2 = k^2 n_{co}^2 (e^{2x/R_1} - e^{2w/R_1}\cos^2\theta_o) \tag{5.54}$$

where the prime in (5.51) denotes differentiation with respect to the argument, C_1 and C_2 are amplitude coefficients and w', corresponds to the turning point given by the relationship

$$kn(w') = \beta \Rightarrow w' = R_1 \ln\left(e^{w/R_1}\cos\theta_o\right) \tag{5.55}$$

in Appendix G we show that away from the turning points w', the large arguments approximation of the Airy functions can be used in (5.51), which in this case becomes identical to (5.6). An important case, which will be further investigated in the following arises when the turning point approaches the lower boundary or equivalently when $w' \approx 0$. As the width w of the tapered bend decreases, this case is related to transition between whispering and non-whispering gallery modes. In the case where $w' \approx 0$, the phase coefficient $\Phi_{\theta_f}(\theta_o)$ can no longer be described by (5.32) or (5.33) but instead as it is proved in Appendix G takes the form

$$\Phi_{\theta_f}(\theta_o) = 2\mathrm{Re}\left\{\arctan\frac{\left(A_i[\xi(0;\vartheta_o)] + B_i[\xi(0;\vartheta_o)]\right) - \xi'(0;\vartheta_o)\left(A_i'[\xi(0;\vartheta_o)] + B_i'[\xi(0;\vartheta_o)]\right)}{\left(A_i[\xi(0;\vartheta_o)] - B_i[\xi(0;\vartheta_o)]\right) - \xi'(0;\vartheta_o)\left(A_i'[\xi(0;\vartheta_o)] - B_i'[\xi(0;\vartheta_o)]\right)}\right\} + 2\Omega \tag{5.56}$$

with

$$\Omega = \begin{cases} \displaystyle\int_{w'}^{0}\kappa_x(x)\,dx, & w' \geq 0 \\ 0, & w' \leq 0 \end{cases} \tag{5.57}$$

by combining (5.32)-(5.33) with (5.56) we can write a unified phase coefficient $\Phi_{\theta_f}(\theta_o)$, due to reflection at the bottom surface, valid in the entire complex angular domain θ_o as

$$\Phi_{\theta_f}(\theta_o)=\begin{cases} 2\arctan\left[i\dfrac{\sqrt{\cos^2\theta_c-e^{2w/R}\cos^2\theta_o}}{\sqrt{e^{2w/R}\cos^2\theta_o-1}}\right], & \mathrm{Re}(e^{w/R}\cos\theta_o)<1 \\ 2\arctan\dfrac{\left(A_i[\xi(0)]+B_i[\xi(0)]\right)-\xi'(0)\left(A_i[\xi(0)]+B_i[\xi(0)]\right)}{\left(A_i[\xi(0)]-B_i[\xi(0)]\right)-\xi'(0)\left(A_i[\xi(0)]-B_i[\xi(0)]\right)}+2\Omega, & \mathrm{Re}(e^{w/R}\cos\theta_o)\cong 1 \\ 2\arctan\left[i\dfrac{\sqrt{\cos^2\theta_c-e^{2w/R}\cos^2\theta_o}}{\sqrt{1-e^{2w/R}\cos^2\theta_o}}\right], & \mathrm{Re}(e^{w/R}\cos\theta_o)>1 \end{cases} \tag{5.58}$$

The importance of the above relationship is that the seeming singularity at $\theta_o=\theta_{wf}$ ($e^{w/R}\cos\theta_{wf}=1$) has been eliminated. This is because in the region where $\theta_o\cong\theta_{wf}$ the fields are described by the Airy functions, (5.51) and the reflection coefficient $\Phi_{\theta_f}(\theta_o)$ by (5.56), which is non-singular everywhere in the waveguide. The resulting phase coefficient $\Phi_{\theta_f}(\theta_o)$ is now analytic over the entire complex angular domain with the exception of one branch-point due to the nominator of the expression.

5.2.5 Analytical continuation of phase functions $\Phi(\theta_o+\omega)$ *and* $\Phi_{\theta_f}(\theta_o)$

The spectral integral (5.8) involves the phase functions $\Phi(\theta_o+\omega)$, $\Phi_{\theta_f}(\theta_o)$ via (5.17) and (5.47). However, these functions contain branch-points, which do not permit direct integration over the whole contour *c*. This problem can be overcome by analytically continuing the phase functions so that the integral in (5.8) is defined everywhere on *c*. We proceed by explaining how to achieve this analytical continuation.

- Phase function $\Phi(\theta_o+\omega)$:

The phase function $\Phi(\theta_o+\omega)$ is given in (5.13) and (5.14) for *l*=0, and has a branch-point due to the numerator when its argument equals to the critical angle θ_c, for reflection on the upper surface. Note that due to the symmetry of the sin functions in (5.13) around π, the point π-θ_c is also a branch point of $\Phi(\theta_o+\omega)$. In exactly the same way as in (3.28), $\Phi(\theta_o+\omega)$, has a first order Taylor expansion around $\theta=(\theta_o+\omega)\rightarrow\theta_c$ of the form:

$$\Phi(\theta)\big|_{\theta\to\theta_c} \cong -2\sqrt{2\cot\theta_c}(\theta_c-\theta)^{1/2} \quad a_o>0 \tag{5.59}$$

As in the homogenous taper case, it is the square root in (5.59), which is responsible for the discussed branch-point. Analytical continuation of $\Phi(\theta)$ close to $\theta = \theta_c$ is again achieved, in the way shown in Fig. 5-6, by replacing $\Phi(\theta)$ with its values on a hemi-circle with infinitely small radius which passes from $\mathrm{Re}(\theta) < \theta_c$ to $\mathrm{Re}(\theta) > \theta_c$ in a clockwise manner. As said in 3.2.1 physical arguments forces us to select the branch where $\Phi(\theta)$ real and negative for $\theta < \theta_c$ (Goos-Hänchen shift), and positive imaginary for $\theta > \theta_c$ (Fresnel loss).

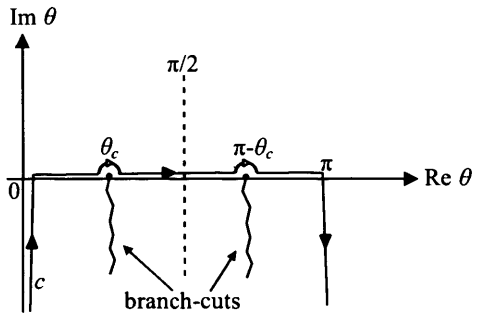

Fig. 5-6. Integration contour c, and analytical continuation of phase function $\Phi(\theta)$, in the complex θ, domain.

- Phase function $\Phi_{\theta_f}(\theta_o)$:

The phase function $\Phi_{\theta_f}(\theta_o)$ is defined in (5.58) and has one branch-point at $\theta_o = \theta_{cf}$ attributed to the numerator of the expression for $\mathrm{Re}(e^{w/R}\cos\theta_o)<1$. The branch point occurs when the following condition for the angle $\theta_o = \theta_{cf}$ is met

$$e^{2w/R}\cos\theta_{cf} = \cos\theta_c \tag{5.60}$$

The angle $\theta_o = \theta_{cf}$ where the branch-point occurs corresponds to the angle that rays form with the propagation axis at the top-surface when they are incident onto the bottom-surface at critical angle. Analytical continuation of $\Phi_{\theta_f}(\theta_o)$, around θ_{cf} follows exactly the same principles as the already described analytical continuation of $\Phi(\theta)$ around θ_c. Close to θ_c we can approximate $\Phi_{\theta_f}(\theta_o)$ as:

$$\Phi_{\theta_f}(\theta_o) \cong -2\sqrt{2\cot\theta_{cf}}\left(\theta_{cf}-\theta_o\right)^{1/2} \theta_o \to \theta_{cf} \tag{5.61}$$

and close to $\theta_o = \theta_{cf}$ we replace $\Phi_{\theta_f}(\theta_o)$ by its values on a semi-circle with infinitely small radius which passes from $\mathrm{Re}(\theta_o) < \theta_c$ to $\mathrm{Re}(\theta_o) > \theta_c$ in a clockwise manner as shown in Fig. 5-7.

The appropriate branch of $\Phi_{\theta_f}(\theta_o)$ in (5.61) is selected so that $\Phi_{\theta_f}(\theta_o)$, has the correct physical behaviour as the branch selected in the case of $\Phi(\theta_o+\omega)$ which again is the one that forces $\Phi_{\theta_f}(\theta_o)$ to be real and negative for $\theta_o < \theta_{cf}$, and positive imaginary for $\theta_o > \theta_{cf}$.

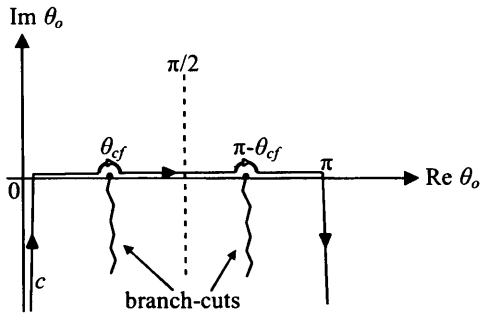

Fig. 5-7. Integration contour c, and analytical continuation of phase function $\Phi_{\theta_f}(\theta_o)$, in the complex θ_o, domain.

- Phase function $\varphi_x(\theta_o)$:

The phase function $\varphi_x(\theta_o)$ is defined in (5.21) for the non-whispering gallery and in (5.22) for the whispering gallery waves. Although (5.21) and (5.22) contain a square root function, $\varphi_x(\theta_o)$ has no branch-points in the complex angular domain. We will proceed by proving this statement. The integrals in (5.21) and (5.22) can be calculated in a closed form to give

$$\varphi_x(\theta_o) = \begin{cases} kn_1R_1\left[e^{w/R_1}\sin\theta_{oq} - e^{w/R_1}\theta_{oq}\cdot\cos\theta_{oq}\right] & ,\ \mathrm{Re}\left(e^{w/R_1}\cos\theta_{oq}\right)\geq 1 \\ kn_1R_1\left(\begin{array}{l}\left[e^{w/R_1}\sin\theta_{oq} - \sqrt{1-e^{2w/R_1}\cos^2\theta_{oq}}\right]- \\ \quad -e^{w/R_1}\cos\theta_{oq}\left[\arccos\left(\cos\theta_{oq}\right)-\arccos\left(e^{w/R_1}\cos\theta_{oq}\right)\right]\end{array}\right) & ,\ \mathrm{Re}\left(e^{w/R_1}\cos\theta_{oq}\right)<1 \end{cases} \tag{5.62}$$

The first branch of (5.62), corresponding to whispering gallery waves, is valid even when $\mathrm{Re}\left(e^{w/R_1}\cos\theta_{oq}\right)=1$ or else even when waves change from being whispering to becoming non-whispering gallery waves. The argument of the square root in the second branch of (5.62) is always non-zero and its phase always different to π in the interval of

consideration, ($\mathrm{Re}(e^{w/R_1}\cos\theta_{oq})<1$). A similar term appears in the expression for the inverse cosine, which is always non-zero and with a phase different to π as well. Therefore, (5.62) is analytic over the entire angular domain.

5.2.6 Evaluation of Error Terms

This section will provide with an approximation of the error terms $E(\theta_o)$, $E_{\theta_f}(\theta_o)$ and $E_{\varphi_y}(\theta_o)$ involved in (5.49).

- Evaluation of $E(\theta_o)$:

Two cases need to be distinguished:

I. Critical angle is larger than $\theta_o+\omega$, ($\theta_o+\omega<\theta_c$):

In this region $E(\theta_o)$ is analytic and since it does not involve any singularity or branch-points, the error is according to the Laplace method, (3.29) and Appendix B

$$E(\theta_o)\approx \mathrm{O}(\omega) \tag{5.63}$$

where the symbol $\mathrm{O}(\omega)$ means that the error is of order ω

II. Critical angle is smaller than $\theta_o+\omega$, ($\theta_o+\omega>\theta_c$) :

In the view of the analytical continuation of $\Phi(\theta_o+\omega)$ (Fig. 5-6), the second integral in (5.44) might traverse the branch-point in which case we need the inclusion of a branch-cut integral. The result of the integral in (5.44) by the steepest descent method [5.21]-[5.22] is as in (3.31)

$$E(\theta_o)\cong -a_o\omega^{1/2}\sum_{q=1}^{\infty}e^{iq\pi/4}\frac{2\sqrt{\pi}}{(q\pi)^{3/2}}+\mathrm{O}(\omega) \tag{5.64}$$

and so the error is

$$E(\theta_o)\approx \mathrm{O}(\omega^{1/2}) \tag{5.65}$$

Therefore, in both cases the error goes ***uniformly*** to zero as $\omega\to 0$ so the error is negligible compared to the rest of the terms.

- Evaluation of $E_{\theta_f}(\theta_o)$:

Again two cases need to be distinguished

I. Angle θ_{cf} is larger than θ_o, ($\theta_o<\theta_{cf}$):

Approximating integrals in (5.45) with the Laplace method (Appendix B) we find that

the error is

$$E_{\theta_f}(\theta_o) \approx O(\omega) \tag{5.66}$$

II. Angle θ_{cf} is smaller than θ_o, ($\theta_o > \theta_{cf}$):

In the view of the analytical continuation of $\Phi_{\theta_f}(\theta_o)$ (Fig. 5-7), the second integral in (5.45) might traverse the branch-point in which case we need the inclusion of a branch-cut integral. Again by using the steepest descent method to approximate the integral in (5.45) we find that the branch-point contributes an $O(\omega^{1/2})$ term and so, as a total estimate for the error we can write

$$E_{\theta_f}(\theta_o) \approx O(\omega^{1/2}) \tag{5.67}$$

Again in both cases (5.66) and (5.67), the error goes ***uniformly*** to zero as $\omega \to 0$.

- Evaluation of $E_{\varphi_x}(\theta_o)$:

The error function $E_{\varphi_x}(\theta_o)$ is analytic over the entire complex angular domain. Approximating integrals in (5.46) with the Laplace method (Appendix B) we find that the error is

$$E_{\varphi_x}(\theta_o) \approx O(\omega) \tag{5.68}$$

Again in (5.68) error goes uniformly to zero as $\omega \to 0$.

5.2.7 Adiabatic tapered bend modes

Combining (5.10), (5.17) and (5.49) we get for the amplitudes of the upward and downward propagating WKB waves

$$\tilde{u}^{\pm}(x,\theta_o) = \exp[iR(\theta_o)] \cdot \exp[-iq\pi\theta_o/\omega] \tag{5.69}$$

$$\begin{aligned} R(\theta_o) = {} & \pm\frac{1}{2}\Phi_{\theta_f}(\theta_o) - \frac{1}{2}\Phi(\theta_o+\omega) - \varphi_x(\theta_o) + \\ & + \frac{1}{2\omega}\int_{\theta_c-\omega}^{\theta_o}\Phi(\hat{\theta}_o+\omega)d\hat{\theta}_o + \frac{1}{2\omega}\int_{\theta_{wf}}^{\theta_o}\Phi_{\theta_f}(\hat{\theta}_o)d\hat{\theta}_o + \frac{1}{\omega}\int_{\theta_c}^{\theta_o}\varphi_x(\hat{\theta}_o)d\hat{\theta}_o \end{aligned} \tag{5.70}$$

Note that in (5.69) and (5.70) we ignored the error terms, (5.49), $E(\theta_o)$, $E_{\varphi_y}(\theta_o)$ and $E_{\theta_f}(\theta_o)$ which go uniformly to zero as $\omega \to 0$, as a first order approximation for the amplitudes $\tilde{u}^{\pm}$. By combining (5.8) with (5.6) and (5.69) we get the total field inside the tapered bend as

$$V^{\pm}(x,y) = \int_c \exp[\, iQ^{\pm}(r,\gamma;\theta_o)] \cdot \exp\left[-iq\pi\theta_o / \omega\right] d\theta_o \tag{5.71}$$

with

$$\exp[\, iQ^{\pm}(r,\gamma;\theta_o)] = \exp[iR(\theta_o)] \cdot \exp\left(ikn_{co}e^{w/R_1}\cos\theta_o r\cos\gamma\right) \cdot \exp\left(\mp i \int_s^{r\sin\gamma} kn_{co}(x')\sin\theta(x')dx'\right) \tag{5.72}$$

where we recall that $s = 0$ for non-whispering waves and $s = w'$ for the whispering gallery case. Equation (5.9) ($V(r,\gamma) = V^{+}(r,\gamma) + V^{-}(r,\gamma)$) defines through (5.71) the intrinsic modes in the tapered bend. These modes are valid (if we do not omit the error terms) for both slow ($\omega \sim 0$) and fast tapers ($\omega >> 0$). However, it is only when we operate in the slow taper regime that an asymptotic calculation of the integral in (5.71) is possible. The integral in (5.71) can be calculated with the steepest descent method. The terms of (5.71) are used to determine saddle points as $\omega \to 0$. The leading order Taylor expansion of $Q^{\pm}$, which is necessary for the calculation of the saddle-points, is given by

$$Q_o^{\pm}(r,\gamma;\theta_o) = \lim_{\omega\to 0}\left[\omega Q^{\pm}(r,\gamma;\theta_o)\right] \tag{5.73}$$

so that for $\omega \to 0$

$$Q^{\pm}(r,\gamma;\theta_o) \cong \omega^{-1}Q_o^{\pm}(r,\gamma;\theta_o) + O(1) \tag{5.74}$$

Saddle-points of the integrand in (5.71) are then calculated as solutions of

$$\frac{\partial Q_o^{\pm}(r,\gamma;\theta_o)}{\partial\theta_o} = q\pi \tag{5.75}$$

The asymptotic behaviour of the waveguide geometry for $\omega \to 0$ is shown in Fig. 5-8. As $\omega \to 0$ the upper boundary rotates so that it becomes parallel to the bottom boundary, while keeping their separation w constant.

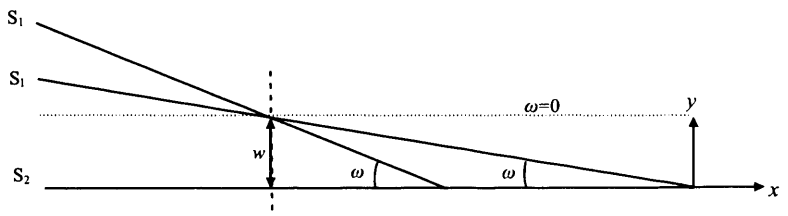

Fig. 5-8. Asymptotic behavior of bend taper geometry as $\omega \to 0$. For a given cross-section boundaries of the waveguide tend to become parallel as $\omega \to 0$, while their separation is kept constant and equals to the ***local*** width of the cross-section w.

Under these assumptions, by combining (5.69), (5.70) and (5.72) we get for $Q_o^{\pm}$

$$Q_o^{\pm}(r,\gamma;\theta_o) = \frac{1}{2}\int_{\theta_c}^{\theta_o}\Phi(\hat{\theta}_o)d\hat{\theta}_o + \frac{1}{2}\int_{\theta_{wf}}^{\theta_o}\Phi_{\theta_f}(\hat{\theta}_o)d\hat{\theta}_o + \int_{\theta_{wf}}^{\theta_o}\varphi x(\hat{\theta}_o)d\hat{\theta}_o = Q_o(r,\gamma;\theta_o) \qquad (5.76)$$

In (5.76) we omitted the ± subscript for Q_o since it takes the same form for upgoing and downgoing waves and we need not distinguish between them any more. Saddle points θ_{oq} are then determined from (5.75) and (5.76) as solutions of the transcendental equation

$$\varphi_x(\theta_{oq}) + \frac{1}{2}\Phi(\theta_{oq}) + \frac{1}{2}\Phi_{\theta_f}(\theta_{oq}) = q\pi \qquad (5.77)$$

with the aid of (5.13), (5.21), (5.22) and (5.58), equation (5.77) takes the following form according to the value of θ_o:

- If $\mathrm{Re}(\theta_o) < \theta_{wf}$, then saddle points for whispering gallery waves are the solutions of the transcendental equation

$$\int_{w'}^{w} kn_{co}\sqrt{e^{2x/R_1} - \cos^2\theta_{oq}}\,dx - \arctan\left[\frac{\sqrt{\cos^2\theta_{oq} - \cos^2\theta_c}}{\sin\theta_{oq}}\right] - \arctan\left[\frac{\sqrt{e^{2w/R}\cos^2\theta_o - \cos^2\theta_c}}{\sqrt{e^{2w/R}\cos^2\theta_o - 1}}\right] = q\pi \qquad (5.78)$$

- If $\mathrm{Re}(\theta_o) > \theta_{wf}$ then saddle points for non-whispering gallery waves are the solutions of the transcendental equation

$$\int_{0}^{w} kn_{co}\sqrt{e^{2x/R_1} - e^{2w/R_1}\cos^2\theta_{oq}}\,dx - \arctan\left[\frac{\sqrt{\cos^2\theta_{oq} - \cos^2\theta_c}}{\sin\theta_{oq}}\right] - \arctan\left[\frac{\sqrt{e^{2w/R}\cos^2\theta_{oq} - \cos^2\theta_c}}{\sqrt{1 - e^{2w/R}\cos^2\theta_{oq}}}\right] = q\pi \qquad (5.79)$$

as can be seen in appendix E, (5.79) is equivalent to the eigenvalue equation of a waveguide bend with local width *w*, as described in [5.10]. Once again, the equations that define the saddle points, (5.78) and (5.79), correspond to the eigenvalue problem, which determines the propagation constants for the local waveguide modes. However, in contrast to the homogenous waveguide case where only one eigenvalue prolem occurs, in the inhomogeneous case the existence of two types of modes (whispering and non-whispering) means that two eigenvalue problem exists.

- Finally, if $\mathrm{Re}(\theta_o) \cong \theta_{wf}$, then saddle points in the transition region between whispering and non-whispering gallery waves are given by

$$\int_{w'}^{w} kn_{co}\sqrt{e^{2x/R_1}-\cos^2\theta_{oq}}\,dx-a\tan\left[\frac{\sqrt{\cos^2\theta_{oq}-\cos^2\theta_c}}{\sin\theta_{oq}}\right]-$$
$$-2\arctan\frac{\left[\frac{1}{2}\frac{\xi''(0)}{\xi'(0)}+\gamma(0)\right]\left(A_i[\xi(0)]+B_i[\xi(0)]\right)-\xi'(0)\left(A_i[\xi(0)]+B_i[\xi(0)]\right)}{\left[\frac{1}{2}\frac{\xi''(0)}{\xi'(0)}+\gamma(0)\right]\left(A_i[\xi(0)]-B_i[\xi(0)]\right)-\xi'(0)\left(A_i[\xi(0)]-B_i[\xi(0)]\right)}+\Omega=q\pi \tag{5.80}$$

We are now ready to find the asymptotic solutions of (5.71). According to the saddle point method we need to deform the integration contour c, to a new one which runs along the steepest descent path c' of $Q_o^{\pm}(x,y;\theta_o)$. The deformed contour is shown in Fig. 5-9. We refer the interested reader to Appendix C for a brief description of the saddle-point method or for a more detailed review to [5.21]-[5.22].

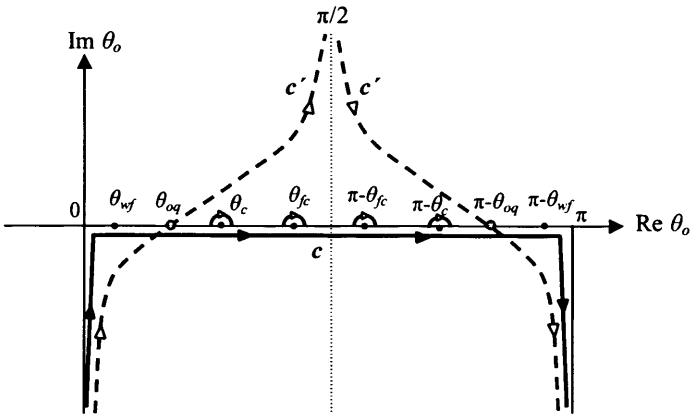

Fig. 5-9. Original contour c (solid line), and deformed contour along the steepest descent c' for a specific saddle point θ_{oq} and its reciprocal $\pi-\theta_{oq}$ (dashed line), in the angular θ_o domain. As can be seen contour c' traverses the two saddle points and asymptotically approaches the line $\mathrm{Re}\theta_o=\pi/2$.

As explained in chapter 3, the first order approximation of the intrinsic mode (5.71) corresponds to the adiabatic mode. Since, we have three different eigenvalue problems (5.78)-(5.80), the adiabatic modes in the tapered bend take three different structural forms. We need to differentiate the following four cases according to the position of the saddle point θ_{oq} in Fig. 5-9.

A. $\theta_{oq}<\theta_{wf}$. This case corresponds to the whispering gallery adiabatic modes in the tapered bend.

Saddle points θ_{oq} are calculated by (5.78). The approximation of the spectral integral (5.71) based on the saddle-point method is inside the core of the taper

$$V^{\pm}(r,\gamma) \approx \frac{\sqrt{2\pi\omega}}{k_o n_1 (\sqrt{e^{2r\sin\gamma/R_1} - e^{2w/R_1}\cos^2\theta_{oq}})^{1/2}} e^{i\pi/4} A_q(r,\omega) e^{-iS_q(r,\omega)} \exp[-i\frac{1}{2}\Phi(\theta_{oq}+\omega)] \cdot$$
$$\exp[\pm i\frac{1}{2}\Phi_{\theta_f}(\theta_{oq})] \cdot \exp\left(\mp i \int_{w'}^{r\sin\gamma} k_o n_1 \sqrt{e^{2x/R_1} - e^{2w/R_1}\cos^2\theta_{oq}}\, dx\right) \tag{5.81}$$

the amplitude $A_q(r,\gamma)$ of the q-th whispering gallery adiabatic mode is given by

$$A_q(r,\gamma) = \left\{ \frac{d}{d\theta_o}\left[\varphi_x(\theta_o) + \frac{1}{2}\Phi(\theta_o) + \frac{1}{2}\Phi_{\theta_f}(\theta_o)\right]\Big|_{\theta_o=\theta_{oq}} \right\}^{-1/2} \tag{5.82}$$

and its phase by

$$S_q(r,\gamma) = \omega^{-1}[Q_o(r,\gamma;\theta_{oq}) - q\pi\theta_{oq}] \tag{5.83}$$

Therefore from (5.9) and (5.81)-(5.82) the q-th adiabatic mode in the taper $V(r,\gamma)$ is

$$V(r,\gamma) \approx \frac{2\sqrt{2\pi\omega}}{k_o n_1 \left(\sqrt{e^{2r\sin\gamma/R_1} - e^{2w/R_1}\cos^2\theta_{oq}}\right)^{1/2}} e^{i\pi/4} \cdot \exp[-i\frac{1}{2}\Phi(\theta_{oq}+\omega)] \cdot A_q(r,\omega) e^{-iS_q(r,\gamma)} \cdot$$
$$\cdot \cos\left(\int_{w'}^{r\sin\gamma} k_o n_1 \sqrt{e^{2x/R_1} - e^{2w/R_1}\cos^2\theta_{oq}}\, dx - \frac{\Phi_{\theta_f}(\theta_{oq})}{2} \right) \tag{5.84}$$

with the above relationship being valid in the region $w' < r\sin\gamma < w$ where the waves are propagating (not evanescent). In the rest of the taper, $w < r\sin\gamma < w'$ (cladding), the field is evanescent and takes the form

$$V(r,\gamma) \approx \frac{2\sqrt{2\pi\omega}}{k_o n_1 \left(\sqrt{e^{2w/R_1}\cos^2\theta_{oq} - e^{2r\sin\gamma/R_1}}\right)^{1/2}} e^{i\pi/4} \cdot \exp[-i\frac{1}{2}\Phi(\theta_{oq}+\omega)] \cdot A_q(r,\gamma) e^{-iS_q(r,\gamma)} \cdot$$
$$\cdot \cosh\left(\int_{r\sin\gamma}^{w'} k_o n_1 \sqrt{\cos^2\theta_{oq} - e^{2x/R_1}}\, dx - i\frac{1}{2}\Phi_{\theta_f}(\theta_{oq}) \right) \tag{5.85}$$

Equation (5.82) corresponds to the amplitude of the adiabatic mode, which does not remain constant as the mode propagates, due to coupling to the rest of the waveguide modes. By performing the differentiation in (5.82) we get the following result for $A_q(r,\gamma)$ which is expressed in terms of the local propagation constant β_q and the wavenumber k_{xq} parameter of the q-th adiabatic mode (equations (5.53) and (5.54) respectively)

$$A_q(r,\gamma)=\left[R_1\left\{k_{xq}(h)-\beta_q+k_{xq}(h)\left[a\cos\left(\frac{\beta_q}{k_{xq}(h)}\right)-a\cos\left(\frac{\beta_q}{k_{xq}(0)}\right)\right]\right\}-\beta_q\frac{\eta_{xq}(h)k_{xq}(0)+\eta_{xq}(0)k_{xq}(h)}{\eta_{xq}(0)\eta_{xq}(h)k_{xq}(0)}\right]^{-1/2} \tag{5.86}$$

and η_{xq} a parameter defined as

$$\eta_{xq}^2(x)=k^2(n_{cl}^2e^{2w/R_1}\cos^2\theta_{oq}-n_{co}^2e^{2x/R_1}) \tag{5.87}$$

Equation (5.83) corresponds to the phase of the adiabatic mode. By expressing the local width w of the taper as $w=z\tan\omega\cong z\omega$ and differentiating with respect to z we get

$$\begin{aligned}\frac{\partial S_q(r,\gamma)}{\partial z}&=\frac{\partial S_q(r,\gamma)}{\partial w}\cdot\frac{\partial w}{\partial z}+\frac{\partial S_q(r,\gamma)}{\partial\theta_q}\cdot\frac{\partial\theta_{oq}}{\partial z}\\&=\frac{\partial\varphi_x(\theta_{oq})}{\partial w}+\omega^{-1}\frac{\partial\theta_{oq}}{\partial z}\left(\varphi_x(\theta_{oq})+\frac{1}{2}\Phi(\theta_{oq})+\frac{1}{2}\Phi_{\theta_f}(\theta_{oq})-q\pi\right)\end{aligned} \tag{5.88}$$

The term in the parenthesis in (5.88) is zero due to the eigenvalue equation (5.77) and so we are left with the result

$$\frac{\partial S_q(r,\gamma)}{\partial z}=\frac{\partial\varphi_y(\theta_{oq})}{\partial w}=\frac{\partial}{\partial w}\left[\int_{\theta_c}^{\theta_{oq}}\int_{w'}^{w}kn_{co}\sqrt{e^{2x/R_1}-e^{2w/R_1}\cos^2\theta_{oq}}\,dx\,d\theta_o\right] \tag{5.89}$$

the inner integral in (5.89) can be calculated in a closed form to give

$$\begin{aligned}&\int_{w'}^{w}kn_{co}\sqrt{e^{2x/R_1}-e^{2w/R_1}\cos^2\theta_{oq}}\,dx=\\&kn_{co}R_1\left\{e^{w/R_1}\sin\theta_{oq}-\sin\theta_{oq}(w')-e^{w/R_1}\cos\theta_{oq}\left[\theta_{oq}-\theta_{oq}(w')\right]\right\}\end{aligned} \tag{5.90}$$

where $\theta_{oq}(w')$ is derived from the following equality

$$e^{w/R_1}\cos\theta_{oq}=e^{y/R_1}\cos\theta_{oq}(x) \tag{5.91}$$

and by combining (5.90) with (5.91) we finally get

$$\begin{aligned}&\frac{\partial S_q(r,\gamma)}{\partial z}=kn_{co}R_1\int_{\theta_c}^{\theta_{oq}}\left\{e^{w/R_1}\sin\theta_{oq}-\sin\theta_{oq}(w')-e^{w/R_1}\cos\theta_{oq}\left[\theta_{oq}-\theta_{oq}(w')\right]\right\}d\theta_{oq}=\\&kn_{co}R_1e^{w/R_1}/R_1\left[-2\cos\theta_{oq}-\theta_{oq}\cdot\sin\theta_{oq}\Big|_{\theta_c}^{\theta_{oq}}\right]+kn_{co}R_1\frac{\partial}{\partial h}\int_{\theta_c}^{\theta_{oq}}\left[\theta_{oq}(w')\cdot\cos\theta_{oq}(w')-\sin\cos\theta_{oq}(w')\right]d\theta_o=\\&\beta_q+terms\end{aligned} \tag{5.92}$$

and so, $S_q(r,\gamma)\sim\int^z\beta_q(z')dz'+terms$. Therefore, as in the case of the homogenous waveguide, as the adiabatic mode in the tapered bend propagates its phase changes

proportionally to the local waveguide mode propagation constant.

B. $\theta_{wf}<\theta_{oq}<\theta_c$. This case corresponds to the non-whispering adiabatic modes in the tapered bend

Saddle points θ_{oq} are calculated from (5.79) for the non-whispering adiabatic modes, with the $\theta_{oq}>\theta_{wf}$ branch of $\Phi_{\theta_f}(\theta_{oq})$, (5.58), being considered.

$$V(r,\gamma)\approx \frac{2\sqrt{2\pi\omega}}{k_o n_1\left(\sqrt{e^{2r\sin\gamma/R_1}-e^{2w/R_1}\cos^2\theta_{oq}}\right)^{1/2}} e^{i\pi/4}\cdot\exp[-i\frac{1}{2}\Phi(\theta_{oq}+\omega)]\cdot A_q(r,\gamma)e^{-iS_q(r,\gamma)}\cdot$$
$$\cdot\cos\left(\int_0^{r\sin\gamma} kn_{co}\sqrt{e^{2x/R_1}-e^{2w/R_1}\cos^2\theta_{oq}}\,dx-\frac{1}{2}\Phi_{\theta_f}(\theta_{oq})\right) \tag{5.93}$$

with the above relationship being valid in the whole core area of the taper $0<r\sin\gamma<w$

C. $\theta_c<\theta_o<\theta_{cf}$. This case corresponds to waves that are leaking from the top boundary while still satisfying the total internal reflection condition at the bottom one

Saddle points θ_{oq} in (5.77) move to the complex angular domain and fields attenuate as they propagate. The integration contour for the approximate calculation of the spectral integral (5.71) is shown in Fig. 5-10 and involves a branch-cut integral around the branch-point (which coincides with the critical angle) θ_c. The solution for the adiabatic mode $V(r,\gamma)$ is this case

$$V(r,\gamma)\approx \frac{2\sqrt{2\pi\omega}}{kn_{co}\left(\sqrt{e^{2r\sin\gamma/R_1}-e^{2w/R_1}\cos^2\theta_{oq}}\right)^{1/2}} e^{-i\pi/4}\cdot\exp[-\frac{1}{2}\left|\Phi(\theta_{oq}+\omega)\right|]\cdot$$
$$A(r,\gamma)e^{-iS(r,\omega)}\cdot\cos\left(\int_0^{r\sin\gamma} kn_{co}\sqrt{e^{2x/R_1}-\cos^2\theta_{oq}}\,dx-\frac{1}{2}\Phi_{\theta_f}(\theta_{oq})\right)+v_1(r,\gamma) \tag{5.94}$$

$$v_1(r,\gamma)\approx \frac{\sqrt{\pi}\sqrt{2\cot\theta_c}\,\omega^{3/2}}{k_o n_1\left(\sqrt{e^{2x/R_1}-e^{2w/R_1}\cos^2\theta_c}\right)^{1/2}} e^{-i\pi/4}\cdot\exp[\frac{1}{2}\omega^{1/2}]\cdot\cos\left(\frac{1}{2}\Phi_{\theta_f}(\theta_c)\right)$$
$$\exp\left(i\omega^{-1}[Q_o(r,\gamma;\theta_c)-q\pi\theta_c]\right)\cdot\left(\int_{w_c}^{r\sin\gamma} kn_{co}\sqrt{e^{2x/R_1}-e^{2w/R_1}\cos^2\theta_c}\,dx\right)^{-5/2}$$

(5.95)

The derivation of (5.95) is the same as the derivation of (3.70) and is describes the "lateral waves" in [5.12]-[5.13], which are excited for modes which reach and go beyond their cut-off and propagate nearly parallel to the waveguide boundaries.

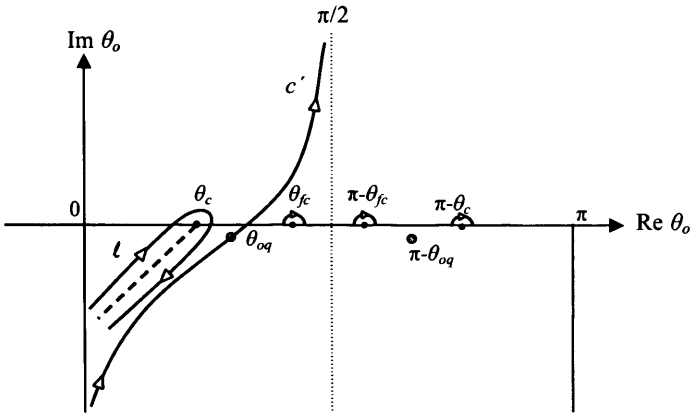

Fig. 5-10. Integration contour along the steepest descent path c' when saddle point θ_{oq} overcomes the critical angle θ_c. Contour is seem to interfere with the branch point θ_c, in which case a branch-cut integral ℓ is required.

D. $\theta_o > \theta_{cf}$. This case corresponds to waves that leak from both core boundaries.

The adiabatic mode takes the following form in this case:

$$V(r,\gamma) \approx \frac{2\sqrt{2\pi\omega}}{kn_{co}\left(\sqrt{e^{2r\sin\gamma/R_1} - e^{2w/R_1}\cos^2\theta_{oq}}\right)^{1/2}} e^{i\pi/4} \cdot \cosh[\frac{1}{2}\Phi_{\theta_f}(\theta_{oq})] \cdot \exp[-\frac{1}{2}\left|\Phi(\theta_{oq}+\omega)\right|]$$
$$\cdot A(r,\gamma)e^{-iS(r,\gamma)} \cdot \cos\left(\int_0^{r\sin\gamma} kn_{co}\sqrt{e^{2x/R_1} - \cos^2\theta_{oq}}\,dx\right) + v_1(r,\gamma) + v_2(r,\gamma) \tag{5.96}$$

$$v_2(r,\gamma) \approx \frac{\sqrt{\pi}\sqrt{2\cot\theta_{cf}}\,\omega^{3/2}}{kn_{co}\left(\sqrt{e^{2x/R_1} - e^{2w/R_1}\cos^2\theta_{cf}}\right)^{1/2}} e^{-i\pi/4} \cdot \exp[\frac{1}{2}\Phi(\theta_{cf})]$$
$$\exp\{i\omega^{-1}[Q_o(r,\gamma;\theta_{cf}) - q\pi\theta_{cf}]\} \cdot \left(\int_{w_{cf}}^{r\sin\gamma} k_o n_1 \sqrt{e^{2x/R_1} - e^{2w/R_1}\cos^2\theta_{cf}}\,dx\right)^{-5/2} \tag{5.97}$$

where the $v_1(r,\gamma)$ term is still given by (5.95). In this case, as we see there are two lateral waves excited, $v_1(r,\gamma)$ and $v_2(r,\gamma)$, since energy is now leaking into the cladding from both waveguide boundaries.

5.2.8 Transition of non-whispering to whispering gallery modes ($\theta_{oq} \cong \theta_{wf}$) and of modes through cut-off ($\theta_{oq} \cong \theta_{cf}$ and $\theta_{oq} \cong \theta_c$).

In the previous section and for the whispering and non-whispering bound adiabatic modes in the taper (5.84)-(5.88), the contribution of the branch points was ignored as being negligible compared to that of the saddle point. However, this is true only for angles θ_o, which are away from the branch points. As angles θ_o approach the two branch points θ_c and θ_{cf} the contribution of the branch-points becomes significant and the steepest path integration method has to be appropriately modified to consider them. This extension is very interesting since as we will see it actually expresses the transition between a bound mode to a mode beyond cut-off. In addition, this section will also focus on another transition occurring in the tapered bend waveguide, which is between a non-whispering and a whispering gallery mode.

A. $\theta_{oq} \cong \theta_{wf}$. As the saddle point approaches and goes beyond the angle, which separates the non-whispering modes from the whispering gallery modes, θ_{wf} (5.50), we have a smooth transition between whispering and non-whispering gallery modes.

Saddle points are determined by the eigenvalue equation (5.80) in this case. As the local width w of the tapered waveguide decreases, the saddle point θ_{oq} (5.80), approaches and proceeds past θ_{wf} (5.50), (see Fig. 5-9 for the location of θ_{wf}). In addition, the turning point w' (5.55), changes sign and from positive becomes negative, which in turn forces the parameter ξ of the Airy functions in (5.51) to change sign from positive to negative in the region between $x = 0$ and $x = w'$. In this transition region and close to $x = 0$, (5.51) should be used to approximate $\psi^{\pm}$ in the spectral integral in (5.71) instead of the WKB solutions used in (5.81) and (5.84) although WKB solutions are still perfectly valid away from this point. The calculation of (5.71) by the steepest descent method then gives the following result with the aid of (5.51)

$$V^{\pm}(r,\gamma) \approx \pi\sqrt{2\omega}e^{i\pi/4} \cdot \exp[-i\frac{1}{2}\Phi(\theta_{oq}+\omega)] \cdot \exp[\pm i\frac{1}{2}\frac{\Phi_{\theta_f}(\theta_{oq})}{2}] \cdot$$
$$A_q(r,\gamma)e^{-iS_q(r,\gamma)}[\xi'(r\sin\gamma)]^{-1/2} \cdot \left(e^{\mp i\pi/4}Ai[\xi(r\sin\gamma)] + e^{\pm i\pi/4}Bi[\xi(r\sin\gamma)]\right) \tag{5.98}$$

Equation (5.98) is accurate everywhere within the core and not only close to $x = 0$. By using the asymptotic expressions for the Airy functions with large arguments, it reduces to the whispering gallery adiabatic mode (5.84) for $w' > 0$ and to the non-whispering gallery mode (5.93) for $w' < 0$, which are derived from the simpler WKB solutions. However, in the transition region between whispering and non-whispering gallery modes the more complicated expression for the adiabatic modes (5.98), has to be used.

B. $\theta_{oq} \cong \theta_c$. This case corresponds to the transition of bound tapered bend adiabatic mode to a leaky mode beyond cut-off.

The saddle points θ_{oq} calculated by (5.71) can approach arbitrary the branch-point θ_c (critical angle for reflection) of the phase function $\Phi(\theta_o)$ as the local waveguide width w decreases, (see Fig. 5-9 for the location of θ_c). In order to overcome the complication raised by θ_c we use the Chester-Friedman-Ursell method described in section 3.2.4 of Chapter 3. We first perform the variable change $t = (\theta_c - \theta_o)^{1/2}$ to equation (5.76) to obtain

$$Q_o(r,\gamma;\theta_o(t)) = \frac{1}{2}\int_{\theta_c}^{\theta_o(t)} \Phi(\hat{\theta}_o)d\hat{\theta}_o + \frac{1}{2}\int_{\theta_{wf}}^{\theta_o(t)} \Phi_{\theta_f}(\hat{\theta}_o)d\hat{\theta}_o + \int_{\theta_{wf}}^{\theta_o(t)} \varphi_x(\hat{\theta}_o)d\hat{\theta}_o \qquad (5.99)$$

Now, if apply the defining equation of the saddle-points

$$\frac{\partial[Q_o(r,\gamma;\theta(t)) - q\pi\theta_o(t)]}{\partial t} = 0 \qquad (5.100)$$

we find that the effect of the transformation is to eliminate the branch-point and to replace it with a second saddle-point at $\theta_{oq} = \theta_c$. This is confirmed if we perform the differentiation in (5.100)

$$\frac{\partial[Q_o(r,\gamma;\theta_o(t)) - q\pi\theta_o(t)]}{\partial t} = \frac{\partial[Q_o(r,\gamma;\theta_o) - q\pi\theta_o]}{\partial\theta_o}\cdot\frac{\partial\theta_o}{\partial t} = -2t\frac{\partial[Q_o(r,\gamma;\theta_o) - q\pi\theta_o]}{\partial\theta_o} \qquad (5.101)$$

From (5.101) and (5.100) we see that apart from the original saddle-point θ_{oq} we now have the addition of a new one at θ_c or $t = 0$. In this way $\Phi(\theta_o)$, which is described by (5.59) when $\theta_o \cong \theta_c$, is transformed to an analytic function and the asymptotic integration in (5.71) is carried out by considering the influence of the two confluent saddle-points θ_{oq} and θ_c. A uniform asymptotic evaluation of the integral (5.71) is in this case obtained by

using the method of Chester-Friedman-Ursell, which gives

$$V^{\pm}(r,\gamma) \approx C_q(r,\gamma)\exp[\,2i\zeta^3/3]\exp[\,\frac{1}{2}\omega^{1/2}]\cdot\exp[\,\pm i\frac{1}{2}\Phi_{\theta_f}(\theta_c)]\left(\sqrt{e^{2x/R_1}-e^{2w/R_1}\cos^2\theta_{oq}}\right)^{-1/2}$$
$$\cdot\exp\left(\mp i\int_0^{r\sin\gamma} k_o n_{co}\sqrt{e^{2x/R_1}-e^{2w/R_1}\cos^2\theta_{oq}}\,dy\right)\left(Ai'\left(\zeta^2 e^{i\pi/3}\right)+\zeta e^{i\pi/6}Ai\left(\zeta^2 e^{i\pi/3}\right)\right) \tag{5.102}$$

with

$$C_q(r,\gamma) = -8\pi e^{-i5\pi/12}\zeta\omega\left(\frac{d^2}{dt^2}(Q_o - q\pi\theta_o)\right)^{-1}\Bigg|_{t=0} \tag{5.103}$$

and

$$\zeta = \omega^{-1/3}\left\{\frac{3}{4}\left[Q_o(r,\gamma;\theta_o(t=0))-Q_o(r,\gamma;\theta_{oq})-(q\pi\theta_c - q\pi\theta_{oq})\right]\right\}^{1/3} =$$
$$\omega^{-1/3}\left\{\frac{3}{4}\int_{\theta_c}^{\theta_o}\left(k_o n_{co}\int_0^w\sqrt{e^{2y/R_1}-e^{2w/R_1}\cos^2\theta_o}\,dx+\Phi_{\theta f}(\theta_o)-\sqrt{2\cot\theta_c}(\theta_c-\theta_o)^{1/2}-q\pi\right)d\theta_o\right\}^{1/3} \tag{5.104}$$

Equation (5.103) can be significantly simplified. At first when $\theta_{oq}\cong\theta_c$ eigenvalue equation (5.77) takes the form

$$kn_{co}\int_0^w\sqrt{e^{2x/R_1}-e^{2w/R_1}\cos^2\theta_{oq}}\,dy+\Phi_{\theta f}(\theta_{oq})-\sqrt{2\cot\theta_c}(\theta_c-\theta_{oq})^{1/2}=q\pi \tag{5.105}$$

where in (5.104) we replaced $\Phi(\theta_o)$ with its value close to θ_c (5.59).

while when the θ_{oq} saddle-point coincides with θ_c (5.77) becomes

$$kn_{co}\int_0^{w_c}\sqrt{e^{2x/R_1}-e^{2w/R_1}\cos^2\theta_c}\,dx+\Phi_{\theta f}(\theta_c)=q\pi \tag{5.106}$$

with w_c the local height of the waveguide where the condition $\theta_{oq}=\theta_c$ is met. By combining (5.104) with (5.105) we get

$$(\theta_c-\theta_{oq})^{1/2}\cong\frac{1}{\sqrt{2\cot\theta_c}}kn_{co}\int_w^{w_c}\sqrt{e^{2x/R_1}-e^{2w/R_1}\cos^2\theta_{oq}}\,dx \tag{5.107}$$

where we have assumed that $\Phi_{\theta_f}(\theta_c)\cong\Phi_{\theta_f}(\theta_q)$

and finally by combining (5.103) with (5.107) we derive the simple expression

$$\zeta = KL^{-2/3} \tag{5.108}$$

$$K = \int_{w}^{w_c} \sqrt{e^{2x/R_1} - e^{2w/R_1}\cos^2\theta_{oq}}\,dx, \quad L = 2\omega^{-1}\sqrt{2\cot\theta_c} \tag{5.109}$$

5.3. SUMMARY – CONCLUSIONS OF THE INTRINSIC MODE THEORY FOR TAPERED BENDS

The intrinsic mode theory has been extended to describe propagation phenomena in tapered bend waveguides. To a first order approximation this theory furnished the adiabatic mode for propagation in the tapered bend. A typical adiabatic mode in the tapered bend starts off as a whispering-gallery type mode (5.84) then converts to non-whispering (5.93) as the width of the waveguide decreases and finally it goes beyond cut-off where it starts attenuating.(5.94)-(5.97). As the whispering-gallery wave transforms to a non-whispering gallery wave, the caustic of the field is moved from inside the core to the cladding and fields are described with the aid of the Airy functions (5.98) close to the bottom boundary. The transition between a bound to a beyond cut-off mode, a situation which the conventional adiabatic theory was failing to accurately describe, is attributed to the confluence of two saddle-points in the spectral integral (5.8), one due to the local eigenvalue problem (5.77) and one due to the branch-point of the phase function for reflection of rays on the upper surface at critical angle (5.13). As the saddle-point arbitrary approaches the critical angle the adiabatic mode takes the form of another set of Airy functions (5.107). The difference between the field described at the transition region between whispering to non-whispering adiabatic modes from the field at the transition between bound to cut-off modes is that in the former, Airy functions (5.98) are necessary only at the vicinity of the caustic close to the bottom boundary and can be replaced with the looser WKB solution (5.84), (5.93) away from it, while in the latter case, the Airy functions (5.107) should be retained within the whole area of the waveguide and can be replaced with their large argument approximations (5.84), (5.93) only when the width of the waveguide is such that allows the saddle-point to be away from the critical angle. Two important features of the adiabatic mode that we derived and that need special attention are its amplitude (5.82), (5.86) and its phase evolution (5.83), (5.92) inside the taper. From (5.86) we see that the amplitude of the tapered bend is not constant in the core of the taper but instead it adjusts itself according to the local waveguide environment. In this respect, the adiabatic mode accounts for the coupling between the

local waveguide modes. In reality, this statement has been proved in [5.18] where Arnold and Felsen have proved that the amplitude of the adiabatic mode derived by their method is equivalent to the amplitude derived by solving the set of differential equations of the normal coupled mode theory [5.19]. Finally, from (5.92) we see that the phase of the mode is analogous to the local propagation constant as expected.

5.4. WAVEGUIDE TAPERED BEND EXPERIMENTS

5.4.1 Description of Waveguides under Investigation

The purpose of this section is to present our experimental results for the insertion loss and the tolerance to source misalignment measured for a range of tapered waveguide bends of various taper ratios and radii of curvature. The tapered waveguide bend arrangement under investigation is shown in Fig. 5-11 and consists of a straight input waveguide, a tapered bend and an output straight waveguide. The input section is a straight waveguide of width w_{in}. The tapered waveguide bend, which follows, transforms the waveguide width from its initial value w_{in} to its final value w_{out} while changing the waveguide's direction by 90°. Finally, the output section is another straight waveguide but of width w_{out}. For simplicity, we refer to this component as the *tapered bend* in the following. The ratio of the output to input width, is referred to as the taper ratio TR ($TR = w_{out} / w_{in}$). Since we always had $w_{out} < w_{in}$ in our experiments, the taper ratio is confined to lie in the region $0 < TR < 1$. Proportionally to the most popular straight waveguide tapers, which are linear, we chose to vary R_1 and R_2 linearly with respect to φ as

$$R_1(\omega) = R_1(0°) + \omega \cdot \varphi, \text{ and } R_2(\omega) = R_2(0°) - \omega \cdot \varphi,$$

with ω, a constant determining the rate of radius change and the boundary conditions

$$R_2(0°) - R_1(0°) = w_{in}, \text{ and } R_2(90°) - R_1(90°) = w_{out}$$

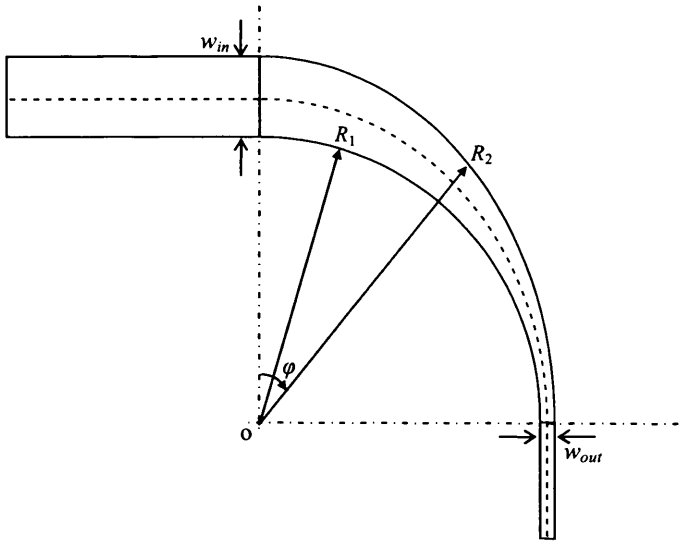

Fig. 5-11. A schematic of a tapered waveguide bend used in our experiments. Although the axis of the curved section, which is shown with a dashed line, is a circular 90° arc, internal R_1 increases linearly and external R_2 radii decreases linearly with respect to the angle φ in order for the width of the waveguide to reduce.

A schematic diagram of the wafer used in the experiments is shown in Fig. 5-12. In Fig. 5-12 we show one basic waveguide group on the wafer, which comprises the tapered bend described above and another three waveguides for calibration and comparison purposes. Starting from the waveguide with the smaller radius R, we meet the tapered bend. The input straight waveguide section has length l_{in} = 11.5 mm and width w_{in} = 50 μm, corresponding to standard multimode waveguides for optical backplane applications. Finally, the output straight waveguide section has length l_{out} = 24.5 mm and width w_{out}. Moving to the next component with radius $R+\Delta R$, we find an input straight – bend – output straight waveguide cascade (which will be referred to as the *waveguide bend* 1 for simplicity). The input and output straight section lengths are again l_{in} and l_{out} respectively, and all three waveguides have the same width w_{in} = 50 μm. The next component with radius $R+2\Delta R$, was another waveguide bend, only that this time the width of all three (input straight – bend – output straight) waveguides was w_{out}, (*waveguide bend* 2). The final component in the group (with radius $R+3\Delta R$), is a combination of an input straight – straight tapered – output straight 1 – bend – output straight 2, waveguides (we will refer to this component as the *straight taper plus bend*). The input straight waveguide has length l_i = 1 mm and width w_{in}. The straight tapered

waveguide was a linear taper from w_{in} to w_{out} with length l_{tap} = 10 mm while the output straight waveguide 1 attached to the taper has length l_o = 0.5 mm. The curved section is a simple 90° bend of radius R, and width w_{out}. Finally, the output straight section 2 has width w_{out} and length l_{out}. This component was designed to compare the performance (insertion loss and tolerance to source misalignment) between straight tapers and tapered bends.

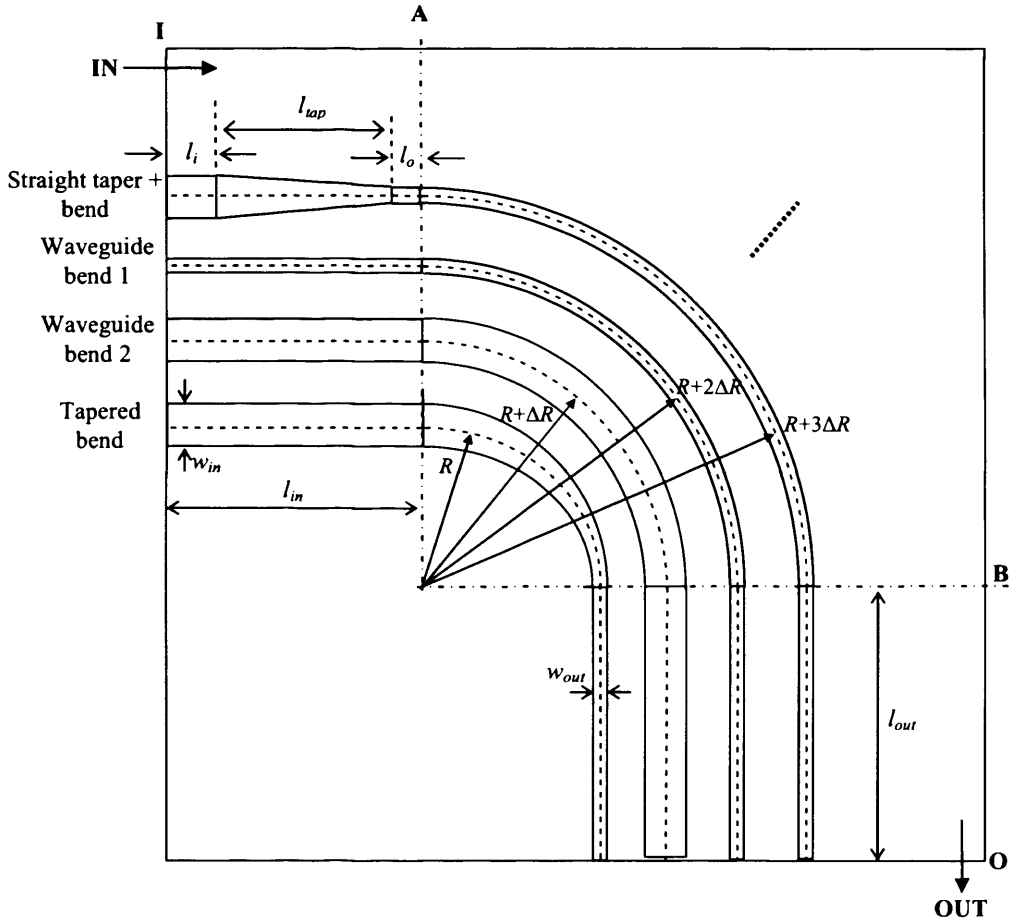

Fig. 5-12. Schematic diagram of one basic group of waveguiding components. From smaller to larger radii, each group contained one tapered bend, one waveguide bend with width w_{in}, one waveguide bend with width w_{out} and finally one straight taper plus a bend. A series of 30 similar basic groups with increasing radii were cascaded on the wafer with TR in the range $0.2 < TR < 0.8$ and radii R in the range 5 mm < R < 34 mm.

The separation between any two successive waveguides in the wafer is ΔR = 250 μm. All waveguides had a 50 μm thickness and the fabrication details of the wafer have already been presented in section 4.3.1 of Chapter 4. As has already been mentioned, the

input width had been set to w_{in} = 50 μm, constant across all waveguides but the output width takes each of the values w_{out} = 10 μm, 20 μm, 25 μm, 30 μm and 40 μm giving corresponding taper ratios *TR* = 0.2, 0.4, 0.5, 0.6 and 0.8. Note that waveguide bends with $w_{in} = w_{out}$ = 50 μm can be alternatively considered as tapered bends or straight tapers plus bends with *TR* = 1. The entire wafer has been constructed as following: The first group was designed so that *TR* = 0.2 and started from *R* = 5 mm. Then a second concentric group was designed starting at $R+4\Delta R$ = 7 mm, with *TR* = 0.4, a third concentric group starting at $R+8\Delta R$ = 8 mm, with *TR* = 0.5, a fourth group starting at $R+12\Delta R$ = 9 mm, with *TR* = 0.6 and a fifth group starting at $R+16\Delta R$ = 10mm, with *T.R* = 0.6. Once we had finished with all 5 available taper ratios we started reusing them until the last group started at *R* = 34 mm. According to our design, we had 30 groups in total, or six groups for each *TR*, with two groups of the same *TR* being separated by $20\Delta R$ = 5 mm. The details of the wafer and the position of each group are summarized in Table 5.1.

TABLE 5.1

DETAILS OF THE WAVEGUIDE GROUPS ON THE TAPERED BEND WAFER

Group no.	Start Radius (mm)	*TR*	Group no.	Start Radius (mm)	*TR*	Group no.	Start Radius (mm)	*TR*
1	5	0.2	**11**	15	0.2	**21**	25	0.2
2	6	0.4	**12**	16	0.4	**22**	26	0.4
3	7	0.5	**13**	17	0.5	**23**	27	0.5
4	8	0.6	**14**	18	0.6	**24**	28	0.6
5	9	0.8	**15**	19	0.8	**25**	29	0.8
6	10	0.2	**16**	20	0.2	**26**	30	0.2
7	11	0.4	**17**	21	0.4	**27**	31	0.4
8	12	0.5	**18**	22	0.5	**28**	32	0.5
9	13	0.6	**19**	23	0.6	**29**	33	0.6
10	14	0.8	**20**	24	0.8	**30**	34	0.8

5.4.2 Straight taper length selection

The length l_{tap}, of the straight taper was selected to ensure that we operated in the adiabatic regime where insertion loss due to the tapering process minimizes. This was supported by BPM simulations of straight tapers like the ones in Fig. 5-12 but with

variable taper length l_{tap}. In these simulations, we analyzed propagation in a cascade of a straight input – straight linearly tapered– straight output waveguides with taper length varying in the range 0.1 mm < l_{tap} < 10 mm. The input width of the tapers was w_{in} = 50 μm while the output width w_{out} =10 μm, therefore, examining the *TR* = 0.2 case. The waveguide thickness was 50 μm, constant. The field at the entrance of the input straight waveguide was a combination of all modes of a multimode fibre added with random phases to resemble closely the field from the mode scrambled step index fibre in Fig. 5-14 that was used in the experiments. The details for the input field and the parameters used in the BPM simulations were the same as the ones used for the simulation of the waveguide bends in section 4.5 of Chapter 4. We refer the reader there for more information. The results of the simulations for the insertion loss of the straight tapers as a function of l_{tap} are shown in Fig. 5-13. There, we can see that for short taper lengths, l_{tap} < 1 mm, insertion loss increases rapidly as l_{tap} decreases. This is because in this regime propagating modes are coupled strongly to each other and to radiation modes increasing insertion loss. In contrast, for l_{tap} > 3 mm, insertion loss saturates to its minimum value ~ -4 dB, which is then maintained independently of l_{tap}. This is strong evidence that the taper starts to operate in the adiabatic regime. In this case, as explained in our theoretical section, propagating modes become independent of each other to a first order approximation and radiate only when the local width of the waveguide reaches their cut-off. Therefore, our selection of l_{tap} = 10 mm in our experiments guaranteed adiabatic operation. In addition, the tapers of the rest taper ratios needed not be simulated as if adiabatic operation is ensured for the lowest *TR* (the most severe taper) then it is secured for all higher *TR*s.

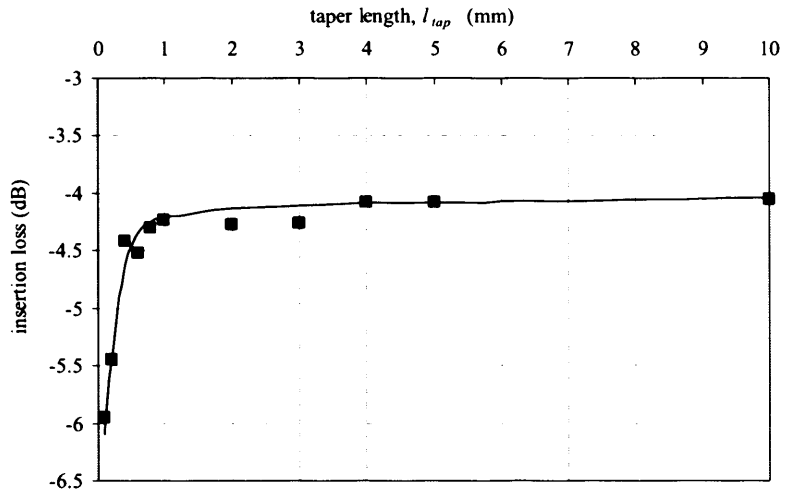

Fig. 5-13. BPM simulation of the input – tapered – output straight waveguides with TR = 0.8 and variable taper lengths for an input field coming from a fully-filled multimode fibre. For taper lengths l_{tap} > 3 mm insertion loss saturates to -4.05 dB independent of l_{tap}, an evidence of adiabatic operation.

5.4.3 Insertion loss measurements

The experimental arrangement for the first set of experiments is shown in Fig. 5-14 and is identical to the method described in Chapter 3 for measuring the insertion loss for the 50 μm × 50 μm waveguide bends. According to Fig. 5-14, light from an 850 nm VCSEL, was launched into a standard 50/125 μm step index MM fibre with $NA_{fibre} = 0.2 < NA_{wg} = 0.302$. After mode scrambling, the fibre was aligned and butt-coupled to one of the waveguides on the wafer. Alignment between fibre and waveguide was achieved by mounting the fibre end on a manual rotation stage and a system of three motorized translation stages with sub-micrometer precision for accurate alignment in x, y, and z directions and then adjusting them respectively to maximize the power at the output of the waveguide. Light from the waveguide output was spatially filtered by a 150 μm diameter circular pinhole to exclude much of the light travelling through the cladding before being collected by an integrating sphere photodetector (PD). Index matching fluid (n = 1.4911 at 850 nm) was applied to both MM fibre - waveguide and waveguide - pinhole interfaces to reduce Fresnel reflection loss due to the index mismatch at the interface and scattering loss due to the surface roughness across the waveguide face.

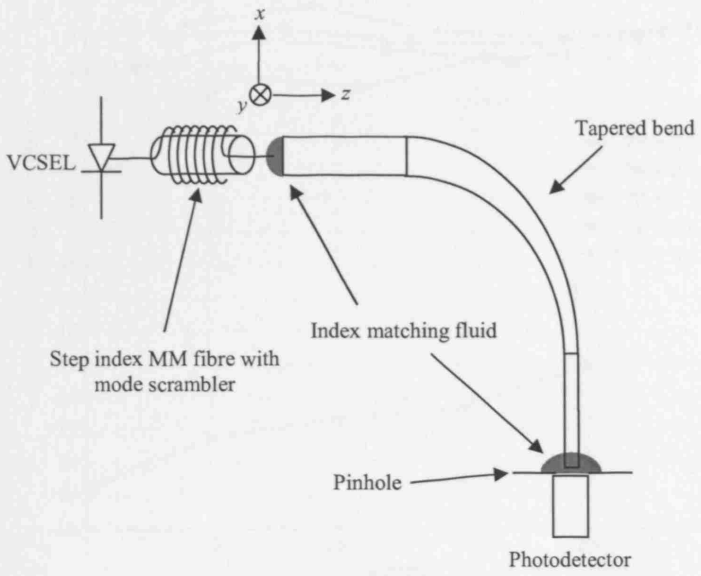

Fig. 5-14. Experimental arrangement used to measure insertion loss in the waveguides on the wafer of Fig. 5-12. Although only a tapered bend waveguide is shown here for illustration, the same method was used for all of the waveguides on the wafer.

The results of the insertion loss measurements for the tapered bends on the wafer are shown in Fig. 5-15. In Fig. 5-15, we show the calibrated insertion loss *Pcal*, as a function of the radius of curvature *R*, for all available taper ratios *TR*. *Pcal* is defined as following: If the power measured at the end of one of the tapered bends is P_{bt} and the power measured at the end of the waveguide bend 2 with width w_{in} next to the tapered bend (Fig. 5-12) is P_b then the calibrated insertion loss P_{cal}, for this tapered bend is calculated as $P_{cal} = P_{bt} - P_b$. Since the radius of the tapered and the waveguide bends are approximately the same (these two waveguides are only 250 μm apart), this calibration step has the advantage of firstly, almost removing the bend loss and secondly, removing the coupling loss. In other words, the calibrated insertion loss is the excess loss that a tapered bend exhibits, compared to the insertion loss of a simple waveguide bend having the same width. This excess loss is due to the tapering process, which we want to reveal with this analysis.

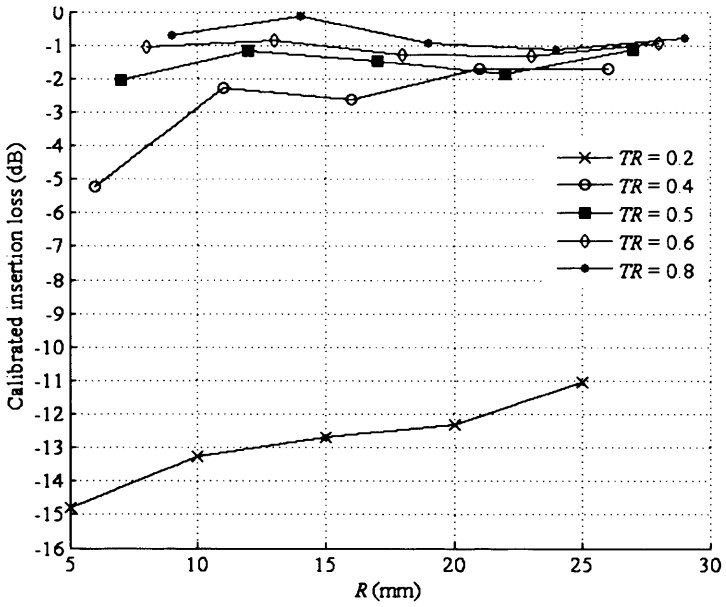

Fig. 5-15. Calibrated insertion loss as a function of radius R of curvature for the tapered bends on the wafer for all available TR.

There two noticeable characteristics from the calibration insertion loss graphs, Fig. 5-15. Firstly, for any R, it is evident that graphs for tapers with higher TR lie above graphs for tapers with lower TR, indicating that as w_{out} becomes smaller the insertion loss increases. This is an expected trend since as we reduce the waveguide width, higher order modes gradually find themselves beyond cut-off and radiate into the cladding. The smaller the final width w_{out}, the more modes will go beyond cut-off. The exception for the TR = 0.4 line which appears to be above the TR = 0.5 one at R = 21 mm is rather attributed to experimental error. The second observation is that for TR = 0.2 and TR = 0.4 the insertion loss gradually improves (insertion loss drops) as R increases, while for the rest of the lines insertion loss appears to be relatively immune to changes in R. One possible explanation is that the radius of curvature has a significant effect on the profile of the modes that propagate inside a curved waveguide. It has been shown that as the radius reduces, the peak of the amplitude of the lower order modes shifts towards the external boundary of the bend [5.24]. Therefore, the field coming from the input straight waveguide tends to excite more high order modes of the waveguide bend in the small radii case than in the large radii case due to greater modal mismatch between these two. However, the lower TR tapers act as high order mode filters and a significant amount of

power coupled into the high-order modes is lost. As the radius increases less high order waveguide bend modes are excited and so the filtering effect is mitigated and more power stays in the waveguides. For larger $TR \geq 0.5$ though the same effect is not as important since as it appears the final waveguide width w_{out}, is large enough to support almost all of the excited bent waveguide modes even for small R.

The tapered bends with $TR = 0.2$ demonstrate high calibrated insertion loss more than -11 dB for all radii and, therefore, they are not suitable for use in a real backplane system where power budget is an important issue. In contrast tapered bends in the range $0.5 < TR < 0.8$ have calibrated insertion loss, which was always less than -2 dB for all radius and so they might be considered to be used.

In Fig. 5-16 (a) – (e), we compare the performance of the tapered bend with the performance of the straight taper plus bend. The graphs show the insertion loss measured for the tapered bends and straight tapers plus bends on the wafer without any calibration to allow direct comparison. The graphs should be read as follows: Fig. 5-16 (a) contains the results for the tapered bend and the straight taper plus bend for the first five groups on the wafer, where all available values of TR were used. Fig. 5-16 (b) shows the results for the groups 6-10, Fig. 5-16 (c) for the groups 11-15, Fig. 5-16 (d) for the groups 16-20 and finally, Fig. 5-16 (e) for the groups 21-25. As has been mentioned before, the waveguide bends with $w_{in} = w_{out} = 50$ μm can be considered as tapered bends or straight tapers plus bends with $TR = 1$. This feature has been utilized in Fig. 5-16 and is very useful since it nicely completes the right end of the graphs. As we can see from Fig. 5-16 (a)-(e) the insertion loss for tapered bends is always less than that of the straight taper plus bend arrangement. This is especially noticeable for the low TR, while as TR increases the two converge to each other. Further work needs to be done to understand why tapered bends operate better than the straight taper plus bend combination but we believe that the main reason is the transition between the straight taper and the intermediate straight waveguide, which does not exist in the tapered bend case and introduces additional loss due to one extra transition involved. For $TR \geq 0.6$ waveguide bend and straight taper plus bend results become almost indistinguishable in all cases. In addition, we can see that, as in Fig. 5-15, the results seem not to significantly depend on the radius, except for the $TR = 0.2$ case where results vary by a large amount and do not have a consistent trend with

R. We believe that the results for *TR* = 0.2 are not very credible since we have previously observed that waveguides with high aspect ratio between their width and thickness have many inaccuracies in their shape after fabrication.

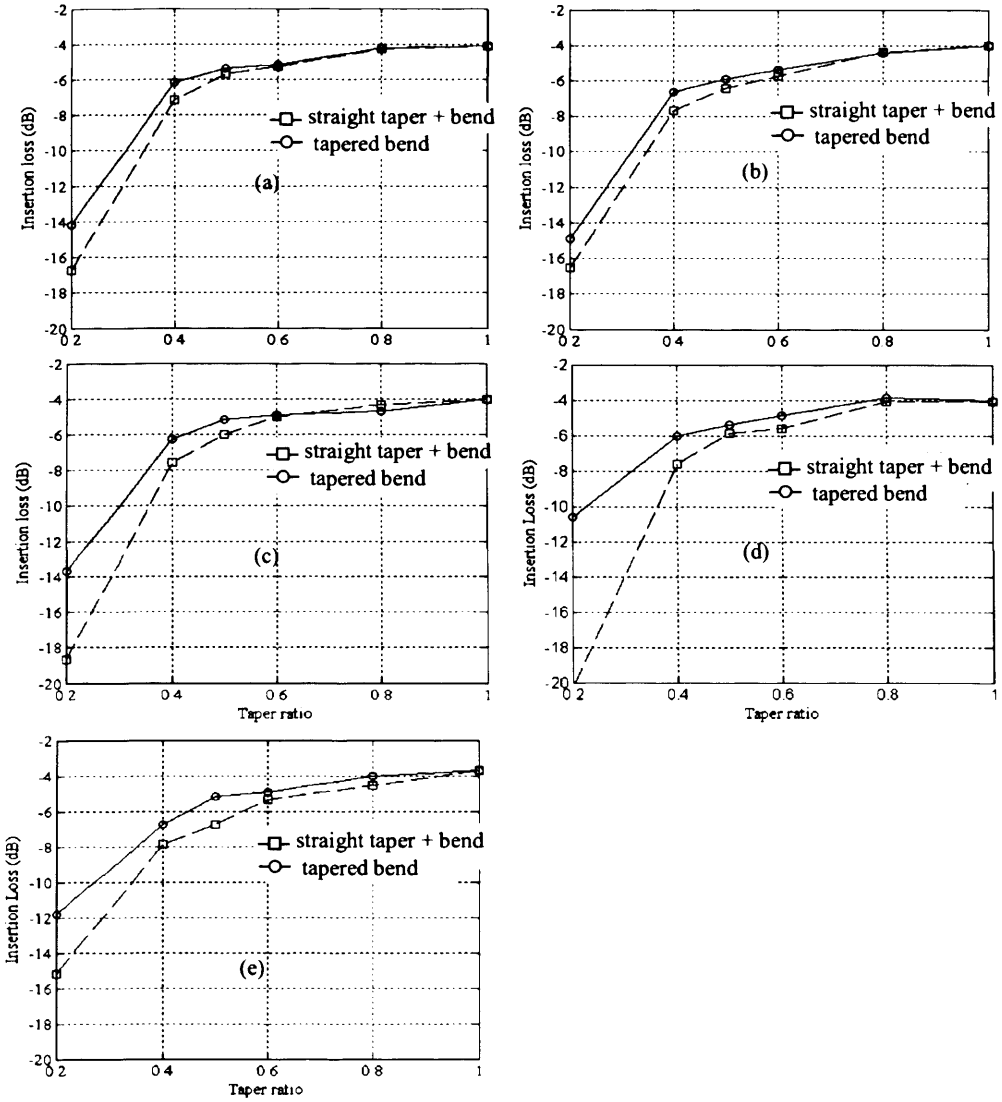

Fig. 5-16. Insertion loss of tapered bent waveguides compared to straight taper plus bend. (a) Results for groups of waveguides 1-5, *R* = 5 mm – 5.75 mm (b) results for groups of waveguides 6-10, *R* = 6 mm – 6.75 mm (c) results for groups of waveguides 11-15, *R* = 7 mm – 7.75 mm (d) results for groups of waveguides 16-20, *R* = 8 mm – 8.75 mm (e) results for groups of waveguides 20-25, *R* = 9 mm – 9.75 mm.

5.4.4 Effect of source misalignment

In the second set of experiments, we were interested in investigating the effect of source misalignment on insertion loss. In this case we replaced the MM fibre of the previous

experiments with a SM fibre and scanned along the lateral direction x, Fig. 5-17, with the aid of the motorized stages while monitoring the power at the other end.

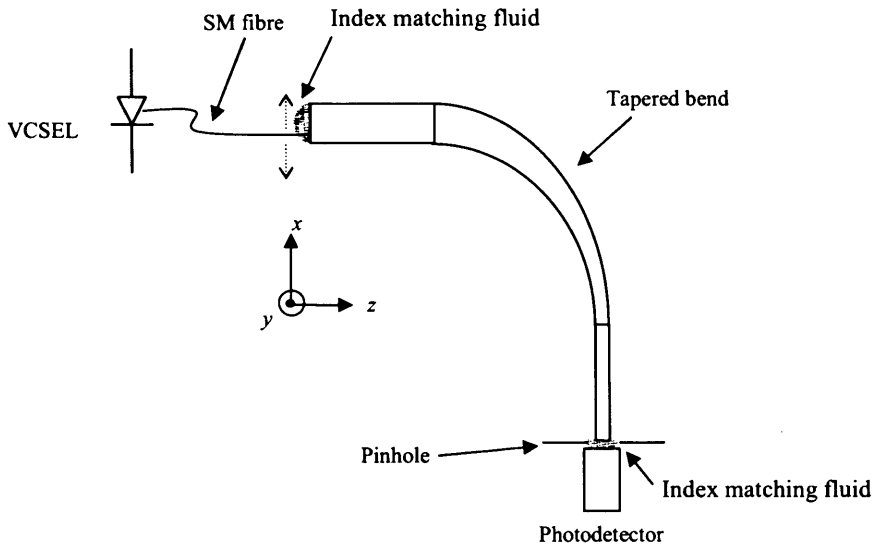

Fig. 5-17. Experimental arrangement used to measure the effect of source misalignment on the performance of the tapered bend.

Figure 4-8 shows the measured insertion loss for two scans, one for a tapered bend with TR = 0.4 (input width 50 μm – output width 20 μm) and one for the waveguide bend 1 with both input and output width of 20 μm for comparison. Both tapered and waveguide bends shown in Fig. 5-18 belonged to the same group of waveguides (group 6, R = 6 mm – 6.75 mm). It is clearly seen in Fig. 5-18 that as fibre moves away from the position of minimum insertion loss (maximum coupling efficiency) x = 0, power drops (insertion loss increases) for both tapered and waveguide bend. However, although they both have the same width, w_{out} = 20 μm at their output, the tapered bend manages to maintain high coupling efficiency for a larger range of fibre misalignment than the waveguide bend. On the other hand, we see that at best coupling position, the insertion loss is lower for the waveguide bend than for the tapered bend. We will come back to this observation later in this section since as will see it is central to the operation of tapers.

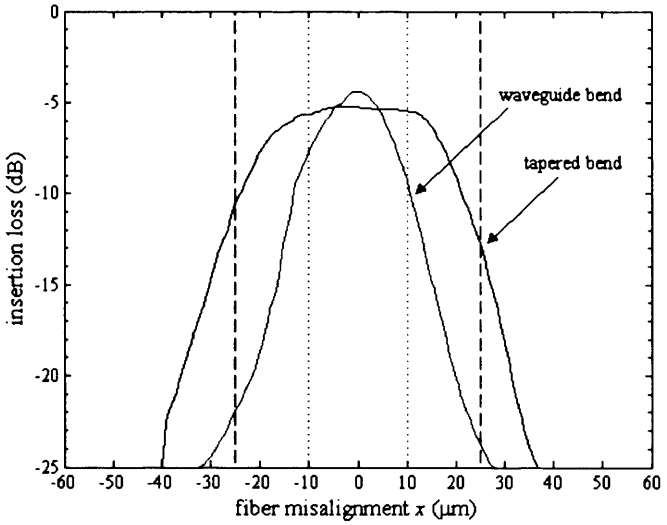

Fig. 5-18. Insertion loss as a function of fibre lateral position x from the position of maximum coupling efficiency (x = 0) for a tapered bend with TR = 0.4 and R = 11 mm and for a waveguide bend with input/output width of 20 μm and R = 11 mm. Dashed lines corresponds to the boundaries of the 50 μm wide entrance of the tapered bend while dotted lines correspond to the boundaries of the 20 μm wide entrance of the waveguide bend. Resolution of the scans was 0.5 μm.

In order to better examine the range of fibre misalignment that is gained when a tapered bend is used we calculated the full width at half maximum (FWHM) of curves such as the ones shown in Fig. 5-18 for the tapered and waveguide bends in groups 7-10 and plotted them in Fig. 5-19 as a function of their output width. According to our design two successive same components, two tapered bends for example, are separated by 1 mm. The tapered bends under examination had radius R = 11 mm (group 7) for output width 20 μm, R = 12 mm (group 8) for output width 25 μm, R = 13 mm (group 9) for output width 30 μm and R = 14 mm (group 10) for output width 40 μm. The waveguide bends which were 500 μm apart from the tapered bends in the same group, had R = 11.5 (group 7) mm for output width 20 μm, R = 12.5 mm (group 8) for output width 25 μm, R = 13.5 mm (group 8) for output width 30 μm and R = 14.5 mm (group 9) for output width 40 μm. In Fig. 5-19, we have also included the measurements for one more bend waveguide with output width 50 μm. In this case, as has been explained, tapered bends degenerate to waveguide bends and this is why FWHM appears to be the same in the graph. This point has been added since it nicely reveals the trend of the curves.

As it is expected, we see that for the waveguide bends FWHM increases steadily as their width increases. For a 20 μm wide waveguide bend FWHM is only 18 μm compared

to 44.5 μm for a 50 μm wide waveguide bend. In contrast, tapered bend FWHM only slightly changes as the output width increases and in all cases, it is steadily better than 40 μm.

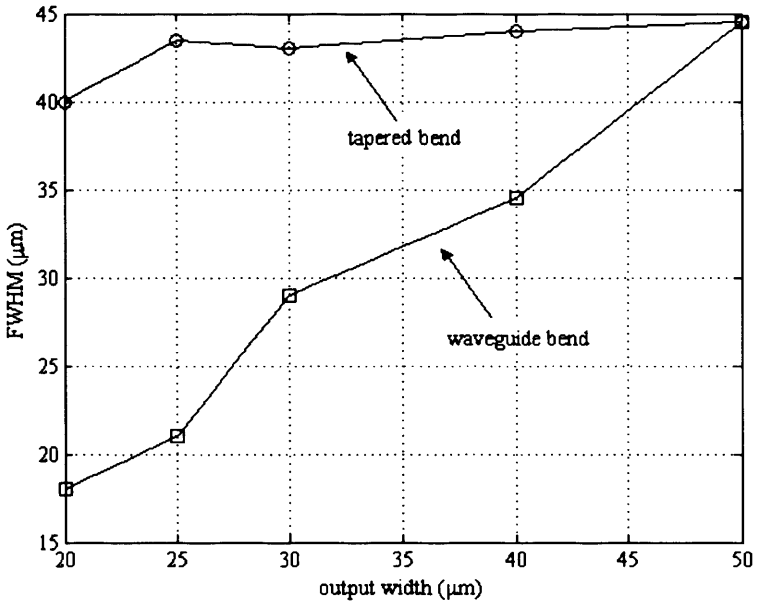

Fig. 5-19. FWHM of the insertion loss as a function of fibre misalignment curves for tapered and waveguide bends in groups 7-10, R = 11 mm – 14.75 mm. FWHM shows the amount that a single-mode fibre can be moved in front of a waveguide before power coupled dropped by 3 dB.

A very revealing graph is derived by plotting the difference, ΔFWHM, between the FWHM obtained for a tapered bend and the FWHM obtained for the waveguide bend of the same output width as this exposes the benefit of using tapers. This graph of ΔFWHM as a function of output width is shown in Fig. 5-20 for the same waveguides as in Fig. 5-19. In the same graph, we plotted the difference between the insertion loss at best coupling position for the tapered bend and the insertion loss measured for the waveguide bends, ΔP, at best coupling position as well. The positive sign of the ΔFWHM across all waveguide widths means that the tapered bend FWHM is always larger than the waveguide bend FWHM. However, the negative sign of ΔP, again for all waveguide widths, means that the tapered bends always have higher insertion loss than the waveguide bends. We highlight the above feature since it summarizes the operation of almost any kind of tapered waveguide: *In multimode tapered waveguides a trade-off exists between the amount of tolerance to source misalignment and the amount of*

insertion loss (or coupling efficiency) experienced. The greater the amount of gain in tolerance the greater the loss in coupling efficiency.

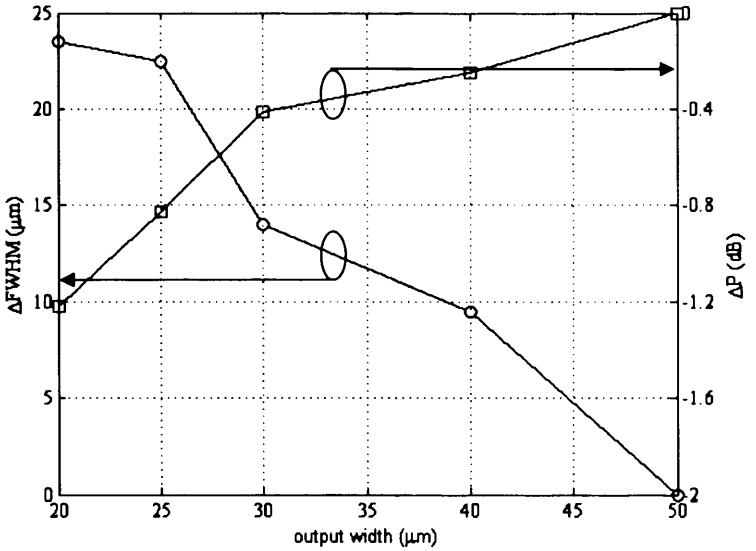

Fig. 5-20. ΔFWHM defined as the difference between the tapered bend FWHM and the waveguide bend FWHM and ΔP defined as the difference between the tapered bend insertion loss and the waveguide bend insertion loss for the same range of waveguides as in Fig. 5-19.

To examine how the radius influences the performance of the tapers we plotted the ΔFWHM for all waveguide groups on the wafer, Fig. 5-21. In Fig. 5-21, we show the ΔFWHM for all four different output waveguide widths (20 μm, 25 μm, 30 μm, 40 μm) as a function of the group number they belong to. It is understood that as group number increases radius of curvature increases too. Surprisingly, there is no noticeable trend within the radius range (5 mm < R < 35 mm) of investigation although the results for the insertion loss of the 50 μm waveguide bends which were presented in Chapter 4 showed significant correlation to the radius for at least the waveguides with R < 10 mm. Perhaps there is actually some mild trend, which could not be identified from Fig. 5-21. If radius is not a parameter, which affects the performance of the tapers, then this is an important observation since it implies that the more compact tapers with tight radius of curvature perform in a similar way to the less compact ones. Therefore, important space conservation can be achieved without significant penalty.

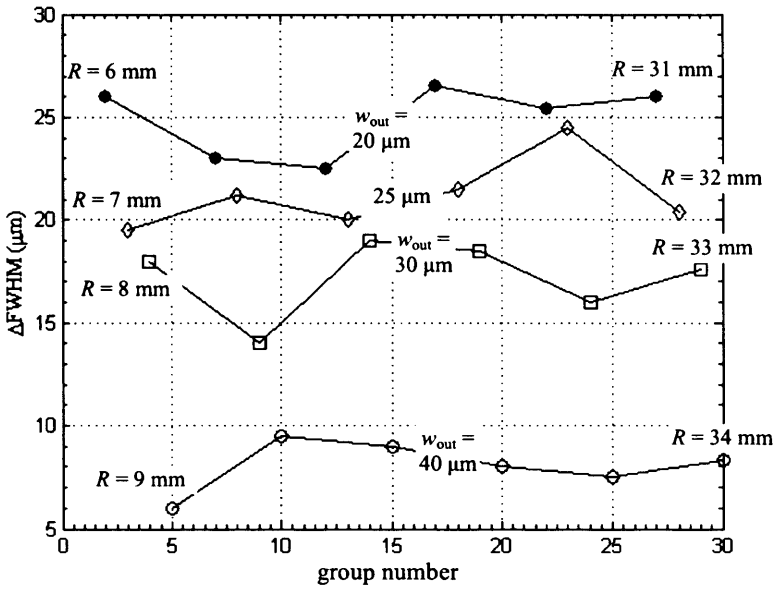

Fig. 5-21. ΔFWHM between tapered and waveguide bends as a function of group number for the various output widths. For a specific output width, there are six groups that contain tapered and bend waveguides of this width (resulting in 6 ΔFWHM). Two successive groups of same output width are separated by 5 mm.

Since we have not identified any dependence of the taper performance on the radius we decided to present all results of the ΔFWHM in a collective way. In Fig. 5-22, we present the mean ΔFWHM for the six waveguides in each set of output widths as well as the mean ΔP for the same. However, rather than plotting the graphs as a function of the output width we used the equivalent taper ratio parameter, *TR*. This is because taper ratio is a more general parameter and can be used for comparison purposes with tapers of other than 50 μm input width.

The error-bars on each point in Fig. 5-22 correspond to the standard deviation from the six measurements of the waveguides with the same *TR*. According to Fig. 5-22 we have an increase of 25.3 μm ± 2.1 μm in FWHM when we use a tapered waveguide with *TR* = 0.4 (50 μm input and 20 μm output) compared to a 20 μm input / output waveguide bend, but we also have -1.51 dB ± 0.38 dB of excess insertion loss. For a tapered bend with *TR* = 0.5 (50 μm input / 25 μm output) the values are 22.0 μm ± 1.5 μm for ΔFWHM and -0.82 dB ± 0.31 dB for ΔP when compared to a 25 μm wide waveguide bend. For *TR* = 0.6 (50 μm input / 30 μm output) we have ΔFWHM = 17.7 μm ± 2.3 μm and ΔP = -0.48 dB ± 0.17 dB when compared to a 30 μm wide waveguide bend. Finally for *TR* = 0.8 (50 μm input / 40 μm output) we have ΔFWHM = 8.1 μm ± 1.2 μm and ΔP = -0.40 dB ± 0.33 dB

when compared to a 40 μm wide waveguide bend.

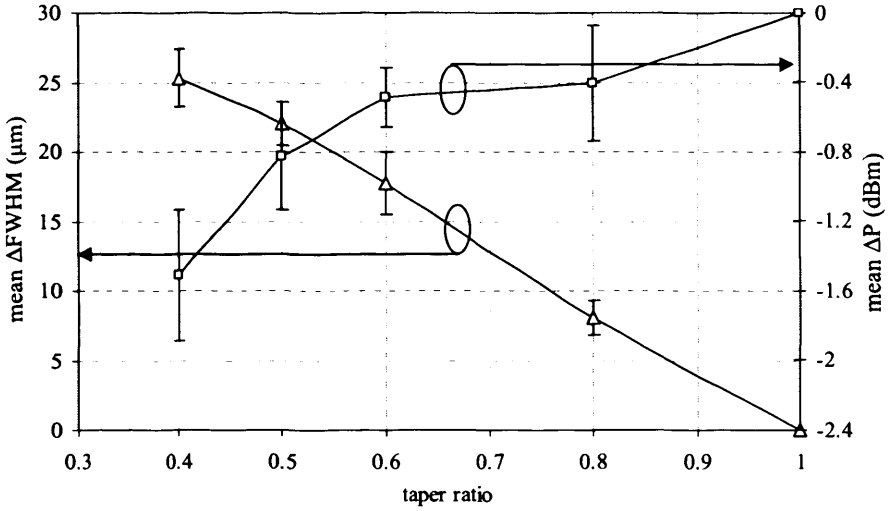

Fig. 5-22. Mean ΔFWHM and ΔP as a function of taper ratio for all tapered bends on the wafer. Error-bars shown correspond to the standard deviation from the six measurements of the waveguides with the same *TR*.

5.5. SUMMARY – CONCLUSIONS OF EXPERIMENTAL MEASUREMENS FOR TAPERED BENDS

We experimentally analyzed tapered bends with fixed input width of w_{in} = 50 μm and variable output width w_{out} = 10 μm, 20 μm, 25 μm, 30 μm and 40 μm giving corresponding taper ratios *TR* = 0.2, 0.4, 0.5, 0.6 and 0.8 and radius of curvature in the range 5 mm < *R* < 35 mm. Experiments with a multimode fibre, which is a standard way of measuring multimode optical components, revealed that for the tapered bends with *TR* > 0.5 insertion loss is always less than -2 dB compared to a 50 μm wide waveguide bend of similar radius, Fig. 5-15. This means that tapered bends can provide the very useful function of waveguide width reduction, but with some penalty loss. In addition, tapered bends always performed better than their counterpart straight tapers plus bends, Fig. 5-16 and so they should be preferred over them in a system design. By using a single mode fibre as the input source and scanning along the waveguide entrances we managed to measure how tolerant, in terms of additional insertion loss, our waveguides are under source misalignment when a tapered bend is used compared to when a waveguide bend is used, Fig. 5-19. According to Fig. 5-19, the higher the taper ratio that is used (the smaller the output width) the more we benefit in misalignment tolerance. However, as shown in

Fig. 5-20 this benefit comes at the expense of higher insertion loss and, therefore, this component's inherent trade off should be taken into account in a system design. Fig. 5-21 revealed that the radius of curvature does not significantly affect the results for the misalignment tolerance gain, ΔFWHM, and, therefore, the tapered bends with the smaller radii should be preferably used as they give the most compact components. Finally, in Fig. 5-22 we combined the measurements from all radii of curvature for each taper ratio and presented the ΔFWHM and additional insertion loss ΔP in a collective way which can be used as design rules or for comparison purposes with tapers of other kinds. According to Fig. 5-22 ΔFWHM varied from 8.1 μm to 25.3 μm and ΔP from -1.51 dB to -0.40 dB for the taper ratios under examination.

REFERENCES

[5.1] L. Vivien, X. Le Roux, S. Laval, E. Cassan, and D. Marris-Morini, "Design, realization, and characterization of 3-D taper for fibre/micro-waveguide coupling," *IEEE J. Sel. Top. Quantum Electron.*, vol. 12, pp. 1354-1358, 2006.

[5.2] T. Mizuno, T. Kitoh, M. Itoh, T. Saida, T. Shibata, Y. Hibino, "Optical spotsize converter using narrow laterally tapered waveguide for planar lightwave circuits," *J. Lightwave Technol.*, vol. 22, pp. 833-839, 2004

[5.3] S. Haxha, E. O. Ladely, M. Mjeku, F. A. Malek, and A. Rahman, "Optimization of compact lateral, vertical, and combined tapered spot-size converters by use of the beam-propagation method," *Appl. Optics*, vol. 45, pp. 288-296, 2006.

[5.4] L. Wu, F. Li, S. Tang, B. Bihari, and R. T. Chen, "Compression-molded three-dimesnional tapered polymeric waveguides for low-loss optoelectronic packaging," *IEEE Photon. Technol. Lett.*, vol. 9, pp. 1601-1603, 1997.

[5.5] K. B. Yoon, I.-K. Cho, and S.-H. Ahn, "10-Gb/s data transmission experiments over polymeric waveguides with 850-nm wavelength multimode VCSEL array," *IEEE Photon. Technol. Lett.*, vol. 16, pp. 2147-2149, 2004.

[5.6] A. W. Snyder, "Coupling of modes on a tapered dielectric cylinder," *IEEE Trans. Microwave Theory and Techniques,* vol. MTT-18, pp. 383-392, 1970.

[5.7] E. A. J. Marcatili, "Dielectric tapers with curved axes and no loss, "*IEEE J. Quantum Electron.*, vol. QE-21, pp. 307-314, 1985.

[5.8] M. L. Wu, P. L. Fan, C. T. Lee, "Completely adiabatic S-shaped bent tapers in optical waveguides," *IEEE Photon. Technol. Lett.*, vol. 9, pp. 212-214, Feb. 1997.

[5.9] A. D. Pierce, "Extension of the method of normal modes to sound propagation in an almost stratified medium," *J. Acoust. Soc. Am*, vol. 37, pp. 19-27, 1965.

[5.10] M. Heiblum and J. H. Harris, "Analysis of curved waveguides by conformal transformation, "*IEEE J. Quantum Electron.*, vol. QE-11, pp. 75-83, 1975.

[5.11] W. Berglund and A. Gopinath, "WKB analysis of bend loss in optical waveguides, "*J. Lightw. Technol.,* vol. LT-18, pp. 1161-1166, Aug. 2000.

[5.12] J. M. Arnold and L. B. Felsen, "Rays and local modes in a wedge-shaped ocean, "*J. Acoust. Soc. Am*, vol. 73, pp. 1105-1119, 1983.

[5.13] J. M. Arnold and L. B. Felsen, "Intrinsic modes in a nonseparable ocean waveguide, "*J. Acoust. Soc. Am*, vol. 76, pp. 850-860, 1984.

[5.14] J. M. Arnold and L. B. Felsen, "Ray invariants, plane wave spectra and adiabatic modes for tapered dielectric waveguides," *Radio Sci.*, vol. 19, pp. 1256-1264, 1984.

[5.15] J. M. Arnold and L. B. Felsen, "Spectral reconstruction of uniformized wave fields from nonuniform ray or adiabatic mode forms for acoustic propagation and diffraction, "*J. Acoust. Soc. Am*, vol. 87, pp. 587-600, 1990.

[5.16] J. M. Arnold and L. B. Felsen, "Local intrinsic modes: layer with nonplanar interface," *Wave Motion*, vol. 8, pp. 1-14, 1986.

[5.17] J. M. Arnold and L. B. Felsen, "Spectral reconstruction of uniformized wave fields from non uniform ray or adiabatic mode forms for acoustic propagation and diffraction," *J. Acoust. Soc. Am*, vol. 87, pp. 587-600, 1990.

[5.18] J. M. Arnold and L. B. Felsen, "Coupled mode theory of intrinsic modes in a wedge," *J. Acoust. Soc. Am*, vol. 79, pp. 31-40, 1986.

[5.19] S. Rutherford, and K. Hawker, "Consistent couple mode theory of sound propagation for a class of non-seperable problems, "*J. Acoust. Soc. Am*, vol. 70, pp. 554-564, 1982.

[5.20] C. Goyal, R. L. Gallawa, and A. K. Ghatak, "Approximate solution to the scalar wave equation for optical waveguides," *Appl. Optics*, vol. 30, pp. 2985-2989, 1991.

[5.21] L. B. Felsen and N. Marcuvitz, *Radiation and Scattering of Waves*, ser. Microwaves and Fields Series, Prentice-Hall, Inc., New Jersey, 1973, pp. 370-441.

[5.22] R. Wong, *Asymptotic Approximations of Integrals*, ser. Computer Science and Scientific Computing, Academic Press, Inc, 1989, pp. 55-60.

[5.23] M. Abramozitz and I. Stegun, "Handbook of mathematical functions and tables," Dover, New York, 1964.

[5.24] C. Goyal, R. L. Gallawa and A. K. Ghatak, "Bent planar waveguides and

whispering gallery modes: A New Method of Analysis," *J. Lightw. Technol.*, vol. LT-8, pp. 768-774, May 1990.

CHAPTER 6

RADIATION MODES, COUPLED POWER THEORY AND MODAL POWER DISTRIBUTION FOR WEAKLY GUIDING DIELECTRIC WAVEGUIDES

6.1. INTRODUCTION

The subject of this chapter is the investigation of the waveguide sidewall roughness effect on the propagation characteristics in multimode buried channel waveguides aimed at optical backplane applications. Roughness has been the subject of a number of papers in optics and photonics [6.1]-[6.25], since it is the main factor accounting for the propagation loss in single mode and multimode waveguides due to scattering. Light propagation under the influence of roughness is a particularly challenging problem, especially for multimode waveguides, as energy keeps redistributing itself among the guided modes and is radiating from the waveguide core into the cladding through coupling of the guided to radiation modes. Marcuse has stated in his famous coupled mode and couple power theories [6.1]-[6.8] that as modes propagate in a waveguide with randomly deformed sidewalls, they converge to a specific distribution, which he called the equilibrium distribution. The average power of each mode remains constant at equilibrium (although the instant power of each mode might vary) and the power distribution over the modes depends on the statistical properties of the waveguide roughness, namely its standard deviation and autocorrelation length. The distance required for equilibrium to be reached was named the equilibrium length by Marcuse. The idea of an equilibrium distribution is very important since the average propagation loss takes a constant value there, which is independent of the initial field that excited the waveguide. In contrast, not only the propagation loss and the modal power distribution both vary as modes propagate in the transition region but they also depend on the excitation source.

Until recently, the coupled mode theory had not been applied to channel waveguides directly. The main reason for this had been that analytical solutions for the channel waveguide radiation modes, which play a central role in the theory, did not exist.

Researchers have tried to deal with this problem by either considering a 2D effective index approximation of the waveguide [6.9]-[6.10] or by approximating the radiation modes with the free-space cladding modes [6.11]-[6.13]. However, both of these methods are only approximate and depending on the type of the problem, they may lead to high inaccuracies. A more precise method, was presented in late 2006 [6.14], where the actual radiation modes of a high-index contrast nanowire were presented. The waveguides examined there were single mode and of submicron dimensions and the focus was again on the propagation loss only. Of course, other methods have dealt with the subject of roughness in rectangular waveguides in the past. One popular method is the volume current method [6.15]-[6.18], which is a far-field approach treating the roughness as an equivalent current source and calculates the loss from the outgoing radiating field. Another method used is ray-tracing [6.19], where modes in the waveguide are approximated by plane waves and loss is found by calculating the scattering matrices of the plane waves on the randomly perturbed waveguide sidewalls. Finally, the Finite Time Difference Method (FTDM) [6.14] has also been used to analyze scattering loss in single mode waveguides. Although some of these methods have demonstrated good agreement with experiments they are either intended for single mode operation only (volume current method), or they are too time consuming for multimode waveguides (FDTD), or finally they can only provide information about the propagation loss (ray-tracing).

Our work here demonstrates for the first time the exact application of the coupled mode and coupled power theories to multimode buried channel waveguides. In order to achieve this, we constructed the radiation modes of a multimode rectangular waveguide in a semi-analytical way by extending the Fourier decomposition (FDM) method for bound modes developed in [6.20] and later modified in [6.21]. Upon construction of the radiation modes, the coupled power theory was applied to a 20 μm × 20 μm test multimode waveguide and the equilibrium loss, length and power distribution as a function of the standard deviation and autocorrelation length of the roughness was investigated.

This chapter has been arranged as following. Section 6.2 reviews the Fourier decomposition method (FDM) for bound modes. Section 6.3 describes our extension to the FDM algorithm, which is used to construct the radiation modes in a channel waveguide. Section 6.4 validates our method by applying it to a slab waveguide and by

comparing it to the available analytic solutions for the slab radiation modes. Section 6.5 presents some results for the calculated radiation modes in buried channel waveguides. Section 6.6 customizes the coupled mode and power theories to the buried channel waveguide environment. Section 6.7 reports the results for the equilibrium loss, length and power distribution for our test waveguide. Finally, section 6.7 concludes.

6.2. REVIEW OF FOURIER DECOMPOSITION METHOD FOR BOUND MODES

6.2.1. Non-Linear Wave Equation Transformation

In this section we briefly review the Fourier decomposition method (FDM) described in [6.21] for calculating the bound modes in rectangular waveguides. We then proceed to the extension of this method and describe how it can be modified to cover the radiation mode regime. A rectangular waveguide such as the one in Fig. 6-1 can support two types of modes according to their polarization. Modes whose dominant electric field component is mainly polarized in x, are called E_x or *TE*-type, while modes whose electric field is polarized in y, are called E_y or *TM*-type [6.26]. In the weakly waveguiding limit, the two polarizations become indistinguishable and, therefore, in the following we focus on the E_x set of modes only.

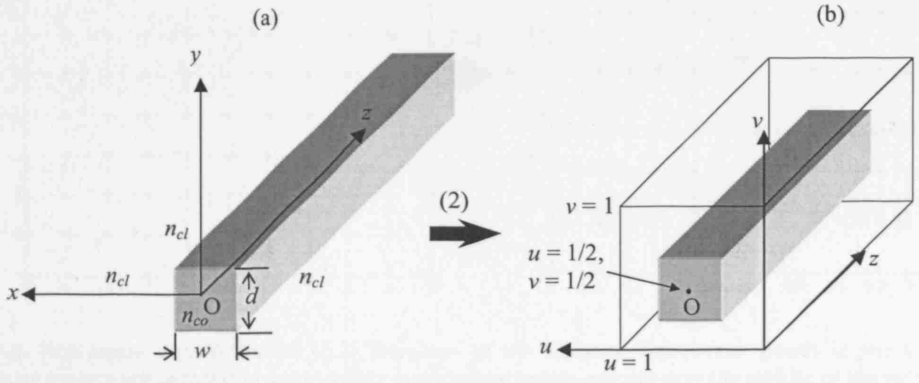

Fig. 6-1. (a) Rectangular waveguide in a Cartesian coordinate system with width w and thickness d. Cladding refractive index is n_{cl} while core refractive index is $n_{co} \cong n_{cl}$. (b) Rectangular waveguide in the transformed uv-domain. The entire xy-space is transformed to the unitary box $0 \le u \le 1$, $0 \le v \le 1$ in the uv-domain. $x = +\infty$, $y = +\infty$ are transformed to $u = 0$, $v = 0$ and $x = -\infty$, $y = -\infty$ are transformed to $u = 1$, $v = 1$. The centre of the waveguide O, is transformed from $(x,y) = (0,0)$ in the original coordinate system to $(u,v) = (1/2,1/2)$ in the new domain. z-axis is let intact from the transformation (6.2).

The dominant transverse electrical field component must satisfy the 3D scalar wave equation anywhere in space [6.26], which for a mode with propagation constant β in z, takes its usual form (time dependence omitted) in a Cartesian coordinate system

$$\left(\frac{\partial^2}{\partial x^2}+\frac{\partial^2}{\partial y^2}+k^2n^2(x,y)-\beta^2\right)E_x(x,y)=0, \tag{6.1}$$

where $k = 2\pi/\lambda$ denotes the free-space wavenumber, and λ the wavelength of operation. The refractive index distribution $n(x,y)$, Fig. 6-1 (a), equals to the refractive index of the core n_{co}, ($n(x,y) = n_{co}$), for $-w/2 \leq x \leq w/2$ and $-d/2 \leq y \leq d/2$ and equals to the refractive index of the cladding ($n(x,y) = n_{cl}$) anywhere else. FDM relies on the non-linear transformation (6.2), which maps the infinite xy-plane onto a unitary box in an alternative uv-coordinate system, Fig. 6-2.

$$\begin{aligned} x &= p\tan\left[\pi\left(u-\frac{1}{2}\right)\right], \\ y &= q\tan\left[\pi\left(v-\frac{1}{2}\right)\right]. \end{aligned} \tag{6.2}$$

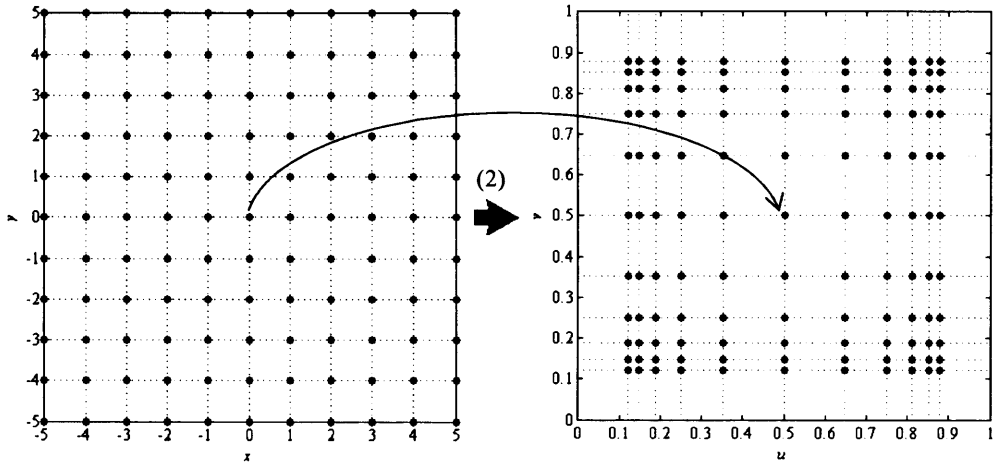

Fig. 6-2. Non-linear transformation (6.2) from xy- to uv- domain. Equidistant points in the Cartesian coordinate system are mapped to a non-linear mesh where points expand near the middle of the unitary box and compress towards its edges. $x, y \rightarrow -\infty$ maps to u, $v = 0$ correspondingly, while $x, y \rightarrow +\infty$ maps to u, $v = 1$.

As described in [6.21] p, q in (6.2) are free scaling parameters, which if chosen appropriately, can result in rapid convergence of the FDM algorithm. Upon application of (6.2) to (6.1) the transformed wave equation in the new uv-coordinate system becomes

$$\left\{\left(\frac{\partial u}{\partial x}\right)^2 \cdot \frac{\partial^2}{\partial u^2} + \frac{\partial^2 u}{\partial x^2} \cdot \frac{\partial}{\partial u} + \left(\frac{\partial v}{\partial y}\right)^2 \cdot \frac{\partial^2}{\partial v^2} + \frac{\partial^2 v}{\partial y^2} \cdot \frac{\partial}{\partial v} + k^2 n^2(u,v) - \beta^2\right\} E_x(u,v) = 0. \quad (6.3)$$

Propagating modes must satisfy the Sommerfeld radiation condition, stating that fields (as well as their transverse derivatives) should go to zero as $x \to \pm\infty$ or $y \to \pm\infty$, which in turn translates as zero field condition when $u \to 0$, 1 or $v \to 0$, 1 in the transformed domain. Solutions for E_x, can then be expressed, [6.21] (for the non cut-off modes), as a linear superposition of a set of sinusoidal functions

$$\begin{aligned} E_z(u,v) &= 4\sum_{m=1}^{M}\sum_{n=1}^{N} c_{mn} \sin(m\pi u)\sin(n\pi v) \\ &= 4\sum_{m=1}^{M}\sum_{n=1}^{N} c_{mn} S_{mn}(u,v). \end{aligned} \quad (6.4)$$

with $S_{mn}(u,v) = \sin(m\pi u)\sin(n\pi v)$. The solutions used in (6.4) physically correspond to the modes of a waveguide with unit width and thickness in the uv-domain, and metallic boundaries. Emphasis should be given to the fact that the proposed set of sinusoidal functions is complete and orthonormal in the fundamental unit square of Fig. 6-1 (b). In addition, they are periodic, with period of 2 unit lengths in u- and v-directions. Odd integer values of m and n represent fields, which have even symmetry about u =1/2 and about v = 1/2 (or about x = 0, y = 0 in the original coordinates) correspondingly, while even m and n represent fields with odd symmetry.

The orthogonality property of the basic functions is used to calculate the coefficients c_{mn}, by first substituting (6.4) in (6.3), multiplying the result with $\sin(m'\pi u)\sin(n'\pi v)$, where m', n' also integers, and integrating over $0 \le u \le 1$ and $0 \le v \le 1$ to get

$$\sum_{m=1}^{M}\sum_{n=1}^{N}\left\{\mathbf{P}_{mn}^{m'n'} + \mathbf{Q}_{mn}^{m'n'} - (\beta^2 - k^2 n_{cl}^2)\delta_{mm',nn'}\right\} \cdot c_{mn} = 0, \quad (6.5)$$

with δ, standing for the Kronecker delta function and the following definitions for the matrices involved in (6.5)

$$\mathbf{P}_{mn}^{m'n'} = \int_0^1\int_0^1 k^2(n^2(u,v) - n_{cl}^2) S_{mn}(u,v) S_{m'n'}(u,v)\,du\,dv \quad (6.6)$$

$$\mathbf{Q}_{mn}^{m'n'} = I_1 + I_2 + I_3 + I_4 \quad (6.7a)$$

$$\mathbf{I}_1 = -m^2\pi^2 \int_0^1\int_0^1 \left(\frac{\partial u}{\partial x}\right)^2 S_{mn}(u,v)S_{m'n'}(u,v)dudv \tag{6.7b}$$

$$\mathbf{I}_2 = m\pi \int_0^1\int_0^1 \frac{\partial^2 u}{\partial x^2}\frac{1}{\tan(m\pi u)} S_{mn}(u,v)S_{m'n'}(u,v)dudv \tag{6.7c}$$

$$\mathbf{I}_3 = -n^2\pi^2 \int_0^1\int_0^1 \left(\frac{\partial v}{\partial y}\right)^2 S_{mn}(u,v)S_{m'n'}(u,v)dudv \tag{6.7d}$$

$$\mathbf{I}_4 = n\pi \int_0^1\int_0^1 \frac{\partial^2 v}{\partial y^2}\frac{1}{\tan(n\pi v)} S_{mn}(u,v)S_{m'n'}(u,v)dudv \tag{6.7e}$$

Equations (6.5), (6.6), (6.7a)-(6.7e), define a matrix eigenvalue problem for the propagation constants, which lie in the region $kn_{cl} < \beta < kn_{co}$,. The real eigenvalues of (6.5), correspond to the propagation constants of the waveguide bound modes, while the magnitudes of its eigenvectors correspond to the amplitudes c_{mn}, of the Fourier expansion (6.4). The imaginary propagation constants correspond to leaky modes in the waveguide and are not of our interest.

6.2.2. Examples of bound TE-like modes

In this section, we present the bound modes of a specific waveguide calculated by the FDM method in 6.2.1. Our example waveguide, Fig. 6-1, has a square cross-section with $w = d = 20$ μm, core refractive index $n_{co} = 1.5560$, cladding index $n_{cl} = 1.5249$, and wavelength of operation $\lambda = 850$ nm. For this waveguide, the bound mode propagation constants lie in the region $11.2720\ \mu m^{-1} < \beta < 11.5019\ \mu m^{-1}$. These values represent a typical multimode waveguide such as the ones used in our optical backplane systems.

As has been mentioned in 6.2.1, bound modes in rectangular waveguides (as well as radiation modes, as we will see in the following) can have any of the following four symmetries

- *Even* symmetry along $x = 0$ and *even* symmetry along $y = 0$. These modes are simply termed Even-Even.
- *Odd* symmetry along $x = 0$, *even* symmetry along $y = 0$. These modes are termed Odd-Even.
- *Even* symmetry along $x = 0$, *odd* symmetry along $y = 0$. These modes are termed

Even-Odd.

– *Odd* symmetry along $x = 0$, *odd* symmetry along $y = 0$. These modes are termed Odd-Odd.

Particularly for square waveguides, only three out of the four sets of symmetries need to be calculated. This is because the even-odd and the odd-even modes are degenerate and so, one can transform to the other by means of a simple 90° rotation in the xy-plane.

In Fig. 6-3, we show the propagation constants calculated with the FDM method, for the three types of symmetry. For these calculations we used $M = N = 96$. The modes have been arranged starting from the one with the highest to the one with the lowest propagation constant, or in other words, from the well-guided modes to the modes, which approach cut-off. There are 47 modes of the even-even symmetry, 43 of the even-odd / odd-even symmetry and, finally, 39 modes of the odd-odd symmetry in our example waveguide. Therefore, in our waveguide we have in total $47 + 2\times43 + 39 = 172$ modes. If we take into account the two polarization states (E_x, E_y), which we have considered as being degenerated, then we have $2\times172 = 344$ modes in total in our 20 μm × 20 μm square waveguide.

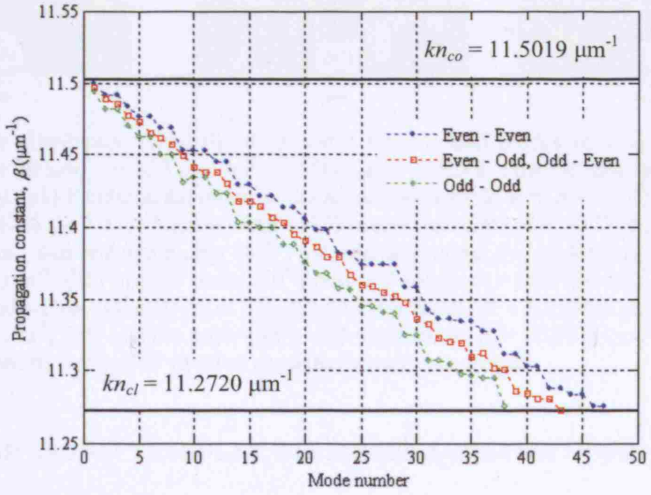

Fig. 6-3. Propagation constants in descending order for the modes of the various symmetry types in a 20 μm × 20 μm square waveguide. All propagation constants are restricted to the region $kn_{cl} < \beta < kn_{co}$.

Figure 6-4 shows some characteristic examples of bound modes for all three symmetry types.

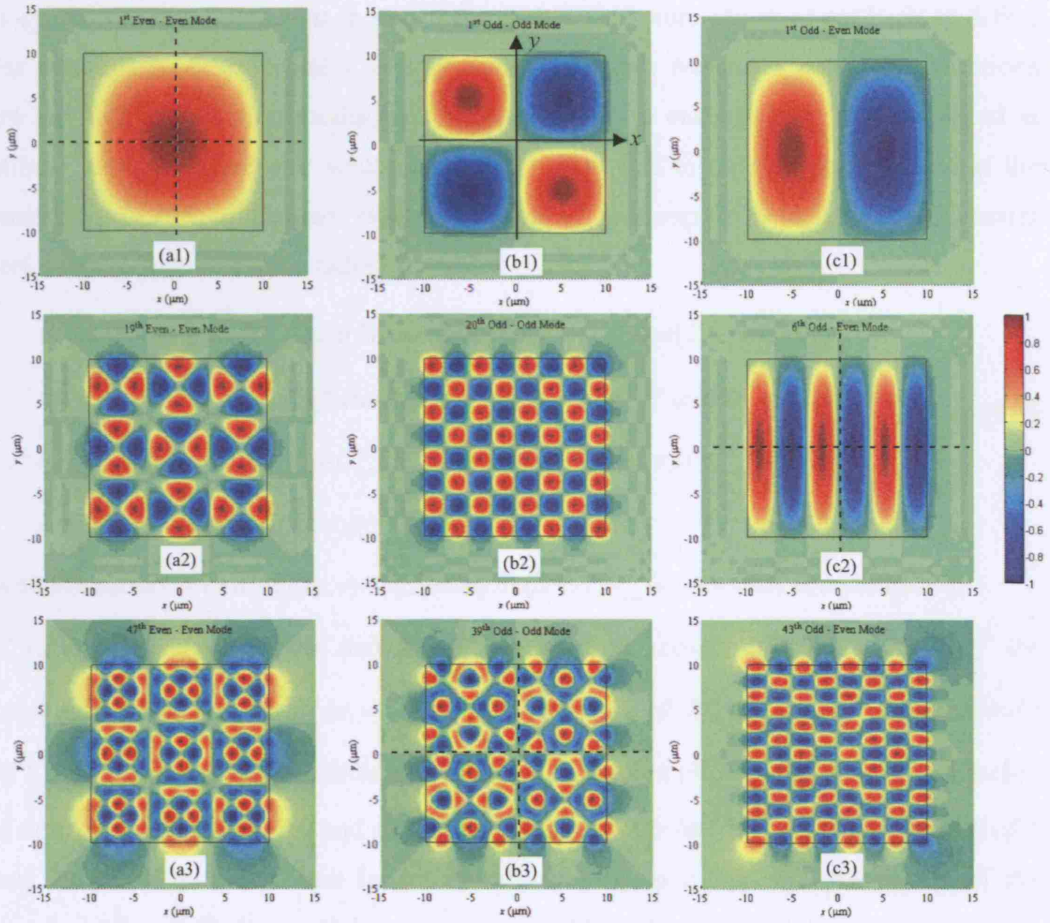

Fig. 6-4. Amplitude distribution (normalized to unity) for 9 bound modes of a square waveguide with parameters: $w = d = 20$ μm, $\lambda = 850$ nm, $n_{cl} = 1.5560$, $n_{co} = 1.5249$. First column (a1)-(a3), modes, with even-even symmetry. (a1) Fundamental mode of the square waveguide with $\beta = 11.50$ μm^{-1}, (a2) 19th even-even mode, $\beta = 11.4134$ μm^{-1}, (a3) highest order (47th) even-even mode, $\beta = 11.2760$ μm^{-1}. Second column (b1)-(b3), modes, with odd-odd symmetry. (b1) First odd-odd mode, $\beta = 11.4940$ μm^{-1}, (b2) 20th odd-odd mode, $\beta = 11.3758$ μm^{-1}, (b3) highest order (39th) odd-odd mode, $\beta = 11.2754$ μm^{-1}. Third column (c1)-(c4), modes, with odd-even symmetry. (c1) First odd-even mode, $\beta = 11.4970$ μm^{-1}, (c2) 6th odd-even mode, $\beta = 11.4655$ μm^{-1}, (c3) highest order (43rd) odd-even mode, $\beta = 11.2736$ μm^{-1}. Even – odd modes result from odd – even modes by 90° rotation about the waveguide centre.

6.3. FDM METHOD AND RECTANGULAR WAVEGUIDE RADIATION MODES

6.3.1. Radiation Mode Construction

In this section, we present our extension to the FDM method, which covers the radiation mode regime or, equivalently, the region where propagation constants satisfy the condition $0 < \beta_r < kn_{cl}$. Radiation mode construction is based on two crucial observations. Firstly, the transformation (6.2) actually leads, not to unique, but to a periodic mapping of

xy-space onto the *uv*-space as shown in Fig. 6-5. This feature serves as our basis to define our radiation modes. Secondly, neither Sommerfeld nor Neumann boundary conditions are satisfied by radiation modes, which are assumed to emerge from sources placed at infinity, and, therefore, our solutions should be allowed to take non-zero values at the boundaries of each unit square. Based on the above, we propose the following 2D Fourier series representation for the radiation modes

$$\begin{aligned} E_x^r(u,v) &= 4\sum_{m=0}^{+\infty}\sum_{n=0}^{+\infty}\left\{C_{mn}^{r,oo}\sin(2m\pi u)\sin(2n\pi v) + C_{mn}^{r,eo}\cos(2m\pi u)\sin(2n\pi v)\right. \\ &\qquad \left. + C_{mn}^{r,oe}\sin(2m\pi u)\cos(2n\pi v) + C_{mn}^{r,ee}\cos(2m\pi u)\cos(2n\pi v)\right\} \\ &= 4\sum_{m=0}^{+\infty}\sum_{n=0}^{+\infty}\left\{C_{mn}^{r,oo}S_{mn}^{oo}(u,v) + C_{mn}^{r,eo}S_{mn}^{eo}(u,v) + C_{mn}^{r,oe}S_{mn}^{oe}(u,v) + C_{mn}^{r,ee}S_{mn}^{ee}(u,v)\right\} \\ &= E_x^{r,oo}(u,v) + E_x^{r,eo}(u,v) + E_x^{r,oe}(u,v) + E_x^{r,ee}(u,v) \end{aligned} \tag{6.8}$$

with the abbreviations, $S_{mn}^{oo}(u,v)=\sin(2m\pi u)\sin(2n\pi v)$, $S_{mn}^{eo}(u,v)=\cos(2m\pi u)\sin(2n\pi v)$, $S_{mn}^{oe}(u,v)=\sin(2m\pi u)\cos(2n\pi v)$ and $S_{mn}^{ee}(u,v)=\cos(2m\pi u)\cos(2n\pi v)$ in (6.8) and $C_{mn}^{r,oo}$ the amplitude coefficient of $S_{mn}^{oo}(u,v)$, $C_{mn}^{r,eo}$ the amplitude of $S_{mn}^{eo}(u,v)$, $C_{mn}^{r,oe}$ the amplitude of $S_{mn}^{oe}(u,v)$ and $C_{mn}^{r,ee}$ the amplitude of $S_{mn}^{ee}(u,v)$. Equation (6.8) consists of a combination of orthonormal cosinusoidal and sinusoidal functions with fundamental spatial period of 1 unit length in *u*- and 1 unit length in *v*-directions, to reflect the periodicity of the transformation (6.2). Sinusoidal terms express fields with odd symmetry about planes $u = (1/2 + q)$ or about planes $v = (1/2 + q)$, $q = 0, \pm1, \pm2, \pm3 \ldots$, while cosinusoidal terms fields with even symmetry. The way these basic sinusoidal and cosinusoidal functions enter (6.8) implies that the total field is expressed as a linear combination of four fields, with each one possessing a different symmetry combination. According to the order they appear in (6.8) these symmetries are the odd-odd ($E_x^{r,oo}$), the even-odd ($E_x^{r,eo}$), the odd-even ($E_x^{r,oe}$) and the even-even ($E_x^{r,ee}$) correspondingly. These symmetries play a central role in the following, since they can be separated from each other, significantly reducing the number of calculations and matrix sizes involved. In a waveguide arrangement, which supports non-symmetrical modes, we can replace the cosine and sine terms in series (6.8) with e^{i2pu}, e^{-i2pu}, e^{i2pv}, and e^{-i2pu} terms at the cost of a fourfold increase at the number of calculations.

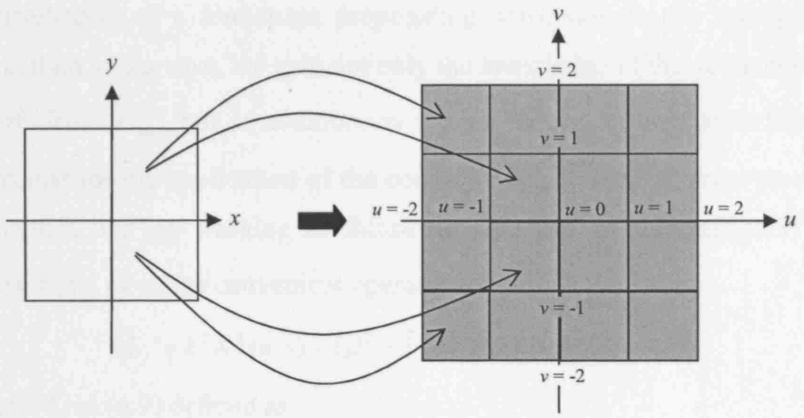

Fig. 6-5. Periodicity property of transformation (6.2). Original *xy*-domain is mapped to an infinite number of periodically arranged unitary squares in the *uv*-domain, with period 1 unit length in both *u*- and *v*-directions.

To calculate the amplitude coefficients of the radiation modes in the various symmetry combinations, we could proceed as in the bound mode case by first substituting (6.8) into the transformed wave equation (6.3), multiplying with an elementary harmonic function $S^{ij}_{m'n'}(u,v)$, $(i,j = e \text{ or } o)$, and integrating over the unitary box. If we did that, then we would reach to an equation, which would be in an equivalent form to (6.5) but with an important difference. Although (6.5) expresses an eigenvalue problem, the equation which would result from the previously described steps would not. The eigenvalue problem in (6.5) is formed exactly because the determinant of the system of linear equations (6.5) vanishes. This enables only to a discrete set of eigenvalues to satisfy it, which correspond to the propagation constants β of the bound modes. However, the determinant of the system for the radiation modes should be non-vanishing so that for the propagation constants to remain arbitrary forming a continuum as expected for radiation modes, [6.2, pp. 23]. The equation that would result from such a process would not be able to be solved for any β. Therefore, a different approach to the bound mode case has to be followed for the calculation of the radiation mode amplitude coefficients C^{ij}_{mn}.

A useful technique for calculating radiation modes in open, dissipationless, dielectric waveguides [6.14],[6.27], is by separating them into a free-space part propagating in an area filled with the cladding material only (without the presence of the waveguide), plus a

response part due to the presence of the waveguide. This in effect means that a radiation mode is a perturbation of a free-space propagating wave due to the waveguide. By applying this method to our case, we gain not only the knowledge of the yet undetermined amplitude coefficients C_{mn}^{ij}, but in addition, as we see, a way to normalize them. This latter step is crucial for the application of the coupled mode theory. In order to calculate the radiation modes, we are working as following: We first reformulate (6.3) for the radiation modes $E_x^r(u,v)$ in the convenient operator form

$$\left(L_f + k^2 N^2(u,v) - (\beta^2 - k^2 n_{cl}^2)\right) \cdot E_x^r(u,v) = 0 \tag{6.9}$$

with the operator L_f in (6.9) defined as

$$L_f = \left(\frac{\partial u}{\partial x}\right)^2 \cdot \frac{\partial^2}{\partial u^2} + \frac{\partial^2 u}{\partial x^2} \cdot \frac{\partial}{\partial u} + \left(\frac{\partial v}{\partial y}\right)^2 \cdot \frac{\partial^2}{\partial v^2} + \frac{\partial^2 v}{\partial y^2} \cdot \frac{\partial}{\partial v} + k^2 n_{cl}^2 \tag{6.10}$$

and

$$N^2(u,v) = \begin{cases} 0, & \text{in cladding} \\ n_{co}^2 - n_{cl}^2, & \text{in core} \end{cases} \tag{6.11}$$

Then we write the radiation mode field $E_x^r(u,v)$ as the combination of a free-space part $E_x^f(u,v)$ and a response part $E_x^R(u,v)$ as

$$E_x^r(u,v) = E_x^f(u,v) + E_x^R(u,v) \tag{6.12}$$

and we substitute (6.12) into (6.9) to obtain

$$\left(L_f + k^2 N^2(u,v) - (\beta^2 - k^2 n_{cl}^2)\right) \cdot E_x^R(u,v) = k^2 N^2(u,v) \cdot E_x^f(u,v) \tag{6.13}$$

Note that in order to derive (6.13) we made use of the fact that since $E_x^f(u,v)$ is a free-space field it has to satisfy the free-space wave equation

$$\left(L_f - (\beta^2 - k^2 n_{cl}^2)\right) \cdot E_x^f(u,v) = 0 \tag{6.14}$$

We next recast (6.8) to reflect the split into free-space and response components as

$$\begin{aligned} E_x^r(u,v) = & \overbrace{4 \sum_{m=0}^{+\infty} \sum_{n=0}^{+\infty} \left\{ C_{mn}^{f,oo} S_{mn}^{oo}(u,v) + C_{mn}^{f,eo} S_{mn}^{eo}(u,v) + C_{mn}^{f,oe} S_{mn}^{oe}(u,v) + C_{mn}^{f,ee} S_{mn}^{ee}(u,v) \right\}}^{E_x^f(u,v)} \\ & + \overbrace{4 \sum_{m=0}^{+\infty} \sum_{n=0}^{+\infty} \left\{ C_{mn}^{R,oo} S_{mn}^{oo}(u,v) + C_{mn}^{R,eo} S_{mn}^{eo}(u,v) + C_{mn}^{R,oe} S_{mn}^{oe}(u,v) + C_{mn}^{R,ee} S_{mn}^{ee}(u,v) \right\}}^{E_x^R(u,v)} \end{aligned} \tag{6.15}$$

and, finally, we substitute the expressions for $E_x^f(u,v)$ and $E_x^R(u,v)$ from (6.15) into

(6.13), multiply with an elementary function $S^{ij}_{m'n'}(u,v)$, (i, j = e or o), and integrate over any of the unitary boxes to get

$$\sum_{m=0}^{M}\sum_{n=0}^{N}\left\{\mathbf{P}^{ij}_{mn,m'n'}+\mathbf{Q}^{ij}_{mn,m'n'}-(\beta^2-k^2n_{cl}^2)\delta_{mm',nn'}\right\}\cdot C^{R,ij}_{mn}=\sum_{m=0}^{M}\sum_{n=0}^{N}\mathbf{P}^{ij}_{mn,m'n'}\cdot C^{f,ij}_{mn}, \tag{6.16}$$

In (6.16) we have truncated the upper limits of m and n from $+\infty$ in (6.8) to M and N. The two new upper limits though, should be large enough to ensure convergence. In addition, we have the following definitions for the matrices involved in (6.16)

$$\mathbf{P}^{ij}_{mn,m'n'}=\int_0^1\int_0^1 k^2N^2(u,v)\cdot S^{ij}_{mn}(u,v)S^{ij}_{m'n'}(u,v)dudv \tag{6.17}$$

$$\mathbf{Q}^{ij}_{mn,m'n'}=I^{ij}_1+I^{ij}_2+I^{ij}_3+I^{ij}_4 \tag{6.18}$$

$$\mathbf{I}^{ij}_1=-m^2\pi^2\int_0^1\int_0^1\left(\frac{\partial u}{\partial x}\right)^2 S^{ij}_{mn}(u,v)S^{ij}_{m'n'}(u,v)dudv \tag{6.19a}$$

$$\mathbf{I}^{ij}_2=m\pi\int_0^1\int_0^1\frac{\partial^2 u}{\partial x^2}\frac{1}{\tan(m\pi u)}S^{ij}_{mn}(u,v)S^{ij}_{m'n'}(u,v)dudv \tag{6.19b}$$

$$\mathbf{I}^{ij}_3=-n^2\pi^2\int_0^1\int_0^1\left(\frac{\partial v}{\partial y}\right)^2 S^{ij}_{mn}(u,v)S^{ij}_{m'n'}(u,v)dudv \tag{6.19c}$$

$$\mathbf{I}^{ij}_4=n\pi\int_0^1\int_0^1\frac{\partial^2 v}{\partial y^2}\frac{1}{\tan(n\pi v)}S^{ij}_{mn}(u,v)S^{ij}_{m'n'}(u,v)dudv \tag{6.19d}$$

The analytic expressions for (6.19a)-(6.19d) are too long to be presented here and so, they are shown in Appendix H.

Equation (6.16) is in the desired form. It is expressed as a system of linear equations, and it implies that the knowledge of the free-space field coefficients $C^{f,ij}_{mn}$ could provide the unknown response coefficients $C^{R,ij}_{mn}$. The radiation mode coefficients $C^{r,ij}_{mn}$ then simply follow from (6.12) and (6.15) as

$$C^{r,ij}_{mn}=C^{f,ij}_{mn}+C^{R,ij}_{mn} \tag{6.20}$$

An important feature of this method is that only one type of symmetry expressed by the indices i, j enters (6.16) at a time. Therefore, radiation modes of different sets of symmetries can be calculated separately from each other, significantly simplifying calculations.

As we see, radiation modes are, by construction, to some degree arbitrary since they

depend on the type of the free-space field used to generate them. A different selection of free-space field would result in a different set of radiation modes. The only requirement for the selected set of free-space modes is to be complete and orthonormal. Guided by our Cartesian coordinate system we choose plane waves in the original xy-domain, to represent the free-space part of the radiation modes. Each plane wave is assumed to emerge from four harmonic sources placed at infinity at planes $x = +\infty$, $x = -\infty$, $y = +\infty$, $y = -\infty$. The four sources are assumed to oscillate with equal amplitudes. If the emerging plane waves are in phase then even symmetry standing waves is achieved while anti-phase waves give odd symmetry standing waves. For example, the free-space mode with even-even symmetry (even in x- and even in y-directions) is generated from four plane waves all oscillating in-phase as

$$\begin{aligned} E_x^{f,ee}(x,y) &= 1/4(A^{ee}e^{+ik_x x}e^{+ik_y y} + A^{ee}e^{-ik_x x}e^{+ik_y y} + A^{ee}e^{+ik_x x}e^{-ik_y y} + A^{ee}e^{-ik_x x}e^{-ik_y y}) \\ &= A^{ee}\cos(k_x x)\cos(k_y y) \end{aligned} \tag{6.21a}$$

The odd-odd free-space mode is generated from four plane waves, which are in anti-phase in pairs as

$$\begin{aligned} E_x^{f,oo}(x,y) &= 1/4i(A^{oo}e^{+ik_x x}e^{+ik_y y} - A^{oo}e^{-ik_x x}e^{+ik_y y} + A^{oo}e^{+ik_x x}e^{-ik_y y} - A^{oo}e^{-ik_x x}e^{-ik_y y}) \\ &= A^{ee}\sin(k_x x)\sin(k_y y) \end{aligned} \tag{6.21b}$$

Similarly, we have for the free-space modes of the remaining symmetries

$$E_x^{f,oe}(x,y) = A^{oe}\sin(k_x x)\cos(k_y y) \tag{6.21c}$$

$$E_x^{f,oo}(x,y) = A^{oo}\sin(k_x x)\sin(k_y y) \tag{6.21d}$$

In (6.21a)-(6.21d), k_x is the wavenumber in x, and k_y the wavenumber in y, which are connected with the usual relationship

$$k_x^2 + k_y^2 + \beta_r^2 = r^2 + \beta_r^2 = k_{ncl}^2 \tag{6.22}$$

with r being the transverse wavenumber $r^2 = k_x^2 + k_y^2$ in (6.22). The propagation constant in z, is confined in the range $0 < \beta_r < kn_{cl}$, as has been mentioned at the beginning of this section for forward propagating radiation modes. If we wanted to include the propagation constants for backward propagating radiation modes then we have to extend β_r to include

the range $-kn_{cl} < \beta_r < 0$. However, for the sake of implementing the coupled mode theory, which is the goal of this chapter backward propagating modes can be ignored as is explained in section 6.6.

It is now a trivial task to transform the fields in (6.21a)-(6.21d), from the *xy*-domain to the *uv*-domain through (6.2) and then to take their Fourier transform to calculate the $C_{mn}^{f,ij}$ coefficients. The radiation mode corresponding to a specific free-space mode would then follow by solving the system of linear equations (6.16) and by adding the response and free-space parts, (6.20). Strictly speaking, the Fourier transforms of (6.21a)-(6.21d) does not exist everywhere in the *uv*-domain. For example the even-even mode $E_x^{f,ee}(x,y)$ (6.21a), takes the following form in the *uv*-domain, $E_x^{f,ee}(x,y) = A^{oo}\cos(k_x x)\cos(k_y y) = A^{oo}\cos(pk_x \tan[\pi(u-1/2)])\cos(qk_x \tan[\pi(v-1/2)]) = E_x^{f,ee}(u,v)$. Due to the tangent functions, this signal has a chirped frequency in both *u*- and *v*-directions, which steadily increases as we move from the centre, (*u*,*v*) = (1/2, 1/2), of the unitary box towards its edges *u*, *v* = 0 and *u*, *v* = 1, until it becomes infinite exactly at the boundary. This can also be seen from Fig. 6-2, if we imagine that each dot represents one peak on a harmonic function (either the sin or the cos) of any free-space mode in (6.21a)-(6.21d). In the *xy*-domain dots are dispersed at equal distances from each other representing the period of the oscillations. However, in the *uv*-domain dots approach each other as we move closer to the boundaries of the unitary box, implying that the frequency of the oscillation does not remain constant but gradually increases until eventually, it becomes infinite at the boundaries. Since an infinite number of oscillations occur within a finite interval, the signals (6.21a)-(6.21d) do not have a Fourier representation on the boundaries of the unitary box in the *uv*-domain. However, their Fourier transform is still valid anywhere else. This minor complication is not restrictive for our purposes since the radiation mode representation fails only at infinity in the original *xy*-domain. Even further, application of the coupled mode theory requires the knowledge of the fields very close to the waveguide only, with the information about the fields anywhere else being redundant. The final remark is about the physical arguments that force the frequency of the free-space oscillations to go to infinity at the boundaries of the boxes in the *uv*-domain. If the frequency of $E_x^{f,ee}(u,v)$ was not infinite at *u*, *v* = 0 and *u*, *v* = 1 then the free-space modes

(6.21a)-(6.21d) would take a well defined value there, which in turn would translate to a well defined value at $x = \pm\infty$ and $y = \pm\infty$ in the original xy-domain. However, this is not possible, as all harmonic functions in (6.21a)-(6.21d) are undefined at infinity (we do not know what the exact value of a sinewave is at infinity, for example). Therefore, the infinite frequency at the boundaries of the unitary box in the uv-domain restores the uncertainty of the harmonic function values at infinity in the xy-domain.

6.3.2. Free-Space Mode Normalization

In this section, we present the normalization of the free-space modes in (6.21a)-(6.21d). This is an important step since with the aid of the normalized free-space modes we can calculate the normalized waveguide radiation modes. In reality, radiation modes carry infinite power [6.1, pp. 313-319] and so, they cannot be normalized with the usual way of unity power flow through a plane perpendicular to the propagation axis. Instead, radiation modes are normalized by demanding a unitary impulse power flow [6.1, pp. 313-319].

The relationship between the normalization of the free-space and the waveguide radiation modes was established in [6.27]. Here we restate the main conclusion of [6.27]: If a radiation mode of an open and dissipationless waveguide is expressed as the sum of a free-space mode plus the response due to the presence of the waveguide then the normalization of the entire radiation mode follows from the normalization of the free-space part only. Therefore, if the free-space modes (6.21a)-(6.21d) are normalized then the radiation modes calculated from (6.16), (6.20) and (6.8) are automatically normalized as well.

We start by calculating all field components of the free-space modes. We follow Marcatilli's approach [6.26] for the field representation, which assumes $E_y = 0$ for the E_x polarized modes, and express all field components as a function of the transverse components as

$$H_x^f = \frac{1}{\omega^2 \mu_o \varepsilon_o n^2(x,y)} \frac{\partial^2 E_x^f}{\partial y^2} \tag{6.23}$$

$$H_y^f = -\frac{1}{\omega^2 \mu_o \varepsilon_o n^2(x,y)} \frac{\partial^2 E_x^f}{\partial x \partial y} - \frac{\beta_r}{\omega \mu_o} E_x^f \tag{6.24}$$

$$H_z^f = \frac{i}{\omega \mu_o} \frac{\partial E_x^f}{\partial y} \tag{6.25}$$

$$E_z^f = -\frac{i}{\omega\mu_o}\left(\frac{\partial H_x^f}{\partial y} + \frac{\partial H_y^f}{\partial x}\right) \tag{6.26}$$

In the previous equations, μ_o is the magnetic permeability, ε_o the vacuum dielectric constant and ω the angular frequency of light. Also, since we are discussing about free-space modes $n(x,y) = n_{cl}$ everywhere. For example, the even-even free-space radiation mode whose E_x component is given in (6.21a) have the following transverse field components

$$E_x^{f,ee} = A^{ee}\cos(k_x x)\cos(k_y y) \tag{6.27}$$

$$E_y^{f,ee} = 0 \tag{6.28}$$

$$H_x^{f,ee} = \frac{A^{ee}k_x k_y}{k^2 n_{cl}^2}\sin(k_x x)\cos(k_y y) \tag{6.29}$$

$$H_y^{f,ee} = A^{ee}\left(\frac{k_x k_y}{k^2 n_{cl}^2}\sin(k_x x)\cos(k_y y) - \frac{\beta_r}{\omega\mu_o}\cos(k_x x)\cos(k_y y)\right) \tag{6.30}$$

We note that (6.23)-(6.26) come directly from Maxwell equations and although are presented here for the free-space modes they are also valid for the bound and the radiation modes.

To calculate the power flow through a waveguide cross-section we need the Poynting vector

$$S_z = \frac{1}{2}\mathrm{Re}\left(\mathbf{E}\times\mathbf{H}^*\right)_z \tag{6.31}$$

The power flow P, through a plane perpendicular to the direction of propagation is found by substituting (6.27)-(6.30) in (6.31) to give

$$P = -\frac{1}{2}\int_{-\infty-\infty}^{+\infty+\infty} S_z\,dxdy = -\frac{1}{2}\int_{-\infty-\infty}^{+\infty+\infty} E_x H_y^*\,dxdy \tag{6.32}$$

$$P = \frac{1}{2}\left(A^{ee}\right)^2 \cdot \int_{-\infty-\infty}^{+\infty+\infty}\cos(k_x' y)\cos(k_y' y)\left(\frac{k_x k_y}{k^2 n_{cl}^2}\sin(k_x x)\cos(k_y y) - \frac{\beta_r}{\omega\mu_o}\cos(k_x x)\cos(k_y y)\right)dxdy \tag{6.33}$$

$$\begin{aligned} P &= \frac{1}{2}\frac{\beta_r\left(A^{ee}\right)^2}{\omega\mu_o}\cdot\int_{0\,0}^{+\infty+\infty}\cos\left((k_x - k_x')x\right)\cos\left((k_y - k_y')y\right)dxdy \\ &= \frac{\pi^2}{2}\frac{\beta_r\left(A^{ee}\right)^2}{\omega\mu_o}\cdot\delta\left((k_x - k_x')x\right)\delta\left((k_y - k_y')y\right) \end{aligned} \tag{6.34}$$

with the symbol δ standing for the Dirac delta (impulse) function in (6.34).

Therefore, for unitary power flow P we have from (6.34)

$$A^{ee} = \left[\frac{2}{\pi^2}\frac{\omega\varepsilon_o}{\beta_r}\right]^{1/2} \tag{6.35}$$

The normalization of the rest of the radiation modes can be proved to be exactly the same and so, $A^{ee} = A^{eo} = A^{oe} = A^{oo} = \left[\frac{2}{\pi^2}\frac{\omega\varepsilon_o}{\beta_r}\right]^{1/2}$.

6.4. METHOD VERIFICATION

In this section, we calculate the radiation modes for a slab waveguide (Fig. 6-6) with our method and directly compare the results with the existing analytical expressions [6.2, pp. 21-28] for the slab radiation modes. The example of the slab waveguide was selected because it is one of the very few waveguide geometries where analytical expressions for radiation modes exist and also its simplicity allows us to better demonstrate our method.

6.4.1. Radiation Modes of a Slab Waveguide

The slab waveguide under examination is shown in Fig. 6-6. The waveguide core extends to $-w/2 < x < w/2$ while it is infinite in y (and as a result $\partial/\partial y = 0$ for the fields). The refractive index of the core is n_{co}, while this of the cladding is n_{cl}.

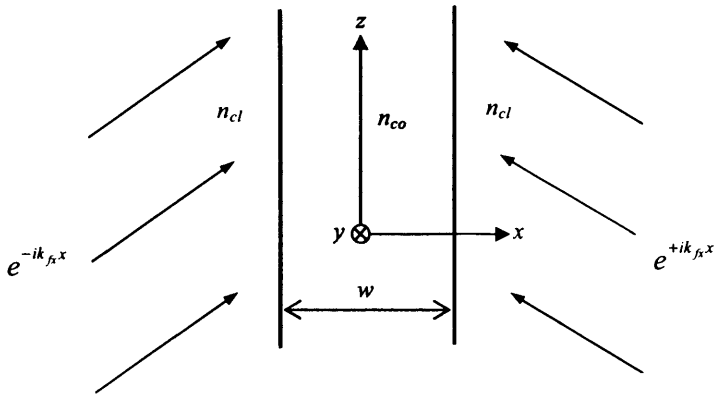

Fig. 6-6. Slab waveguide geometry used for the radiation mode calculation. Also shown, the free-space modes which are plane waves coming from sources placed at infinity. If sources at infinity oscillate in phase then free-space modes with even symmetry about $x = 0$ are generated. If sources are 180° out of phase then waves with odd symmetry are generated.

In the following we concentrate on the *TE* radiation modes of the slab waveguide, which

have the components E_x, H_x and H_z. According to [6.2, pp. 21-28] the analytic expressions for the electrical field of the radiation modes which have even symmetry about the $x = 0$ plane are

$$E_x^e = \begin{cases} \dfrac{2\omega\mu_o}{\pi\beta_r}\cos[\eta(x-w/2)+a\tan(k_x/\eta\tan(k_x w/2))], & w/2 < x < +\infty \\ \dfrac{2\omega\mu_o}{\pi\beta_r}\left[\cos^2(k_x w/2)+\dfrac{k_x^2}{\eta^2}\sin^2(k_x w/2)\right]\cos(k_x x), & -w/2 < x < w/2 \\ \dfrac{2\omega\mu_o}{\pi\beta_r}\cos[\eta(x+w/2)-a\tan(k_x/\eta\tan(k_x w/2))], & -\infty < x < -w/2 \end{cases} \tag{6.36a}$$

while, the electric field for the radiation modes with odd symmetry about the plane $x = 0$ is

$$E_x^o = \begin{cases} \dfrac{2\omega\mu_o}{\pi\beta_r}\sin[\eta(x-w/2)-a\tan(\eta/k_x\tan(k_x w/2))], & w/2 < x < +\infty \\ \dfrac{2\omega\mu_o}{\pi\beta_r}\left[\sin^2(k_x w/2)+\dfrac{k_x^2}{\eta^2}\cos^2(k_x w/2)\right]\sin(k_x x), & -w/2 < x < w/2 \\ \dfrac{2\omega\mu_o}{\pi\beta_r}\sin[\eta(x+w/2)+a\tan(\eta/k_x\tan(k_x w/2))], & -\infty < x < -w/2 \end{cases} \tag{6.36b}$$

where the propagation constant β_r is connected to the wavenumber k_x in x inside the core through the relationship, $k_x^2 + \beta_r^2 = k^2 n_{co}^2$ and to the wavenumber η in x inside the cladding through the relationship, $\eta^2 + \beta_r^2 = k^2 n_{cl}^2$. In both (6.36a) and (6.36b), radiation modes have been normalized to unitary impulse power flow (power flow, which is a delta function with unitary amplitude).

6.4.2. FDM Constructed Radiation Modes

We now proceed to construct the same radiation modes as in (6.36a) and (6.36b) but with the use of our method. Equations (6.15) – (6.19) need to be slightly modified in this case to reflect the fact that in the slab waveguide we have one dimension less involved than in the rectangular waveguide case, since $\partial/\partial y = 0$. In this case (6.15) and (6.16) become

$$E_x^{r,i}(u) = 2\sum_{m=0}^{M} C_m^{r,i} S_m^i(u) = \overbrace{2\sum_{m=0}^{M} C_m^{f,i} S_m^i(u)}^{E_x^{f,i}(u)} + \overbrace{2\sum_{m=0}^{M} C_m^{R,i} S_m^i(u)}^{E_x^{R,i}(u)}. \tag{6.37}$$

$$\sum_{m=0}^{M}\left\{\mathbf{P}_{m',m}^i + \mathbf{Q}_{m',m}^i - (\beta_r^2 - k^2 n_{cl}^2)\delta_{mm'}\right\}\cdot C_m^{R,i} = \sum_{m=0}^{M} P_{m',m}^i \cdot C_m^{f,i} \tag{6.38}$$

where, $S_m^e(u) = \cos(m\pi u), S_m^o(u) = \sin(m\pi u)$ and the matrices involved in (6.38) are also adjusted to a single dimension as

$$\mathbf{P}^i_{m',m} = \int_0^1 k^2 N^2(u) \cdot S^i_m(u) S^i_{m'}(u) du \tag{6.39}$$

$$\mathbf{Q}^i_{m',m} = \mathbf{I}^i_1 + \mathbf{I}^i_2 \tag{6.40}$$

$$\mathbf{I}^i_1 = -m^2\pi^2 \int_0^1 \left(\frac{\partial u}{\partial x}\right)^2 S^i_m(u,v) S^i_{m'}(u) du \tag{6.41a}$$

$$\mathbf{I}^i_2 = m\pi \int_0^1 \frac{\partial^2 u}{\partial x^2} \frac{1}{\tan(m\pi u)} S^i_m(u) S^i_{m'}(u) du \tag{6.41b}$$

with $N^2(u) = n_{co}^2 - n_{cl}^2$ in the core and $N^2(u) = 0$ in the cladding. We now need to define the free-space modes $E_x^{f,i}(u)$, which trigger the response field $E_x^{R,i}(u)$ in (6.38). Guided by the system geometry we select two plane waves emerging from sources placed at x = $+\infty$ and x = $-\infty$ as our free-space modes, Fig. 6-6. Such plane waves generate free-space modes with even symmetry about x = 0 if combined in phase, while they generate free-space modes with odd symmetry if they combine in anti-phase. According to the above, free-space modes are expressed as

$$E_x^{f,e} = \frac{1}{2}\left(Ae^{+ik_{fx}x} + Ae^{-ik_{fx}x}\right) = A\cos(k_{fx}x) \tag{6.42a}$$

$$E_x^{f,o} = \frac{1}{2}\left(Ae^{+ik_{fx}x} - Ae^{-ik_{fx}x}\right) = iA\sin(k_{fx}x) \tag{6.42b}$$

with k_{fx} being the free space wave vector in x, connected to the propagation constant β_r through the relationship, $k_{fx}^2 + \beta_r^2 = k^2 n_{cl}^2$. We next need to switch to the u-domain. This is achieved by using the transformation (6.2) to give

$$E_y^{f,e}(u) = 2A\cos\left(k_{fx} p \tan\left[\pi\left(u - \frac{1}{2}\right)\right]\right) \tag{6.43a}$$

$$E_y^{f,o}(u) = 2iA\sin\left(k_{fx} p \tan\left[\pi\left(u - \frac{1}{2}\right)\right]\right) \tag{6.43b}$$

At this point, we have to mention that the transformation (6.2) retains the modal symmetry. The even mode in the x-domain (6.42a) transforms to a field, which is even about u = 1/2 in the u-domain (6.43a), while the odd mode (6.42b) transforms to an odd

field about $u = 1/2$ (6.43b). In addition, as mentioned earlier the free parameter p plays an important role in helping the FDM algorithm to converge fast. We will come back to this point later when we will explore the relationship between p and the radiation modes in the transformed domain.

The next step of the algorithm is to Fourier transform (6.43a) and (6.43b) in order to derive the free-space spectrum coefficients $C_m^{f,i}$ ($i = o$ or e)

$$C_m^{f,i}(u) = \int_0^1 E_y^{f,i}(u) S_m^i(u) du, \quad m = 0,1...M \tag{6.44}$$

We then replace the known (6.39), (6.40) and (6.44) into (6.38) and we solve the resulting system of linear equations to calculate the M+1 unknown coefficients $C_m^{R,i}$. To make this step clearer we write (6.38) in its equivalent matrix form (6.45).

$$\begin{array}{c} \\ m'=0 \\ m'=1 \\ \vdots \\ m'=M \end{array}\begin{array}{c} \begin{array}{cccc} m=0 & m=1 & & m=M \end{array} \\ \underbrace{\begin{bmatrix} P^i_{0,0}+Q^i_{0,0}-(\beta^2-k^2n_{cl}^2) & P^i_{0,1}+Q^i_{0,1} & \cdots & P^i_{0,M}+Q^i_{0,M} \\ P^i_{1,0}+Q^i_{1,0} & P^i_{1,1}+Q^i_{1,1}-(\beta^2-k^2n_{cl}^2) & & P^i_{1,M}+Q^i_{1,M} \\ \vdots & & \ddots & \\ P^i_{M,0}+Q^i_{M,0} & \cdots & & P^i_{M,M}+Q^i_{M,M}-(\beta^2-k^2n_{cl}^2) \end{bmatrix}}_{A} \end{array} \cdot \underbrace{\begin{bmatrix} C_0^{R,i} \\ C_1^{R,i} \\ \vdots \\ C_M^{R,i} \end{bmatrix}}_{X} = \underbrace{\begin{bmatrix} P^i_{0,0} & P^i_{0,1} & \cdots & P^i_{0,M} \\ P^i_{1,0} & P^i_{1,1} & & P^i_{M,1} \\ \vdots & & \ddots & \\ P^i_{M,0} & \cdots & & P^i_{M,M} \end{bmatrix}}_{C} \cdot \begin{bmatrix} C_0^{f,i} \\ C_1^{f,i} \\ \vdots \\ C_M^{f,i} \end{bmatrix} \tag{6.45}$$

Equation (6.45) is in the usual form of a system of linear equations $A \cdot X = C$. The matrix A is of size (M+1)×(M+1), the size of X is (M+1) ×1 and the size of C is (M+1)×(M+1). As the index m increases from 0 to M the columns of the matrices A and C are filled while as m' increases from 0 to M the rows of A and C are filled. In the case of the 3D rectangular waveguide, the sizes of the corresponding matrices change as following. The size of matrix A becomes $(M+1)^2 \times (N+1)^2$, the size of X is $(M+1) \times (N+1)$ and finally the size of C becomes $(M+1)^2 \times (N+1)^2$. The increase to the matrix sizes is due to the additional summation, which involves the n and n' indices in (6.16). Therefore, the effect of the extra dimension is to raise the number of elements and thus the number of calculations required to the power of two.

Once we have calculated $C_m^{R,i}$ we use (6.20) to calculate the radiation mode spectrum coefficients $C_m^{r,i}$, and the inverse Fourier transform (6.37) to calculate the radiation mode in the u-domain. The last step is to use (6.2) to transform the radiation mode back to the original x-domain. All steps of the algorithm are summarized in Fig. 6-7 for the more

general rectangular waveguide case.

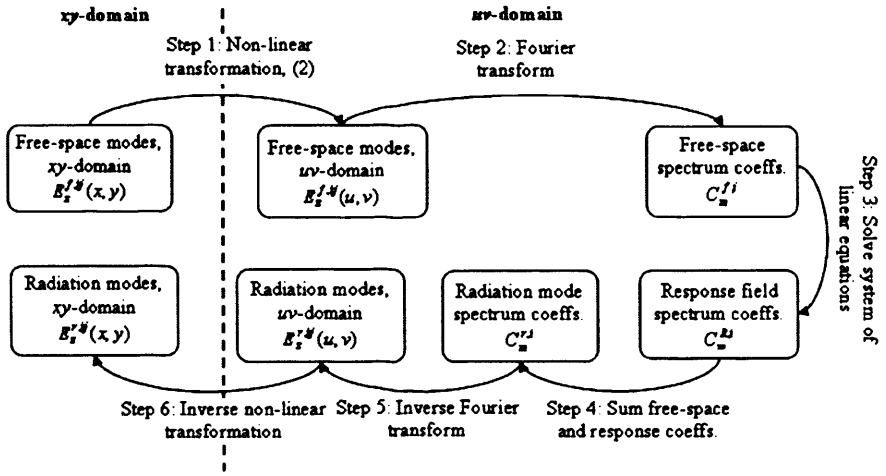

Fig. 6-7. Algorithm for the calculation of the rectangular waveguide radiation modes with the FDM method.

6.4.3. Comparison between Analytical and FDM Constructed Radiation Modes

In this section, we proceed to compare the analytical expressions for the radiation modes presented in 6.4.1, with the radiation modes constructed with the FDM method 6.4.2 for specific waveguide examples. In the process of comparing the two we highlight how to correctly select the two most important parameters associated with the FDM method, which are the scaling parameter p of the non-linear transformation (6.2), (p and q in the rectangular waveguide case), and the size M of the Fourier series (6.37) ($M \times N$ in the case of the rectangular waveguide).

In the first representative example, we examine the radiation modes of a slab waveguide with w = 10 μm, n_{co} = 1.556, n_{cl} = 1.5249 and operational wavelength λ = 0.85 μm. For this waveguide, the radiation mode propagation constants are found in the region $0 < \beta <$ 11.272 μm^{-1}. Fig. 6-8 presents the results for two cases of interest. Fig. 6-8 (a) presents the even radiation mode with propagation constant β = 10.632 μm^{-1} while Fig. 6-8 (b) the odd radiation mode with β = 11.247 μm^{-1}. The analytical radiation modes for the even and the odd case as calculated from (6.36a) and (6.36b) have been plotted with grey colour in Fig. 6-8 (a) and Fig. 6-8 (b) correspondingly. The same radiation modes calculated with the FDM algorithm have been plotted with black colour. We chose the representation to be in the u-domain rather than in the Cartesian system because the comparison is easier

due to the compression of the entire space into the unitary box. As we see, in both Fig. 6-8 (a) and Fig. 6-8 (b) FDM results agree excellent with the real results in the vicinity of the waveguide. However, as we approach $u = 0$ or $u = 1$, which correspond to $x = -\infty$ and $x = +\infty$ respectively in the original domain, the FDM mode fails to follow the high frequency oscillations of the analytic solution. Better agreement at higher frequencies could be achieved at the cost of using a larger number of Fourier harmonics, M. Fig. 6-9 shows the free-space mode, the response field and the calculated radiation mode for the two cases in Fig. 6-8 but in the x-domain this time. In Fig. 6-9 (a) we see the free-space mode, which when combined with the response field in Fig. 6-9 (b) gives the even radiation mode in Fig. 6-8 (c). Similarly in Fig. 6-9 (d) we see the free-space mode, which when combined with the response field in Fig. 6-9 (e) gives the odd radiation mode in Fig. 6-9 (f).

Next, we discuss the optimization of the parameters involved in the FDM algorithm. In order to explain our main points we use the two examples in Fig. 6-10, to help discuss the selection of the scaling parameter p in (6.2). In these two examples we investigate a slab waveguide with the following properties, $w = 20$ μm, $n_{co} = 1.556$, $n_{cl} = 1.5249$ and $\lambda = 0.85$ μm. In the first case, we examine an even radiation mode with $\beta = 11.247$ μm^{-1} and our aim is to illustrate the effect of choosing a "very small" p. In Fig. 6.10 (a) we have plotted the real radiation mode calculated from the analytical expressions (6.36a), and the FDM calculated mode for $p = 2.3$ and $M = 256$, both in the u-domain. On a second y-axis, we have plotted the Cartesian coordinate x as a function of u calculated from (6.2). As we see, in Fig. 6-10 (a), a "very small" p causes the boundaries of the waveguide to be placed very close to the boundaries of the unitary box in the u-domain. In this regime, we operate in the non-linear region of the *tan* function which relates x and u via (6.2), and, therefore, small deviations in u cause very large deviations in x ($\partial x/\partial u$ is very large). Now, the radiation mode is an oscillating signal in the x-domain. When mapped to the u-domain the peaks of the signal are well separated from each other close to $u = 1/2$ where x changes slowly with u, but close to $u = 0$ and $u = 1$ where x changes very fast with u, peaks are brought very close to each other resulting in a high frequency signal. Due to its high spatial frequencies, FDM algorithm fails to resolve the radiation mode correctly close to the waveguide boundaries for the specific M. Nevertheless, situation changes dramatically

if we choose a larger p. In Fig. 6-10 (b) we again show the analytic and FDM obtained radiation mode but for $p = 31$ this time.

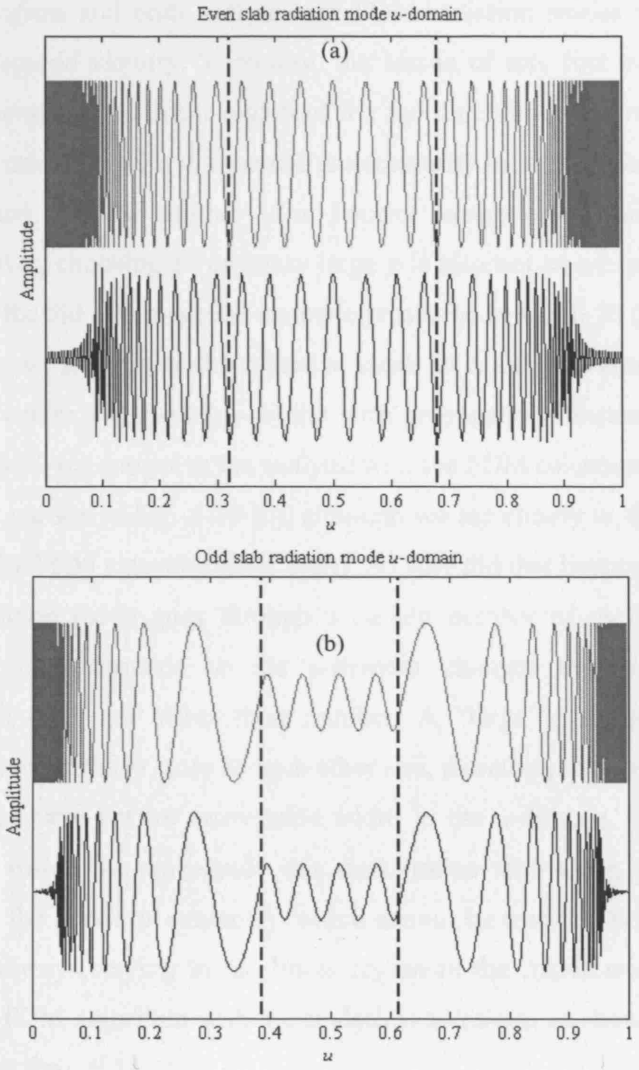

Fig. 6-8. Examples of two radiation modes in the transformed u-domain for a slab waveguide with $w = 10$ μm, $n_{co} = 1.556$ and $n_{cl} = 1.5249$ and operational wavelength $\lambda = 0.85$ μm. The radiation modes obtained with the analytical expressions (36a)-(36b) are shown with grey colour and the modes calculated with the FDM method with black colour. (a) Even radiation mode with propagation constant $\beta = 10.632$ μm^{-1}. The parameters used for the FDM calculations were $M = 256$ and $p = 30$. (b) Odd radiation mode with propagation constant $\beta = 11.247$ μm^{-1}. The parameters used for the FDM calculations were $M = 256$ and $p = 10$. Dashed lines correspond to the boundaries of the waveguide in the u-domain, which appear to be in different locations in the two examples due to the different scaling parameters used.

The number of terms in the Fourier series has remained *unchanged* at $M = 256$ as in Fig. 6-10 (a). The result of increasing p is to bring the waveguide boundaries closer to each

other and so, as seen in Fig. 6-10 (b) to operate in the linear region of the *tan* function this time. As a consequence, the waveguide boundaries have now been moved away from the high frequency regime and both analytic and FDM radiation modes agree well at least close to the waveguide vicinity. Therefore, the lesson of this first example is that we should always operate in the linear region of the *tan* function in the transformation (6.2) where x changes smoothly with u, to avoid unnecessarily increasing the frequency of the radiation mode and thus the number M of Fourier components required to describe it accurately. However, choosing an arbitrary large p is also not an adequate solution. This is explained with the aid of our second example presented in Fig. 6-10 (c) and 5-10 (d). In these two graphs, we investigate the radiation mode of a slab waveguide with the same properties as the one in Fig. 6-10 (a)-(b) but with propagation constant $\beta = 10.972\ \mu m^{-1}$ this time. Figure 5-10 (c) compares the analytic with the FDM calculated field for $p = 156$ and $M = 256$. As we see in Fig. 6-10 (c), although we are clearly in the linear region of the *tan* function the FDM algorithm fails again. So why did that happen? The explanation is that each radiation mode goes through a certain number of oscillations inside the waveguide. The transformation to the u-domain changes the frequency of these oscillations but it does not affect their number. A "large" p causes the waveguide boundaries to be brought very close to each other and, therefore, these oscillations have to squeeze within the very narrow waveguide width in the u-domain. This causes a high frequency signal inside the waveguide this time (rather than close to the unitary box boundaries, as in the previous example), which cannot be resolved with the selected M. Relaxing p (but always staying in the linear region of the transformation), gives good agreement of the FDM algorithm with the analytical solutions, as shown in Fig. 6-10 (d), for the same M but for $p = 53$.

The two examples show that the correct choice of the scaling parameter p is very important for the FDM solutions to resolve accurately the radiation modes in the waveguide regime. A good choice for p is the one, which balances the frequency components required to describe accurately the radiation modes inside the waveguide and just outside of it. With this, we mean that p should be small enough so that high frequency components inside the waveguide are avoided, but also p should be large enough for the boundaries of the waveguide to stay within the linear region of the

transformation (6.2).

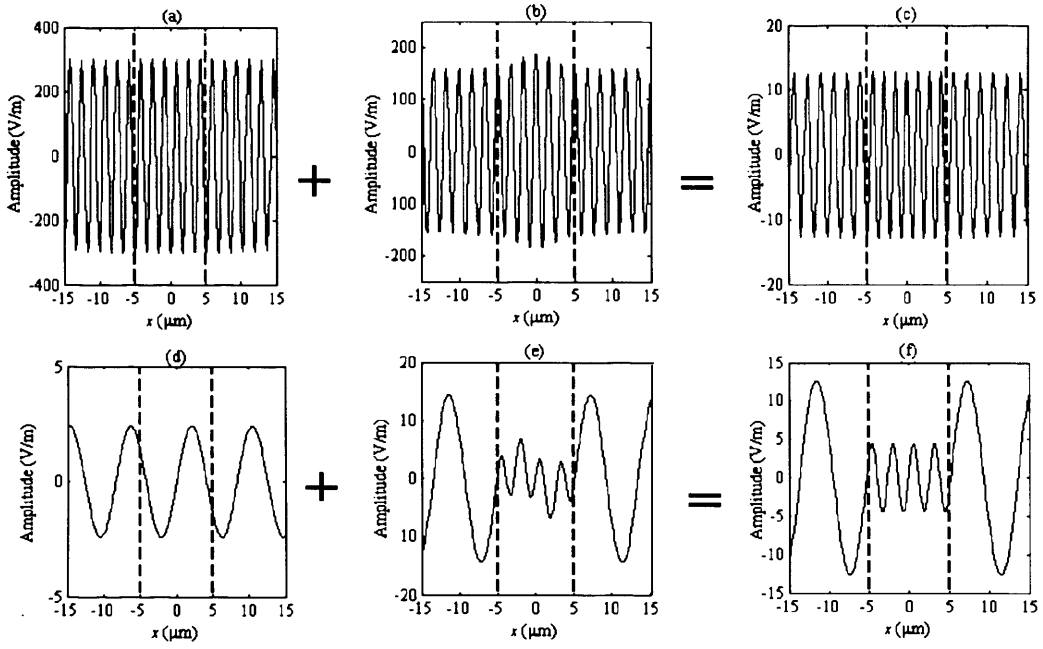

Fig. 6-9. (a) Free-space mode, (b) response field, and (c) resulting radiation mode for the even radiation mode of Fig. 6-8 (a). (d) free-space mode, (e) response field, and (f) resulting radiation mode for the odd radiation mode of Fig. 6-8 (b).

Our last remark discusses the number of frequency components M required for convergence. Not all radiation modes have the same demands for Fourier components. This can be better understood with the aid of (6.36a) and (6.36b), which give the analytic expressions for the radiation modes. Take for example the part of the even radiation modes inside the waveguide (6.36a). If we ignore the constant terms, then it is simply described by the harmonic function $\cos(k_x x)$ and so, the wavenumber k_x equals to the angular frequency of the radiation mode oscillations in the x-direction. Since k_x is related to the propagation constant as $k_x^2 = k^2 n_{co}^2 - \beta_r^2$ and the propagation constant lies in the region $0 < \beta_r < kn_{cl}$, k_x is small when $\beta_r \cong kn_{cl}$ and the radiation mode oscillates with low frequency. In this case, with a clever choice of p a small number of Fourier components M should be adequate to describe these modes. On the other hand, for propagation constants with $\beta_r << kn_{cl}$, the wavenumber k_x becomes large resulting to high frequency radiation modes. These modes require a larger M in general in order to be resolved.

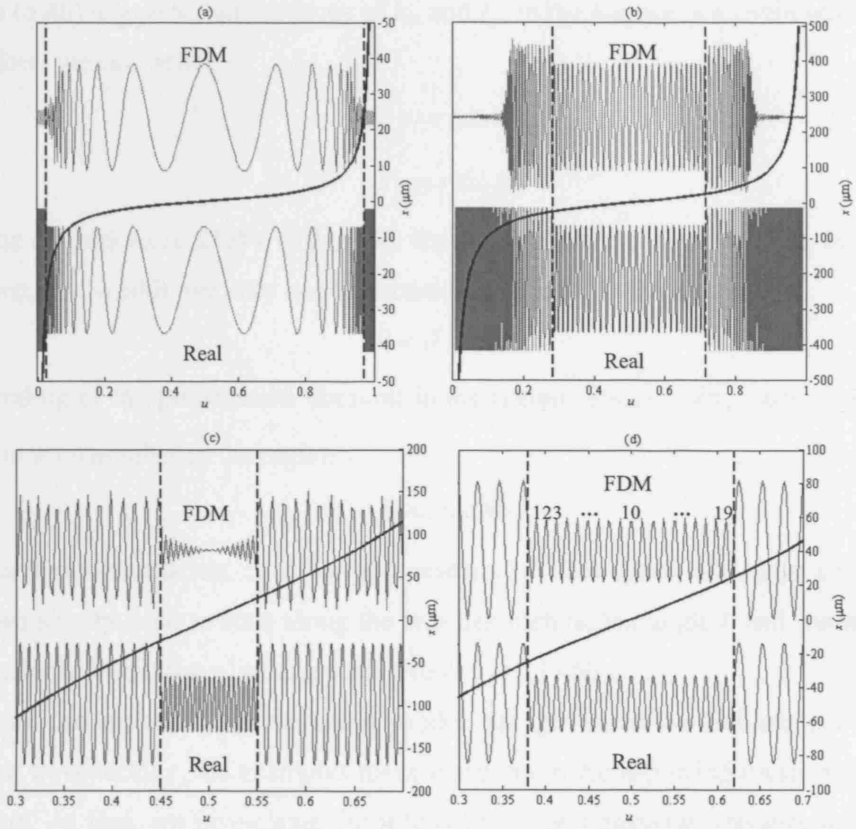

Fig. 6-10. (a) Even radiation mode in the u-domain for $\beta = 11.247\ \mu m^{-1}$. $M = 256$ and $p = 2.3$ for the FDM obtained solution which fails to resolve the rapidly oscillating part of the radiation mode close to the waveguide boundaries. (b) Same radiation mode as in (a) but with $p = 31$. In this case, FDM solution accurately converges to the analytic one inside the waveguide and close to its boundaries. (c) Even radiation mode in the u-domain for $\beta = 10.972\ \mu m^{-1}$. $M = 256$ and $p = 156$ for the FDM obtained solution which fails inside the waveguide. (d) Same radiation mode as in (c) but with $p = 53$. Again good convergence is observed inside and near the waveguide. Waveguide parameters: $w = 20\ \mu m$, $n_{co} = 1.556$, $n_{cl} = 1.5249$ and $\lambda = 0.85\ \mu m$

6.5. BURIED CHANNEL WAVEGUIDE RADIATION MODES

After validating our method for constructing radiation modes, we are now ready to proceed to the buried channel waveguide case. The cladding free-space modes that generate the radiation modes have been defined in (6.21a) – (6.21d), for the four possible types of symmetry in a buried channel waveguide. We begin by presenting a convenient formulation that simplifies the radiation mode construction. We first reproduce the definition of the transverse wavenumber r from (6.22), which relates r to the x-wavenumber k_x, and the y-wavenumber k_y

$$r^2 = k_x^2 + k_y^2 \tag{6.46}$$

Equation (6.46) suggests that the locus of k_x, and k_y, in the k-space is a circle with radius r. Therefore, we can write,

$$k_x = r\cos\theta \tag{6.47}$$

$$k_y = r\sin\theta \tag{6.48}$$

Due to the definitions (6.21a) – (6.21d) for the four symmetries (even – even, even – odd, odd – even, odd – odd), we only need to consider angles θ, in the region

$$0 < \theta < \pi/2 \tag{6.49}$$

The bounding of the propagation constant in the region, $0 < \beta_r < kn_{cl}$, also confines the transverse wavenumber in the region

$$0 < |r| < kn_{cl} \tag{6.50}$$

With this new formulation, in order to construct all free-space, and thus all radiation modes, we simply need to scan along the two parameters, the angle θ and the transverse wavenumber r, within their limiting values (6.49) and (6.50).

Since the properties of the radiation modes are governed by the angle θ and the transverse wavevector r, the examples that we present in the following focus on these two parameters. At first, we investigate the influence of the transverse wavevector r, on the buried channel waveguide radiation modes. Figure 6-11 shows the amplitude contour maps for three representative radiation modes and their free-space fields for a waveguide with physical parameters, $w = d = 5$ μm, $\lambda = 850$ nm, $n_{cl} = 1.5560$, $n_{co} = 1.5249$, $kn_{co} = 11.5019$ μm^{-1}, $kn_{cl} = 11.2720$ μm^{-1}. The three radiation modes under investigation follow the odd-odd symmetry and they all have $\theta = 45°$, that gives $k_x = k_y$ from (6.47)-(6.48). Their transverse wavenumbers are $r_1 = 0.2123$ μm^{-1} ($\beta_{r1} = 11.27$ μm^{-1}), $r_2 = 1.2720$ μm^{-1} ($\beta_{r2} = 11.20$ μm^{-1}), $r_3 = 2.4613$ μm^{-1} ($\beta_{r3} = 11$ μm^{-1}), respectively. The free-space fields of the three modes are shown in the left column of Fig. 6-11, while the radiation modes are shown in the right column. The waveguide boundary is shown as a black square in the middle of the graphs. It is understood that in the case of the free-space modes the waveguide does not actually exist, as the whole space is filled with cladding material only. The presence of the black square in this case is only for reference and for comparison with the radiation modes.

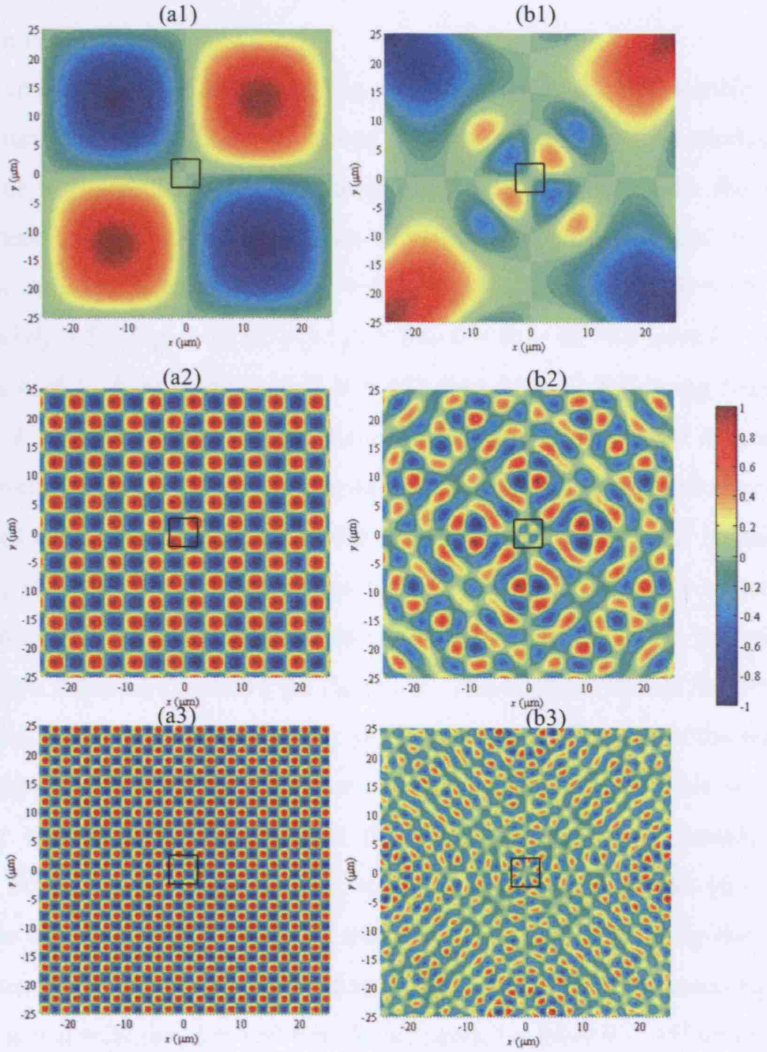

Fig. 6-11. Three representative odd – odd radiation modes for a waveguide with $w = d = 5$ μm, $\lambda = 850$ nm, $n_{cl} = 1.5560$, $n_{co} = 1.5249$, $kn_{co} = 11.5019$ μm^{-1}, $kn_{cl} = 11.2720$ μm^{-1}. (a1) Free-space field and (b1) radiation mode for $r_1 = 0.2123$ μm^{-1}. (a2) Free-space field and (b2) radiation mode for $r_2 = 1.2720$ μm^{-1}. (a3) Free-space field and (b3) radiation mode for $r_3 = 2.4613$ μm^{-1}. In all three cases, $\theta = 45°$.

The first important observation from Fig. 6-11 is that the presence of the waveguide significantly distorts the free-space fields in the vicinity of the waveguide, in all three cases. In addition, we see in Fig. 6-11 that for a certain θ, as the transverse wavenumber r increases, the spatial frequency of the radiation modes in both transverse x- and y-directions increases as well. Although evident from (6.46), this feature has important implications for the implementation of our method since higher spatial frequencies require more Fourier components, (6.28), for accurate representation and, thus, result to

longer simulation times.

The second example, which is shown in Fig. 6-12, discusses the relationship between the radiation modes and the angle θ. We chose the even – odd radiation modes for this demonstration for a waveguide with the same physical properties as in the previous example. The transverse wavenumber was set to r = 1.2720 μm^{-1} constant in this case. The angle θ, was varied to take the values θ_1 = 45° (Fig. 6-12 (a1)-(b1)), θ_2 = 15° (Fig. 6-12 (a2)-(b2)), and θ_3 = 5° (Fig. 6-12 (a3)-(b3)). When $\theta = \theta_1 = 45°$ we have $k_x = k_y$. In the rest of the cases $k_x \neq k_y$. More precisely if $\theta < 45°$ then $k_x > k_y$, following from (6.47), (6.48), while if $\theta > 45°$ then $k_x < k_y$. In the case we are examining, θ decreases and therefore the wavenumber k_x gradually increases with respect to the wavenumber k_y. As k_x increases so does the spatial frequency of the radiation mode in x, with respect to the spatial frequency in y. The implication of this feature is that for $\theta < 45°$ a larger number of Fourier components, (6.8), are required to resolve the field in x than the number of Fourier components required to resolve the field in y. The opposite occurs for $\theta > 45°$.

The last example, which is presented in Fig. 6-13, shows the influence of the waveguide core and cladding refractive index difference on the radiation modes. This is important since a number of papers have suggested that radiation modes in weakly guiding waveguides can be approximated by their corresponding free-space modes [6.11]-[6.13]. Figure 5-13 tests this assumption, which if true can significantly simplify the radiation mode calculations. Our test case this time refers to three even – even radiation modes of a waveguide with $w = d$ = 20 μm, λ = 850 nm. In all cases, we have θ = 45° and so, $k_x = k_y$ for simplicity.

The transverse wavenumber has been fixed to the constant value r = 0.7045 μm^{-1}. In order to examine the effect of the core and cladding refractive index difference, we have kept the refractive index of the cladding constant at the value n_{cl} = 1.5249, and varied the refractive index of the core between the three examples as following. In the first example, Fig. 6-13 (a1), we present the radiation mode of a waveguide with n_{co} = 1.5560 (Δn = 1.9%). This waveguide has been extensively used by our group for optical backplane applications. In the second example, Fig. 6-13 (a2) we present the radiation mode of a waveguide with n_{co} = 1.5400 (Δn = 0.9%). In the last example, Fig. 6-13 (a3) we present the radiation mode of a waveguide with n_{co} = 1.5260 (Δn = 0.07%).

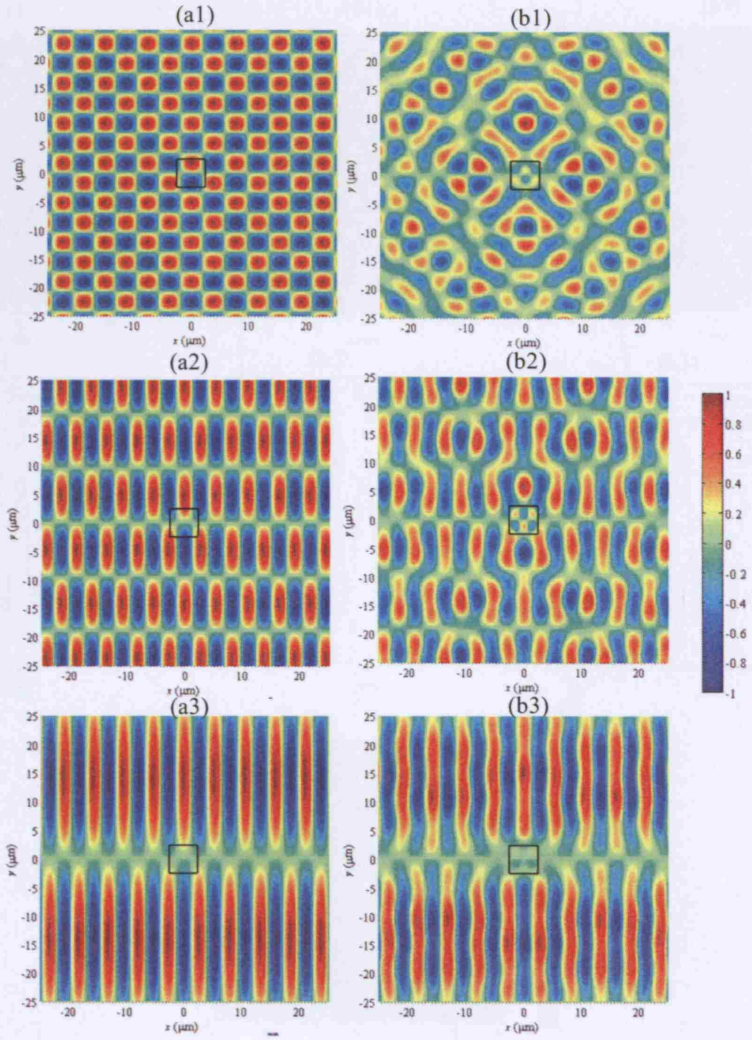

Fig. 6-12. Three representative even– odd radiation modes for a waveguide with $w = d = 5$ μm, $\lambda = 850$ nm, $n_{cl} = 1.5560$, $n_{co} = 1.5249$, $kn_{co} = 11.5019$ μm^{-1}, $kn_{cl} = 11.2720$ μm^{-1}. (a1) Free-space field and (b1) radiation mode for $\theta_1 = 45°$. (a2) Free-space field and (b2) radiation mode for $\theta_2 = 15°$. (a3) Free-space field and (b3) radiation mode for $\theta_3 = 5°$. In all three cases, $r = 1.2720$ μm^{-1}.

In addition to the amplitude contour maps of the radiation modes, we have plotted a horizontal cut of the fields at $y = 0$, in Fig. 6-13 (b1), Fig. 6-13 (b2), Fig. 6-13 (b3) for the three cases of interest respectively. In the same graphs we have also plotted with red colour the horizontal cut of the free-space mode at $y = 0$ for comparison. Note that since the cladding index remains constant, the free-space mode (Fig. 6-13 (c)) is the same in all three examples. According to our selections for n_{co}, the refractive index of the core becomes closer to this of the cladding as we move from the first example to the third.

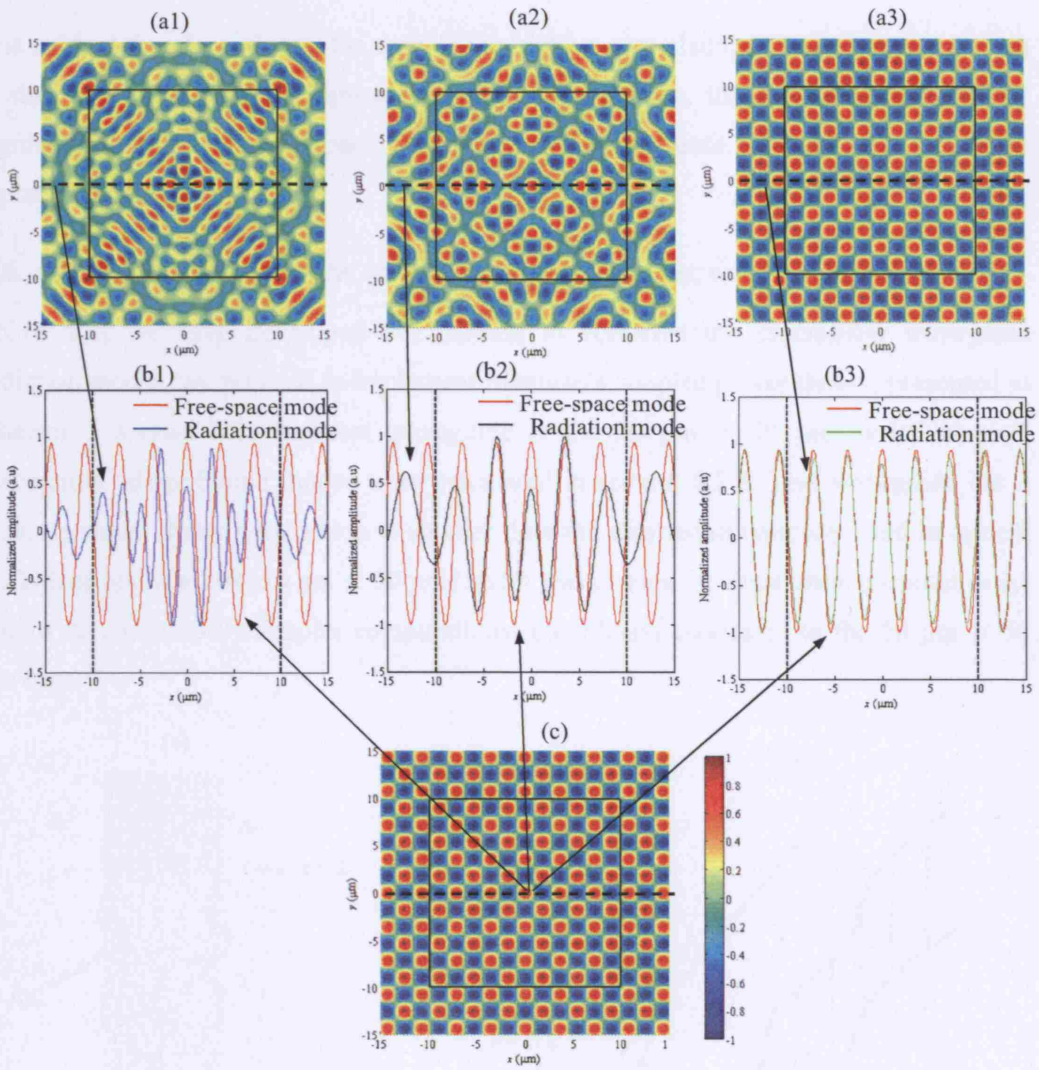

Fig. 6-13. Three representative even–even radiation modes for a waveguide with w = d = 20 μm, λ = 850 nm, n_{cl} = 1.5249, θ = 45°, and r = 0.7045 μm^{-1} with varying core refractive index. (a1), radiation mode transverse profile for n_{co} = 1.556 and (b1) radiation mode horizontal cut at x = 0 for same. (a2) Radiation mode transverse profile for n_{co} = 1.54 and (b2) radiation mode horizontal cut at x = 0 for same. (a3) Radiation mode transverse profile for n_{co} = 1.526 and (b3) radiation mode horizontal cut at x = 0 for same. (c) Free-space mode.

As we see in Fig. 6-13 (a1)-(b1), the radiation mode for the waveguide with the highest refractive index contrast departs significantly from the cladding free-space mode Fig. 6-13 (c). As the refractive index of the core approaches that of the cladding, Fig. 6-13 (a2)-(b2), the radiation mode starts looking similar to the free-space mode. Eventually, as the core index gets very close to the clad index, Fig. 6-13 (a3)-(b3), the waveguide becomes almost transparent and free-space and radiation modes become almost indistinguishable.

It is evident therefore, that in the case of the highest core-cladding index contrast, which is the most interesting for optical backplane applications, the radiation modes differ significantly from the free space modes and for an accurate analysis they cannot be replaced by them.

6.6. COUPLED MODE AND COUPLED POWER THEORY FOR RECTANGULAR WAVEGUIDES

Now that we have developed our method to construct the rectangular waveguide radiation modes, we proceed to implement Marcuse's coupled power theory, presented in Chapter 3 section 3.3. Our test waveguide is the 20 μm × 20 μm buried channel waveguide whose bound modes were calculated in section 6.2.2. This waveguide has a cross-sectional dimension, which is smaller than the dimension typically used in optical backplane applications (50 μm × 50 μm) and it was chosen for illustration purposes only, due to its significantly simpler computational complexity compared to the 50 μm × 50 μm case.

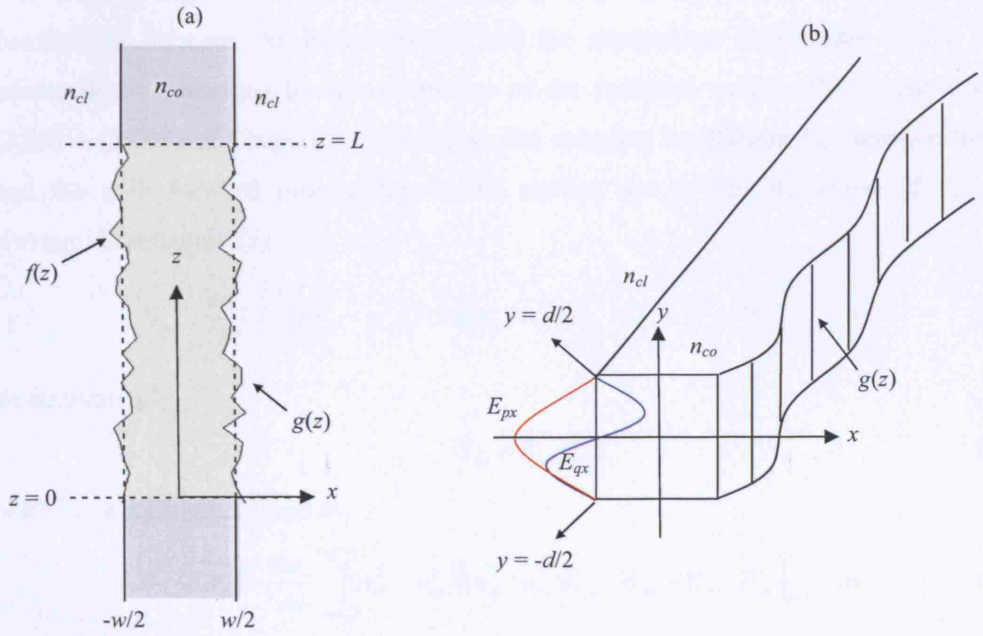

Fig. 6-14. (a) Top-view of a buried channel waveguide with sidewall roughness. The distortion function of its left sidewall is the random distribution $f(z)$, which is statistically independent from the random distortion function of its right sidewall $g(z)$. (b) Angled-view of the randomly deformed waveguide. The 1D deformation, $g(z)$, affects the width of the waveguide, while its thickness d remains constant. Also shown the E_{px} field of the even p-th mode in y and E_{qx} field of the even q-th mode in y, on the waveguide left boundary.

We remind from our theory review Chapter 3, that we consider waveguides whose sidewalls have been randomly distorted during their fabrication process, Fig. 6-14. Specifically for waveguides fabricated photolithographically, it has been observed [6.22]-[6.25] that the sidewall distortion results from the roughness of the mask due to etching, which is then replicated onto the waveguides. In this case, it is usually sufficient to assume that the roughness is one-dimensional only and that it affects the waveguide width only but not its thickness (roughness is independent of the y-coordinate in Fig. 6-14), [6.22]-[6.25]. In addition, we assume that the distortion function of the left core boundary is a stationary random process described by the function $f(z)$ and that of the right a stationary random process described by the function $g(z)$. The two processes are assumed statistically independent.

6.6.1. Coupling Coefficients between Bound Modes in Rectangular Waveguides

In order to implement the coupled power theory we need to calculate the coupling coefficients between the bound modes and the attenuation coefficients of the bound modes due to coupling to the continuum of the radiation modes. We repeat equation (3.99) – (3.101) of Chapter 3, which give the coupling coefficient S_{pq} between the p-th and the q-th forward propagating bound modes due to the distortion of the right waveguide sidewall $f(z)$

$$S_{pq} = \frac{\omega\varepsilon_o}{4i}\left\{\int_{-d/2}^{d/2}(n_{cl}^2 - n_{co}^2) f(z)\left[(n_{cl}^2/n_{co}^2)\mathbf{E}_{px}^* \cdot \mathbf{E}_{qx} + \mathbf{E}_{pz}^* \cdot \mathbf{E}_{qz}\right]_{x=w/2} dy\right\} \tag{6.51}$$

or equivalently

$$S_{pq} = T_{pq} f(z) \tag{6.52}$$

with T_{pq} a constant defined as

$$T_{pq} = \frac{\omega\varepsilon_o}{4i}\int_{-d/2}^{d/2}(n_{cl}^2 - n_{co}^2)\left[(n_{cl}^2/n_{co}^2)\mathbf{E}_{px}^* \cdot \mathbf{E}_{qx} + \mathbf{E}_{pz}^* \cdot \mathbf{E}_{qz}\right]_{x=w/2} dy \tag{6.53}$$

According to (3.166) the power coupling coefficient h_{pq}, which expresses the power exchange between the two modes is

$$h_{pq} = T_{pq}^2 \int_{-\infty}^{+\infty}\langle f(z) f(z-u)\rangle \exp\left[-i(\beta_q - \beta_p)u\right] du = T_{pq}^2 \left\langle \left|F(\beta_q - \beta_p)\right|^2 \right\rangle \tag{6.54}$$

Note that compared to (3.99)-(3.101) the y-field components have been omitted, since they are zero for the *TE*-like rectangular waveguide modes according to (6.28). Close observation of equations (6.51)-(6.53) lead us to a very important conclusion. According to (6.51)-(6.53) the coupling coefficient S_{pq} between any two bound modes (the p-th and the q-th modes for example) is proportional to the product of their electric field values taken on the waveguide boundary and then integrated in the direction of its thickness. However, if the two modes have different symmetries along the waveguide thickness, the p-th mode has even symmetry in y and the q-th mode has odd symmetry in y in Fig. 6-14 for example, then their product is an odd function whose integral along a symmetrical interval about $y = 0$ is exactly zero. According to the modal symmetries defined in section 6.2, the modes with the even – even and odd – even symmetry can only couple to the modes of the same group of symmetries (even – even and odd – even). Similarly, the waveguide modes with odd – odd and even – odd symmetry can only couple to odd – odd and even – odd modes only.

6.6.2. Attenuation Coefficients due to Coupling of Bound to Radiation Modes

Equation (6.54) through (6.53) expresses the power coupling coefficient between two bound modes. However, if one of the modes was of the radiation kind, then the same equation would still hold but this time it would describe power coupling between bound and radiation modes. The difference in that case is that the radiation modes are not normalized to unity power P, but rather to unity delta power through (6.34)-(6.35). Therefore, similarly to (6.54), if we replace the q-th bound mode with the r-th radiation mode we get for the power coupling coefficients H_{pr}, between bound and radiation modes

$$H_{pr} = T_{pr}^2 \left| F(\beta_q - \beta_r) \right|^2 \tag{6.55}$$

with the constant T_{pr} given from (6.53) by replacing q with r. According to (3.122) in Chapter 3, the attenuation coefficient a_p of the p-th guided mode due to coupling to the radiation modes is given by integrating over the propagation constants of all radiation modes as

$$2a_p = \sum_{4} \int_{-kn_{cl}}^{kn_{cl}} \left| G_{pr} \right|^2 \left| F(\beta_r - \beta_q) \right|^2 (|\beta_r| / r) d\beta_r \tag{6.56}$$

with r the transverse wavenumber of the r-th radiation mode, (6.46). The Σ symbol in

(6.56) implies summation over the four radiation modes of the four different symmetries. We note that similar arguments as in the bound-to-bound mode coupling case, suggest that bound modes of a specific symmetry group (the even – even / odd – even symmetry group for example) can lose energy due to coupling to radiation modes of the same symmetry group only (radiation modes with even – even / odd – even in this example).

6.6.3. Atomic Force Microscope Measurements of Waveguide Sidewall Roughness

We performed measurements of the sidewall nano-roughness with the aid of an atomic force microscope (AFM). A typical roughness profile is shown in Fig. 6-15 (a). Measurements of this example were taken on a 601-point linear grid extending in the propagation direction of the waveguide. The spacing between two successive points on the grid was Δz = 50 nm and so, we measured in total 30 μm of the waveguide. The results have been leveled to a zero median value. The standard deviation of the roughness was calculated in the specific case to be σ = 27.39 nm and the autocorrelation length was calculated to be L_c = 4.3529 μm.

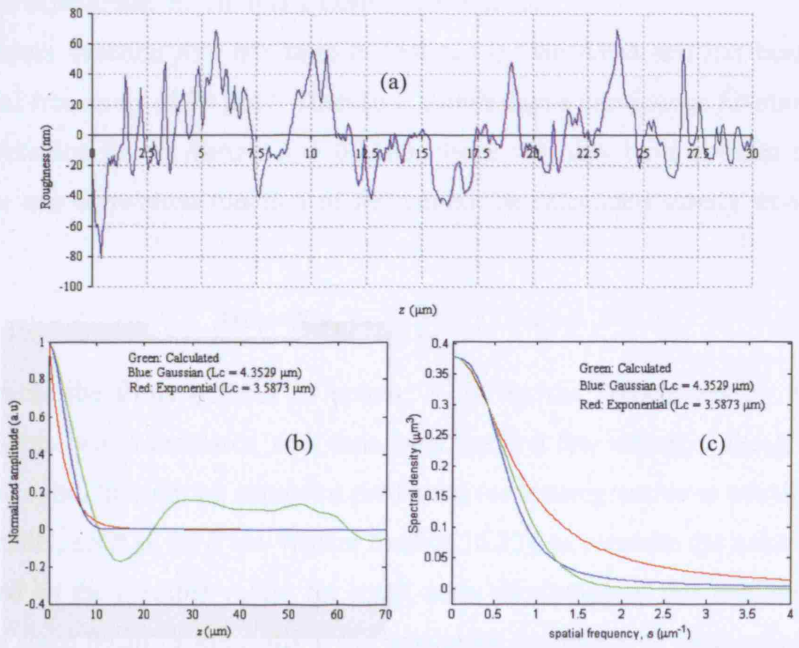

Fig. 6-15. (a) Waveguide sidewall roughness profile, $f(z)$, measured for a 30 μm sample. (b) Autocorrelation functions as calculated by the Yule-Walker autoregression method for Gaussian and exponential models. (c) Spectral density of the roughness calculated from the autocorrelation functions in (b).

As showed in the previous section, the coupling coefficients of the various waveguide modes depend on the spectral density $F(s)$, of the side wall roughness function $f(z)$, (6.54). In order to calculate the spectral density $F(s)$, we make use of the fact that $f(z)$ is considered a stationary random process. Since spectral density and autocorrelation functions are just Fourier transform pairs, we only need to work out the autocorrelation function of the measured profile in Fig. 6.15 (a). Two statistical models, the Gaussian (6.57) and the exponential (6.58), [6.2], have been, in general, considered to model the autocorrelation function, $R(u)$, and the spectral density, $F(s)$, of undeterministic functions:

$$R(u) = \sigma^2 \exp\left(-\frac{u^2}{L_c^2}\right) \xleftrightarrow{FT} \sqrt{\pi}\sigma^2 L_c \exp\left(-\frac{s^2 L_c^2}{4}\right) = F(s) \tag{6.57}$$

$$R(u) = \sigma^2 \exp\left(-\frac{|u|}{L_c}\right) \xleftrightarrow{FT} \sigma^2 \frac{2L_c^2}{1+s^2 L_c^2} = F(s) \tag{6.58}$$

where σ, corresponds to the standard deviation of the roughness and L_c, to its autocorrelation length in (6.57)-(6.58). From the above equations, we see that the spectral density of a Gaussian function is another Gaussian function (6.57), while the spectral density of an exponential function is a Lorentzian function.

The roughness function $f(z)$, has been discretized by the AFM and has been sampled with a spatial frequency of 20 μm^{-1}. Therefore, rather than a continuous function we have a discrete function $f(z) = f(n\Delta z)$, n = 0...600. Since we only have a finite number of samples, the autocorrelation function of $f(z)$ cannot be calculated simply from its usual formula

$$R(u) = R(u_k) = \frac{1}{N}\sum_{n=0}^{N} f_n f_k, \quad k = 0..N \tag{6.59}$$

This is because the finite number of points, N, forces the autocorrelation function to degrade artificially as k increases, and, thus, only the first few values of $R(u_k)$, calculated by (6.59) are valid. Instead, we can use a predicting (or autoregressive as usually found in statistics) model, such as the Yule-Walker method [6.23], to estimate the values $R(u_k)$ for large k based on the credible values for small ones. According to this method, which is presented in some detail in Appendix I, the roughness function f_n at some point n (with n large), is calculated to be an average of its past Q-values with the addition of a white noise distortion e_n as

$$f_n = -\sum_{q=0}^{Q} \varphi_q f_{n-q} + e_n \tag{6.60}$$

The spectral density of the roughness signal $f(z)$, can then be expressed as

$$F(s) = \frac{\sigma_\varepsilon^2 \Delta z}{2\pi} \left| \sum_{q=0}^{Q} \varphi_q e^{-isq\Delta z} \right|^{-2} \tag{6.61}$$

with, φ_q the autoregression coefficients and σ_ε, the standard deviation of the white noise, which can be obtained from the following expressions

$$\sum_{q=0}^{Q} \varphi_q f_{n-q} = -f_n \tag{6.62}$$

$$\sum_{q=0}^{Q} \varphi_q f_q = \sigma_\varepsilon^2 \tag{6.63}$$

The steps of the Yule-Walker method are the following. Firstly, the system of equations (6.62) is solved for the unknown φ_q for a small initial Q. Secondly, the standard deviation of the white noise term σ_ε is calculated from (6.63). Finally, (6.61) is used to calculate the desired spectral density. The process is then repeated for increasing Q, until the spectral density converges. The spectral density function calculated by this method is shown in Fig. 6.15 (c) with green colour. In the same graph, we also show a Gaussian fit (blue line) and an exponential fit (red line). It is evident that for the specific case exponential statistics are more valid. The autocorrelation length of the roughness function $f(z)$, found from the exponential fit is L_c = 4.36 μm. For other samples we have calculated autocorrelation functions, which vary approximately in the range 2 μm < L_c < 8 μm. The standard deviation σ, for these samples was found to vary within the range 9 nm < σ < 74 nm.

6.7. Application of the Coupled Power Theory to a Square Cross-Section Waveguide

In this section we apply the coupled power theory described in section 6.6 to a multimode buried channel waveguide, Fig. 6-1, with parameters $w = d$ = 20 μm, λ = 850 nm, n_{cl} = 1.5560, n_{co} = 1.5249. The aim of the section is to calculate the power distribution of the modes at equilibrium, to calculate the steady state propagation loss and finally to estimate the distance needed for the equilibrium to be reached. Based on the evidence from our AFM measurements, Fig. 6.15, we are examining a waveguide with a

random deformation whose standard deviation varies in the range 10 nm < σ < 100 nm and has autocorrelation lengths that vary in the range 4 μm < L_c < 10 μm. The bound modes of the waveguide under examination have been calculated with the aid of the FDM method of section 6.3. The radiation modes have been calculated with the new method described in this thesis, section 6.4.

6.7.1. Segmentation of Radiation Modes

The attenuation of any guided mode is calculated by integration along the continuum of the radiation mode propagation constants, (6.56). However, since our method is semi-analytical a direct calculation of this integral cannot be performed. In contrast, the radiation mode spectrum has to be segmented and all integrations involved have to be performed numerically. The segmentation should be fine enough to guarantee convergence without jeopardizing the accuracy of the calculations, but also not too fine, which could lead to impractical simulation times. As has been explained in detail in section 6.5, the radiation modes are constructed by two parameters, the angle θ, which lies in the range $0 < \theta < \pi/2$, (6.49), and the transverse wavenumber r, which lies in the range $0 < r < kn_{cl}$, (6.50). In order to construct all free-space, and thus all radiation modes, we simply need to scan along the two parameters, the angle θ and the transverse wavenumber r, within their limiting values. In reality, for the transverse wavenumber r case we do not need to calculate the free-space modes across the whole region defined in (6.50), but we can rather confine our calculations in the vicinity of kn_{cl}. This is because the power coupling coefficients between bound and radiation modes, (6.55), are proportional to the spectral density function of the waveguide roughness, (6.57)-(6.58). However, irrespectively of the nature of the statistics applicable (Gaussian (6.57) or exponential (6.58)), the spectral density decreases rapidly as the radiation mode propagation constant, β_r, increases. If we assume the propagation constant of the last guided mode (closer to cut-off) in the waveguide to be $\beta_q \cong kn_{cl}$, and, we assume that there are no contributions to the power coupling coefficients (6.55), when the spectral density function has dropped by more than 0.001 from its maximum value, then for Gaussian statistics we find from (6.57) an upper limit, r_{lim}, for β_r and r

$$r_{\text{lim}} = r_{\text{lim}}(L_c) = \sqrt{-4\log(0.001)/L_c^2} = 5.356/L_c \tag{6.64}$$

We can therefore assume that β_r and r are now confined within the new regions

$$0 < \beta_r < r_{\text{lim}}, \qquad kn_{cl} - r_{\text{lim}} < r < kn_{cl} \tag{6.65}$$

The two free-space mode parameters θ and r, are finally segmented in M and N discrete steps respectively, Fig. 6-16 (a) as

$$\theta = m\Delta\theta,\ m\ =\ 0,...,M, \Delta\theta = \pi / 2M \tag{6.66}$$

$$r = kn_{cl} - \text{n}\Delta r,\ n\ =\ 0,...,N, \Delta r = r_{\text{lim}} / N \tag{6.67}$$

After initial tests carried out we chose M = 18 giving $\Delta\theta = 5^o$. Based on the AFM measurements presented in Fig. 6-15, for L_c = 4 μm we have r_{lim} = 1.32 μm^{-1}. Based on our tests we chose N = 40 giving $\Delta r = 0.033$. Our tests aimed at converging of the coupling and attenuation coefficients to two decimal points. With these values, a total of 2880 radiation modes were generated.

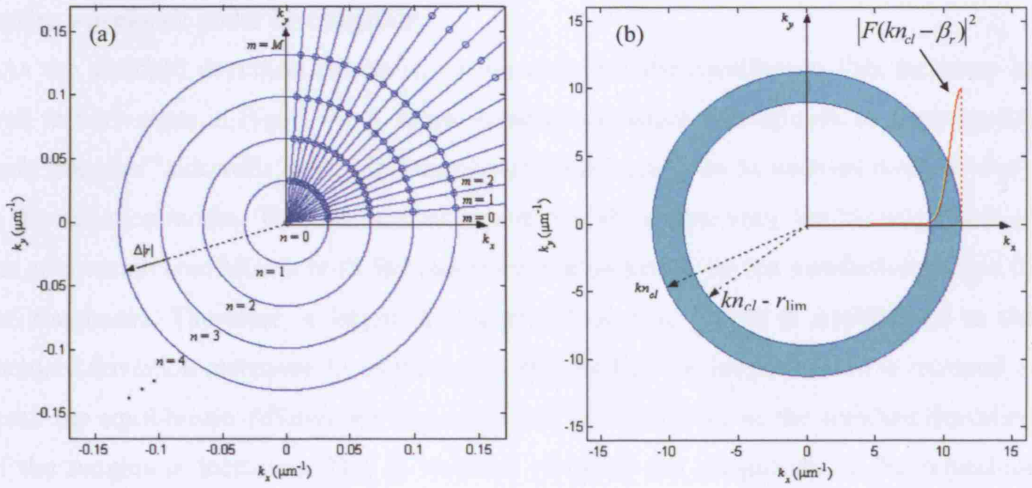

Fig. 6-16. (a) Constellation diagram of k_x and k_y wavenumbers used to discretize the free-space mode spectrum. (b) Although $0 < r < kn_{cl}$, in reality the thin annulus with $kn_{cl} - r_{\text{lim}} < r < kn_{cl}$ is sufficient for the bound-to-radiation coupling and attenuation coefficient calculation.

6.7.2. Modal Equilibrium for 20 μm × 20 μm Multimode Waveguides

We now apply Marcuse's coupled power theory to examine propagation in our test 20 μm × 20 μm waveguide. Firstly, we examine the effect of the roughness standard deviation on the equilibrium loss and equilibrium length. This is shown in Fig. 6-17 for a waveguide whose roughness autocorrelation length has been fixed to L_c = 4 μm and its standard deviation was varied in the range 10 nm < S_d < 100 nm. As has been mentioned

in section 6.6.1, one major difference between a rectangular cross-section waveguide and a slab or an optical fibre is that in the case of the rectangular waveguide, not all modes are coupled to each other. The even-even and odd-even modes (bound or radiation) can couple only to each other. Similarly, the odd-odd and even-odd modes can also couple only to each other. Coupling between any of the modes of the even-even / odd-even modal ensemble with any of the modes of the odd-odd / even-odd modal ensemble and vice versa cannot occur. Therefore, our theory predicts that there are going to be two independent and uncorrelated distributions at equilibrium, one for each set of symmetries. The equilibrium loss and length for the even-even and odd-even ensemble are shown with open circles in Fig. 6-17, while the same for the odd-odd, even-odd ensemble are shown with open rectangles. For comparison purposes, we also show the equilibrium loss and length for a slab waveguide with the same physical parameters (w, n_{cl}, n_{co}, S_d, L_c) as the square waveguide under investigation.

As the standard deviation increases, we observe that the equilibrium loss increases as well in both cases in Fig. 6-17. A larger standard deviation corresponds to a waveguide with "rougher" sidewalls, which in turn causes bound modes to be coupled more strongly to the radiation modes. This can be readily understood by observing that the magnitude of the attenuation coefficients in (6.56) increases proportionally to the standard deviation of the roughness. Therefore, a larger propagation loss is expected at equilibrium as the standard deviation increases. In addition, we observe that the length, which is required to reach the equilibrium, follows the opposite trend and decreases as the standard deviation of the roughness increases. This is because, not only the magnitude of the bound-to-radiation coupling coefficients increase, but also the magnitude of the bound-to-bound coupling coefficients increase. As bound modes are coupled more strongly to each other, they exchange energy at faster rates and equilibrium is reached in shorter lengths. Compared to the square waveguide, a slab waveguide with similar properties has higher steady state loss and shorter equilibrium loss. However, the results for the slab waveguide are of the same order of magnitude as those of the square waveguide. Therefore, a slab waveguide can be used in cases were a fast but relatively inaccurate approximation for the propagation loss and length is required. The steady state loss for the even-even, odd-even ensemble appears to be slightly higher than that of the odd-odd and even-odd ensemble. It

is not yet clear why this occurs.

As a particular example, a waveguide with L_c = 4 μm and S_d = 30 nm, has a steady state loss for the even-even, odd-even modes of a_{eeoe} = 0.0069 dB/cm and equilibrium length L_{eeoe} = 10.3 m. The odd-odd and even-odd modes have a steady state loss of a_{ooeo} = 0.0062 dB/cm, and equilibrium length L_{ooeo} = 18 m. The calculations for the slab waveguide showed a steady state loss of 0.0138 dB/cm and equilibrium length of 3.14 m. These calculations show that for the 20 μm × 20 μm waveguide the equilibrium is never reached for typical backplane distances (< 1m).

The next set of calculation we performed had the objective to study the effect of the autocorrelation length of the roughness. For this purpose we set the standard deviation to S_d = 25 nm and varied the autocorrelation length in the range, 3 μm < L_c < 10 μm, Fig. 6-18. As seen in Fig. 6-18, the steady state loss follows a descending trend as the autocorrelation length increases while the opposite trend is followed by the equilibrium length, which increases. The explanation for the above trends is similar to the previous case. Without loss of generality, assume that we are considering Gaussian statistics for the roughness function (6.57). The key observation this time is that the autocorrelation length enters the formulas for the bound-to-bound (6.54) and the bound-to-radiation coupling coefficients (6.55), as the coefficient in the exponent of the spectral density (6.57). Since the magnitude of coupling between any two modes is proportional to the value of the spectral density function taken at the difference between the propagation constants of the two modes under examination, a shorter autocorrelation length results in a broader Gaussian function (a Gaussian function whose value drops slower), and therefore to stronger coupling. Proportionally, longer autocorrelation lengths results in narrower Gaussian functions and weaker coupling between modes. Similar arguments were used when calculating the integration limit for the transverse wavenumber r, Fig. 6-16 (b). Shorter autocorrelation lengths mean that the r_{lim}, defined in (6.64), becomes larger and, therefore, the area of the disk in Fig. 6-16 (b) that determines which radiation modes contribute to the loss mechanism, increases as well. Since more radiation modes participate in the loss process and with stronger magnitudes the equilibrium loss increases.

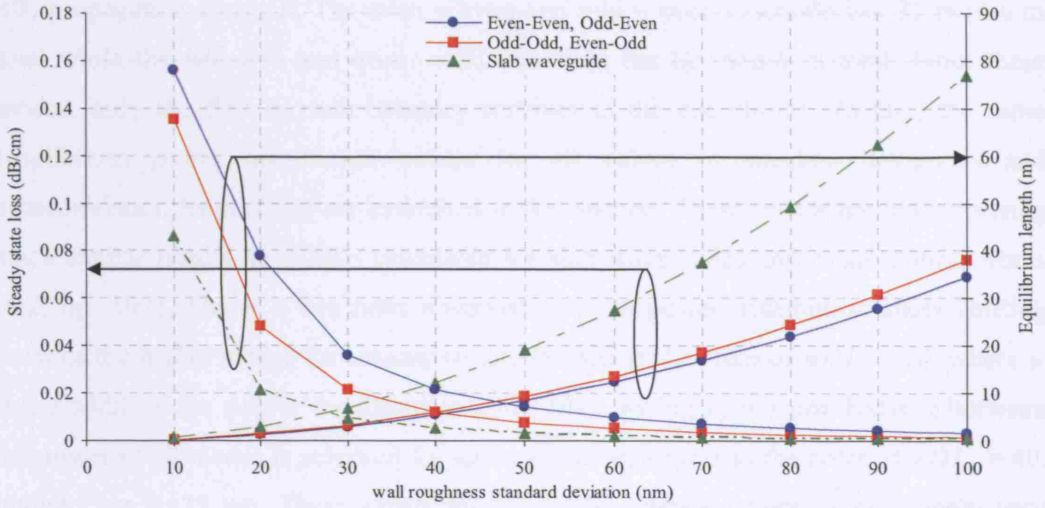

Fig. 6-17. Steady state loss and equilibrium length as a function of the sidewall roughness standard deviation for L_c = 4 μm. The results for a slab waveguide with same parameters as the square channel waveguide are also shown for comparison.

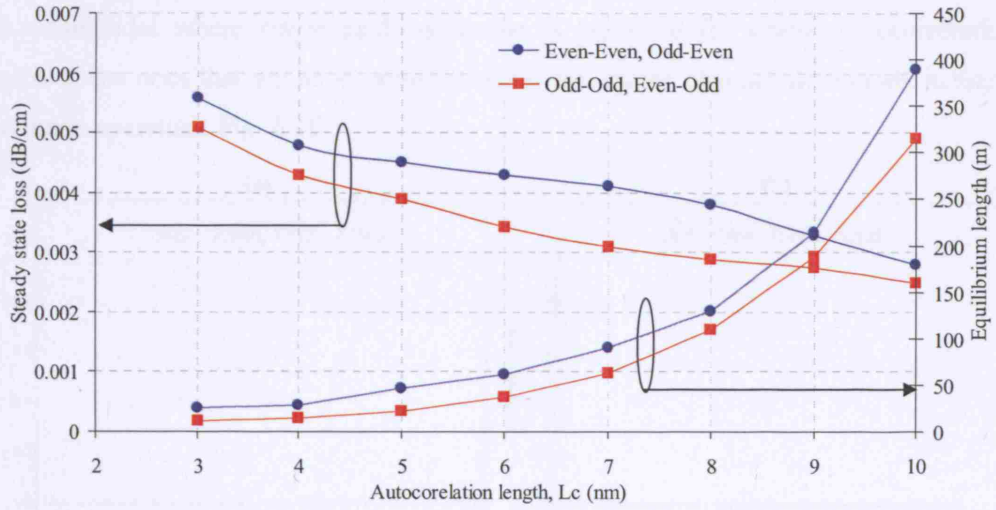

Fig. 6-18. Steady state loss and equilibrium length as a function of the roughness autocorrelation length for S_d = 25 μm.

The final property that we investigate is the distribution of power between the guided modes at equilibrium. This is shown in Fig. 6-19 for the special case of σ = 25 nm, L_c = 4 μm. In Fig. 6-19, we present the normalized power distribution as a function of the mode number for the two sets of symmetries. The modes have been arranged according to their propagation constant in descending order. The first mode corresponds to the one with the

highest propagation constant while the last mode to the one with the lowest (closer to cut-off) propagation constant. The even – even and odd – even ensemble has 91 modes in total while the odd–odd and even - odd ensemble has 82 modes in total. From these modes, only the first in each category survives at the equilibrium. In fact, the same equilibrium power distribution occurs for all values of standard deviations and autocorrelation lengths that are examined in this section. These results are not surprising since similar results have been calculated for slab waveguides and round optical fibres [6.2, pp. 197]. There, it has been observed that the power distribution starts shifting towards the higher modes for autocorrelation lengths in the order of $w/2L_c = 10$, where w is the width of the slab or the diameter of the fibre, giving $L_c = 1$ μm. Balance between the power of all modes is achieved for autocorrelation lengths in the order of $w/2L_c = 40$, giving $L_c = 0.125$ μm. These values for the autocorrelation lengths, which imply very random sidewall roughness, are not in the range of the autocorrelation lengths that we have measured. At this point, we need to emphasize that in contrast to the fibres and the slab waveguides where single mode operation is predicted for similar autocorrelation lengths to the ones that we have examined here, the square channel waveguide exhibits *dual* mode operation, Fig. 6-19.

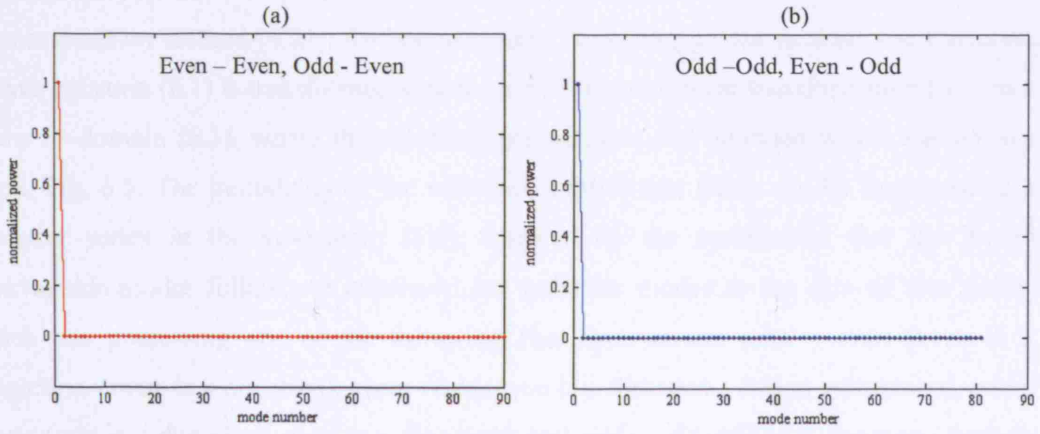

Fig. 6-19. Power distribution among the bound modes at equilibrium for a 20 μm × 20 μm square waveguide having a sidewall roughness with statistical parameters, $S_d = 25$ nm, $L_c = 4$ μm. (a) Even - even, even – odd mode ensemble. (b) Odd - odd, even – odd mode ensemble.

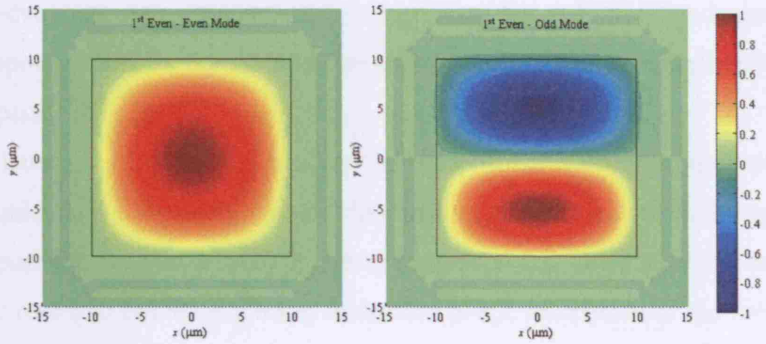

Fig. 6-20. Amplitude distribution (normalized to unity) of the two bound modes that survive at the modal equilibrium for a 20 μm × 20 μm square waveguide having a sidewall roughness with statistical parameters, S_d = 25 nm, L_c = 4 μm. (a) The first even – even mode, which is also the waveguide fundamental mode, with β = 11.50 μm^{-1} is the only one to survive from the even - even, odd – even mode ensemble. (b) The first even – odd mode, with β = 11.4970 μm^{-1} is the only one to survive from the odd - odd, even – odd mode ensemble.

6.8. SUMMARY – CONCLUSIONS

The subject of this chapter has been the investigation of modal propagation in buried channel waveguides under the influence of the randomly deformed waveguide sidewalls. Throughout this chapter, we have concentrated our efforts on two main elements. Firstly, we developed a novel method to calculate the radiation modes in buried channel waveguides, Section 6.3, which extended an existing method based on the Fourier decomposition method [6.21], for bound modes. According to our method, the Cartesian wave equation (6.1) is transformed with the aid of the non-linear transformation (6.2) to a new *uv*-domain (6.3), where the solutions are periodic and bounded within the unitary box, Fig. 6.5. The periodicity of the solutions implies that fields can be expressed as a Fourier series in the *uv*-domain (6.8). Inspired by the symmetries that the bound waveguide modes follow, we expressed our radiation modes as the sum of four fields, each one possessing one of the following four symmetries: *even – even* (even in *x* direction - even in *y* direction), *even – odd* (even in *x* direction - odd in *y* direction), *odd – even* (odd in *x* direction - even in *y* direction), and *odd – odd* (odd in *x* direction - even in *y* direction), in (6.8). Radiation modes do not form an eigenvalue problem, as in the bound mode case, and working with them directly is rather prohibitive. This problem was resolved by splitting the field into a cladding free-space mode and the response coming from the waveguide (6.20). The knowledge of the free-space fields (6.21a)-(6.21d) allowed us to calculate the response field by solving the system of linear equations (6.16).

A significant advantage was also gained by separating the radiation mode into a free-space and a response field, as the radiation mode was normalized by simply normalizing the free-space part [6.27], (6.35).

Section 6.4 focused on the validation of our method by generating the radiation modes in a slab waveguide and comparing them to the existing analytical solutions, Fig 5-8, Fig. 6-9. The comparison showed excellent agreement between those constructed by our method and the real slab radiation modes. In section 6.4.3, we discussed the optimization of our method with respect to the scaling parameters p and q of the transformation (6.2). As explained with the aid of Fig. 6-10, the correct choice of p and q should be the one that does not allow the core boundaries to approach the edges of the unitary box in the uv-domain, as fields become highly oscillating there and an unnecessary large number of Fourier components would be required to resolve them. In addition, p and q should not bring the waveguide boundaries too close to each other, as this would compress the field inside the waveguide also creating high frequency spatial components.

Section 6.5 demonstrated for the first time a number of rectangular multimode waveguide radiation modes and discussed their behaviour in connection with the transverse wavenumber r, (6.50), and angle θ, (6.49). We showed in Fig. 6.8 that as r increases both free-space and radiation modes oscillate with higher spatial frequencies. Therefore, a larger number of Fourier components are required to resolve fields as r increases. However, for the sake of studying the interaction between guided and radiation modes, not the entire range of r (6.50), needs to be taken into account. In reality, we can limit ourselves to within a narrow range of r close to $r = 0$, in most if the cases of practical interest. The exact limits of the calculations should be always considered in regards to the statistical properties of the sidewall perturbation (6.74), (6.75), as they are directly connected to the autocorrelation length of the perturbation through (6.81). The effect of the angle θ, is to alter the spatial frequencies in x- and y- directions. For $\theta > 45°$ we have $k_x < k_y$ and, therefore, the radiation mode oscillates faster in x than in y. The opposite occurs for $\theta < 45°$. Finally, in section 6.5, Fig. 6-13 we demonstrated that although the radiation modes closely resemble the free-space modes, as the refractive index of the waveguide core approaches that of the cladding, this is not the case for the refractive indices used in our applications. The radiation mode in Fig. 6-13 (a) with $n_{co} =$

1.556, n_{cl} = 1.5249 (Δn = 1.9%) deviates significantly from the free-space field and approximating the former with the latter is not advisable.

Section 6.5 customized the bound-to-bound mode coupling coefficients (6.51)-(6.54) and the bound mode attenuation coefficients (6.55)-(6.56) to the rectangular waveguide environment. The expression in (6.53), led us to conclude that for waveguides with 1D sidewall deformation, even - even modes can only couple to each other and to odd – even modes. Similarly odd – odd modes can only coupled to each other and to even – odd modes. Based on this observation we have proposed for the first time that two independent and uncorrelated modal power distributions exist at equilibrium.

Finally, in section 6.6 we combined the radiation modes calculated by our method and the coupled mode theory to examine propagation in a 20 μm × 20 μm burried channel waveguide. The other waveguide parameters were λ = 850 nm, n_{cl} = 1.5560, n_{co} = 1.5249. More particularly, we were interested in investigating the propagation loss at the equilibrium state, the equilibrium distance, and the distribution of power at the equilibrium as the statistical properties of the waveguide, namely the standard deviation σ and the autocorrelation length L_c of the roughness, were varying. In Fig. 6-18 we showed the results for the propagation loss and equilibrium length as a function of the roughness standard deviation, for L_c = 4 μm and 10 nm < σ < 100 nm. As the standard deviation increased, propagation loss also increased for both even – even, odd – even and odd – odd, even – odd ensembles. In contrast, equilibrium length decreased as standard deviation increased. For example for σ = 10 nm the propagation loss for the even – even, odd - even ensemble was 0.0008 dB/cm and the equilibrium length 67.6 m. The propagation loss was 0.0007 dB/cm and the equilibrium length 78 m for the odd – odd, even – odd ensemble. The same values for σ = 100 nm were 0.076 dB/cm and 0.97 m for the even – even, odd - even ensemble, and 0.069 dB/cm and 1.73 m for the odd – odd, even - odd ensemble correspondingly. This behaviour was explained by noting that as the standard deviation increased, both bound-to-bound coupling coefficients and bound mode attenuation coefficients increased. The coupling between modes was stronger and, therefore, power was lost at a higher rate and power was distributed among them faster giving shorter equilibrium lengths. Figure 5-19 examined the effect of increasing L_c while keeping σ = 25 nm, constant. The trend was for the propagation loss to decrease as the

autocorrelation length increased and the equilibrium length to increase. This trend was explained by noting that as the autocorrelation length increases the roughness spectral distribution (6.57)-(6.58), became narrower. That meant that both the coupling and the attenuation coefficients became smaller. In addition, the number of radiation modes, which contribute to the loss mechanism reduced. This caused longer equilibrium lengths and less propagation loss. The last property we examined was the power distribution at equilibrium. Our calculations predicted that for the whole range of standard deviations and autocorrelation lengths that we considered dual mode operation occurs with one mode from each symmetry ensemble surviving. The first even – even mode β = 11.50 μm^{-1} dominates the even – even, odd – even symmetry set, while the first even – odd mode with β = 11.4970 μm^{-1} dominates the odd – odd, even – odd modal symmetry set, Fig. 6-20.

REFERENCES

[6.1] D. Marcuse, *Light Transmission Optics*. London, U.K.: Van Nostrand Reinhold, 1972.

[6.2] D. Marcuse, *Theory of Dielectric Waveguides*, London, U.K: Academic, 1991.

[6.3] D. Marcuse, "Radiation losses of dielectric waveguides in terms of the power spectrum of the wall distortion function," *Bell Syst. Tech. J.,* vol. 48, pp. 3233-3243, Dec. 1969.

[6.4] D. Marcuse, "Mode conversion caused by surface imperfections of a dielectric slab waveguide," *Bell Syst. Tech. J.,* vol. 48, pp. 3186-3214, Dec. 1969.

[6.5] D. Marcuse, "Derivation of coupled power equations," *Bell Syst. Tech. J.,* vol. 51, pp. 229-237, Jan. 1972.

[6.6] D. Marcuse, "Power distribution and radiation losses in multimode dielectric slab waveguides," *Bell Syst. Tech. J.,* vol. 51, pp. 429-454, Feb. 1972.

[6.7] D. Marcuse, "Higher-order scattering losses in dielectric waveguides," *Bell Syst. Tech. J.,* vol. 51, pp. 1801-1817, Oct. 1972.

[6.8] D. Marcuse, "Higher-order loss processes and the loss penalty of multimode operation," *Bell Syst. Tech. J.,* vol. 51, pp. 1819-1836, Oct. 1972.

[6.9] K. K. Lee, D. R. Lim, H.-C. Luan, A. Agarwal, J. Foresi, and L. C. Kimerling, "Effect of size and roughness on light-transmission in a Si/SiO_2 waveguide: Experiments and model," *Appl. Phys. Lett.*, vol. 77, pp. 1617-1619, 2000.

[6.10] F. Grillot, L. Vivien, S. Laval, D. Pascal, and E. Cassan, "Size influence on the propagation loss induced by sidewall roughness in ultrasmall SOI waveguides," *IEEE Photon. Technol. Lett.*, vol. 16, pp. 1661-1663, Jul. 2004.

[6.11] D. Lenz, D. Erni, and W Bächtold, "Modal power loss coefficients for highly overmoded rectangular dielectric waveguides based on free space modes," *Opt. Express,* vol. 12, pp. 1150-1156, Mar. 2004.

[6.12] M. Reed, T. M. Benson, P. Sewell, P. C. Kendall, G. M. Berry, S. V. Dewar, "Free space radiation mode analysis of rectangular dielectric waveguides," *Opt. Quantum. Elctron.* vol. 28, pp. 1175-1179, 1996.

[6.13] Z. H. Wang, "Free space mode approximation of radiation modes for weakly guiding planar optical waveguides," *IEEE J. Quantum Electron.*, vol. 4, pp. 680-685, Apr. 1998.

[6.14] C. G. Poulton, C. Koos, M. Fujii, A. Pfrang, T. Schimmel, J. Leuthold, W. Freude, "Radiation modes and roughness loss in high index-contrast waveguides," *IEEE J. Sel. Top. Quantum Electron.*, vol. 12, pp. 1306-1320, Nov./Dec. 2006.

[6.15] S. G. Johnson, M. L. Povinelli, M. Soljacic, A. Karalis, S. Jacobs, and J. D. Joannopolous, "Roughness losses and volume-current methods in photonic-crystal waveguides," *Appl. Phys. B*, vol. 81, pp. 283-293, 2005.

[6.16] M. Kuznetsov, and H. A. Haus, "Radiation loss in dielectric waveguide structures by the volume current method," *IEEE J. Quantum Electron.*, vol. QE-19, pp. 1505-1514, Oct. 1983.

[6.17] T. Barwicz, and H. A. Haus, "Three-dimensional analysis of scattering losses due to sidewall roughness in microphotonic waveguides," *J. Lightwave Technol.*, vol. 23, pp. 2719-2732, Sep. 2005.

[6.18] J. P. R. Lacey, and F. P. Payne, "Radiation loss from planar waveguides with random wall imperfections," *Proc. IEE*, vol. 137, pp. 282-288, Aug. 1990.

[6.19] T. Bierhoff, A. Wallrabenstein, A. Himmler, E. Griese and G. Mrozynski, "Ray tracing technique and its verification for the analysis of highly multimode optical waveguides with rough surfaces," *IEEE Trans. Magnetics*, vol. 37, pp. 3307-3310, Sep. 2001.

[6.20] C. H. Henry, and B. H.Verbeek, "Solution of the scalar wave equation for arbitrarily shaped dielectric waveguides by two-dimensional Fourier analysis," *J. Lightwave Technol.*, vol. 7, pp. 308-383, Feb. 1989.

[6.21] S. J. Hewlett, and F. Ladoucer, "Fourier decomposition method applied to mapped infinite waveguides: Scalar analysis of dielectric waveguides down to modal cut-off," *J. Lightwave Technol.*, vol. 13, pp. 375-383, Mar. 1995.

[6.22] F. Ladoucer, J. D. Love, and T. J. Senden, "Measurement of surface roughness in burried channel waveguides," *Electron. Lett.*, vol. 28, pp. 1321-1322, Jul. 1992.

[6.23] F. Ladoucer, J. D. Love, and T. J. Senden, "Effect of side wall roughness in buried channel waveguides," *IEE Proc. Optoelectron.*, vol. 141, pp. 242-248, Aug. 1994.

[6.24] F. Ladoucer, and L. Poladian, "Surface roughness and backscattering," *Optics Lett.*, vol. 21, pp. 1833-1835, Nov. 1996.

[6.25] F. Ladoucer, "Roughness, inhomogeneity, and integrated optics," *J. Lightwave Technol.*, vol. 15, pp. 1020-1025, Jun. 1997.

[6.26] E. A. J. Marcatili, "Dielectric rectangular waveguide and directional coupler for integrated optics," *Bell Syst. Tech. J.,* vol. 48, pp. 2071-2101, Dec. 1969.

[6.27] R. A. Sammut, "Orthogonality and normalization of radiation modes in dielectric waveguides," *J. Opt. Soc. Am.*, vol. 72, pp. 1335-1337, Oct. 1982.

CHAPTER 7

LOW COST, PRECISION SELF-ALIGNMENT TECHNIQUE FOR COUPLING LASER AND PHOTODIODE ARRAYS TO POLYMER WAVEGUIDE ARRAYS ON PCBs

7.1. INTRODUCTION

Connectors will probably be the most important components in Optical printed circuit boards (OPCBs), since as it is projected they will dominate reliability and cost issues [7.1]. The key specifications of OPCB connector designs include passive, low cost and highly accurate component alignment, repeatability over multiple engagement cycles, reliability in time and environmental changes, size compactness and reproducibility [7.2]-[7.14]. In addition, OPCB connectors should be made compatible with existing PCB fabrication methods such as reactive ion etching, laser ablation, laser writing and photolithography to reduce complexity and, thus, save cost and manufacturing time.

The most common OPCB connector designs use a Vertical Cavity Surface Emitting Laser (VCSEL) array emitting normally into the planar surface of the waveguide layer and a 45° angled plane mirror, which reflects the light through 90° into the waveguides [7.2]-[7.11]. Although the 45° mirror fabrication techniques have given losses as low as 0.5 dB – 1.5 dB per mirror [7.2]-[7.11] they are still being optimized to reduce the fabrication cost and to reproducibly give the correct angle and surface flatness over large OPCB areas. A more direct technique in which VCSELs are butt-coupled to the end of the waveguides [7.12]-[7.14] gives lower loss due to the absence of the mirror but is difficult to align and can only be used at the edges or in holes in the OPCB.

A popular method to achieve passive and accurate alignment between arrays of components is the mechanically transferable (MT) technology [7.2]-[7.20]. MT-connectors are comprised of a plug part, which carries two MT-pins, and a socket part, which carries two MT-holes, with an array of optical components being mounted on each of the plug and the socket. The component arrays are very precisely positioned in respect to the MT-pins in the plug case, and the MT-holes in the socket

case and so, accurate alignment is achieved upon registration of the MT-pins into the MT-holes. MT-technology is very attractive to be used in optical backplane connectors because VCSELs can be easily cleaved in arrays along cleaving lines and located against alignment features or projections in the plug so that their alignment with respect to the MT-pins can be achieved to within 1 μm of accuracy [7.21]. In addition, standard industrial fabrication methods, such as injection molding, can be used to fabricate MT-ferrules in almost any shape and size and so, these connectors can be mass produced. For these reasons, MT-connectors have been considered by several research groups [7.4]-[7.5], [7.7], [7.11]-[7.14] for their OPCB designs. However, the most serious problem in all reported designs up to date is in aligning the MT-socket to the waveguides and this has prevented a practical, low cost, detachable connector being brought to the market.

This chapter focuses on the connector developed during the Storlite project for optical backplane interconnection applications. The solution of direct coupling between the VCSEL array and the OPCB waveguides was employed, in order to avoid the problems associated with the 45° mirrors. A novel method where an array of GRIN lenses imaging the field emitted by the VCSELs onto the waveguide input facets was used to protect the VCSEL wire bonds being knocked off when butt-coupled to the waveguides. Alignment between the MT-socket and the OPCB waveguides relied on mechanical alignment features formed on the OPCB at the same fabrication step as the waveguides. Due to the simultaneous fabrication of waveguides and alignment features and with the aid of the same photolithographic mask, very accurate positioning of these two was guaranteed. The assembly of the connector, the choice of components and the design of all electronics was accomplished by our industrial partner Xyratex Ltd. [7.15]. The fabrication of the waveguides was carried out by Exxelis Ltd. [7.24]. Finally, the design of the masks and the experiments presented in this Chapter were part of this PhD.

The present chapter is arranged as following: Section 7.2 describes our low cost, passive, self-alignment technique. Section 7.3 describes the structure of a prototype multiple channel connector and its individual components namely the MT-plug, MT-socket, waveguides and alignment features and compares our method to the previously published work. Section 7.4 describes the experiments performed to validate the operation of the connector. These include VCSEL characterization, backplane waveguide characterization, insertion loss and cross-talk measurements as a

function of connector misalignment and repeatability over multiple connector engagements. Finally, Section 7.5 concludes.

7.2. DEVELOPMENT OF A TECHNIQUE FOR SELF-ALIGNMENT OF THE MT-SOCKET TO THE WAVEGUIDES

7.2.1 Difficulties of Alignment

Low cost PCBs are made from FR4, which is a non-uniform glass woven material, having various temperature expansion coefficients in different directions [7.21], while its thickness might vary significantly from sample to sample [7.22]. So, if the MT-socket is attached to the bottom of the FR4 substrate firstly it will move with respect to the top of the substrate where the waveguides are formed resulting in misalignment, and secondly different wafers would align with variable accuracy to the socket due to poor control on the FR4 thickness.

In addition, the woven pattern of the FR4 often results in a rippling of its surface [7.22]. As a result, if the MT-socket is attached to the top of the FR4 layer there will be a large uncertainty in the alignment to the waveguide cores. Such wafers can be planarized by depositing a sufficiently thick layer of lower waveguide cladding polymer, but there is still a large uncertainty in its final thickness [7.23]. Therefore, not only FR4, but cladding layer dimensions are unreliable and so, any alignment method should be made independent of the thickness of both.

One popular photosensitive acrylate polymer is Truemode^{TM}, which has low loss at 850 nm wavelength and is robust to humidity and thermal cycling but it must be used wet after spinning it onto the substrate [7.24]. In the case of lithographic fabrication, the mask must be offset by about 100 μm above the surface of the wet polymer to avoid adhesion effects and this spacing may vary from run to run [7.24]. The offset can cause a less well defined waveguide with walls sloping outwards towards its base, which might be overexposed giving wider waveguides than those defined on the dark field mask. If the MT-socket is laterally aligned in the plane to visual alignment features such as electrical vias or exposed copper tracks on the FR4 surface then for the socket to align to the waveguides the waveguides must be fabricated so that they align to the FR4 visual alignment features. However, the mask required is a dark field mask so it is difficult to see alignment features through the clear wet polymer layer. Moreover, since the mask is 100 μm plus the thickness of the core and lower cladding above the FR4 it is not possible to bring the visual alignment features on the FR4 and

the waveguides into focus together resulting in poor lateral alignment. Tighter process control can improve reproducibility of results but at an increased cost penalty to the fabrication of the complete structure.

7.2.2 Practical Self-Alignment Technique

We propose the use of an MT-socket interposer, Fig. 7-1, which is micro-mechanically aligned to the waveguides.

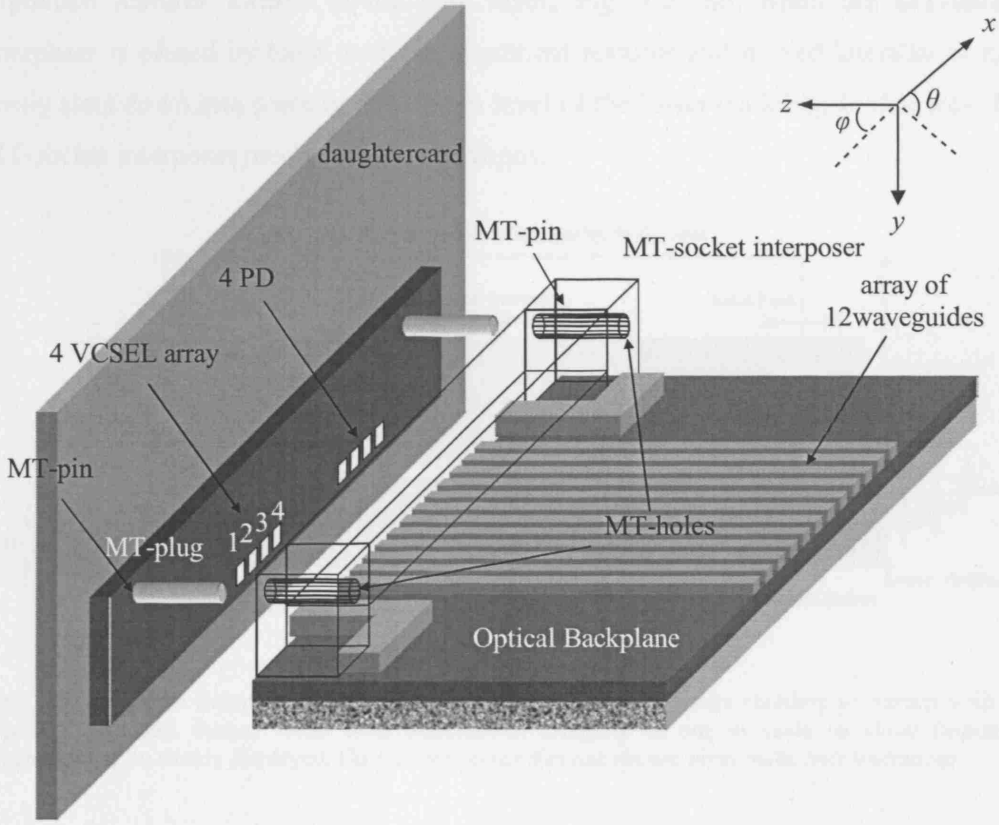

Fig. 7-1. Alignment method based on MT concept. After registering the MT-pins of the plug into the MT-holes of the socket interposer accurate alignment between the VCSEL's – PIN diodes of the mezzanine board and the waveguides of the backplane is achieved.

The MT-socket interposer, Fig. 7-1 and Fig. 7-2, is an inverted U-shaped polymer structure that fits over the linear array of waveguides. The first key aspect of the alignment technique is that the two feet of the MT-socket interposer stand on the top of the lower cladding layer, which acts as the datum layer with respect to which the alignment is achieved. As the waveguides are also formed on the same datum layer, the MT-socket interposer maintains the same *y*, alignment with the waveguides irrespective of any lower layers.

The second key aspect of the alignment technique is that the mask used to fabricate

the waveguides is also used to fabricate mechanical alignment features at the same time in the core layer having the same thickness as the waveguides with sidewalls running parallel to the waveguides. This ensures correct lateral positioning of the alignment features due to the high positional accuracy (nm accuracy) of the e-beam mask layout. The spacing between the inner faces of the MT-socket interposer legs is designed to match the spacing between the outer sidewalls of the mechanical alignment features formed in the core layer, Fig. 7-2. So, when the MT-socket interposer is placed by hand over the alignment features and moved laterally in x, it neatly slots down into place on the datum level of the lower cladding. In this way, the MT-socket interposer mechanically self-aligns.

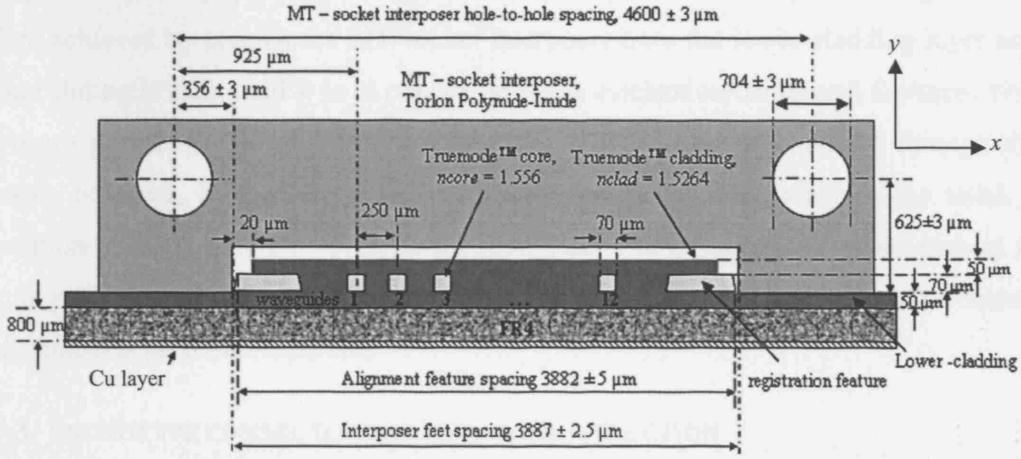

Fig. 7-2. MT-socket interposer slotted into place on the top of the lower cladding in contact with the exposed alignment feature walls with dimensions. Diagram is not in scale to allow important dimensions to be clearly displayed. Critical connector dimensions are given with their tolerances.

The alignment in z, is achieved by forming the mechanical alignment features to have backstops so that once the MT-socket interposer has been slotted into place laterally it can simply be slid back into contact with the backstops. Finally, while clamping the MT-socket interposer in place glue can be put around its legs to lock it into place.

The third key aspect is that when the waveguides are covered with the upper cladding to bury them, it (the cladding) does not cover the aligning side wall nor back stop wall of the mechanical alignment features so that these remain exposed and available, Fig. 7-1, for mechanical contact alignment of the feet of the MT-socket interposer. Provided the upper cladding is sufficiently stepped back from the alignment wall in the core layer then the lateral tolerance for positioning the upper

cladding layer need not be very tight.

The side walls sometimes slope outwards towards the base of the waveguide, Fig. 7-2, and are often over exposed giving waveguides and alignment features that are larger than on the mask by a certain amount. This irregularity needs to be taken into account in designing the spacing of the two feet of the MT-socket interposer, as the feet will make contact with the bottom of the waveguide walls. Generally, the lateral positions of the sidewalls of the mechanical alignment features are reproducible but if the process control is insufficient, there may be an uncertainty in the lateral position of the sidewalls. In this case, the MT-socket interposer feet can be shaped to be wider away from the cut edge of the waveguides. Similarly, the alignment features can be angled so that they are wider away from the cut edge of the waveguides. Alignment is then achieved by placing the MT-socket interposer onto the lower cladding layer and then sliding it back until it is in contact with the mechanical alignment features. This ensures perfect lateral alignment irrespective of over or under exposure through the mask, however, it is at the expense of some increased uncertainty in the axial, z position of the socket. However, as we show later a large amount of misalignment in *z*, is possible without serious ill effects on the coupling loss whereas accurate lateral alignment is far more important.

7.3. PROTOTYPE CONNECTOR DESIGN AND CONSTRUCTION

A prototype connector was designed to make use of the novel micro-mechanical alignment technique and so that the degree of alignment of this technique could be assessed and the effect of the misalignment on the optical coupling, insertion loss and cross-talk assessed. It is desirable to have no active devices on the optical PCB backplane, as this is usually an intimate part of the rack-based system and difficult to remove. Therefore, all of the active devices were put into the MT-plug of the connector and the MT-socket had no active devices. The connector was designed to have 4 duplex channels capable of operating at 10 Gb/s with a linear array of 4 laser sources and 4 photodiode detectors and the MT-socket receptacle was placed over 12 waveguides although in this demonstration only the 4 at each end were used.

7.3.1 MT-Plug

As already mentioned, the MT-plug hosted all active components. These included 10 Gb/s 850 nm Oxide-confined VCSELs with 7 μm active diameters [7.26] from ULM

photonics and 10 GHz GaAs PIN diodes with 75 μm active diameters [7.27] from Microsemi corporation. VCSELs and PDs were arranged in linear arrays of four, on a pitch of 250 μm which matched the waveguide to waveguide spacing. Active component arrays were first aligned and glued onto the MT-plug header using its raised alignment features, and then they were wire bonded to electrical contacts, Fig. 7-3 (b), (c). The VCSELs were arranged to launch into waveguides 1-4 and PDs to receive from waveguides 9-12. Waveguides 5-8 were unused in this first approach. We adopted a novel approach by using an array of GRIN lenses to image the VCSELs and PDs to a position onto the exterior face of the GRIN lens towards the waveguides, Fig. 7-3 (c), to avoid the bond wires being knocked off when butt-coupled to the waveguides. GRIN lenses were designed to allow them to be positioned beyond the bond wires of the VCSEL so that they were not affected. In addition, GRIN lenses could be physically butt coupled to the waveguides with some degree of force without damaging the VCSELs. The GRIN lenses were mounted on silicon V-grooves in a ceramic holder, Fig. 7-3 (b). The ceramic lens holder had two 705 ± 3 μm diameter holes corresponding to, but having a slightly larger diameter than the MT-plug pins. The MT-pins were first slipped through the holes and then the ceramic holder was adjusted in x, and y under a microscope until the VCSEL and PD images were brought into focus at the centre of the front surface of the GRIN lenses, Fig. 7-3 (c). Subsequent measurement of the assembly showed that in fact the active devices were imaged 2 μm beyond the face of the GRIN lenses towards the waveguides.

7.3.2MT-socket, Waveguides and Alignment Features

The MT-socket interposer, Fig. 7-3 (a), for the prototype was machined from a block of Torlon Polyimide, which has a thermal expansion coefficient of 14.4 ppm / °C chosen to be compatible with that of the FR4. The interposer was designed to be injection molded to minimize cost in a final product. Each waveguide was designed to have an approximately square cross section of 70 μm × 70 μm. This choice of waveguide dimensions was based on preliminary experimental results, which suggested that for the given VCSELs and PDs, 70 μm × 70 waveguide cross-sections maximized coupling efficiency while minimizing cross-talk from adjacent waveguides. This experiment will be presented in detail in section 7.5.1. The 12 straight waveguides in the array were on a pitch of 250 μm and they were 10 cm long. The FR4 wafer had a thickness of 800 μm and was coated in a copper layer of 17 μm

on the surface away from the waveguides. One dark field e-beam (Fig. 7-4 (a)) and one light field laser written mask (Fig. 7-4 (b)) were used for the fabrication of the optical features, which took place in three distinctive phases, Fig. 7-5. In phase A, the ~50 μm thick lower cladding layer was developed following spinning and UV curing. In phase B, the core layer was spun on to a thickness of 70 μm and waveguides and alignment features with backstops were formed photolithographically from the e-beam dark field mask, Fig. 7-4 (a), after UV exposure through the mask and removal of the unexposed core material. In phase C, a ~50 μm layer of upper cladding polymer was initially spun over the whole substrate. A second light field photomask, Fig. 7-4 (b) was then aligned to the visual cross alignment features left in the core layer from the first mask, shown in Fig. 7-4 (a), and the upper cladding was formed by UV illumination through the second mask and subsequent clearing of the unexposed residual material. Critical visual alignment between the marks left in the core during phase B and the marks on the second mask was not necessary, since a gap of 20 μm had been left, Fig. 7-2, between the edge of the upper cladding and the exposed core alignment feature walls. This also meant that a lower cost lower resolution photomask was sufficient. The upper cladding polymer was the same as the lower cladding polymer and had the same lower refractive index than the core when cured. The refractive index of the core after UV exposure was $ncore$ = 1.556 and that of the cladding was $nclad$ = 1.5264, as measured by the prism coupler method, giving a waveguide numerical aperture of NA = 0.302.

The separation of the internal faces of the MT-interposer feet was designed to be 5 μm wider than the spacing between the outer walls of the alignment features on the mask to allow for the expected overexposure and wall slope which caused widening of the alignment feature wall spacing.

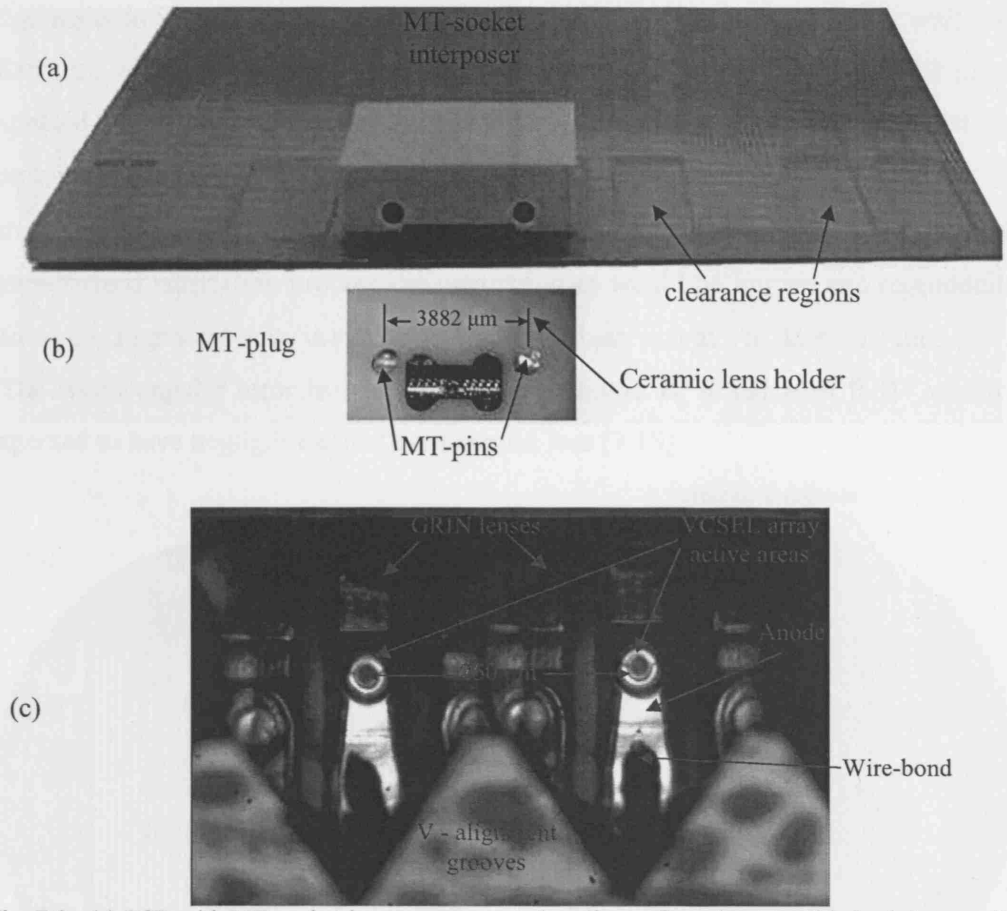

Fig. 7-3. (a) PCB with MT-socket interposer mounted on the surface about to slide back into position against backstops. (b) MT-plug with ceramic lens holder in place. (c) An array of GRIN-lenses held on V-alignment grooves aligned to the array of VCSELs (2 out of the 4 GRIN-lenses and VCSELs in the array are shown) was used to protect the wire bonds. Lenses were designed to image VCSEL output to the exterior surface of the lenses. Picture was taken under a microscope with a 30x microscope objective lens.

7.3.3 Connector Alignment Tolerances

Translational misalignments can occur in the horizontal direction in-plane x, in the vertical direction normal to the plane y, and in the axial direction z. In addition, angular misalignments can occur in θ and φ. The amount of misalignment is determined by the fabrication accuracies of each of the MT-plug, MT-socket and OPCB features. The individual and combined tolerances are summarized in Table 7-1 for all three translational directions. The tolerances for the MT-plug and MT-socket were obtained from the manufacturers while those for the OPCB features were measured by shadowgraph after fabrication, Fig. 7-6. According to this technique, highly collimated white light was passed through the MT-socket and waveguide assembly and cast a shadow on a screen that was then magnified. The shadowgraph clearly shows the waveguides, alignment features and the MT-socket interposer

alignments in x, and y. The measured separation of the alignment feature walls was 3886 μm, which is larger than the separation designed on the mask of 3882 μm as expected due to over exposure and wall slope. As seen from Table 7-1, the worst case combined misalignment between VCSELs/PDs to waveguides along x, is $\Delta x = \pm 11$ μm, along y, is $\Delta y = \pm 7$ μm and along z, is $\Delta z = +12.5$ μm. However, on a well-characterized fabrication process the overexposure would be known and reproducible and so the alignment error in x reduces to $\Delta x = \pm 6$ μm and in z to $\Delta z = +10$ μm.

The worst angular error in standard MT connectors is, θ and φ of 0.01° which is expected to have negligible effect on insertion loss [7.18].

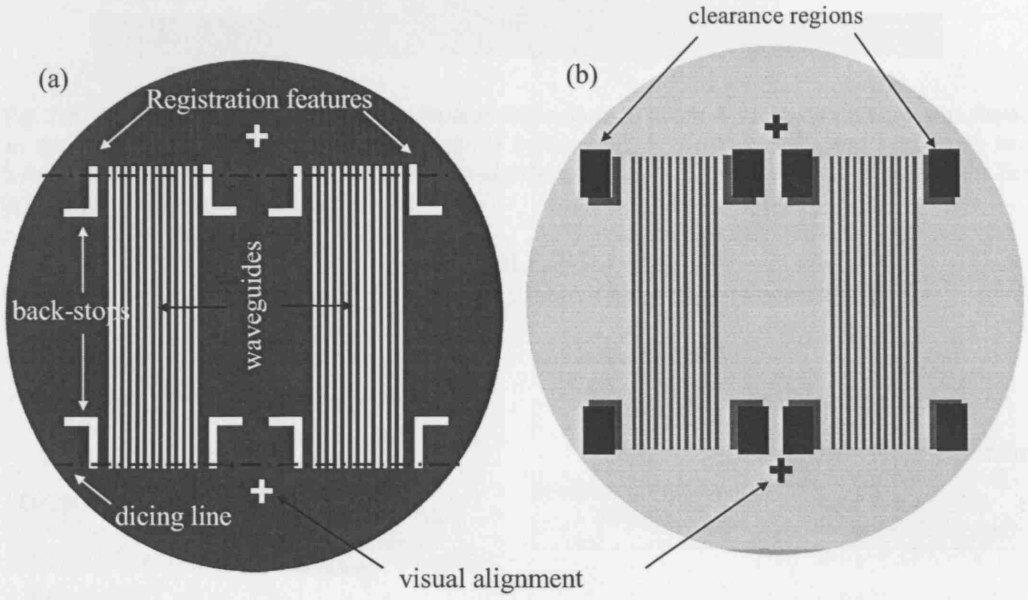

Fig. 7-4. (a) Core layer mask. Waveguides, mechanical registration features, mechanical backstops and optical alignment marks for the cladding-mask are shown. (b) Upper-cladding mask as it appears in the mask aligner on top of an incompletely processed wafer. Features of cladding mask are opaque and shown in black while core features on the wafer are shown in gray.

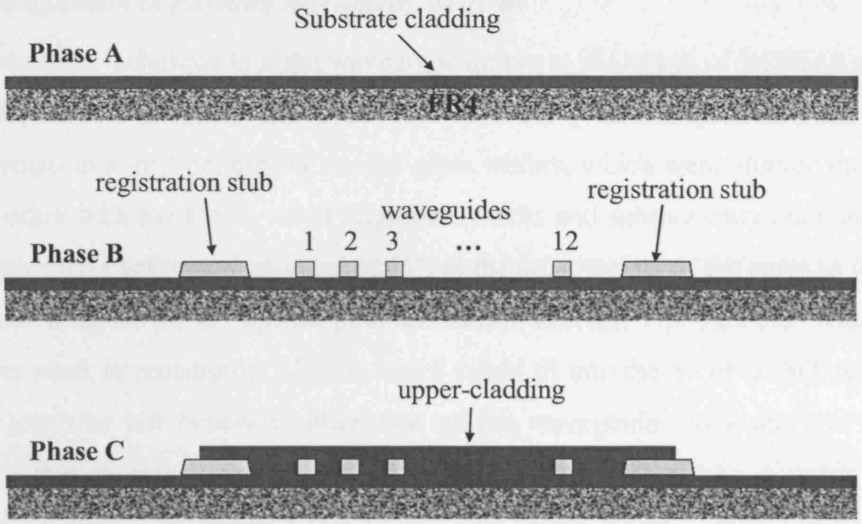

Fig. 7-5. Schematic diagram of optical backplane fabrication. In Phase A substrate cladding was formed on the top of an 7" × 7" FR4 wafer. In phase B waveguides, registration stubs and back stops were formed simultaneously while in Phase C upper-cladding was specially deposited to leave the area next to the registration stubs unfilled.

TABLE 7-1

TOLERANCES ALONG *x*, *y* AND *z* FOR CONNECTOR COMPONENTS

	x	*y*	*z*
MT-plug	±3 μm (pin-to-pin)	±3 μm (pin-to-GRIN)	_____
MT-socket	±3 μm (hole-to-hole)	±3 μm (hole-to-waveguide)	_____
OPCB features	+2.5 μm (increase in registration wall-to-wall spacing due to overexposure) ±2.5 μm (due to 5 μm extra spacing between feet of interposer)	±1 μm (core thickness control)	+10 μm (accuracy of dicing in respect to the dicing lines on the board) +2.5 μm (backstop shift due to overetching)
Tolerance of MT interposer socket to waveguides	±8 μm or **±3 μm** if overexposure widening is known and reproducible	±4 μm	+12.5 μm or **+10 μm** if overexposure widening is known and reproducible
Combined tolerance of VCSEL and PIN to waveguides	±11 μm or **±6 μm** if overexposure widening is known and reproducible	±7 μm	+12.5 μm or **+10 μm** if overexposure widening is known and reproducible

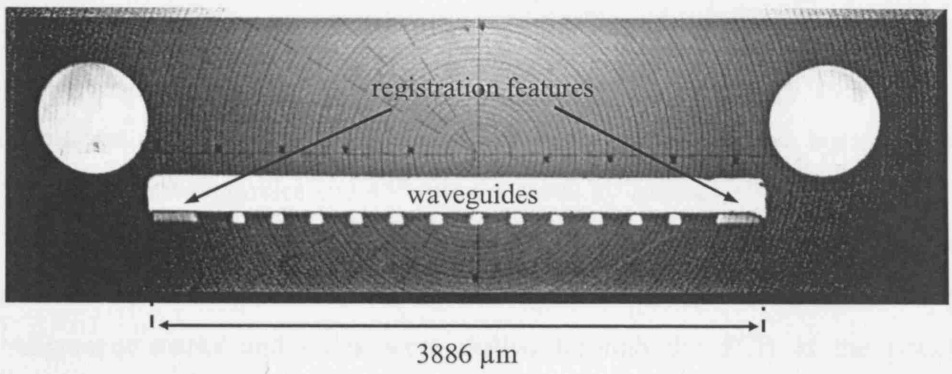

Fig. 7-6. Shadowgraph picture showing the actual alignment of the components.

7.3.4 Comparison to Existing Alignment Methods

An interesting technique to align waveguide arrays to 2D arrays of VCSELs and PDs using MT sockets and plugs has been reported in [7.3]. In this approach, waveguides were formed in a grid pattern on several glass wafers, which were aligned on the top of each other with the aid of visual alignment marks and subsequently laminated. The resulting wafer-stack was then diced at 45°, at the cross-points of the cores to form 3D waveguide arrays with 45° optical path redirection mirrors. The final step was to dice the wafer-stack in rectangular blocks, which could fit into the pit of an MT ferrule. A 50 μm gap was left between either side of the waveguide block and the MT pit probably due to inaccuracies involved in the dicing process. As a result, lateral alignment between waveguides and VCSEL/PD arrays along x- direction had to be active. Vertical alignment along y though, was passive as the glass wafer thickness was controlled with very good accuracy. The last two features significantly differentiate the work reported in [7.3] from the work described here. Firstly, in our case there is a large uncertainty in the thickness of the cladding and core layers, which results from the spin coating fabrication step, with a maximum 10% [7.23] variation in the thickness of each layer to be expected. Therefore, alignment in y could not rely on the under-layers for polymer waveguides made photolithographically. This problem was overcome in our technique by resting the feet of the MT-socket interposer on the top of the under-cladding layer as shown in Fig. 7-2. In this way, vertical MT-hole to waveguide alignment, y, was made dependent on the distance between the bottom of the interposer feet to the centre of the MT-holes only, which could be very precisely controlled. Secondly, as explained in 6.2.2 the lateral alignment x, mainly depends on the position of the alignment features Fig. 7-2, with respect to the waveguides. Since both are formed simultaneously and with the aid of the same e-beam mask, accurate alignment in x, is guaranteed. In conclusion, alignment in our connector was achieved completely passively along the two critical x- and y- directions without any active step being involved.

The authors in [7.4] described an optical backplane connector based on MT-technology with waveguides and 45° mirrors made by laser ablation. In their system, VCSEL to waveguide coupling was achieved with the aid of microlenses made on a Si-substrate. According to their method, waveguides were made in the same step as the alignment marks and holes were drilled through the PCB at the positions

specified by the alignment marks for the MT-pins. Then, a thin Si-plate with two holes of diameter and separation matching those of the MT-technology, were registered on an MT-plug of a fibre ribbon. The spots created on the Si-plate upon illumination of the fibre ribbon were used as reference to form perfectly aligned (to the spots) microlenses. Subsequently, MT-pins were inserted on the MT-holes of the PCB and the Si-plate with the microlenses was registered in the MT-pins. The first difference of this method to our approach was that in their case holes were drilled in the PCB, which was hosting the MT-pins, in contrast to our case where MT-plug was a separate to the PCB component. In addition, in their case MT-socket was carrying a fibre ribbon rather than active components. In reality, in their demonstrator, signals were coming from fibres and active components were not used at all. Finally, they used the laser ablation method to write waveguides and alignment in the PCB. Although this is a popular and established method in today's electrical PCBs, it is mainly used to drill holes. It is unclear whether laser ablation can write waveguides fast enough to allow for manufacturing on a mass scale. On the other hand, photolithography is a fast and reliable method since all waveguides and marks replicate the mask features in a single illumination step.

In [7.7] VCSELs and PDs were wire bonded on the top surface of an arrangement, which included one optical waveguide film laminated between two conventional electrical PCBs, in a surface mount approach. Holes were drilled with a CO2-laser through the PCB and waveguide film layers to form vias. Then a fibre ribbon, called the optical connection rod, which was carried by an MT-ferrule, was inserted into the vias and alignment was achieved by MT-holes, which were also drilled through the PCB. Optical fibre end faces were polished at 45° degrees to deflect light perpendicularly from the fibres into the waveguides of the PCB. Unfortunately, they did not provide with many details as how they aligned the fibres to the VCSELs and PDs or about how vias were drilled with accuracy in respect to the waveguides to allow for the MT-pins to be registered accurately. The system they presented needed lots of optimization as they reported 8 dB of insertion loss, which is unusually high.

Finally authors in [7.11]-[7.12] reported an MT based connector for a flexible PCB. There they managed to mount a flexible PCB made of Pyrex with UV curable resin. Although they claim that alignment between PCB waveguides and MT-holes/pins was passive they give no further details. The reason we mention this approach is because our alignment technique although demonstrated on a rigid PCB is also suitable for use

on flexible PCBs as the MT-socket is mounted on the top of the cladding area a flexible PCB cladding layer can well be used and the interposer is only glued over a small area of the PCB. The same technique can also be extended for use with multiple layers of waveguides by using two-dimensional arrays of VCSELS, PDs and GRIN lenses in the MT-plug.

7.4. VCSEL CHARACTERIZATION

7.4.1 L-I curve and Coupling Efficiency

Fig. 7-7 shows a typical VCSEL L-I characteristic that we measured for one of the lasers in the array. The rest of the VCSELs exhibited very similar curves. From Fig. 7-7 we see that threshold current is at $I_{th} \sim 0.7$ mA. At $I_{bias} = 3.3$ mA the VCSEL output power reached 1 mW (0 dBm) while for $I_{bias} > 9$ mA power began to saturate.

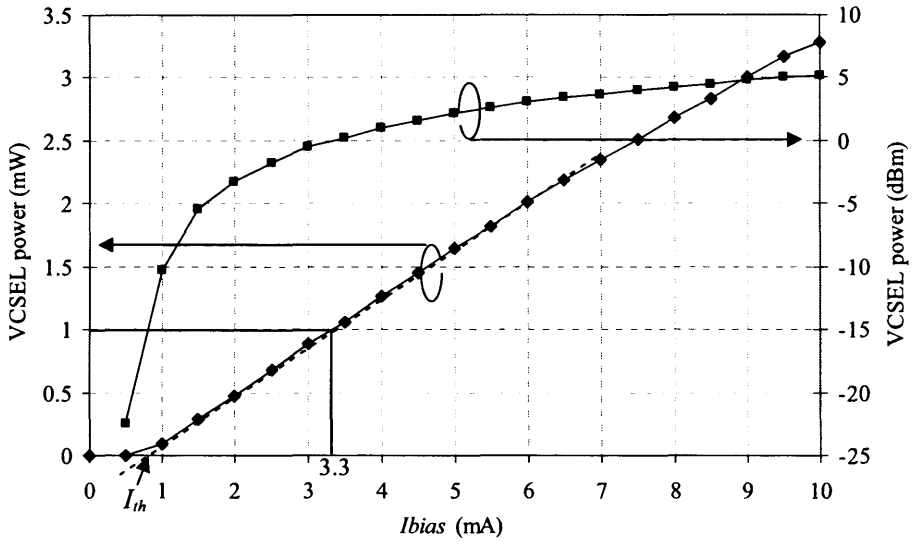

Fig. 7-7. L-I characteristic of a typical VCSEL used in our experiments. The threshold current is $I_{th} \sim$ 0.8 mA. The power reaches 0 dBm at $I_{bias} = 3.3$ mA and begins saturating for $I_{bias} > 9$ mA.

One important aspect of an optical link is how much of the light emitted by the laser source is actually coupled into the waveguides. The coupling efficiency is a parameter, which is not constant with I_{bias} but it heavily depends on the driving conditions of the VCSELs. Figure 6-8 shows the power received at the end of one of the waveguides in the wafer as a function of I_{bias}, as well as the power emitted from the VCSEL (L-I characteristic of Fig. 7-7). Measurements were calibrated to exclude propagation loss through the waveguides. This calibration step will be explained in section 7.5.2. At the moment, it is enough to know that propagation loss, which is a

variable dependent on the waveguide length only and would distort results if left intact, has been removed. On the same graph, we have plotted the coupling loss, which is defined as the difference (in dB) between the power emitted by the VCSEL and the power measured at the end of the waveguide, and the VCSEL-to-waveguide coupling efficiency (power coupled into the waveguides as a percentage of the light emitted by the VCSEL). Since propagation loss has been calibrated out, coupling loss is the combination of Fresnel reflection losses and loss due to mismatch between VCSEL and waveguide modes. No index matching fluid was used for these experiments.

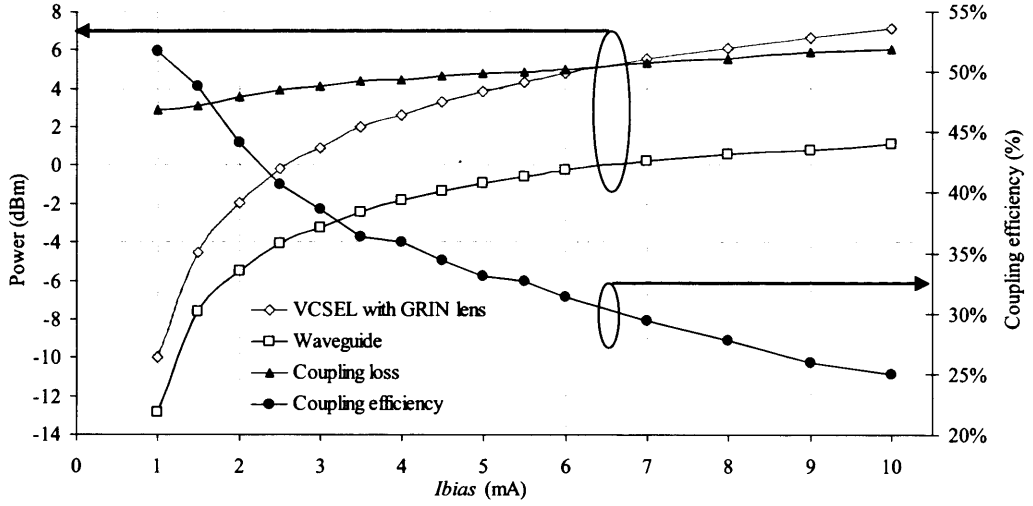

Fig. 7-8. Primary *y*-axis: VCSEL power, power at the output of the waveguides of the board, coupling loss, and coupling efficiency as a function of I_{bias}. Secondary *y*-axis: VCSEL to waveguide coupling efficiency. Measurements taken at room temperature 25° C.

Figure 6-8 reveals that as I_{bias} increases, the coupling loss increases as well, or equivalently coupling efficiency drops. At currents just above threshold, I_{bias} = 1 mA, coupling loss takes its minimum value of 2.86 dB, while it increases to 6.031 dB for I_{bias} = 10 mA. In equivalent coupling efficiency terms, at I_{bias} = 1 mA, 51.8 % of light is coupled into the waveguide while at I_{bias} = 10 mA only 24.9 % of light couples into it. In a binary optical system, a modulation (or drive) current is superimposed onto the bias current and 1's and 0's are represented by different levels of optical power. Therefore, for given bias and drive currents, Fig. 7-8 can be utilized in optical link power budgets calculations.

Similar coupling behaviour has been observed before, between VCSELs and multimode fibres [7.28]-[7.29]. There it was shown that in multi-transverse mode emitting VCSELs, as the ones we are using, the coupling efficiency strongly depends

on the VCSEL active diameter and number of transverse modes. In their experimental and modelling results, the coupling efficiency was good for VCSELs whose active diameter was similar to the diameter of the multimode fibre as better spatial matching was achieved between the modes of the two. In addition, the coupling efficiency was better for low I_{bias} where VCSELs exhibited nearly single mode operation than for higher I_{bias}, which tended to excite high order modes, as they found that higher transverse modes are more spatially dissimilar to fibre modes than low order modes and therefore they cannot be coupled with the same efficiency into the fibre.

7.4.2 Near and Far-Field Measurements

In order to investigate how the VCSEL bias current affects its modal characteristics and, therefore, the coupling efficiency in our waveguides, we measured the near and far field intensities for a range of I_{bias}. The spatial distribution of the VCSEL near-field intensity was recorded for various values of I_{bias} with the aid of a 40x microscope objective lens and a CCD camera placed at the focal plane of the lens. In Fig. 7-9 we show the results for three drive currents of interest, I_{bias} = 1.5 mA, I_{bias} = 3 mA and I_{bias} = 10 mA correspondingly, presented I_{bias} in a greyscale intensity contour plot format. Modes are numbered according to the order they appear in the near-filed pattern as we increase I_{bias}. From Fig. 7-9 we derive two notable conclusions. At first, as the bias current increases the part of the active area, which illuminates broadens. Secondly, the number of bright spots (white spots) increases from one for I_{bias} = 1.5 mA to two for I_{bias} = 3 mA and then gradually to five for I_{bias} = 10 mA. Each of these spots corresponds to (at least) one transverse mode [7.30], and therefore as the gain of the cavity increases we pass from single to multimode operation. Modes, which are adjacent or overlap each other (1 and 3, 2 and 4 in Fig. 7-9) compete for the gain of the cavity. This experiment confirmed that our VCSELs exhibit multi-transverse modal operation.

To further investigate the relationship between the VCSEL emitted field and the coupling efficiency we measured the VCSEL far-field intensity distribution as a function of I_{bias}. To obtain the far-field measurements, the CCD camera was directly placed 20 mm away from the VCSEL. No lens was used in this case. Fig. 7-10 (a) shows a horizontal cut of the far-field intensity for three representative bias currents I_{bias} = 1 mA, I_{bias} = 3.3 mA and I_{bias} = 6 mA. The far-field pattern was normalized to a unitary peak. From Fig. 7-10 (a) we see that as I_{bias} increases, the far-field divergence,

defined as the full-width at e^{-2}, increases as well and more peaks, corresponding to multimode operation, make their appearance. After obtaining the far-field intensity patterns for all I_{bias} in the range 1 mA < I_{bias} < 10 mA, we proceeded by plotting the far-field divergence as a function of bias current, Fig. 7-10 (b). In the same graph, we plotted the coupling efficiency as a function of I_{bias} on a second axis (repeated from Fig. 7-8). Fig. 7-10 (b) shows a strong correlation between far-field divergence and coupling efficiency. As I_{bias} increased far-field divergence increased while coupling efficiency dropped even though in all cases VCSEL emitted light within the waveguide NA = 0.302 which corresponds to ~34° of full acceptance angle.

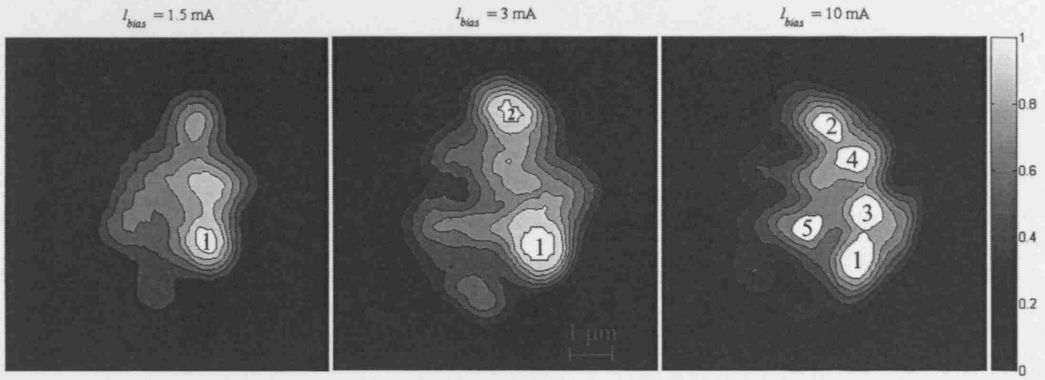

Fig. 7-9. Normalized (to unity maximum value) intensity contour plots of VCSEL near-field measurements for three representative bias currents, I_{bias} = 1.5 mA, I_{bias} = 3 mA and I_{bias} = 10 mA. Pictures were taken with the aid of a 40x microscope objective lens focusing the VCSEL aperture onto a CCD camera. Greyscale plots of intensity are constructed with 12 contours, with white color corresponding to the highest intensity and black to the lowest. As I_{bias} increases, the near-field pattern broadens and more transverse modes (white spots) appear. Modes are numbered according to the order they appear in the near-filed pattern as we increase I_{bias}.

At I_{bias} = 1 mA far-field divergence was 11.64° and coupling efficiency 51.8%. For I_{bias} = 3 mA far-field divergence reached 21.07° and coupling efficiency decreased to 36.86%. Finally at I_{bias} = 10 mA far-field divergence was 29.62° and coupling efficiency dropped to 24.9%. We note that as the far-field angle increases Fresnel reflection losses increase as well. This is another reason why coupling efficiency drops as I_{bias} increases, in addition to the assessments in [7.28]-[7.30].

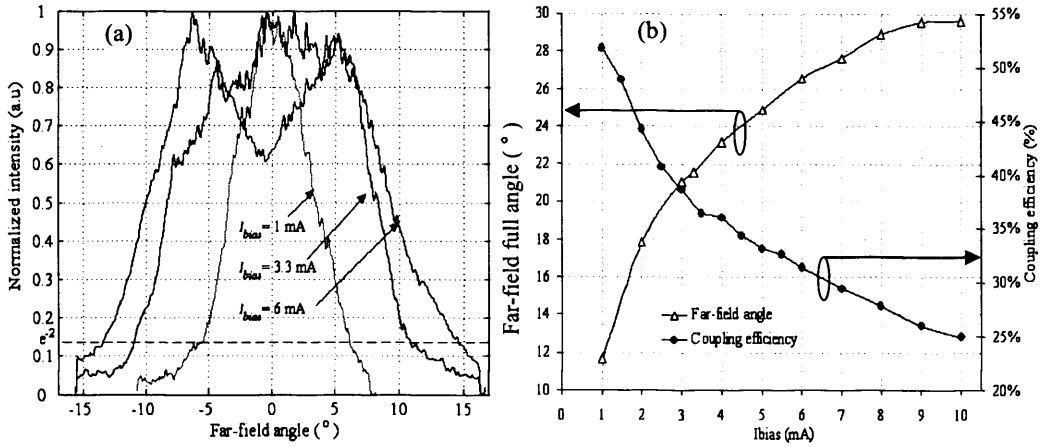

Fig. 7-10. (a) VCSEL far-field intensity (linear units normalized to unity maximum value) measured I_{bias} = 1 mA, I_{bias} = 3.3 mA and I_{bias} = 6 mA. For I_{bias} = 3.3 mA, which is the bias current used in the connector evaluation experiments, far-field divergence was ~23°. (b) Far-field divergence (defined as the full angle at e^{-2} from maximum intensity of the far-field intensity) and coupling efficiency as a function of I_{bias}.

7.5. PROTOTYPE BACKPLANE AND CONNECTOR CHARACTERIZATION

7.5.1 Waveguide Cross-Section Dimension Selection

The choice of 70 μm square cross-section waveguides was based on evidence from preliminary measurements of the insertion loss and cross-talk in an array of 15 waveguides with various widths, Fig. 7-11. The thickness of these former waveguides was 50 μm, constant throughout the array, while their width was varying from 10 μm to 150 μm with 10 μm difference between successive waveguides. The lateral separation between two adjacent waveguides was 250 μm. For these experiments, we positioned an MT-plug, after its pins had been removed, on a system of three *xyz*-motorized stages and we brought the GRIN-lenses in contact with the input of the waveguides on the wafer. One of the waveguide's output was then butt-coupled to a 75 μm pinhole attached to a GaAs photodetector, to simulate the GRIN lens / PD combination aperture, and the MT-plug and pinhole/photodetector were moved along the two lateral directions (*x* and *y*) until the power received by the photodector was maximized. After the measurement of the power coupled into the waveguide under investigation was taken, we moved the MT-plug holding the VCSEL array first by 250 μm to the left and then by 250 μm to the right of this waveguide while still recording the power at the photodetector (which remained in its initial position). In this way, we measured the signal to cross-talk ratio (*SCR*) that the reference waveguide would experience from one waveguide on its left and one waveguide on its

right in a real system. We then moved the pinhole / photodetector and VCSEL to the next waveguide, repeated the same measurements, and continued in the same way to cover all 15 waveguides in the array. The results are presented in Fig. 7-12. As shown in Fig. 7-12, the insertion loss was minimized for the waveguides with widths in the range between 50 μm – 80 μm. Minimum signal to cross-talk ratio was exhibited by the 70 μm – 80 μm wide waveguides. Therefore, the waveguides, which showed minimum insertion loss, combined with minimum *SCR* were found to be in the range between 70 μm – 80 μm. This prompted our selection for 70 μm square waveguides in our prototype demonstrator.

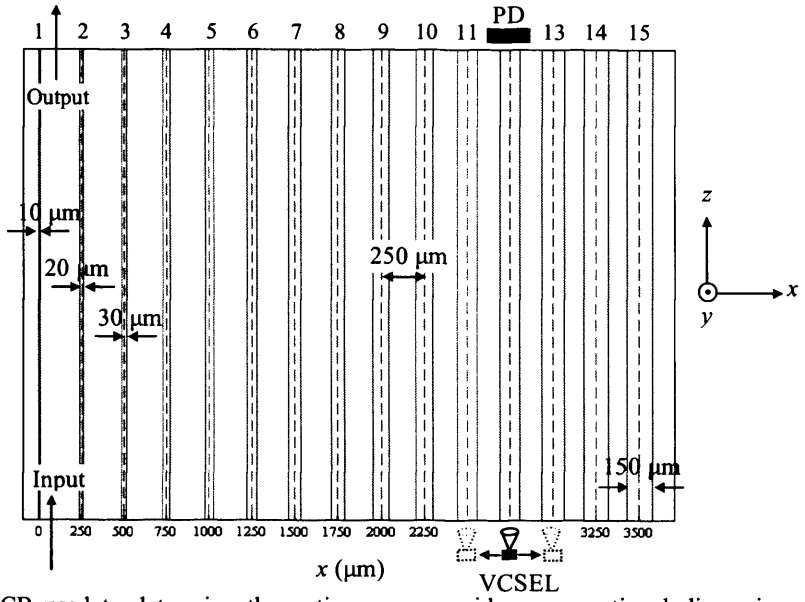

Fig. 7-11. Test PCB used to determine the optimum waveguide cross-sectional dimensions in the prototype connector design. Insertion loss and signal to cross-talk was measured for an array of 15 waveguides with chirped width varying from 10 μm to 150 μm and 250 μm spacing. In the arrangement shown in the figure, one of the VCSELs of the MT-plug is aligned at the input of waveguide 12. The PD is aligned at the output of the same, 12th, waveguide and in this way insertion loss is measured. If VCSEL is moved laterally along *x*, by 250 μm towards the left while PD is left intact, then the cross-talk coming from waveguide 11 is measured. Similarly, by moving the VCSEL 250 μm to the right the cross-talk coming from waveguide 13 is measured.

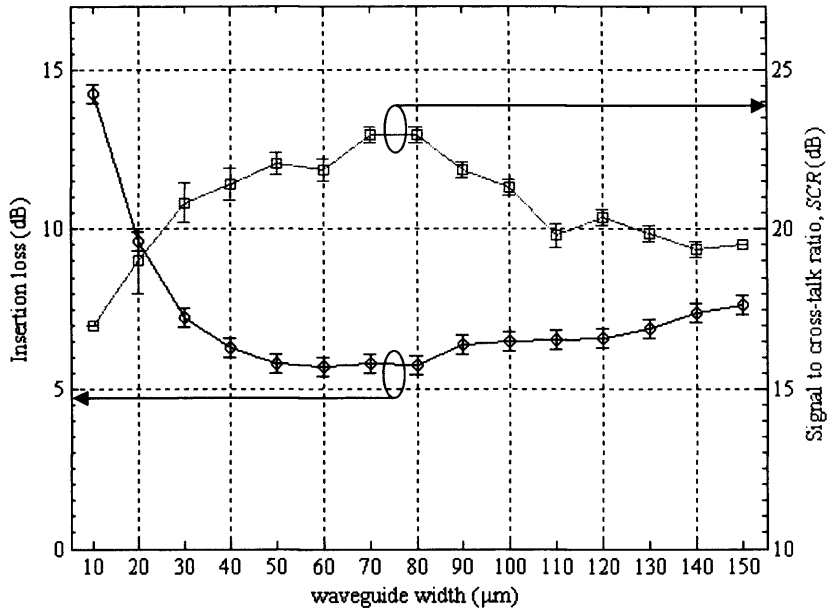

Fig. 7-12. Coupling efficiency and *SCR* measured for an array of 15 waveguides with chirped widths varying from 10 μm to 150 μm. For a given waveguide, the *SCR* shown corresponds to the mean signal to cross-talk value due to one waveguide on its left and one waveguide on its right. The maximum value of the error bar corresponds to the *SCR* resulting from the left while the minimum value to the *SCR* resulting from the right waveguide.

7.5.2 Misaligned Insertion Loss

In order to measure the insertion loss as a function of the three possible translational misalignments x, y and z in our prototype connector design we again used the same system of motorized stages / MT-plug, as in section 7.5.1, but this time we scanned continuously across the waveguides. The VCSEL bias current was set to I_{bias} = 3.3 mA, DC, which provided an output optical power of 0 dBm. The position of maximum coupling efficiency (or equivalently minimum insertion loss) corresponded to $\Delta x = 0$, $\Delta y = 0$, $\Delta z = 0$. Scanning along x and y at different values of z and monitoring the power at the waveguide output, allowed us to generated the xy-contour maps of insertion loss due to VCSEL misalignment, Fig. 7-13 (a) (Δz = 0 μm) and (c) (Δz = 60 μm). Figure 6-13 (a), Δz = 0 μm, corresponds to the case where the VCSELs are butt-coupled to the waveguides. Figure 6-13 (c), Δz = 60 μm, is just an example case to illustrate the effect of Δz on the contour maps. The insertion loss in the contour maps shown in Fig. 7-13, is relative to the minimum insertion loss measured at $\Delta x = 0$, $\Delta y = 0$, $\Delta z = 0$.

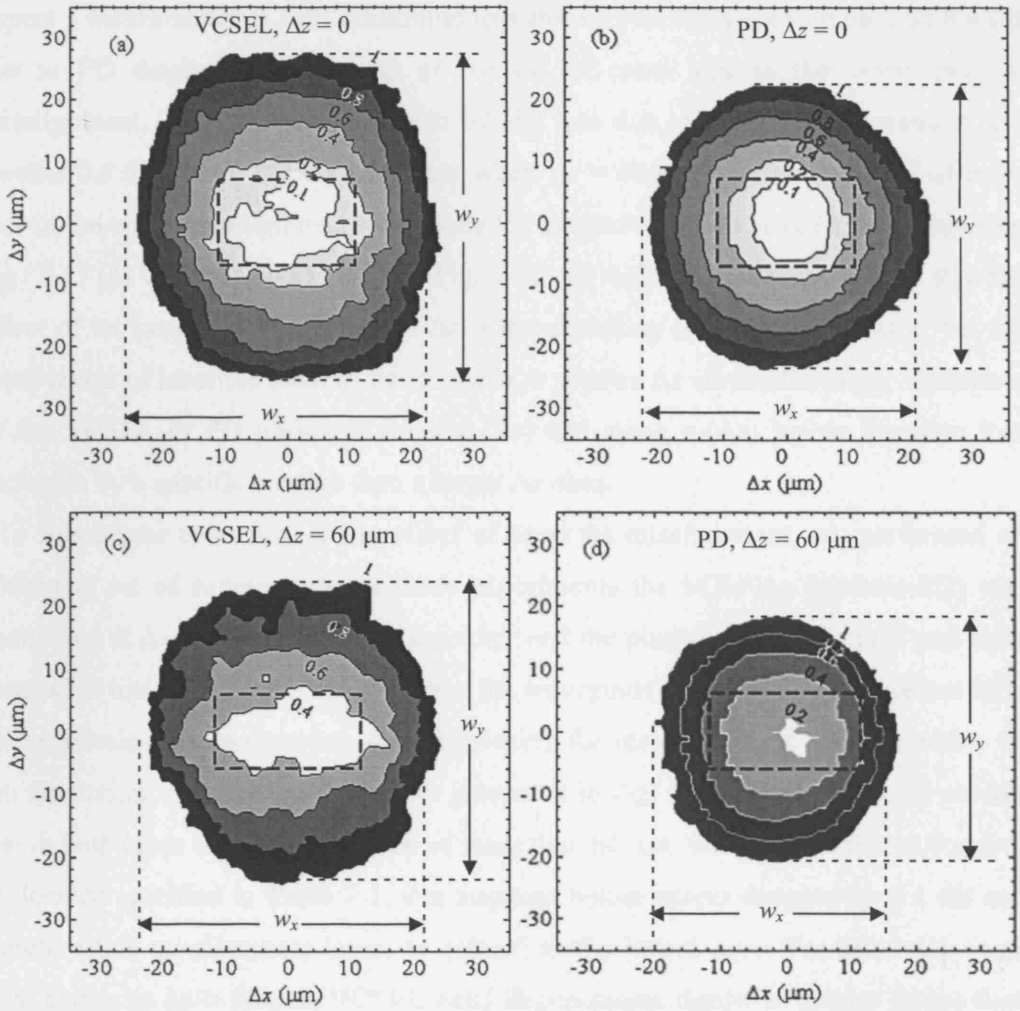

Fig. 7-13. (a) Contour map of relative insertion loss compared to the maximum coupling position for VCSEL misalignments along x and y (Δx, Δy) at $\Delta z = 0$. (b) Same for x and y, PD misalignments at $\Delta z = 0$. (c) Contour map of relative insertion loss for x and y, VCSEL misalignments at $\Delta z = 60$ μm. (d) Same for x and y, PD misalignments at $\Delta z = 60$ μm. Resolution step was $\Delta x = \Delta y = 1$ μm. Dashed rectangle in the middle of the maps corresponds to the expected relative insertion loss according to the manufacturing tolerances along x and y reported in Table 7-1 for our connector design.

To investigate the effect of PD misalignments, we exchanged the position of the PD and MT-plug on the motorized stages and repeated the experiments. We generated *xy*-contour maps of the relative insertion loss due to PD misalignment, Fig. 7-13 (b) (for $\Delta z = 0$ μm) and (d) (for $\Delta z = 60$ μm). The contour maps indicate the accuracy that the position of either the VCSEL or the PD should be controlled in order to achieve a targeted insertion loss. Therefore, from these graphs we can extract the requirements for a connector design. The dashed rectangles in the middle of Fig. 7-13 (a), (b), (c) and (d) indicate the maximum additional insertion loss due to the expected misalignments in Table 7-1 due to our connector design. As we see for $\Delta z = 0$ μm, we

expect a maximum of 0.2 dB additional loss due to VCSEL displacement and 0.4 dB due to PD displacement, a total of 0.6 dB of extra loss in the worst case of misalignment. These values change to 0.6 dB loss due to VCSEL displacement and another 0.6 dB due to PD displacement when Δz = 60 μm, a total of 1.2 dB of extra loss in the worst misalignment case along the dashed rectangular borders. Comparing Fig. 7-13 (a) with Fig. 7-13 (b), and Fig. 7-13 (c) with Fig. 7-13 (d), we see that the effect of an increased misalignment Δz is the shrinking of the contour maps, for the same levels of insertion loss. In other words, a smaller Δz allows for larger tolerances of the VCSEL or PD positions along x (Δx) and along y (Δy) before insertion loss increases by a specific amount than a larger Δz does.

To investigate even further the effect of axial Δz misalignment, we performed an additional set of experiments. In these experiments the MT-Plug (pinhole-PD) was positioned at $\Delta x = \Delta y = 0$, while at the other end the pinhole-PD (MT-plug) was butt-coupled to the waveguides. The power at the waveguide output was monitored as MT-plug (pinhole-PD) was moving axially covering the range $0 < \Delta z < 200$ μm with a 10 μm resolution step and the results are presented in Fig. 7-14. From Fig. 7-14 we see that in both cases an axial separation of more than 80 μm, well beyond the 12.5 μm of z tolerance specified in Table 7-1, was required before power dropped by 0.1 dB and therefore this misalignment is not as critical as the lateral *ones*. For relatively large axial distances $\Delta z > 80$ μm, VCSEL axial displacement results in greater losses than PD axial displacement. This can be readily explained after observing the far-field coming from the waveguide output, Fig. 7-15. A horizontal cross-section of the waveguide far-field revealed an angular divergence (full angle at e^{-2} of maximum intensity) of 13°, well below the 23° of the angular divergence measured for the VCSEL (Fig. 7-10 for I_{bias} = 3.3 mA). As the VCSEL is moving away (axially) from the waveguide, its emitted field keeps diffracting until for some certain z, the diffracted field's spot size becomes larger than the waveguide aperture and the power coupled into the waveguide reduces. The same occurs at the other side of the waveguide only that this time it is the field coming from the waveguide, which diffracts before being collected by the PD. Since the angular divergence of the VCSEL is larger than this of the waveguide, an incremental positional change Δz results in a larger expansion of the VCSEL spot size compared to the expansion of the waveguide spot size for the same Δz. Therefore, the larger angular divergence of the VCSEL far-field results in power dropping faster in the case where VCSEL moves

away from the waveguide compared to the power drop when PD moves away from the waveguide.

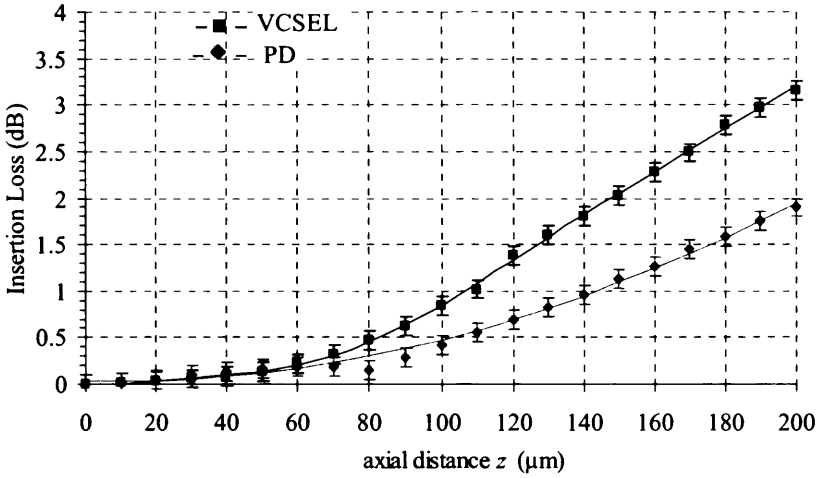

Fig. 7-14. Relative insertion loss of VCSEL and PD as they move away (along z) from the OPCB waveguides. Lateral position was set at the maximum coupling position, $x = y = 0$.

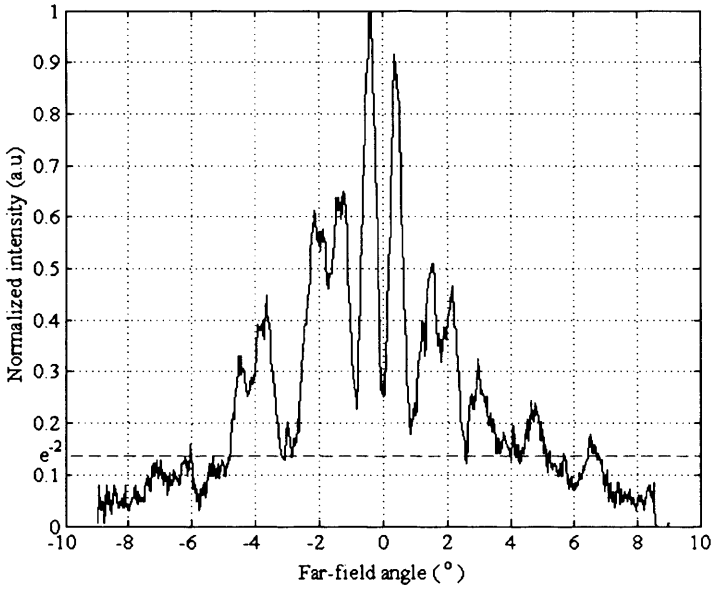

Fig. 7-15. Far-field coming from waveguide for I_{bias} = 3.3 mA which corresponds to 0 dBm of VCSEL emitted power. Far-field divergence (measured at e^{-2} from maximum power) is ~13°.

Contour maps like the ones presented in Fig. 7-13 are very useful for the construction of general design rules. In Fig. 7-16 (a) and (b) the diameter of the 1 dB contours along horizontal cut $\Delta x = 0$ (w_x), and vertical cut $\Delta y = 0$ (w_y) were drawn for both VCSEL and PD. These diameters were calculated after contour maps similar to those of Fig. 7-13 were composed for $0 < \Delta z < 100$ μm with a 20 μm step. From Fig. 7-16 (a) and (b) we see that VCSEL and PD 1 dB contour diameters remain almost constant in the region $0 < \Delta z < 40$ μm while in the rest of the region $60 < \Delta z < 100$

μm VCSEL curves drop faster than PD ones for the same amount of axial displacement z. This trend is similar to the one observed in Fig. 7-14 and again attributed to the higher divergence of the VCSEL field compared to the divergence of the field from the waveguide output. Fig. 7-16 simply reveals the amount of Δx and Δy misalignment allowed for a given Δz before insertion loss exceeds 1 dB. Therefore, they can serve as design rules for the connector tolerances. Of course, similar graphs can be generated for any insertion loss level.

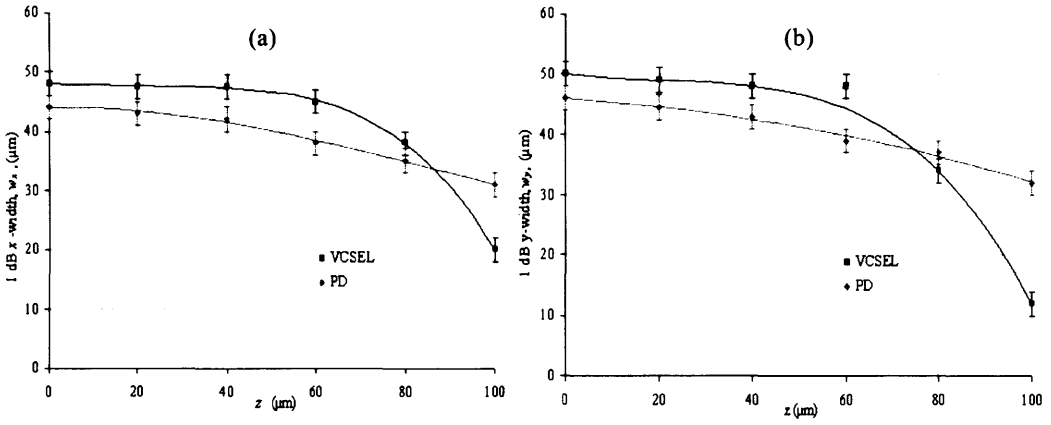

Fig. 7-16. (a) Plot 1 dB x-width, w_x, (horizontal cut of contour plots in Fig. 7-13) as a function of z for VCSEL source and PD. (b) Plot of 1 dB y-width, w_y, (vertical cut of contour plots in Fig. 7-13) as a function of z for VCSEL source and PD.

7.5.3 Loss Components

At best coupling position, the insertion loss was 4.4 dB – 4.8 dB without index matching fluid depending on the choice of waveguide and experimental conditions, such as the way the substrate was mounted. When index-matching fluid, n = 1.557 (n_{core} = 1.556), was applied results improved by 2.1 dB – 2.7 dB which is the loss due to Fresnel reflections and scattering from the waveguide entrance and exit faces. We note that the waveguides were diced but not polished in a low cost approach and they were quite rough with a ~250 nm RMS roughness [7.25]. Therefore, waveguide entrances and exits were relatively rough and therefore coupling loss was expected to be quite high.

Propagation loss due to material absorption and scattering from the sidewalls was calculated with the aid of three 1 m spiral waveguides made under the same conditions with our wafer, Fig. 7-17. Propagation loss measurements are summarized in Table 7-2 for the three spiral waveguides. The average propagation loss was measured to be $\alpha = 0.08 \pm 0.01$ dB/cm. Therefore, our 10 cm long waveguides exhibit

0.8 dB of loss in total due to propagation. This loss is higher than the usually quoted figure of 0.03-0.04 dB/cm for Truemode™ polymer [7.24]. This is likely to be because Exxelis Ltd., the company that fabricated the OPCB, moved clean rooms and the equipment had not been used for waveguide fabrication before and so, had not been characterized nor optimized. The higher loss may also be because the earlier figures were measured for 50 μm square waveguides rather than for our 70 μm square waveguides. If we remove Fresnel reflections / scattering and propagation loss from the insertion loss (2.1 dB – 2.7 dB when index matching fluid used), then the remaining 0.9 - 1.9 dB is the coupling loss between VCSEL and waveguide and between waveguide and PD.

Compared to other published work on waveguide connectors based on MT technology, an optimum insertion loss of 3.5 dB was reported for the active interposer in [7.2] but the authors did not report whether the waveguides used were polished. The authors in [7.3] reported a 1.6 dB insertion loss for their waveguide to waveguide connector but their waveguides were polished and active lateral alignment was used. A loss of 0.6 dB was reported in [7.10], for a multimode fibre to flexible film waveguide connector, with index matching fluid being used for their measurements and waveguides being polished. Finally, an insertion loss of 8 dB was reported for the backplane connector in [7.6], without index matching fluid. Therefore, when index matching fluid was used, our system's insertion loss was close to the lowest loss levels reported in the literature.

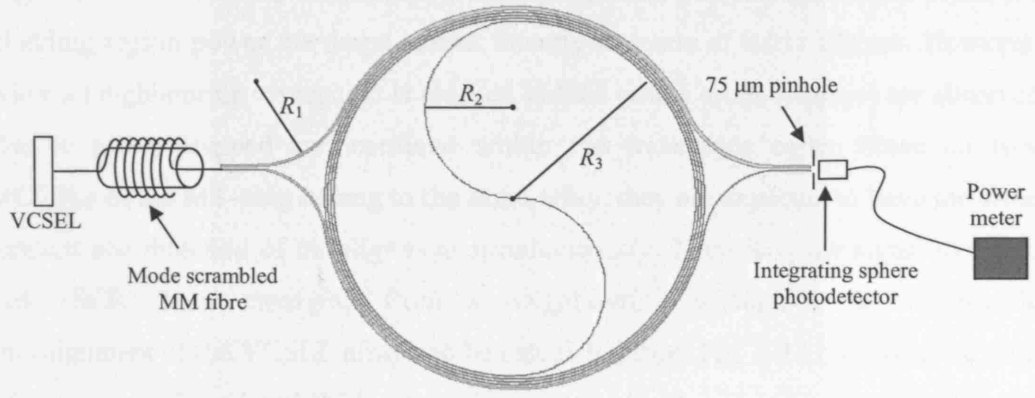

Fig. 7-17. 1m-spiral, 70 μm × 70 μm, waveguide used to measure propagation loss. The input-output waveguide bend radius was R_1 = 18 mm, the S-shape radius was R_2 = 16 mm, while the external ring radius was R_3 = 32 mm. These values were ensuring minimization of the waveguide bend transition loss according to Chapter 3. VCSEL light was coupled to the spiral waveguide through a MM mode scrambled fibre. A 75 μm pinhole at the waveguide output spatially filtered cladding light out allowing an integrating sphere photodetector to collect light from the waveguide core only.

TABLE 7.2

PROPAGATION LOSS IN SPIRAL WAVEGUIDES

Spiral 1 α_1 (dB/cm)	Spiral 2 α_2 (dB/cm)	Spiral 3 α_3 (dB/cm)	Average α (dB/cm)
0.089	0.076	0.077	0.081 ± 0.007

7.5.4 Misaligned Cross – Talk and SNR Discussion

Misaligned components not only contribute to insertion loss but also to cross-talk which may substantially limit performance of high-bit rate systems. In order to examine cross-talk in our system, the following experiment was performed. One VCSEL of the MT-plug was positioned at $\Delta y = 0$, $\Delta z = 0$ in front of a waveguide (named 0th waveguide in Fig. 7-18). Then the VCSEL was moved laterally in the range $-300\ \mu m < \Delta x < 1600\ \mu m$ in 1 μm steps, while the power at the end of the 0th waveguide was monitored at every step. Since the waveguide lateral separation is 250 μm we covered the whole region between one waveguide to the left and six waveguides to the right of the 0th. For as long as our VCSEL was scanning within the boundaries of the 0th waveguide, the recorded power corresponded to the power coupled into this waveguide as a function of the lateral misalignment, Δx. However, when the VCSEL was scanning the core area of the waveguides adjacent to the 0th waveguide, the detected power corresponded to the cross-talk originating from the other VCSELs of the same array that would be coupled to these waveguides. From Fig. 7-18 we see that as VCSEL moves away from the 0th waveguide and enters the cladding region power the drops almost linearly at a rate of 0.011 dB/μm. However, when a neighbouring waveguide is reached sudden power drops (valleys) are observed due to power trapped and confined within the waveguide cores. Since all four VCSELs of the MT-plug belong to the same array, they are expected to have the same amount and direction of misalignment simultaneously. Therefore, the signal to cross-talk (SCR) level emerging from a neighbouring waveguide for a specific misalignment of the VCSEL array can be calculated from Fig. 7-18 by taking the ratio of the power when the VCSEL is emitting into the waveguide of interest (0th) to the power detected when the VCSEL has been moved to the same position relative to the centre of the core in the neighbour waveguide. According to this assertion, the lowest cross-talk levels are achieved when perfect alignment occurs between VCSELs and waveguides as can be seen from Fig. 7-18. As the VCSELs move away from the

centre of the other waveguides while still remaining in the core area the received power increased, indicating worsening of cross-talk.

In Fig. 7-19 (a) we have plotted the cross-talk that the 0^{th} waveguide will suffer from each one of its six neighbouring waveguides, calculated as explained above. Fig. 7-19 (a) clearly shows that the nearest to the 0^{th} waveguide contribute more cross-talk than the more remote ones. In a real system cross-talk from all neighbouring waveguides combine. The aggregate *SCR* for the arrangement of our prototype connector design is shown in Fig. 7-19 (b). Not all of the waveguides in our system are expected to have the same *SCR*. The waveguides which are against the two external VCSELs of the array (numbered 1 and 4 in Fig. 7-1) have only one immediate waveguide next to them that can contribute to cross-talk. On the other hand, waveguides which are against the two middle VCSELs (2 and 3 in Fig. 7-1) have two immediate waveguides next to them, one on each of side of them and, therefore, will suffer from more cross-talk (or equivalently less *SCR*). Two curves are shown in Fig. 7-19 (b), one for the waveguides of VCSELs 1 and 4, and one for waveguides of VCSELs 2 and 3. At perfect alignment *SCR* is 17.76 dB for waveguide 2 and 3 and 19.46 dB for waveguide 1 and 4. The *SCR* at worst estimated misalignment, taken from Table 7-1, is 17.43 dB for waveguide 2 and 3 and 19.07 dB for waveguide 1 and 4. To the best of our knowledge, these are the first results of cross-talk reported in optical backplane systems as a function of source misalignment. Note that in real systems cross-talk might be a bit different to the ones measured here. This is because the beams from multiple lasers interfere at the waveguide output facets creating fringes which might affect the measured bit error rate.

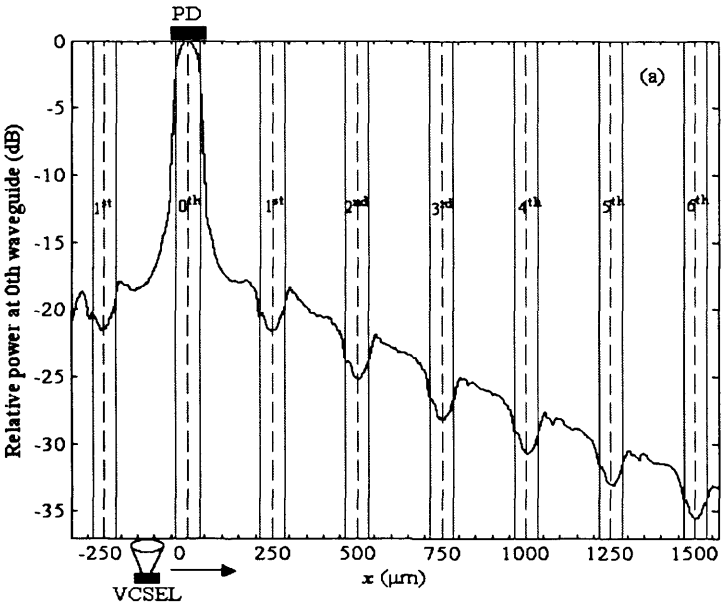

Fig. 7-18. Power received at the end of 0th waveguide as a function of the lateral distance of the VCSEL from its center. The boundaries and the centres of the waveguides on the backplane are marked. In the cladding power drops at a rate of 0.011 dB/μm.

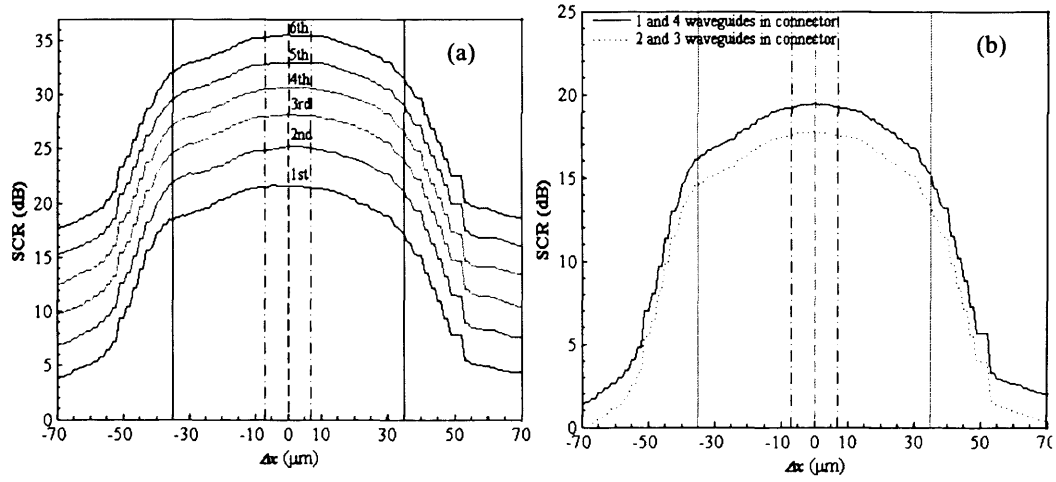

Fig. 7-19. (a) Signal-to-cross-talk (SCR) levels that 0th waveguide experiences from its adjacent waveguides. (b) SCR experienced by waveguides number 1 and 4 and of waveguides number 2 and 3 from the array of four in the connector if all were in use. Dashed-dot lines determine the boundaries of the maximum expected cross-talk based on current connector tolerances.

7.5.5 Repeatability

We measured insertion loss and cross-talk for the best channel in our prototype connector design as we engaged the MT-socket into the MT-plug 75 times, Fig. 7-20 (a). For the insertion loss measurements, only one VCSEL (VCSEL 1 in Fig. 7-1) was switched on and set to 0 dBm output power, while the other three VCSELs in the

array were switched off. The average insertion loss measured was 5.19 ± 0.16 dB. The histogram of insertion loss shown in Fig. 7-20 (b) has the usual form of a one-sided Gaussian [7.16], [7.32] of a well aligned connector. The most frequently encountered insertion loss was in the range of 5.1 – 5.2 dB. This variation agrees well with that expected from the contour maps values, Fig. 7-13, within the worst estimated misalignment. The standard deviation of insertion loss achieved by our connector was 0.16 dB, which is better than the 0.34 dB reported in [7.10] and comparable to the 0.12 dB in [7.32] although both [7.10] and [7.32] refer to single mode systems.

For the cross-talk measurements, we switched VCSEL 1 off while the other three VCSELs (2-4) were switched on and each set to 0 dBm output power. Therefore, the combined cross-talk of the three VCSELs was recorded. The average received cross-talk was -19.95 ± 0.27 dB in close agreement with values obtained from Fig. 7-19 (b) at the worst estimated misalignment.

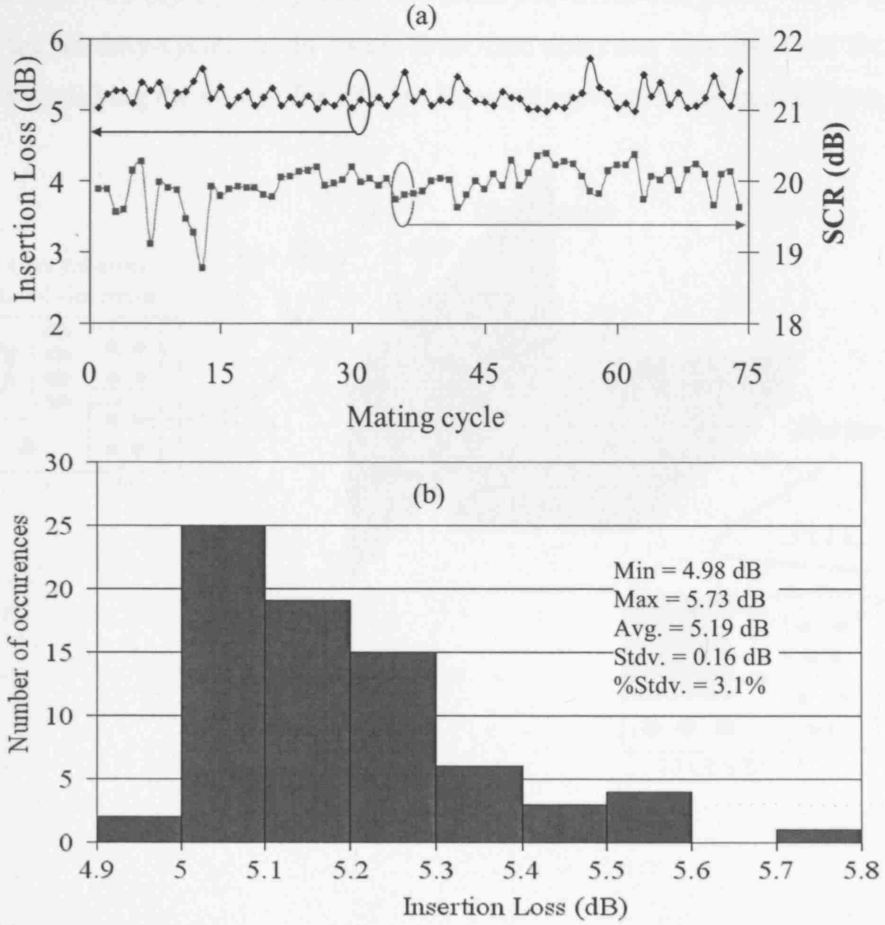

Fig. 7-20. (a) Insertion loss and signal to cross-talk (SCR) as a function of mating cycle for 75 engagements. (b) Histogram of insertion loss.

7.5.6 High-Speed Data Measurements

In addition to the DC experiments described in the previous sections, we measured the bit error rate (BER) performance of our system at 10 Gb/s data transmission. For our BER tests we used the configuration shown in Fig. 7-21 (a). 10 Gb/s Ethernet data generated by an Ethernet protocol generator were coupled into a MM fibre. The pattern randomness bit sequence (PRBS) was 10^{-21}. The fibre was plugged onto an XFP (10 Gb/s Small Form Factor Pluggable) transceiver integrated into the daughtercard of our prototype connector design. After the optical to electrical transformation at the XFP, data were fed to the laser driver circuits, which modulated one of the four available VCSELs. Light generated was then coupled into one of the backplane waveguides and collected at the other end from a MM fibre, which was connected, to the receiver of the bit error rate tester (BERT). With this arrangement, we were able to test individual channels only. Typical eye-diagrams obtained are shown in Fig. 7-21 (b). Eye-diagrams were clean with measured jitter < 38 ps (or less 38% of the bit duty-cycle), in all cases. Error-free operation was observed for more than 48 h qualifying the system for 10 Gb/s Ethernet protocol based applications.

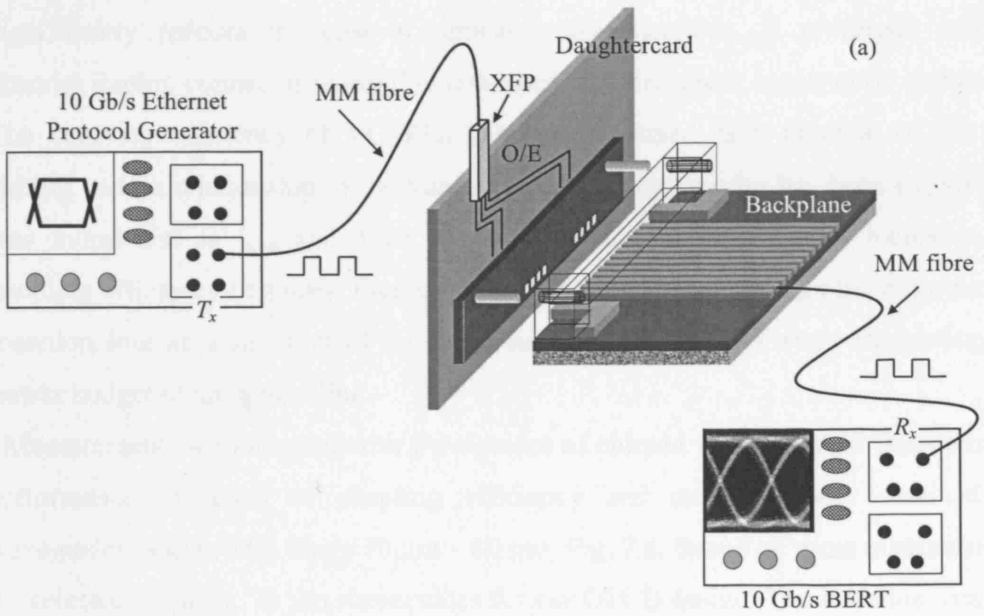

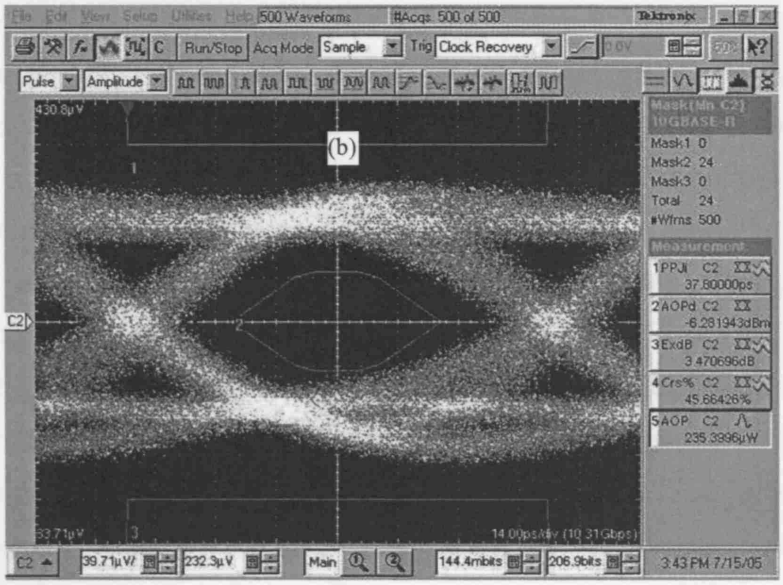

Fig. 7-21. (a) Experimental set-up for BER measurements. (b) Eye-diagram at 10 Gb/s.

7.6. CONCLUSIONS

A passive, precision, self-alignment technique has been reported for coupling arrays of VCSELs and photodiodes to an array of buried channel waveguides, which significantly reduces the cost of optical interconnections. A prototype multiple channel duplex connector using this approach was designed, constructed and tested. The coupling efficiency of VCSELs has been assessed as a function of the bias current and its relationship to the transverse laser cavity modes has been explored. It was found that as I_{bias} and, thus, the number of transverse modes increases, the coupling efficiency degrades. Figure 6-8, which shows the coupling efficiency and the insertion loss as a function of I_{bias}, can serve as a guideline when calculating the power budget of an optical link.

Measurements with a board with waveguides of chirped width showed that optimum performance in terms of coupling efficiency and cross-talk was obtained for waveguides in the width range 70 µm – 80 µm, Fig. 7.8. Based on these measurements we selected 70 µm × 70 µm waveguides for our OPCB design. The insertion loss was measured and at best was found to be 4.4 dB total or 3.6 dB if propagation loss is calibrated out. This was reduced to 0.9 - 1.9 dB of loss, depending on the waveguide, by using index matching fluid. In a practical system there is therefore the potential to reduce the loss by this amount by polishing, optimizing the dicing process and use of

sufficient contact force.

The variation of optical coupling loss as a function of mechanical misalignments in x, y and z of both the laser source and of the photodetector were measured to assess how much misalignment may be permitted. The proposed self-alignment technique was estimated to have at worst tolerances in x $\Delta x = \pm 11$ μm, in y $\Delta y = \pm 7$ μm and in z $\Delta z = +12.5$ μm, which were shown to cause less than 0.2 dB additional insertion loss for the VCSEL and less than 0.4 dB additional insertion loss for the PD, Fig. 7-13. However, these tolerances are reproducible and with proper design could reduced to $\Delta x = \pm 6$ μm, $\Delta y = \pm 7$ μm and $\Delta z = +10$ μm. Insertion loss increases slowly with axial, z, offsets to 80 μm, but increases at increasing rates beyond this. The loss due to PDs however, does not increase so quickly with distance, Fig. 7-16. PDs are less sensitive to z but more sensitive to x and y misalignments due to the narrow 13° divergent beam from the waveguide and their 75 μm diameters in contrast to VCSELs due to their wider 23° divergent beam and 7 μm diameters.

The signal to cross-talk ratio (*SCR*) was found to decrease as the VCSEL was moved away from its perfectly aligned position. When VCSEL was aligned, *SCR* was 19.46 dB, dropping to 19.07 dB when moved to the worst position specified by the connector tolerances, Table 7-1, for the waveguides at the edge of the group of four. *SCR* was 17.43 dB at alignment and 17.76 dB at worst position for the middle waveguides on the board. Ideally, the cross-talk should be 10 dB better than this so cross-talk suppression measures must be developed for the nearest neighbour waveguides. Alternatively, since experiments with index matching fluid showed significant improvement of cross-talk, waveguides could be polished after dicing them. These were the first recorded measurements of cross-talk between adjacent and near neighbour waveguides when the connector is misaligned, which is crucial as this is on of the main reasons this technology is being considered for replacing copper tracks.

During 75 repeated attaching and detaching cycles of the connector the insertion loss was 5.19 ± 0.16 dB and the cross-talk was -19.95 ± 0.27 dB, Fig. 7-20, in reasonable agreement with the value, 19.43 dB, for the same waveguide obtained from misaligned insertion loss measurements at the worst estimated misalignment, giving a low variation and good reproducibility. To the best of our knowledge, these were also the first results of loss distribution after mating cycle reported for PCB connectors

based on MT. Finally, we demonstrated error free operation for more than 48h with clean eye-diagrams, Fig. 7-21.

REFERENCES

[7.1] International Electronics Manufacturing Initiative (iNEMI), "Cost analysis: Copper vs. optical backplanes, available at http://www.onboard-technology.com/pdf_settembre2005/090502.pdf, last time accessed 31/12/2007.

[7.2] S. Hiramatsu, and T. Mikawa, "Optical design of active interposer for high-speed chip level optical interconnects," *J. Lightw. Technol.*, vol. 24, pp. 927-934, Sep. 2006.

[7.3] S. Hiramatsu, and M. Kinoshita, "Three dimensional waveguide arrays for coupling between fibre-optic connectors and surface-mounted optoelectronic devices," *J. Lightw. Technol.*, vol. 23, pp. 2733-2739, Sep. 2005.

[7.4] G. V. Steenberge, P. Geerinck, S. V. Put, J. V. Koetsem, H. Ottevaere, D. Morlion, H. Thienpont, and P. V. Daele, "MT-compatible laser-ablated interconnections for optical printed circuit boards," *J. Lightw. Technol.*, vol. 22, pp. 2083-2090, Sep. 2004.

[7.5] C. Choi, L. Lin, Y. Liu, J. Choi, L. Wang, D. Haas, J. Magera, and R. T. Chen, "Flexible optical waveguide film fabrications and optoelectronic devices integration for fully embedded board-level optical interconnects," *J. Lightw. Technol.*, vol. 22, pp. 2168-2176, Sep. 2004.

[7.6] B. S. Rho, H. S. Cho, H.-H. Park, S.-W. Ha, and B.-H. Rhee, "PCB-compatible optical interconnection using 45°-ended connection rods and via-holed waveguides," *J. Lightw. Technol.*, vol. 22, pp. 2128-2134, Sep. 2004.

[7.7] T. Sakamoto, H. Tsuda, M. Hikita, T. Kagawa, K. Tateno, and C. Amano, "Optical interconnection using VCSELs and polymeric waveguide circuits," *J. Lightw. Technol.*, vol. 22, pp. 2083-2090, Sep. 2004.

[7.8] K. Katsura, M. Usui, N. Sato, A. Ohki, N. Tanaka, N. Matsuura, T. Kagawa, K. Tateno, M. Hikita, R. Yoshimura, and Y. Ando, "Packaging for a 40-channel parallel optical interconnection module with an over-25-Gbit/s throughput," *IEEE Trans. Adv. Packag.*, vol. 22, pp. 551-560, Nov. 1999.

[7.9] K. Byoung, I.-K. Cho, S. H. Ahn, M. Y. Jeong, D. J. Lee, Y. U. Heo, B. S. Rho, H.-H. Park, and B.-H. Rhee, "Optical backplane system using waveguide-embedded PCBs and optical slots," *J. Lightw. Technol.*, vol. 22,

pp. 2119-2127, Sep. 2004.

[7.10] M. Hikita, R. Yoshimura, M. Usui, S. Tomaru, and S. Imamura, "Polymeric optical waveguides for optical interconnection," *Thin Solid Films*, vol. 331, pp. 303-308, 1998.

[7.11] M. Hikita, S. Tomarum K. Enbutsu, N. Ooba, R. Yoshimura, M. Usui, T. Yoshida, and S. Imamura , "Polymeric optical waveguide films for short-distance optical interconnects," *IEEE J. Sel. Top. Quantum. Electron*, vol. 5, pp. 1237-1242, Sep/Oct 1999.

[7.12] H. Kosaka, M. Kajita, M. Yamada, and Y. Sugimoto, "A 16 × 16 optical full-cross-bar connection module with VCSEL-array push/pull module and polymer-waveguide coupler connector," *IEEE Photon. Technol. Lett.*, vol. 9, pp. 244-246, Feb. 1997.

[7.13] M. Schmatz, B. J. Offrein, K. Vey: (2005, April 25). "Optical Interconnects: Intra-system data transfer with light," Available: http://www.zurich.ibm.com/pdf/sys/Optical_Interconnects @IBM-ZRL_2005-04_E.pdf. Last time accessed 16/06/07.

[7.14] J. Moisel, J. Guttman, H.-P. Huber, O. Krumpholz, M. Rode, R. Bogenberger, and K.-P. Kuhn, "Optical backplanes with integrated polymer waveguides", *Opt. Eng.*, vol. 39, pp. 673-679, March 2000.

[7.15] www.xyratex.com/technology/white-papers.aspx, "Pluggable optical backplane technology", white paper, last time accessed 20/02/2008.

[7.16] S. Nagasawa, Y. Yokohama, F. Ashiya, and T. Satake, "A High-Performance Single-Mode Multifibre Connector Using Oblique and Direct End-Face Contact between Multiple Fibres Arranged in a Plastic Ferrule," *J. Lightw. Technol.*, vol. 13, pp. 987-994, Jun. 1995.

[7.17] M. Takaya, and K. Shibata, "Design and performance of very-high-density 60-fibre connectors," *J. Lightw. Technol.*, vol. 21, pp. 1549-1556, Jun. 2003.

[7.18] M. Kihara, S. Nagasawa, and T. Tanifuji, "Design and Performance of an Angled Physical Contact Type Multifibre Connector," *J. Lightw. Technol.*, vol. 14, pp. 542-548, Apr. 1996.

[7.19] K. Tatsuno, K, Harada, K. Yoshida, S. Takahashi, H. Naka, S. Gardner, D. Spear, and J. Severn, "Fibre-Pigtail_detachable Plastic MiniDIL Trasnmitter Module With a Tool-Free Optical Connector," *J. Lightw. Technol.*, vol. 21,

pp. 1066-1077, Apr. 2003.

[7.20] TIA-604-5. Fibre Optic Connector Intermateability Standard, Type MPO.

[7.21] C. Fu, R. C. Brown, and C. Ume, "Temperature-dependent material characterizations for thin epoxy FR-4/E-Glass woven laminate," *in Proc. 43rd Electronics Components and Technology Conf.*, Orlando, 1993, pp. 560–562.

[7.22] MIL-P-13949. Military specification for plastic sheet, laminated, metal-clad for printed wiring board. Available: http://www.thetestlab.com/data/13949_ss.pdf.

[7.23] N. Suyal, Exxelis Ltd., private communication, Jul. 2006.

[7.24] Exxelis Ltd., "TruemodeTM wet film datasheet". Available at http://www.exxelis.com/products/truemode.php. Last time accessed 16/06/07.

[7.25] A. Graham, "Novel optoelectronic devices for guided-wave and free-space optical interconnects," PhD thesis, School of Engineering and Physical Sciences, Herriot-Watt Univ., Edinburgh, Scotland, UK, Apr. 2005.

[7.26] ULM photonics, 10 Gb/s VCSEL array data-sheet. Available at http://www.ulm-photonics.de/docs/products_new/datasheets/VCSEL-ULM850-10-chips.pdf. Last time accessed 16/06/2007.

[7.27] Microsemi corporation, LX3045 10 Gb/s coplanar GaAs PIN photodiode data-sheet. Available at http://www.microsemi.com/datasheets/lx304x.pdf. Last time accessed 16/06/2007.

[7.28] J. Heinrich, E. Zeeb, and K. J. Ebeling, "Butt-Coupling Efficiency of VCSEL's into Multimode Fibres," *IEEE Photon. Technol. Lett.*, vol. 9, pp. 1555-1557, Dec. 1997.

[7.29] Y. Wakazono, K. Kikuchi, A. Suzuki, K. Suzuki, S. Suzuki, T. Yamaguchi, H. Nakagawa, M. Aoyagi and O. Ibaragi, "Fundamental analysis of VCSEL emission for evaluation of optical coupling," *Proc. of the 7th Electron. Packag. Technol. Conf.*, pp. 380-383, Singapore, 7-9 Dec. 2005.

[7.30] K. J. Knopp, D. H. Christensen, G. V. Rhodes, J. M. Pomeroy, B. B. Goldberg, and M. S. Unlu, "Spatio-Spectral Mapping of Multimode Vertical Surface Emitting Lasers," *J. Lightw. Technol.*, vol. 17, pp. 1429-1435, Aug. 1999.

[7.31] V. N. Morozov, J. A. Neff, and H. Zhou, "Analysis of Vertical-Cavity Surface-Emitting Laser Multimode Behavior," *IEEE J. Quantum. Electron.*, vol. 33, pp. 980-988, 1997.

[7.32] Timothy S. Barry, Daniel L. Rode, Marcelo H. Cordaro, Robert R. Krchnavek, and Kenichi Nakagawa "Efficient Multimode Optical Fibre-to-Waveguide Coupling for Passive Alignment Applications in Mutlichip Modules," *IEEE Trans. on Components, Packaging and Manufacturing Technology – Part B*, vol. 18, pp. 685-690, Nov. 1995.

CHAPTER 8

CONCLUSIONS AND FUTURE WORK

8.1. SUMMARY - CONCLUSIONS

The subject of this thesis has been the investigation of board-to-board 10 Gb/s parallel optical interconnects for backplane applications. In particular, our focus has been on polymer multimode buried channel waveguides embedded in FR4 printed circuit boards (PCBs) to realize optical links, and on 1D arrays of 10 Gb/s Vertical Cavity Surface Emitting Lasers (VCSELs) for the optical transmission sources. Throughout our work, we followed a hybrid approach, which combined designing and performing appropriate experiments to investigate important practical aspects of optical interconnects (Chapter 4 and Chapter 7), as well as extending existing theories in order to understand light propagation in multimode waveguides (Chapter 5 and Chapter 6).

Chapter 1 introduced this thesis and gave the motivation behind the work carried out on optical backplanes. Chapter 2 reviewed the most important projects in optical interconnections worldwide with emphasis on the manufacturing technologies and materials used, and it summarized their outcomes. Chapter 3 introduced the intrinsic mode theory and the coupled mode and coupled power theories, which were used as the basis for the analysis of modal propagation in tapered waveguide bends in Chapter 5 and in waveguides with sidewall roughness in Chapter 6.

Chapter 4 analyzed the insertion loss introduced by curved multimode polymer waveguides. We experimentally measured the insertion loss of a series of nested waveguide bends for three different waveguide widths (w = 50 μm, w = 75 μm, w = 100 μm) and core-cladding refractive index difference Δn = 0.0296 (= 1.9% of core index). The thickness of the waveguides was d = 50 μm constant, and the radii of curvature under investigation varied in the range 5.5 mm < R < 34.5 mm. Our experiments showed that the optimum bend radius for polymer waveguide backplanes, Fig. 4-3, Table 4.1, was 13.5 mm for 50 μm × 50 μm waveguide cross-sections giving 0.73 dB loss, 15.3 mm for 75 μm × 50 giving 0.84 dB loss and 17.7 mm for 100 μm × 50 giving 1.16 dB loss. The

wider waveguides appear to have higher insertion loss than the narrower ones. It is inadvisable to have much smaller radii of curvature than ~10 mm since loss increases quickly as the radius is reduced, although if very tight bends are required to meet layout constraints then Fig. 4-4 can be used as a design curve to establish the loss for the link power budget calculation. Our beam propagation method (BPM) simulations showed that for small radii of curvature (R < 10 mm), the dominant loss component in the waveguide bend system, is the transition loss at the junction between the straight waveguide and the waveguide bend. However, as the radius increased the contribution of the rest of the loss factors were growing in importance, until for large radii of curvatures (R > 20 mm) the propagation loss took over as the main loss component. Our geometric optics model showed that the numerical aperture (NA) of a bend waveguide is not held constant but it varies across a bend waveguide cross-section along the in-plane direction. The NA of the waveguide bend equals the NA of an equivalent straight waveguide at the outer edge of the bend but it reduces as we move towards the inner edge of it. This mismatch between the NA of the straight waveguide and the NA of the waveguide bend is responsible for the transition loss at their junction. Using the fact that as the radius of curvature of a waveguide bend increases, its length increases proportionally, we calculated the propagation loss for all three waveguide widths. In doing so, we assumed that the propagation loss is uniform among straight and bend waveguides and independent of the radius of curvature for at least the waveguides with large radii (R > 20 mm). The calculated propagation loss was 0.129±0.041 dB/cm for the 50 μm × 50 μm waveguides, 0.124±0.040 dB/cm for the 75 μm × 50 waveguides and 0.117±0.060 dB/cm for the 100 μm × 50 waveguides, Table 4.3.

Chapter 5 introduced a novel waveguiding component, which we called the tapered bend. This component combined a waveguide taper with a waveguide bend, and compared to a straight taper - waveguide bend combination is more space efficient. The first half of Chapter 5 was dedicated to the theoretical investigation of adiabatic modal propagation in 2D tapered bends. Two types of adiabatic modes propagate inside the tapered bend, the whispering gallery modes and the non-whispering gallery modes. A mode, which starts as a whispering gallery (5.84), undergoes two successive transformations as it propagates inside a tapered bend. As the width of the waveguide

decreases, it firstly converts to the non-whispering gallery type (5.93), and as the width decreases even further, it eventually goes beyond cut-off and it starts radiating into the cladding (5.94)-(5.97). In contrast, a non-whispering mode undergoes one transformation only as it propagates, from guided to beyond cut-off. As an adiabatic whispering gallery mode transforms to the non-whispering gallery one, the caustic of the field (point where fields change propagation direction) is moving from inside the core towards the cladding. WKB solutions however, are singular at the region of the caustic and the transition process is described by replacing the fields with the more general Airy functions (5.98). The transition from a mode that is bound, to a mode that is beyond cut-off, is equivalent to WKB waves approaching the critical angle of total internal reflection on the waveguide boundaries. However, the critical angle corresponds to a branch-point of the phase reflection coefficient (5.13) and the saddle-point approximation of the integrals (5.8) involves a branch-cut. This branch-cut integral leads to another set of Airy functions (5.94), (5.95) to describe this transition process. Probably the two most important features of the adiabatic mode are its amplitude (5.82), (5.86) and its phase evolution (5.83), (5.92) inside the taper. From (5.86) we see that the amplitude of the tapered bend is not constant but instead it adjusts itself as the mode propagates to adapt to the local waveguide environment. Finally, in (5.92) it was proved the intuitively expected result; the phase of the adiabatic mode at a certain waveguide cross-section is analogous to the propagation constant of the local waveguide mode taken at the same cross-section. The second half of Chapter 5 presented our experimental results for a number of tapered bends with varying taper ratios (defined as the ratio of input to output width). These experiments investigated the additional insertion loss that tapered bends introduced and the amount of improvement to the source misalignment tolerance that they exhibited, compared to simple waveguide bends of similar widths. Tapered bends were also compared to straight tapers plus bends of similar taper ratios. The tapered bends that we analyzed had all fixed input width w_{in} = 50 μm, typical for multimode waveguides aimed at backplane applications, and variable output width w_{out} = 10 μm, 20 μm, 25 μm, 30 μm and 40 μm, giving corresponding taper ratios TR = 0.2, 0.4, 0.5, 0.6 and 0.8. The radius of curvature of the tapered bends varied in the range 5 mm < R < 35 mm. Our measurements showed that the insertion loss for the tapered bends was always worse than

the insertion loss of the simple waveguide bends for all *TR* and radii of curvature, Fig. 5-15. In addition, as *TR* decreased the insertion loss performance of the tapered bends was worsening. Tapered bends with $TR > 0.5$ however, exhibited less than 2 dB of higher insertion loss compared to the insertion loss of the waveguide bends, for any radius of curvature, Fig. 5-15. Depending on the power budget of the links, these levels of insertion loss can be tolerable and tapered bends can be utilized. Compared to the straight taper – waveguide bend combination, tapered bends exhibited slightly better insertion loss performance for the *TR*s of interest ($TR > 0.5$), Fig. 5-16, and so they should be preferred over them in a system design. Regarding the misalignment tolerance experiments, Fig. 5-19, we found that the gain in misalignment tolerance increased as the taper ratio of the tapered bends increased. More specifically, the Full Width at Half Maximum (FWHM) of the insertion loss versus misalignment curve for the tapered bend with $TR = 0.4$ (input width 50 μm, output width 20 μm) was 40 μm, compared to only 17 μm for the waveguide bend with both input and output width of 20 μm. This means that in the case of the tapered bend, the input field was allowed to be misaligned by an extra 23 μm compared to the simple waveguide bend case, before the insertion loss curve dropped by 3 dB from its optimum value. However, as shown in Fig. 5-20 this gain in misalignment tolerance came to the cost of higher optimum insertion loss. Taking again for example the tapered bend with $TR = 0.4$, its optimum insertion loss is 1.2 dB higher than this of the waveguide bend although as we said it is more resistant to source misalignments by 23 μm. As *TR* increased, the misalignment tolerance gain for the tapered bend dropped but its optimum insertion loss got closer to this of the waveguide bend. For example, the values for extra misalignment tolerance and extra optimum loss were 7 μm and 0.3 dB respectively for a tapered bend with $TR = 0.8$ (input width 50 μm, output width 40 μm) compared to a waveguide bend with a 40 μm input and a 40 μm output. Our graphs 5-15, 5-16 and 5-21 analyzing the insertion loss, the misalignment tolerance, and their trade-offs can be used as design rules by optical backplane designers.

The subject of Chapter 6 has been the investigation of modal propagation in buried channel waveguides under the influence of the randomly deformed waveguide sidewalls. At first, we developed a novel method to calculate the radiation modes in buried channel waveguides, Section 6.3, which extended an existing method based on the Fourier

decomposition method [6.21], for bound modes. Our method was validated by generating the radiation modes of a slab waveguide and by comparing them to the existing analytical solutions, Fig 6-8, Fig. 6-9. The comparison showed excellent agreement between the constructed from our method radiation modes and the analytic slab radiation modes. In addition, we customized Marcuse's coupled mode and power theories to the special case of buried channel waveguides, section 6.5. The expressions of the coupling coefficients (6.69)-(6.70) and (6.73), leaded us to conclude that for waveguides with 1D sidewall deformation, even - even modes can only couple to each other and to odd – even modes. Similarly odd – odd modes can only coupled to each other and to even – odd modes. Based on this observation, we have proposed for the first time that two independent and uncorrelated modal power distributions exist at equilibrium. Finally, in section 6.6 we combined the radiation modes calculated by our method with the coupled mode theory and examined multimode propagation in a 20 μm × 20 μm buried channel waveguide with physical parameters, λ = 850 nm, n_{cl} = 1.5560, and n_{co} = 1.5249. Particularly, we were interested in investigating the steady state propagation loss, the equilibrium distance, and the distribution of power at the equilibrium, as the statistical properties of the waveguide roughness, namely its standard deviation S_d and its autocorrelation length L_c, varied. For a waveguide with L_c = 4 μm and standard deviation in the range 10 nm < S_d < 100 nm our calculations showed, Fig. 6-18, that as the standard deviation increased propagation loss also increased, for both even – even / odd – even and odd – odd / even – odd symmetry ensembles. In contrast, equilibrium length followed the opposite trend and decreased as standard deviation increased. For example, for S_d = 10 nm the propagation loss for the even – even / odd - even ensemble was 0.0008 dB/cm and the equilibrium length 67.6 m. For the same S_d, the propagation loss was 0.0007 dB/cm and the equilibrium length 78 m for the odd – odd / even – odd ensemble. The propagation loss and the equilibrium length values for S_d = 100 nm were 0.076 dB/cm and 0.97 m for the even – even / odd - even ensemble, and 0.069 dB/cm and 1.73 m for the odd – odd / even - odd ensemble correspondingly. The last property that we examined was the power distribution at equilibrium. Our calculations predicted that for the whole range of standard deviations and autocorrelation lengths that we considered, dual mode operation occurs with one mode from each symmetry ensemble to be surviving. The first even –

even mode $\beta = 11.50\ \mu m^{-1}$ dominates in the even – even / odd – even symmetry set, while the first even – odd mode with $\beta = 11.4970\ \mu m^{-1}$ dominates in the odd – odd / even – odd modal symmetry set, Fig. 6-20. Since our analysis showed that the equilibrium distances are out of the reach of optical backplane sizes (max 1m), the problem of multimode propagation should be examined at the transition region.

Chapter 7 presented our novel passive, precision, self-alignment technique for coupling VCSEL and photodiode arrays to buried channel waveguide arrays embedded on FR4 PCBs. Our alignment method tolerances were calculated to be 6 μm horizontally, 7 μm of vertically and 12 μm axially. The proposed alignment method significantly reduces the cost of optical interconnections and although demonstrated here for single optical layer printed circuit boards it can be used in multilayer, as well as in flexible PCBs. A prototype multiple channel duplex connector using this approach was designed, constructed and tested. The VCSEL sources used in our demonstrator were characterized, and their coupling efficiency to the PCB waveguides was measured. The threshold current of the VCSELs was measured at $I_{th} \sim 0.8$ mA. Power saturation started occurring for $I_{bias} > 9$ mA. The experiments of the coupling efficiency versus bias current, Fig. 7-2, revealed that the coupling efficiency significantly dropped as the bias current increased. For example, the coupling efficiency was 52% at the threshold current $I_{th} = 0.8$ mA but dropped to 33% when the bias current increased to $I_{bias} = 5$ mA, and to 25% when the bias current increased to $I_{bias} = 10$ mA. Non-return-to-zero (NRZ) transmission, which is usually employed in optical backplane links, uses higher drive currents to represent 1s than the drive currents it uses to represent 0s. Therefore, according to our measurements 1s will suffer from higher insertion loss than 0s, an effect, which has to be taken into account in a system design. The insertion loss for all demonstrator channels was measured, and was found to vary in the range 4.4 dB – 5.1 dB, or in the range 3.6 dB – 4.3 dB if propagation loss was calibrated out. These levels of insertion loss were significantly reduced to 0.9 - 1.9 dB, depending on the channel measured, by using index matching fluid. In a practical system there is therefore the potential to reduce the loss by this amount by polishing, optimizing the dicing process and use of sufficient contact force. The variation of the optical coupling loss as a function of the misalignments in x, y and z for both the laser source and the photodetector were measured to assess how much

misalignment may be permitted, Fig. 7-13, Fig. 7-14. According to the tolerances of our alignment method a maximum 0.2 dB of additional insertion loss due to the VCSEL misalignment, and a maximum of 0.4 dB of additional insertion loss due to the PD misalignment should be expected. These almost insignificant additional loss levels demonstrate the high efficiency of our alignment method. For the first time in multichannel optical backplanes, the signal to cross-talk ratio (SCR) was measured as a function of the VCSEL array misalignment, Fig. 7-18 – Fig. 7-19. As expected, SCR was stronger for the waveguides, which were immediately next to each other but dropped, as the waveguides were further apart. For example, the waveguides separated by 250 μm from each other experience ~ 20 dB of SCR, which improves to ~ 24 dB for waveguides 500 μm apart and to ~ 27 dB for waveguides 750 μm apart, Fig. 7-19. In a real system, a number of channels operate simultaneously and for a specific waveguide the cross-talk from the rest of the channels builds up. The SCR exhibited by our demonstrator was 19.46 dB for the channels that were placed at the edge of the board and therefore, had only one immediate waveguide next to them. The SCR worsen to 17.76 dB for the waveguides that were placed further toward the middle of the board and therefore, had two immediate waveguides next to them. During 75 repeated attaching and detaching cycles of the connector the insertion loss variation was measured 5.19 ± 0.16 dB and the cross-talk variation was measured -19.95 ± 0.27 dB in reasonable agreement with our evaluation experiments. The repeatability experiments showed that our connector design had low variation and good reproducibility.

8.2. FUTURE WORK

Although our study in Chapter 4, showed that a radius of curvature of less than 10 mm should be avoided, it is more than certain that much tighter bends will be required in real optical backplane applications. Therefore, any future work should be aiming at investigating new ways of reducing the radius of curvature while keeping the insertion loss within acceptable levels. We recommend that the design rules extracted from this study for a single refractive index difference ($\Delta n = 0.0296$) should be complemented with measurements on waveguides of a range of Δn. Several studies have suggested that the bend transition loss can be reduced for waveguides utilizing a higher Δn. However, as Δn

increases both coupling loss and propagation loss increase due to higher reflectivity of the waveguide facets and enhanced influence of the waveguide sidewall roughness correspondingly. Therefore, a detailed study taking into account all loss components, as we did in this chapter, is required to reveal the optimum Δn, which balances the loss components.

Regarding the adiabatic mode theory in tapered waveguides, Chapter 5, in the future it should be extended from the 2D slab-tapered bends to the 3D buried channel tapered bends. In addition, related to the practical aspect, a way to realize tapers in both horizontal and vertical directions should be invented and new 3D tapers should be designed and tested.

The theory of propagation in multimode buried channels waveguide with sidewall roughness, Chapter 6, should be extended in two ways. Firstly, since our calculations showed that equilibrium is beyond the typical backplane length, we need to investigate the transition region. The propagation loss and the energy redistribution between modes should then be examined in connection to the excitation field. In addition, the theory should be extended to cover pulse propagation in multimode waveguides with roughness. Issues, such as modal dispersion and modal noise, which usually limit the bandwidth in multimode waveguide links, should be investigated.

Finally, regarding the work on the optical connector, Chapter 7, future work should address the problem of the relatively high cross-talk observed. Waveguides can be polished (all waveguides reported in this work have been unpolished) and connectors can be designed so that larger contact forces are applied. In addition, trenches between two adjacent waveguides could be investigated to reduce cross-talk. Another future extension is to redesign the optical connector for multilayer optical PCBs and for flexible PCBs.

APPENDIX A

STORLITE OPTICAL BACKPLANE CONNECTOR (*StorConn*) COMMERCIAL EVALUATION

A.1 INTRODUCTION

This chapter assesses the commercial potential of the optical backplane connector (*StorConn*) developed during Storlite [A1], a 27 months EPSRC funded research project via the LINK Information Storage and Displays grant GR/S28136/01. The academic partners of Storlite were the University College London, [A2], and the University of Edinburgh, [A3], while the industrial collaborate of Storlite was Xyratex Ltd., [A4]. The work in this chapter was sponsored by the Centre for Scientific Enterprise Limited (CSEL), [A5]. Storlite aimed at interconnecting electronic daughtercards in storage drive card systems via an optical backplane, with embedded polymer buried channel waveguides. The need for such optical backplane systems is driven by the well-known electronic wire bottleneck related to electromagnetic interference and bandwidth constraints in electronic circuits, [A6]-[A7]. Figure A-1 demonstrates the concept of an optically interconnected backplane.

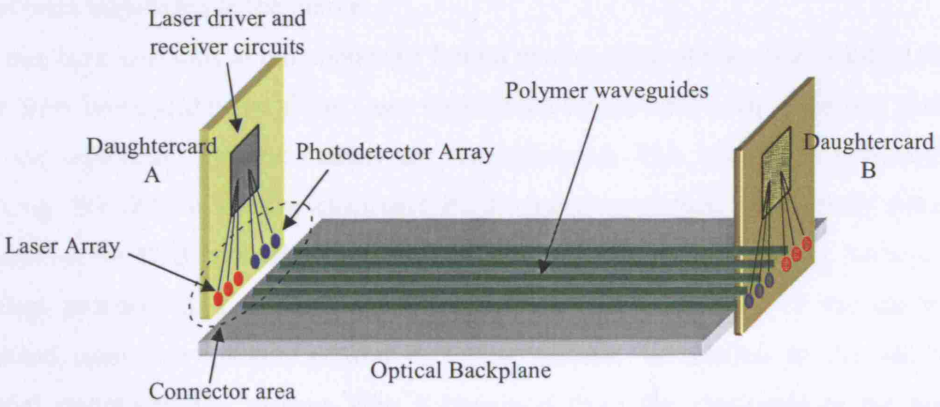

Fig. A-1. Storlite prototype optical backplane system. Laser and photodetector array of daughtercard A are in a mirror arrangement with respect to the laser and photodetector array of daughtercard B. Using this technique bi-directional point-to-point communication between the two electronic daughtercards was demonstrated at 10 Gb/s. The backplane could be redesigned to host multiple sets of daughtercards.

The main components appearing in Fig. A-1 are

- Laser - photodetector arrays mounted on the daughtercards
- High-speed electronic laser drivers and receiver electronic circuits
- Backplane with surface embedded optical waveguides
- Connector mechanism that ensures precise alignment between the active component arrays on the daughtercard and the waveguides on the backplane, at low cost.

Each of these components could be viewed as a different point on an optical backplane value chain. Storlite, focused on developing the drive circuits for the lasers and the receivers, designing optical devices, such as wavelength division multiplexers (WDM), and developing a novel backplane connector. We used commercially available arrays of lasers and photodetectors, and backplane fabrication was outsourced to Exxelis Ltd., [A8], who acted as a subcontractor in the project. Soon after the project began, we decided that the most commercially attractive research outcome was the Storlite connector (*StorConn*), with the aid of which connectivity was achieved between the daughtercard laser and PD arrays and the backplane waveguide, and we decided to commit our efforts in bringing it into the market. This decision was based on the fact that although a number of companies had been already active commercialising other types of components, a reliable, passive aligning, cost effective connector for rigid backplanes had yet not been introduced in the market.

Our aim here is to look at our connector from a market point of view and identify niches where *StorConn* could better fit in. Once appropriate niches have been identified, paths to bring the connector into the market are recommended. This chapter is structured as following: We first review the electronic PCB connector market, and identify potential segments of the PCB connector market to be served by an optical product, section A.2. We then proceed to a more detailed macro- and micro-analysis of the electronic backplane connector market, section A.3, and discuss, in relation to the identified potential customers, the reasons why a transition from the electronic to the optical technology is likely to happen. After briefly reviewing the technical aspects of our product in A.4, we proceed to analyse the electronic PCB connector industry in section A.5. Having discussed the market our product serves and the industry we have to compete

in, we assess the route of our OPCB connector to the market.

A.2 GLOBAL PCB CONNECTOR MARKET REVIEW

This section reviews the electronic printed circuit board (PCB) connector market and identifies the growth potential and the challenges within this market. A summary of the entire connector market is necessary in order to identify niches and opportunities for *StorConn*.

A.2.1. Types of Electronic Connectors

Connectors are classified according to their application into four categories:

A. **Backplane connectors**. Backplane connectors are used for backplane / mid-plane / motherboard, daughtercard-to-daughtercard interconnection at right angles. Typical applications include high-speed backplane connectors for telecommunication use equipment such as switches and high-density routers, networking equipment such as servers and storage systems, and mid-speed connectors for computer and notebook motherboards. The backplane connectors provide high-speed interfaces between PCBs and they follow the prong sleeve approach. The male part of the connector with the prong pins is placed on the daughtercard, and connection is achieved by pushing it into the female part with the sleeve jackets placed on the backplane. State of the art copper based connectors [A14] can achieve good signal integrity for frequencies up to 12 GHz but connectors operating at higher frequencies suffer from signal attenuation, reflections, non-uniform impedance and other parameters, which distort the signal and make their design a big challenge.

B. **Mezzanine connectors**. Mezzanine connectors are high-density, high-speed connectors with typically a small pitch, used to stack various modules onto a single daughtercard. Mezzanine connectors are mainly used to separate components that are often replaced or redesigned such as for example high-speed modules and thus significantly reduce board design cost and repair cost. The most commonly used mezzanine connectors are the industry pack (IP) and the PCI mezzanine (PMC) connectors. The first utilizes 50-pin connectors while the second utilized 64-pin connectors.

C. **Board-to-board connectors**. Board-to-Board connectors consist of the two-piece

male-female configuration and are utilized for direct right angle interconnection between boards without having to go through a backplane.

D. **Board-to-wire connectors**. Board-to-wire connectors are a variation of the board-to-board type connectors that allow flexing. Board-to-board and board-to-wire connectors are usually of mid- and low-speed and they find a large variety of applications mainly in consumer electronics such as in digital cameras, MP3 players, PDAs, mobile phones.

Figure A-2 shows the revenue for the PCB connectors and the percentage growth for the entire sector for the period 2001-2011. The graphs are based on the report by Frost&Sullivan published in 2005, [A13]. The revenues for the period 2001-2004 are based on real data, while the revenues for the period 2005-2011 are based on prediction. Figure A-3 shows the percentage of the share that each type of connector (backplane, mezzanine, board-to-board and board-to-wire) is predicted to capture for the same period [A13]. A healthy annual growth of revenue between 10% - 16% is predicted for the whole period of forecast, with all types of connectors expected to benefit from the growth trend. Revenue generated by the PCB connectors, is expected to reach $13 billion in 2011. The backplane connectors are expected to dominate the PCB connector market and their share is predicted to reach 44.8% 2011 up from 39% in 2001. The main reasons for the growth of the backplane connector market are the continuing expansion of the telecommunication and data communication sectors, which constitute the two main customers for these products, and the growing importance of niche but high margin markets such as the automotive and medical diagnostic equipment. The backplane connector market is the market our product mainly targets, and is analyzed in more detail in the next section. Mezzanine connector growth drive factors are the trend for miniaturization, which leads to the adoption of connectors with smaller footprints, the growth in the datacomm market and especially the increasing demand for blade servers and high-speed routers where mezzanine connectors are extensively employed and, finally, the development of high speed interconnections between boards, which require newer high-speed connectors. Board-to-board and board-to-wire connectors are the two classes of PCB connectors with the highest sales in terms of units sold. They both benefit from the growth in telecommunications (especially mobile handsets), the expanding GDP in the developed

and especially the developing countries which fuels the demand for consumer electronics, computing and automotive products and finally from the high growth in niche verticals, as for example the medical applications.

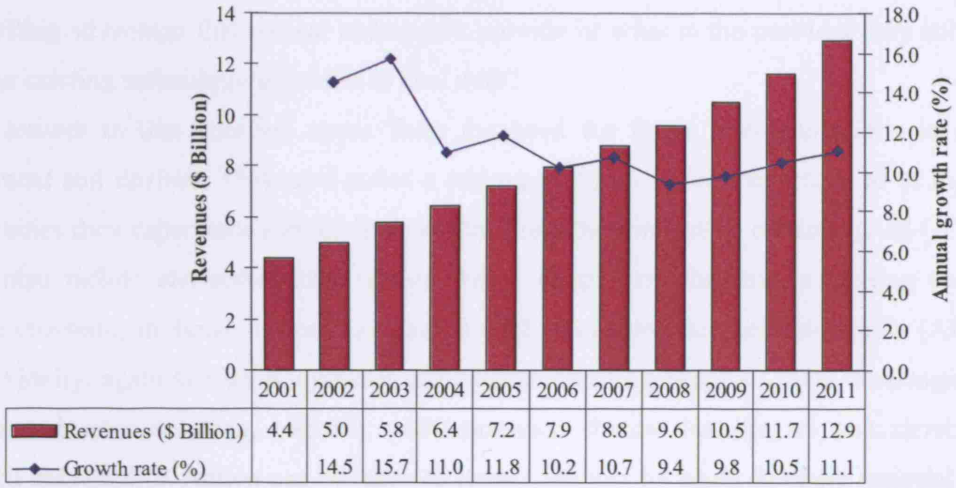

	2001	2002	2003	2004	2005	2006	2007	2008	2009	2010	2011
Revenues ($ Billion)	4.4	5.0	5.8	6.4	7.2	7.9	8.8	9.6	10.5	11.7	12.9
Growth rate (%)		14.5	15.7	11.0	11.8	10.2	10.7	9.4	9.8	10.5	11.1

Fig. A-2. Global PCB connector market. Combined revenues of all four connector types for the period 2001-2011. Source: *Frost&Sullivan.*

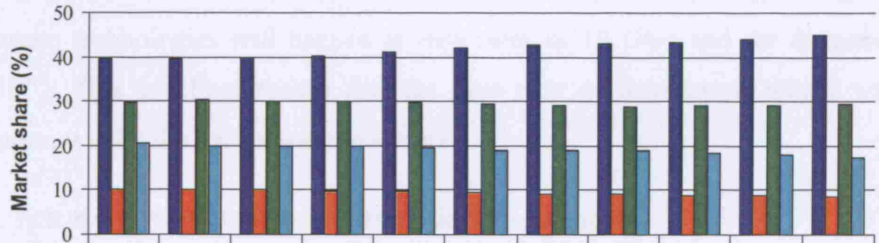

	2001	2002	2003	2004	2005	2006	2007	2008	2009	2010	2011
Backplane (%)	39.4	39.6	39.8	40.1	41.1	42.0	42.6	42.9	43.5	44.1	44.8
Mezzanine (%)	10.0	10.2	10.2	9.9	9.7	9.5	9.3	9.2	9.0	8.8	8.6
Board-Board (%)	29.9	30.4	30.2	30.0	29.7	29.4	29.1	28.9	29.0	29.1	29.3
Board-Wire (%)	20.7	19.8	19.8	20.0	19.5	19.1	19.0	18.9	18.5	18.0	17.4

Fig. A-3. Global PCB connector market. Share of revenues per connector type for the period 2001-2011. Source: *Frost&Sullivan.*

A.2.2. Market for an Optical Printed Circuit Board Connector

All connector types described so far are, up to today, electronic. However, the product we wish to introduce is an optical connector and, therefore, a technology transition from electronics to optics is required. Any such transition is painful as it is very demanding in

both capital and labour effort in order for the new products to be designed, developed, and tested from scratch and then brought into the market. Industries usually are reluctant to take on new technologies unless they offer some serious advantage over the existing ones. Therefore, the question that we have to answer is the following: What is the compelling advantage that optical connectors provide or what is the problem they solve that the existing technology is unable to deal with?

The answer to this question stems from the need for faster interconnections in all equipment and devices. This need poses a serious problem for copper tracks as at high frequencies they experience serious loss, which limits the connection distance [A6]-[A7]. They also radiate electromagnetic waves, which couple to other tracks causing such severe crosstalk, in dense systems, so that the bit error rate becomes intolerable [A6]-[A7]. Finally, again at high frequencies impedance matching becomes more challenging in the connector resulting, together with increased current leakage, to considerably reduced data quality. Action can be taken to reduce the loss by using Rodgers material in the printed circuit board and using adaptive equalisers and pulse pre-emphasis, but these are costly and can consume more power, so a different approach is needed. According to the international electronics manufacturing initiative (iNEMI) roadmap [A17], [A19], the transition between technologies will happen at data rates of 10 Gb/s and for distances longer than 19". This in effect means that the first type of connectors, which will incorporate optics, will be the backplane connectors.

A.3 OPTICAL PCB BACKPLANE CONNECTORS. MARKET ANALYSIS

Having identified the backplane connector sector as being the one more likely to adopt optical technology in the short- and mid-term, we proceed by analyzing the macro- and micro-levels for the market domain. This section focuses on issues such as the size of the backplane connector market, the reasons for its growth and the general trends, which will sustain this growth in the long term.

A.3.1. PCB backplane connector market: Macro-level Analysis

Backplane connector market size and growth prospects

The PCB backplane connector market is a market of growing importance, which as we

mentioned before it is expected have the highest revenue share among all types of connectors by 2011. Figure A-4, shows the predicted revenues for the backplane connectors for the period 2001-2011, [A13]. Revenues are expected to reach $5.79 billion in 2011, up from $1.72 billion in 2011. The average annual growth is expected to be 12.3%.

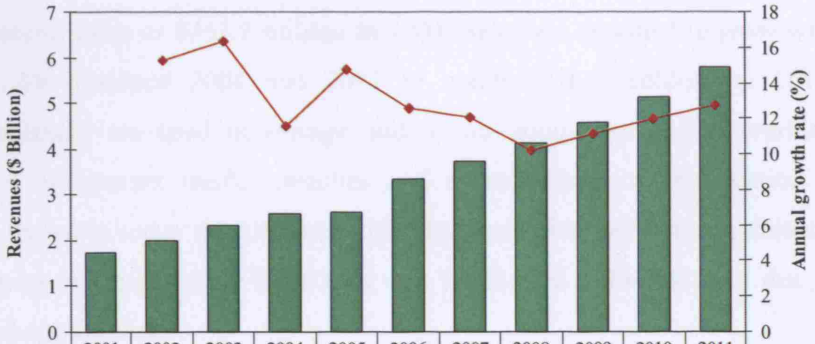

	2001	2002	2003	2004	2005	2006	2007	2008	2009	2010	2011
Revenues ($ Billion)	1.72	1.98	2.31	2.58	2.62	3.33	3.73	4.12	4.58	5.13	5.79
Growth rate (%)		15.3	16.4	11.6	14.8	12.6	12.1	10.3	11.2	12.0	12.8

Fig. A-4. Backplane connector market. Predicted revenues generated by backplane connector sales for the period 2001-2011. Source: *Frost&Sullivan*.

Backplane connector customers

Backplane connectors find a wide range of applications within the electronics industry. The customers of the backplane connectors are divided into nine categories:

a) *Telecommunications*. Telecommunications was the highest contributor to the backplane connector market in 2004 with a share in the total sales, which reached 22.7% or $585.7 million, Fig. A-5. Backplane connectors find applications in telecom equipment such as in switches, voice compression equipment, high-density routers, base station equipment and others. The demand for backplane connectors, is expected to remain strong for the whole period of discussion due to high demand for high-speed applications and introduction of new protocols such as the 10G Ethernet, 10 Gb/s Fibre Channel etc. In the period 2004 – 2011, telecom related backplane connector sales are expected to grow with an average rate of 10.9% and capture a share of 20.8% of the whole backplane connector sales or $1.20 billion by the end of this period.

b) *Computing applications.* Backplane connectors for computing applications, mainly refer to the connectors between motherboards and computer cards in desktops and notebooks. The computing sector accounted for 22.2% of the whole backplane connector sales or $572.8 million. Sales are expected to grow with a healthy average of 12% between 2004 and 2011 to reach $1.26 billion by 2011 as show in Fig. A-5.

c) *Data communications.* Data communications accounted for 14.1% of the whole backplane connector sales or $363.8 million in 2004. Sales are expected to grow with an average 11.4% between 2004 and 2011 to reach $776.7 million by 2011. Backplane connectors are used in storage and server equipment and networking equipment such as internet traffic switches and routers. Data communication is expected to be the main sector together with the telecommunication sector to demand optical backplanes and connectors since they can justify the additional cost due to their high-speed applications.

d) *Consumer electronics.* Consumer electronics accounted for 11.1% of the whole backplane connector sales or $296.7 million in 2004, Fig. A-5. Sales are expected to reach $776.7 million by 2011. Applications, which will demand optical connectors, lie in the high-end of the consumer electronics and include game consoles and high-definition TV screens.

e) *Medical.* Medical applications accounted for 4.3% of the whole backplane connector sales or $100.9 million in 2004. It is a rapidly growing sector with sales expected to grow with an average 25.4% between 2004 and 2011 to reach $550.7 million, by the end of the period. Medical is a niche were optical backplanes are expected to find broad application, especially in diagnostic equipment such as scan axial tomographers, which handle a large amount of data that need to be stored and to be transferred.

f) *Aerospace/defense.* The aerospace/defense sector accounted for 7.5% of the whole backplane connector sales or $193.5 million in 2004. Sales are expected to grow with an average of 9.2% between 2004 and 2011 to reach $359.4 million by 2011 as can be seen in Fig. A-5. Navigation and guidance as well as sensing systems in aircrafts and ships are the main applications for backplane connectors. Entertainment systems are another quickly growing niche in commercial aircraft.

g) *Automotive.* Automotive is another interesting sector, which exhibits an increasing demand for backplane connectors. In 2004 automotive added just $74.8 million or 2.9% market share to the backplane connector sales. However, this sector is expected to experience high growth with an average growth of 26% to reach $376.8 million in 2011. This is due to the expanded use of electronics in navigation, entertainment and sensing systems, which has initially started from the high-end cars but it is gradually migrating to the mid- and low-end vehicles.

h) *Industrial.* Although the highest contributor to the backplane connector sales in 2001 with a market share of 20.5%, industrial connectors gradually lose ground compared to the rest of the sectors. In 2004, it accounted for 9.5% of the whole backplane connector sales or $245.1 million. A very mild expansion of an annual average 3% is expected for the period 2004-2011 which indicates that the sector is saturated, and sales are expected to reach $301.4 million by the end of the period. Backplane connectors are utilized for scientific instruments, production equipment and industrial control equipment within this market segment. Scientific instruments such as high frequency network analyzers, bit error rate testers and oscilloscopes are likely candidates to adopt optical connectors.

i) *Others.* This segment includes all electronic equipment used for business, retail and transportation electronic applications. In 2004, it accounted for 5.3% of the total backplane connector sales or $136.7. A strong growth is expected with an average annual growth of 17% to reach $411.6 million by 2011, Fig. A-5. This is another interesting niche.

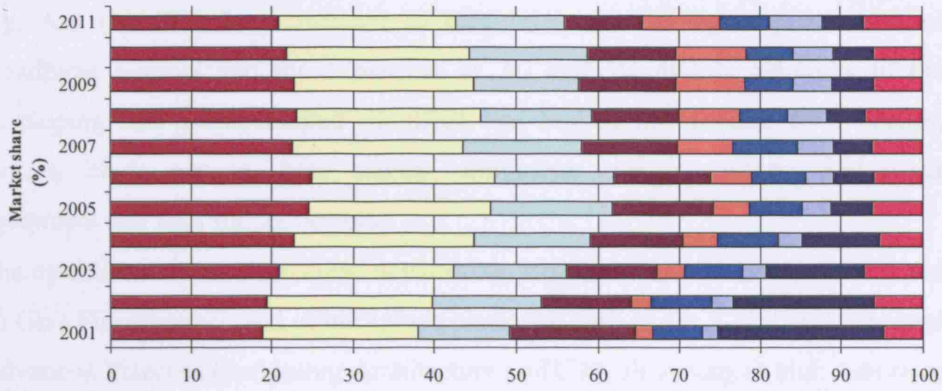

	2001	2002	2003	2004	2005	2006	2007	2008	2009	2010	2011
Others (%)	4.7	5.9	7.2	5.3	6.2	5.9	6.1	7	5.9	6	7.1
Industrial (%)	20.5	17.5	12	9.5	5.1	5	4.9	4.7	5.2	4.9	5.2
Automotive (%)	2	2.5	3	2.9	3.5	3.5	4.3	4.8	4.8	5	6.5
Aerospace (%)	6	7.5	7.1	7.5	6.5	6.6	8	6	5.9	5.7	6.2
Medical (%)	2.2	2.5	3.5	4.3	4.5	5.1	6.9	7.5	8.5	8.7	9.5
Cons. Electronics (%)	15.5	11	11.1	11.5	12.4	12	11.8	10.8	12.1	11	9.5
Datacomm (%)	11.1	13.4	13.7	14.1	14.8	14.5	14.5	13.5	12.8	14.3	13.4
Computing (%)	19	20.2	21.4	22.2	22.5	22.5	21	22.7	22.1	22.5	21.8
Telecom (%)	19	19.5	21	22.7	24.5	24.9	22.5	23	22.7	21.9	20.8

Fig. A-5. Backplane connector market. Share of revenues per industry for the period 2001-2011. The base year is 2004. Source: *Frost&Sullivan*.

Market Trends

In Fig. A-4, we saw that the backplane connector generated revenues are expected to rise by 337% globally in the decade 2001-2011. The purpose of this paragraph is to investigate the general trends driving this growth. As it has been briefly mentioned a combination of technological and economic trends are behind the market growth. Specifically, the major factors contributing to the expansion of the backplane connector market are

– *Technological advancements*. The main technological advancements, which assist to the backplane connector market growth are:
  - The expansion of the telecommunications and data communications sectors. As shown in Fig. A-6 (a) the required capacity for the US backbone network alone was predicted to reach 230 Tb/s in 2006 up from almost 75 Tb/s in 2003 [A19], and the trend is towards rapid increase in the capacity demand. To cope with this demand, backplane capacity should reach 1 Tb/s by 2011 up from almost 0.2 Tb/s in 2006 [A21], which corresponds to a fivefold increase in 5 years as shown in

Fig. A-6 (b). This large increase to data rates, due to higher penetration of broadband internet and the expansion of 2G and 3G mobile networks in the developing and the developed countries, has fuelled the demand for switches, routers, blade servers, base station equipment, storage systems and other equipment and thus for connectors.

- The establishment of high-speed networking protocols such as 10G Ethernet and 10 Gb/s Fibrechannel, and of backplane platforms such as the XAUI and the serial Advanced Telecom Computing Architecture (ATCA), all aiming at high data rates request newer, faster and more robust connectors as replacement for the older and slower ones.
- Advances in plating of plastic materials, which can more easily handle impedance non-uniformities and resulting mismatches has enabled the design and fabrication of faster and denser connectors. This has helped to increase the demand for high-speed connectors.
- Recent advances in the flip-chip technology and the SMT (surface mount technology) technique are leading to high-density connectors with reduced power consumption and labour cost. These new products give more flexibility to the PCB backplane designers and, thus, are expected to have high demand.
- Advances in medical equipment (mainly diagnostic), which require the handling of large amount of data will fuel demand for faster connectors. Medical is a very fast growing niche.
- Advances in automotive and avionics are expected to be rapid in the next few years mainly due to sensing applications, navigation and entertainment systems.
- Finally, more electronic equipment is expected to be used for business, retail and transportation, which will significantly contribute to the backplane connector growth.

– *Economic trends*. The increased GDP especially in the developing countries is expected to generate a huge new number of consumers in the next decade. These consumers will turn to electronic and computing devices such as mobile phones, desktops, notebooks, PDA etc that in turn will increase the demand for motherboard connectors as well as increase investments of telecommunications and internet service

providers in equipment.

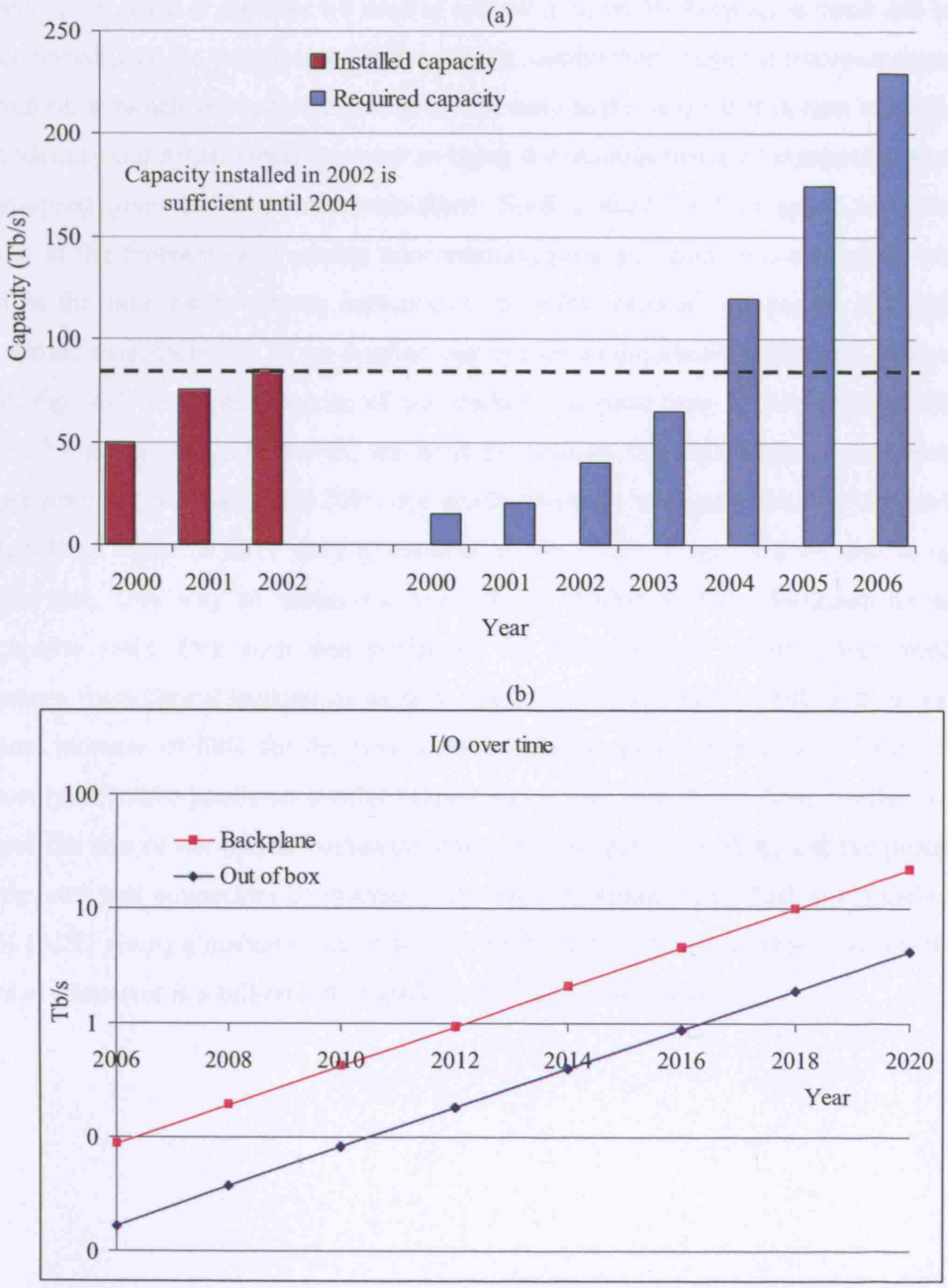

Fig. A-6. (a) Long haul backbone network capacity in the US for the period 2000-2006. Source: *Goldman Sachs&McKinsey* (b) Forecast backplane capacity for the period 2006-2020. source: *Intel*.

A.3.2. Optical backplane connectors market: A micro-level look

In the previous section, we quantified the size of the backplane market to $5.74 billion

by the year 2011, Fig. A-4. However, the question that arises is whether the entire market is within our reach or whether we need to narrow it down. By keeping in mind that optical interconnections are substitutes for the already established copper interconnections and, therefore, a switch between technologies will only make sense if it is cost effective, we can identify our initial target segment as being the manufacturers of equipment requiring high-speed (over 5 Gb/s) interconnections. Such a need for high-speed interconnects exists at the moment only among telecommunication and data communication vendors and in the near future among automotive, avionics, medical equipment and high-end electronic manufacturers. If we confine our market to the above mentioned sectors then from Fig. A-7 we expect the size of our market to expand from $1.38 billion in 2004 to $3.27 billion in 2011. However, we need to mention that this estimate constitutes an upper limit for our market. In 2004, the whole revenues were generated by copper-based connectors, while in 2011 only a fraction of the $3.27 billion will be due to optical connectors. One way to assess the size of our market is from forecasts on optical backplane sales. One such was performed by ElectroniCast [A19], which predicted revenues from optical backplanes sales to reach $2.565 billion by 2008, with an average annual increase of 68% for the period 2003-2008 as shown in Fig. A-8. BPA in their report [A20] have predicted similar market sizes, Fig. A-9. From these studies, we can assess the size of the optical backplane connector market by working out the percentage of the cost that connectors contribute to the total backplane cost. This is typically 30%-40% [A22] giving a market share of $0.77 – $1.03 billion. From the above we see that the optical connector is a billion dollar market with excellent prospects.

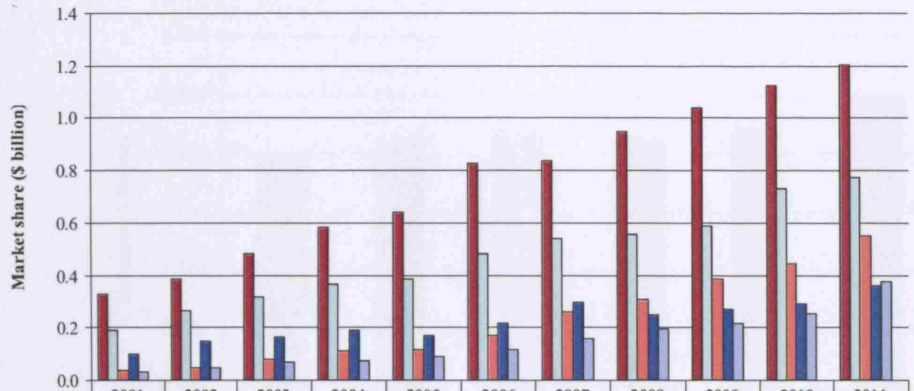

	2001	2002	2003	2004	2005	2006	2007	2008	2009	2010	2011
Telecom ($B)	0.33	0.39	0.49	0.59	0.64	0.83	0.84	0.95	1.04	1.12	1.20
Datacomm ($B)	0.19	0.27	0.32	0.36	0.39	0.48	0.54	0.56	0.59	0.73	0.78
Medical ($B)	0.04	0.05	0.08	0.11	0.12	0.17	0.26	0.31	0.39	0.45	0.55
Aerospace ($B)	0.10	0.15	0.16	0.19	0.17	0.22	0.30	0.25	0.27	0.29	0.36
Automotive ($B)	0.03	0.05	0.07	0.07	0.09	0.12	0.16	0.20	0.22	0.26	0.38
Total ($B)	0.69	0.90	1.12	1.33	1.41	1.82	2.10	2.26	2.51	2.85	3.27

Fig. A-7. Backplane connector market. Revenues per potential customer sector for optical backplane connectors for the period 2001-2011. The base year is 2004. Source: *Frost&Sullivan*.

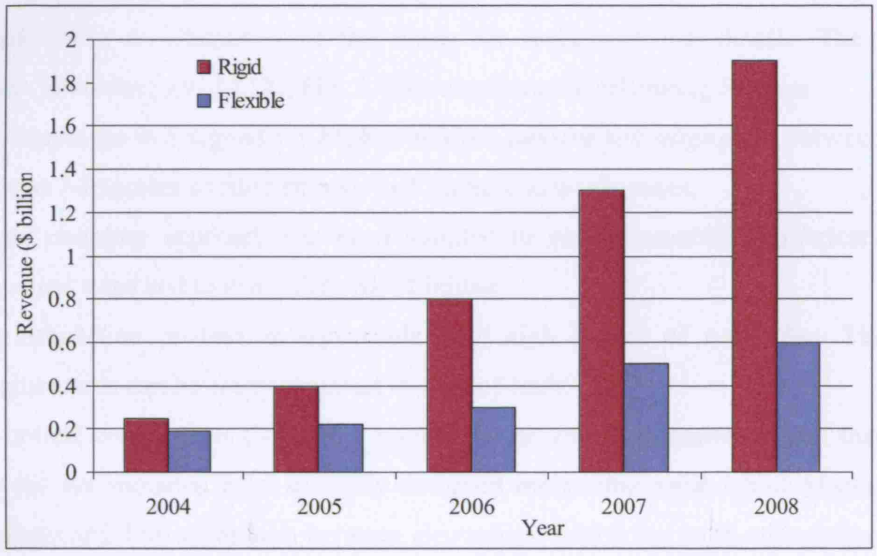

Fig. A-8. Optical Backplane market. Revenues per sector for the period 2000-2008. Source: *ElectroniCast*.

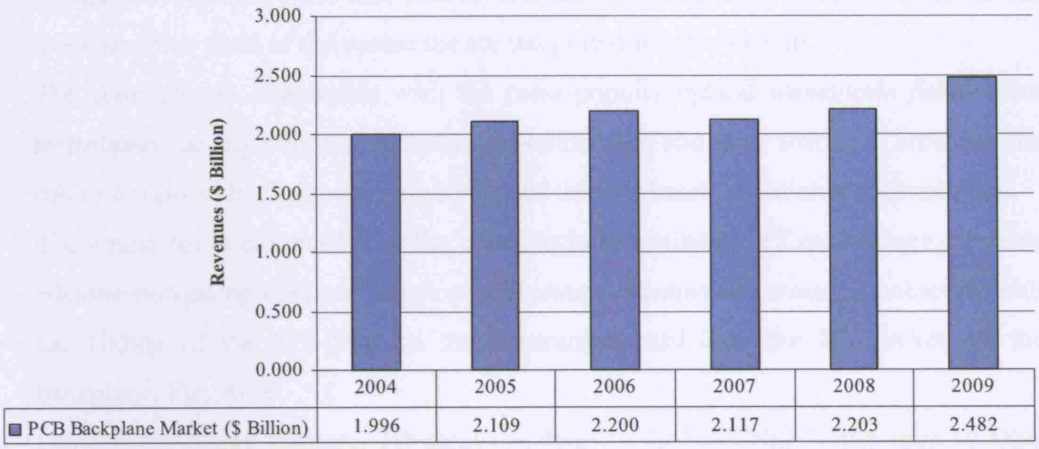

Fig. A-9. PCB backplane market. Predicted revenues generated by backplane sales for the period 2004-2009. Source: *BPA consulting*.

A.4 StorConn description

In this section, we give a brief description of our connector. We refer the more interested reader to Chapter 7 of the thesis for more technical details. The Storlite connector *StorConn* [A9]-[A12], Fig. A-10, comprises the following features:

- The connector is designed for ***high precision***, ***passive self-alignment*** between arrays of lasers / detectors or fibre ribbons and backplane waveguides.
- ***Direct coupling*** approach has been adopted to reduce number of fabrication and alignment steps and to minimize risk of failing.
- The connection process is ***repeatable*** with high degree of ***reliability.*** Therefore, daughtercards can be easily replaced in case of fault.
- All optical components (VCSEL - photodetector arrays, microlenses and their drive circuits) are mounted on a specially designed ***mezzanine card***, which stacks on the daughtercard. Full separation between electronics, which are on the daughtercard and optics, which are on the mezzanine card, is therefore achieved. In this way, optics can be treated as a black box from the PCB designers who can still use the same design tools as in the case of the copper only daughtercards. Since mezzanine cards and connectors are commonly used in the PCB industry, this characteristic makes the switch to the optical technology easier.
- The connector is designed to operate within the backplane "harsh" environmental

conditions. Flexible parts that ***absorb vibrations*** before they are transferred to the most sensitive parts of the connector are integrated into the design.

- The connector is ***compatible*** with the most popular optical ***waveguide fabrication techniques*** namely photolithography, hot-embossing and laser writing. Therefore, the can fit to optical backplanes made by any of the previously mentioned technologies.
- The connector is ***compatible*** to the commercially available ***MT technology for fibre ribbons*** mitigating cost and development issues. Passive alignment is achieved with the sliding of the MT-plug on the mezzanine card into the MT-socket on the backplane, Fig. A-10.
- Our current design supports 1D arrays of four 10 Gb/s VCSEL's and four 10 Gb/s photoreceivers. An integrated ***80 Gb/s duplex bandwidth*** has been recently demonstrated but up to 120 Gb/s overall bandwidth can be supported (an array of 6 VCSEL's and 6 photoreceivers).
- Connector design is easily scalable to carry ***2D arrays*** of components.

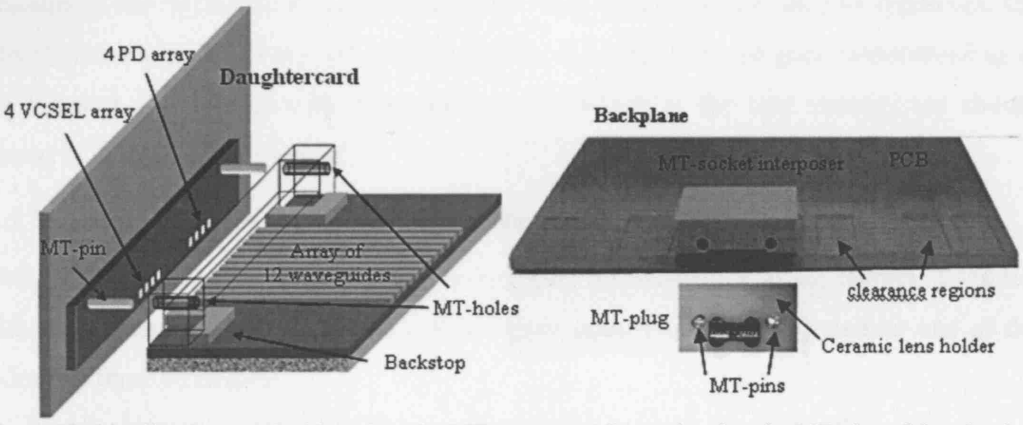

Fig. A-10. (a) Alignment method based on the MT concept. After registering the MT-pins of the plug into the MT-holes of the socket accurate alignment between the VCSEL's – PIN diodes of the mezzanine board and the waveguides of the backplane is achieved. (b) Optoelectronic PCB with MT-socket interposer mounted on the surface about to slide back into position against backstops and MT-plug with ceramic lens holder in place

A.4.1. StorConn performance

StorConn connector has been subjected to extensive laboratory testing. The findings have been accepter for publication to a leading *IEEE* journal [A9]. The details of the testing can be found in Chapter 7. The key results were:

- We achieved **error free operation** for all channels at targeted data rates of 10 Gb/s

after **24h** of continuous operation.

- The **maximum lateral misalignment** between laser arrays in a system can potentially be ±6 μm, which is very satisfactory for optical backplane applications.
- The **additional coupling loss** under most severe misalignment conditions is **0.4 dB** at each end of the link.
- **Signal to cross talk ratio** is **-20 dB** at best coupling position.
- A histogram of 75 repetitive engagements of the connector showed uniform coupling power measurements with small variation, meaning that the connector exhibits **excellent reproducibility**.

We believe that these results are very satisfactory for a prototype connector and we think that there is good potential for the connector to be commercialized.

A.5 ROUTE TO MARKET AND INDUSTRY ANALYSIS

The final section of this chapter concentrates on the very important issue of identifying ways to bring our product to the market. In order to do so, we need to examine the current situation in the backplane connector industry. This is because we need to appreciate the attractiveness of the industry we wish to step in. It is also because good understanding of the industry provides us with a guidance about which is the best strategy we should pursue to introduce our product.

A.5.1. Strategies to Bring Product to the Market

We start by listing the potential ways in bringing our connector to the market. Together with our industrial partner Xyratex Ltd. we have mainly considered pursuing one of the following three strategies:

1) Xyratex sets-up an optical PCB connector company and a manufacturing site.
2) Xyratex acquires an existing connector company, which starts producing *StorCon*.
3) We license our core patents to an established player in the market who develops and produces *StorCon* and we receive a margin from the revenue.

A.5.2. Backplane Connector Industry Domain Analysis

In order to investigate the industry attractiveness we use the Porter's five forces tool [A16]. The analysis that is presented is from the optical backplane connector point of

view.

Threat of Entry

We consider the threat of new entrants in the optical backplane connector industry to be low in the short- and mid- term after the technology is introduced to the market, but to be more serious in the long- term when the technology is established and rivalry intensifies. This is because capital requirements for research, equipment and production lines, set a high barrier for new companies to enter. Finally, in order for optical connector companies to be competitive they have to follow the paradigm of electronic PCB connector companies' business plan. A new company must set up their manufacturing centre in Asia and China, in order to keep production cost low, and must have experience of the Northern American, European and Japanese markets, where most of the customers are based. Such a combination can only be achieved by a leading connector company. However, as optical technology becomes more popular and starts expanding towards consumer products we expect more entries in the industry.

Supplier power

We consider supplier power to be one of the most unfavourable forces in our industry in the short-term. However, its impact is expected to reduce in time. This assessment is because currently there is a limited number of suppliers, for most of the components necessary to built the optical connector, who can set high margins. Costly components include 1D or 2D arrays of 10 Gb/s or faster VCSELs, 1D or 2D arrays of 10 Gb/s or faster photoreceivers, 1D or 2D arrays of custom made microlenses (if used), custom made MT-ferrules and polymers for the backplane fabrication. However, we expect these products to exhibit a price elastic behaviour and their price to reduce significantly as the purchase volumes increase. An analogous example is demonstrated in Fig. A-11 with the very similar 10 Gb/s transponders used in SONET/SDH applications. Their cost reduced exponentially when the demand for these products soared [A21].

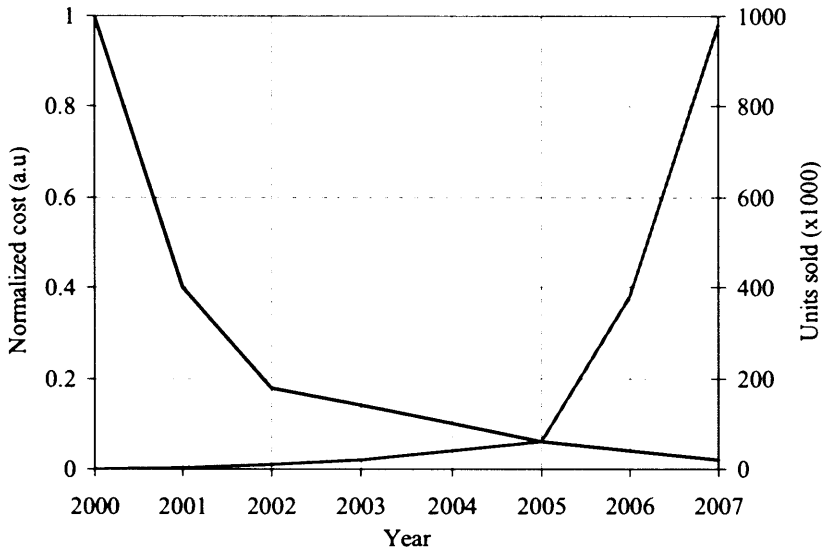

Fig. A-11. Price elasticity for 10 Gb transponders. An exponential increase to the demand led to a similar reduction to the price of the transponders. Source: *Intel*

Buyer power

The power of the optical backplane connector customers is medium. The factors that weaken the buyers bargaining power is the low concentration of companies (at the initial stages) offering optical backplane connectors, the high-switching costs for buyers to other optical connector manufacturers, the lack of industrial standards for optical connectors which will lead to high differentiation of the products between optical connector vendors. Another factor is the increasing importance of the connector companies to the quality of the buyer final products, due to their involvement in more aspects of the final system such as the design and testing. The factors that increase the buyers power are the existence of the alternative copper connectors and the reluctance of the buyers to switch to the costly optical technology (in the short-term), the trend of buyers towards multi-sourcing agreements and the good knowledge of buyers of the structures of connector companies.

Threat of substitutes

The threat of substitutes is considered high in the short-term, and initially is expected to affect the adoption rate of the optical technology. However, in time we expect the advantages of the optical connectors to surpass all alternative solutions. The main substitutes of the optical backplane connectors are:

- New generation high-speed copper based two piece PCB connectors
- Coaxial cable PCB connectors
- Fibre optic PCB connectors for optical backplanes

Competitive rivalry

We start by looking at the current rivalry among electronic backplane connector manufacturers. Figure A-12 shows how the revenues were distributed among the electronic backplane connector vendors in 2004. Tyco electronics captured 21.6% of the market, FCI Connect 19.2%, Molex 10.2%, Teradyne 9.8%, Erni 5.5%, Foxconn 5.1%, Harting 7.1%, while no other single company had a significant market share. It is worth noting that the two leading companies combined share was 40.8%. The main reasons, which explain this high concentration of market share among a small number of companies, are

- Backplane connectors are very specialized high commodity, innovative products. Existing companies are rich in intellectual property and active in research for high-speed products. Barriers due to research cost are too high for smaller companies to compete in the high-speed connector market.
- Large vendors usually become part of the backplane design, building strong ties with the customer, which makes it difficult for smaller companies to replace them.
- There is an ongoing trend for partnerships between large connector vendors across all stages of a connector cycle, from the designing and manufacturing to their testing. For example, the partnership between Tyco and Erni has enabled them to increase their product lines and reduce the manufacturing lead-time. In addition, the multi-source agreement between

We expect similar rivalry environment in the optical backplane connector industry. The combination of high capital requirements for research and development of new optical backplane connector products, the need for strong global distribution centres and supply chains and high quality manufacturing cites in Asia to keep production costs low, the lack of industrial standards, the trend for partnering between existing companies, and the ability of the big players to offer added value services, such as to participate in the backplane design, leaves enough room for only a few players in the industry. However, as

optical interconnects tend to spread from advanced equipment to consumer products we expect the entrance of more companies and, thus, we expect the competition to be intensified.

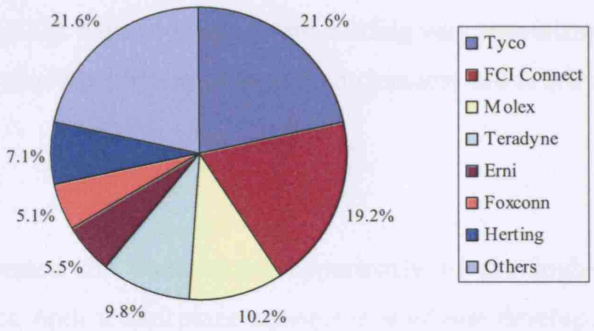

Fig. A-12. Backplane connector market. Share of revenues per backplane connector manufacturer in 2004. Source: *Frost&Sullivan*.

A.5.3. Best Route to the Market

We are now ready to asses the best strategy in bringing *StorConn* in the market. We present our arguments based on the findings from the industry analysis.

1) Xyratex starts a manufacturing site producing optical backplane connectors: This choice has been rejected mainly because of the capital needed to build a production plant. In addition, long time would be required before a hypothetical manufacturing site was set up, which would jeopardize our chances of being among the first companies to offer an optical connector to the market. Finally, even if production started breaking into, the dominated by a limited number of players, market would be very challenging.
2) Xyratex acquires an existing connector company, which starts producing *StorCon*: The arguments are more or less the same as in the previous case. Acquiring a connector company would save Xyratex the time from setting up a new manufacturing plan but it would still be very capital intensive. In addition, an acquisition would possibly aim at a small size connector company, as the larger ones

of Fig. A-12 are multinational corporations with billions of dollars of revenue. However, as we have said optical connectors are high-commodity products that only the bigger players can offer.

3) License the patents to an existing player in the electronic PCB connector industry: According to our view, this is the most sensible and the lowest risk approach. In fact, we have already taken this step and we have collaborated with the US connector manufacturer Samtec [A23]. Samtec is an up and coming very specialized high-speed connector company. It also has efficient distribution channels and is active in all main markets worldwide.

A.6 CONCLUSIONS

In this chapter, we assessed the commercial opportunity of the high-speed, high-precision passive alignment, optical backplane connector *StorConn* developed during the Storlite project. A transition form the electronic to the optical technology will be unavoidable in the next years to confront the electronic interconnection bottleneck. Market analysis showed that the demand for such products will be high in the years to come and will mainly be fuelled from the traditional backplane connector customers in the telecommunication and data-communication industries. Optical connectors will be required by these industries to cope with the anticipated increase in the interconnection bit-rates. However, a number of emerging markets will be also demanding optical solutions and these will be proved significant niches in the future. Niche applications include medical diagnostic equipment, navigation and entertainment automotive systems, high-end consumer electronics and avionics applications.

Industry analysis showed a highly unfavourable environment for newcomers in the PCB connector industry. Parameters such as the high capital requirements for research and development, the alliances between existing PCB connector companies which gives them the ability to offer more integrated solutions, the enhanced personal relationships between customers and connector companies due to the customized nature of these products and the need for strong global distribution centres and supply chains leave enough room for only a few players in the industry. As a result, probably the only choice to bring *StorConn* to the market is to collaborate with an established player.

REFERENCES

[A1] www.photonics.org.uk/ISD/www/storlite.php, last time accessed 11/01/2007.

[A2] www.ucl.ac.uk, last time accessed 30/09/2007.

[A3] http://www.ed.ac.uk/, last time accessed 30/09/2007.

[A4] www.xyratex.com, last time accessed 30/09/2007.

[A5] http://www.cselondon.com/, last time accessed 30/09/2007.

[A6] Dawei Huang, Theresa Sze, Anders Landin, Rick Lytel, and Howard L. Davidson,, "Optical Interconnects: Out of the Box Forever?," *IEEE J. Sel. Top. Quantum. Electron*, vol.12, pp. 614-623, Mar/Apr 2003.

[A7] J. A. Davis and J. D. Meindl, "Is interconnect the weak link?," *IEEE Circuits Devices Mag.*, vol. 14, no. 2, pp. 30–36, Mar. 1998.

[A8] www.exxelis.com, last time accessed 30/09/2007.

[A9] I. Papakonstantinou, D. R. Selviah, R. A. Pitwon and D. Milward "Low cost, precision, self-alignment technique for coupling laser and photodiode arrays to waveguide arrays," *IEEE Trans. Adv. Packag.*, Accepted for publication.

[A10] Patent: K. Hopkins, R. A. Pitwon, "*A backplane for a data communications system, a data communication system, a host and a method of communication*".

[A11] Patent: Richard Pitwon, Ken Hopkins, "*An optical Connector, a communication system and a method of connecting a user circuit to an optical backplane*".

[A12] Patent: I. Johnson, R. Pitwon, D. R. Selviah, I. Papakonstantinou ,"*An optical printed circuit board and a method of manufacturing an optical printed circuit board*", available at http://v3.espacenet.com/textdoc?DB=EPODOC&IDX=WO2007010184&F=2&QPN=WO2007010184, last time accessed 30/09/2007.

[A13] Frost&Sullivan, "*World printed circuit board (PCB) connector markets*", A708-25, 2005.

[A14] Tyco electronics, "*High-speed backplane interconnect solutions*," http://catalog.tycoelectronics.com/TE/Presentations/1654263-1_01.pdf, last time accesed 12/07/2007.

[A15] Frost&Sullivan, "*Emerging technologies development in chip/board level interconnects,*" D435, 2005.

[A16] John W. Mullins, "*The New Business Road Test: What Entrepreneurs and Executives Should Do Before Writing a Business Plan*," FT Prentice Hall, London, Dec. 2003, ISBN: 0-273-66356-9.

[A17] iNEMI, "NEMI cost analysis: Optical versus copper backplanes," http://thor.inemi.org/webdownload/newsroom/Presentations/Opto_Copper_APEX04.pdf, page 4, last time accessed 12/01/2007.

[A18] Intel, "Market, Technical, Cost and Solution Considerations for HSSG," http://grouper.ieee.org/groups/802/3/hssg/public/nov06/peeters_01_1106.pdf, page 4, last time accessed 12/01/2005.

[A19] iNEMI, "NEMI Project on Cost-Performance Modeling of High Speed Backplanes, Copper vs. Optical, " http://thor.inemi.org/webdownload/newsroom/Presentations /IEEE_highspeed04.pdf, page 32, last time accessed, 12/01/2007.

[A20] http://www.emsnow.com/newsarchives/archivedetails.cfm?ID=6796, last time accessed 12/01/2007.

[A21] Intel, "Market, Technical, Cost and Solution Considerations for HSSG," http://grouper.ieee.org/groups/802/3/hssg/public/nov06/peeters_01_1106.pdf, page 11, last time accessed 12/01/2005.

[A22] Ken Hopkins, Xyratex Ltd., private communication.

[A23] Samtec corporation website, http://www.samtec.com/. Last time accesed 03/08/07.

APPENDIX B

POISSON SUMMATION, EULER-MACLAURIN FORMULA AND LAPLACE APPROXIMATION OF COMPLEX INTEGRALS

B1. Poisson Summation of Reflection Coefficients and Euler-Maclaurin Approximations

Assume that $F(l)$, is a continuous and finite function in the interval $0 < l \leq 1$. Then, from Fourier theory, [3.11], we know that the following equality is valid

$$\frac{1}{2}[F(0)+F(1)]=\sum_{q=-\infty}^{+\infty}\int_0^1 F(l)e^{-2\pi iql}\,dl \tag{B1}$$

The series in (B1) is definitely convergent. To involve the phase function of the Rayleigh reflection coefficient Φ in (3.6) in Chapter 3, or in (5.13) in Chapter 5 we write F, in the following form

$$F(l) = \Phi(l+L) \tag{B2}$$

where L can be any integer in (B2). The phase function Φ, satisfies all requirements of (B1) since it is continuous and bounded as $-\pi/2 < \Phi \leq \pi/2$, and also it is differentiable. If we apply (B1) to (B2) we get

$$\frac{1}{2}[\Phi(L)+\Phi(L+1)]=\sum_{q=-\infty}^{+\infty}\int_0^1\Phi(L+l)e^{-2\pi iql}\,dl=\sum_{q=-\infty}^{+\infty}\int_L^{L+1}\Phi(l)e^{-2\pi iql}\,dl \tag{B3}$$

If we sum (B3) over integer values L, in the range $L_1 \leq L \leq L_2$, we obtain the Poisson formula

$$\sum_{l=L_1}^{L_2}\Phi(l)=\frac{1}{2}[\Phi(L_1)+\Phi(L_2)]+\sum_{q=-\infty}^{+\infty}\int_{L_1}^{L_2}\Phi(l)e^{-2\pi iql}\,dl \tag{B4}$$

It can be easily verified that the Poisson formula (B4) is equivalent to the Euler-Maclaurin formula

$$\sum_{l=L_1}^{L_2}\Phi(l)=\frac{1}{2}[\Phi(L_1)+\Phi(L_2)]+\int_{L_1}^{L_2}\Phi(l)dl+E \tag{B5}$$

if the error term E is expressed as

APPENDIX B: *Poisson Summation. Euler-Maclaurin Formula and Laplace Approximation of Complex Integrals*

$$E = 2\sum_{q=+1}^{+\infty}\int_{L_1}^{L_2}\Phi(l)\cos(2\pi q l)\,dl \tag{B6}$$

As it is implied in (B5), the dominant contribution to the Euler-Maclaurin formula arises from the term for which $q = 0$. The rest of the terms are affected by the oscillatory functions $\cos(2\pi q l)$, $q \neq 0$ which cause rapid cancellations for $q>>$. By applying (B4) and (B5) to the series $\sum_{l=0}^{m}\Phi(\theta^{(l)})$ in (3.16) with $L_1 = 0$ and $L_2 = m$, Chapter 3, we obtain (3.17) and (3.18). Similarly, by applying (B4) and (B5) to the series, $\sum_{l=0}^{m}\Phi(\theta_f^{(l)})$, $\sum_{l=0}^{m}\Phi(\theta_o^{(l)}+\omega)$ and $\sum_{l=0}^{m}\varphi_x(\theta_o^{(l)})$ in (5.19) we obtain (5.25), (5.27) and (5.29) respectively.

B2. Laplace Integral Formula

The magnitude of the error terms $\hat{E}(\theta^{(m)},\theta)$, (3.23) in Chapter 3, and $\hat{E}_{\theta_f}(\theta_o^{(m)},\theta_o)$, $\hat{E}_{\varphi_y}(\theta_f^{(m)},\theta_f)$ and $\hat{E}_{\varphi_y}(\theta_o^{(m)},\theta_o)$, (5.26), (5.28) and (5.30) respectively in Chapter 5, can be estimated with the Laplace method in the region where they are analytic and where no branch-points or singularities interfere. We write all error terms with the single notation $\hat{E}(\theta_o)$ as

$$\hat{E}(\theta_o) = \omega^{-1}\sum_{q=1}^{+\infty}\int_{+i\infty}^{0} f(\theta_o+\psi)\cdot\exp(iq\pi\psi/\omega)\,d\psi + \omega^{-1}\sum_{q=1}^{+\infty}\int_{-i\infty}^{0} f(\theta_o+\psi)\cdot\exp(-iq\pi\psi/\omega)\,d\psi \tag{B7}$$

with $f(\theta_o)$ in (B7) standing for any of the following phase functions: $f(\theta_o) = \Phi(\theta_o)$ if we refer to the error term (3.23), in Chapter 3, and $f(\theta_o) = \Phi(\theta_o+\omega)$, $f(\theta_o) = \Phi_{\theta_f}(\theta_o)$ and $f(\theta_o) = \varphi_y(\theta_o)$, for the error terms in (5.26), (528) and (5.30) respectively, Chapter 5. The variable change $\psi = i\psi$ transforms (B7) to

$$\hat{E}(\theta_o) = i\omega^{-1}\sum_{q=1}^{+\infty}\int_{0}^{+\infty}[f(\theta_o+i\psi)-f(\theta_o-i\psi)]\cdot\exp(-q\pi\psi/\omega)\,d\psi \tag{B8}$$

The function $\hat{E}(\theta_o)$ in (B7) satisfies the following validity conditions of the Laplace

asymptotic approximation theorem [3.11]:

(a) The argument of the exponent ($q\pi\psi/\omega$) takes its minimum value at the lower limit of the integration interval $\psi=0$ and is monotonically increasing for $\psi>0$.

(b) The argument of the exponent can be expanded in a power series of ψ around $\psi=0$.

(c) The functions $f(\theta_o+i\psi)$ and $f(\theta_o-i\psi)$ are continuous in a neighbourhood of $\psi=0$ (but not necessarily continuous at $\psi=0$). and can be approximated by a power series of ψ around $\psi=0$ as

$$[f(\theta_o+i\psi)-f(\theta_o-i\psi)]\approx[f(\theta_o+i\psi)-f(\theta_o-i\psi)]_{\psi=0}+\left.\frac{\partial[f(\theta_o+i\psi)-f(\theta_o-i\psi)]}{\partial\psi}\right|_{\psi=0}\cdot\psi+\ldots= \quad \text{(B9)}$$

$$=p_1\psi+p_2\frac{\psi^2}{2!}+..+p_n\frac{\psi^n}{n!}$$

with p_1, p_2, ..., p_n the coefficients of the Taylor expansion in (B9). We note that in the expansion of (B9) the DC terms (for $\psi=0$) cancel each other. Since the above requirements (B) – (c) are satisfied, $\hat{E}(\theta_o)$ can be approximated by the following asymptotically converging Laplace series [3.11]

$$\hat{E}(\theta_o)\approx\omega^{-1}\sum_{q=1}^{+\infty}\sum_{s=0}^{+\infty}\Gamma(s+2)c_s\omega^{(s+2)} \quad \text{(B10)}$$

where in (B10) Γ, stands for the Gamma function and the coefficients c_s, are definitely finite. For the purpose of the error estimation it is sufficient to keep the dominant term only for $s = 0$ in (B10) and write

$$\hat{E}(\theta_o)\approx\omega^{-1}\left[\sum_{q=1}^{+\infty}\Gamma(2)\frac{b_2}{(q\pi)^2}\omega^2+\mathrm{O}(\omega^3)\right]=\omega p_2\Gamma(2)\sum_{q=1}^{+\infty}\frac{1}{(q\pi)^2}+\mathrm{O}(\omega^2) \quad \text{(B11)}$$

in (B11) we replaced c_o, with its value calculated by the Laplace theorem (B11) and, which is $c_o=\frac{b_2}{(q\pi)^2}$ with b_2 a finite coefficient. Therefore, since the geometric series $\Sigma(1/q\pi)^2$ is definitely convergent we can write as a total estimate for all error terms expressed by $\hat{E}(\theta_o)$:

$$\hat{E}(\theta_o)\approx\mathrm{O}(\omega) \quad \text{(B12)}$$

APPENDIX C

SADDLE POINT METHOD FOR THE ASYMPTOTIC EVALUATION OF COMPLEX INTEGRALS

In this section we briefly present the method of saddle points to approximate the spectral integrals (3.34), in Chapter 3, and (5.71) in chapter 5. For a more detailed analysis, please refer to [3.10]. Spectral integrals (3.34) and (5.71) take the form.

$$I^{\pm}(\omega) = \int_c g^{\pm}(\theta_o) \cdot e^{p(\theta_o)/\omega} d\theta_o \tag{C1}$$

with

$$p(\theta_o) = i\left[Q_o(r,\gamma;\theta_o) - q\pi\theta_o\right] \tag{C2}$$

and

$$g^{\pm}(\theta_o) = \exp\left[\mp \frac{i}{2}\Phi(\theta_o)\right] \tag{C3A}$$

$$Q_o(r,\gamma;\theta_o) = -kn_{co}w\cos(\theta_o) + \frac{1}{2}\int_{\theta_c}^{\theta_o}\Phi(\hat{\theta}_o)d\hat{\theta}_o + \frac{\pi\theta_o}{2}$$

in the case of the homogenous tapered waveguide (3.34) or

$$g^{\pm}(\theta_o) = \exp i\left[\pm\frac{1}{2}\Phi_{\theta_f}(\theta_o) - \frac{1}{2}\Phi(\theta_o+\omega) - \varphi_x(\theta_o) + ikn_{co}e^{w/R_1}\cos\theta_o r\cos\gamma\right] \tag{C3B}$$

$$Q_o(r,\gamma;\theta_o) = \frac{1}{2}\int_{\theta_c}^{\theta_o}\Phi(\hat{\theta}_o)d\hat{\theta}_o + \frac{1}{2}\int_{\theta_{wf}}^{\theta_o}\Phi_{\theta_f}(\hat{\theta}_o)d\hat{\theta}_o + \int_{\theta_{wf}}^{\theta_o}\varphi_x(\hat{\theta}_o)d\hat{\theta}_o$$

in the case of the transformed tapered bend (5.71). In both cases, the end points of the contour c lie at infinity. If the real values of the function $p(\theta_o)$ in (C1), take their maximum value at some point $\theta_o = \theta_{oq}$ then the parameter $A = \left|e^{p(\theta_o)/\omega}\right|$ also takes its maximum value at $\theta_o = \theta_{oq}$, and since we consider angles ω for which $\omega \to 0$, A decreases rapidly away from θ_{oq}. In this case, the integral in (C1) can be asymptotically approximated in the region very close to $\theta_o \cong \theta_{oq}$. By using Cauchy's theorem, we can always deform the initial contour c to a new contour c' that passes through $\theta_o = \theta_{oq}$.

These points $\theta_o = \theta_{oq}$, where $\mathrm{Re}\,p(\theta_{oq}) = \max[\mathrm{Re}\,p(\theta_o)]$ are called ***saddle-points*** and satisfy the condition $\partial p(\theta_o)/\partial\theta_o|_{\theta_o=\theta_{oq}} = 0$. The deformed contour c' is termed the ***steepest descent path*** (SDP) in the saddle-point theory, and the main contribution to the integral in (C1) along c' arise from the integration in the vicinity of θ_{oq}. It can be shown [3.10], that the steepest descent paths are those contours in the complex domain, along which the imaginary part of $p(\theta_o)$ stays constant and satisfies the condition, $\mathrm{Im}\,p(\theta_o) = \mathrm{Im}\,p(\theta_{oq})$. If any of the $g(\theta_o)$ or $p(\theta_o)$ functions have any singularities such as poles or branch points along the integration path, then these should be taken into account in the asymptotic calculation of the integrals.

In the following we focus our attention on the types of integrals appearing in the main text. Saddle-points are classified as first- or higher-order depending on whether the first derivative only or higher derivatives are zero at $\theta_o = \theta_{oq}$. In chapters 3 and 5, we meet saddle points of the first-order at $\theta_o = \theta_{oq}$, which are affected by a branch-point singularity at $\theta_o = \theta_c$, (3.27), the critical angle for reflection on the bottom surface in the homogenous tapered waveguide described in Chapter 3.

(a) When $\theta_{oq} < \theta_c$ then the contribution of the saddle point θ_{oq} dominates over the contribution of the branch-point, which can then be ignored. The saddle-point method with one ***first-order*** saddle-point is then used to approximate asymptotically the integrals in (C1).

(b) As the local width *h* of the taper decreases, the saddle-point θ_{oq} approaches θ_c, Fig. 3-5. When $\theta_{oq} \approx \theta_c$ then the influence of the branch-point should be taken into account. In this case the Chester-Friedman-Ursell [3.11] method should be used, which transforms the branch-point to a ***second-order*** saddle-point. In this case, we need the saddle-point method for two first order saddle points that can arbitrary approach each other to approximate asymptotically the integrals in (C1).

(c) When $\theta_{oq} > \theta_c$ then the contribution of the branch-point at θ_c should still be taken into account, but this case differs from the previous one in that the two saddle-points can be considered as being well separated and making two distinct contributions. In this

case saddle point method with ***one first-order*** saddle point and ***one branch-integral*** should be used to approximate integrals.

In the tapered bend case, Chapter 5 we meet a first order saddle points at $\theta_o = \theta_{oq}$, which is affected by two branch-points (as opposed to one in the homogenous waveguide). The first branch-point singularity is at $\theta_o = \theta_c$, the critical angle for reflection on the top surface, and the second branch-point at $\theta_o = \theta_{cf}$, (5.60), the critical angle for reflection on the bottom surface. We distinguish the following cases:

(d) When $\theta_{oq} < \theta_c$ then the contribution of the saddle point θ_{oq} dominates over the contribution of both branch-points, which are ignored and the ***first-order*** saddle-point is used to calculate the integrals in (C1).

(e) As the local width h of the taper decreases the saddle-point θ_{oq} approaches the first branch-point θ_c. Near to $\theta_{oq} \approx \theta_c$ the influence of the first branch-point should be taken into account and the Chester-Friedman-Ursell method for ***second-order*** saddle-points, is again used for the approximations of the integrals. However, the second branch-point at $\theta_o = \theta_{cf}$ is not interfering, and can still be ignored.

(f) In the region where, $\theta_c < \theta_{oq} < \theta_{cf}$ the contribution from both the branch-point at $\theta_o = \theta_c$ and the saddle point at $\theta_o = \theta_{oq}$ is considered, (while the contribution from θ_{cf} can be still ignored). However, as in the homogenous case we need to calculate the distinct contributions of a ***first-order*** saddle point and one ***branch-cut*** integral to calculate the integrals in (C1).

(g) As θ_{oq} approaches θ_{cf}, $\theta_{oq} \cong \theta_{cf}$ and goes past θ_{cf}, $\theta_{oq} > \theta_{cf}$, the contribution from the second branch-point has to be included. These cases can be treated using exactly the same way as the previous two cases, with the only difference that the distinct contribution of the first branch-point (it contributes a branch-cut integral) should be taken into account. The cases when $\theta_{oq} \cong \theta_{cf}$ and $\theta_{oq} > \theta_{cf}$ will not be analysed in detail due to their similarity with the cases in (e) and (f).

(h) Finally, as $\theta_{oq} > \theta_{cf}$ we have the contribution of one first-order saddle-point and two and the distinct contribution of two branch-cut integrals associated with the critical

angle for reflection at the top surface θ_c and the critical angle for reflection at the bottom surface θ_{cf}. The distinct contribution of the saddle-point can be treated as in d), while the contributions of each of the branch-points can be calculated as in (f), and so, we will not analyse this case here.

Based on the above remarks we present the general formulas for asymptotic approximation of integrals by the saddle point method for all cases of interest:

A. ***Saddle-point method for integrals with one first order saddle-point:*** $\partial p(\theta_o)/\partial\theta_o\big|_{\theta_o=\theta_{oq}} = 0,\ \partial^2 p(\theta_o)/\partial\theta_o^2\big|_{\theta_o=\theta_{oq}} \neq 0$.

We first transform $p(\theta_o)$ to a second order polynomial as

$$p(\theta_o) = p(\theta_{oq}) - s^2 \tag{C4}$$

the saddle-point in the s-domain is at $s = 0$ while the SDP is along the real s axis as it can be easily confirmed. Upon the variable change (C4) the integral in (C1) is transformed to

$$I(\omega) = e^{p(\theta_{oq})/\omega} \int_{-\infty}^{+\infty} G(s)\cdot e^{-s^2/\omega}\, ds \tag{C5}$$

where in (C5) the end points lie at infinity and $G(s)$ is given by

$$G(s) = g(\theta_{oq})\left(\frac{d\theta_o}{ds}\right)_{s=0},\quad \left(\frac{d\theta_o}{ds}\right)_{s=0} = \frac{-2s}{p'(\theta_{oq})} = \sqrt{\frac{2}{|p''(\theta_{oq})|}}\, e^{\pm i\pi/4} \tag{C6}$$

The square root in (C6) is a multivalued function as seen from the two phase choices ($\pm\pi/4$). The (+) sign should be chosen if $p''(\theta_{oq})>0$ (as is the case with the integrals throughout Chapter 3 and Chapter 5), while the (-) when $p''(\theta_{oq})<0$. For a full explanation about how to resolve the sign ambiguity in (C6) consult [3.11]. Since we have assumed that $g(\theta_o)$ and $p(\theta_o)$ are regular around θ_{oq} then $G(s)$ is regular around $s = 0$ and we can expand it into a power series

$$G(s) = G(0) + G'(0)s + G''(0)\frac{s^2}{2!} + \ldots \tag{C7}$$

If we only keep the first term (dominant term) of the power series (C7) and substitute the result to (C5) we get

$$I(\omega) \approx G(0)e^{p(\theta_{oq})/\omega}\int_{-\infty}^{+\infty} e^{-s^2/\omega}ds = \sqrt{\frac{2\pi\omega}{|p''(\theta_{oq})|}}g(\theta_{oq})e^{p(\theta_{oq})/\omega}e^{\pm i\pi/4} \qquad \text{(C8)}$$

where we used the equality $\int_{-\infty}^{+\infty} e^{-s^2/\omega}ds = \sqrt{\pi\omega}$ to derive the final result in (C8). The error involved in ignoring the higher order terms of the power series (C6) can be shown to be $O(\omega^{3/2})$.

B. Saddle-point method when a first order saddle-point approaches a branch-point.

The phase function $\Phi(\theta_o)$ defined in (3.6) for the homogenous waveguide and in (5.13) for the tapered bend, has a branch-point at θ_c which is passed to $p(\theta_o)$ through (C2). As the saddle-point θ_{oq} arbitrary approaches the branch point of the phase function, the contribution of θ_c should be considered. In order to overcome the singularity at $\theta_o = \theta_c$ we first apply the variable change

$$t = (\theta_c - \theta_o)^{1/2} \qquad \text{(C9)}$$

which has the effect of eliminating the branch-point and replacing it with a second saddle-point. This is easily confirmed by writing

$$\frac{\partial[Q_o(x,y;\theta_o(t)) - q\pi\theta_o(t)]}{\partial t} = \frac{\partial[Q_o(x,y;\theta_o) - q\pi\theta_o]}{\partial\theta_o}\cdot\frac{\partial\theta_o}{\partial t} = -2t\frac{\partial[Q_o(x,y;\theta_o) - q\pi\theta_o]}{\partial\theta_o} \qquad \text{(C10)}$$

and since saddle-points are determined by the relationship

$$\frac{\partial[Q_o(x,y;\theta(t)) - q\pi\theta_o(t)]}{\partial t} = 0 \qquad \text{(C11)}$$

we see that apart from the original saddle-point θ_{oq} we have the addition of a new one at θ_c or $t = 0$. In this way, $\Phi(\theta_o)$ is transformed to an analytic function and the asymptotic integration in (C1) is carried out by considering the influence of two confluent saddle-points in contrast to one saddle-point that we examined in the previous paragraph. Under the variable change (C9) the integral in (C1) becomes

$$I(\omega) = \int\frac{d\theta_o}{dt}g(\theta_o(t))\cdot e^{p(\theta_o(t))/\omega}dt = \int(-2t)g(t)\cdot e^{p(t)/\omega}dt \qquad \text{(C12)}$$

A uniform asymptotic evaluation of the integral (C12) is obtained by using the method of Chester-Friedman-Ursell. According to this method we associate Q_o with a third order polynomial as

$$\omega^{-1} p(t) = if_o - if_1 \frac{s^2}{2} - \frac{s^3}{3} = f(s) \tag{C13}$$

and the integral (C11) is transformed into the new s-domain

$$I(\omega) = \int \left[(-2t(s)) g(s) \frac{dt}{ds} \right] \cdot e^{p(s)/\omega} dt = \int G(s) \cdot e^{p(s)/\omega} ds \tag{C14}$$

In the new s-domain, the two saddle-points s_1 and s_2 are given by

$$\frac{\partial f(s)}{\partial s} = s(-if_1 - s) = 0 \Rightarrow \begin{cases} s_1 = 0 \\ s_2 = -if_1 \end{cases} \tag{C15}$$

without loss of generality we assume that s_1 corresponds to the saddle-point with t=0 and s_2 to θ_{oq}. Therefore, as $\theta_{oq} \rightarrow \theta_c$ we have $s_2 \rightarrow s_1 = 0$ in the s-domain.

With the help of (C13) and (C14) we can write

$$\omega^{-1} p(t = 0) = \tau(s_1) = if_o \tag{C16}$$

$$\omega^{-1} p\left[t(\theta_o = \theta_{oq})\right] = \tau(s_2) = i\left(f_o + \frac{1}{6} f_1^3 \right) \tag{C17}$$

the coefficient f_o is given directly by (C1) while f_1 can be calculated from (C16) and (C17)

$$f_1^3 = 6\omega^{-1} \left(p\left[t(\theta_o = \theta_{oq})\right] - p(t = 0) \right) \tag{C18}$$

in order to proceed with our asymptotic calculation of the integral in (C14) as $s_2 \rightarrow s_1 = 0$, we need the Taylor expansion of $G(s)$ around s=0

$$G(s) = G(0) + G'(0)s + G''(0) \frac{s^2}{2!} + \ldots \tag{C19}$$

The major difference from the previous case with the one saddle-point is that in this case we have

$$G(0) = (-2t) g(s) \left. \frac{dt}{ds} \right|_{t=s=0} = 0 \tag{C20}$$

and we need to keep the second term as a first order approximation of (C13), which involves the derivative of $G(s)$ and, which can be written

$$\left.\frac{dG(s)}{ds}\right|_{s=t=0} = \frac{d}{ds}\left[(-2t)g(s)\frac{dt}{ds}\right]_{s=t=0} \tag{C21}$$

in order to calculate (C21) we first need to calculate the *dt/ds* term. This can be done by differentiating (C13) in respect to s and by keeping in mind that $t = 0$ is a saddle-point which eliminates *dp(t)/dt* we get

$$\left.\frac{dt}{ds}\right|_{s=0} = \left.\frac{-if_1 s - s^2}{dp(t)/dt}\omega\right|_{s=t=0} \xrightarrow{\text{L'Hospital}} \left.\frac{dt}{ds}\right|_{s=0} = \sqrt{\frac{-i\omega f_1}{p''(t=0)}} \tag{C22}$$

with the aid of (C22) we get after some straight forward calculations the result for (C21) is

$$G'(0) = 2g(t=0)\frac{i\omega f_1}{p''(t=0)} \tag{C23}$$

by replacing (C23) to (C14) we take as a first order approximation for the integral I

$$I(\omega) = 2g(t=0)\frac{i\omega f_1 e^{if_o}}{p''(t=0)}\int e^{-i\frac{f_1}{2}s^2} e^{-\frac{s^3}{3}} ds \tag{C24}$$

the integral I in (C24), can be expressed with the aid of the Airy-function of first kind and its derivative with the aid of the relationship [3.12]

$$\int_{+\infty e^{2\pi i/3}}^{+\infty} e^{-iax^2} e^{-\frac{x^3}{3}} dx = -2\pi e^{2ia^3/3} e^{-i\pi/4} e^{-i\pi/12}\left[Ai'\left(a^2 e^{i\pi/3}\right) + e^{i\pi/6} Ai\left(a^2 e^{i\pi/3}\right)\right] \tag{C25}$$

and finally by replacing (C25) to (C23) we get the result for the asymptotic calculation of integrals when a saddle-point is arbitrary close to a branch-point as

$$I(\omega) = -4\pi g(t=0)\frac{i\omega f_1 e^{if_o}}{p''(t=0)} e^{2i(f_1/2)^3/3} e^{-i\pi/4} e^{-i\pi/12}\left[Ai'\left(\zeta e^{i\pi/3}\right) + e^{i\pi/6} Ai\left(\zeta e^{i\pi/3}\right)\right] \tag{C26}$$

$$\zeta = \left\{\frac{3}{4}\left[p(\theta_{oq}) - p(t=0)\right]\right\}^{1/3} / \omega^{1/3} \tag{C27}$$

C. Saddle-point method for asymptotic calculation of integrals around a branch-cut.

The last integral that we calculate is related to the cases (c) and (f) where the saddle-point is well separated from the branch point and the distinct contribution of the branch-point needs to be calculated. When the integration path traverses a branch-cut as it happens for example in the case when the saddle point θ_{oq} is larger than the critical angle θ_c, then the

path should be deformed to surround the branch-cut in the context shown in Fig. 3-5, Fig. 5-10. In this case, this integral, which is called a branch-cut integral, gives a distinct contribution. The branch-cut integral can be calculated in the following way: We first use the same variable change as in (C9) which transforms the general integral (C1) into the form shown in (C12). As mentioned in paragraph B the branch-point has now been transformed to a saddle-point at $t = 0$. The difference, however, from the previous case is that now we do not have to take into account the contribution from the second saddle point at $\theta_o = \theta_{oq}$ since we assume that $\theta_{oq} >> \theta_c$ and the two saddle-points are considered to be well separated, and thus giving two distinct contributions. Since we can treat the branch-point at θ_c as a saddle-point, we can use the same method presented in paragraph A to calculate its contribution. Following the lines drew in paragraph A, we apply the transformation (C4) to the integral in (C12) to obtain

$$I(\omega) = \int(-2t)g(t)\cdot e^{p(t)/\omega}dt = \int\left[(-2t(s))\,g(t(s))\frac{dt}{ds}\right]\cdot e^{-s^2/\omega}ds = \int_{-\infty}^{+\infty}G(s)\cdot e^{-s^2/\omega}ds \tag{C28}$$

The difference to the case in section A is that after expanding $G(s)$ around 0 as in (C6) the first term $G(0)$ is zero and, therefore, we need to use higher terms for the asymptotic calculation of (C28). The second term of the power series (C7) is proportional to s, and since the function $se^{-s^2/\omega}$ is an odd function, it gives a zero contribution upon integration in the [-∞, +∞] interval. Therefore, it is the third term of the series in (C7) that dominates the asymptotic calculation. By keeping the third term only we can approximate $G(s)$ as

$$G(s) \approx G''(0)\frac{s^2}{2!} \tag{C29}$$

and so we get a final approximation for the integral I in (C28)

$$I(\omega) = G''(0)\int_{-\infty}^{+\infty}s^2e^{-s^2/\omega}ds = \frac{\sqrt{\pi}}{2}\omega^{3/2}G''(0) \tag{C30}$$

where in order to derive (C30) we used the identity

$$I(\omega) = \int_{-\infty}^{+\infty}s^n e^{-s^2/\omega}ds = \begin{cases}\Gamma[(1+n)/2]\omega^{(1+n)/2}, & n \text{ even}\\ 0, & n \text{ odd}\end{cases} \tag{C31}$$

with Γ standing for the Gamma function, and the identity

$$\Gamma[(1+n)/2] = \frac{(n-1)}{2}\sqrt{\pi} \tag{C32}$$

In order to evaluate the integral I in (C30) we need to calculate the second derivative of $G(s)$ at $s = 0$ with $G(s)$ defined in (C29). After performing the derivations we obtain

$$G''(s=0) = z''(t=0)[\varphi(s=0)]^3 + 3z'(t=0)\varphi(s=0)\varphi'(s=0) \tag{C33}$$

where primes in (C33) are understood as differentiation in respect to the implied argument and the following definitions for the parameters involved in (C33)

$$z(t) = (-2t)g(t) \tag{C34}$$

$$\varphi(s=0) = \left.\frac{dt}{ds}\right|_{s=0} = \sqrt{\frac{2}{\left|d^2p(t)/dt^2\right|_{t=0}}}e^{\pm i\pi/4} \tag{C35}$$

$$\varphi'(s=0) = \frac{2}{3}\sqrt{\frac{\left[d^3p(t)/dt^3\right]_{t=0}}{\left[d^2p(t)/dt^2\right]^2_{t=0}}}e^{\pm i\pi/4} \tag{C36}$$

where again the sign in the $\exp(\pm\pi/4)$ factor is resolved in conjunction to the sign of $d^2p(t)/dt^2$ as in (C6) in section A.

APPENDIX D

PLANE WAVES IN WAVEGUIDE BENDS

D1. Power flow through a straight waveguide cross-section

The ray trace method implies that the bound modes of the waveguide can be approximated by plane waves, which propagate by successive reflections at the waveguide boundaries. The E_x field component of a *TE*-polarized plane wave propagating in the waveguide core is given by

$$E_x = Ae^{-ik_x x}e^{-ik_y y}e^{-i\beta z} \tag{D1}$$

with A, the amplitude of the plane wave, β its propagation constant, k_x its wavenumber along x, and k_y its wavenumber along y. The k-vector of such a plane wave subtends angles θ_x, θ_y, φ with the x, y, z axes as shown in Fig. D1. If the wavenumber in free space is $\kappa = 2\pi/\lambda$ (λ the wavelength of operation) and the refractive index of the core is n_{co}, then the amplitude of the k-vector is related to k_x , k_y and β through the relationships,

$$k^2 = k_x^2 + k_y^2 + \beta^2 = \kappa^2 n_{co}^2 ,$$

$$k_x = k\cos\theta_x,\ k_y = k\cos\theta_y,\ \beta = k\cos\varphi \tag{D2}$$

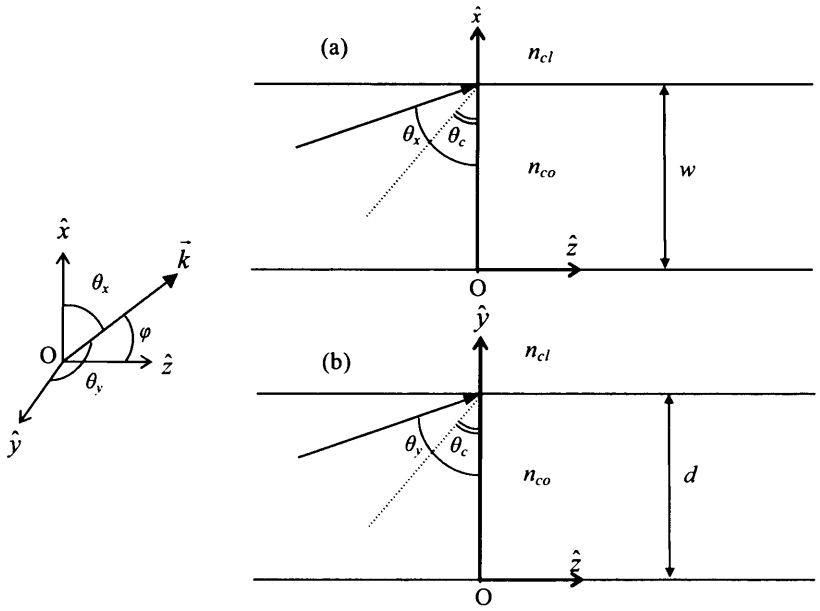

Fig. D1. Plane wave approximation of modal propagation in waveguides. (a) *xz*-plane view of propagating rays, (b) *yz*-plane view of propagating rays

Plane waves propagate inside the waveguide without attenuation if and only if they reflect at the boundaries with angles larger than the critical one, θ_c measured from the normal to the surface, Fig. D1. The critical angle for reflection on a planar surface between two dielectrics with refractive indices n_{co} (core) and n_{cl} (cladding) is given by the relationship

$$\sin\theta_{cr} = \frac{n_{cl}}{n_{co}} \Rightarrow \theta_{cr} = \arcsin\left(\frac{n_{cl}}{n_{co}}\right) \tag{D3}$$

The parameter $NA = \sin(\theta_c)$ is termed the numerical aperture and is a useful quantity in waveguiding theory, which determines the range of angles that a waveguide can accept for propagation. According to what we have said about reflection with angles more than the critical one, plane waves will be guided inside the waveguide if the angles they subtend with the x and y axes satisfy the conditions

$$\theta_{cr} < \theta_x < \frac{\pi}{2} \quad \text{or} \quad -\frac{\pi}{2} < \theta_x < -\theta_{cr} \quad \text{and} \quad \theta_{cr} < \theta_y < \frac{\pi}{2} \quad \text{or} \quad -\frac{\pi}{2} < \theta_y < -\theta_{cr} \tag{D4}$$

where, the positive range of θ_x (θ_y) angles should be taken for propagation towards the positive x-direction (y-direction), and the negative ranges of θ_x (θ_y) for propagation towards the negative directions. In addition, the angles of the planes waves propagating inside a waveguide are not continuous but take some district values within the ranges in (D4), defined by imposing the appropriate dielectric boundary conditions, at the core-cladding interfaces, on the exact solutions of the wave equation. However, for highly multimode waveguides, like the ones we are considering in this PhD, the large number of bound modes allow us to consider the angles to be continuous and to cover the entire ranges defined in (D4), [4.31], [4-32], [4.35].

The calculation of the power flow of any plane wave (D1), through a waveguide transverse cross-section requires the knowledge of the z-component of the Poynting vector S_z, which is given by [4.38]

$$S_z = \frac{1}{2}\varepsilon_o \omega \frac{\beta}{k^2} E_x \cdot E_x^* = \frac{A^2}{2}\varepsilon_o \omega \frac{\beta}{k^2} \tag{D5}$$

The power flow P_{θ_x,θ_y}, of this plane wave can be then calculated by integrating the Poynting vector over a waveguide transverse cross-section as

$$P_{\theta_x,\theta_y} = \frac{A^2}{2}\varepsilon_o\omega\frac{\beta}{k^2}\int_{-w/2}^{w/2}\int_{-d/2}^{d/2}dxdy = \frac{A^2wh}{2}\varepsilon_o\omega\frac{\beta}{k^2} = \frac{A^2wh}{2}\frac{\varepsilon_o\omega}{k}\cos\varphi = \frac{A^2wh}{2}\frac{\varepsilon_o\omega}{k}\sqrt{1-\cos^2\theta_x-\cos^2\theta_y} = I(\theta_x,\theta_y) \tag{D6}$$

where in (D6) we made use of (D2). Equation (D6) assumes all the energy of the waves to be confined inside the core of the waveguide, which is true for at least the strongly guided modes. The total power flow I_o from all plane waves, is calculated by summing the incremental power flow contributions from each plane wave guided in the waveguide, which with the aid of (D3) becomes

$$I_o = \int_{\theta_x=\theta_{cr}}^{\pi/2}\int_{\theta_y=\theta_{cr}}^{\pi/2} + \int_{\pi/2}^{-\theta_{cr}}\int_{\pi/2}^{-\theta_{cr}} I(\theta_x,\theta_y)d\theta_x d\theta_y = 2A^2wh\frac{\varepsilon_o\omega}{k}\int_{\theta_x=\theta_{cr}}^{\pi/2}\int_{\theta_y=\theta_{cr}}^{\pi/2}\sqrt{1-\cos^2\theta_x-\cos^2\theta_y}\,d\theta_x d\theta_y \tag{D7}$$

D2. Loss due to transition from a straight to a curved waveguide

Inside the curved section, angles θ_y are preserved since reflections still occur on the planar surfaces $y = 0$ and $y = d$, (the curvature is only in the xz plane). However, θ_x and so φ have to change to account for reflections along the curved surfaces. On the upper curved boundary, rays are reflected with angles ψ, measured on a local polar coordinate system moving with the radius of curvature of the upper boundary R, Fig. D2, which are given by applying the law of sines to the **AOB** triangle as

$$\sin\psi = [(R - x_o)/R]\sin\theta_x, \quad 0 < x_o < w \tag{D8}$$

where x_o, is the distance along the x-axis between the upper curved boundary and the position from where the ray enters the curved section and w the width of the waveguide. Equation (D8) shows that $\sin\psi < \sin\theta_x$ and so, $\psi < \theta_x$ and therefore some rays, which previously belonged to propagating waves in the straight waveguide section might reflect at angles less than the critical angle inside the bend, resulting in radiation loss. In addition, for rays entering from the same position x_o, decreasing θ_x leads to decreasing ψ and so it is easier for the high order modes ($\theta_x \sim \theta_c$) of the straight waveguide to go beyond cut-off in the bend, rather than the low order modes ($\theta_x \sim \pi/2$). This implies that curved waveguides behave like mode filters, filtering out the higher order modes. The worst case is for rays passing through $x_o = w$, as these rays travel further into the

waveguide before reflecting from its walls, as happens with the two parallel rays r_1 and r_2 shown in Fig. D2.

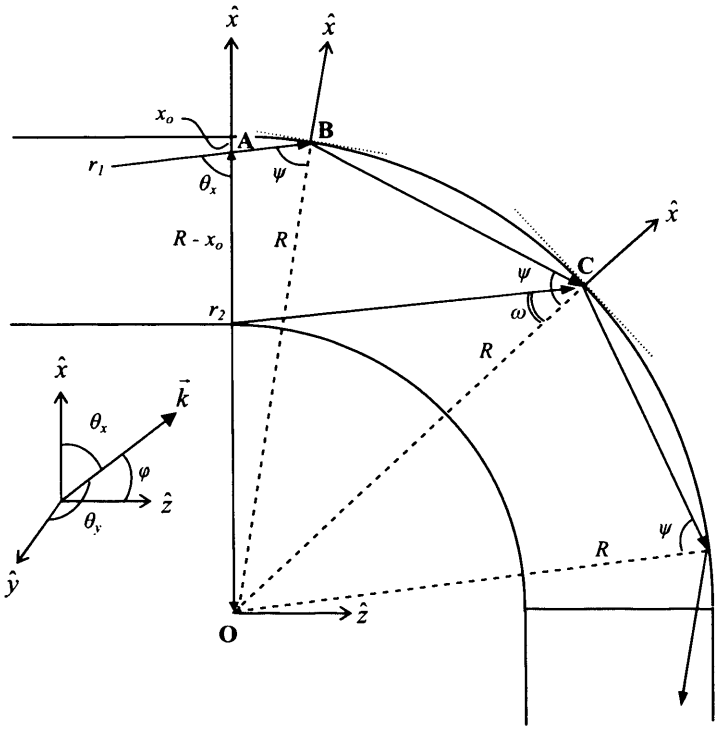

Fig. D2. Schematic diagram of rays entering the waveguide bend from the input straight waveguide for the geometrical ray optical calculation of acceptance angle and numerical aperture. In the diagram we observe two parallel rays r_1 and r_2, which both subtend angle θ_x with the x-axis, to enter the waveguide bend from two different points on the straight waveguide – waveguide bend interface. Due to the waveguide curvature, r_1 is reflected from the upper boundary of the bend with angle $\psi < \theta_x$. If ψ is smaller than the critical angle $\psi < \theta_c$ then r_1 will find itself beyond cut-off inside the bend and will be lost. The second ray r_2, is reflected with angle $\omega < \psi < \theta_x$ inside the bend. Therefore, r_2 is more likely to be lost than r_1.

Therefore, the first ray to be lost will pass from $x_o = w$, and it is reflected by the upper bent boundary with the critical angle ($\psi = \theta_c$). By replacing $\sin\psi \rightarrow \sin\theta_{cr} = n_{cl}/n_{co}$ and $x_o = w$ in (D8), we find that all plane waves with angles θ_x satisfying the condition

$$\theta_x < \theta_o = \arcsin\left[\frac{n_2}{n_1}\frac{(R-w)}{R}\right] \tag{D9}$$

contain some rays, which are reflected with angles beyond the critical angle inside the bend and thus, are rapidly lost. Each plane wave with $\theta_x < \theta_o$, has a window on its wavefront, which radiates away from the waveguide. This is the part in the range $x_o'(\theta_x) < x_o <$ w where $x_o'(\theta_x)$ is found from (D8) as ψ approaches the critical angle

$$x_o'(\theta_x) = R\left(1 - \frac{n_{cl}}{n_{co}} \frac{1}{\sin\theta_x}\right) \tag{D10}$$

If (D8) was solved for θ_x, as $\sin\psi \rightarrow \sin\theta_{cr}$ instead, then we could interpret in an alternative way.

$$\theta_x = \theta_o(x) = \arcsin\left[\frac{n_{cl}}{n_{co}} \frac{R}{R - x_o}\right] \tag{D11}$$

Equation (D11) implies that rays entering the curved section from a given x_o, survive as they propagate inside the bend if they belong in the range $\theta_o < \theta_x < \pi/2$ while they go beyond cut-off inside the bend if they belong in the range $\theta_c < \theta_x < \theta_o$. Therefore, the angle θ_o is in some ways the equivalent to the acceptance angle which determines the *NA* in straight waveguides. The difference is that in curved waveguides θ_o, and thus, the *NA* varies along the waveguide aperture with x. Each plane wave with $\theta_x < \theta_o$ experiences some degree of transition loss, while those with $\theta_x > \theta_o$ do not experience any attenuation. For a certain plane wave with $\theta_x < \theta_o$, the power I_α, which is lost, is found by integrating the Poynting vector, (D5) along the window of loss $x_o'(\theta_x) < x_o < w$, (D10).

$$I_\alpha(\theta_x, \theta_y) = \int_{x_o(\theta_x)}^{x_o = w} \int_{y=0}^{h} \frac{A^2 wh}{2} \frac{\varepsilon_o \omega}{k} \sqrt{1 - \cos^2\theta_x - \cos^2\theta_y}\, dx dy = \frac{A^2 h}{2} \frac{\varepsilon_o \omega}{k} (w - x_o(\theta_x)) \sqrt{1 - \cos^2\theta_x - \cos^2\theta_y} \tag{D12}$$

Finally, the total power lost from all plane waves propagating from the straight waveguide into the waveguide bend is found from (D12) by summing the incremental loss contributions from each plane wave, in a similar manner as in (D7)

$$I_\alpha = 4 \int_{\theta_x = \theta_0}^{\pi/2} \int_{\theta_y = \theta_{cr}}^{\pi/2} I_\alpha(\theta_x, \theta_y) d\theta_x d\theta_y \tag{D13}$$

Therefore, the loss due to transition between a straight and a curved waveguide *TransA*, is given by

$$TransA = \frac{I_\alpha}{I_o} \tag{D14}$$

APPENDIX E

EIGENVALUE EQUATION OF A TRANSFORMED WAVEGUIDE BEND

The aim of this appendix is to prove that the eigenvalue equation (5.78), which determines the discrete set of angles θ_o of the rays that propagate inside the local cross-sections, agrees exactly with the eigenvalue equation (24) in [5.10], which gives the propagation constants of a waveguide bend with a width equal to the local width of the tapered bend. First we repeat (5.79) for convenience

$$\int_0^w kn_{co}\sqrt{e^{2y/R_1}-e^{2w/R_1}\cos^2\theta_{oq}}\,dy-\arctan\left[\frac{\sqrt{\cos^2\theta_{oq}-\cos^2\theta_c}}{\sin\theta_{oq}}\right]-\arctan\left[\frac{\sqrt{e^{2w/R}\cos^2\theta_{oq}-\cos^2\theta_c}}{\sqrt{1-e^{2w/R}\cos^2\theta_{oq}}}\right]=q\pi \tag{E1}$$

the integral in (E1) can be calculated in a closed form to give

$$\begin{aligned}&kn_{co}R_1\left\{e^{w/R_1}\sin\theta_{oq}-\sqrt{1-e^{2w/R_1}\cos^2\theta_{oq}}\right]-e^{w/R_1}\cos\theta_{oq}\left[\cos^{-1}(\cos\theta_{oq})-\cos^{-1}\left(e^{h/R_1}\cos\theta_{oq}\right)\right]\Big\}\\&-\arctan\left[\frac{\sqrt{\cos^2\theta_{oq}-\cos^2\theta_c}}{\sin\theta_{oq}}\right]-\arctan\left[\frac{\sqrt{e^{2w/R}\cos^2\theta_{oq}-\cos^2\theta_c}}{\sqrt{1-e^{2w/R}\cos^2\theta_{oq}}}\right]=q\pi\end{aligned} \tag{E2}$$

by using the definitions

$$\beta=kn_{co}e^{w/R_1}\cos\theta_{oq} \tag{E3}$$

$$w=R_1\ln\left(\frac{R_2}{R_1}\right) \tag{E4}$$

and combining (E2), (E3) and (E4) with the definition for the critical angle $\cos\theta_c=n_{cl}/n_{co}$ we derive

$$\begin{aligned}&\beta R_1\left\{\left[\sqrt{\frac{k^2n_{co}^2}{\beta^2}\cdot\frac{R_2^2}{R_1^2}-1}-\sqrt{\frac{k^2n_{co}^2}{\beta^2}-1}\right]-\left[\cos^{-1}\left(\frac{\beta}{kn_{co}}\cdot\frac{R_1}{R_2}\right)-\cos^{-1}\left(\frac{\beta}{kn_{co}}\right)\right]\right\}\\&-a\tan\left[\frac{\sqrt{\frac{R_1^2}{R_2^2}\beta^2-k^2n_{cl}^2}}{\sqrt{k^2n_{co}^2-\frac{R_1^2}{R_2^2}\beta^2}}\right]-a\tan\left[\frac{\sqrt{\beta^2-k^2n_{cl}^2}}{\sqrt{k^2n_{co}^2-\beta^2}}\right]=q\pi\end{aligned} \tag{E5}$$

if we take as reference the refractive index on the top surface and use the notation

$$n'_{co} = n_{co}\frac{R_2}{R_1}, n'_{cl} = n_{cl}\frac{R_2}{R_1} \tag{E6}$$

then (E5) is transformed to

$$\begin{aligned}&\beta R_2\left\{\left[\sqrt{\frac{k^2 n'^2_{cl}}{\beta^2}-1}-\sqrt{\frac{k^2 n'^2_{cl}}{\beta^2}\cdot\frac{R_1^2}{R_2^2}-1}\right]-\cos^{-1}\left(\frac{\beta}{kn'_{co}}\right)+\cos^{-1}\left(\frac{\beta}{kn'_{co}}\cdot\frac{R_2}{R1}\right)\right\}\\&-\arctan\left[\frac{\sqrt{\beta^2-k^2n'^2_{cl}}}{\sqrt{k_o^2n'^2_{co}-\beta^2}}\right]-\arctan\left[\frac{\sqrt{\beta^2-k_o^2n'^2_{cl}\frac{R_1^2}{R_2^2}}}{\sqrt{\frac{R_1^2}{R_2^2}k_o^2n'^2_{co}-\beta^2}}\right]=q\pi\end{aligned} \tag{E7}$$

Equation (E7) agrees precisely with (24) in [5.10].

APPENDIX F

REFLECTION COEFFICIENTS FOR WHISPERING GALLERY WAVES

The phase coefficient $\Phi_{\theta_f}(\theta_o)$ due to wave reflection on the bottom surface, takes a more complicated form in the case of the whispering gallery modes, compared to the non-whispering gallery mode phase coefficient (5.31). The phase coefficient $\Phi_{\theta_f}(\theta_o)$ in this case can be calculated by making use of the electromagnetic theory in multilayer waveguides. If the angle that rays form with the z-axis θ_o, at the top boundary S_2 is shallow, then as rays propagate from the top surface of the waveguide to the bottom they gradually bend until they finally become parallel to the waveguide boundaries. The point where the rays become parallel to the waveguide is called the caustic or turning point and occurs at a distance w' measured from the bottom boundary, which from (5.7) is given by

$$e^{w'/R_1} = e^{w/R_1}\cos\theta_o \tag{F1}$$

where in order to extract (F1) we took into account that the angle that the rays form with the z-axis is at the turning point $x = w'$ is $\theta(w') = 0$. Whispering gallery waves are formed for all angles θ_o, for which $w' > 0$. At $x = w'$ a caustic is formed for the field in the waveguide and the denominator of the WKB field expression in (5.6) goes to zero. To overcome the problem of the singular field at the turning points we use a method in which we assume that the continuous refractive index is replaced by two infinitely thin layers of constant refractive index as shown in Fig. F-1. The refractive index n, in the core region around $x = w'$ is taken to be

$$n = \begin{cases} n_1 e^{(w'+\Delta x)/R_1}, & w' < x < w' + \Delta x \\ n_1 e^{(w'-\Delta x)/R_1}, & w' - \Delta x < x < w' \end{cases} \tag{F2}$$

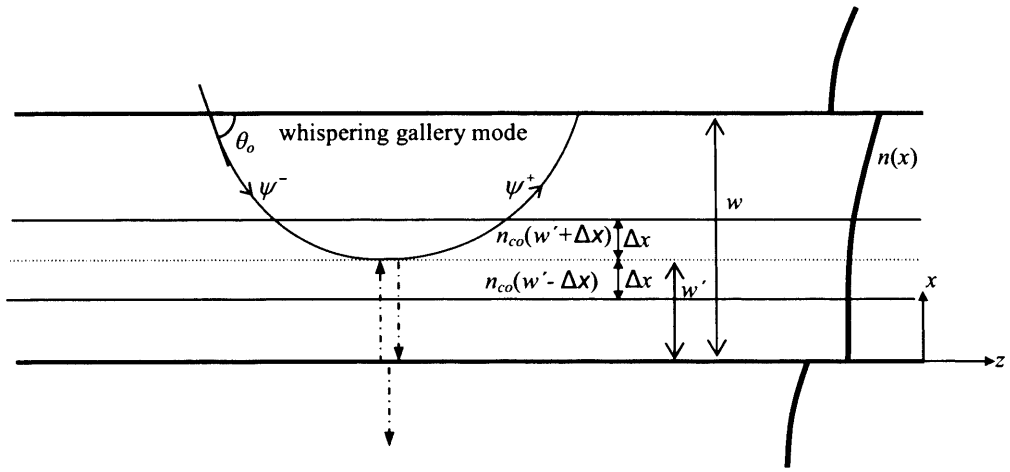

Fig. F-1. Evaluation of phase coefficient for the whispering gallery type eigenfunctions. To overcome the singularity of the wavefunctions (caustics) at the turning point, we replace the waveguide core region close to h' with two infinitely thin slabs with constant refractive index and an index difference of $\Delta n = n_{co}(w'+\Delta x) - n_{co}(w'-\Delta x)$. The phase coefficient for the continuous index case is taken as the limiting case of the Rayleigh coefficient for the phase change in this slab waveguide system as $\Delta x \to 0$. Evanescent waves are shown with dashed-dotted lines and their contribution is taken into account in the same way as in the case of multilayer waveguides.

We then take the following representations for the electric and magnetic components of a *TE* type field in the two slab regions

For $w' < x < w' + \Delta x$:

$$E_z : \psi_1^{\pm} = a^{\pm} \exp\left[\mp ikn_{co}\sqrt{e^{2(w'+\Delta x)/R_1} - e^{2w/R_1}\cos^2\theta_o}\cdot(x-w')\right]$$

$$H_x : i\frac{\partial \psi_1^{\pm}}{\partial y} = \pm a^{\pm} kn_{co}\sqrt{e^{2(w'+\Delta x)/R_1} - e^{2w/R_1}\cos^2\theta_o}\exp\left[\mp ikn_{co}\sqrt{e^{2(w'+\Delta x)/R_1} - e^{2w/R_1}\cos^2\theta_o}\cdot(x-w')\right] \tag{F3}$$

and for $w' - \Delta x < x < w'$:

$$E_z : \psi_2^{\pm} = b^{\pm} \exp\left[\pm kn_{co}\sqrt{e^{2w/R_1}\cos^2\theta_o - e^{2(w'-\Delta x)/R_1}}\cdot(x-w')\right]$$

$$H_x : i\frac{\partial \psi_2^{\pm}}{\partial x} = \pm ib^{\pm} kn_{co}\sqrt{e^{2w/R_1}\cos^2\theta_o - e^{2(w'-\Delta x)/R_1}}\exp\left[\pm kn_{co}\sqrt{e^{2w/R_1}\cos^2\theta_o - e^{2(w'-\Delta x)/R_1}}\cdot(x-w')\right] \tag{F4}$$

where in (F3) the argument of the exponents in the electric and magnetic field components is imaginary expressing propagating waves and it is real in (F4) to express evanescent waves. Also without loss of generality and in order to simplify calculations we took the zero phase level to occur at $x = w'$ in (F3) and (F4). Boundary conditions require continuity of the tangential field components at $x = w'$, which can be expressed as

$$\left.\begin{aligned}\psi_1^+ + \psi_1^- &= \psi_2^+ + \psi_2^- \\ \frac{\partial\psi_1^+}{\partial x} + \frac{\partial\psi_1^-}{\partial x} &= \frac{\partial\psi_2^+}{\partial x} + \frac{\partial\psi_2^-}{\partial x}\end{aligned}\right|_{x=w'} \tag{F5}$$

combining (F5) with (F3) and (F4) we get the boundary conditions in a matrix form

$$\begin{bmatrix} \dfrac{1}{\sqrt{e^{2(w'+\Delta x)/R_1} - e^{2w/R_1}\cos^2\theta_o}} & -\dfrac{1}{\sqrt{e^{2(w'+\Delta x)/R_1} - e^{2w/R_1}\cos^2\theta_o}} \end{bmatrix} \begin{bmatrix} a^+ \\ a^- \end{bmatrix} =$$

$$= \begin{bmatrix} \dfrac{1}{+i\sqrt{e^{2w/R_1}\cos^2\theta_o - e^{2(w'-\Delta x)/R_1}}} & \dfrac{1}{-i\sqrt{e^{2w/R_1}\cos^2\theta_o - e^{2(w'-\Delta x)/R_1}}} \end{bmatrix} \begin{bmatrix} b^+ \\ b^- \end{bmatrix}$$

which, after some calculations can be written as

$$\begin{bmatrix} a^+ \\ a^- \end{bmatrix} = \frac{1}{2A} \cdot \begin{bmatrix} (A+iB) & (A-iB) \\ (A-iB) & (A+iB) \end{bmatrix} \begin{bmatrix} b^+ \\ b^- \end{bmatrix} \tag{F6}$$

$$\begin{aligned} A &= \sqrt{e^{2(w'+\Delta x)/R_1} - e^{2w/R_1}\cos^2\theta_o} \\ B &= \sqrt{e^{2w/R_1}\cos^2\theta_o - e^{2(w'-\Delta x)/R_1}} \end{aligned} \tag{F7}$$

At $x = 0$ we have an abrupt change of the refractive index from n_{co} to n_{cl}. To see the effect of the step index change on the phase coefficient, we write the fields in the region of continuous refractive index $0 < x < w'\text{-}\Delta x$.

$$\begin{aligned} E_z : \psi_3^\pm &= b^\pm \exp\left[\pm k n_{co} \int_0^x \sqrt{e^{2w/R_1}\cos^2\theta_o - e^{2x'/R_1}}\, dx' \right] \\ H_x : \frac{\partial\psi_3^\pm}{\partial x} &= \pm i b^\pm k n_{co} \sqrt{e^{2w/R_1}\cos^2\theta_o - e^{2x/R_1}} \exp\left[\pm k n_{co} \int_0^x \sqrt{e^{2w/R_1}\cos^2\theta_o - e^{2x'/R_1}}\, dx' \right] \end{aligned} \tag{F8}$$

Note that in (F8) the same amplitude coefficients $b^\pm$, were chosen as in (F4) since at the interface between the slab waveguide and the region with the inhomogeneous index at $x = w'\text{-}\Delta x$ the refractive index is continuous and thus no other intermediate reflections are involved.

Finally in the $x < 0$ region we write for the fields

$$\begin{aligned} E_z : \psi_4^+ &= c^+ \exp\left[+ k n_{cl} \int_0^x \sqrt{\frac{n_{co}^2}{n_{cl}^2} e^{2w/R_1}\cos^2\theta_o - e^{2x'/R_1}}\, dx' \right] \\ H_x : i\frac{\partial\psi_4^+}{\partial x} &= i c^+ k n_{cl} \sqrt{\frac{n_{co}^2}{n_{cl}^2} e^{2w/R_1}\cos^2\theta_o - e^{2w/R_1}} \exp\left[+ k n_{cl} \int_0^x \sqrt{\frac{n_{co}^2}{n_{cl}^2} e^{2w/R_1}\cos^2\theta_o - e^{2x'/R_1}}\, dx' \right] \end{aligned} \tag{F9}$$

where only the (+) solution was selected in (F9) to satisfy the Sommerfeld radiation condition for finite fields at infinity. The $\frac{n_{co}^2}{n_{cl}^2}$ factor in the argument of the square roots in ψ_4^+ and in $\frac{\partial \psi_4^+}{\partial x}$ appears because of the Snell's law (5.14), which is valid even for imaginary angles at $x = 0$. The boundary conditions at $x = 0$ will then read

$$\left.\begin{aligned} \psi_3^+ + \psi_3^- &= \psi_4^+ \\ \frac{\partial \psi_3^+}{\partial x} + \frac{\partial \psi_3^-}{\partial x} &= \frac{\partial \psi_4^+}{\partial x} \end{aligned}\right|_{x=0}$$

or in a matrix form

$$\begin{bmatrix} \dfrac{1}{in_{co}\sqrt{e^{2w/R_1}\cos^2\theta_o - 1}} & -in_{co}\sqrt{e^{2w/R_1}\cos^2\theta_o - 1} \end{bmatrix} \begin{bmatrix} b^+ \\ b^- \end{bmatrix} = \begin{bmatrix} \dfrac{1}{in_{cl}\sqrt{\dfrac{n_{co}^2}{n_{cl}^2}e^{2w/R_1}\cos^2\theta_o - 1}} \end{bmatrix} c^+$$

which after some calculations take the form

$$\begin{bmatrix} b^+ \\ b^- \end{bmatrix} = \frac{1}{-2n_{co}\sqrt{e^{2w/R_1}\cos^2\theta_o - 1}} \begin{bmatrix} -n_{co}\sqrt{e^{2w/R_1}\cos^2\theta_o - 1} - n_2\sqrt{\dfrac{n_{co}^2}{n_{cl}^2}e^{2w/R_1}\cos^2\theta_o - 1} \\ -n_{co}\sqrt{e^{2w/R_1}\cos^2\theta_o - 1} + n_{cl}\sqrt{\dfrac{n_{co}^2}{n_{cl}^2}e^{2w/R_1}\cos^2\theta_o - 1} \end{bmatrix} c^+ \tag{F10}$$

Finally by combining (F6) and (F10) we derive the relationship between the amplitude a^+ of the upward travelling part and the amplitude a^- of the downward travelling part of a whispering gallery wave as

$$\begin{bmatrix} a^+ \\ a^- \end{bmatrix} = \frac{c^+}{2AD} \cdot \begin{bmatrix} AD + iBC \\ AD - iBC \end{bmatrix} \tag{F11}$$

$$\begin{aligned} C &= \sqrt{e^{2w/R_1}\cos^2\theta_o - \cos^2\theta_c} \\ D &= \sqrt{e^{2w/R_1}\cos^2\theta_o - 1} \end{aligned} \tag{F12}$$

As we see in (F11) $a^- = a^{+*}$, with the asterisk sign denoting complex conjugate and also $|a^-| = |a^+| = 1$. Therefore we can extract the argument of the reflection coefficient a^+ / a^- as

$$\Phi = Arg\left(a^{+}/_{a^{-}}\right) = 2\,Arg\left(a^{+}\right)$$

$$= 2\arctan\left[\frac{\sqrt{e^{2w/R_1}\cos^2\theta_o - e^{2(w'-\Delta x)/R_1}}}{\sqrt{e^{2(w'+\Delta x)/R_1} - e^{2w/R_1}\cos^2\theta_o}} \cdot \frac{n_{cl}\sqrt{\frac{n_{co}^2}{n_{cl}^2}e^{2w/R_1}\cos^2\theta_o - 1}}{n_{co}\sqrt{e^{2w/R_1}\cos^2\theta_o - 1}}\right] \tag{F13}$$

Finally as mentioned in the above the phase coefficient $\Phi_{\theta f}$ for the whispering gallery waves is takes as the limiting case of Φ when $\Delta x \to 0^{+}$ which with the aid of (F1) is calculated as

$$\Phi_{\theta f}(\theta_o) = \lim_{\Delta x \to 0^{+}}(\Phi) = \lim_{\Delta x \to 0^{+}}\left(2a\tan\left[\frac{\not{e}^{w'/R_1}\sqrt{1-e^{-2\Delta x/R_1}}}{\not{e}^{w'/R_1}\sqrt{e^{2\Delta x/R_1}-1}} \cdot \frac{n_{cl}\sqrt{\frac{n_{co}^2}{n_{cl}^2}e^{2w/R_1}\cos^2\theta_o - 1}}{n_{co}\sqrt{e^{2w/R_1}\cos^2\theta_o - 1}}\right]\right) =$$

$$= 2\arctan\left[\frac{\sqrt{e^{2w/R_1}\cos^2\theta_o - \frac{n_{cl}^2}{n_{co}^2}}}{\sqrt{e^{2w/R_1}\cos^2\theta_o - 1}}\right] = 2\arctan\left[\frac{\sqrt{e^{2w/R_1}\cos^2\theta_o - \cos^2\theta_c}}{\sqrt{e^{2w/R_1}\cos^2\theta_o - 1}}\right] \tag{F14}$$

which can be also be written if (F1) is used once again as

$$2\Phi_{\theta f} = \arctan\left[\frac{n_{cl}\sqrt{\frac{n_{co}^2}{n_{cl}^2}e^{2w'/R_1} - 1}}{n_{co}\sqrt{e^{2w'/R_1} - 1}}\right] \tag{F15}$$

To validate the above expression for the phase coefficient we examine the following two limiting cases

A) Assume that the second boundary did not exist (or equivalently that $w \to +\infty$) then from (F14) we would take

$$\underset{w\to+\infty}{2\Phi_{\theta f}} = \underset{w\to+\infty}{\arctan}\left[-\frac{\not{e}^{w/R_1}\sqrt{n_{co}^2\cos^2\theta_o - n_{cl}^2 e^{-2w/R_1}}}{n_{co}\not{e}^{w/R_1}\sqrt{\cos^2\theta_o - e^{-2w/R_1}}}\right] = a\tan(1) = \frac{\pi}{4} \tag{F16}$$

as expected for whispering gallery waves without bottom boundary.

B) Assume that θ_o was such, that rays changed direction exactly at the bottom boundary (or else assume that $w' = 0$) then we would then take from (F15)

$$2\Phi_{\substack{\theta f \\ w'\to 0^+}} = \arctan_{w'\to 0^+}\left[\frac{n_{cl}\sqrt{\frac{n_{co}^2}{n_{cl}^2}e^{2w'/R_1}-1}}{n_{co}\sqrt{e^{2w'/R_1}-1}}\right] = a\tan(+\infty) = \frac{\pi}{2} \tag{F17}$$

As expected for rays incident on the interface of two different index regions at grazing angle.

The phase function $\Phi_{\theta f}$ for the non-whispering gallery waves is given in (5.32) and is reproduced below for clarity.

$$\Phi_{\theta_f}(\theta_o) = 2\arctan\left[i\frac{\sqrt{\cos^2\theta_c - e^{2w/R}\cos^2\theta_o}}{\sqrt{1-e^{2w/R}\cos^2\theta_o}}\right] = 2\arctan\left[-\frac{\sqrt{e^{2w/R}\cos^2\theta_o - \cos^2\theta_c}}{\sqrt{1-e^{2w/R}\cos^2\theta_o}}\right] \tag{F18}$$

It is convenient to write a unified phase coefficient for both whispering and non-whispering modes as

$$\Phi_{\theta_f}(\theta_o) = \begin{cases} 2\arctan\left[i\dfrac{\sqrt{\cos^2\theta_c - e^{2w/R}\cos^2\theta_o}}{\sqrt{e^{2w/R}\cos^2\theta_o - 1}}\right], & e^{w/R}\cos\theta_o < 1 \\ 2\arctan\left[i\dfrac{\sqrt{\cos^2\theta_c - e^{2w/R}\cos^2\theta_o}}{\sqrt{1-e^{2w/R}\cos^2\theta_o}}\right], & e^{w/R}\cos\theta_o > 1 \end{cases} \tag{F19}$$

The unified phase coefficient $\Phi_{\theta f}$ is analytical and continuous everywhere except at the two common branch points which occur for these angles θ_o, that zero the square root functions in the numerator and denominator.

APPENDIX G

FIELDS AND REFLECTION COEFFICIENTS IN THE PROXIMITY OF A CAUSTIC

In this Appendix, we analyze the transformed waveguide bend of Fig. 5-3. 5-4, when the turning point h', is close to the lower interface, which is when $y = h' \approx 0$. In this case, the solutions of the scalar wave equation for the electric *TE* field can be written in the core and the cladding as [5.19]

$$\psi(x,z) = \exp(-i\beta z)\begin{cases} F\dfrac{e^{-\int_x^0 \gamma(x)dx}}{\sqrt{\gamma(x)}}, & x \geq h \\ C_1[\xi'(x)]^{-1/2} A_i[\xi(x)] + C_2[\xi'(x)]^{-1/2} B_i[\xi(x)], & 0 \leq x \leq h \\ D\dfrac{e^{\int_0^x \gamma(x)dx}}{\sqrt{\gamma(y)}}, & x \leq 0 \end{cases} \quad \text{(G1)}$$

with F, C_1, C_2 and D constants that will be defined from the boundary conditions and $\xi(y)$, β and h' defined in (5.63)-(5.66) but reproduced below for convenience

$$\xi(x) = \left[\int_{h'}^{x}\sqrt{-\frac{3}{2}\kappa_x^2(u)du}\right]^{2/3} = \begin{cases} -\left[\int_{h'}^{x}\sqrt{\frac{3}{2}}\kappa_x(u)du\right]^{2/3}, & x > h' \\ +\left[\int_{h'}^{x}\sqrt{\frac{3}{2}}\eta(u)du\right]^{2/3}, & x < h' \end{cases} \quad \text{(G2)}$$

$$\beta = kn_{co}e^{h/R_1}\cos\theta_o \quad \text{(G3)}$$

$$\kappa_x^2(y) = k^2n^2(x) - \beta^2 = k^2n_{co}^2(e^{2x/R_1} - e^{2h/R_1}\cos^2\theta_o) \quad \text{(G4)}$$

$$\eta^2(x) = -\kappa_x^2(x) = k^2n_{co}^2(e^{2h/R_1}\cos^2\theta_o - e^{2x/R_1}) \quad \text{(G5)}$$

$$e^{h'/R_1} = e^{h/R_1}\cos\theta_o \quad \text{(G6)}$$

and $\gamma(x)$ is given by the relationship

$$\gamma^2(x) = k^2(n_{co}^2e^{2h/R_1}\cos^2\theta_o - n_{cl}^2e^{2x/R_1}) \quad \text{(G7)}$$

note that in (G1) we made use of the Airy functions for the fields in the core only but we

kept the WKB approximations for the fields in the cladding since at $x = h'$ we have a caustic only for the core but not for the cladding field ($\kappa_y(h') = 0$ but $\gamma(h') \neq 0$).

Firstly, we will show that the WKB approximations for the fields in the core (G1) coincide with the WKB solution (6) away from the caustic, which is in the region where $x >> h'$. To achieve this we will use the large argument approximations for the Airy functions with negative argument which read [5.22]

$$\begin{aligned} Ai(-z) &\approx \pi^{-1/2} z^{-1/4} \sin\left(\zeta + \frac{\pi}{4}\right) \\ Bi(-z) &\approx \pi^{-1/2} z^{-1/4} \cos\left(\zeta + \frac{\pi}{4}\right), \qquad \zeta = \frac{2}{3} z^{3/2} \end{aligned} \tag{G8}$$

Substituting (G8) into (G1) in the region $0 \leq x \leq h$ we get after some straight forward calculations

$$\psi(X) = C_1 \pi^{-1/2} \frac{\sin\left(\int_{h'}^{y} \kappa_x(x) + \frac{\pi}{4}\right)}{\sqrt{\kappa_x(x)}} + C_2 \pi^{-1/2} \frac{\cos\left(\int_{h'}^{y} \kappa_x(x) + \frac{\pi}{4}\right)}{\sqrt{\kappa_x(x)}} \tag{G9}$$

where we made use of the following equality to derive (G9)

$$[\xi'(x)]^{-1/2} = \frac{\xi(x)^{1/4}}{\sqrt{\kappa_x(x)}} \tag{G10}$$

we can easily confirm that (G9) can take the alternative form

$$\psi(x) = \frac{\pi^{-1/2}}{2} \frac{\sqrt{2}}{2} \left\{ \frac{\exp\left(i \int_{h'}^{x} \kappa_x(x)\right)}{\sqrt{\kappa_x(x)}} [(C_1 + C_2) + i(C_1 - C_2)] + \frac{\exp\left(-i \int_{h'}^{x} \kappa_x(x)\right)}{\sqrt{\kappa_x(x)}} [(C_1 + C_2) - i(C_1 - C_2)] \right\} \tag{G11}$$

direct comparison between (5.6) and (G11) reveals that they become identical if the constants involved are connected to each other as

$$\begin{aligned} C^+ &= \frac{\pi^{-1/2}}{2} \frac{\sqrt{2}}{2} [(C_1 + C_2) + i(C_1 - C_2)] \\ C^- &= (C^+)^* \end{aligned} \tag{G12}$$

with the asterisk in (G12) denoting complex conjugate. Therefore, the fields described by the Airy functions in (G1) become identical to the WKB solutions away from the caustic.

In this respect, we can associate the upward and downward propagating WKB solutions (5.6) with the Airy solutions (G11) by inverting (G12) as

$$\psi^{\pm}(x,z) = C^{\pm}\sqrt{\pi}\left(e^{\mp\pi/4}[\xi'(x)]^{-1/2}A_i[\xi(x)] + e^{\pm\pi/4}[\xi'(x)]^{-1/2}B_i[\xi(x)]\right)\exp(-i\beta z) \tag{G13}$$

From (G11) and (G12) we can extract the phase difference between the amplitude of the upgoing WKB wave C^+ and the amplitude C^- of the downgoing WKB wave as

$$\Delta\varphi = Arg\left[\frac{C^-}{C^+}\right] = 2a\tan\frac{C_2 - C_1}{C_2 + C_1} \tag{G14}$$

In the next we calculated the phase coefficient $\Phi_{\theta_f}(\theta_o)$, which corresponds to the phase shift induced due to reflection of the fields on the bottom boundary $x = 0$ for the special case where $h' \approx 0$. The phase coefficient $\Phi_{\theta_f}(\theta_o)$ will be found after applying appropriate boundary conditions for the tangential electric and magnetic fields on the bottom interface. The tangential magnetic field component can be calculated from (G1) as

$$\frac{\partial\psi(x,z)}{\partial y} = \exp(-i\beta z)\begin{cases} -F\sqrt{\gamma(x)}e^{-\int_h^x \gamma(x)dx}, & x \geq h \\ -\frac{1}{2}C_1[\xi'(x)]^{-3/2}\xi''(x)A_i[\xi(x)] + C_1[\xi'(x)]^{-1/2}A_i'[\xi(x)] - \\ -\frac{1}{2}C_2[\xi'(x)]^{-3/2}\xi''(x)B_i[\xi(x)] + C_2[\xi'(x)]^{-1/2}B_i'[\xi(x)], & 0 \leq x \leq h \\ D\sqrt{\gamma(x)}e^{\int_x^0 \gamma(x)dx}, & x \leq 0 \end{cases} \tag{G15}$$

continuity of electric field (G1) at $y = 0$ requires

$$C_1[\xi'(0)]^{-1/2}A_i[\xi(0)] + C_2[\xi'(0)]^{-1/2}B_i[\xi(0)] = \frac{D}{\sqrt{\gamma(0)}} \tag{G16}$$

while magnetic field (G15) continuity at $x = 0$ requires

$$\begin{aligned} &-\frac{1}{2}C_1[\xi'(0)]^{-3/2}\xi''(0)A_i[\xi(0)] + C_1[\xi'(0)]^{-1/2}A_i'[\xi(0)] - \\ &-\frac{1}{2}C_2[\xi'(0)]^{-3/2}\xi''(y)B_i[\xi(0)] + C_2[\xi'(0)]^{-1/2}B_i'[\xi(0)] = D\sqrt{\gamma(0)} \end{aligned} \tag{G17}$$

by combining (G16) and (G17) and omitting D, we get a relationship which connects C_1 and C_2

$$\frac{C_1}{C_2} = -\frac{B_i[\xi(0)] - \xi'(0)B_i'[\xi(0)]}{A_i[\xi(0)] - \xi'(0)A_i'[\xi(0)]} \tag{G18}$$

Finally, after combining (G14) with (G18) we calculate the phase difference $\Delta\varphi$ between upward and downward propagating waves upon reflection as

$$\Delta\varphi = 2a\tan\frac{\left(A_i[\xi(0)] + B_i[\xi(0)]\right) - \xi'(0)\left(A_i'[\xi(0)] + B_i'[\xi(0)]\right)}{\left(A_i[\xi(0)] - B_i[\xi(0)]\right) - \xi'(0)\left(A_i'[\xi(0)] - B_i'[\xi(0)]\right)} \tag{G19}$$

Equation (G19) is the main outcome of this section and is related to the phase shift upon reflection on the bottom surface when the turning point is close to this surface. In the case where $h' >> 0$, (G19) should asymptotically be related to (5.32), that gives $\Phi_{\theta_f}(\theta_o)$ for whispering gallery waves. Similarly, if $h' << 0$, (G19) should asymptotically be related to (29B) which gives $\Phi_{\theta_f}(\theta_o)$ for non-whispering gallery waves. We proceed to establish this relation.

If $h' << 0$ then by first combining the asymptotic approximations of the Airy function (G3) with (G19) and second neglecting terms analogous to $\xi''(0)/\xi'(0)$, an assumption which is anyway central to WKB theory we get

$$\Delta\varphi = 2a\tan\left[\frac{\frac{\gamma(0)}{\kappa_x(0)} - \tan\left(\int_{h'}^{0}\kappa_x(x)dx\right)}{1 + \frac{\gamma(0)}{\kappa_x(0)}\tan\left(\int_{h'}^{0}\kappa_x(x)dx\right)}\right] = 2a\tan\left[\frac{\gamma(0)}{\kappa_x(0)}\right] - \int_{h'}^{0}\kappa_x(x)dy = \Phi_{\theta f}^{-} - \Delta\Phi_L \tag{G20}$$

and with the aid of (G4) and (G7) we can write for the term $\Phi_{\theta_f}^{-}$ in (G20)

$$\Phi_{\theta f}^{-} = 2\arctan\left[\frac{\sqrt{n_{co}^2 e^{2h/R}\cos^2\theta_o - n_{cl}^2}}{n_{co}\sqrt{1 - e^{2h/R}\cos^2\theta_o}}\right] = 2\arctan\left[\frac{\sqrt{e^{2h/R}\cos^2\theta_o - \cos^2\theta_c}}{\sqrt{1 - e^{2h/R}\cos^2\theta_o}}\right] = \Phi_{\theta_f}^{-}(\theta_o) \tag{G21}$$

Equation (G21) states that $\Phi_{\theta_f}^{-}$ equals to the phase coefficient $\Phi_{\theta_f}(\theta_o)$ for the non-whispering waves (5.32). We therefore see that if $h' << 0$ then $\Delta\varphi$ is expressed as the sum of the phase coefficient $\Phi_{\theta_f}(\theta_o)$ due to reflection of the downward WKB wave to the

upward WKB wave at the bottom boundary, plus the phase introduced to the waves because of the optical path $\Delta\Phi_L$ between the turning point $x = h'$ and the bottom boundary $x = 0$.

If $h' >> 0$ then $\xi(0)$ is positive and we need the asymptotic approximations of the Airy functions with positive arguments [5.22]

$$\begin{aligned} Ai(z) &\approx \frac{1}{2}\pi^{-1/2}z^{-1/4}e^{-\zeta} \\ Bi(z) &\approx \pi^{-1/2}z^{-1/4}e^{\zeta}, \qquad \zeta = \frac{2}{3}z^{3/2} \end{aligned} \tag{G22}$$

Equation (G22) combined with (G19) and after neglecting terms analogous to $\xi''(0)/\xi'(0)$ as previously gives

$$\Delta\varphi = 2\arctan\left[\frac{\frac{\gamma(0)}{\eta(0)} - \tan\left(i\int_{h'}^{0}\delta_x(x)dx\right)}{1+\frac{\gamma(0)}{\eta(0)}\tan\left(i\int_{h'}^{0}\delta_x(x)dx\right)}\right] = 2\arctan\left[\frac{\gamma(0)}{\eta(0)}\right] - i\int_{h'}^{0}\delta_x(x)dx = \Phi_{\theta f}^{+} + iE \tag{G23}$$

with the aid of (G4) and (G7) we can write for the term $\Phi_{\theta f}^{+}$ in (G23)

$$\Phi_{\theta f}^{+} = 2\arctan\left[\frac{\sqrt{e^{2h/R}\cos^2\theta_o - \cos^2\theta_c}}{\sqrt{e^{2h/R}\cos^2\theta_o - 1}}\right] = \Phi_{\theta_f}^{+}(\theta_o) \tag{G24}$$

which equals the phase coefficient $\Phi_{\theta_f}(\theta_o)$ for whispering gallery waves (5.33). We therefore see that if $h' >> 0$ then $\Delta\varphi$ is the sum of the phase shift $\Phi_{\theta_f}(\theta_o)$, which occurs when a downward WKB wave reverses its direction after passing through the turning point and becoming an upward travelling WKB wave, plus an imaginary term iE, due to extension of the evanescent wave from $x = 0$ to $x = h'$.

The field solutions based on Airy functions (G1) are needed close to the turning points only since the fields very rapidly converge to the WKB solutions away from the caustics. However for the phase difference between upward and downward waves upon reflection at $x = 0$ in the case where we have for the turning point that $h' \approx 0$ the error involved by using the WKB solutions is significant and even further when the condition $h' = 0$ is

satisfied WKB solutions are singular and cannot be used at all. In this case, we need to use the modified reflection coefficient presented in (G19). From (G20) and (G23) we see that $\Delta\varphi$ is the combination of the phase coefficient $\Phi_{\theta_f}(\theta_o)$ due to reflection and the propagation phase shift $\Delta\Phi_L$ (or the imaginary term iE, in the evanescent wave case). Therefore we can express (G19) as

$$\mathrm{Re}(\Delta\varphi) = \Phi_{\theta_f}(\theta_o) - \Omega \tag{G25}$$

with

$$\Omega = \begin{cases} \int_{h'}^{0} \kappa_x(x)dx, & h' \geq 0 \\ 0, & h' \leq 0 \end{cases} \tag{G26}$$

where the real parts were kept only since imaginary parts do not contribute to phase changes. Finally by combining (G19) and (G25)-(G26) we derive the phase coefficient $\Phi_{\theta_f}(\theta_o)$ when $h' \approx 0$ as

$$\Phi_{\theta_f}(\theta_o) = 2\mathrm{Re}\left\{ a\tan\frac{(A_i[\xi(0)] + B_i[\xi(0)]) - \xi'(0)(A_i[\xi(0)] + B_i[\xi(0)])}{(A_i[\xi(0)] - B_i[\xi(0)]) - \xi'(0)(A_i[\xi(0)] - B_i[\xi(0)])} \right\} + 2\begin{cases} \int_{h'}^{0} \kappa_x(x)dx, & h' \geq 0 \\ 0, & h' \leq 0 \end{cases} \tag{G26}$$

APPENDIX H

INTEGRAL CALCULATION FOR RADIATION MODE FOURIER DECOMPOSITION METHOD

The matrices involved in (6.19b)-(6.19e) take the following analytical form. Note that in all integrals δ stands for the Kronecker delta function

$$\left(\frac{\partial u}{\partial x}\right)^2 = \frac{1}{8\pi^2 a_x^2}\left[3-4\cos(2\pi u)+\cos(4\pi u)\right] \tag{H1}$$

$$\frac{\partial^2 u}{\partial x^2} = \frac{1}{2\pi a_x^2}\left[3\sin(\pi u)-\sin(3\pi u)\right] \tag{H2}$$

$$\left(\frac{\partial v}{\partial y}\right)^2 = \frac{1}{8\pi^2 a_y^2}\left[3-4\cos(2\pi v)+\cos(4\pi v)\right] \tag{H3}$$

$$\frac{\partial^2 v}{\partial y^2} = \frac{1}{2\pi a_y^2}\left[3\sin(\pi v)-\sin(3\pi v)\right] \tag{H4}$$

$$\begin{aligned}\mathbf{I}_1^{oo} &= -m^2\pi^2\int_0^1\int_0^1\left(\frac{\partial u}{\partial x}\right)^2 S_{mn}^{oo}(u,v)S_{m'n'}^{oo}(u,v)dudv \\ &= \frac{m^2}{a_x^2}\left\{\frac{3}{2}\delta_{m,m'}-\delta_{m,m'+1}-\delta_{m,m'-1}+\frac{1}{4}\delta_{m,m'+2}+\frac{1}{4}\delta_{m,m'-2}-\frac{1}{4}\delta_{m,2-m'}\right\}\delta_{n,n'}\end{aligned} \tag{H5}$$

$$\begin{aligned}\mathbf{I}_2^{oo} &= m\pi\int_0^1\int_0^1\frac{\partial^2 u}{\partial x^2}\frac{1}{\tan(m\pi u)}S_{mn}^{oo}(u,v)S_{m'n'}^{oo}(u,v)dudv \\ &= \frac{m}{2a_x^2}\left\{\delta_{m,m'+1}-\delta_{m,m'-1}-\frac{1}{2}\delta_{m,m'+2}+\frac{1}{2}\delta_{m,m'-2}+\frac{1}{2}\delta_{m,2-m'}\right\}\delta_{n,n'}\end{aligned} \tag{H6}$$

$$\begin{aligned}\mathbf{I}_3^{oo} &= -n^2\pi^2\int_0^1\int_0^1\left(\frac{\partial v}{\partial y}\right)^2 S_{mn}^{oo}(u,v)S_{m'n'}^{oo}(u,v)dudv \\ &= \frac{n^2}{a_y^2}\left\{\frac{3}{2}\delta_{n,n'}-\delta_{n,n'+1}-\delta_{n,n'-1}+\frac{1}{4}\delta_{n,n'+2}+\frac{1}{4}\delta_{n,n'-2}-\frac{1}{4}\delta_{n,2-n'}\right\}\delta_{m,m'}\end{aligned} \tag{H7}$$

$$\begin{aligned}\mathbf{I}_4^{oo} &= n\pi\int_0^1\int_0^1\frac{\partial^2 v}{\partial y^2}\frac{1}{\tan(n\pi v)}S_{mn}^{oo}(u,v)S_{m'n'}^{oo}(u,v)dudv \\ &= \frac{n}{2a_y^2}\left\{\delta_{n,n'+1}-\delta_{n,n'-1}-\frac{1}{2}\delta_{n,n'+2}+\frac{1}{2}\delta_{n,n'-2}+\frac{1}{2}\delta_{n,2-n'}\right\}\delta_{m,m'}\end{aligned} \tag{H8}$$

APPENDIX H: *Integral Calculation for Radiation Mode Fourier Decomposition Method*

$$\mathbf{I}_1^{eo} = -m^2\pi^2 \int_0^1\int_0^1 \left(\frac{\partial u}{\partial x}\right)^2 S_{mn}^{eo}(u,v) S_{m'n'}^{eo}(u,v)\,du dv$$
$$= \frac{m^2}{a_x^2}\left\{\frac{3}{2}\delta_{m,m'} - \delta_{m,m'+1} - \delta_{m,m'-1} + \frac{1}{4}\delta_{m,m'+2} + \frac{1}{4}\delta_{m,m'-2} - \frac{1}{4}\delta_{m,2-m'}\right\}\delta_{n,n'} \tag{H9}$$

$$\mathbf{I}_2^{eo} = m\pi \int_0^1\int_0^1 \frac{\partial^2 u}{\partial x^2}\frac{1}{\tan(m\pi u)} S_{mn}^{eo}(u,v) S_{m'n'}^{eo}(u,v)\,du dv$$
$$= \frac{m}{2a_x^2}\left\{\delta_{m,m'+1} - \delta_{m,m'-1} - \frac{1}{2}\delta_{m,m'+2} + \frac{1}{2}\delta_{m,m'-2} - \frac{1}{2}\delta_{m,2-m'}\right\}\delta_{n,n'} \tag{H10}$$

$$\mathbf{I}_3^{eo} = -n^2\pi^2 \int_0^1\int_0^1 \left(\frac{\partial v}{\partial y}\right)^2 S_{mn}^{eo}(u,v) S_{m'n'}^{eo}(u,v)\,du dv$$
$$= \frac{n^2}{a_y^2}\left\{\frac{3}{2}\delta_{n,n'} + \frac{3}{2}\delta_{n,0} - \delta_{n,n'+1} - \delta_{n,n'-1} - \delta_{n,1-n'} + \frac{1}{4}\delta_{n,n'+2} + \frac{1}{4}\delta_{n,n'-2} + \frac{1}{4}\delta_{n,2-n'}\right\}\delta_{m,m'} \tag{H11}$$

$$\mathbf{I}_4^{eo} = n\pi \int_0^1\int_0^1 \frac{\partial^2 v}{\partial y^2}\frac{1}{\tan(n\pi v)} S_{mn}^{eo}(u,v) S_{m'n'}^{eo}(u,v)\,du dv$$
$$= \frac{n}{2a_y^2}\left\{\delta_{n,n'+1} - \delta_{n,n'-1} + \delta_{n,1-n'} - \frac{1}{2}\delta_{n,n'+2} + \frac{1}{2}\delta_{n,n'-2} - \frac{1}{2}\delta_{n,2-n'}\right\}\delta_{m,m'} \tag{H12}$$

$$\mathbf{I}_1^{oe} = -m^2\pi^2 \int_0^1\int_0^1 \left(\frac{\partial u}{\partial x}\right)^2 S_{mn}^{oe}(u,v) S_{m'n'}^{oe}(u,v)\,du dv$$
$$= \sum_{m=1}^{M}\sum_{n=1}^{N}\frac{m^2}{a_x^2}\left\{\frac{3}{2}\delta_{m,m'} + \frac{3}{2}\delta_{m,0} - \delta_{m,m'+1} - \delta_{m,m'-1} - \delta_{m,1-m'} + \frac{1}{4}\delta_{m,m'+2} + \frac{1}{4}\delta_{m,m'-2} + \frac{1}{4}\delta_{m,2-m'}\right\}\delta_{n,n'}$$

(H13)

$$\mathbf{I}_2^{oe} = m\pi \int_0^1\int_0^1 \frac{\partial^2 u}{\partial x^2}\frac{1}{\tan(m\pi u)} S_{mn}^{oe}(u,v) S_{m'n'}^{oe}(u,v)\,du dv$$
$$= \frac{m}{2a_x^2}\left\{\delta_{m,m'+1} - \delta_{m,m'-1} + \delta_{m,1-m'} - \frac{1}{2}\delta_{m,m'+2} + \frac{1}{2}\delta_{m,m'-2} - \frac{1}{2}\delta_{m,2-m'}\right\}\delta_{n,n'} \tag{H14}$$

$$\mathbf{I}_3^{eo} = -n^2\pi^2 \int_0^1\int_0^1 \left(\frac{\partial v}{\partial y}\right)^2 S_{mn}^{oe}(u,v) S_{m'n'}^{oe}(u,v)\,du dv$$
$$= \frac{n^2}{a_y^2}\left\{\frac{3}{2}\delta_{n,n'} - \delta_{n,n'+1} - \delta_{n,n'-1} + \frac{1}{4}\delta_{n,n'+2} + \frac{1}{4}\delta_{n,n'-2} - \frac{1}{4}\delta_{n,2-n'}\right\}\delta_{m,m'} \tag{H15}$$

APPENDIX H: *Integral Calculation for Radiation Mode Fourier Decomposition Method*

$$\mathbf{I}_4^{eo} = n\pi \int_0^1 \int_0^1 \frac{\partial^2 v}{\partial y^2} \frac{1}{\tan(n\pi v)} S_{mn}^{oe}(u,v) S_{m'n'}^{oe}(u,v) du dv$$
$$= \frac{n}{2a_y^2} \left\{ \delta_{n,n'+1} - \delta_{n,n'-1} - \frac{1}{2}\delta_{n,n'+2} + \frac{1}{2}\delta_{n,n'-2} - \frac{1}{2}\delta_{n,2-n'} \right\} \delta_{m,m'} \tag{H16}$$

$$\mathbf{I}_1^{ee} = -m^2\pi^2 \int_0^1 \int_0^1 \left(\frac{\partial u}{\partial x} \right)^2 S_{mn}^{ee}(u,v) S_{m'n'}^{ee}(u,v) du dv$$
$$= \frac{m^2}{a_x^2} \left\{ \frac{3}{2}\delta_{m,m'} + \frac{3}{2}\delta_{m,0} - \delta_{m,m'+1} - \delta_{m,m'-1} - \delta_{m,1-m'} + \frac{1}{4}\delta_{m,m'+2} + \frac{1}{4}\delta_{m,m'-2} + \frac{1}{4}\delta_{m,2-m'} \right\} \delta_{n,n'} \tag{H17}$$

$$\mathbf{I}_2^{ee} = m\pi \int_0^1 \int_0^1 \frac{\partial^2 u}{\partial x^2} \frac{1}{\tan(m\pi u)} S_{mn}^{ee}(u,v) S_{m'n'}^{ee}(u,v) du dv$$
$$= \frac{m}{2a_x^2} \left\{ \delta_{m,m'+1} - \delta_{m,m'-1} + \delta_{m,1-m'} - \frac{1}{2}\delta_{m,m'+2} + \frac{1}{2}\delta_{m,m'-2} - \frac{1}{2}\delta_{m,2-m'} \right\} \delta_{n,n'} \tag{H18}$$

$$\mathbf{I}_3^{ee} = -n^2\pi^2 \int_0^1 \int_0^1 \left(\frac{\partial v}{\partial y} \right)^2 S_{mn}^{ee}(u,v) S_{m'n'}^{ee}(u,v) du dv$$
$$= \frac{n^2}{a_y^2} \left\{ \frac{3}{2}\delta_{n,n'} + \frac{3}{2}\delta_{n,0} - \delta_{n,n'+1} - \delta_{n,n'-1} - \delta_{n,1-n'} + \frac{1}{4}\delta_{n,n'+2} + \frac{1}{4}\delta_{n,n'-2} + \frac{1}{4}\delta_{n,2-n'} \right\} \delta_{m,m'} \tag{H19}$$

$$\mathbf{I}_4^{ee} = n\pi \int_0^1 \int_0^1 \frac{\partial^2 v}{\partial y^2} \frac{1}{\tan(n\pi v)} S_{mn}^{ee}(u,v) S_{m'n'}^{ee}(u,v) du dv$$
$$= \frac{n}{2a_y^2} \left\{ \delta_{n,n'+1} - \delta_{n,n'-1} + \delta_{n,1-n'} - \frac{1}{2}\delta_{n,n'+2} + \frac{1}{2}\delta_{n,n'-2} - \frac{1}{2}\delta_{n,2-n'} \right\} \delta_{m,m'} \tag{H20}$$

APPENDIX I

AUTOREGRESSIVE COEFFICIENT CALCULATION WITH THE YULE-WALKER METHOD

I1. Estimate for the Wall Roughness Spectral Density

In this Appendix, we briefly review the Yule-Walker method [6.23] for calculating the autoregressive coefficients (6.70)-(6.71). Firstly, we repeat equation (6.69), which corresponds to our predictive model, expressing the n-th value of the wall-roughness stochastic random process e_n, as a sum of the past Q-values plus a white noise contribution.

$$\sum_{q=0}^{Q} \varphi_q f_{n-q} = e_n \tag{I1}$$

where in (I1) the summation started from $q = 0$ rather than $q = 1$ as in (69), with $\varphi_0 = 1$. Another way of interpreting (I1) is by noting that the left hand side of the equation is the discrete value convolution between $f(z)$ and a function $\varphi(z)$ with $\varphi_q = \varphi(z_q) = \varphi(q\Delta z)$. In equivalent terms, the n-th value of the roughness random process is expressed as the response of the linear filter $\varphi(z)$ with $f(z)$ input plus the white noise term. If we assume that the variance of the white noise is ε, then we can write for the spectral density $F(s)$ of the signal $f(z)$:

$$|\Phi(s)|^2 F(s) = \frac{\varepsilon^2}{2\pi} \tag{I2}$$

with $\varepsilon^2/2\pi$ corresponding to the white noise spectral density and $\Phi(s)$ corresponding to the filter impulse response defined by

$$\Phi(s) = \int_{-\infty}^{+\infty} \varphi(z) e^{-isz} dz \cong \sum_q \varphi_q e^{-isq\Delta z} \tag{I3}$$

Finally, by combining (I2) with (I3) we derive an estimate for the spectral density of the waveguide sidewall roughness function

$$F(s) = \frac{\varepsilon^2}{2\pi} \left| \sum_{q=0}^{Q} \varphi_q e^{-isq\Delta z} \right|^{-2} \tag{I4}$$

Therefore, in order to calculate an estimate for $F(s)$, we need to know the variance ε, of

the white noise and the coefficients φ_q. This estimate will be provided by the Yule-Walker method.

I2. Yule-Walker Autoregressive Coefficients

By defining the average (or expectance) operator as

$$\langle g_n \rangle_n = \lim_{N\to\infty} \frac{1}{N} \sum_{n=0}^{N} g_n \tag{I5}$$

we can write the autocorrelation function as

$$W_n = \langle g_q g_{q+n} \rangle_q \tag{I6}$$

upon multiplication of (I1) with g_{n-p}, and averaging over n, we get

$$\sum_{q=0}^{Q} \varphi_q \langle g_{n-q} g_{n-p} \rangle_n = \langle g_{n-p} e_n \rangle_n \tag{I7}$$

Using the fact that white noise is uncorrelated with the signal $f(z)$, the right hand side of (I7) is zero. Therefore, (I7) is written, by considering (I6) and by also noting that $\varphi_0 = 1$, as

$$\sum_{q=1}^{Q} \varphi_q W_{p-q} = -W_p \tag{I8}$$

The system of linear equations (I8), can be readily solved to calculate the linear filter coefficients φ_q, $q = 1 \ldots Q$. Finally, by multiplying (I1) with e_n and following the same steps as for the calculation of φ_q, we can show that

$$\langle g_n e_n \rangle_n = \varepsilon^2 \tag{I9}$$

By replacing the values for e_n, from (I1) we get the estimation for the white noise variance

$$\varepsilon^2 = \sum_{q=0}^{Q} \varphi_q W_q \tag{I10}$$

APPENDIX J

COMPARISON BETWEEN FDM AND BPM METHODS FOR THE CALCULATION OF BOUND MODES

In this Appendix, we present a brief comparison of the modal fields generated with the Fourier Decomposition Method of section 6.2 and the BPM method. The commercially available program BeamProp by Rsoft design group has been used for the BPM calculations.

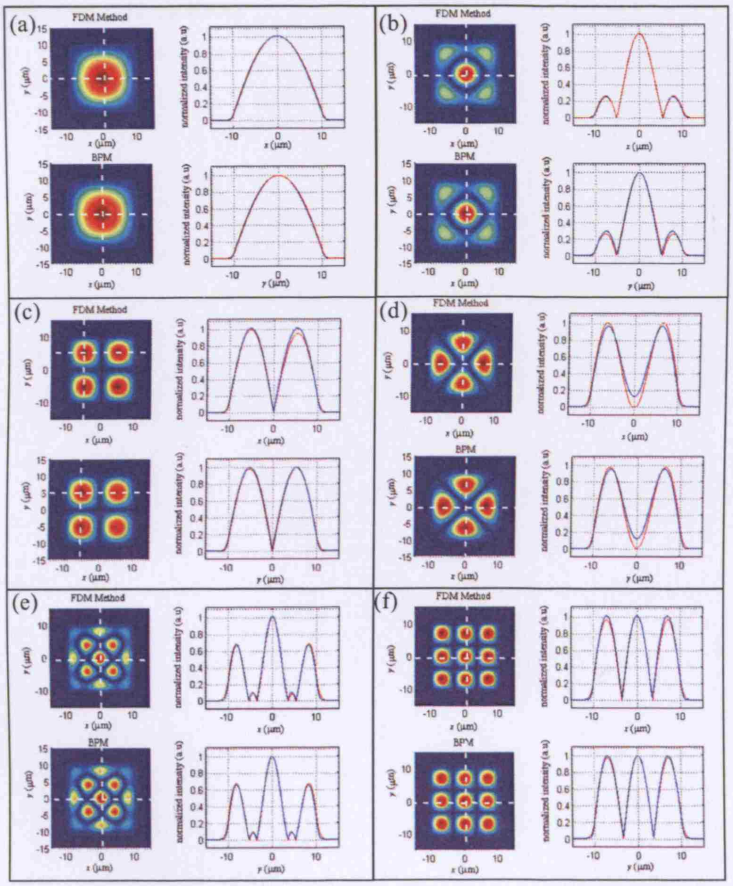

Fig. J-1. FDM and BPM generated mode profiles for a 20 μm × 20 μm buried channel waveguide. Also, comparison along horizontal and vertical cuts shown with the dashed white lines of the modal fields. Blue line correspond to the FDM modes while red lines to the BPM. (a) Fundamental waveguide mode, (b) Second Even-Even type mode, (c) First Odd-Odd type mode, (d) Second Odd-Odd type mode, (e) Third

Even-Even type mode, (f) Fourth Even-Even type mode.

In Fig. J-1 we present the modal fields along the transverse waveguide cross-section for six representative modes in contour map format, calculated by the FDM and BPM methods. We also compare the fields along 1D horizontal and vertical cuts on the waveguide cross-section for more clarity, (blue lines for FDM method, red lines for BPM). The modes that are shown there are: The first and second Even – Even symmetry modes (I1 (a) and (I1 (b) respectively), the first and second modes of Odd-Odd symmetry (I1 (c) and G1 (d)) and the third and fourth modes of Even-Even symmetry (I1 (e) and G1 (f)). In all cases, very good convergence between the FDM and the BPM obtained results is observed validating our method.